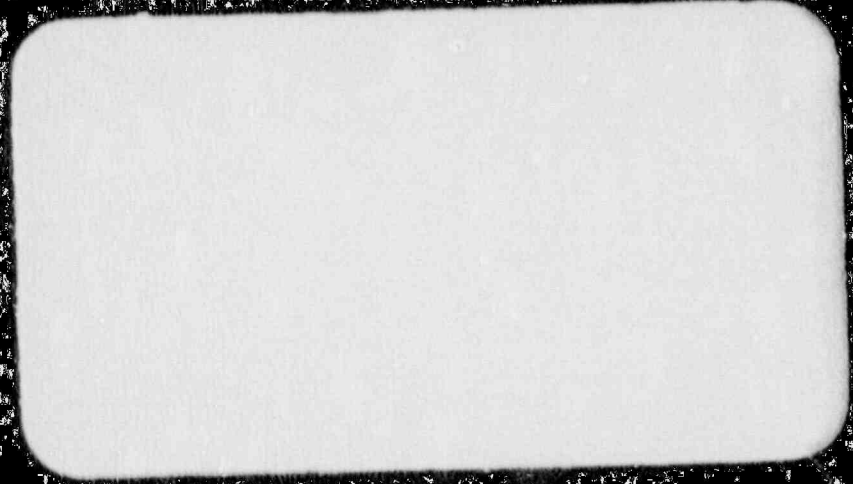


Westinghouse Energy Systems



8912070380 891122  
PDR TOPRF EMWEST  
B PDC



Westinghouse Energy Systems



8912070380 891122  
PDR TOPRP EMVWEST  
B PDC

WESTINGHOUSE CLASS 3

WCAP-12391

WESTINGHOUSE BOILING WATER REACTOR  
EMERGENCY CORE COOLING SYSTEM EVALUATION MODEL:  
CODE DESCRIPTION AND QUALIFICATION

By

D. B. Ebeling-Koning  
M. E. Nissley  
J. T. Dederer  
A. F. Gagnon  
J. M. Brennan

October 30, 1989

WESTINGHOUSE ELECTRIC CORPORATION  
Nuclear Energy Systems  
P. O. Box 355  
Pittsburgh, Pennsylvania 15230



UNITED STATES  
NUCLEAR REGULATORY COMMISSION  
WASHINGTON, D. C. 20555

August 22, 1989

Mr. W. J. Johnson, Manager  
Nuclear Safety Department  
Westinghouse Electric Corporation  
Nuclear Energy Systems  
P. O. Box 355  
Pittsburgh, Pennsylvania 15230

Dear Mr. Johnson:

SUBJECT: ACCEPTANCE FOR REFERENCING OF LICENSING TOPICAL  
REPORTS WCAP-11284 AND WCAP-11427 REGARDING THE  
WESTINGHOUSE BOILING WATER REACTOR EMERGENCY  
CORE COOLING SYSTEM EVALUATION MODEL

We have completed our review of the subject topical reports. We find these reports acceptable for referencing in license applications to the extent specified and under the limitations delineated in the reports and the associated NRC evaluation which is enclosed. The evaluation defines the basis for acceptance of the reports.

We do not intend to repeat our review of the matters described in the reports and found acceptable when the reports appear as references in license applications except to assure that the material presented is applicable to the specified plant involved. Our acceptance applies only to the matters described in the reports.

In accordance with procedures established in NUREG-0390, it is requested that Westinghouse publish accepted versions of WCAP-11284 and WCAP-11427, proprietary and non-proprietary, within 3 months of receipt of this letter. The accepted versions should incorporate this letter and the enclosed evaluation between the title page and the abstract. The accepted versions shall include an -A (designating accepted) following the report identification symbol.

Should our criteria or regulations change such that our conclusions as to the acceptability of the reports are invalidated, Westinghouse and/or the licensees referencing the topical reports will be expected to revise and

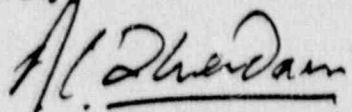
W. J. Johnson

- 2 -

August 22, 1989

resubmit their respective documentation, or submit justification for the continued effective applicability of the topical reports without revision of their respective documentation.

Sincerely,



Ashok C. Thadani, Assistant Director  
for Systems  
Division of Engineering & Systems Technology  
Office of Nuclear Reactor Regulation

Enclosure:  
Evaluation Report

## ENCLOSURE

### SAFETY EVALUATION BY THE OFFICE OF NUCLEAR REACTOR REGULATION RELATING TO THE WESTINGHOUSE ELECTRIC CORPORATION BOILING WATER REACTOR EMERGENCY CORE COOLING SYSTEM EVALUATION MODEL

#### 1.0 INTRODUCTION

By letter dated September 30, 1986, Westinghouse Electric Corporation submitted for review licensing topical report WCAP-11284 entitled "Westinghouse Boiling Water Reactor Emergency Core Cooling System Evaluation Model: Code Description and Qualification" (Ref. 1). By letter dated June 30, 1987, Westinghouse submitted WCAP-11427 entitled "Westinghouse Boiling Water Reactor Emergency Core Cooling System Evaluation Model: Code Sensitivity" (Ref. 2) which was reviewed by the NRC concurrently with WCAP-11284. The staff requested assistance in the review from Los Alamos National Laboratory (LANL). LANL identified additional information needs to which Westinghouse responded in an amendment document, WCAP-11284-Amendment 1/WCAP-11427-Amendment 1, "Westinghouse Boiling Water Reactor Emergency Core Cooling System Evaluation Model: Response to Request for Additional Information and Errata" (Ref. 3).

The Office of Nuclear Reactor Regulation (NRR) is responsible for the review and evaluation of licensing analyses and methodology. The review was conducted to provide a technical assessment of conformance of the Westinghouse emergency core cooling system (ECCS) model to Appendix K of 10 CFR Part 50 (Code of Federal Regulations - Energy). The ECCS model will be part of the safety analysis methodology applicable to boiling water reactor (BWR) fuel manufactured and marketed by Westinghouse Electric Corporation. The ECCS loss-of-coolant accident (LOCA) methodology was developed by ASEA-ATOM, Sweden, and has been in use in Europe in the study of boiling water reactor performance.

This safety evaluation (SE) documents the review of Westinghouse large-break and small-break LOCA analysis methods applicable to BWR types 2 through 6 plants. The SE is divided into eight sections. Section 2 presents a summary

of the topical reports and Section 3 provides a code description summary and assessment (WCAP-11284). Section 4 discusses the code sensitivity studies and assessment (WCAP-11427). Section 5 describes the integral system qualifications, and Section 6 discusses compliance with Appendix K requirements. Section 7 provides the staff conclusions resulting from this review, and Section 8 contains the references applicable to the review.

## 2.0 SUMMARY OF TOPICAL REPORTS

Westinghouse uses the GOBLIN system of computer codes (Ref. 1) to evaluate ECCS performance during postulated LOCAs in BWRs. The system codes calculate the BWR transient responses to both large-break and small-break LOCAs. The system is composed of three major computer codes (GOBLIN, DRAGON, and CHACHA-3C), an auxiliary code (BILBO), and several input/output data processors (HOBIT, FRODO, CHINE, PLOAUX, and SUPERB). A brief description of the more important codes follows.

GOBLIN - Analyzes the LOCA blowdown and reflood thermal-hydraulic transient for the entire reactor, including the interactions with various control and safety systems. GOBLIN calculates the pressure and enthalpy at the core inlet and outlet, using the core power generation, system geometry, ECCS performance, and the break type.

DRAGON - Performs the hot fuel channel, thermal-hydraulic transient calculations. DRAGON is virtually identical to GOBLIN except several calculation models are bypassed. Using channel power, geometry, and boundary conditions from the GOBLIN calculations, DRAGON calculates the coolant temperature and pressure, the void fraction, and the heat-transfer coefficients.

CHACHA-3C - Performs detailed temperature calculations at a specified axial level within the fuel assembly previously analyzed by the DRAGON code. All necessary fluid boundary conditions are obtained from the DRAGON calculation. CHACHA-3C calculates the time-dependent, pellet-to-clad gap, heat-transfer coefficients, as well as clad swelling and potential burst. It determines the temperature distribution of each rod throughout the transient and ultimately

determines the peak clad temperature (PCT) and cladding oxidation at the axial plane under investigation. It also provides input for the calculation of total hydrogen generation by supplying the local oxidation at a number of axial and radial locations in the core.

Westinghouse has performed integral system qualification analyses to compare the code simulation with the two-loop test apparatus (TLTA) test data. The objective of this verification program is to demonstrate the code's ability to predict plant responses to a design-basis LOCA correctly. To support the LOCA evaluation methodology to be used in the licensing calculations for a BWR/5, Westinghouse also has performed sensitivity studies (Ref. 2) that consider hydraulic models, plant parameters, numerical convergence, and nodalization.

### 3.0 CODE DESCRIPTION AND ASSESSMENT

#### 3.1 Thermal-Hydraulic Analysis Codes: GOBLIN/DRAGON

The GOBLIN code performs one-dimensional, thermal-hydraulic calculations for the entire reactor during a postulated LOCA. The system response from blowdown through reflood is calculated for both small- and large-break events. GOBLIN is divided into four main sections.

The power generation model calculates the heat generation resulting from fission, decay heat, and metal-water reactions. Fission power is determined by a point kinetics model that allows for up to six delayed neutron groups. Reactivity feedback is included for void fraction, moderator (coolant) temperature, fuel temperature, and reactor control rods. The decay power generation is calculated by the sum of 11 fission product decay groups and the actinide decay of U-239 and Np-239. The Baker-Just model is used to determine the heat generation from the metal-water reactions.

The hydraulic model solves the mass, energy, and momentum conservation equations together with the equation of state for each control volume. This model includes empirical constitutive correlations for the calculation of



pressure drops, two-phase energy flow (drift flux), two-phase level tracing, spray-fluid interaction, and critical flow rate.

The system models contain detailed models of the various reactor components and the safety systems that are activated after a LOCA. They include the ECCS; the steam separators and dryers; the reactor level measurement, trip, and depressurization systems; and the recirculation and jet pumps.

The thermal model calculates the heat conduction and heat transfer from the fuel rods, pressure vessel, and internals (plates) to the coolant. The model solves the material heat conduction equation and calculates the heat transfer from the fuel and structures to the coolant. The heat-transfer coefficients couple the hydraulic solution to the thermal conduction solution through the coolant state and surface temperature. Empirical heat-transfer coefficient correlations are modeled for single-phase liquid-heat transfer, two-phase non-dryout transition boiling, post-dryout heat transfer and single-phase vapor, and surface-to-surface radiation heat transfer.

DRAGON is used to simulate the hot fuel channel by specifying the inlet and outlet plenum pressures and enthalpies from the GOBLIN simulation. DRAGON incorporates the channel power and geometry and inlet/outlet hydraulic properties to produce coolant temperature and pressure, void fraction, and heat-transfer coefficients. The following subsections describe the key models in the GOBLIN/DRAGON code.

### 3.1.1 Decay of Actinides and Fission Products

Three actinide decay groups are modeled. The decay time constants and effective energy fractions are taken from a Westinghouse fuel design code, PHOENIX, that has received NRC approval. The fission product decay model uses decay constants and effective energy fractions that best fit the 1971 American Nuclear Society (ANS) decay power guideline. An uncertainty of 20 percent is added to the resultant fission product power generation. Westinghouse assumes that the total gamma energy deposition fraction outside of the fuel rod is 2

percent of the total power generation. Westinghouse has performed sensitivity studies and identified that the effect on the PCT is negligible by delaying the time to increase the power generation fraction from 96 percent to 98 percent of the total power generation (see Reference 3, response to Question 2). The sensitivity studies performed by Westinghouse are in response to an Appendix K, Section I.A.4 requirement to justify a gamma energy deposition fraction outside the fuel rod that is less than 1.0. Westinghouse also has partitioned pellet and cladding power distribution and found that the no-partition case would be more conservative, that is, would produce a higher PCT. The differences in PCT as reported in the Reference 3 sensitivity studies confirmed that the effect of the assumption of a 2-percent energy deposition fraction outside the fuel rod is small.

### 3.1.2 Two-Phase Energy Flow Model

The enthalpy flow rate for the two-phase flow is determined using a drift-flux correlation developed from the work of J.A. Holmes (Ref. 4) and includes a counter-current flow limitation (CCFL) correlation of the form defined by H.B. Wallis (Ref. 5). The constants used in the CCFL correlations originally were derived from formulations and data developed by R.V. Bailey (Ref. 6) and S.O. Eriksson (Ref. 7). Westinghouse has performed a series of experiments to test the conservatism of the CCFL correlation. The results indicate that the CCFL correlation used in the GOBLIN/DRAGON is 25 percent more restrictive in the liquid drain flow rate than was observed in the experiment.

### 3.1.3 Two-Phase Level Tracking

GOBLIN can specify a series of control volumes in which a two-phase level is to be calculated and tracked with time. The level tracking model replaces a fixed control volume boundary with a moving boundary located at the two-phase level. The flow rate through the boundary is determined by maintaining continuity of the phasic flow rates through the two-phase level for a given level velocity. The phasic flow rates are calculated for the volume above and below the level by the drift-flux correlation. With level tracking, the control volume boundaries continuously change with time. Hence, the boundaries

of the level-tracking region become a significant nodalization parameter. The use of moving boundaries at the two phase level is consistent with other ECCS evaluation models which have been approved by the staff.

#### 3.1.4 Frictional and Local Form Pressure Drop Correlations

The original two-phase multipliers in WCAP-11284 for the frictional and local form pressure drop were modified for the QUAD+ fuel design modelled for the sensitivity studies reported in WCAP-11427. Other modifications will be required when the methodology is applied to an accepted fuel design.

#### 3.1.5 Injection-Flow/Vessel-Fluid Interaction

The external water is added to a control volume as a mass and energy source item. If the water level falls below the injection point, the injection water is added to the liquid in the uppermost liquid control volume, together with the steam that has condensed from the upper control volume. A falling distance of 0.3 meter assumed in the GOBLIN analysis is based on experimental data (Ref. 8) that demonstrates that the injection water has essentially reached saturation in that distance.

#### 3.1.6 Critical Flow Model

The GOBLIN code uses the Moody critical flow model for the two-phase break flow and a modified Bernoulli model that assumes zero flow resistance from stagnation point to the exits for the subcooled critical flow. Both models are typical of those used in approved ECCS evaluation models.

#### 3.1.7 Heat-Transfer Regimes

The heat-transfer regimes modeled in GOBLIN are identified in Sections 2 and 3 of WCAP-11284. The regimes are characterized by dryout conditions, single- and two-phase fluid conditions, and Reynolds' Number. Void fraction limits denote transition to dispersed flow conditions and transition from inverted annular flow to dispersed flow.

During its review, the staff noted that a maximum differential of 2.5 percent in voids could result in an oscillatory solution instability. However, Westinghouse responded that no oscillatory solutions have been observed before core reflood.

### 3.1.8 Dryout Correlation

The boiling transition between non-dryout heat transfer and post-dryout heat transfer is determined from a critical heat flux (CHF) correlation. The CHF used is the maximum between a flow-boiling and a pool-boiling correlation. Westinghouse has conducted steady-state and transient CHF tests using a simulated QUAD+ mini-bundle. The resulting test data were used to develop and verify the WB-1 correlation (for QUAD+ fuel), which uses the critical quality boiling length formulation. This correlation was intended to replace the AA-74 correlation for use in the QUAD+ fuel analysis. The staff has not reviewed the WB-1 correlation; a staff-approved correlation must be used when the subject ECCS methodology is used in a licensing analysis.

### 3.2 Rod Heatup Analysis Codes: CHACHA-3C/BILBO

Detailed fuel rod heatup calculations are performed with the CHACHA-3C code using boundary conditions of the coolant pressure and temperature supplied by DRAGON. The prime use of CHACHA-3C is to determine the PCT at the hottest axial plane in the peak power bundle. It also is used to determine the total hydrogen generation by evaluating local cladding oxidation at a number of axial and radial locations in the core.

The major components of the CHACHA-3C code include: (1) a fuel rod conduction model; (2) a channel temperature model; (3) a heat generation model; (4) a metal-water reaction model; (5) a gas plenum temperature and pressure model; (6) a pellet/cladding-gap, heat-transfer model; (7) a cladding strain-and-rupture model; (8) a thermal radiation model; and (9) a spray heat-transfer model. The first two models use a conventional finite-difference method to

treat heat conduction in the fuel rod and channel. The heat generation model in CHACHA-3C is identical to that in GOBLIN/DRAGON. The gas plenum temperature-and-pressure model and the pellet/cladding-gap, heat-transfer model use the analytical models in the NRC-approved PAD code. The cladding strain-and-rupture model uses the NRC-approved materials properties data from MATPRO Version II and General Electric (GE) stress/strain correlations, including cladding strain versus temperature before perforation, circumferential strain versus cladding differential pressure, and a lower bound curve for the data for strain versus temperature taken from NEDO-20566 (Ref. 9). The following subsections describe the thermal radiation and channel rewet models.

### 3.2.1 Thermal Radiation Model

The thermal radiation model was formulated using the following assumptions:

- (1) All surfaces in the rod bundle are gray, diffuse, and nontransparent.
- (2) The emission of radiation takes place isotropically.
- (3) Reflection of radiation is divided into isotropic and anisotropic components.
- (4) The anisotropic reflection reverts back to the origin of radiation.
- (5) Absorption, emission, and dispersion in coolant are omitted.
- (6) All surfaces are in thermal quasi-equilibrium during each time step.

The gray-body factors are calculated by the auxiliary code BILBO, which evaluates geometric view factors for two geometries: (1) all rods at normal dimensions, and (2) all rods fully strained. The emissivities of dry and wet surfaces are taken as 0.67 and 0.96, respectively.

The thermal radiation model is considered conservative and adequate because of (1) the derivation of the dry emissivities taking into consideration oxide buildup as a function of local burnup, and (2) the omission of coolant absorption.

### 3.2.2 Spray Heat-Transfer Model

ASEA-ATOM (A-A) has performed experiments using the A-A 8x8 design and demonstrated that the Appendix K coefficients acceptable for the 7x7 fuel are applicable to the A-A 8x8 design, when an isotropic radiation model was used. A-A also developed the convective heat-transfer coefficients that when applied with an anisotropic model would match the 8x8 temperature distributions calculated with the Appendix K coefficients and the isotropic model. This new set of coefficients then was reduced by 15 percent for the QUAD+ fuel bundle design.

The Westinghouse ECCS evaluation model compliance with Appendix K, Sections I.D.6 and I.D.7, use convective heat transfer coefficients derived from the Appendix K-recommended values. The experimental data used to verify the values should be justified as applicable to the particular fuel design for which the overall methodology is to be applied.

## 4.0 CODE SENSITIVITY STUDIES AND ASSESSMENT

### 4.1 Nodalization

Westinghouse has performed sensitivity studies for the nominal (six volumes), coarse (five volumes), and fine (eight volumes) cases near the break location. The pressure and void at the break indicate that the coarse noding is nonconservative because of a lower break flow. However, the fine and nominal cases compare well throughout the transient.

Westinghouse also performed sensitivity studies in the bypass and upper plenum to demonstrate adequate noding at injection locations of the ECCS. Five cases were studied, and the results show that the mid-plane reflood times compare

well when the level tracking scheme was used. The sensitivity to the location of the bottom of level trackings is negligible. A coarser noding case results in a slightly different time of refilling guide tubes and bypasses. However, the final reflooding time of the mid-plane (a parameter in determining the PCT) remains within a time period of one second of the standard noding case.

The standard CHACHA-3C fuel rod noding consists of seven pellet nodes of equal volume and three cladding nodes of equal thickness. The sensitivity of the PCT to fuel-rod noding was evaluated by comparing results obtained from the standard case to those obtained with 5-pellet/2-cladding nodes and 10-pellet/4-cladding nodes. The results indicate negligible difference in the PCT calculated from three cases. As a result, it is concluded that standard fuel noding is appropriate for CHACHA-3C. CHACHA-3C uses the watercross thickness to calculate channel temperature. The sensitivity to the thickness of channel and watercross was evaluated, and results show that the PCT is relatively insensitive to the channel noding and is overestimated by 16°F using the watercross thickness.

#### 4.2 Plant Parameter Studies

The sensitivity of the nuclear peaking factors, including the axial peaking factor, bundle relative power, and peaking location, was evaluated. Five cases were studied, and the results show that the cases with a higher bundle relative power dried out and uncovered faster than the cases with a lower bundle relative power. The PCT for the peak-to-top power is slightly higher than that for the cosine power (by 25°F). However, the peak-to-top power would correspond to an operation with the control rods inserted approximately halfway into the core, which is inconsistent with the full-power operation. Because of the relative insensitivity to the power distribution and the inherent tendency of BWRs operating with slightly peak-to-bottom power shapes, the 1.5 cosine shape has been used in the DRAGON model. Axial peaking factors were considered as part of the power distribution sensitivity studies by Westinghouse. The sensitivity study for axial peaking factors in the range 1.5 to 1.6 covers the upper bound normally expected for a BWR/5. It is

concluded that adequate consideration has been given to the sensitivity of the nuclear peaking factors.

Westinghouse has performed studies varying the plant initial conditions and transient conditions (scram time, time of main steam isolation valve (MSIV) closure, initial water level, pressure form-loss coefficients, and feedwater and recirculation pump coast-down rates) to determine their effect on the time of mid-plane dryout. The results show that the largest change in mid-plane dryout time as a consequence of any of these sensitivities was about 1 second. As a result, the plant variables used in the Westinghouse evaluation models are considered adequate.

A reduced core flow sensitivity was performed for 66 percent of rated core flow and 104.3 percent rated power. Because of the initial lower enthalpy in the lower plenum, the reduced core flow case would delay the lower plenum flashing by 1 second and extend the midplane dryout by 2.5 seconds. As a result, the reference LOCA would result in a higher PCT and is more conservative.

#### 4.3 Numerical Convergence

Westinghouse has varied convergence criteria and time steps to show that the calculated solution is unique and within acceptable limits of the ideal asymptotic solution. Three convergence criteria were involved: thermal-hydraulic, fuel rod temperature, and surface heat transfer. A range of convergence criteria (by three orders of magnitude), time-step size (by one order of magnitude), and surface heat transfer (by one order of magnitude) were studied.

Three key system parameters, steamdome pressure, rod surface temperature, and core void fraction calculated from GOBLIN/DRAGON, demonstrated an asymptotic solution as the time-step size was reduced. The calculation of pressure shows the sensitivity of hydraulic models; the surface temperature calculation demonstrates the sensitivity of the heat transfer models; and the void fraction calculation warrants the adequacy of core flow rate, heat rate, and pressure. Varying the convergence criteria has negligible effect on the GOBLIN/DRAGON solutions.



Convergence criteria in CHACHA-3C also have been changed by an order of magnitude: the relative change in both rod surface heat flux and rod surface temperature, the absolute change in nodal temperature, and the relative change in channel temperature were the parameters identified in Reference 2, Section 7. The results show identical PCTs in the two runs. In order to evaluate the sensitivity of time-step sizes, values of time-step sizes were reduced by 80 percent for different phases: blowdown, dryout, dryout to uncovering, uncovering to reflood. The results show a difference of approximately 2°F in PCT.

It is concluded that the time-step/convergence criteria study conducted by Westinghouse demonstrates convergence of the GOBLIN/DRAGON and CHACHA-3C codes to a unique asymptotic solution.

#### 4.4 Break Spectrum

The limiting break is a combination of break size, location, and single failure that yields the highest PCT. The break spectrum studied by Westinghouse included:

- Case I: A full guillotine break in a recirculation suction line with failure of the low-pressure core spray (LPCS) diesel generator.
- Case II: A full guillotine break in a recirculation suction line with failure of the high-pressure core spray (HPCS) system.
- Case III: A 0.0084-m<sup>2</sup> (0.09-ft<sup>2</sup>) split break in a recirculation suction line with failure of the HPCS system.
- Case IV: A full break in a spray line with failure of the LPCS diesel generator (Division I).

For Case I, additional break sizes of 80 percent, 60 percent, and 40 percent of the full break were analyzed. Based on the results from Case I (four break sizes) and Case II, the full-size break in Case I would result in a higher PCT

of 1897°F. This was mainly because of a larger break size (compared with fractional break sizes) and smaller ECC flow (loss of LPCS versus HPCS flow). Cases III and IV are considered to be small breaks. Both cases result in a substantially lower PCT than that from the Case I full break by about 800°-900°F. The Westinghouse results were compared with those from the GE 8x8 safety analysis for the reference BWR. The Westinghouse-calculated PCTs are relatively consistent with the GE results. The differences in the PCTs can be attributed to a different maximum linear heat generation rate used (Westinghouse 14.5 kW/ft versus GE 13.4 kW/ft) and an earlier calculated low level 1 signal in the Westinghouse analysis. An earlier low level 1 signal would result in an earlier MSIV closure, an earlier automatic depressurization system actuation, and an earlier subsequent ECC injection. Regardless, in either analysis, the result is the same; namely, that the small LOCA is significantly less limiting than the 100 percent, double-ended guillotine recirculation pipe break.

#### 4.5 Transition Core

Reload analyses have been performed by Westinghouse using GOBLIN for a full QUAD+ core, a mixed core of GE 8x8 fuel and QUAD+ fuel core, and a full core of GE 8x8 fuel. The key phenomena compared include the core inlet flow rate during blowdown, the vessel depressurization rate, and the time of core reflood. The core inlet flow dictates the time of boiling transition and uncovering. The vessel depressurization rate determines the time at which spray flow is initiated. The reflood time determines the time at which the fuel rod heatup is terminated.

A full core of GE 8x8 fuel was modeled by GOBLIN with necessary modifications of the noding set for the QUAD+ fuel. The general system responses are similar for the GE 8x8 fuel core and the QUAD+ fuel core. The QUAD+ active core flow is slightly higher before lower plenum flashing as a result of draining of the watercross. The mid-plane dryout times are almost the same (by a 0.7 second difference). The vessel depressurization rate is almost identical. The mid-plane reflood times differ by 7 seconds because the watercross helps refill

the lower plenum slightly faster in the QUAD+ core. Therefore, similar system responses for the two fuel designs were concluded for the limiting LOCA.

Westinghouse also did a mixed-core LOCA system response analysis to demonstrate that each fuel design does not have an adverse effect on the other fuel design. A GOBLIN calculation was made with one third 8x8 fuel and two thirds QUAD+ fuel. The results of times for the initial blowdown phenomena, depressurization, and core flood closely follow that for a full core of QUAD+ fuel. The active core inlet flow and flow rate at the top of each fuel type are similar, and both assemblies receive comparable ECC flow rates. The potential of an uneven flow distribution of ECC power into different fuel assemblies during the refill/reflood phase was studied and excluded.

In summary, results from the analyses for the 8x8 fuel, QUAD+ fuel, and a mixed core fuel showed very minor changes in the timing of the key phenomena. As a result, introducing the QUAD+ fuel in a transition core of GE 8x8 fuel will not adversely affect the fuel-type-specific LOCA maximum average planar linear heat generation rate limits determined on the basis of a full core of the respective fuel type.

The use of a different fuel design other than QUAD+ fuel in a transition core should be addressed in a generic Reference Safety Report.

## 5.0 INTEGRAL SYSTEM QUALIFICATIONS

The system codes were assessed against several tests. These tests provided information on the integral system behavior under the influence of many interacting thermal-hydraulic phenomena. Westinghouse provided comparisons using the experimental data from TLTA Test 6425/2 (average power and average ECC), TLTA Test 6423/3 (high power and low ECC), TLTA Tests 6007/26 and 6006/3 (blowdown heat transfer), TLTA-5B and -5C small-break LOCA tests, and the FIX-II break spectrum tests. The results from a preliminary assessment indicated that the comparison of the Westinghouse simulations and these tests was unsatisfactory, particularly in the areas of time-zero offsets, system pressure, bundle mass, break flow rate, and fuel rod temperature. Other issues

needing clarification included code versions (the Westinghouse version versus the A-A version) and supporting plot data.

Westinghouse responded to our request for additional information by performing additional analyses using TLTA 6423/3, which involves a large-break LOCA with high power and low ECC. Major improvements made in these analyses included a much better match of the initial and boundary conditions with the tests, particularly for the initial downcomer mass inventory, lower plenum enthalpy, and steamline flow rate. The downcomer mass affects the initial depressurization through the recirculation line uncovering; the lower plenum enthalpy affects the time of lower plenum flashing; and modeling of the steamline valve closure improves the early pressure transient.

The GOBLIN simulation of TLTA Test 6423/3 excluded several Appendix K evaluation model requirements in order to best simulate the test phenomena. The differences between the simulation assumption/modeling and the Appendix K requirements are as follows:

- ° Rewetting of the fuel rods was allowed.
- ° The best-estimate homogeneous equilibrium critical flow model with subcooled flow multipliers on TLTA orifice critical flow data was used, replacing the Appendix K-required Moody model.
- ° The actual test power history was used instead of the Appendix K-required ARS 1971 decay heat curve plus a 20 percent conservatism.

The calculated system pressure and mass flow were compared with measured data. The calculated pressure before the MSIV closure compares well with the measured data. The bundle inlet flow for the initial phase of the transient agrees with the experiment. The good agreement of the total mass inventory and system pressure confirms the accurate calculation of the break flow through the transient. Westinghouse also provided data on the mass inventory in the components of the system. The mass inventory distribution, including downcomer, bypass, guide tube, upper plenum, and lower plenum, was provided and

compared fairly well with the test results. Comparisons of the test thermocouple measurements at various elevations with GOBLIN predictions show general agreement in trends and timing (Ref. 3); the selection of nodes for the rod dryout, heatup, and rewet comparisons is acceptable.

To demonstrate the conservative margin, Westinghouse performed more rod temperature analyses incorporating portions of the Appendix K requirement (no rewetting of the rods, zero heat-transfer coefficient following uncovering, and Appendix K-prescribed heat-transfer coefficients during spray cooling and after reflood). The resulting rod temperature shows about a 380°F margin. An additional PCT margin is inherent in the evaluation model because of other conservative Appendix K requirements excluded from the simulation (that is, the Moody break flow model and decay heat curve plus 20 percent conservatism).

#### 6.0 COMPLIANCE WITH APPENDIX K REQUIREMENTS

Appendix K to 10 CFR Part 50 sets forth certain required and acceptable features of evaluation models for calculating ECCS performance to demonstrate that the acceptance criteria of 10 CFR 50.46 are met. These required and acceptable features involve both individual calculational models and inputs to the licensing model.

The staff, with assistance from LANL, has conducted a review of the Westinghouse boiling water reactor ECCS evaluation model (BWR ECCS EM) to verify compliance of the model with 10 CFR Part 50 Appendix K, requirements and to ensure that the methodology provides an acceptable calculational framework for evaluating the behavior of a BWR reactor system during a postulated loss-of-coolant accident in the classes of boiling water reactors presently licensed for operation. The review included those aspects of the methodology relevant to the calculation of peak cladding temperature (PCT) and hydrogen generation for a spectrum of break sizes.

Conformance of the Westinghouse BWR ECCS EM to each applicable item of the requirements established in 10 CFR Part 50, Appendix K, concerning ECCS evaluation models is addressed in the following.

## I. Required and Acceptable Features of the Evaluation Models

### I.A. Sources of Heat During the LOCA

All licensing basis LOCA calculations will be performed for a power level 1.02 times the licensed power level as required by Appendix K.

I.A.1. The Initial Stored Energy in the Fuel -- Fuel rod conditions at the initiation of the postulated LOCA are generated using an approved methodology (the PAD code). An evaluation was performed to determine a conservative burnup for the reference fuel design. These considerations result in acceptable compliance with Appendix K.

I.A.2. Fission Heat -- Fission power and point kinetics parameters are developed using an NRC-approved methodology (the PHOENIX code).

I.A.3. Decay of Actinides -- The actinide decay power is determined using a model described in American Nuclear Society Standard 5.1 "Decay Energy Release Rates Following Shutdown of Uranium-Fueled Thermal Reactors." This model is used for the calculations at the time in the fuel cycle that yields the highest calculated fuel temperature during the LOCA, as required by Appendix K.

I.A.4. Fission Product Decay -- The acceptable model ANS Standard 5.1 is used with a 1.2 multiplier as prescribed in Appendix K.

I.A.5. Metal-Water Reaction Rate -- The rate of energy release, hydrogen generation, and cladding oxidation is determined from the Baker-Just equation which is acceptable as specified in Appendix K.

I.A.6. Reactor Internals Heat Transfer -- Heat transfer from non-fuel reactor components have been considered, as required by Appendix K.

#### I.B. Swelling and Rupture of the Cladding and Fuel Rod Thermal Parameters

As discussed in Section 3.2 of this Safety Evaluation, the cladding burst model employed in the Westinghouse BWR ECCS EM is a model developed for CHACHA-3C and which uses NRC-approved materials properties data. Cladding stress/strain functions are taken from a previously approved methodology.

#### I.C. Blowdown Phenomena

I.C.1. Break Characteristics and Flow -- The sensitivity study provided by Westinghouse included the results of a break spectrum analysis for a BWR/5. Plant-specific applications should include or reference a sensitivity study applicable to the facility BWR class. The discharge model used in BWR ECCS EM is the Moody model as specified in Appendix K and is acceptable.

I.C.2. Frictional Pressure Drops -- The frictional losses are calculated with commonly accepted relationships of friction factor and Reynolds number and two-phase friction multipliers as required by Appendix K.

I.C.3. Momentum Equation -- The momentum equation used in the GOBLIN series of codes includes all terms specified in Appendix K.

I.C.4. Critical Heat Flux -- A staff-approved correlation must be used when the subject methodology is used in a licensing analysis.

I.C.5. Post-Critical Heat Flux Heat Transfer Correlations -- The heat transfer correlations used in GOBLIN are the Groeneveld 5.7 correlation specified in Appendix K or other NRC-approved correlations.

I.C.6. Pump Modeling -- The recirculation pump model used in GOBLIN is developed from a basic conservation of angular momentum equation. Single-phase and degraded two-phase pump performance are modeled through performance curves which are addressed in a plant-specific application. The jet pump model in GOBLIN accounts for momentum and resistance effects as required by this rule item.

Section I.C.7 is not applicable to BWRs.

I.D. Post-Blowdown Phenomena; Heat Removal by the ECCS

I.D.1. Single Failure Criterion -- The sensitivity studies provided by Westinghouse included relevant single failure considerations and comparisons with previous evaluations by the nuclear steam supply system vendor. This is acceptable.

I.D.2. Containment Pressure -- GOBLIN analyses will conservatively assume atmospheric pressure in the containment volume throughout the LOCA transient. This assumption adequately addresses the requirements for this feature of Appendix K.

Sections I.D.3 through I.D.5 are not applicable to BWRs.

I.D.6. Convective Heat Transfer Coefficients for BWR Fuel Rods Under Spray Cooling -- The Westinghouse CHACHA-3C code will use the rod surface heat transfer coefficients calculated by DRAGON before the end of lower plenum flashing. After this period, the convective coefficients will be derived from Appendix K recommendations. Heat transfer coefficients developed from experimental data should be justified as applicable to the particular fuel design for which the overall methodology is to be used.

I.D.7. The Boiling Water Reactor Channel Box Under Spray Cooling -- The Westinghouse CHACHA-3C code will use the convective heat transfer coefficients calculated by DRAGON prior to the end of lower



plenum flashing. After this period but prior to core spray reaching rated flow, the channel convective heat transfer coefficient will be set to zero. Experimental data used to verify the applicability of heat transfer coefficients derived from Appendix K recommended values should be justified as applicable to the particular fuel design for which the overall methodology is to be used. The channel wetting time will be determined based on the modified Yamanouchi correlation plus 60 seconds, as prescribed by Appendix K.

## II. Required Documentation

The documentation provided in References 1 through 3 was in sufficient detail which (1) allowed technical review of the analytical approach, (2) provided sensitivity studies of pertinent variables, system and fuel noding, and calculational time step, (3) provided adequate comparisons with experimental data, and (4) demonstrated an acceptable margin of safety comparable to other acceptable evaluation models.

The staff has confirmed that Westinghouse has addressed those features of Appendix K applicable to BWRs.

## 7.0 CONCLUSIONS

The Westinghouse BWR ECCS evaluation model (WCAP-11284) and sensitivity studies (WCAP-11427) were reviewed in reference to the Appendix K requirements. We conclude that Westinghouse/ASEA-ATOM has developed and documented an adequate information data base to address and meet the Appendix K requirements. Westinghouse also has performed an integral system qualification analysis to compare the ECCS model calculations against applicable groups of test data.

From our present evaluation of the adequacy of the models used in the Westinghouse BWR ECCS EM and the conformance of the calculations to Appendix K requirements, it is concluded that the model described in Reference 1 will provide adequately representative and conservative predictions for large-break

and small-break LOCAs in boiling water reactors. Because the analysis predictions were based on data and characteristics of a fuel design (QUAD+) not presently scheduled for production and commercial use, this conclusion is subject to certain conditions before use of the methodology for licensing actions. These conditions are specified in the following Regulatory Position.

#### Regulatory Position

- (1) The staff concludes that the Westinghouse BWR ECCS EM provides an acceptable evaluation model of loss-of-coolant accidents for use in calculations of peak clad temperature (PCT) and hydrogen generation made in accordance with Appendix K licensing calculations for large-break and small-break LOCAs in boiling water reactor BWR/2 through BWR/6 plants. The basis for this position is the staff review of licensing topical reports WCAP-11284 (Ref. 1) and WCAP-11427 (Ref. 2) and the evaluation summarized in this safety evaluation. This conclusion is subject to the conditions described in paragraphs 2 and 3 below.
- (2) The staff concludes that the Westinghouse BWR ECCS EM has provisions and options to conform with the required modelling features of Appendix K. Conformance to plant-specific requirements of Appendix K (e.g., I.C.6, Pump Modeling) for use in licensing calculations must be specified in the license application reload safety analysis report. This report should include or reference a sensitivity study for the BWR type identified in the license application.
- (3) Certain specific model areas of the Westinghouse BWR ECCS EM discussed in WCAP-11284 are specific to a fuel design (QUAD+). These areas are the critical heat flux (CHF) and fuel design characteristics for the QUAD+ fuel assemblies. A staff-approved CHF correlation must be used when the subject ECCS methodology is used in a licensing analysis (Section 3.1.8). The experimental data used to verify the convective spray heat transfer coefficients should be justified as applicable to the particular fuel design for which the overall methodology is to be applied (Section 3.2.2). The use of a fuel design other than QUAD+ fuel in a transition core should also be addressed.

## 8.0 REFERENCES

1. D. B. Ebeling-Konig, M. E. Nissley, J. T. Dederer, A. G. Gagnon, and J. M. Brennan, "Westinghouse Boiling Water Reactor Emergency Core Cooling System Evaluation Model: Code Description and Qualification," Westinghouse report WCAP-11284 (September 30, 1986).
2. D. B. Ebeling-Konig, M. E. Nissley, and R. M. Jakub, "Westinghouse Boiling Water Reactor Emergency Core Cooling System Evaluation Model: Code Sensitivity," Westinghouse report WCAP-11427 (June 30, 1987).
3. "Westinghouse Boiling Water Reactor Emergency Core Cooling System Evaluation Model: Response for Additional Information and Errata," WCAP-11284-Amendment 1/WCAP-11427-Amendment 1 (July 18, 1988).
4. J. A. Holmes, "Description of the Drift Flux Model in the LOCA Code RELAP-UK," Conference on Heat and Fluid Flow in Water Reactor Safety, I. Mech. E. Manchester, 1977.
5. G. B. Wallis, One-Dimensional Two-Phase Flow (New York: McGraw-Hill, Inc., 1969).
6. R. V. Bailey et al., "Transport of Gases Through Liquid-Gas Mixtures," AIChE New Orleans Meeting (1956).
7. S. O. Eriksson et al., "Experiment Med Motriktade Angfloden I Strilkylningskretsen," GOTA Studsvik report, AES-15 (1977).
8. P. W. Ianni, "Effectiveness of Core Standby Cooling Systems for General Electric Boiling Water Reactors," APED-5458, March 1968.
9. NEDO-20566, "General Electric Company Analytical Model for Loss-of-Coolant Accident Analysis in Accordance with 10 CFR Part 50, Appendix K," January 1976.

## ACKNOWLEDGEMENTS

Foremost, Westinghouse wishes to thank ASEA-ATOM of Sweden, for furnishing the reports RCC-80-43 and RCC-81-30, Rev. 1, which supplied the basis for a significant portion of this document. Special thanks are due to Hjalmar Wijkström of ASEA-ATOM, for contributing much valuable insight information to this document. The authors would like to recognize the following people within Westinghouse for their contributions to this document: L. E. Hochreiter, A. C. Cheung, J. J. Besspiata, G. E. Collier, K. A. Ewing, C. Cooper, S. L. Washington, K. I. R. Knippel, K. F. McNamee, J. M. Boyd, and Nuclear Safety word processing.

## TABLE OF CONTENTS

	<u>Page</u>
ACKNOWLEDGEMENTS	i
LIST OF FIGURES	vii
LIST OF TABLES	xii
1. INTRODUCTION	1-1
1.1 Evaluation Model	1-1
1.2 References	1-2
2. SUMMARY OF ANALYSIS CODES	2-1
2.1 GOBLIN/DRAGON	2-1
2.1.1 Hydraulic Models	2-2
2.1.2 System Models	2-4
2.1.3 Thermal Models	2-5
2.1.4 Power Generation Models	2-6
2.1.5 Numerical Methods	2-7
2.1.6 DRAGON	2-7
2.2 CHACHA-3C/BILBO	2-8
2.2.1 Heatup Analysis: CHACHA-3C	2-8
2.2.2 Radiation Gray Body Factors: BILBO	2-10
2.3 References	2-11
3. THERMAL-HYDRAULIC ANALYSIS CODES: GOBLIN/DRAGON	3-1
3.1 Basic Conservation Equations	3-1
3.1.1 Mass Conservation Equation	3-2
3.1.2 Energy Conservation Equation	3-3
3.1.3 Momentum Conservation Equation	3-8
3.2 Fluid State Equations	3-17
3.2.1 Thermodynamic and Fluid Properties of Water and Steam	3-17
3.2.2 State of Equation	3-18

## TABLE OF CONTENTS (Cont.)

		<u>Page</u>
3.3	Constitutive Models	3-19
	3.3.1 Two-Phase Energy Flow Model	3-19
	3.3.2 Two-Phase Level Tracking	3-28
	3.3.3 Frictional Pressure Drop Correlations	3-30
	3.3.4 Form Pressure Drop Correlations	3-33
	3.3.5 Injection Flow-Fluid Interaction	3-35
	3.3.6 Critical Flow Model	3-36
3.4	System Models	3-41
	3.4.1 Recirculation Pump Model	3-41
	3.4.2 Jet Pump Model	3-46
	3.4.3 Separator and Dryer Model	3-49
	3.4.4 Feedwater and Steamline Systems	3-52
	3.4.5 BWR Systems	3-53
3.5	Heat Transfer Models	3-55
	3.5.1 Heat Transfer Regimes	3-56
	3.5.2 Convective Heat Transfer Coefficients	3-56
	3.5.3 Dryout Correlation	3-63
	3.5.4 Transient Boiling	3-71
	3.5.5 Radiation Heat Transfer	3-75
3.6	Heat Conduction Models	3-75
	3.6.1 Plate Heat Conduction	3-75
	3.6.2 Rod Conduction	3-76
	3.6.3 Material Properties	3-78
3.7	Power Generation Models	3-80
	3.7.1 Point Kinetics Model	3-80
	3.7.2 Metal-Water Reaction Model	3-83

## TABLE OF CONTENTS (Cont.)

	<u>Page</u>
3.8 Numerical Methods	3-85
3.8.1 Reactor Point Kinetic Solution	3-86
3.8.2 Hydraulic Model Solution	3-87
3.8.3 Heat Conduction and Transfer Solution	3-91
3.9 Nodalization	3-94
3.10 Nomenclature	3-95
3.11 References	3-99
Appendix 3A	3-103
4. ROD HEAT-UP ANALYSIS CODES: CHACHA-3C/BILBO	4-1
4.1 Fuel Rod Conduction Model	4-2
4.2 Channel Temperature Model	4-13
4.3 Heat Generation Model	4-15
4.4 Metal-Water Reaction Model	4-16
4.5 Thermal Radiation Model	4-21
4.5.1 Model Derivation	4-21
4.5.2 Gray Body Factor Code BILBO	4-26
4.5.3 Derivation of Consistent Spray Cooling Heat Transfer Coefficients	4-28
4.6 Gas Plenum Temperature and Pressure Model	4-29
4.6.1 Plenum Temperature Model	4-31
4.6.2 Internal Rod Gas Pressure Model	4-33
4.7 Channel Wetting Model	4-34
4.8 Pellet-Clad Gap Heat Transfer Model	4-36
4.9 Cladding Strain and Rupture Model	4-41
4.9.1 Cladding Rupture Model	4-41
4.9.2 Cladding Strain Model	4-41
4.9.3 Pellet-Cladding Gap Model	4-44
4.10 Nomenclature	4-46
4.11 References	4-50
Appendix 4A	4-52

TABLE OF CONTENTS (Cont.)

	<u>Page</u>
5. EVALUATION MODEL COMPLIANCE WITH 10CFR50 APPENDIX K	5-1
5.1 Introduction	5-1
5.2 Specific Compliance With Appendix K	5-1
5.2.1 Sources of Heat During LOCA	5-1
5.2.1 Initial Stored Energy in Fuel	5-2
5.2.3 Fission Heat	5-4
5.2.4 Decay of Actinides	5-5
5.2.5 Fission Product Decay	5-6
5.2.6 Metal-Water Reaction Rate	5-7
5.2.7 Reactor Internals Heat Transfer	5-8
5.2.8 Swelling and Rupture of the Cladding and Fuel Rod Thermal Parameters	5-8
5.2.9 Break Spectrum Analysis	5-9
5.2.10 Discharge Model	5-10
5.2.11 Noding Near the Break and the ECCS Injection Points	5-11
5.2.12 Frictional Pressure Drops	5-12
5.2.13 Momentum Equation	5-13
5.2.14 Critical Heat Flux	5-13
5.2.15 Post-CHF Heat Transfer Correlations	5-16
5.2.16 Pump Modeling	5-18
5.2.17 Single Failure Criterion	5-19
5.2.18 Containment Pressure	5-20
5.2.19 Convective Heat Transfer Coefficient for BWR Fuel Rods Under Spray Cooling	5-21
5.2.20 The Boiling Water Reactor Channel Box Under Spray Cooling	5-22
5.3 References	5-24



## TABLE OF CONTENTS (Cont.)

	<u>Page</u>
6. QUALIFICATION	6-1
6.1 Separate Effects Qualification	6-2
6.1.1 Drift Flux	6-2
6.1.2 Level Swell	6-5
6.1.3 Countercurrent Flow Limitation	6-7
6.1.4 Fuel Bundle Pressure Drop	6-10
6.1.5 Jet Pump	6-11
6.1.6 CHF Correlation	6-14
6.1.7 Post-Dryout Heat Transfer	6-15
6.1.8 Reactor Power Generation Model	6-17
6.1.9 Fuel Rod Conduction Model	6-19
6.1.10 Cladding Strain and Rupture Model	6-22
6.1.11 Radiation Heat Transfer Model	6-24
6.1.12 Spray Cooling and Channel Wetting	6-26
6.2 TLTA-5A Integral System Qualification	6-27
6.2.1 Objective	6-27
6.2.2 TLTA Facility Description	6-27
6.2.3 Average Power and Average ECC Test	6-30
6.2.4 High Power and Low ECC Test	6-34
6.2.5 Summary	6-35
6.3 Additional Integral System Qualification	6-36
6.3.1 TLTA-4 Blowdown Heat Transfer Tests	6-36
6.3.2 TLTA Small Break Tests	6-37
6.3.3 FIX-II Break Spectrum Tests	6-37
6.4 Nomenclature	6-39
6.5 References	6-40
7. CONCLUSIONS	7-1

## LIST OF FIGURES

<u>Figure</u>	<u>Title</u>	<u>Page</u>
1-1	Flow of Information Between Computer Codes	1-3
1-2	Interaction Between Computer Codes	1-4
2-1	Sample GOBLIN Geometrical Representation of Reactor	2-12
2-2	Structure of GOBLIN Code	2-13
3-1	Mass Balance Control Volume	3-109
3-2	Energy Balance Control Volume	3-110
3-3	Momentum Balance Control Volume	3-111
3-4	Weighted Mean Rise Velocity of Steam Through Stagnant Water at Atmospheric Pressure	3-112
3-5	Intersection of Drift Flux and Countercurrent Flow Limitation Correlations	3-113
3-6	Nomenclature Convention in Application of Drift Flux Model	3-114
3-7	Mass Drift Flux/CCFL Relation for $\alpha_y \geq \alpha_z$	3-115
3-8	Mass Drift Flux/CCFL Relation for $\alpha_y < \alpha_z$	3-116
3-9	Flow Conservation and Calculation at Two-Phase Level	3-117
3-10	Condensation Rate Function	3-119
3-11	Critical Break Flow Model Regimes	3-120
3-12	Typical Homologous Hydraulic Torque Curve	3-121
3-13	Frictional Torque as Function of Pump Speed	3-122
3-14	Typical Homologous Pump Head Curves	3-123
3-15	Jet Pump Recirculation System	3-124
3-16	Schematic of Jet Pump Model	3-125
3-17	Schematic of Steam Separator Model	3-126
3-18	Schematic of Steam Dryer Unit	3-127

LIST OF FIGURES (Cont.)

<u>Figure</u>	<u>Title</u>	<u>Page</u>
3-19	Heat Transfer Flow Regime Map	3-128
3-20	Dryout Quality and Maximum Heat Flux Calculation Based on Critical Power Ratio	3-129
3-21	Transition Boiling Model	3-130
3-22	Plate Heat Conduction Model Nodalization	3-131
3-23	Simplified Flow Chart of GOBLIN Computational Sequence	3-132
3-24	Simultaneous Solution of Conduction and Convective Heat Transfer	3-133
3-25	Conduction/Heat Transfer Solution for Various Heat Transfer Regimes	3-134
4-1	Fuel Rod Conduction Model Nodalization	4-59
4-2	UO <sub>2</sub> Pellet Radial Power Distribution	4-60
4-3	Components of Radiation at Surface i	4-61
4-4	Top End of Fuel Rod	4-62
4-5	Heat Transfer Paths for Plenum Temperature Model	4-63
4-6	Fission Gas Release vs. Time at High Temperature	4-64
4-7	CHACHA-3C Rod Burst Correlation	4-65
4-8	Cladding Strain After Perforation	4-66
4-9	Plastic Strain Prior to Cladding Perforation	4-67
6-1	Comparison of Drift Flux Model with FRIGG Data at 6.8 MPa (990 psia)	6-45
6-2	Comparison of Drift Flux Model with FRIGG Data at 4.8 MPa (700 psia)	6-46
6-3	DRAGON Nodalization of TLTA Bundle	6-47
6-4	Axial Power Distribution for TLTA Bundle	6-48
6-5	Comparison of Void Fractions for 790 psia Test (100 sec)	6-49

LIST OF FIGURES (Cont.)

<u>Figure</u>	<u>Title</u>	<u>Page</u>
6-6	Comparison of Void Fractions for 195 psia Test (200 sec)	6-50
6-7	Level Swell Test Apparatus	6-51
6-8	Level Swell Qualification, Pressure Transient for Test 1	6-52
6-9	Level Swell Qualification, Level Transient for Test 1	6-53
6-10	Level Swell Qualification, Mass Transient for Test 1	6-54
6-11	Level Swell Qualification, Pressure Transient for Test 2	6-55
6-12	Level Swell Qualification, Level Transient for Test 2	6-56
6-13	CCFL Correlation Comparison for the GE Upper Tie Plate	6-57
6-14	CCFL Correlation Comparison for the Bypass Region	6-58
6-15	CCFL Correlation Comparison for the Side Entry Orifice	6-59
6-16	Nodalization for Jet Pump Qualification	6-60
6-17	Comparison of Measured and Calculated Jet Pump Performance	6-61
6-18	Post-Dryout Heat Transfer Coefficient Comparison with G-1 Test Data	6-62
6-19	Post-Dryout Heat Transfer Coefficient Comparison with G-2 Data	6-63
6-20	Post-Dryout Heat Transfer Coefficient Comparison with FLECHT Low Flow Reflooding Data	6-64
6-21	TVO-1 Internal Recirculation Pump Plant	6-65
6-22	GOBLIN Nodalization of TVO-1 for Pump Trip Transient	6-66
6-23	Comparison of Core Channel Inlet Flow Rate for TVO-1 Pump Trip Transient	6-67
6-24	Comparison of Fission Power for TVO-1 Pump Trip Transient	6-68
6-25	Conduction Model Qualification - Step Change in Surface Temperature	6-69
6-26	Conduction Model Qualification - Step Change in Coolant Temperature with Convection	6-70

## LIST OF FIGURES (Cont.)

<u>Figure</u>	<u>Title</u>	<u>Page</u>
6-27	Comparison of Rod Burst Correlation with Data	6-71
6-28	Comparison of Rod Burst Correlations	6-72
6-29	Cross-Section of Bundle Used for Radiation-Only Tests	6-73
6-30	CHACHA-3C Comparison with Radiation-Only Data	6-74
6-31	TLTA-5A Facility Schematic	6-75
6-32	GOBLIN Noding Diagram for TLTA-5A	6-76
6-33	Bundle Flowrate for TLTA-5A Test 6425/2	6-77
6-34	Bundle Mass for TLTA-5A Test 6425/2	6-78
6-35	Lower Plenum Mass for TLTA-5A Test 6425/2	6-79
6-36	Bypass Mass for TLTA-5A Test 6425/2	6-80
6-37	System Pressure for TLTA-5A Test 6425/2	6-81
6-38	Break Flow for TLTA-5A Test 6425/2	6-82
6-39	Broken Jet Pump Flow Rate for TLTA-5A Test 6425/2	6-83
6-40	Bundle Flowrate for TLTA-5A Test 6423/3	6-84
6-41	Bundle Mass for TLTA-5A Test 6423/3	6-85
6-42	Lower Plenum Mass for TLTA-5A Test 6423/3	6-86
6-43	Bypass Mass for TLTA-5A Test 6423/3	6-87
6-44	System Pressure for TLTA-5A Test 6423/3	6-88
6-45	Break Flow for TLTA-5A Test 6423/3	6-89
6-46	Broken Jet Pump Flow Rate for TLTA-5A Test 6423/3	6-90
6-47	System Pressure Transient for TLTA-4 Test 6007 Run 26	6-91
6-48	Bundle Inlet Flow for TLTA-4 Test 6007 Run 26	6-92
6-49	Jet Pump Flow Rates for TLTA-4 Test 6007 Run 26	6-93

LIST OF FIGURES (Cont.)

<u>Figure</u>	<u>Title</u>	<u>Page</u>
6-50	Rod Temperatures at 79 Inch Elevation for TLTA-4 Test 6007 Run 26	6-94
6-51	Steam Dome Pressure for TLTA-5C	6-95
6-52	Upper Plenum and Downcomer Levels for TLTA-5C	6-96
6-53	Steam Dome Pressure for FIX-II Test 3061, 100% Break at 2.51 kW	6-97
6-54	Midplane Rod Temperature for Fix-II Test 3061, 100% Break at 2.51 kW	6-98

## LIST OF TABLES

<u>Table</u>	<u>Title</u>	<u>Page</u>
2-1	Heat Transfer Regimes	2-12
3-1	Factor $f_4$ in Westinghouse UHI Correlation	3-105
3-2	Fission Product and Actinide Decay Effective Energy Fraction and Decay Constants	3-106
3-3	Comparison of 11 Group Fission Product Decay Curve with Tabulated Proposed 1971 ANS Standard 5.1	3-107
4-1	Inputs Required to Calculate Heat Generation Rates	4-57
4-2	Appendix K Spray Heat Transfer Coefficients for A-A 8x8 Fuel	4-58
4-3	Appendix K Spray Heat Transfer Coefficients for QUAD+ Fuel	4-58
6-1	FRIGG Void Measurement Test Conditions	6-43
6-2	Rod-Burst Data Sources	6-44

## 1. INTRODUCTION

### 1.1 Evaluation Model

The Westinghouse Boiling Water Reactor (BWR) Evaluation Model used to calculate the performance of the Emergency Core Cooling (ECC) System during a postulated Loss-of-Coolant Accident (LOCA) is known as the GOBLIN series of codes.

The GOBLIN series of codes, as described in this document include thermal hydraulic models that comply with all applicable 10 CFR Part 50.46 and Appendix K (Ref. 1-1) requirements and therefore represents an overall conservative calculation of the fuel cladding temperature and oxidation following a LOCA. Westinghouse at a future time may elect to modify the models described in this report as a result of new information obtained through either Westinghouse experiments or public sources. Information as a result of Westinghouse experiments may demonstrate either excessive conservatism in Appendix K requirements or LOCA margin inherent in the Westinghouse BWR fuel assembly design.

The GOBLIN series of codes uses one-dimensional assumptions and solution techniques to calculate the BWR transient response to both large and small break LOCAs. The series is composed of three major computer codes--GOBLIN, DRAGON and CHACHA-3C; an auxiliary code--BILBO; and several input/output data processors--HOBIT, FRODO, CHINE, PLOAUX, and SUPERB. DRAGON is virtually identical to GOBLIN except several calculation models are bypassed. A brief description of each code follows.

GOBLIN - Performs the analysis of the LOCA blowdown and reflood thermal hydraulic transient for the entire reactor, including the interaction with various control and safety systems.

DRAGON - Performs the hot fuel channel thermal hydraulic transient calculations using boundary conditions from the GOBLIN calculation.



CHACHA-3C - Performs detailed temperature calculations at a specified axial level within the fuel assembly previously analyzed by the DRAGON code. All necessary fluid boundary conditions are obtained from the DRAGON calculation. CHACHA-3C calculates the time-dependent pellet to clad gap heat transfer coefficients along with clad swelling and potential burst. It determines the temperature distribution of each rod throughout the transient and ultimately the peak clad temperature (PCT) and cladding oxidation at the axial plane under investigation. It also provides input for the calculation total hydrogen generation, by supplying the local oxidation at a number of axial and radial locations in the core.

BILBO - Calculates the radiation gray body factors for input into GOBLIN, DRAGON, and CHACHA-3C.

HOBIT - Performs input processing for GOBLIN and DRAGON.

FRODO - Performs restart data processing for GOBLIN and DRAGON.

CHINE - Transfers the thermal hydraulic boundary conditions from the DRAGON calculation to CHACHA-3C.

PLOAUX - Processes output data for generating plots.

SUPERB - Generates the plot diagrams.

The flow of information between GOBLIN, DRAGON and CHACHA is shown in Fig. 1-1. Figure 1-2 shows the interaction between the GOBLIN series of computer codes.

## 1.2 References

- 1-1. Code of Federal Regulations, Title 10 Part 50, Office of the Federal Register, National Archives and Records Administration, 1986.

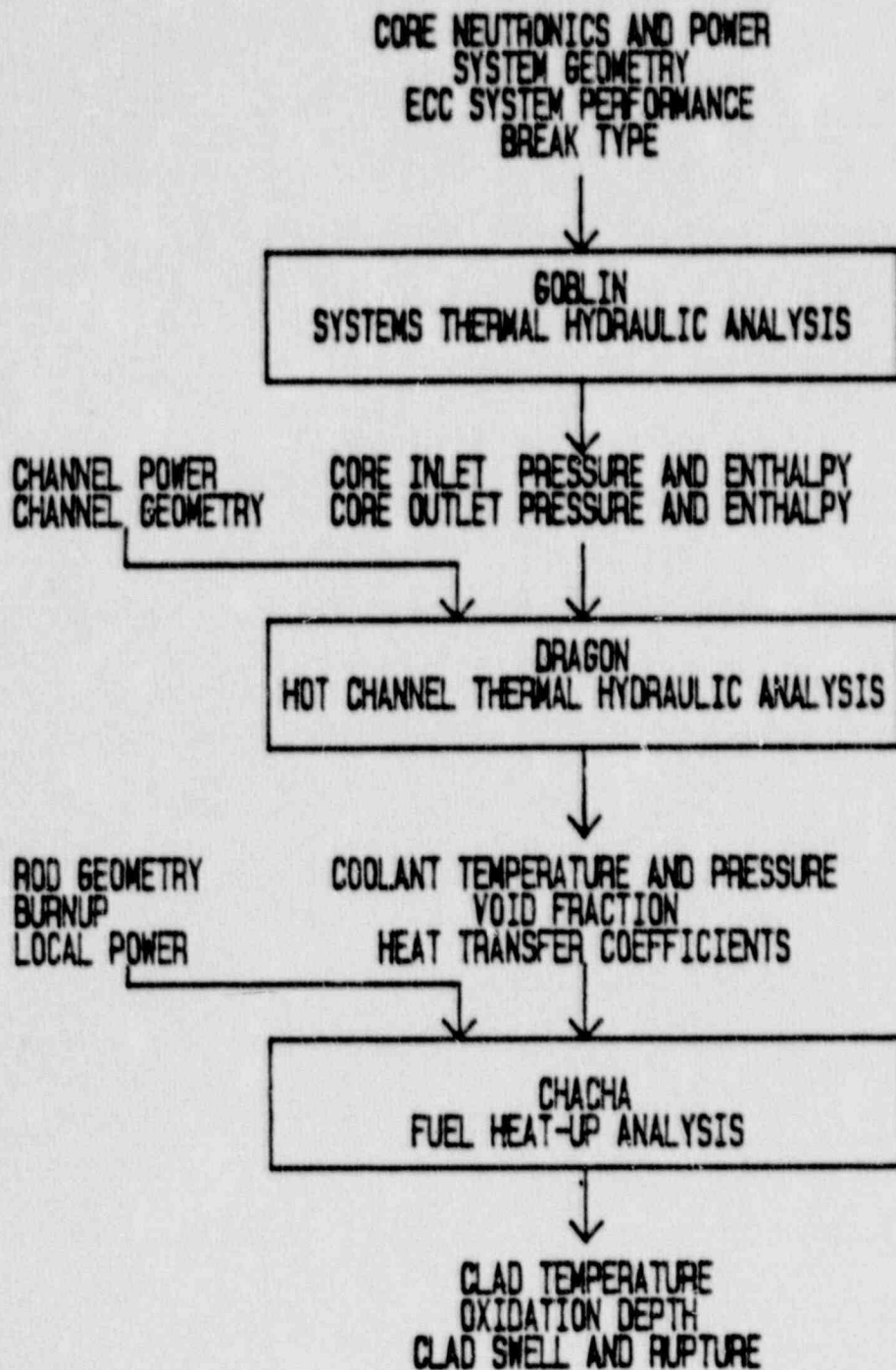


Figure 1-1 - Flow of Information Between Computer Codes

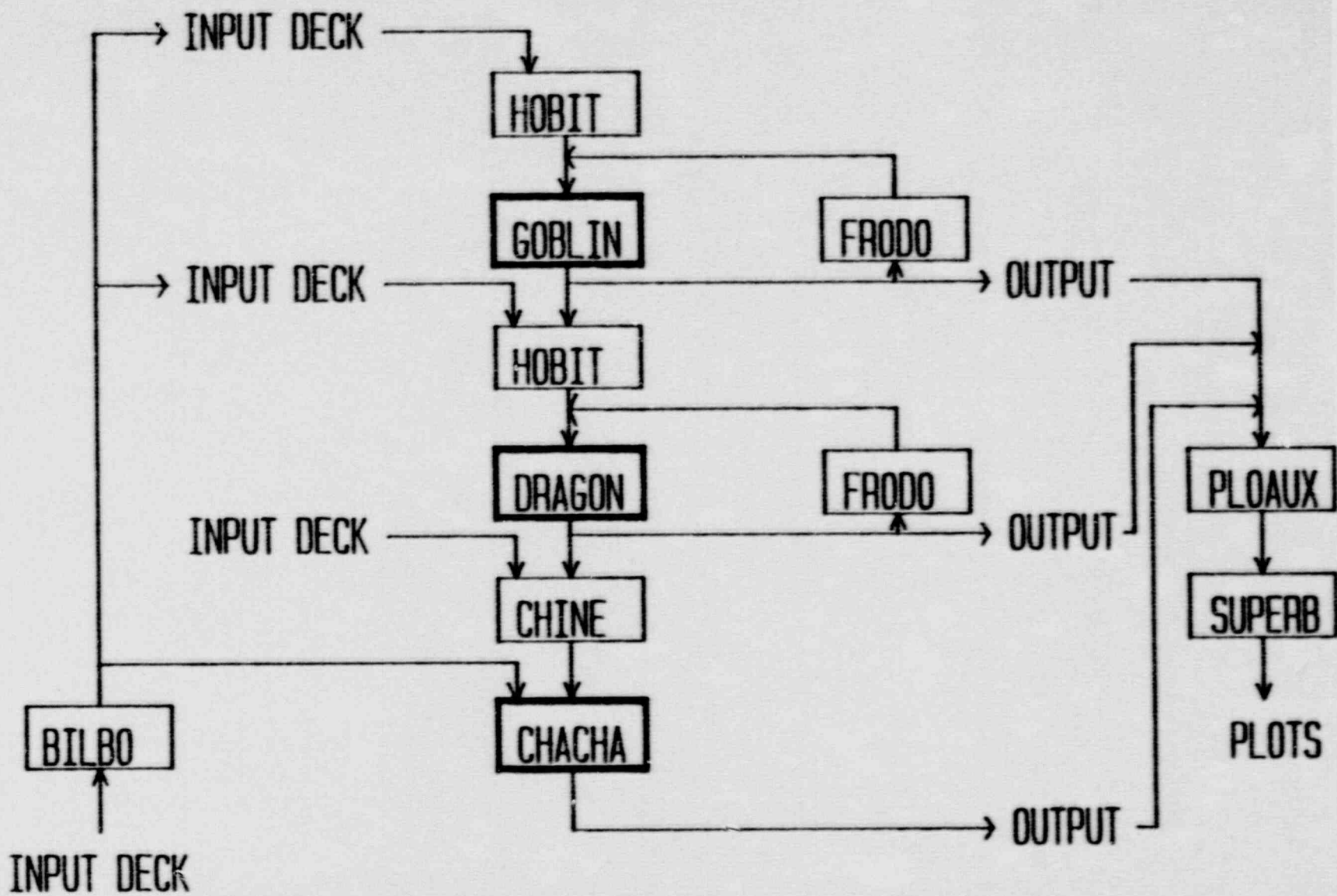


Figure 1-2 - Interaction Between Computer Codes

## 2. SUMMARY OF ANALYSIS CODES

### 2.1 GOBLIN/DRAGON

The GOBLIN code performs the thermal hydraulic calculations for the entire reactor during a postulated LOCA using one-dimensional assumptions. The system response from blowdown through reflood is calculated by GOBLIN for both large and small break events.

The reactor is divided into a user specified number of mass/energy control volumes and flow paths. The flow paths represent momentum control volumes between adjacent mass/energy control volumes. Figure 2-1 shows a sample geometric representation for the GOBLIN code.

The GOBLIN code can be divided into four main sections (Fig. 2-2):

- o The hydraulic model solves the mass, energy, and momentum conservation equations together with the equation of state for each control volume. This model includes empirical constitutive correlations for the calculation of pressure drops, two-phase energy flow (drift flux), two-phase level tracking, spray-fluid interaction, and critical flow rate.
- o The system models contain detailed models of the various reactor components, and the safety systems that are activated after a LOCA. They include the steam separators and dryers; reactor level measurement, trip, and depressurization systems; recirculation and jet pumps; and emergency core cooling systems.
- o The thermal model calculates the heat conduction and heat transfer from the fuel rods, pressure vessel, and internals (plates) to the coolant. This model solves the material heat conduction equation and calculates the heat transfer from the fuel and structures to the coolant.

- o The power generation models calculate the heat generation due to fission, decay heat, and metal-water reaction. Fission power is determined by a reactor point kinetics model.

A fully implicit numerical method is used to solve the hydraulic model and the simultaneous heat transfer and thermal conduction solution. Only the heat flux into the coolant is treated explicitly.

The following provides a summary description of the main GOBLIN/DRAGON models. A detailed description is given in Sec. 3.

### 2.1.1 Hydraulic Model

The hydraulic model solves the governing equations for the coolant flow. They are:

- o Mass Conservation
- o Energy Conservation
- o Momentum Conservation
- o Equation of State

The fluid conservation equations (Sec. 3.1 and 3.2) include all terms in the theoretical derivations for one-dimensional, drift-flux, thermal equilibrium flow with the exception of the kinetic and potential energy terms in the energy balance. These terms are negligible in the type of calculation considered here.

The above set of equations together with the necessary secondary relations and constitutive correlations form a complete system of equations for calculating the fluid flow phenomena.

The conservation equations for the fluid flow are integrated over "control volumes" and the resulting set of equations are cast into finite-difference form using a fully implicit scheme.

The control volumes for the mass and energy equations consist of fluid volumes prescribed by the user. The control volumes for the momentum balance consist of the volume between the centers of adjacent fluid volumes and are denoted by flow paths as shown in Fig. 2-1.

For each control volume, values of pressure, enthalpy, mass inventory, and boundary coolant flow are determined by the solution of the conservation equations. From secondary relations and the constitutive correlations, properties such as steam qualities, void fractions, fluid temperatures, two-phase level, etc., are calculated.

Several empirical constitutive correlations are necessary to complete formulation of the basic fluid equations. The most important correlations in the hydraulic model of the GOBLIN code are:

- o Two-phase energy flow (drift flux) correlations (Sec. 3.3.1)
- o Two-phase level tracking (Sec. 3.3.2)
- o Friction and local pressure drop correlations (Sec. 3.3.3 - 3.3.4)
- o Correlations for the interaction between injected water and the reactor inventory fluid (Sec. 3.3.5)
- o Critical flow rate correlations (Sec. 3.3.6)

In the pressure drop calculation, correlations are provided for single-phase friction factors and two-phase friction and local form pressure drop multipliers. The two-phase energy transport between volumes is calculated by a relation based on drift flux and countercurrent flow limitation (CCFL) correlations. The CCFL correlation is a general formulation applicable to different flow geometries.

The interaction of emergency core cooling (ECC) water introduced into a control volume with the fluid in the volume is modeled. Specifically the model calculates the condensation rate of steam when the ECC water is injected above a two-phase level.

The choked flow model is comprised of the Moody model (Ref. 2-1) with a subcooled extension according to P. Pana (Ref. 2-2).

### 2-1.2 System Models

GOBLIN includes models for the following boiling water reactor system and components.

- o The main recirculation pumps (Sec. 3.4.1)
- o The jet pumps (Sec. 3.4.2)
- o The separators and dryers (Sec. 3.4.3)
- o The feedwater and steamline systems (Sec. 3.4.4)
- o The reactor protection system (Sec. 3.4.5)
- o The reactor level measurement system (Sec. 3.4.5)
- o The pressure relief system (Sec. 3.4.5), and
- o The emergency core cooling (ECC) injection and spray systems (Sec. 3.4.5).

The speed of the main circulation pumps is determined from the solution of the angular momentum balance for the pump impeller. This equation is solved simultaneously with the fluid conservation equations. The applied torque represents the net torque from all sources, i.e., the hydraulic interaction between the fluid and the pump impeller (usually referred to as the "hydraulic torque"), frictional losses in the rotating machinery, and torque supplied by the pump motor. The pump head and hydraulic torque are determined from user supplied homologous curves which are a function of pump speed, volumetric flow rate, and void fraction.

The jet pump model modifies the one-dimensional momentum equation to account for the spatial and temporal acceleration due to the significant momentum exchange occurring between the jet pump drive and suction flows.

Models describing the efficiency of the steam separators and the steam dryer are included. The model is based on the separation efficiency expressed by the carryover fraction (water entrained in the steam to the steam dome) and carry-under fractions (steam entrained in the water to the downcomer).

The steamline flow and moisture content can be specified as a function of time. The feedwater system flow and enthalpy also can be specified with time.

Included in GOBLIN is a model to calculate the response of the level measurement system, which is used to determine trip time and ECC system start times. The loss-of-offsite power can be modeled to occur at anytime during the transient with the subsequent diesel start, pump, and valve delays. The steam pressure relief/safety valve system including the automatic depressurization system (ADS) is modeled in sufficient detail to account for opening and reseal delays. The ECC systems for both spray and injection are modeled using tables of flow rates as a function of differential pressure between the reactor and the containment wetwell.

### 2.1.3 Thermal Model

The thermal model in the GOBLIN code calculates the heat transferred from the fuel rods, reactor vessel, and internals to the coolant, for use in the hydraulic transient calculation. The surface heat transfer and material heat conduction problems are solved simultaneously to determine the total heat transfer to the coolant.

The heat transfer coefficient couples the hydraulic solution to the thermal conduction solution through the coolant state and surface temperature. Empirical heat transfer coefficient correlations are modelled for: single-phase liquid heat transfer, two-phase non-dryout heat transfer, transition boiling, two-phase post-dryout heat transfer, single-phase vapor



and surface to surface radiation heat transfer (see Sec. 3.5). The specific regimes modeled are summarized in Table 2-1. The above heat transfer package is used in the GOBLIN and DRAGON simulations only. The conservative requirements of 10 CFR 50 Appendix K (Ref. 2-9) are applied in the CHACHA-3C fuel heat-up simulation.

The radial heat conduction equation is solved for the fuel rods (axial conduction is neglected) using an implicit finite-difference technique and the appropriate heat transfer coefficients as boundary conditions (Sec. 3.6).

Detailed models for heat transfer from the pressure vessel and the internal are also included. These components are referred to as "plates". The user can specify any number of heat transferring plates which can be in contact with coolant on both sides or isolated on either side. The one-dimensional heat conduction equation is solved for a user specified nodal subdivision of each plate using a finite difference technique. Each plate can be composed of several different materials (Sec. 3.6).

#### 2.1.4 Power Generation Models

The power generation portion of GOBLIN calculates the fission power, decay power, and heat due to metal-water reaction in the reactor core (Sec. 3.7). The fission power generation in the core is calculated by a reactor point kinetics model allowing for up to six delay neutron groups. Reactivity feedback is included for void fraction, moderator (coolant) temperature (Doppler broadening), fuel temperature, and reactor control rods.

The decay power generation is calculated by the sum of eleven fission product decay groups and the actinide decay of Uranium-239 and Neptunium-239. The power fraction deposited in the fuel and coolant can be specified with time.

The power generation due to the exothermic reaction between the Zircaloy cladding and water is also modelled. The Baker-Just Model (Ref. 2-4) model is used to determine the heat generation due to metal-water reaction.

### 2.1.5 Numerical Methods

The mass, momentum, energy, and state equations along with the pump speed equations are solved simultaneously using Newton's method. The Jacobian matrix includes all derivatives and is inverted using a sparse matrix technique by A. R. Curtis and J. K. Reid (Ref. 2-5). In cases where the solution is close but converges slowly, a predictor-corrector method may be invoked to speed the convergence (Sec. 3.8).

The rod and metal plate conduction equations are solved by Gaussian elimination and back substitution. The conduction equation and the surface heat transfer are solved iteratively for the surface temperature. The point kinetics model is solved using a second order integration method (Sec. 3.8).

The hydraulic model is solved implicitly with time. The thermal conduction and heat transfer models are also solved implicitly with time. The hydraulic and conduction solutions are coupled through the surface heat transfer. The hydraulic fluid conditions are treated implicitly in the heat conduction and heat transfer solution. The surface heat transfer, however, is treated explicitly in the hydraulic solution (Sec. 3.8).

### 2.1.6 DRAGON

The DRAGON code is identical to the GOBLIN code minus several reactor system component models. It also utilizes the GOBLIN code option of specifying external boundary conditions from the results of another transient calculation. The hydraulics, power generation, and thermal models are all identical to that of GOBLIN.

DRAGON is used to simulate the hot fuel channel by specifying the inlet and outlet plenum hydraulic conditions (i.e., pressure and enthalpy) from a GOBLIN simulation. Since DRAGON uses boundary conditions supplied by the full GOBLIN simulation, calculations of the containment, emergency core cooling, reactor protection, level measurement, steam flow, and feedwater flow systems are not required. Hence, calculation of these systems is skipped in a DRAGON simulation. The detailed discussion in Section 3 pertains to both GOBLIN and DRAGON (although most references in the discussion are made only to the GOBLIN code).

## 2.2 CHACHA-3C/BILBO

The CHACHA-3C code calculates the temperature response of each fuel rod at a specified axial location in the hot bundle. Hydraulic boundary conditions are furnished from the DRAGON hot channel thermal hydraulic calculation. The fuel bundle radiation view factors and gray body factors used by CHACHA-3C (and GOBLIN/DRAGON) are calculated by the auxiliary code BILBO.

The following is a summary description of the CHACHA-3C and BILBO codes. A detailed description is given in Sec. 4.

### 2.2.1 Heat-up Analysis: CHACHA-3C

CHACHA-3C contains all of the calculational models necessary for a detailed fuel rod heat-up analysis during a postulated BWR LOCA. The key models in the code are summarized below:

- o The fuel rod conduction model calculates the temperature response throughout the transient of each fuel rod in the bundle cross-section at an axial location (Sec. 4.1). The conduction equation is set up in one-dimensional radial form and solved using an implicit finite-difference method. Heat transfer coefficients at the fuel rod surfaces are supplied by DRAGON for the portions of the transient when Appendix K surface heat transfer coefficients are not required. The coolant temperature used to calculate convective heat transfer is also supplied by DRAGON.
- o The channel temperature model determines the channel temperature transient throughout the postulated LOCA (Sec. 4.2). Heat addition to the channel due to radiation from the rods and gamma heating is accounted for. Convective heat transfer to the coolant is calculated in the same manner as for the fuel rods.
- o The heat generation model calculates the heat generation rates in the fuel, cladding and channel throughout the transient (Sec. 4.3). The magnitude and distribution of the heat sources are specified through input.

- o The metal/water reaction model calculates the heat generation in the cladding due to the exothermic reaction between Zircaloy and water (steam) which occurs at high cladding temperatures (Sec. 4.4). The effect of cladding strain on the reaction rate is included. Reaction on the clad inner surface is also calculated if rod perforation is predicted. The oxide front is tracked throughout the transient, with the heat generated added as a heat source to the appropriate cladding node(s).
  
- o The thermal radiation model calculates the radiation exchange between the fuel rods and the channel surface when the elevation of interest is uncovered (Sec. 4.5). The model allows for anisotropic reflection of radiation. Appendix K-equivalent spray cooling convective heat transfer coefficients which are compatible with the anisotropic reflection assumption are used.
  
- o The gas plenum temperature and pressure model determines the internal gas conditions for each rod throughout the transient (Sec. 4.6). Three gas regions are considered--the plenum, the pellet/cladding gap and the free volume within the pellet stack. The plenum gas temperatures are calculated using a detailed heat transfer model. The effective rod gap and free volume gas temperatures are conservatively assumed to be equal to the gap and pellet average temperatures, respectively, at the elevation of interest. The gas pressure is determined from the ideal gas law.
  
- o The surface wetting model determines the time delay from spray initiation to rewetting of the channel surface at the elevation of interest (Sec. 4.7). This model is based on the modified Yamanouchi correlation recommended in Appendix K. When rewet is calculated to occur the channel temperature is set to saturation, and gray body factors consistent with a wet channel surface are used in the radiation calculation.

- o The pellet/cladding gap heat transfer model calculates the gap conductance throughout the transient based on the gap dimensions and the composition, pressure, and temperature of the gas in the gap (Sec. 4.8). A radiation heat transfer component is added to obtain the total gap heat transfer.
  
- o The cladding strain and rupture model calculates the change in cladding dimensions throughout the transient and determines whether rod perforation has occurred (Sec. 4.9).

### 2.2.2 Radiation Gray Body Factors: BILBO

The gray body factors (GBF) for the anisotropic radiation model are calculated by the auxiliary code BILBO (Sec. 4.5.2). GBF are calculated for wet and dry channel walls, and for strained and unstrained cladding prior to running CHACHA-3C. For each time step in the calculation for which radiation heat transfer is evaluated, CHACHA-3C selects the set of GBF which corresponds to the correct bundle conditions.

BILBO also calculates GBF for the radiation model of the GOBLIN/DRAGON codes. The GBF are for the lumped rod geometries used in the GOBLIN and DRAGON calculations.

## 2.1 References

- 2-1 F. J. Moody, "Maximum Flow Rate of a Single-Component Two-Phase Mixture," J. of Heat Transfer, Trans. ASME, Vol. 87, No. 1, 1965, pp. 134-142.
- 2-2 P. Pana and M. Muller, "Subcooled and Two-Phase Critical Flow States and Comparison with Data," Nuclear Engineering and Design, Vol. 45, pp. 117-120.
- 2-3. Code of Federal Regulations, Title 10 Part 50, Office of the Federal Register National Archives and Records Administration, 1986.
- 2-4 L. Baker, L. C. Just "Studies of Metal-Water Reactions at High Temperatures: III Experimental and Theoretical Studies of Zirconium-Water Reaction," ANL-6548, 1962.
- 2-5 A. R. Curtis and J. K. Reid, "FORTRAN Subroutine for the Solution of Sparse Sets of Linear Equations," AERE-R6844.

TABLE 2-1  
Heat Transfer Regimes

Single-Phase Liquid

- o Laminar Natural Convection
- o Turbulent Natural Convection
- o Laminar Forced Convection
- o Turbulent Forced Convection

Two-Phase Mixture

- o Non-Dryout
  - o Subcooled Boiling
  - o Nucleate Boiling
  - o Flow Boiling
- o Transition Boiling
- o Post-Dryout
  - o Low Flow Film Boiling
  - o Flow Film Boiling
  - o Dispersed Flow
- o Condensation

Single-Phase Vapor

- o Laminar Natural Convection
- o Turbulent Natural Convection
- o Laminar Forced Convection
- o Turbulent Forced Convection

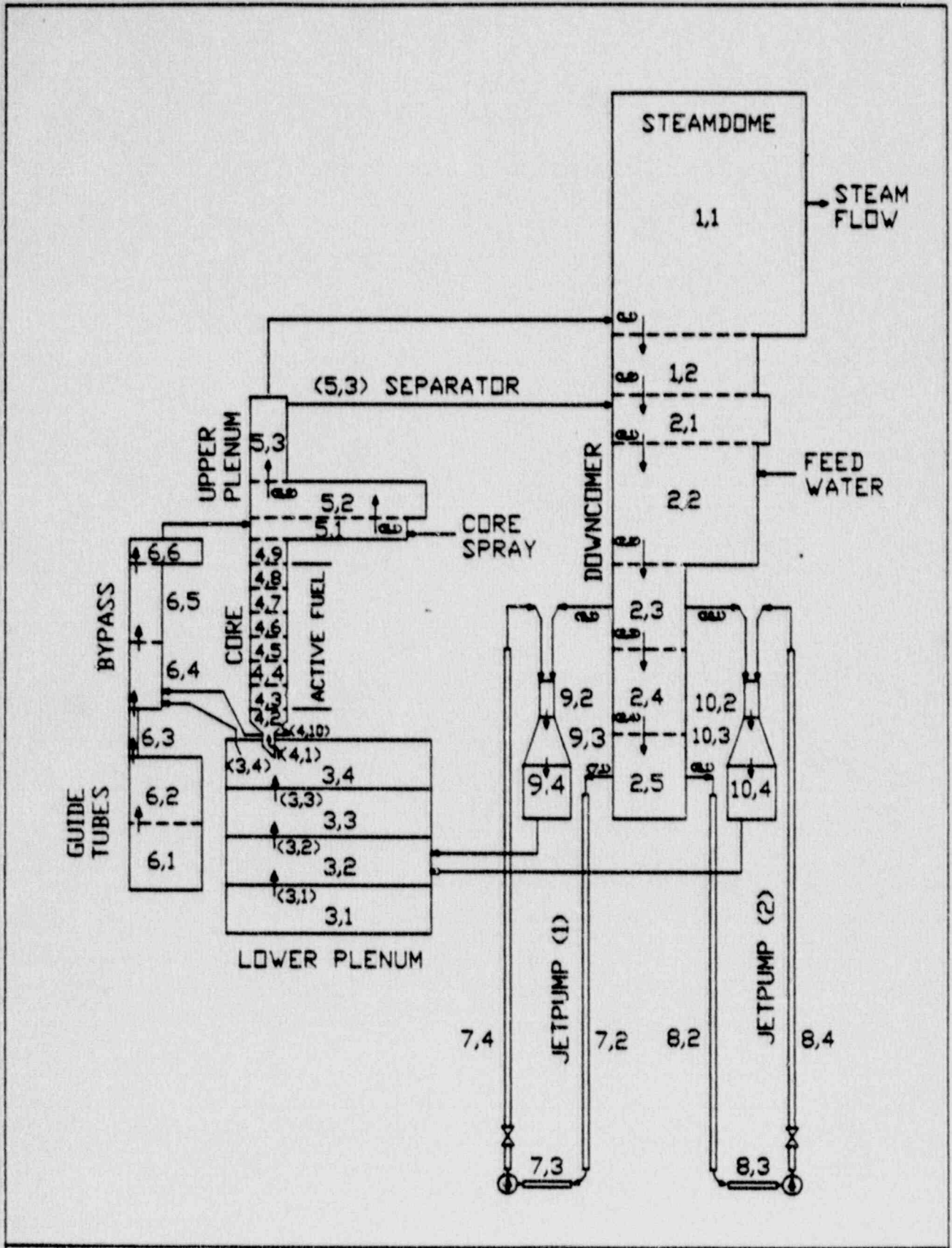


Figure 2-1 - Sample GOBLIN Geometrical Representation of Reactor



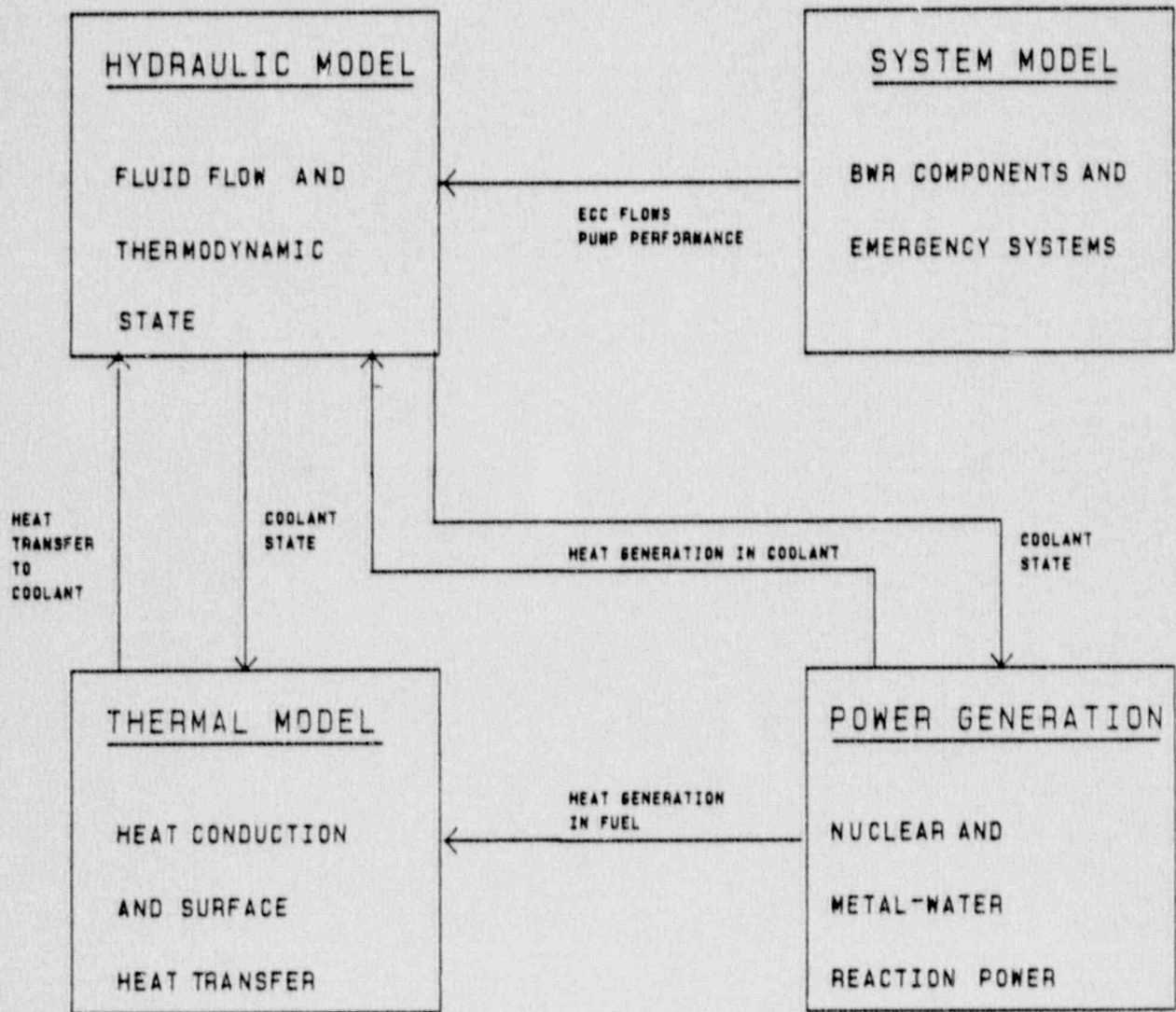


Figure 2-2 - Structure of GOBLIN Code

### 3. THERMAL HYDRAULIC ANALYSIS CODES: GOBLIN/DRAGON

In this chapter the conservation equations, constitutive models, and numerics of the GOBLIN and DRAGON codes are described in detail. The hydraulic conservation equations and associated constitutive and component models are presented first. The thermal heat transfer and conduction models are described next, followed by the power generation models, and then the numerical solution methods.

#### 3.1 Basic Conservation Equations

The basic equations for the mass, energy, and momentum conservation are formulated together with an equation of state. The equations are based on the assumptions of one-dimensional, drift-flux, thermal-equilibrium flow. The calculation of fluid energy transport accounts for the different flow velocities and flow directions of the liquid and vapor phases.

The conservation equations are integrated over control volumes. Source and sink terms are added to the integrated mass and energy balances to account for break flow, steam line flow, steam-water separator and steam dryer behavior, and coolant injection from various systems.

The derivations shown in the following consider a single inlet and outlet flow. Actually in the GOBLIN code the inlet and outlet flows may be comprised of several flow paths.

### 3.1.1 Mass Conservation Equation

#### Theoretical Basis

The mass conservation equation for the mixture (Ref. 3-1) is

$$\frac{\partial \rho}{\partial t} = -\nabla \cdot (\rho \underline{U}) \quad (3.1-1)$$

Integrating Eq. (3.1-1) over a one-dimensional control volume as shown in Figure 3-1(a), yields

$$\frac{\partial M}{\partial t} = w_1 - w_2 + w_{src} \quad (3.1-2)$$

where  $w$  is the mass flow rate and  $w_{src}$  accounts for mass source and sink terms;

$$w_{src} = -w_{br} + w_{st} + w_{sep} + w_{cond}$$

$$w_{br} = \text{Break flow rate from control volume}$$

$$w_{st} = \text{Coolant inflow to control volume from various systems (e.g. feedwater, spray)}$$

$$w_{sep} = \text{Coolant inflow to control volume from separator outlets}$$

$$w_{cond} = \text{Coolant inflow to control volume from steam dryer outlets}$$

$$w_1 = \text{Inlet flow to control volume}$$

$$w_2 = \text{Exit flow from control volume}$$

Calculation of break flows, coolant inflow from separator and steam dryer outlets and the inflow from the systems are described in Sec. 3.3 and 3.4.

### Finite Difference Formulation of the Mass Equation

Consider the following flow path shown in Fig. 3-1(b). The integrated mass conservation equation is written in finite difference form using a fully implicit finite difference scheme. Hence Eq. (3.1-2) becomes:

$$\frac{m_i^{n+1} - m_i^n}{\Delta t} - w_{i-1}^{n+1} + w_i^{n+1} - w_{src,i}^{n+1} = 0 \quad (3.1-3)$$

where superscripts n and n+1 denote time  $t_n$  and  $t_{n+1}$ , respectively, and the subscripts denote fluid control volumes.

### 3.1.2 Energy Conservation Equation

#### Theoretical Basis

The general form of the conservation of energy equation (Ref. 3-1) is

$$\frac{\partial(e\rho)}{\partial t} + \nabla \cdot (e\rho\mathbf{u}) + \nabla \cdot \mathbf{q}'' - \mathbf{q}''' - \nabla \cdot (\mathbf{q} \cdot \mathbf{u}) = 0 \quad (3.1-4)$$

where

$$e = e_{int} + e_{kin} + e_{pot} = \text{total specific energy} \quad (3.1-5)$$

$$e_{int} = \text{internal (thermodynamic) energy}$$

$$e_{kin} = \frac{1}{2} \mathbf{u} \cdot \mathbf{u} = \text{kinetic energy}$$

$e_{\text{pot}}$  = potential energy

$\rho$  = density

$\underline{u}$  = velocity field vector

$q''$  = heat flux

$q'''$  = internal heat generation per unit volume

$\sigma$  = stress tensor

The specific enthalpy  $h$  is introduced, (3.1-6)

$$h = e_{\text{int}} + p/\rho$$

and the stress tensor is divided into a normal and shear stress

$$\sigma_{ij} = -p\delta_{ij} + \bar{\sigma}_{ij} \quad (3.1-7)$$

where  $\delta_{ij}$  is the kronecker delta, defined

$$\delta_{ij} = \begin{cases} 0 & \text{if } i \neq j \\ 1 & \text{if } i = j \end{cases} \quad (3.1-8)$$

$p$  = Local static pressure

and

$$\bar{\sigma}_{ij} = \sigma_{ij} - \left( \sum_{k=1}^3 \frac{\sigma_{kk}}{3} \right) \cdot \delta_{ij} \quad (3.1-9)$$

The term  $\sigma_{ij}$  is the stress deviator representing the part of the forces in the fluid which are due to relative motion of nearby particles in the fluid.

Equation (3.1-4) is now rewritten

$$\begin{aligned} \frac{\partial}{\partial t} (h\rho - p) + \nabla \cdot (h\rho \underline{u}) + \nabla \cdot \underline{q}'' - \dot{q}''' = \\ - \frac{\partial}{\partial t} (\rho(e_{kin} + e_{pot})) - \nabla \cdot (\rho(e_{kin} + e_{pot})\underline{u}) \\ + \nabla \cdot (\underline{q} \cdot \underline{u}) \end{aligned} \quad (3.1-10)$$

The right hand side of Eq. (3.1-10) represents the contributions from kinetic and potential energy, and dissipation due to stress. In Appendix 3A it is demonstrated that the right hand side of equation (3.1-10) can be neglected, hence the energy equation used in the GOBLIN code is

$$\frac{\partial}{\partial t} (h\rho - p) + \nabla \cdot (h\rho \underline{u}) + \nabla \cdot \underline{q}'' - \dot{q}''' = 0 \quad (3.1-11)$$

#### Finite Difference Formulation of the Energy Equation

Equation (3.1-11) is integrated over the control volume shown in Fig. 3-2. The integration is performed below term by term.

The first term is

$$\begin{aligned} \int_V \frac{\partial}{\partial t} (h\rho - p) dV &= \frac{d}{dt} \int_V (h\rho - p) dV \\ &= \frac{d}{dt} (m \cdot \bar{h}) - V \frac{d}{dt} \bar{p} \end{aligned} \quad (3.1-12)$$

where

$$m = \int_V \rho dV \quad = \text{The mass of the control volume}$$

$$\bar{h} = (\int_V h \rho dV) / m \quad = \text{Mean enthalpy of the control volume}$$

$$\bar{p} = \int_V \rho dV / \int_V dV \quad = \text{Mean pressure of the control volume}$$

The second term, applying the divergence theorem, gives

$$\int_V \nabla \cdot (h \rho \underline{u}) dV = \int_S h \rho \cdot \underline{u} \cdot \underline{n} dS$$

Since  $\underline{u} = 0$  on the rigid boundaries, the surface integral reduces to

$$\begin{aligned} \int_V \nabla \cdot (h \rho \underline{u}) dV &= \int_{A_2} h \rho u_x dA + \int_{A_1} h \rho u_x dA + \int_{A_{src}} h \rho \underline{u} \cdot \underline{n} dA \\ &= wh_2 - wh_1 + wh_{src} \end{aligned} \quad (3.1-13)$$

The calculation of the enthalpy flow terms,  $wh$ , is discussed in detail in Section (3.3.1).

The term  $wh_{src}$  is the enthalpy flow source due to leaks or coolant addition to the control volume (e.g., break flow, feedwater flow).

The third term, applying the divergence theorem, gives

$$\begin{aligned} \int_V \nabla \cdot \underline{q}'' dV &= \int_S \underline{q}'' \cdot \underline{n} dS \\ &= Q_A \end{aligned} \quad (3.1-14)$$

where  $Q_A$  is the surface heat transfer and the conduction over the fluid surfaces  $A_1$  and  $A_2$  have been neglected.

The heat flux due to conduction within the fluid clearly can be neglected for LOCA analysis when comparing the magnitude of terms two and three. The fluid conduction is of the order

$$q'' = -k \cdot dT/dx = - (0.7 \text{ W/m}^\circ\text{K}) (10^\circ\text{K/m}) = 7 \text{ W/m}^2 (2.2 \text{ Btu/hr ft}^2)$$

or less, which is clearly negligible when compared to the energy transported by the fluid of the order  $10^9 - 10^{10} \text{ W/m}^2$  ( $3.2 \times 10^8 - 3.2 \times 10^9 \text{ Btu/hr-ft}^2$ ).

The calculation of  $Q_A$  is described in Sec. 3.5 and 3.6.

The fourth term

$$\int_V q''' dV = Q_V$$

The term  $Q_V$  consists of internal heat generation due to neutron and gamma absorption and scattering in the fluid. The term  $Q_V$  is lumped together with  $Q_A$  and the sum is the net heat source

$$Q = Q_A + Q_V \tag{3.1-15}$$

The integrated energy equation can now be written

$$d(M\bar{H})/dt - V \cdot d\bar{p} + wh_2 - wh_1 - wh_{src} - Q = 0 \tag{3.1-16}$$



The fully implicit finite difference form of Eq. (3.1-16), used in GOBLIN, is

$$\frac{m_i^{n+1} h_i^{n+1} - m_i^n h_i^n}{\Delta t} - \frac{V_i (p_i^{n+1} - p_i^n)}{\Delta t} + (wh)_i^{n+1} - (wh)_{i-1}^{n+1} - Q^{n+1} - (wh)_{src,i}^{n+1} = 0 \quad (3.1-17)$$

Figure 3-2(b) shows schematically the energy control volume.

### 3.1.3 Momentum Conservation Equation

#### Theoretical Basis

The general formulation for the momentum equation (Ref. 3-1) is

$$\frac{\partial}{\partial t} (\rho \underline{u}) = - [\nabla \cdot \rho \underline{u} \underline{u}] - \nabla p \quad (3.1-18)$$

(a)                      (b)                      (c)

$$- [\nabla \cdot \tau] - \rho \underline{g}$$

(d)                      (e)

where the terms in Eq. (3.1-18) are

- (a) - Rate of increase of momentum
- (b) - Rate of momentum gain by convection
- (c) - Pressure force
- (d) - Rate of momentum gain due to viscous stress
- (e) - Gravitational force

Equation (3.1-18) is integrated over a fixed control volume  $V$  with solid surfaces  $S$ ,

$$\iiint_V \frac{\partial}{\partial t} (\rho \underline{u}) dV = \iiint_V (- [\nabla \cdot \rho \underline{u} \underline{u}] - \nabla p - [\nabla \cdot \underline{\tau}] - \rho \underline{g} ) dV \quad (3.1-19)$$

The Gauss divergence theorem is applied to the first and third terms on the right-hand side of Eq. (3.1-19) giving

$$\iiint_V \nabla \cdot \rho \underline{u} \underline{u} dV = \iint_S \rho \underline{u} \underline{u} \cdot \underline{n} dS \quad (3.1-20)$$

$$\iiint_V \nabla \cdot \underline{\tau} dV = \iint_S \underline{\tau} \cdot \underline{n} dS \quad (3.1-21)$$

where  $\underline{n}$  is the outward normal vector of surface element  $dS$ .

Substituting Eq. (3.1-20) and (3.1-21) into Eq. (3.1-19) yields

$$\begin{aligned} \iiint_V \frac{\partial}{\partial t} (\rho \underline{u}) dV = & - \iint_S \rho \underline{u} \underline{u} \cdot \underline{n} dS - \iiint_V \nabla p dV \\ & - \iint_S \underline{\tau} \cdot \underline{n} dS - \iiint_V \rho \underline{g} dV \end{aligned} \quad (3.1-22)$$

Assuming the flow is one-dimensional the left-hand side of Eq. (3.1-22) can be integrated from a point 1 to a point 2, at a distance  $2\Delta x$  from point 1 (see Fig. 3-3(a)), gives

$$\begin{aligned} \iiint_V \frac{\partial}{\partial t} (\rho \underline{u}) dV &= \frac{\partial}{\partial t} \int_{x_1}^{x_2} \left[ \iint_{A(x)} \rho \underline{u} dA \right] dx \\ &= \frac{\partial}{\partial t} \int_{x_1}^{x_2} \rho \underline{u} A(x) dx = \bar{A} \frac{\partial(\rho \underline{u})}{\partial t} 2\Delta x \end{aligned} \quad (3.1-23)$$

The bar represents an average value. The first term on the right-hand side of Eq. (3.1-22) can be rewritten

$$\begin{aligned} - \iint_S \rho \underline{u} \underline{u} \cdot \underline{n} dS &= - \left[ \iint_{A_1} \rho u^2 (-dA) + \iint_{A_2} \rho u^2 dA \right] \\ &= \rho_1 u_1^2 A_1 - \rho_2 u_2^2 A_2 \end{aligned} \quad (3.1-24)$$

since the solid surfaces do not contribute to this term ( $\underline{u} \cdot \underline{n} = 0$ ).

For a one-dimensional flow the second term on the right-hand side of Eq. (3.1-22) can be similarly integrated and expressed in terms of average values

$$\begin{aligned} - \iiint_V \nabla p dV &= - \int_{x_1}^{x_2} \left[ \iint_{A(x)} \frac{\partial p}{\partial x} dA \right] dx \\ &= - \bar{A} \frac{\partial p}{\partial x} 2\Delta x \end{aligned} \quad (3.1-25)$$

The third term on the right-hand side of Eq. (3.1-22) is the unrecoverable friction loss term and can be rewritten as

$$- \iint_S \underline{\tau} \cdot \underline{n} dS = - \int_{x_1}^{x_2} \tau P_w dx = - \overline{\tau \cdot P_w} 2\Delta x \quad (3.1-26)$$

where  $P_w$  is the wetted perimeter.

The fourth term on the right-hand side of equation (3.1-22) can be similarly integrated yielding

$$-\iiint_V \rho g \, dV = -\bar{A} g (\rho_2 z_2 - \rho_1 z_1) \quad (3.1-27)$$

where  $z$  is the vertical distance between points 1 and 2.

Substituting Eqs. (3.1-24) through (3.1-27) into equation (3.1-22) yields

$$\begin{aligned} \bar{A} \frac{\partial(\bar{\rho}U)}{\partial t} 2\Delta x &= \rho_1 u_1^2 A_1 - \rho_2 u_2^2 A_2 - \bar{A} \frac{\partial p}{\partial x} 2\Delta x \\ &\quad - \tau P_w 2\Delta x - \bar{A} g(\rho_2 z_2 - \rho_1 z_1) \end{aligned} \quad (3.1-28)$$

Dividing by  $2\Delta x$  and taking the limit as  $\Delta x$  goes to 0, yields

$$A \frac{\partial(\bar{\rho}U)}{\partial t} = - \frac{\partial}{\partial x} (\rho U^2 A) - A \frac{\partial p}{\partial x} - \tau P_w - A \frac{\partial}{\partial x} (\rho g z) \quad (3.1-29)$$

Expressing equation (3.1-29) in terms of mass flow rate

$$w = \rho A U$$

and dividing by  $A$  give the one-dimensional momentum equation used in GOBLIN

$$\frac{1}{A} \frac{\partial w}{\partial t} = - \frac{1}{A} \frac{\partial}{\partial x} \left( \frac{w^2}{\rho A} \right) - \frac{\partial p}{\partial x} - \frac{\tau P_w}{A} - \frac{\partial}{\partial x} (\rho g z) \quad (3.1-30)$$

### Finite Difference Formulation of The Momentum Equation

In this section the mathematical formulation of the momentum equation will be written in the finite difference form used in GOBLIN.

Consider the following flow path shown in Fig. 3-3(b). Equation (3.1-30) is integrated between points  $x_i$  and  $x_{i+1}$  to give

$$\int_{x_i}^{x_{i+1}} \frac{1}{A} \frac{\partial w}{\partial t} dx = \int_{x_i}^{x_{i+1}} \frac{1}{A} \frac{\partial}{\partial x} \left( \frac{w^2}{\rho A} \right) dx$$

$$- \int_{x_i}^{x_{i+1}} \frac{\partial p}{\partial x} dx - \int_{x_i}^{x_{i+1}} \frac{\tau P}{A} w dx - \int_{x_i}^{x_{i+1}} \frac{\partial}{\partial x} (\rho g z) dx \quad (3.1-31)$$

### Temporal acceleration term

The temporal acceleration between control volumes at  $i$  and  $i+1$  is modelled as an inertia,  $I_i$ , times the fluid acceleration, thus

$$\int_{x_i}^{x_{i+1}} \frac{1}{A} \frac{\partial w}{\partial t} dx = \frac{\partial w_i}{\partial t} \int_{x_i}^{x_{i+1}} \frac{1}{A} dx = I_i \frac{\partial w_i}{\partial t} \quad (3.1-32)$$

### Pressure gradient

$$- \int_{x_i}^{x_{i+1}} \frac{\partial p}{\partial x} dx = - (p_{i+1} - p_i) \quad (3.1.33)$$

### Gravitation

$$\int_{x_i}^{x_{i+1}} \frac{\partial}{\partial x} (\rho g z) dx = \int_{x_i}^{x_i + \Delta x_i} \frac{\partial}{\partial x} (\rho g z) dx + \int_{x_i + \Delta x_i}^{x_{i+1}} \frac{\partial}{\partial x} (\rho g z) dx$$

$$= (\rho_i \Delta z_i + \rho_{i+1} \Delta z_{i+1}) g \quad (3.1-34)$$

where

$$\Delta z_i = z_{junc} - z_i$$

$$\Delta z_{i+1} = z_{i+1} - z_{junc}$$

$$z_{junc} = \text{Junction elevation}$$

$$z_i = \text{Elevation of the midpoint of control volume } i$$

Unrecoverable pressure losses

The unrecoverable pressure losses are divided into a wall friction term,  $\Delta p_f$ , and a term corresponding to unrecoverable pressure losses,  $\Delta p_l$ , due to area changes.

$$-\int_{x_i}^{x_{i+1}} \frac{\tau_w}{A} dx = -\Delta p_{f,i} - \Delta p_{f,i+1} - \Delta p_{l,i} \quad (3.1-35)$$

$$\Delta p_{f,i} = f_i \frac{\Delta x_i}{D_{h,i}} \frac{\bar{w}_i}{2} \frac{|\bar{w}_i|}{A_i^2} \frac{1}{\rho_i} \beta_i^2 \quad (3.1-36)$$

where

$$f_i = \text{Single-phase friction factor (see Sec. 3.3.2)}$$

$$\beta_i^2 = \text{Two phase wall friction multiplier (see Sec. 3.3.2)}$$

$$\beta_i^2 = \begin{cases} p_{f,i} & \text{For single-phase liquid and two-phase mixture when } w_{f,i} \geq 0 \\ p_{f,i+1} & \text{For single-phase liquid and two-phase mixture when } w_{f,i} < 0 \\ p_{g,i} & \text{For single-phase vapor when } w_{g,i} \geq 0 \\ p_{g,i+1} & \text{For single-phase vapor when } w_{g,i} < 0 \end{cases}$$

The area change pressure loss is calculated according to

$$\Delta p_{l,i} = \xi_k \frac{\bar{w}_i \cdot |\bar{w}_i|}{2 A_L^2} \cdot \frac{1}{\rho_L} \rho_L^2 \quad (3.1-37)$$

where

$\xi_k$  = Flow resistance coefficient (which may depend on the flow direction) (see Sec. 3.3.4)

$$k = \begin{cases} i & \text{if } \bar{w}_i \geq 0 \\ i+1 & \text{if } \bar{w}_i < 0 \end{cases}$$

$A_L$  = Local restriction flow area

$\phi_L^2$  = Local pressure drop two-phase multiplier (see Sec. 3.3.4)

### Spatial acceleration

The momentum flux term

$$\int_{x_i}^{x_{i+1}} \frac{1}{A} \frac{\partial}{\partial x} \left( \frac{w^2}{\rho A} \right) dx$$

is formulated using the ZIP differencing technique (Ref. 3-2).

$$\int_{x_i}^{x_{i+1}} \frac{1}{A} \frac{\partial}{\partial x} \frac{w^2}{\rho A} dx = \frac{1}{A^*} \left[ \frac{\bar{w}_i \bar{w}_{i+1}}{A_{i+1} \rho_{i+1}} - \frac{\bar{w}_i \bar{w}_{i-1}}{\rho_i A_i} \right] \quad (3.1-38)$$

The area  $A^*$  is derived by comparing the momentum to the Bernoulli equation for steady, incompressible, inviscid fluid flow. The Bernoulli equation is

$$p_i - p_{i+1} = \frac{1}{2} \frac{w^2}{\rho A_{i+1}^2} - \frac{1}{2} \frac{w^2}{\rho A_i^2} \quad (3.1-39)$$

The momentum equation is

$$p_i - p_{i+1} + \frac{1}{A^*} \left[ \frac{w^2}{\rho} \left( \frac{1}{A_i} - \frac{1}{A_{i+1}} \right) \right] = 0 \quad (3.1-40)$$

Equating the two equations, and eliminating the pressure difference terms,

$$\frac{1}{2} \frac{w^2}{\rho} \left( \frac{1}{A_{i+1}^2} - \frac{1}{A_i^2} \right) = \frac{1}{A^*} \frac{w^2}{\rho} \left( \frac{1}{A_{i+1}} - \frac{1}{A_i} \right) \quad (3.1-41)$$

and solving for  $A^*$  gives

$$\frac{1}{A^*} = \frac{1}{2} \left( \frac{1}{A_i} + \frac{1}{A_{i+1}} \right) \quad (3.1-42)$$

Finally inserting Eqs. (3.1-32) through (3.1-38) into Eq.

(3.1-31) yields

$$I_i \frac{\partial \bar{w}_i}{\partial t} = p_i - p_{i+1} - 0.5 \bar{w}_i \left| \bar{w}_i \right| \left\{ f_i \frac{\Delta x_i}{D_{h,i}} \frac{\beta_i^2}{A_i^2 \rho_L} + f_{i+1} \frac{\Delta x_{i+1}}{D_{h,i+1}} \frac{\beta_{i+1}^2}{A_{i+1}^2 \rho_L} + \epsilon_k \cdot \frac{\beta_1^2}{A_k^2 \rho_L} \right\} - (\rho_i \Delta z_i + \rho_{i+1} \Delta z_{i+1}) g$$



$$\begin{aligned}
& - \frac{1}{A^*} \left[ \frac{\bar{w}_i \bar{w}_{i+1}}{p_{i+1} A_{i+1}} - \frac{\bar{w}_i \bar{w}_{i-1}}{p_i A_i} \right] \\
& + FP_i \cdot \Delta p_{\text{pump}}
\end{aligned} \tag{3.1-43}$$

where

$$FP_i = \begin{cases} 0 & \text{if no pump is present in control volume } i \\ 1 & \text{if a pump is present in control volume } i \end{cases}$$

A fully implicit finite difference scheme is used to represent the momentum equation. The time derivative is approximated by

$$\frac{\partial w_i}{\partial t} = \frac{\bar{w}_i^{n+1} - \bar{w}_i^n}{\Delta t} \tag{3.1-44}$$

All other state variables are calculated at  $t_{n+1}$ . Thus the momentum equation programmed in GOBLIN is

$$\begin{aligned}
I_i \frac{\bar{w}_i^{n+1} - \bar{w}_i^n}{\Delta t} &= p_i^{n+1} - p_{i+1}^{n+1} \\
-0.5 \bar{w}_i^{n+1} | \bar{w}_i | & \left[ f_i \frac{\Delta x_i}{D_{h,i}} \frac{\beta_i^2}{A_{iP_L}^2} + f_{i+1} \frac{\Delta x_{i+1}}{D_{h,i+1}} \frac{\beta_{i+1}^2}{A_{i+1P_L}^2} \right. \\
& \left. + \xi_k \cdot \frac{\beta_L^2}{A_{LP_L}^2} \right]^{n+1} \\
& - (p_i \Delta z_i + p_{i+1} \Delta z_{i+1})^{n+1} g
\end{aligned}$$

$$\begin{aligned}
& - \frac{1}{A^*} \left[ \frac{\bar{w}_i \bar{w}_{i+1}}{p_{i+1} A_{i+1}} - \frac{\bar{w}_i \bar{w}_{i-1}}{p_i A_i} \right]^{n+1} \\
& + F p_i \cdot \Delta p^{n+1}
\end{aligned}
\tag{3.1-45}$$

## 3.2 Fluid State Equation

### 3.2.1 Thermodynamic and Fluid Properties of Water and Steam

During one calculation cycle within the GOBLIN code many evaluations of thermodynamic and transport properties of water and steam are made. The quantities evaluated are:

- Density of subcooled and saturated water
- Density of superheated and saturated steam
- Saturation temperature
- Enthalpy of saturated water
- Enthalpy of saturated steam
- Temperature of subcooled water
- Temperature of subcooled steam
- Dynamic viscosity of water and steam
- Surface tension
- Heat capacity of water and steam
- Thermal conductivity of water and steam
- Volume coefficient expansion for steam

These quantities are computed according to Ref. 3-3 which is based upon 1967 IFC formulation of properties of steam. The basic independent variables in the GOBLIN code are pressure and enthalpy. In the IFC formulation the pressure and temperature are usually the independent variables. Hence, given the pressure and the enthalpy, the temperature is first calculated then the other property.

### 3.2.2 Equation of State

The equation of state

$$\rho = \rho(p, h) \quad (3.2-1)$$

is included in a volume balance for each control volume

$$m_i/\rho_i - V_i = 0 \quad (3.2-2)$$

For single-phase liquid or vapor the density,  $\rho$ , is given by Eq. (3.2-1) through correlations of the thermodynamic properties. For two-phase flow, the mixture density is calculated from

$$\rho = \rho_f + \alpha (\rho_g - \rho_f) \quad (3.2-3)$$

where the void fraction,  $\alpha$ , is given by

$$\alpha = \frac{h - h_f}{h \left(1 - \frac{\rho_g}{\rho_f}\right) + h_g \frac{\rho_g}{\rho_f} - h_f} \quad (3.2-4)$$

### 3.3 Constitutive Models

#### 3.3.1 Two-Phase Energy Flow Model

In single-phase flow the enthalpy flow rate is determined by

$$\dot{w}h = \dot{w} \cdot h$$

where the "donor cell" concept is used i.e., the enthalpy,  $h$ , is taken as that of the control volume from which flow is leaving. The enthalpy flow rate for two-phase flow is determined from a drift-flux correlation developed from the work of Holmes (Ref. 3-4) and includes a countercurrent flow limitation correlation of the form defined by Wallis (Ref. 3-5).

#### Drift Flux Formulation

The drift flux formulation for relative motion between two phases (Ref. 3-6) is

$$j_g = C_0 j_a + V_{gj} a \quad (3.3-1)$$

where  $j$  is the superficial velocity and the concentration coefficient,  $C_0$ , and the drift velocity  $V_{gj}$  are defined by empirical correlations.

The above expression can be transformed into an analogous expression for mass flux.

$$G_g = X^* G + G_d \quad (3.3-2)$$

or

$$G_d = (1-X^*) G_g - X^* G_f \quad (3.3-3)$$

where  $G$  is the mass flux,  $G_d$  is the mass drift flux and  $X^*$  is the flow quality. The flow quality for local homogeneous flow is related to the void fraction by

$$X^* = \frac{a C_o}{a C_o + \frac{P_f}{P_g} (1 - a C_o)} \quad (3.3-4)$$

The mass drift flux is related to  $V_{gj}$  by

$$G_d = \frac{P_f X^*}{C_o} V_{gj} \quad (3.3-5)$$

Hence  $G_d$  and  $X^*$  used in GOBLIN are analogous to the coefficients  $C_o$  and  $V_{gj}$ .

#### Concentration Coefficient Correlation

The flow quality,  $X^*$ , is evaluated from Eq. (3.3-4) for a given void fraction, phase densities, and concentration coefficient. The concentration coefficient,  $C_o$ , is given by (Ref. 37).

$$C_o = \frac{1}{a + (1-a)a^b} \quad (3.3-6)$$

where

$$a = \left[ \begin{array}{l} \\ \\ \end{array} \right]^{a, c, g} \quad (3.3-7)$$

$$b = \left[ \begin{array}{l} \\ \\ \end{array} \right] \quad (3.3-8)$$

and  $P_{crit}$  is the critical pressure (221.2 bar) and  $P_{1000}$  is the pressure at 1000 psia (68.94 bar).

### Countercurrent Flow Limitation Correlation

The mass drift flux,  $G_d$ , is determined from requiring the drift flux correlation to be tangent to the countercurrent flow limitation (CCFL) correlation and then assumed applicable at all mass fluxes for a given  $X^*$  (void fraction and pressure).

First the CCFL correlation used in GOBLIN is described, then an expression for  $G_d$  is derived.

In the countercurrent flow region, there is a physical limit to the downward water flow for a given upward steam flow. Countercurrent flow limitation has been described by Wallis (Ref. 3-5) for flow in vertical tubes, with the dimensionless relationship,

$$\left( \frac{j_g^{1/2}}{g \cos \theta D (\rho_f - \rho_g)} \right)^{1/4} + \left( \frac{K_1 (-j_f)^{1/2}}{g \cos \theta D (\rho_f - \rho_g)} \right)^{1/4} = K_2 \quad (3.3-9)$$

where  $K_1 = 1.0$  and  $K_2 = 0.8-1.0$  depending on water inlet geometry.

Defining the characteristic length as

$$D_L = \left[ \frac{\sigma}{g \Delta \rho} \right]^{1/2}$$

dividing both sides by  $D_L^{1/4}$  and multiplying by  $D^{1/4}$  gives

$$\frac{j_g^{1/2}}{(\cos^2 \theta \frac{\sigma g \Delta \rho}{2})^{1/8} \rho_g} + \frac{K_1 (-j_f)^{1/2}}{(\cos^2 \theta \frac{\sigma g \Delta \rho}{2})^{1/8} \rho_f} = \frac{K_2 D^{1/4}}{\frac{\sigma}{g \Delta \rho}}^{1/8} = Ku^{1/2} \quad (3.3-10)$$

The value of the coefficients that best fit the ASEA-ATOM 8x8 bundle geometry data (Ref. 3-7) are

$$K_1 = [ \quad ]^{a,c,g}$$

$$K_u = [ \quad ]^{a,c,g}$$

where the constant  $[ \quad ]^{a,c,g}$  is meter<sup>1/4</sup> and is based on the bundle area. The pressure dependence of  $D_L$  is small, about 4 percent between 1 and 5 bar (15-75 psia). At a pressure of 1 bar  $K_u = [ \quad ]^{a,c,g}$ . This value is used in the subsequent correlation.

The experiments in Ref. 3-7 cover a relatively high values of void fraction. At lower void fractions, another approach is necessary. This is described later in this section.

Holmes (Ref. 3-4) reported a geometry dependence of CCFL as a function of the dimensionless pipe diameter  $D^*$  in the form  $(D^*-2)/(D^*+2.5)$  where

$$D^* = \left( \frac{g \Delta \rho}{\sigma} \right)^{1/2} \cdot D = \frac{D}{D_L} \quad (3.3-11)$$

and  $D$  is the pipe diameter.

Replacing  $D$  by  $P_w/\pi$  in Eq. (3.3-11) where  $P_w$  is the wetted perimeter for the geometry in question, and incorporating Holmes geometry dependence, gives

$$K_1 = [ \quad ]^{a,c,g}$$

$$K_{u1} = [ \quad ]^{a,c,g} \quad (3.3-12)$$

where

$$D^* = P_w / (\pi D_L)$$

This expression is valid for both pipes and rod bundle with void fractions between  $[\alpha]^{a,c,g}$ . The value of  $[\alpha]^{a,c,g}$  is justified since for rod bundle  $P_w \gg D_L$  and  $Ku_1$  reduces to  $[\alpha]^{a,c,g}$ . The slight pressure dependent of  $Ku$  in Eq. (3.3-11) which is not accounted for here is within the normal scatter of the data for  $Ku$  between 1-10 bars (15-150 psia).

According to the data of Bailey et al, Ref. 3-8 there is a transition between two relations for  $Ku$  as void fraction increases. The above relation is applicable at  $[\alpha]^{a,c,g}$  and the other relation is applicable at  $[\alpha]^{a,c,g}$ . This latter relation, given by Holmes has been modified to include the geometry dependences, thus

$$Ku_2 = \left[ \frac{D_h}{D} \right]^{a,c,g} \quad (3.3-13)$$

where  $D_h$  is the hydraulic diameter.

For the transition interval between  $[\alpha]^{a,c,g}$   $Ku$  is of the form

$$Ku = f(\alpha) Ku_2 + [1 - f(\alpha)] Ku_1 \quad (3.3-14)$$

where

$$f(\alpha) = (\alpha - \alpha_2)^2 / [(\alpha - \alpha_2)^2 + (\alpha - \alpha_1)^2]$$

$$\alpha_1 = [\alpha]^{a,c,g}$$

$$\alpha_2 = [\alpha]^{a,c,g}$$

This expression is due to Holmes, and fits the Bailey data well (see Fig. 3-4).

The resultant CCFL correlation used is Eq. (3.3-10) with  $K_1 = [\alpha]^{a,c,g}$  and  $Ku$  is calculated from Eq. (3.3-12), (3.3-13) or (3.3-14) for void fraction ranges of  $[\alpha]^{a,c,g}$ , respectively.



### Mass Drift Flux

Now the mass drift flux,  $G_d$ , can be calculated from the CCFL correlation. Using the following definitions

$$j_g = G_g/\rho_g ; j_f = G_f/\rho_f ; V_c = \left( \frac{g \Delta p_c}{\rho_f} \right)^{1/4} \quad (3.3-15)$$

in Eq. (3.3-10) give

$$\left( \frac{G_g \sqrt{\rho_f/\rho_g}}{\rho_f K_u V_c} \right)^{1/2} + \left( \frac{-G_f}{\rho_f K_u V_c} \right)^{1/2} = 1 \quad (3.3-16)$$

For the countercurrent flow regime, and for void fractions greater than  $\left[ \quad \right]^{a,c,g}$ , the drift flux relation, Eq. (3.3-3) gives lines of constant  $\alpha$  which are tangential to the CCFL limit curve, Eq. (3.3-16). This relationship is shown in Fig. 3-5. The resultant expression is

$$G_d = \frac{X^*(1-X^*)\rho_f K_u V_c}{1 - X^* \sqrt{\frac{\rho_f}{\rho_g}} X^*} \quad (3.3-17)$$

### Application of the Drift Flux Model in GOBLIN

The mass drift flux correlation used in GOBLIN is

$$G_g = X^* G + G_d \quad (3.3-18)$$

where  $X^*$  is given by Eq. (3.3-4),  $G_d$  is given by Eq. (3.3-17). Then

$$\begin{aligned}
 G_f &= G - G_g \\
 &= (1-X^*) G - G_d
 \end{aligned}
 \tag{3.3-19}$$

The drift flux correlation is used to split the total mass flux  $G$  into its steam and water components,  $G_g$  and  $G_f$ , so that the enthalpy transport,  $wh$ , can be calculated from

$$wh = A \cdot (G_g \cdot h_s + G_f \cdot h_w) \tag{3.3-20}$$

To explain the calculation of the energy transport between two volumes, consider the case of a vertical flow path between two volumes  $y$  and  $z$  with the positive direction corresponding to upward flow (see Fig. 3-6). The steam and water enthalpy in Eq. (3.3-20) are determined from

$$h_s = \begin{cases} h_{sy} & G_g \geq 0 \\ h_{sz} & G_g < 0 \end{cases} \tag{3.3-21}$$

$$h_w = \begin{cases} h_{wy} & G_f \geq 0 \\ h_{wz} & G_f < 0 \end{cases} \tag{3.3-22}$$

The flow quality used in Eq. (3.3-18) is calculated from Eq. (3.3-4), which is a function of pressure and void fraction. The average pressure,  $p_m$ , between volumes  $y$  and  $z$  is used

$$p_m = 0.5 \cdot (p_z + p_y) \tag{3.3-23}$$

The void fraction used in evaluating the flow quality and the mass drift flux, Eq. (3.3-17), depends on the respective void fractions of the adjacent volumes and total mass flux.

Two somewhat different situations occur if the void fraction above the flow path is less than the void fraction below or if the reverse is true. In both cases it is clear that if the total mass flux is positive and large the void

fraction of volume  $y$  should be used and if the total mass flux is negative and the absolute value is large the void fraction of node  $z$  should be used.

Case 1:  $\alpha_y \geq \alpha_z$

This situation is illustrated in Fig. 3-7 where the drift flux curves corresponding to the two void fractions (Eq. 3.3-16) are shown together with lines of constant mass flux

$$G = G_f + G_g \quad (3.3-24)$$

Also shown in Fig. 3-7 is the CCFL curve.

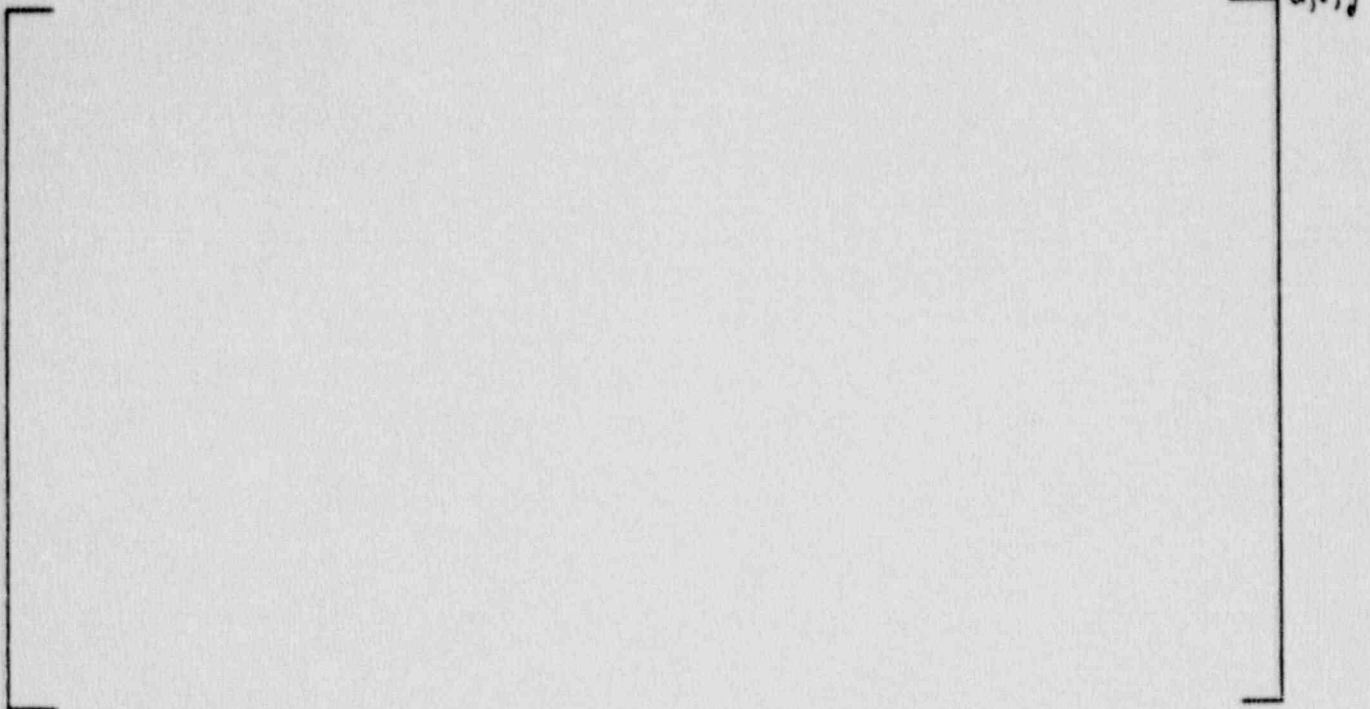
a,c,g

a,c,g

In all equations when applying the drift flux correlation the value of  $K_u$  that is taken is calculated using the void fraction in node  $y$ .

Case 2:  $\alpha_y < \alpha_z$

This situation is illustrated in Fig. 3-8.



Inclined and horizontal flow paths are accounted for by using the component of gravity in the flow path direction in the CCFL correlation (Eq. (3.3-10)). Therefore, in the limit of a horizontal flow path  $G_d$  becomes zero.

### 3.3.2 Two-Phase Level Tracking

The GOBLIN code has the capability to specify a series of control volumes in which a two phase level is to be calculated and tracked with time. The level tracking model replaces a fixed control volume boundary with a moving boundary located at the two-phase level. The flow rate through the boundary is determined by maintaining continuity of the phasic flow rates through the two-phase level for a given level velocity. The phasic flow rates are calculated for the volume above and below the level by the drift flux correlation. The velocity of the two-phase level is determined from the change in the level position

$$u_{lev} = \frac{z_{lev}^{n+1} - z_{lev}^n}{\Delta t} \quad (3.3-30)$$

The two-phase level position is a primary variable, solved for in the solution matrix, replacing the mass flow rate.

### Flow Rate Through Level

A relation between the motion of the two-phase level and the flow rate through the level is required to define the level position and provide closure of the solution. This relation is obtained by forcing conservation of the phasic mass flow rates leaving and entering the volumes above and below the level, as predicted by the drift flux correlation.

Conservation of phasic flow components (see Fig. 3-9) is

$$\left[ \begin{array}{c} \\ \\ \\ \end{array} \right]^{a,c,g} \quad (3.3-31a)$$

$$\left[ \begin{array}{c} \\ \\ \\ \end{array} \right] \quad (3.3-31b)$$

The vapor velocities are determined by the drift flux correlation (Eq. 3.3-1) rewritten here in terms of relative velocity.

$$\left[ \begin{array}{c} \\ \\ \\ \end{array} \right]^{a,c,g} \quad (3.3-32a)$$

$$\left[ \begin{array}{c} \\ \\ \\ \end{array} \right] \quad (3.3-32b)$$

$$\left[ \begin{array}{c} \\ \\ \\ \end{array} \right] \quad (3.3-33)$$

$$\left[ \quad \quad \quad \right]^{a,c,g} \quad (3.3-34)$$

The solution of Eq. (3.3-31) and (3.3-32) gives the phasic flow rates  $G_g$  and  $G_f$  for a given two-phase level velocity,  $u_{lev}$ .

### Two-Phase Level at a Flow Path

When the two-phase level is at the elevation of a flow path, the liquid and vapor energy flow rates are evaluated according to the level elevation. The energy partitions is performed for a flow path designated as "pure" flow path and the partitioning is based on the density weighted vertical flow area projection below and above the two-phase level (see Fig. 3-9(c))

$$h_1 = ah_z + (1-a) h_y \quad (3.3-35)$$

where

$$a = \rho_z A_{\ell,z} / (\rho_z A_{\ell,z} + \rho_y A_{\ell,y}) \quad (3.3-36)$$

### 3.3.3 Frictional Pressure Drop Correlations

The frictional pressure drop is calculated from Eq. (3.1-36). The friction factor,  $f_i$ , and the two-phase multiplier,  $\phi_i^2$ , correlations are described below. Also the application of Eq. (3.1-36) for countercurrent flow is described.

#### Single-Phase Friction Factors

The single-phase friction factors are calculated for turbulent flow in the fuel bundles by (Ref. 3-9)

$$f_i = C_1 Re^{-C_2} \quad (3.3-37)$$

where

$$C_1 = [ \quad ]^{a,c,g}$$

$$C_2 = [ \quad ]^{a,c,g}$$

$$Re_i = \frac{W D_h}{A \mu}$$

For two-phase flow  $\mu = \mu_f$ . This correlation may be modified later to reflect test data applicable to Westinghouse fuel.

For turbulent flow in other parts of the flow loop the Colebrook's correlation is used (Ref. 3-10)

$$f_i = 5.5 \times 10^{-3} \left[ 1 + \left( 2 \times 10^4 \frac{\epsilon}{D_h} + \frac{10^6}{Re} \right) \right]^{1/3} \quad (3.3-38)$$

where  $\epsilon$  is the surface roughness.

For laminar flow the friction factor is

$$f_i = 64/Re \quad (3.3-39)$$

The transition between laminar and turbulent flow is the Reynolds number where the two friction factors are equal.

#### Two-Phase Friction Multiplier

The two-phase friction multiplier is calculated according to the AA-correlation

$$\phi_i^2 = [ \quad ]^{a,c,g} \quad (3.3-40)$$



$$\Gamma = \left( \frac{p_f}{p_g} \frac{f_g}{f_f} \right)^{1/2} \quad (3.3-41)$$

$$B_C = \left[ \quad \right]^{a,c,g} \quad (3.3-42)$$

$$A_C = \left[ \quad \right]^{a,c,g} \quad (3.3-43)$$

$$G_f = \left[ \quad \right]^{a,c,g} \quad (3.3-44)$$

$$FF = \left[ \quad \right]^{a,c,g} \quad (3.3-45)$$

$$B_F = \left[ \quad \right]^{a,c,g} \quad (3.3-46)$$

This correlation is based on full scale measurement in the ASEA-ATOM FRIGG test loop (Ref. 3-9) and the Baroczy correlation database (Ref. 3-11). The number of data points used is 288 and the mean and standard deviations are 0.3 percent and 8.3 percent respectively. The correlation covers the pressure range from 1 to 100 bar, the mass flow range from 1 to 3000 kg/m<sup>2</sup>-s, and the quality range from zero to 100 percent.

The two-phase multiplier is one for single-phase flow and evaluated from Eq. (3.3-40) for cocurrent two-phase flow in the bundle. For other geometries the homogeneous flow two-phase multiplier is used (Eq. 3.3-54).

#### Countercurrent Flow Pressure Drop

In countercurrent flow the frictional pressure drop is evaluated by the following expression

$$\Delta p_{f,i} = \frac{f_{g,i} \cdot \Delta x_i}{D_{h,i}} \cdot \frac{|w_{g,i}| \cdot w_{g,i}}{A_i^2 \cdot 2 \cdot \rho_{g,i}}$$

$$+ \frac{f_{f,i} \cdot \Delta x_i}{D_{h,i}} \cdot \frac{|w_{f,i}| \cdot w_{f,i}}{A_i^2 \cdot 2 \cdot \rho_{f,i}} \quad (3.3-47)$$

which replaces Eq. (3.1-36).

The single-phase friction factors  $f_{f,i}$  and  $f_{g,i}$  obtained from Eq. (3.3-37) through (3.3-39), are evaluated using water and steam Reynolds numbers

$$Re_f = (w_f/A) \cdot (D_h/\mu_f) \quad (3.3-48)$$

$$Re_g = (w_g/A) \cdot (D_h/\mu_g) \quad (3.3-49)$$

### 3.3.4 Local Form Pressure Drop Correlations

The local irreversible pressure drop is calculated from Eq. (3.1-37) where the loss coefficient,  $\xi_k$ , and the local two-phase multiplier,  $\phi_k^2$ , are specified correlation.

#### Local Loss Coefficient

The local loss coefficient  $\xi_k$  is a user specified constant which is flow direction dependent. Two sets of constants may be specified, ones for bundle spacer grids and ones for non-spacer grids. Each set has two values, one for positive flow direction and one for reverse flow.

#### Local Form Loss Two-Phase Multiplier

Two different two-phase multipliers,  $\phi_k^2$ , are used for local form losses. For bundle sources grids the pressure drop is calculated using the following correlation for the two-phase multiplier

$$\phi_{k, \text{spacer}}^2 = \left[ \quad \right]^{a,c,g} \quad (3.3-50)$$

where

$$\Gamma = \left( \frac{p_f}{p_g} \right)^{1/2} \quad (3.3-51)$$

$$A_c = \left[ \quad \right]^{a,c,g} \quad (3.3-52)$$

$$B_c = \left[ \quad \right]^{a,c,g} \quad (3.3-53)$$

and

$A_B$  = fuel bundle flow area

$w$  = coolant flow through the fuel bundle

The correlation is based on the full scale measurements in the FRIGG loop (Ref. 3-9). It may be modified in the future to reflect test data applicable to Westinghouse fuel.

For all other local pressure drops the homogeneous flow two-phase multiplier is used:

$$\beta_k^2 = 1 + X^* \cdot \left( \frac{p_f}{p_g} - 1 \right) \quad (3.3-54)$$

#### Countercurrent Local Form Pressure Drop

In countercurrent flow the local pressure drop is evaluated from

$$\Delta p_{l,i} = \xi_k \frac{w_{g,i} |w|_{g,i}}{A_l^2 \cdot 2 \cdot p_g} + \xi_k \frac{w_{f,i} |w|_{f,i}}{A_l^2 \cdot 2 \cdot p_f} \quad (3.3-55)$$

where  $\xi_k$  is the appropriate directional loss coefficient for the direction of each phase.

### 3.3.5 Injection Flow - Fluid Interaction

External water can be added to the reactor as core spray, feedwater and flooding injection water. The external water is added to a control volume as mass and energy source terms. If the two-phase level falls below the injection point the injected water is added to the liquid in the upper most liquid control volume together with any steam that has condensed from the upper control volume.

The rate of steam condensation due to the injected water is calculated by the formula

$$w_{fg} = F_{cs} \cdot (h_{fsat} - h_{in}) / h_{fg} \cdot f(z_{lev}) \cdot w_{in} \quad (3.3-56)$$

where

- $w_{fg}$  = Steam mass condensation rate
- $F_{cs}$  = Maximum condensation
- $h_{fsat}$  = Saturation enthalpy of water
- $h_{in}$  = Enthalpy of injected water
- $h_{fg}$  = Latent heat of vaporization
- $f(z_{lev})$  = Two-phase level dependent function
- $w_{in}$  = Injected mass flow rate

The two-phase level dependence,  $f(z_{lev})$ , in Eq. (3.3.56) is shown in Fig. 3-10. The falling distance  $z_{cond}$  is user specified as is the maximum

condensation factor  $F_{cs}$ . According to Ref. 3-12 injected water typically reaches 95 percent of saturation when falling approximately 0.3 meters (1 foot) through steam.

### 3.3.6 Critical Flow Model

The GOBLIN code uses the Moody critical flow model for two-phase break flow and a modified Bernoulli model for subcooled critical flow. The Moody model complies with the requirements of 10 CFR 50 Appendix K and the modified Bernoulli model is considered a conservative prediction of the subcooled break flow.

The break mass flow rate is calculated for a given coolant state (pressure, enthalpy, and if applicable, water level) at the break, receiver (downstream) pressure, break area, and flow loss coefficient. The break flow path is an additional source flow entering into the conservation equations. For guillotine pipe breaks the two break locations are specified and the flow path connecting the two pipe sections is closed off.

Critical flow checks may also be specified for any flow path. For a flow path being checked the evaluated mass flow rate is compared to the mass flow rate calculated by the critical flow model and limited to this value if warranted.

#### The Moody Model

The model according to F. J. Moody is included in the GOBLIN code. This model is described in Ref. 3-13.

The assumptions used in the model, which includes friction in the pipe, are

- o Straight pipe with constant flow area and adiabatic walls
- o Steady flow

- o Annular flow without entrainment and liquid in contact with the wall
- o Liquid and vapor in thermodynamic equilibrium at any section
- o Uniform and linear velocities of each phase

For this model an equivalent flow loss coefficient (velocity heads) is specified.

### Subcooled Flow

A subcooled flow model based on the work of P. Pana (Ref. 3-14) has been included in the GOBLIN code. For subcooled flow this model calculates the maximum flow rate from

$$G_{\max} = \left( \frac{2(p_0 - p_s(T_2)) \cdot p_f(T_2)}{1 + \xi} \right)^{1/2} \quad (3.3-57)$$

where

$p_0$  = Stagnation pressure upstream of break

$p_s(T_2)$  = Saturation pressure at the exit

$T_2$  = Exit temperature

$\xi$  = Flow resistance coefficient from stagnation point 0 to exit.

Point 0 is the upstream location and Point 2 the break location. Equation (3.3-57) is used for subcooled or saturated liquid exit conditions (point 2), i.e.,  $T_2$  less than or equal to  $T_{\text{sat}}(p_2)$ .

The exit pressure ( $p_2$ ) is calculated from

$$p_2 = p_0 - (1+\xi) \frac{G^2}{2\rho_0} \quad (3.3-58)$$

and the exit temperature,  $T_2$ , from

$$T_2 = T_0 - \frac{G^2}{2 c_{pf,0} \rho_0} (1+\xi) \left( (T_2+273.15) - \frac{\xi}{1+\xi} \right) \quad (3.3-59)$$

where  $c_{pf,0}$  is the specific heat of water at entrance conditions.

The above equation was derived assuming isentropic nozzle inlet flow and isentropic flow from the inlet to the outlet of the pipe.

The Moody model is used for saturated or two-phase inlet conditions. A linear interpolation between the two-phase model and the subcooled model, Eq. (3.3-57), is used in the intermediate region where flashing occurs upstream of the break even though the inlet conditions are subcooled. This is illustrated in Fig. 3-11.

The inlet conditions corresponding to saturated outlet conditions ( $X_2 = 0$ ) are calculated from

$$G(T_s) = \begin{cases} aT_s^3 + bT_s^2 + cT_s + d & ; T_s \geq 80^\circ\text{C} \\ eT_s & ; T_s < 80^\circ\text{C} \end{cases} \quad (3.3-60)$$

$$p_2 = p_0 - (1+\xi) \frac{G(T_s)^2}{2\rho_f(T_2)} \quad (3.3-61)$$

$T_s = T_{\text{sat}}(p_2)$  = saturation temperature at the exit pressure

where the coefficients in Eq. (3.3-60) for the Moody model are

$$\begin{matrix} a = \\ b = \\ c = \\ d = \\ e = \end{matrix} \left[ \begin{matrix} \\ \\ \\ \\ \end{matrix} \right]^{a,c}$$

Equations (3.3-60) and (3.3-61) are solved for the mass flux,  $G$ , and exit pressure  $p_2$ .

### Superheated Steam

For superheated steam flow isentropic expansion is assumed and the critical flow rate is given by

$$G = \left( \frac{\gamma p_o p_o}{(1 + \frac{\gamma}{2}) \frac{\gamma+1}{\gamma}} \right)^{1/2} \quad (3.3-62)$$

where

$$\gamma = \frac{c_p}{c_v} \quad (3.3-63)$$

If the coefficient  $\gamma$  is assumed to be constant the continuous variation of the mass flow rate with inlet stagnation state is achieved by using

$$G_{\max}(p_o, h_o) = G_{\max}(p_o, X_o = 1) \cdot \left( \frac{p_g(p_o, h_o)}{p_{g\text{sat}}(p_o)} \right)^{1/2} \quad (3.3-64)$$

where  $h_o$  is the inlet stagnation enthalpy which is greater than the saturated vapor stagnation enthalpy, and  $G_{\max}(p_o, X_o = 1)$  is the saturated steam critical mass flow rate based on the Moody model.



### Subcritical Flow

For receiver pressures,  $P_B$ , greater than the pipe exit pressure based on critical flow,  $P_2$ , the mass flow rate is calculated from

$$G = \frac{2(P_0 - P_B) \rho_0(P_0, h_0)}{(1+\xi)} \quad (3.3-65)$$

where  $\xi$  is the flow resistance of the pipe. The critical flow exit pressure in the pipe,  $P_2$ , is calculated according to Eq. (3.3-58). If the vessel pressure is less than the receiver pressure,  $P_B$ , it is assumed that saturated steam is entering the vessel from the surroundings.

### 3.4 System Models

In this section models for the systems and components of a boiling water reactor are described. These includes models for the recirculation pumps, jet pumps, steam separators and dryers, feedwater and steam flow, reactor protection, level measurement, and emergency core cooling systems.

#### 3.4.1 Recirculation Pump Model

The behavior of the main recirculation line reactor coolant pumps are modelled for single and two-phase flow conditions under normal operation and coastdown conditions.

##### Pump Speed and Torque

The behavior of the main recirculation pump is modelled by the conservation of angular momentum

$$I \frac{d\omega}{dt} = T \quad (3.4-1)$$

where

$\omega$  = Angular velocity

$t$  = Time

$T$  = Net torque

$I$  = Momentum of inertia

The difference formulation of Eq. (3.4-1) is

$$\frac{\omega^{n+1} - \omega^n}{\Delta t} - \frac{T^{n+1}}{I} = 0 \quad (3.4-2)$$

The pump equation is solved at every time step simultaneously with the basic conservation equations.

The torque  $T$  represents the net torque on the pump impeller. It consists of three components:

- (1) The hydraulic component,  $T_{hyd}$ , due to the interaction between the fluid and the pump impeller,
- (2) The frictional component,  $T_{fric}$ , due to frictional losses in the bearing and rotating machinery, and
- (3) The pump motor torque,  $T_m$ .

The net torque,  $T$ , is calculated as

$$T = T_m - T_{hyd} + T_{fric} \quad (3.4-3)$$

The pump motor torque is evaluated at the initial time, when the pump speed is constant and there is no net torque on the pump impeller (See Eq. (3.4-1)). Thus

$$T_m(t) = T_{hyd}(t = 0) - T_{fric}(t = 0) \quad (3.4-4)$$

This value for  $T_m(t)$  is maintained until the pumps are tripped at a time specified by the user. After the pump trip,  $T_m(t)$  is set equal to zero.

The user inputs homologous curves for hydraulic torque as four tables of dimensionless hydraulic torque versus the ratio between dimensionless flow and speed (or its reciprocal). The tabulated curves are:

<u>Table</u>	<u>Independent Variable</u>	<u>Dependent Variable</u>
1	$v/\alpha$	$\beta/\alpha^2$
2	$\alpha/v$	$\beta/v^2$
3	$v/\alpha$	$\beta/\alpha^2$
4	$\alpha/v$	$\beta/v^2$

where

$$\beta = T_{\text{hyd}}/T_{\text{hyd,ref}}$$

$$v = Q/Q_{\text{ref}}$$

$$\alpha = \omega/\omega_{\text{ref}}$$

A typical example is given in Fig. 3-12.

For a specified volume flow,  $Q$ , through the pump and a specified pump speed,  $\omega$ , the dimensionless hydraulic torque is calculated by quadratic interpolation from the appropriate table.

<u>Table Used</u>	<u>Criteria</u>
1	$ \alpha  \geq  v , \alpha \geq 0$
2	$ \alpha  <  v , v < 0$
3	$ \alpha  \geq  v , \alpha < 0$
4	$ \alpha  <  v , v \geq 0$

The absolute hydraulic torque is then calculated from

$$T_{\text{hyd}} = \beta \cdot T_{\text{hyd,ref}} \cdot \left(\frac{\rho}{\rho_{\text{ref}}}\right) \quad (3.4-5)$$

where

$\rho$  = Density of fluid in the pump

$\rho_{\text{ref}}$  = Reference pump fluid density

The friction torque,  $T_{\text{fric}}$ , is calculated by

$$T_{\text{fric}} = \begin{cases} HC_2 \cdot (\omega^{n+1})^2 \cdot \psi & \text{for } |\omega^{n+1}| > HC_3 \\ HC_4 \cdot \psi & \text{for } |\omega^{n+1}| < HC_3 \end{cases} \quad (3.4-6)$$

where

$$\psi = \begin{cases} +1 & \text{for } \omega^n < 0 \\ -1 & \text{for } \omega^n \geq 0 \end{cases} \quad (3.4-7)$$

The above expression applies if  $\omega^{n+1}$  and  $\omega^n$  have the same sign. If not,  $T_{\text{fric}}$  is calculated from

$$T_{\text{fric}} = \frac{HC_4 \cdot \psi}{0.01 \cdot HC_3^2} (\omega^{n+1} + 0.01 \cdot HC_3 \cdot \psi) \quad (3.4-8)$$

The constants  $HC_2$ ,  $HC_3$ ,  $HC_4$  and  $HC_5$  are user specified and represent the friction torque coefficient ( $HC_2$ ) at angular speeds greater than  $HC_3$  and the friction torque ( $HC_4$ ) when the angular speed is less than  $HC_3$ . The constant  $HC_5$  is the friction torque that must be overcome to start the pump from zero speed (See Fig. 3-13).

If the pump speed at the earlier time step ( $\omega^n$ ) was less than a user specified value ( $\omega_0$ ), the pump will stop. Only if the hydraulic torque is greater than the maximum friction torque at rest ( $HC_5$ ), will the pump start running again.

The friction torque as a function of the pump speed is shown in Fig. 3-13.

### Pump Hydraulic Head

The momentum equation of the control volume containing the pump includes a term for the pump head (see Eq. 3.1-43). The user inputs homologous curves for head as four tables of dimensionless pump head versus ratio between dimensionless flow and speed (or its reciprocal). The tabulated curves are

<u>Table</u>	<u>Independent Variable</u>	<u>Dependent Variable</u>
1	$v/\alpha$	$h/\alpha^2$
2	$\alpha/v$	$h/v^2$
3	$v/\alpha$	$h/\alpha^2$
4	$\alpha/v$	$h/v^2$

A typical example is shown in Fig. 3-14.

For a specified volume flow,  $Q$ , and pump speed,  $\omega$ , the dimensionless hydraulic head is calculated by quadratic interpolation from the appropriate table:

<u>Table Used</u>	<u>Criteria</u>
1	$ \alpha  \geq  \nu , \alpha \geq 0$
2	$ \alpha  <  \nu , \nu < 0$
3	$ \alpha  \geq  \nu , \alpha < 0$
4	$ \alpha  <  \nu , \nu \geq 0$

For a specified volume flow,  $Q$ , and pump speed,  $\omega$ , the pump head is calculated from

$$\Delta p_{\text{pump}} = g \cdot \rho_{\text{pump}} \cdot (h \cdot h_{\text{ref}} - HC_{10} \cdot Q \cdot |Q|) \quad (3.4-8)$$

where  $HC_{10}$  is the pump diffuser head loss coefficient.

#### Two-Phase Pump Behavior

The pump head under two-phase flow conditions is determined by a user specified set of homologous differential head curves and a two-phase multiplier which is a function of void fraction. The two-phase dimensionless head is then calculated from

$$h_{2\phi} = h_{1\phi} - M(\alpha) \cdot h_D \quad (3.4-9)$$

where  $M(\alpha)$  is the tabulated multiplier and  $h_D$  is the difference between the single and two-phase pump head at a reference void fraction. The single-phase head,  $h_{1\phi}$ , is calculated as described in the previous section. This formulation is adapted from Ref. 3-15.

The two-phase pump head is then calculated from Eq. (3.4-8).

### 3.4.2 Jet Pump Model

In some boiling water reactor designs a jet pump recirculation system is used to force flow through the reactor core.

In a jet pump recirculation system a fraction of the total recirculation flow is taken out side the reactor vessel and given a high mechanical energy by passing through a drive pump. This high energy drive flow is then used to accelerate the remaining recirculation flow (suction flow) by momentum mixing. The velocity of the total flow is converted to static head in a diffuser. A drawing of the jet pump recirculation system is shown in Fig. 3-15.

The jet pump recirculation lines and diffuser sections are modeled with normal GOBLIN control volumes and conservation equations. The drive line recirculation pump performance is calculated as described in Sec. 3.4.1. The jet pump drive and suction flow path momentum equations are modified to account for the two-dimensional temporal and spatial acceleration effects of momentum mixing.

#### Jet Pump Momentum Equation

The momentum equation for the jet pump drive and suction flow paths are modified to account for the momentum exchange between the two flow paths (see Fig. 3-16).

The temporal acceleration term in Eq. (3.1-32) for the drive flow path is

$$\int_{x_D}^{x_T} \frac{1}{A} \frac{dw}{dt} dx = \int_{x_D}^{x_M} \frac{1}{A} \frac{dw}{dt} dx + \int_{x_M}^{x_T} \frac{1}{A} \frac{dw}{dt} dx \quad (3.4-10)$$



$$= \frac{dw_D}{dt} \int_{x_D}^{x_{M1}} \frac{1}{A} dx + \frac{dw_D}{dt} \int_{x_m}^{x_{T1}} \frac{1}{A_D} dx \quad (3.4-11)$$

$$+ \frac{dw_S}{dt} \int_{x_M}^{x_{T1}} \frac{1}{A_S} dx$$

$$= I_D \frac{dw_D}{dt} + I_{DS} \frac{dw_S}{dt} \quad (3.4-12)$$

where  $I_D$  and  $I_{DS}$  are the flow path inertias due to the drive flow and suction flows.

The suction flow temporal acceleration term is analogous (interchange subscripts D and S).

For the drive and suction flows, the spatial acceleration term, Eq. (3.1-38), is also modified to account for the increased mixing losses in the throat region when a density difference exists between the drive and suction fluids. The spatial acceleration term for the drive flow is

$$\int_{x_D}^{x_{T1}} \frac{1}{A} \frac{\partial}{\partial x} \left( \frac{w^2}{\rho A} \right) dx = \int_{x_D}^{x_{M1}} \frac{1}{A} \frac{\partial}{\partial x} \left( \frac{w^2}{\rho A} \right) dx$$

$$+ \int_{x_M}^{x_D} \frac{1}{A} \frac{\partial}{\partial x} \left( \frac{w^2}{\rho A} \right) dx \quad (3.4-13)$$

$$\begin{aligned}
&= \frac{w_D^2}{2\rho_D} \left( \frac{1}{A_2^2} - \frac{1}{A_{DN}^2} \right) \\
&+ \left( \frac{w_T^2}{\rho_T A_T^2} - \frac{w_S^2}{\rho_S A_S^2} - \frac{w_D^2}{\rho_D A_D^2} \right) \cdot f_1 \cdot f_2 \left( \frac{\rho_D}{\rho_S} \right)
\end{aligned}
\tag{3.4-14}$$

where

$$f_1 = \begin{cases} 1 & w_D > 0 \\ 0 & w_D < 0 \end{cases}
\tag{3.4-15}$$

and the factor  $f_2$  accounts for the additional mixing losses due to the density difference between the suction and drive flow. The factor  $f_2$  has been calculated analytical by solving the momentum equation in the jet pump throat for two adjacent streams of differing density. The factor  $f_2$  has been correlated for a range of jet pump flow and density differences, by

$$f_2 = \begin{cases} \frac{a_1 (1+a_2) \cdot (\rho_D/\rho_S)}{a_2 + (\rho_D/\rho_S)} & \text{for } \rho_D/\rho_S > 1 \\ \frac{a_1 (1+a_2) \cdot (\rho_S/\rho_D)}{a_2 + (\rho_S/\rho_D)} & \text{for } \rho_D/\rho_S \leq 1 \end{cases}
\tag{3.4-16}$$

where  $a_1$  is  $\left[ \quad \right]^{a,c,g}$  and  $a_2$  is  $\left[ \quad \right]^{a,c,g}$

The spatial acceleration for the suction flow path is analogous to Eq. (3.4-16) (interchange subscripts D and S).

### 3.4.3 Separator and Dryer Models

Models are incorporated in GOBLIN to simulate the steam-water separators and steam dryers in a boiling water reactor. The models mechanistically determine the steam and water phase separation and the component pressure drop.

The pressure drop for each component is modelled as a local form loss analogous to the form loss pressure drops of other GOBLIN control volumes (see Sec. 3.3.4). The phase separation model is described below.

### Steam Separator Model

Figure 3-17 shows a schematic diagram of the steam-water separator. For a known inlet steam and water flow rates and user specified water carryover,  $x_{co}$ , and steam carry-under,  $x_{cu}$ , fractions, the phase separation can be calculated. The carryover and under are defined as

$$x_{co} = \frac{w_{fs}}{w_{fs} + w_{gs}} \quad (3.4-17)$$

$$x_{cu} = \frac{w_{gp}}{w_{fp} + w_{gp}} \quad (3.4-18)$$

where the subscript s is secondary flow path and p is primary flow path. A mass balance of each component is performed on the separator to find the components flow rates.

A mass balance of each phase is

$$w_{g,in} = w_{gs} + w_{gp} \quad (3.4-19)$$

$$w_{f,in} = w_{fs} + w_{fp} \quad (3.4-20)$$

Equations (3.4-17) through (3.4-20) can be solved for the separation components

$$w_{fp} = (1-x_{cu}) \frac{w_{g,in} x_{co} - w_{f,in} (1-x_{co})}{x_{cu} - (1-x_{co})} \quad (3.4-21)$$

$$w_{fp} = w_{f,in} - w_{fp} \quad (3.4-22)$$

$$w_{gp} = x_{cu} \frac{w_{g,in} x_{co} - w_{f,in} (1-x_{co})}{x_{cu} - (1-x_{co})} \quad (3.4-23)$$

$$w_{gs} = w_{g,in} - w_{gp} \quad (3.4-24)$$

The above equations are valid under normal flow conditions. The limiting conditions are:

- (1) If there is insufficient liquid flow to meet the carryover fraction all available liquid is carried over ( $w_{fs}$ ).
- (2) If there is insufficient steam flow to meet the carry-under fraction all available steam is carried under ( $w_{gp}$ ).
- (3) If the flow is countercurrent or downflow the carryover and carry-under fractions are zero ( $w_{fs} = w_{gp} = 0$ ).

During the LOCA blowdown transient the flow through the steam separators is of very high quality steam. The separator performance, therefore, is of minor significant to the overall transient response.

### Dryer Model

The flow from the steam dome to the steam lines passes through a steam dryer unit where most of the remaining liquid is removed. The removed liquid is returned to the downcomer.

The steam dryer model is similar to the separator model. Figure 3-18 shows the nomenclature convention for the dryer unit. The carryover,  $x_{co}^D$ , and carry-under,  $x_{cu}^D$ , fractions for the dryer are defined as

$$x_{co}^D = \frac{w_{fp}}{w_{gp} + w_{fp}} \quad (3.4-25)$$

$$x_{cu}^D = \frac{w_{gs}}{w_{gs} + w_{fs}} \quad (3.4-26)$$

By substituting  $x_{cu} = 1 - x_{co}^D$  and  $x_{co} = 1 - x_{cu}^D$  in Eq. (3.4-21) through (3.4-24) an analogous expression for the dry separation fraction is developed

$$w_{fp} = x_{co}^D \frac{w_{g,in} (1 - x_{cu}^D) - w_{f,in} x_{cu}^D}{(1 - x_{co}^D) - x_{co}^D} \quad (3.4-27)$$

$$w_{fp} = w_{f,in} - w_{gp} \quad (3.4-28)$$

$$w_{gp} = (1 - x_{co}^D) \frac{w_{g,in} (1 - x_{cu}^D) - w_{f,in} x_{cu}^D}{(1 - x_{co}^D) - x_{co}^D} \quad (3.6-29)$$

$$w_{gp} = w_{g,in} - w_{fp} \quad (3.4-30)$$

The limiting conditions for the dryer model are

- (1) If there is insufficient water for carryover, all the liquid flow available is carried over ( $w_{fp}$ ).
- (2) If there is insufficient steam flow for carry-under, all the steam flow available is carried under ( $w_{gs}$ ).
- (3) If the inlet liquid flow is negative the carryover flow is also negative ( $w_{fp} = w_{f,in}$ ).

- (4) If the inlet vapor flow is negative (unusually condition) both the carryover and carry-under are zero ( $w_{fp} = w_{gs} = 0$ ).

#### 3.4.4 Feedwater and Steamline Systems

The entire steamline, turbine, and feedwater system is not modelled in GOBLIN. The interface between the reactor vessel and the balance of plant is modelled as user specified curves of feedwater and steam flow as a function of time through the transient. The influence of the reactor vessel response on the balance of plant is small and of negligible significance to the overall LOCA blowdown transient.

#### 3.4.5 Reactor Measurement and Protection Systems

The boiling water reactor has several reactor control, measurement, and protection systems. The systems for which perform a function during a LOCA event are modelled in GOBLIN. These include the level measurement system, reactor protection system, pressure relief valve system, high pressure emergency core cooling (ECC) system and low pressure ECC system.

##### Level Measurement System

The level measurement system simulates the measurement, process, and interpretation of the reactor vessel level measurements. The influence of the ambient temperature and reactor pressure on the level indication also may be included. Low and high level actuation signals are modelled either by pressure differential switches or level float switches. The processed level signals may be used to actuate the pressure relief and ECC systems.

##### Reactor Protection System

The control functions of the reactor protection system associated with the pressure relief and ECC systems are modelled in GOBLIN. Signals may be actuated on reactor fluid conditions or at a user specified time. Various isolation signals, power train failure, loss of offsite power and associated diesel start time delays can be simulated.

### Pressure Relief Valve System

A series of relief, safety, and controlled depressurization valves are located on the steamline of a boiling water reactor. Several of these valves may be associated with the automatic depressurization system (ADS). All these valves can be simulated in GOBLIN. The valve model includes the capability to simulate delay times in opening and closing, force open and force close signals, low power close interlocks, and a programmed controlled opening, as in the control depressurization valves.

### High Pressure ECC Systems

The high pressure ECC systems of boiling water reactors vary for different plant designs. GOBLIN has the capability to specify up to four high pressure injection or spray flow trains. The flow rate of each train is calculated from a user specified curve of volumetric flow versus differential pressure between the reactor and the wetwell. The flow enthalpy is determined by the fluid conditions of the suppression pool. An initial period of fluid suction from the condensate storage tank also can be modelled.

### Low Pressure ECC Systems

The low pressure ECC systems also vary for different boiling water reactor plants. The models for the low pressure ECC are analogous to the high pressure ECC model described above. The major difference is flow suction is always from the suppression pool.

### 3.5 Heat Transfer Models

The coupling between the hydraulic and thermal model is through the surface to fluid heat transfer. The surface heat transfer appears in the energy conservation equation (Eq. 3.1-17) as the component  $Q_A$  (defined in Eq. (3.1-14)) of the term  $Q$ . The surface heat transfer is divided into a convective and a radiative component

$$Q_A = Q_C + Q_R \quad (3.5-1)$$

The convective heat transfer is calculated by an average convective heat transfer coefficient,  $H$ , defined by

$$Q_C = H A_{HT} (T_w - T_c) \quad (3.5-2)$$

where  $T_w$  is the surface temperature and  $T_c$  is the coolant bulk temperature. The convective heat transfer is calculated using an empirical correlation which is primarily a function of fluid properties, flow, surface material, surface temperature.

The radiative heat transfer is calculated from

$$Q_R = \sum_k GBF_k \sigma_R (T_w^4 - T_{w,k}^4) \quad (3.5-3)$$

where  $GBF_k$  are the gray body factors for the surface  $k$  and  $\sigma_R$  is the Stefan-Boltzmann constant.

In many heat transfer regimes, the heat transfer coefficient is surface temperature dependent. The solution method used in GOBLIN accounts for this dependency by solving the heat transfer and heat conduction problems simultaneously (see Sec. 3.8).

This section describes the heat transfer regimes, convective heat transfer correlations, dryout correlation, Leidenfrost temperature and boiling transition correlation, and the radiative heat transfer model.

### 3.5.1 Heat Transfer Regimes

The various heat transfer regimes modelled in GOBLIN are listed in Table 2-1. The heat transfer flow regime map is shown in Fig. 3-19. The transition void fractions are:



$$\begin{matrix} \alpha_1 \\ \alpha_2 \\ \alpha_3 \\ \alpha_4 \end{matrix} = \left[ \begin{matrix} \\ \\ \\ \end{matrix} \right]^{a, c, g}$$

In Fig. 3-19 the cross hatched regions signifies where the heat transfer is linearly interpolated between the two adjacent regimes. The Reynolds number transitions are where the heat transfer for the two regimes become equal.

### 3.5.2 Convective Heat Transfer Coefficients

#### Laminar and Turbulent Natural Convection Regime

The heat transfer coefficient for natural convection of steam or water is from M. Jakob (Ref. 3-16) for vertical plates.

$$Nu = C \cdot (Gr \cdot Pr)^n \quad (3.5-4)$$

$$H = k_{flm} \cdot Nu/L \quad (3.5-5)$$

where  $L$  is the film length,

$$Pr = \frac{\mu_{flm} \cdot c_{p,flm}}{k_{flm}} \quad (3.5-6)$$

and

$$Gr = g \cdot \beta_{flm} \cdot L^3 \cdot |T_w - T_c| \cdot \left( \frac{\rho_{flm}}{\mu_{flm}} \right)^2 \quad (3.5-7)$$

The subscript "flm" means that properties shall be evaluated at film temperature,  $T_{flm}$

$$T_{f1m} = \begin{cases} \min(0.5(T_w + T_c); T_s) & \text{for water} \\ \max(0.5(T_w + T_c); T_s) & \text{for steam} \end{cases} \quad (3.5-8)$$

and  $L$  is the characteristic length.

The coefficients  $C$  and  $n$  for laminar natural convection, are

$$C = 1.35; n = 0.15 \quad \text{for } 1 < Gr \cdot Pr < 5554$$

$$C = 0.57; n = 0.25 \quad \text{for } 5554 \leq Gr \cdot Pr \leq 1.057 \times 10^8$$

and for turbulent natural convection

$$C = 0.13; n = 0.333 \quad \text{for } 1.057 \times 10^8 < Gr \cdot Pr$$

#### Laminar Forced Convection Regime

For laminar forced convection of steam and water the correlation of Sieder-Tate (Ref. 3-17) is used

$$Nu = 1.86 \left( Re_i \cdot Pr_i \cdot \frac{D_H}{L} \right)^{1/3} \cdot \left( \frac{\mu_i}{\mu_w} \right)^{0.14} \quad (3.5-9)$$

$$H = k_i \cdot Nu / D_H \quad (3.5-10)$$

where subscript  $i$  is  $f$  for the water regime and  $g$  for the steam regime.

The Reynolds number is

$$Re_f = |G_f| D_H / (\mu_f (1-\alpha)) \quad (3.5-11)$$

$$Re_g = |G_g| D_H / (\mu_g \alpha) \quad (3.5-12)$$

$$Pr_i = \mu_i \cdot c_{p,i} / k_i \quad (3.5-13)$$

The wall viscosity,  $\mu_w$ , is evaluated at

$$T = \begin{cases} \min(T_w, T_{sat}) & \text{for water} \\ \max(T_w, T_{sat}) & \text{for steam} \end{cases} \quad (3.5-14)$$

### Turbulent Forced Convection Regime

Dittus-Boelter correlation (Ref. 3-18) is used for turbulent forced convection of steam and water

$$Nu = 0.023 \cdot Re_i^{0.8} \cdot Pr_i^{0.4} \quad (3.5-15)$$

$$H = k_i \cdot Nu/D_h \quad (3.5-16)$$

where again subscript  $i$  is  $f$  for water regime and  $g$  for the steam regime. The Reynolds and Prandtl number are defined in Eq. (3.5-11) through (3.5-13).

### Two-phase Subcooled, Nucleate, and Flow Boiling Regime

For nucleate and nondryout flow boiling the Chen's correlation (Ref. 3-19) is used

$$H = 0.023 \cdot \frac{k_f}{D_h} Re^{0.8} Pr^{0.4} \cdot F + 0.00122 \cdot \frac{k_f^{0.79} C_{pf}^{0.45} \cdot p_f^{0.49}}{\sigma^{0.5} \cdot \mu_f^{0.29} \cdot h_{fg}^{0.24} \cdot \rho_g^{0.24}}$$

$$(T_w - T_s)^{0.24} \cdot (p_w - p)^{0.75} \cdot S \quad (3.5-17)$$

where

$$Re = G_f D_h / \mu_f \quad (3.5-18)$$

$$Pr = \mu_f c_{p,f} / k_f \quad (3.5-19)$$

$$T_w = \max (T_w, T_s)$$

$$p_w = p_{sat} (T_w)$$

The two-phase Reynolds number Factor, F, is

$$F = \begin{cases} 1.0 & \text{for } X_{tt}^{-1} \leq 0.1 \\ 2.3511447 \cdot (X_{tt}^{-1+0.213})^{0.736} & \text{for } X_{tt}^{-1} > 0.1 \end{cases} \quad (3.5-20)$$

where

$$X_{tt}^{-1} = \left( \frac{X}{1-X} \right)^{0.9} \cdot \left( \frac{p_f}{p_g} \right)^{0.5} \cdot \left( \frac{\mu_g}{\mu_f} \right)^{0.1} \quad (3.5-21)$$

and X is the quality which is limited to less than 0.99.

The subcooling suppression factor, S, is

$$S = \begin{cases} 1/(1+0.012 Re_{TP}^{1.14}) & \text{for } Re_{TP} < 32.5 \\ 1/(1+0.042 Re_{TP}^{0.78}) & \text{for } 32.5 \leq Re_{TP} < 70 \\ 0.1 & \text{for } Re_{TP} \geq 70 \end{cases}$$

where

$$Re_{TP} = 10^{-4} \cdot |G| \cdot (1-X) D_h / \mu_f \cdot F^{1.25}$$

### Low Flow Film Boiling Regime

For low mass flow the post dryout film boiling regimes modelled are inverted annular and the dispersed flow. For the inverted annular regime a modified Bromley correlation (Ref. 3-20) is used

$$H = Nu \cdot k_g/L_H + H_{rad} \quad (3.5-23)$$

The Nussett number is given by

$$Nu = 0.62 [Ra_z \cdot h_{fg} (c_{p,g} \Delta T_w)^{-1}]^{1/4} \quad (3.5-24)$$

where

$$Ra_z = \frac{L_H^3 g \rho_g (\rho_f - \rho_g) Pr_g}{\mu_g^2} \quad (3.5-25)$$

and  $L_H$  is the Helmholtz instability length

$$L_H = 16.24 \cdot [\sigma^4 h_{fg}^3 \mu_g^5 / (\rho_g (\rho_f - \rho_g)^5 g^5 k_g^3 \Delta T_w^3)]^{1/11} \quad (3.5-26)$$

$$H_{rad} = \epsilon_w \sigma_R ((T_w^4 - T_s^4) / (T_w - T_s)) \quad (3.5-27)$$

where  $\epsilon_w$  is the emissivity of the surface and  $\sigma_R$  is the Stefan-Boltzmann's constant.

### Low Flow Dispersed Film Boiling Regime

In the low flow post-dryout dispersed regime the heat transfer coefficient is calculated using the steam natural convection or forced convection heat transfer coefficients as described previously.

### Flow Film Boiling Regime for High Pressures

For pressures above 23.8 bar (350 psia) the Groeneveld post-dryout correlation (Ref. 3-21) is used. Because the Groeneveld correlation has a low pressure singularity, for pressures below 13.8 bar (200 psia) the Westinghouse UHI correlation (Ref. 3-22) is used. In the intermediate pressure range a linear interpolation transition between the two correlations is used.

The Groeneveld correlation is

$$H = \frac{k_g}{D_H} a \left[ Re_g \left( X + \frac{p_g}{p_f} (1-X) \right) \right]^b \left[ Pr_{gw} \right]^c \gamma^d \quad (3.5-28)$$

$$\gamma = 1 - 0.1 \left( \frac{p_f}{p_g} - 1 \right)^{0.4} \cdot (1 - X)^{0.4} \quad (3.5-29)$$

where

$$a = 5.2 \cdot 10^{-2}$$

$$b = 0.688$$

$$c = 1.26$$

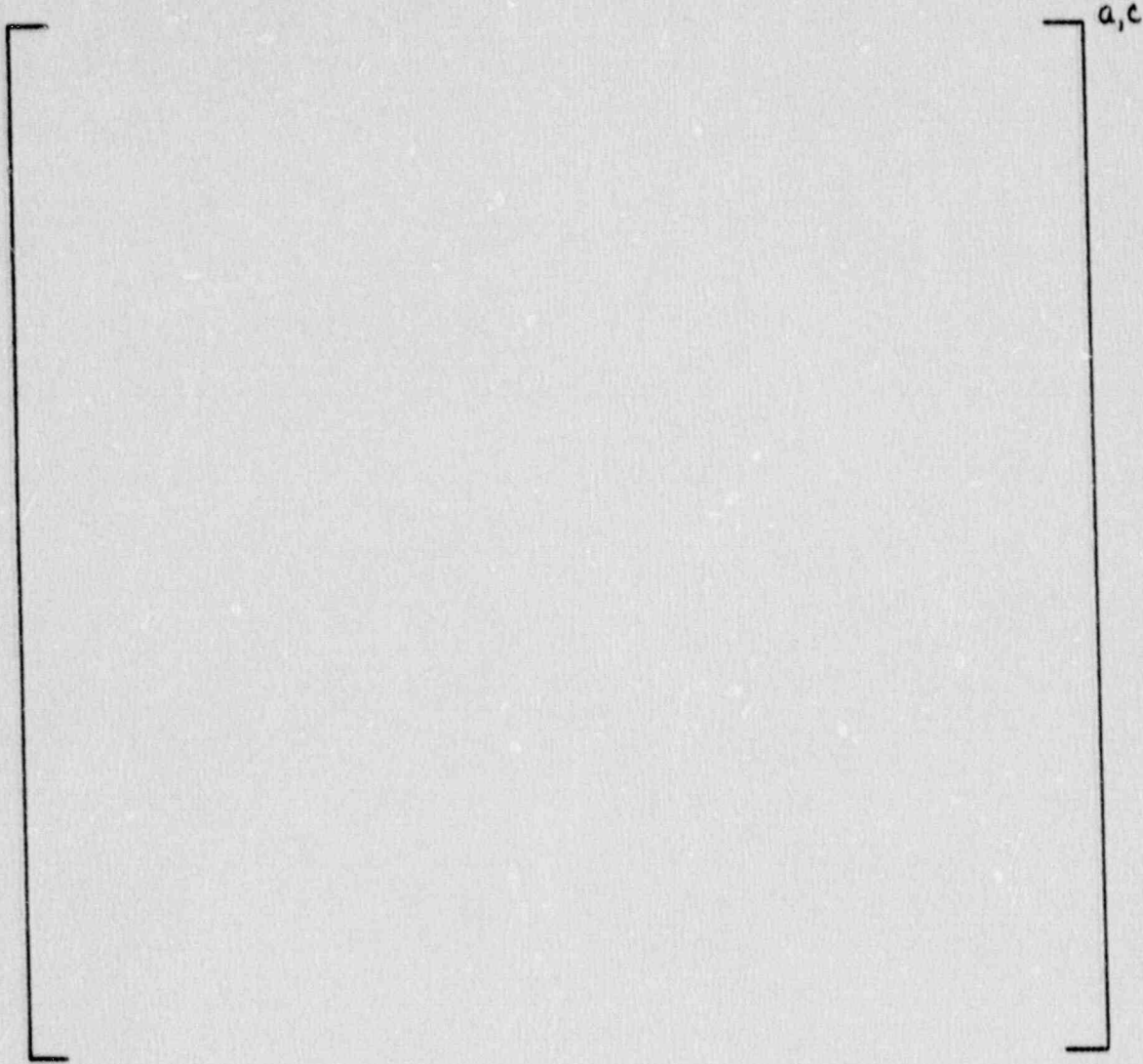
$$d = -1.06$$

### Flow Film Boiling Regime for Low Pressures

The Westinghouse UHI correlation is a low pressure flow film boiling correlation for cocurrent and countercurrent flow. It is based on experimental data from the G-1 and G-2 test facility (Ref. 3-23, 3-24). The formulation is derived from the Doughall-Rohsenow post dryout correlation (Ref. 3-25).

$$H = f_1 f_2 f_3 f_4 \frac{k_g}{D_h} \left[ Re_g \left( X + \frac{p_g}{p_f} (1-X) \right) \right]^{0.8} Pr_g^{0.4} \quad (3.5-30)$$

The four factors are empirical correlations of quality, pressure, flow rate, void fraction and flow direction



And  $f_4$  is  $\left[ \begin{matrix} a,c \\ \cdot \end{matrix} \right]$ . Then it is the product of the three coefficients interpolated from Table 3-1.

## Condensation

If the metal plate temperature drops below the saturation temperature for a two-phase coolant, then condensation will take place. An average heat transfer coefficient of  $20,000 \text{ W/m}^2 \text{ }^\circ\text{C}$  is used.

### 3.5.3 Dryout Correlation

The boiling transition between nondryout heat transfer and post-dryout heat transfer is determined from a critical heat flux correlation.

The critical power ratio (CPR) is a measure of the margin to dryout, for on a given critical heat flux correlation. The critical power ratio at an axial location is defined as the ratio of the integrated bundle power from the inlet to to the dryout location, to the actual integrated bundle power over the same length.

The critical heat flux used is the maximum between a flow boiling and a pool boiling correlation

$$q''_{\text{crit}} = \max [q''_{\text{cr}}, q''_{\text{pc}}] \quad (3.5-34)$$

### Flow Boiling Critical Heat Flux

The current flow critical heat flux (CHF) correlation in GOBLIN is the AA-74 correlation (Ref. 3-26). This correlation will developed from ASEA-ATOM 8x8 fuel assembly CHF test data. This correlation will be modified or replaced by a new one to reflect experimental critical heat flux data for the Westinghouse fuel design.

The AA-74 correlation is comprised of a base equation, a low, and a high quality equation. Corrections for pressure and mass flux are included. The critical heat flux is



$$q''_{cr} = \begin{cases} q''_{base} \cdot C_1(p,G); & |G| \leq G_{tran} \\ \max [\min (q''_{LX}, q''_{base}), q''_{HX}] \cdot C_1(p,G); & G_{tran} < |G| \end{cases} \quad (3.5-35)$$

The base correlation is

$$q''_{base} = A_2 - B_2 \cdot X \quad (3.5-36)$$

where

$$A_2 = \left[ \begin{array}{c} \phantom{A_2} \\ \phantom{A_2} \\ \phantom{A_2} \\ \phantom{A_2} \end{array} \right]^{a,c,g} \quad (3.5-37)$$

$$B_2 = \left[ \begin{array}{c} \phantom{B_2} \\ \phantom{B_2} \\ \phantom{B_2} \\ \phantom{B_2} \end{array} \right]^{a,c,g} \quad (3.5-38)$$

$$A^* = \left[ \begin{array}{c} \phantom{A^*} \\ \phantom{A^*} \\ \phantom{A^*} \\ \phantom{A^*} \end{array} \right]^{a,c,g} \quad (3.5-39)$$

$$B^* = \left[ \begin{array}{c} \phantom{B^*} \\ \phantom{B^*} \\ \phantom{B^*} \\ \phantom{B^*} \end{array} \right]^{a,c,g} \quad (3.5-40)$$

For low steam qualities

$$q''_{LX} = A_1 - B_1 X \quad (3.5-41)$$

where

$$A_1 = \left[ \begin{array}{c} \phantom{A_1} \\ \phantom{A_1} \\ \phantom{A_1} \\ \phantom{A_1} \end{array} \right]^{a,c,g} \quad (3.5-42)$$

$$B_1 = 0$$

For high steam qualities

$$q_{HX}'' = A_3 - B_3 \cdot X \quad (3.5-43)$$

where

$$\begin{matrix} A_3 = [ & ]^{a,c,g} \\ B_3 = [ & ] \end{matrix} \quad (3.5-44)$$

The above critical heat flux expressions are for a pressure of 7.0 MPa, and with a spacer distance of 400 mm. For pressures other than 7.0 MPa, a pressure and flow rate correction is applied

$$C_1(p,G) = f_1(p) \cdot g_1(p,G) \quad (3.5-45)$$

where

$$\begin{matrix} f_1(p) = [ & ]^{a,c,g} \\ p^* = [ & ]^{a,c,g} \end{matrix} \quad (3.5-46)$$

and

$$\begin{matrix} g_1(p,G) = [ & ]^{a,c,g} \\ p^{**} = [ & ]^{a,c,g} \end{matrix} \quad (3.5-47)$$

The transition mass flux is

$$G_{\text{tran}} = \left[ \right]^{a,c,g}$$

where  $D_{\text{heat}}$  is the equivalent diameter for heat transfer.

### Pool Boiling Critical Heat Flux

The critical heat flux in pool boiling is calculated from a modified Zuber (Ref. 3-27) correlation. The original Zuber correlation was

$$q''_{\text{pc,Z}} = \frac{\pi}{24} \cdot h_{\text{fg}} \cdot \rho_{\text{g}} \left( \frac{\sigma g (\rho_{\text{f}} - \rho_{\text{g}})}{\rho_{\text{g}}^2} \right)^{1/4} \left( \frac{\rho_{\text{f}}}{\rho_{\text{f}} + \rho_{\text{g}}} \right)^{1/2} \quad (3.5-49)$$

According to Griffith (Ref. 3-28) this should be modified for two-phase mixtures by multiplying by  $(1-\alpha)$ , where  $\alpha$  is the void fraction.

Hence, the final correlation for the critical heat flux in pool boiling is

$$q''_{\text{pc}} = (1-\alpha) \cdot \frac{\pi}{24} \cdot h_{\text{fg}} \cdot \rho_{\text{g}} \left( \frac{\sigma g (\rho_{\text{f}} - \rho_{\text{g}})}{\rho_{\text{g}}^2} \right)^{1/4} \left( \frac{\rho_{\text{f}}}{\rho_{\text{f}} + \rho_{\text{g}}} \right)^{1/2} \quad (3.5-50)$$

## Critical Power Ratio

In order to determine the critical temperature defined in the heat transfer regime map, it is necessary to first calculate the critical power ratio (CPR) and maximum allowable heat flux. The critical power ratio is a measure of the margin to dryout conditions. Calculation of the critical power ratio and maximum allowable heat flux are described below including correction factors for bundle internal power peaking and grid spacer locations.

The critical power ratio is defined as

$$\text{CPR}(z=z_0) = \frac{Q_{\text{DO}}(z=z_0)}{Q(z=z_0)} \cdot C_S(\Delta S) \cdot C_F(F_{\text{INT}}) \quad (3.5-51)$$

where

- $Q_{\text{DO}}(z=z_0)$  = Bundle power integrated from zero to  $z_0$  necessary to cause dryout to occur at  $z = z_0$
- $Q(z=z_0)$  = Actual bundle power to coolant flow from inlet to  $z = z_0$
- $C_S(\Delta S)$  = Spacer distance correction (given below for the AA-74 correlation)
- $C_F(F_{\text{INT}})$  = Internal power distribution correction (calculated according to (Ref. 3-29) for the AA-74 correlation).
- $F_{\text{INT}}$  = Bundle internal power peaking factor

For AA-74 correlation  $C_S$  is

$$C_S(\Delta S) = \left[ \quad \right]^{a,c,g} \quad (3.5-52)$$

where  $\Delta S$  is the spacer distance.

To evaluate the critical power ratio the integrated bundle power that yields dryout at  $z_0$ ,  $Q_{DO}(z_0)$ , is needed. To get  $Q_{DO}(z_0)$ , first the dryout quality  $X_{DO}$  is found by solving the critical heat flux correlation and an integral heat balance simultaneously. Then  $Q_{DO}(z_0)$  is determined from substituting  $X_{DO}$  back in the integral heat balance. Finally the CPR and maximum allowable heat flux can be calculated.

An integral heat balance to location  $z_0$ , assuming steady flow, is

$$Q_{DO}(z_0) = w h_{fg}(X_{DO}(z_0) - X_{in}) \quad (3.5-53)$$

$$Q(z_0) = w h_{fg}(X_s(z_0) - X_{in})$$

where  $X_{DO}$ ,  $X_s$ , and  $X_{in}$  are the dryout quality and actual quality at  $z_0$ , and the inlet quality, respectively.

Substituting the above into Eq. (3.5-51), the CPR can be expressed as

$$CPR(z=z_0) = \frac{X_{DO}(z=z_0) - X_{in}}{X_s(z=z_0) - X_{in}} \cdot C_S(\Delta S) \cdot C_F(F_{INT}) \quad (3.5-54)$$

The dryout limiting quality,  $X_{DO}$  is found by equating  $q''_{cr}$  from the critical heat flux equation

$$q''_{cr}(z=z_0) = (A_i - B_i \cdot X_{DO}(z=z_0)) \cdot C_1(p,G) \quad (3.5-55)$$

with the heat flux at dryout,  $q''_{DO}(z=z_0)$  for the peak rod, expressed as (see Fig. 3-20)

$$q''_{DO}(z=z_0) = \left. \frac{\partial q''}{\partial X} \right|_{z=z_0} \cdot (X_{DO}(z=z_0) - X_{in}) \quad (3.5-56)$$

where

$$\left. \frac{\partial q''}{\partial X} \right|_{z=z_0} = \frac{q''(z=z_0) \cdot F_{INT}}{X_s(z=z_0) - X_{in}} \quad (3.5-57)$$

which includes the effect of internal bundle peaking.

In Eq. (3.5-55) for the AA correlation  $C_1(p,G)$ ,  $A_i$ , and  $B_i$  are according to the appropriate equations of (3.5-37) through (3.5-47).

Equation Eq. (3.5-55) and (3.5-56) gives:

$$X_{DO_i} = \frac{A_i C_1(p,G) + \left. \frac{\partial q''}{\partial X} \right|_{z=z_0} \cdot X_{in}}{\left. \frac{\partial q''}{\partial X} \right|_{z=z_0} + B_i C_1(p,G)} \quad (3.5-58)$$

$$X_{DO}(z=z_0) = \max[\min[(X_{DO_1}(z=z_0), X_{DO_2}(z=z_0)], X_{DO_3}(z=z_0))] \quad (3.5-59)$$

The flow boiling critical power ratio (CPR) can now be evaluated using Eq. (3.5-54).

The pool boiling CPR is also calculated by replacing Eq. (3.5-55) with Eq. (3.5-50)

$$CPR_{PB} = q''_{pc}(z=z_0)/q''(z=z_0) \cdot F_{INT} \quad (3.5-60)$$

Then the final CPR is

$$CPR = \max[CPR \text{ (Eq. (3.5-54))}; CPR_{PB}] \quad (3.5-61)$$

Last, the maximum allowable heat flux can be determined for a given minimum critical power ratio, MCPR, internal bundle power peaking,  $F_{INT}$ , power peaking distribution correction  $C_F(F_{INT})$  and spacer location correction  $C_S(\Delta S)$ . To calculate a maximum allowable heat flux, Eq. (3.5-54) is first rewritten as

$$X_{DO} = \frac{MCPR (X_s(z=z_0) - X_{in})}{C_S(\Delta S) \cdot C_F(F_{INT})} + X_{in} \quad (3.5-62)$$

This dryout limiting quality is then used to calculate a critical heat flux by substituting into the appropriate critical heat flux correlation.

Then the maximum allowable heat flux is given by rewriting Eq. (3.5-51).

$$q''_{max}(z=z_0) = \frac{q''_{crit} \cdot C_S(\Delta S) \cdot C_F(F_{INT})}{MCPR \cdot F_{INT}} \quad (3.5-63)$$

where  $C_S(\Delta S)$  and  $C_F(F_{INT})$  are set to one for pool boiling.

#### Rod Critical Temperature

The critical temperature is calculated from

$$T_{crit} = \frac{q''_{max}}{h_{crit}} + T_c \quad (3.5-64)$$

where

$q''_{max}$  = Maximum heat flux (Eq. (3.5-63))

$h_{crit}$  = Heat transfer coefficient in the two-phase boiling regime.

### Plate Critical Temperature

The critical temperature for the reactor vessel and internals (metal plates) is calculated from (Ref. 3-30)

$$T_{crit} = T_{sat} + 23^{\circ}\text{C} \quad (3.5-65)$$

where  $T_{sat}$  is the saturation temperature.

#### 3.5.4 Transition Boiling

Transition boiling occurs when the surface temperature is above the critical temperature,  $T_{crit}$ , but below the Leidenfrost temperature,  $T_{Leid}$ . This regime is called the unstable dryout regime.

The heat flux in the unstable dryout regime is calculated by interpolation between the critical heat flux and Leidenfrost point heat flux (see Fig. 3-21). A model in terms of surface temperature can be generated by solving the models for the heat conduction and convective heat transfer simultaneously.

The transient solution to the heat conduction equation can be written as

$$q_T'' = g(\xi_i, T_w) \quad (3.5-66)$$

where

- $g$  = Function representing the heat conduction equation
- $\xi_i$  = Various parameters (power generation, geometry, material properties)
- $T_w$  = Surface temperature
- $q_T''$  = Surface heat flux



In the transition boiling region, Eq. (3.5-66) is evaluated for surface temperatures at both the critical and Leidenfrost temperatures:

$$q_T''(T=T_{crit}) = g(\xi_i, T_{crit}) \quad (3.5-67)$$

$$q_T''(T=T_{Leid}) = g(\xi_i, T_{Leid}) \quad (3.5-68)$$

The solution to the heat conduction equation for temperatures between the critical and the Leidenfrost temperatures is approximated by the linear interpolation relationship:

$$q_T''(T=T_w) = q_T''(T=T_{crit}) - f_T \cdot [q_T''(T=T_{crit}) - q_T''(T=T_{Leid})] \quad (3.5-69)$$

where

$$f_T = \frac{T_w - T_{crit}}{T_{Leid} - T_{crit}} \quad (3.5-70)$$

Alternatively, the surface heat fluxes at the two boundaries temperatures of the transition boiling regime also can be calculated from the convective heat transfer correlations as follows.

At the critical temperature:

$$q_H''(T=T_{crit})_{2\phi} = H_{2\phi} (T_{crit} - T_c) \text{ for two-phase flow} \quad (3.5-71)$$

$$q_H''(T=T_{crit})_g = H_g (T_{crit} - T_c) \text{ for single-phase steam} \quad (3.5-72)$$

At the Leidenfrost temperature:

$$q_H''(T=T_{Leid})_{2\phi} = H_{DO} (T_{Leid} - T_c) \text{ for two-phase flow} \quad (3.5-73)$$

$$q_H''(T=T_{Leid})_g = H_g (T_{Leid} - T_c) \text{ for single-phase steam} \quad (3.5-74)$$

The surface convective heat flux for surface temperatures between the critical and Leidenfrost temperatures is approximated by the interpolation relationship

$$q_H''(T=T_w) = (1-F_g) \cdot [q_H''(T=T_{crit})_{2\theta} + (q_H''(T=T_{Leid})_{2\theta} - q_H''(T=T_{crit})_{2\theta}) \frac{(1+a) \cdot f_T}{f_T+a}] + F_g [q_H''(T=T_{crit})_g + (q_H''(T=T_{Leid})_g - q_H''(T=T_{crit})_g) \cdot f_T] \quad (3.5-75)$$

where "a" is a curvature parameter equal to 0.1 and  $F_g$  is

$$F_g = \max [0, \min [1.0, \frac{\alpha - \alpha_1}{\alpha_2 - \alpha_1}]] \quad (3.5-76)$$

where  $\alpha_1$  and  $\alpha_2$  are the transition void fractions defined in Sec. 3.5.1.

The heat conduction and heat transfer heat fluxes in the boiling transition regime are equated to solve for the surface temperature. Hence, the simultaneous solution to Eq. (3.5-69) and (3.5-75) gives:

$$T_w = T_{crit} + C_T \cdot (T_{Leid} - T_{crit}) \quad (3.5-77)$$

where

$$C_T = -a_1 + (a_1^2 - 4a_0a_2) / (2a_2) \quad (3.5-78)$$

$$a_0 = (F_g \cdot q_H''(T=T_{crit})_g + (1-F_g) \cdot q_H''(T=T_{crit})_{2\theta})^2$$

$$q_T''(T=T_{crit}) \cdot a \quad (3.5-79)$$

$$a_1 = F_g \cdot q_H''(T=T_{crit})_g - q_T''(T=T_{crit}) +$$

$$(1-F_g) \cdot q_H''(T=T_{Leid})_{2\theta} +$$

$$a [F_g (q_H''(T=T_{Leid})_g - q_H''(T=T_{crit})_g) +$$

$$q_T''(T=T_{crit}) - q_T''(T=T_{Leid}) +$$

$$(1-F_g) (q_H''(T=T_{Leid})_{2\theta} - q_H''(T=T_{crit})_{2\theta})] \quad (3.5-80)$$

$$a_2 = F_g (q_H''(T=T_{Leid})_g - q_H''(T=T_{crit})_g) +$$

$$q_T''(T=T_{crit}) - q_T''(T=T_{Leid}) \quad (3.5-81)$$

Equation (3.5-77) gives the wall temperature in the unstable dryout regime for a given  $T_{crit}$  and  $T_{Leid}$ . The calculation of  $T_{crit}$  was described in Section 3.5.3. The calculation of  $T_{Leid}$  is described below.

### Leidenfrost Temperature

The Leidenfrost temperature,  $T_{Leid}$ , for fuel rods is calculated from (Ref. 3-31)

$$T_{Leid} = T_{sat} + f_{Leid} (9.0945 \cdot 10^{-3} + \frac{3.6963 \cdot 10^3}{p})^{-1} \quad (3.5-82)$$

The pressure,  $p$ , is in Pascals. The value of the multiplier  $f_{Leid}$  is 2.0 based on comparisons of rewet times with experimental data (Ref. 3-35).

### 3.5.5 Radiation Heat Transfer

The surface to surface radiation is calculated by Eq. (3.5-3). The gray body factors are input into GOBLIN for the geometry of interest. These gray body factors are calculated using the auxiliary code BILBO described in Sec. 4.5.2. Radiation heat transfer is only calculated in the dispersed and steam flow regimes.

### 3.6 Heat Conduction Models

The thermal model in GOBLIN consists of two one-dimensional conduction models, cylindrical coordinates is used for the fuel rods and Cartesian coordinates for the reactor vessel and internals (plates). The properties of the structural materials, are also considered.

The heat conduction model accounts for the influence of a moving two-phase water level on the heat transfer. This is done by subdividing any rod or plate into a portion above and below the water level and performing separate heat conduction calculations for each subdivision.

#### 3.6.1 Fuel Rod Conduction Model

The fuel rod conduction model in GOBLIN is essentially the same as the CHACHA-3C model described in detail in Sec. 4.1.

In CHACHA-3C the boundary conditions of coolant temperature and heat transfer coefficient are specified as inputs. In GOBLIN the coolant conditions are specified by the hydraulic model and the heat transfer coefficient is solved implicitly with the heat conduction solution. The GOBLIN model also can simulate several axial fuel rod segments. The axial conduction between fuel rod segments is not modelled, as they are negligible.

### 3.6.2 Plate Conduction Model

GOBLIN can model any number of heat-transferring plates (simulating parts of the vessel or the internals) which are in contact (cooled) with coolant on both sides or insulated on either side. The one-dimensional heat conduction equation is solved using a finite difference technique and a user-specified nodal subdivision of each plate. Each plate can be composed of different materials.

The one-dimensional heat conduction equation

$$\rho c \frac{\partial T}{\partial t} = k \frac{\partial^2 T}{\partial x^2} \quad (3.6-1)$$

is integrated over the conduction nodes (see Fig. 3-22).

For node  $i$  we have

$$\begin{aligned} \rho_i c_i V_i \frac{\partial T_i}{\partial t} = & -A_{i-1,i} \cdot k_{i-1,i} \left. \frac{\partial T}{\partial x} \right|_{i-1,i} \\ & + A_{i,i+1} \cdot k_{i,i+1} \left. \frac{\partial T}{\partial x} \right|_{i,i+1} \end{aligned} \quad (3.6-2)$$

The partial derivatives are approximated by the following differences

$$\frac{\partial T_i}{\partial t} = \frac{T_i^{n+1} - T_i^n}{\Delta t} \quad (3.6-3)$$

$$\left. \frac{\partial T}{\partial x} \right|_{i-1,i} = \frac{T_i - T_{i-1}}{0.5(\Delta x_i + \Delta x_{i-1})} \quad (3.6-4)$$

$$\left. \frac{\partial T}{\partial x} \right|_{i,i+1} = \frac{T_{i+1} - T_i}{0.5(\Delta x_i + \Delta x_{i+1})} \quad (3.6-5)$$

$$\left. \frac{\partial T}{\partial x} \right|_{L,1} = \frac{T_1 - T_{CL}}{0.5 \Delta x_1} \quad (3.6-6)$$

$$\left. \frac{\partial T}{\partial x} \right|_{N,R} = \frac{T_{CR} - T_N}{0.5 \Delta x_N} \quad (3.6-7)$$

The thermal conductivities at the boundaries of the nodes are calculated using the requirement of a continuous heat flux across the node boundaries.

$$k_{i,i+1} = \frac{k(T_i) k(T_{i+1}) \cdot (\Delta x_i + \Delta x_{i+1})}{k(T_i) \cdot \Delta x_{i-1} + k(T_{i+1}) \cdot \Delta x_i} \quad (3.6-8)$$

Equation (3.6-2) is written in the finite difference form using the method developed by Crank and Nicolson (Ref. 3-36):

$$\begin{aligned} \rho_i V_i c (T_i^n) \frac{T_i^{n+1} - T_i^n}{\Delta t} = \\ - \frac{A_{i-1,i} k_{i-1,i}^n}{0.5 (\Delta x_i + \Delta x_{i-1})} [\theta T_i^{n+1} + (1-\theta) T_i^n - \theta T_{i-1}^{n+1} - (1-\theta) T_{i-1}^n] \\ + \frac{A_{i,i+1} k_{i,i+1}^n}{0.5 (\Delta x_i + \Delta x_{i+1})} [\theta T_{i+1}^{n+1} + (1-\theta) T_{i+1}^n - \theta T_i^{n+1} - (1-\theta) T_i^n] \end{aligned} \quad (3.6-9)$$

where  $\theta$  is the implicitness factor (a value of one is used in GOBLIN/DRAGON).

For the left boundary, the following equation is used

$$-k(T_1^n) \frac{T_0^{n+1} - T_1^{n+1}}{0.5 \Delta x_1} \cdot A_{0,1} = H_L^n \cdot A_L (T_0^{n+1} - T_{CL}) \quad (3.6-10)$$

and for the right boundary

$$-k(T_N^n) \cdot \frac{T_N^{n+1} - T_{N+1}^{n+1}}{0.5 \Delta x_N} A_{N,N+1} = H_R^n \cdot A_R (T_{N+1}^{n+1} - T_{CR}) \quad (3.6-11)$$

### Solution Method

Once the hydraulic model has been solved, the heat conduction problem for the plates is solved using Eq. (3.6-9) through (3.6-11). These form a system of equations in the unknown temperatures of the form

$$\underline{A} \underline{T} = \underline{B} \quad (3.6-12)$$

where A is a tridiagonal matrix. This system of equations is solved using a Gaussian elimination technique accounting for the structure of the matrix A.

### 3.6.3 Material Properties

Several material property equations as a function of temperature are incorporated into GOBLIN. The material properties of interest are thermal conductivity, heat capacity, and density.

The fuel rod material properties for Zircaloy-2 and Uranium dioxide are presented in Appendix 4A. The following are the other structural material properties in GOBLIN.

#### Carbon Steel ASME 508 Class 2 or 3

$$\begin{aligned} k &= 55.14 - 0.03054 \cdot T && (\text{W/m}^\circ\text{K}) \\ c &= 453.6 + 0.444 \cdot T && (\text{J/Kg}^\circ\text{K}) \\ \rho &= 7830 && (\text{Kg/m}^3) \end{aligned}$$

Stainless steel SIS 2333

$$\begin{aligned}k &= 14.73 + 0.01346 \cdot T && (\text{W/m}^\circ\text{K}) \\c &= 432.25 + 0.391 \cdot T - 1.8\text{E-}4 \cdot T^2 && (\text{J/Kg}^\circ\text{K}) \\p &= 7900 && (\text{Kg/m}^3)\end{aligned}$$

Carbonsteel ASME SA 533 Grade B

$$\begin{aligned}k &= 55.14 - 0.03054 \cdot T && (\text{W/m}^\circ\text{K}) \\c &= 453.6 + 0.444 \cdot T && (\text{J/Kg}^\circ\text{K}) \\p &= 7810 && (\text{Kg/m}^3)\end{aligned}$$

Inconel 600

$$\begin{aligned}k &= 14.47 + 0.01635 \cdot T && (\text{W/m}^\circ\text{K}) \\c &= 444 && (\text{J/Kg}^\circ\text{K}) \\p &= 8420 && (\text{Kg/m}^3)\end{aligned}$$

Stainless steel SIS 2333 with boron carbide

$$\begin{aligned}k &= 14.73 + 0.01346 \cdot T && (\text{W/m}^\circ\text{K}) \\c &= 435.1 + 0.2436 \cdot T && (\text{J/Kg}^\circ\text{K}) \\p &= 7900 && (\text{Kg/in}^3)\end{aligned}$$



### 3.7 Power Generation Models

The volumetric heat generation in the fuel and coolant are calculated in GOBLIN. The heat sources for the fuel appear in the heat conduction equation as the volumetric heat generation term,  $q'''$ , in Eq. (4.1-1). The heat sources for the coolant appear as the volumetric heat generation term,  $Q_V$  in the energy equation (see Eq. (3.1-15)).

Heat generation due to reactor power and decay power is modelled as the sum of heat generated from three basic sources -- fission power, fission product decay, and actinide decay. The total power is distributed throughout the core via user specified deposition fractions associated with various user defined regions of the fuel and coolant. The reactor fission power is calculated from a neutron point kinetics model. The fission products and actinide decay power are calculated by a 14 decay group model.

The heat generation due to Zircaloy metal-water reaction is also modelled. It is calculated by the Baker-Just reaction model (Ref. 3-32). The heat is deposited in the cladding node containing the oxidation interface.

#### 3.7.1 Point Kinetics Model

The power generation in the reactor core may be determined from the solution of the reactor point kinetics equations. These equations describe the time behavior of the core power level with the total reactivity acting as the controlling parameter.

The reactor point kinetics equations include effects arising from the direct fission power and the decay of fission products and actinides. The total power generation is the sum of the fission and decay power

$$Q(t) = Q_f(t) + Q_d(t) \quad (3.7-1)$$

The instantaneous fission power is given

by

$$Q_f(t) = \rho(t) \cdot E_Q \quad (3.7-2)$$

where  $E_Q$  is the conversion factor between neutron power generation and neutron flux density.

The decay heat generation rate is

$$Q_d(t) = \sum_{j=1}^M \lambda_j H_j \quad (3.7-3)$$

where  $\lambda_j$  is the decay group decay constant and  $H_j$  is the decay power for group  $j$ .

The neutron flux density and decay group power over time are determined by solving the point kinetics equations

$$\frac{d\rho}{dt} = \frac{r-\beta}{\ell^*} \rho + \frac{1}{\ell^*} \sum_{i=1}^n \lambda_i C_i \quad (3.7-4)$$

$$\frac{dC_i}{dt} = \beta_i \rho - \lambda_i C_i, \quad i=1, n \quad (3.7-5)$$

$$\frac{dH_j}{dt} = -\lambda_j H_j + E_j \cdot (Q_o/Q_{\text{neutron}}) \cdot \rho \cdot E_Q, \quad j = 1, m \quad (3.7-6)$$

where

$\theta$	= The neutron flux density
$\lambda_i$	= Delay neutron group decay constant
$C_i$	= Delay neutron group flux density
$\beta_i$	= Delay neutron group yield
$r$	= Reactivity
$\ell^*$	= Mean neutron lifetime
$H_j$	= Decay group power
$E_j$	= Decay group energy fraction
$\gamma_j$	= Decay group decay constant

The prompt jump approximation of

$$\frac{d\theta}{dt} = 0 \quad (3.7-7)$$

is used in Eq. (3.7-4), yielding

$$\theta = \sum_{i=1}^n \lambda_i C_i / (\beta - r) \quad (3.7-8)$$

Then Eq. (3.7-5) becomes

$$\frac{dC_i}{dt} = \beta_i \cdot \frac{\sum_{i=1}^n \lambda_i C_i}{(\beta - r)} - \lambda_i C_i, \quad i=1, n \quad (3.7-9)$$

Equation (3.7-9) is solved using a second order iterative method, for the delay neutron flux densities. The neutron flux density is found from Eq. (3.7-8). Then the decay group power is then found from Eq. (3.7-6). Finally the reactor power is calculated from Eq. (3.7-1) through (3.7-3).

The kinetics model is initialized such that the initial power generation equals the specified steady state power. Up to six delay neutron groups,

i.e., delay neutron fractions,  $\beta_i$ , and time constants,  $\lambda_i$ , may be specified by the user.

The fission product decay is modelled by eleven groups. The constants and effective energy fractions for these eleven group is based on a fit to the proposed American Nuclear Society Standard 5.1 of 1971 (Ref. 3-33). Three actinide decay groups are also modelled. The decay time constants and effective energy fractions also are based on Ref. 3-33. Table 3-2 lists the time constants and energy fractions for the 14 decay groups. Table 3-3 shows a comparison of the eleven group fission product curve with the tabulated standard. The agreement is close and conservative. An uncertainty of 20 percent as required by Appendix K of 10CFR50, is added to the resultant fission product power generation. The reactivity,  $r$ , includes models for the reactivity change due to fuel temperature, moderator temperature, void fraction, and control rod insertion. The first three reactivity changes are calculated from user specified correlations. The control rod reactivity is input versus time after reactor scram.

The fission power or total power versus time also may be specified by the user eliminating the kinetic calculation (this option is used in a DRAGON calculation).

### 3.7.2 Metal-Water Reaction Model

The heat generation due to metal-water reaction between the Zircaloy cladding and the coolant is calculated using the reaction rate model developed by Baker and Just (Ref. 3-32).

The power generated per unit length of rod is the energy release per mass reacted times the rate of cladding oxidation

$$Q_{MWR} = \frac{\Delta E \rho_{Zr} (V_{Zr}/\Delta z)}{\Delta t} \quad (3.7-10)$$

where  $\rho_{Zr}$  is  $6560 \text{ kg/m}^3$  and

$$\Delta E \text{ (J/kg)} = 6.669 \times 10^6 - 257 T \text{ (}^\circ\text{K)} \quad (3.7-11)$$

The reacted volume is calculated from the oxidation rate equation

$$\frac{dr}{dt} \text{ (m/s)} = \frac{3.937 \times 10^{-5}}{r} \exp\left(\frac{-22898.84}{T \text{ (}^\circ\text{K)}}\right) \quad (3.7-12)$$

Integrating Eq. (3.7-12) gives the radius oxidized over time  $\Delta t$ . The volume per unit length oxidized is thus

$$\left(\frac{V_{Zr}}{\Delta z}\right) \text{ (m}^2\text{)} = 2\pi \left(\frac{2r_o}{r_1 + r_2} - 1\right) (3.937 \times 10^{-5}) \exp\left(\frac{-22898.84}{T \text{ (}^\circ\text{K)}}\right) \Delta t \quad (3.7-13)$$

where  $r_o$ ,  $r_1$ , and  $r_2$  are respectively the outer cladding radius, initial oxidation front radius and final front radius in time  $\Delta t$ .

The power generation calculated from Eq. (3.7-10) is added in the cladding conduction calculation for the node(s) between radius  $r_1$ , and  $r_2$ .

### 3.8 Numerical Solution

Several numerical methods are employed in GOBLIN to solve the power generation, hydraulic, and heat conduction/transfer models. A simplified flow chart of the calculational sequence is shown in Fig. 3-23.

After initialization of the problem, the first quantities evaluated for each calculational time step are the boundary conditions (e.g. ECC flow rates) and power generation. The reactor point kinetics model, used in evaluating the power generation, is solved by a second order Runge-Kutta method.

Next the hydraulic model is solved iteratively for the primary variables. The hydraulic problem is solved by a simultaneous solution of the conservation equations, equations of state, and pump speed equations using relaxed Newton's method.

The primary variables are pressure, enthalpy, mass, and flow rate or two-phase elevation. Secondary variables are calculated from auxiliary expressions. A predictor-corrector calculation may be employed to accelerate convergence, if the solution is close to converged. A variable transient time step logic based on the transient hydraulics is used to optimize the computational time. If the hydraulic problem does not converge the time step is reduced and the calculation restarted.

Once the hydraulic problem is solved the coolant state is used in finding the solution of the rod and the plate heat conduction and problems. The conduction and surface heat transfer equations are solved iteratively for the surface temperature and heat transfer coefficient. The conduction equation is solved by Gaussian elimination and back substitution. Fractional steps of a hydraulic time step may be employed to find a unique solution for the surface temperature. The convective and radiative heat fluxes are then calculated from the known temperatures and heat transfer coefficient.

For a given calculational time the hydraulic and thermal solutions, and the hydraulic to thermal coupling are treated fully implicitly. The convective heat flux used in the hydraulic solution, however, is treated explicitly.

The numerical solution methods are described in more detail below.

### 3.8.1 Reactor Point Kinetics Solution

The differential equations for the delayed neutron flux densities Eq. (3.7-9) are written the form

$$\frac{dY_i}{dt} = f(\underline{Y}) \quad (3.8-1)$$

where  $\underline{Y}$  is the vector of the delay neutron fluxes  $C_i$ . Eq. (3.8-1) are numerically integrated over kinetics model time steps  $\Delta t_k$ , using a second order Runge-Kutta method.

$$Y_i^{n+1} = Y_i^n + \frac{\Delta t_k}{2} [f(\underline{Y}^n) + f(\underline{Z}^{n+1})] \quad (3.8-2)$$

where

$$\underline{Z}^{n+1} = \underline{Y}^n + \Delta t_k [f(\underline{Y}^n)] \quad (3.8-3)$$

The time step,  $\Delta t_k$ , is two percent of the smallest delay neutron time constant, (i.e.,  $0.02/\max(\lambda_i)$ ), or the hydraulic time step size if smaller.

Once the delayed neutron flux densities at the new time step are known, the total neutron flux is calculated from Eq. (3.7-8). Last the decay fission product group power  $H_j$  is calculated from the integration of Eq. (3.7-6)

$$H_j^{n+1} = H_j^n \cdot \exp(-\alpha_j \cdot \Delta t_k) + \frac{E_j}{\alpha_j} \frac{Q_0}{Q_{\text{neutron}}} \beta^n (1 - \exp(-\alpha_j \cdot \Delta t_k)) - \beta^{n+1} \quad (3.8-4)$$

where

$$\eta = [1 - \exp(-\lambda_j \cdot \Delta t_k)] / (\lambda_j \cdot \Delta t_k) \quad (3.8-5)$$

which assumes that the total flux  $\phi$  varies linearly over  $\Delta t$ . The total power at the new kinetics time step is

$$Q^{n+1} = E_Q \cdot \phi^{n+1} + \sum_{j=1}^m \lambda_j \cdot H_j^{n+1} \quad (3.8-6)$$

The power generation for the hydraulic time step is the integrated average of each kinetics time step.

### 3.8.2 Hydraulic Model Solution

The fluid conservation equations together with the momentum balance for the main recirculation pumps are put in the form

$$\underline{F}(\underline{Y}^{n+1}) = 0 \quad (3.8-7)$$

where  $\underline{Y}^{n+1}$  is the system state vector, representing the primary variables at the new time step,

$$\underline{Y}^{n+1} = (\underline{Y}_1^{n+1}, \underline{Y}_2^{n+1}, \dots, \underline{Y}_N^{n+1}) \quad (3.8-8)$$

The primary variables in the GOBLIN code are:

$$\begin{aligned} Y_1 &= \omega_1 &= \text{angular speed of pump wheel 1} \\ &\vdots & \\ Y_{N_p} &= \omega_{N_p} &= \text{angular speed of pump wheel } N_p \\ Y_k &= p &= \text{Pressure of control volume } i \\ Y_{k+1} &= m &= \text{Mass inventory of control volume } i \end{aligned}$$



$Y_{k+2} = h$  = Enthalpy of control volume  $i$

$Y_{k+3} = w$  = Mass flow rate out of control volume  $i$

For a control volume with a two phase level as the control volume boundary  $Y_{k+3}$  is replaced with

$Y_{k+3} = z_{lev}$  = Elevation of boundary of control volume  $i$

The value of  $k$  ranges from the number of pumps plus one,  $N_p + 1$ , to the total number of control volumes,  $K$ .

The total number of primary variables,  $N$  is

$$N = N_p + K \quad (3.8-9)$$

The equations to be solved in the GOBLIN code are:

$F_1$  = Momentum balance of recirculation pump number 1  
 $F_{N_p}$  = Momentum balance of recirculation pump number  $N_p$   
 $F_k^p$  = Equation of state of control volume  $i$   
 $F_{k+1}$  = Energy balance of control volume  $i$   
 $F_{k+2}$  = Mass balance of control volume  $i$   
 $F_{k+3}$  = Momentum balance of control volume flow out of  $i$

When a two-phase level is present the equation for  $F_{k+3}$  is replaced with an equation for volume conservation between the two control volumes adjacent to the two-phase level.

#### Newton's Method

The system of non-linear equations is solved using a relaxed Newton's method,

$$\underline{y}_{m+1}^{n+1} = \underline{z}_m^{n+1} - \underline{J}^{-1} \cdot \underline{F}(\underline{z}_m^{n+1}) \quad (3.8-10)$$

where superscript n is the time step and subscript m is the iteration count, and  $\underline{Z}_m$  is the relaxed previous iteration primary variable vector

$$\underline{Z}_m = \underline{Y}_m + f_{\text{relax}} \cdot (\underline{Y}_m - \underline{Y}_{m-1}) \quad (3.8-11)$$

The relaxation factor,  $f_{\text{relax}}$ , is a scalar quantity based on the rate of convergence of the previous iterations.

The matrix  $\underline{J}$  is the Jacobian of  $\underline{F}$ . The elements of  $\underline{J}$  are

$$J_{ij} = \frac{\partial F_i}{\partial Y_j} \quad (3.8-12)$$

The elements are calculated analytically where this can be done readily, others are evaluated numerically. Optionally,  $\underline{J}$  can be calculated completely numerically. The Jacobian is normally recalculated for each iteration although an option is available by which the Jacobian is recalculated only once each time step.

The starting guess for the Newton iteration is normally a linearly-extrapolated solution from the last two time steps. However at restarts the starting guess is taken to be the last accepted solution.

The linear system of equations of Eq. (3.8-10) are solved using an adopted version of the methods developed by A. R. Curtis and J. K. Reid (Ref. 3-34). The method is based on Gaussian elimination in a form suitable for sparse matrices (the matrix  $\underline{J}$  above is sparse). Linked lists and great freedom to choose a pivot element make the method very efficient. The pivot sequence used is also stored in case a later system of equations with the same pattern of coefficients appears, in which case the solution is faster. The Jacobian is also scaled before it is processed.

The convergence criteria for the Newton iteration is

$$\max \left\{ \frac{|Y_{i,m+1}^{n+1} - Y_{i,m}^{n+1}|}{1000 + |Y_{i,m}^{n+1}|} \right\} < \epsilon \quad (3.8-13)$$

for all  $i$  from 1 to  $N$ . The convergence requirement,  $\epsilon$ , is typically  $10^{-4}$ , and two to five iterations are normally sufficient.

### Predictor-Corrector Method

A predictor-corrector method is employed in the solution of the hydraulic problem if the convergence using Newton's method is slow. The predictor-corrector method is used only after several Newton iterations if the time steps and errors are sufficiently small.

The residual errors from the last Newton iteration are used as the predictor and the primary variable vector is corrected using Euler's method

$$Y_{-m+1}^{n+1} = Y_{-m}^{n+1} + \Delta t \cdot F(Y_{-m}^{n+1}) \quad (3.8-14)$$

Iteration  $m+1$  is the converged solution.

### 3.8.3 Heat Conduction and Transfer Solution

The solution of the heat conduction equation (Sec. 3.6) and the surface heat transfer equation (Sec. 3.5) is performed simultaneously by solving iteratively for the wall surface temperature.

The heat transfer and heat conduction problems can be written as

$$q'' = H(\xi_i, T_w) \cdot (T_w - T_c) \quad (3.8-15)$$

and

$$q'' = g(\eta_i, T_w) \quad (3.8-16)$$

where Eq. (3.8-15) expresses the heat flux given a surface temperature,  $T_w$ , ( $\xi_i$ , represents other variables affecting the heat transfer coefficient), and Eq. (3.8-16) expresses the solution to the heat conduction equation for the fuel rod or plate given the surface temperature as a boundary condition. Equation (3.8-15) and (3.8-16) are shown in Fig. 3-24. The system of Eq. (3.8-15) and (3.8-16) are rewritten as:

$$F(T_w) = H(\xi_i, T_w) (T_w - T_c) - g(\eta_i, T_w) = 0 \quad (3.8-17)$$

Equation (3.8-17) is then solved by using Newton-Raphson's method

$$T_{w_{i+1}} = T_{w_i} - F(T_{w_i}) / \left. \frac{\partial F}{\partial T_w} \right|_{T=T_{w_i}} \quad (3.8-18)$$

where

$$\left. \frac{\partial F}{\partial T_w} \right|_{T=T_{w_i}} = \frac{F(T_{w_{i-1}}) - F(T_{w_i})}{T_{w_{i-1}} - T_{w_i}} \quad (3.8-19)$$

Two starting guesses are needed ( $T_{w_0}$  and  $T_{w_1}$ ), which depend on the previous time fluid conditions. For non-dryout conditions:

$$T_{w_0} = T_{crit} \quad (3.8-20)$$

$$T_{w_1} = \min (T_x, T_{crit} - 1)$$

and for dryout conditions:

$$T_{w_0} = T_{Leid} \quad (3.8-21)$$

$$T_{w_1} = \max (T_x, T_{Leid} + 1)$$

where  $T_x$  is the coolant temperature,  $T_c$  plus 5°C in steady state and the old surface temperature for a transient calculation.

During the iterations the derivative  $\frac{\partial F}{\partial T_w}$  in Eq. (3.8-18) is reevaluated only if  $|F(T_{w_{i-1}}) - F(T_{w_i})|$  exceeds one. Furthermore, for the

solution of  $T_{w_i}$  and  $T_{w_{i+1}}$ , the temperature with the largest value of  $|F(T_w)|$

is rejected from the next iteration.

To determine whether dryout or non-dryout conditions apply, the following procedure is used. The maximum permissible heat flux ( $q''_{max}$ ) is determined from Eq. (3.5-62). The critical temperature is then calculated according to Eq. (3.5-64) or (3.5-65) and the Leidenfrost temperature by Eq. (3.5-82). The heat fluxes

$$q''_H(T=T_{crit}) = H(\xi_i, T_{crit}) \cdot (T_{crit} - T_c)$$

$$q''_T(T=T_{crit}) = g(\eta_i, T_{crit})$$

$$q''_H(T=T_{Leid}) = H(\xi_i, T_{Leid}) \cdot (T_{Leid} - T_c)$$

$$q''_T(T=T_{Leid}) = g(\eta_i, T_{Leid})$$

and the conditions at the last time step are then used to determine the heat transfer regime and described below. The procedure is illustrated graphically in Fig. 3-25 and described below.

(1) If  $q_T''(T=T_{crit}) \leq q_H''(T=T_{crit})$  and there was no dryout during the last time step, then non-dryout conditions still apply.

(2) If  $q_T''(T=T_{Leid}) \geq q_H''(T=T_{Leid})$  and the surface was in the dryout heat transfer regime during the last time step or  $q_T''(T=T_{crit}) > q_H''(T=T_{crit})$  then stable dryout conditions apply.

(3) If  $q_T''(T=T_{crit}) > q_H''(T=T_{crit})$  and

$q_T''(T=T_{Leid}) \leq q_H''(T=T_{Leid})$ , then transition boiling is applicable.

(4) If  $q_T''(T=T_{crit}) \leq q_H''(T=T_{crit})$  and

$q_T''(T=T_{Leid}) \geq q_H''(T=T_{Leid})$  and transition boiling applied last time

step, then the time step is halved until a unique solution is achieved.

If the time step is halved, an average heat flux to the coolant is calculated and used in the energy balance equation for the coolant flow

$$q''_{AVG} = \frac{\sum_{i=1}^N q_i''}{N} \quad (3.8-22)$$

where  $q_i''$  is heat flux during sub-time step number  $i$  and  $N$  is number of sub-time steps.

### 3.9 Nodalization

The GOBLIN code has minimal restrictions on the nodalization configuration used for a plant model. Individual mass/energy control volumes are defined and momentum control volumes are defined which connect two adjacent mass/energy volumes. A double index notation is used to identify each control volume. Several momentum control volumes may be connected to a mass/energy volume. Any number of jet pumps, recirculation loops, recirculation pumps, fuel channels, fuel rods, structural plates, separators, dryers units, can be modelled. A sample GOBLIN nodalization diagram is shown in Figure 2-1.

Two types of boundary condition control volumes can be modelled:

- o A pressure and enthalpy boundary condition
- o A pressure, enthalpy and mass flow rate boundary condition

The boundary conditions may be supplied versus time by the user or they may be obtained from an output of a previous GOBLIN or DRAGON simulation.

### 3.10 Nomenclature

<u>Variable</u>	<u>Definition</u>
A	Area
$A_c$	Coefficient in friction factor correlation
a	Constant
B	Constant
$B_f$	Coefficient in friction factor correlation
C	Constant
$C_0$	Drift flux distribution parameter
$C_1, C_2$	Friction factor coefficients
$C_1$	CHF correlation correction factor
$C_i$	Delay neutron flux density
$C_f$	CPR correlation spacer coefficient
$C_r$	Conversion ratio
$C_s$	CPR correlation internal power coefficient
CPR	Critical power ratio
c	Heat capacity
$c_p$	Heat capacity at constant pressure
D	Diameter
$D_L$	Dimensionless property diameter
$D_h$	Hydraulic equivalent diameter
$D^*$	CCFL correlation dimensionless diameter
$D_{heat}$	Heated equivalent diameter
$E_Q$	Fission power conversion factor
$E_j$	Decay group effective energy fraction
e	Total energy
F	Two-phase Reynolds suppression factor
$\underline{F}$	Solution equation vector
$F_{cs}$	Maximum condensation rate factor
f	Friction factor
f	Function
G	Mass flux
$G_d$	Mass drift flux



<u>Variable</u>	<u>Definition</u>
$G_{tran}$	CHF correlation transition mass flux
GBF	Gray body factor
g	Gravity
H	Heat transfer coefficient
$H_j$	Decay group power
HC	Recirculation pump coefficients
h	Enthalpy
$h_{fg}$	Latent heat of vaporization
I	Inertia
J	Jacobian matrix
$\underline{j}$	Superficial velocity
K	Number balance equations
$K_1, K_2$	CCFL correlation coefficients
Ku	Kutateladze number
k	Conductivity
L	Length
$L_H$	Helmholtz instability length
$\ell^*$	Neutron mean lifetime
M	Two-phase pump multiplier
m	Mass
MCPR	Minimum critical power ratio
N	Total number solution equations
$N_p$	Number of pump equation
$\underline{n}$	Normal vector
$P_w$	Wetted perimeter
Pr	Prandtl number
p	Pressure
Q	Total heat generation
Q	Volumetric flow rate
$Q_V$	Volume heat generation
$Q_A$	Surface heat generation
$q''$	Heat flux

<u>Variable</u>	<u>Definition</u>
$q'''$	Volumetric heat rate
Re	Reynolds number
Ra	Rayleigh number
r	Radius
r	Reactivity
S	Surface
S	Subcooling suppression factor
S	Slip factor
T	Temperature
T	Torque
$T_s$	Saturation temperature
t	Time
u	Velocity
$u_r$	Relative velocity
V	Volume
$V_c$	CCFL correlation characteristic velocity
$V_{gj}$	Drift velocity
w	Mass flow rate
x,y,z	Cartesian coordinates
X	Static quality
$X^*$	Flow quality
$X_{tt}$	Martinelli property parameter
$\underline{Y}$	Primary variable vector
$\underline{Z}$	Corrected primary variable vector
z	Elevation
$\alpha$	Void fraction
$\alpha$	Dimensionless pump speed
$\beta$	Dimensionless pump torque
$\beta$	Volume coefficient of expansion
$\beta$	Delay neutron fraction
$\beta_i$	Delay neutron group fraction
$\Gamma$	Chisholm parameter

<u>Variable</u>	<u>Definition</u>
$\gamma$	Heat capacity ratio ( $c_p/c_v$ )
$\gamma_j$	Decay group decay constant
$\delta_{ij}$	Kronecker delta
$\epsilon$	Convergence error criteria
$\epsilon$	Roughness
$\epsilon_w$	Emissivity
$\theta$	Differencing weighting factor
$\lambda_i$	Delay neutron decay constant
$\mu$	Viscosity
$\nu$	Dimensionless pump volumetric flow rate
$\xi$	Local form pressure loss coefficient
$\pi$	3.14159...
$\rho$	Density
$\sigma$	Neutron cross section
$\sigma$	Surface tension
$\sigma_R$	Stefan-Boltzmann constant
$\underline{\sigma}$	Stress tensor
$\tau$	Shear stress
$\beta$	Neutron flux density
$\beta^2$	Two-phase multiplier
$x$	Parastic phase mass fraction
$\psi$	Pump direction coefficient
$\omega$	Pump speed

### 3.11 References

- 3-1 R. B. Byrd, W. E. Steward, E. N. Lightfoot, Transport Phenomena, John Wiley and Sons, 1960.
- 3-2 C. W. Hirst, "Heuristic Stability Theory for Finite-Difference Equation," Journal of Computational Physics, Vol. 2, 1968.
- 3-3 E. Schmith, "Properties of Water and Steam in SI-Units," Springer-Verlag, Berlin, 1969.
- 3-4 J. A. Holmes, Description of the Drift Flux Model in the LOCA Code RELAP-UK, Conference in Heat and Fluid Flow in Water Reactor Safety, I Mech E Manchester, 1977.
- 3-5 G. B. Wallis, One-dimensional Two-phase Flow, New York, McGraw-Hill, Inc., 1969.
- 3-6 R. T. Lahey and F. J. Moody, The Thermal-Hydraulics of a Boiling Water Nuclear Reactor, ANS Monograph, 1977.
- 3-7 S. O. Eriksson et al, Experiment Med Motriktade Ångflöden I Strilkylningskretsen, GÖTA, Studsvik, AES-15, 1977.
- 3-8 R. V. Bailey et al, "Transport of Gases Through Liquid-gas Mixtures," Paper presented at the AIChE New Orleans Meeting, 1956.
- 3-9 "OF64. Results of pressure drop measurements," FRIGG PM-71, May 26, 1970.  
"OF646. Pressure drop measurements," FRIGG PM-111, December 21, 1970.
- 3-10 F. Colebrook, "Turbulent Flow in Pipes with Particular Reference to the Transition Region between the Smooth and Rough Pipes" J. Inst. Civil Engineers, No. 4, 1938.

- 3-11 C. J. Baroczy, "A Systematic Correlation for Two-Phase Pressure Drop," Chem. Enging. Prog. Symp. Series, No. 64, Vol 62, 1965.
- 3-12 P. W. Ianni, "Effectiveness of Core Standby Cooling Systems for General Electric Boiling Water Reactors," APED-5458, March 1968.
- 3-13 F. S. Moody, "Maximum Flow Rate of a Single Component, Two-Phase Mixture," ASME Paper 64-HT-35, August, 1964.
- 3-14 P. Pana and M. Muller, "Subcooled and Two Phase Critical Flow States and Comparison with Data," Nuclear Engineering and Design Vol. 45, 1978, pp 117-125.
- 3-15 WREM: Water Reactor Evaluation Model (Rev. 1), NUREG-75/056, National Technical Information Service, May 1975.
- 3-16 M. Jakob, Heat Transfer, Vol. 1, Wiley, 1949, pg. 529.
- 3-17 E. N. Sieder and G. E. Tate, "Heat Transfer and Pressure Drop of Liquids in Tubes," Ind. Eng. Chem. 28, 1936, pg. 1429.
- 3-18 F. W. Dittus and L. M. K. Boelter, Pub. Eng. 2, Univ. of Calif., Berkeley, 1930, pg. 433.
- 3-19 J. C. Chen, "A Correlation for Boiling Heat Transfer of Saturated Fluids in Convective Flow," ASME paper 63-HT-34, 1963.
- 3-20 NEDO 20566-1 Rev. 1, Calculation of Low Flow Film Boiling Heat Transfer for BWR LOCA Analysis, 1977.
- 3-21 D. C. Groeneveld, "An Investigation of Heat Transfer in the Liquid Deficient Regime," AECL-3281, Aug. 1969.
- 3-22 W Emergency Core Cooling System Evaluation Model Application to Plants Equipped with Upper Head Injection, WCAP-8479-P Rev. 2.

- 3-23 ECCS Heat Transfer Experiments with Upper Head Injection, WCAP-8400.
- 3-24 G-2 17 x 17 Refill Heat Transfer Test and Analysis, WCAP-8793-P, August 1976.
- 3-25 R. S. Dougall and W. M. Rohsenow, "Film Boiling on the Inside of Vertical Tubes with Upward Flow of the Fluid at Low Qualities," M&T Report No 9079-26, Cambridge, Massachusetts Sept. 1963.
- 3-26 "AA-74 Dryout Correlation. An extended and reoptimized version of the previous dryout design correlation (AA-69)," ASEA-ATOM Report RM-RCB-74-55, Rev. 1, 1974.
- 3-27 N. Zuber, M. Tribus, J. W. Westwater, "The Hydrodynamic Crisis in Pool Boiling of Saturated and Subcooled Liquids," International Developments in Heat Transfer Part II, 1961, pg. 230-236.
- 3-28 P. Griffith, K. T. Avedisian, J. F. Walkush, "Countercurrent Flow Critical Heat Flux," National Heat Transfer Conference San Francisco, Aug. 1975.
- 3-29 "En approximative method for bestamning av interna effektfordelningens inverkan pa dryout," English Translation: "An approximate method for determination of the impact of the internal power distribution on dryout," ASEA-ATOM Report PM RCB 75-54, Aug. 27, 1975.
- 3-30 "Berechnung des instationaren Temperatur-verlaufes im Behalter eines Druckwasser-reaktors bei Notkuhlung," Brennst-Warme-Kraft 25, Nr. 5 1973, pp. 199-203.
- 3-31 "Heating in a Reactor Fuel Element Rod under Transient Conditions Part II DINO Temperatures during a Loss of Coolant Accident," RISO-M-1533, Sept. 1972.

- 3-32 L. Baker and L. C. Just, "Studies of Metal-Water Reactions at High Temperatures: III Experimental and Theoretical Studies of the Zirconium-Water Reaction," ANL-6548, 1962.
- 3-33 Proposed American Nuclear Society Standard 5.1 "Decay Energy Release Rates following Shutdown of Uranium-Fueled Thermal Reactors," Oct. 1971, Revised Oct. 1973.
- 3-34 A. R. Curtis and J. K. Reid, "Fortran Subroutine for the Solution of Sparse Sets of Linear Equations," AERE-R6844.
- 3-35 GOBLIN - Comparison with FIX-II Break Spectrum Tests, ASEA-ATOM Report KPA-85-71, May 8, 1985.
- 3-36 J. Crank and P. Nicolson, "A Practical Method for Numerical Evaluations of Solutions of Partial Differential Equations of the Heat Conduction Type" Proc. Cambridge Phil. Soc. Vol. 43, 1947.
- 3-37 O. Nylund and R. Eklund OF-64. Results of Void Measurement, FRIGG PM-69, February 9, 1970.

### Appendix 3A: Impact of Kinetic, Potential, and Dissipation Energy

The kinetic energy, potential energy, and dissipation terms are omitted in Eq. (3.1-10). The following demonstrates that these terms are to be negligible below. During a typical LOCA transient the maximum values of  $e_{kin}$  and  $e_{pot}$  are

$$e_{kin} = 1/2 u^2 = 1/2 (15 \text{ m/s})^2 \approx 100 \text{ J/kg} \quad (3A-1)$$

$$e_{pot} = gz = 9.8 \text{ m/s}^2 \cdot 10 \text{ m} \approx 100 \text{ J/kg} \quad (3A-2)$$

One hundred J/kg corresponds to a change in water temperature of about 0.02°C. Hence, these terms are clearly negligible compared to the fluid internal energy.

In order to justify omission of dissipation effects, the dominating terms of  $\nabla \cdot (\underline{g} \cdot \underline{u})$ , the dissipation term, must be examined

$$\begin{aligned} \nabla \cdot (\underline{g} \cdot \underline{u}) &\approx \frac{\partial}{\partial y} (\bar{\sigma}_{yx} u_x) \\ &= \frac{\partial \bar{\sigma}_{yy}}{\partial y} \cdot u_x + \bar{\sigma}_{yx} \frac{\partial u_x}{\partial y} \\ &\approx \bar{\sigma}_{yx} \frac{\partial u_x}{\partial y} \end{aligned} \quad (3A-3)$$

when  $x$  is the main flow direction and  $y$  is perpendicular to  $x$ . The term  $\sigma_{yx}$  can be estimated by an equation for frictional pressure drop

$$\tau_{wall} \cdot P_w = \Delta P_{fric} / \Delta x \cdot A \quad (3A-4)$$



which for a typical rod bundle a typical is

$$\begin{aligned}\tau_{\text{wall}} &= \frac{\Delta p_{\text{fric}}}{\Delta x} \frac{A}{P_w} = \frac{1}{4} \frac{\Delta p_{\text{fric}}}{\Delta x} D_h = \\ &= 1/4 \cdot 5000 \cdot 0.01 = 10 \text{ N/m}^2\end{aligned}\quad (3A-5)$$

Furthermore

$$\frac{\partial u_x}{\partial x} \approx \frac{u}{D_h} \approx \frac{15}{0.01} \approx 1500 \text{ s}^{-1}\quad (3A-6)$$

substituting into Eq. (3A-3) the dissipation term gives

$$\nabla \cdot (\bar{q} \cdot \underline{u}) \approx 10 \cdot 1500 \text{ N/m}^2 \text{ s} = 0.015 \text{ MW/m}^3\quad (3A-7)$$

When compared to the power density of the core (per cubic meter coolant)

$$q''' \approx (3000 \cdot 10^6 \text{ W})/24 \text{ m}^3 \approx 100 \text{ MW/m}^3\quad (3A-8)$$

the dissipation term is clearly negligible.

TABLE 3-1  
Factor  $f_4$  in Westinghouse UHI Correlation

$$f_4 = f_p f_G f_X$$

Pressure (psia)

[

$f_p$

] <sup>a,c</sup>

Mass flux (lbm/ft<sup>2</sup>sec)

[

$f_G$

] <sup>a,c</sup>

Quality

[

$f_X$

] <sup>a,c</sup>

TABLE 3-2  
Fission Product and Actinide Decay  
Effective Energy Fractions and Decay Constants

Group	$E_j$	$\lambda_j$ (sec <sup>-1</sup> )
1	0.00299	1.772
2	0.00825	0.5774
3	0.01550	$6.743 \times 10^{-2}$
4	0.01935	$6.214 \times 10^{-3}$
5	0.01165	$4.739 \times 10^{-4}$
6	0.00645	$4.810 \times 10^{-5}$
7	0.00231	$5.344 \times 10^{-6}$
8	0.00164	$5.726 \times 10^{-7}$
9	0.00085	$1.036 \times 10^{-7}$
10	0.00043	$2.959 \times 10^{-8}$
11	0.00057	$7.585 \times 10^{-10}$
12	$C_r \cdot \frac{\sigma_{25}}{\sigma_{f25}} \cdot 2.28E-3$	4.91E-4
13	$C_r \cdot \frac{\sigma_{25}}{\sigma_{f25}} \cdot 2.18519E-3$	3.41E-6
14	$C_r \cdot \frac{\sigma_{25}}{\sigma_{f25}} \cdot (-1.519E-5)$	4.91E-4

where

$$C_r \frac{\sigma_{25}}{\sigma_{f25}} = \text{Uranium -239 produced per fission}$$

TABLE 3-3

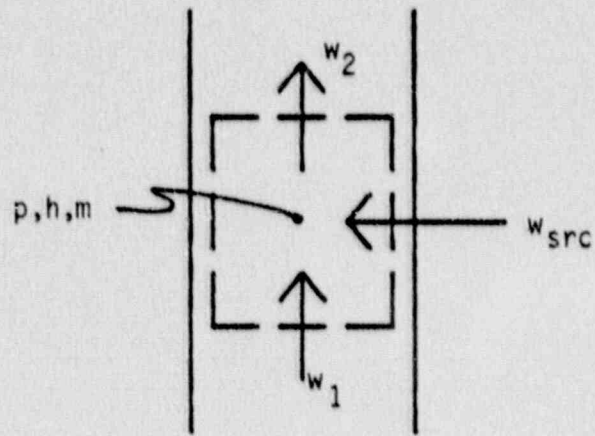
Comparison of 11 Group Fission Product Decay Curve with  
Tabulated Proposed 1971 ANS Standard 5.1 (Ref. 3-33)

<u>Time After Shutdown (sec)</u>	<u>Relative Power</u>	
	<u>ANS71</u>	<u>GOBLIN</u>
1 x 10 <sup>-1</sup>	0.0675	0.0689
1	0.0625	0.0628
2	0.0590	0.0593
4	0.0552	0.0554
6	0.0533	0.0531
8	0.0512	0.0514
1 x 10 <sup>+1</sup>	0.0500	0.0500
2 x 10 <sup>+1</sup>	0.0450	0.0449
4 x 10 <sup>+1</sup>	0.0396	0.0398
6 x 10 <sup>+1</sup>	0.0365	0.0372
8 x 10 <sup>+1</sup>	0.0346	0.0353
1 x 10 <sup>+2</sup>	0.0331	0.0337
2 x 10 <sup>+2</sup>	0.0275	0.0284
4 x 10 <sup>+2</sup>	0.0235	0.0234
6 x 10 <sup>+2</sup>	0.0211	0.0213
8 x 10 <sup>+2</sup>	0.0196	0.0201
1 x 10 <sup>+3</sup>	0.0185	0.0192
2 x 10 <sup>+3</sup>	0.0157	0.0162
4 x 10 <sup>+3</sup>	0.0128	0.0128
6 x 10 <sup>+3</sup>	0.0112	0.0112
8 x 10 <sup>+3</sup>	0.0105	0.0104
1 x 10 <sup>+4</sup>	0.00965	0.00976
2 x 10 <sup>+4</sup>	0.00795	0.00801
4 x 10 <sup>+4</sup>	0.00625	0.00625
6 x 10 <sup>+4</sup>	0.00566	0.00546
8 x 10 <sup>+4</sup>	0.00505	0.00506

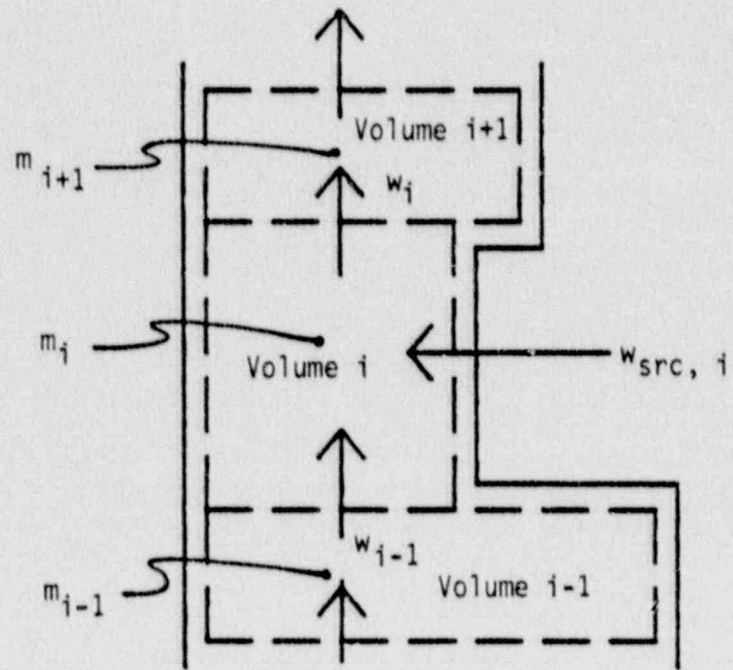
TABLE 3-3 (Continued)

Comparison of 11 Group Fission Product Decay Curve with  
Tabulated Proposed 1971 ANS Standard 5.1 (Ref. 3-33)

<u>Time After Shutdown (sec)</u>	<u>Relative Power</u>	
	<u>ANS71</u>	<u>GOBLIN</u>
1 x 10 <sup>+5</sup>	0.00475	0.00480
2 x 10 <sup>+5</sup>	0.00400	0.00409
4 x 10 <sup>+5</sup>	0.00339	0.00340
6 x 10 <sup>+5</sup>	0.00310	0.00305
8 x 10 <sup>+5</sup>	0.00282	0.00284
1 x 10 <sup>+6</sup>	0.00267	0.00269
2 x 10 <sup>+6</sup>	0.00215	0.00219
4 x 10 <sup>+6</sup>	0.00166	0.00168
6 x 10 <sup>+6</sup>	0.00143	0.00144
8 x 10 <sup>+6</sup>	0.00130	0.00130
1 x 10 <sup>+7</sup>	0.00117	0.00119
2 x 10 <sup>+7</sup>	0.00089	0.00091
4 x 10 <sup>+7</sup>	0.00068	0.00070
6 x 10 <sup>+7</sup>	0.00062	0.00062
8 x 10 <sup>+7</sup>	0.00057	0.00058
1 x 10 <sup>+8</sup>	0.000550	0.00055
2 x 10 <sup>+8</sup>	0.000485	0.00049
4 x 10 <sup>+8</sup>	0.000415	0.00042
6 x 10 <sup>+8</sup>	0.000360	0.00036
8 x 10 <sup>+8</sup>	0.000303	0.00031
1 x 10 <sup>+9</sup>	0.000267	0.00027

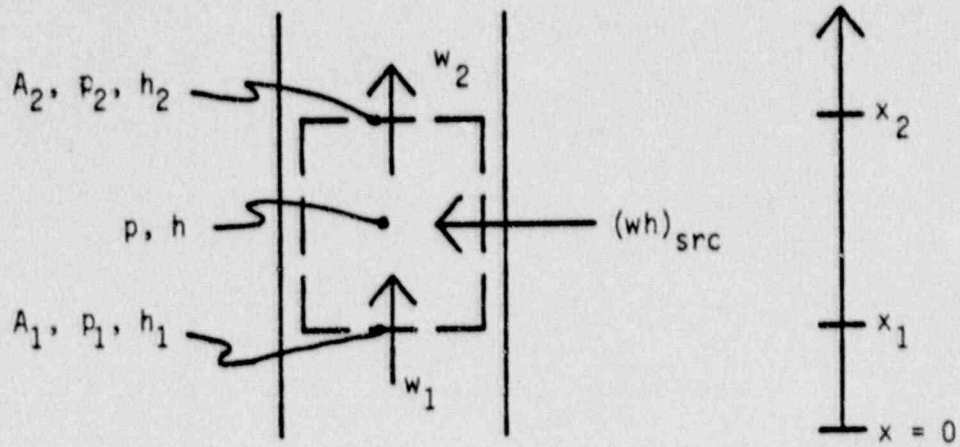


(a)

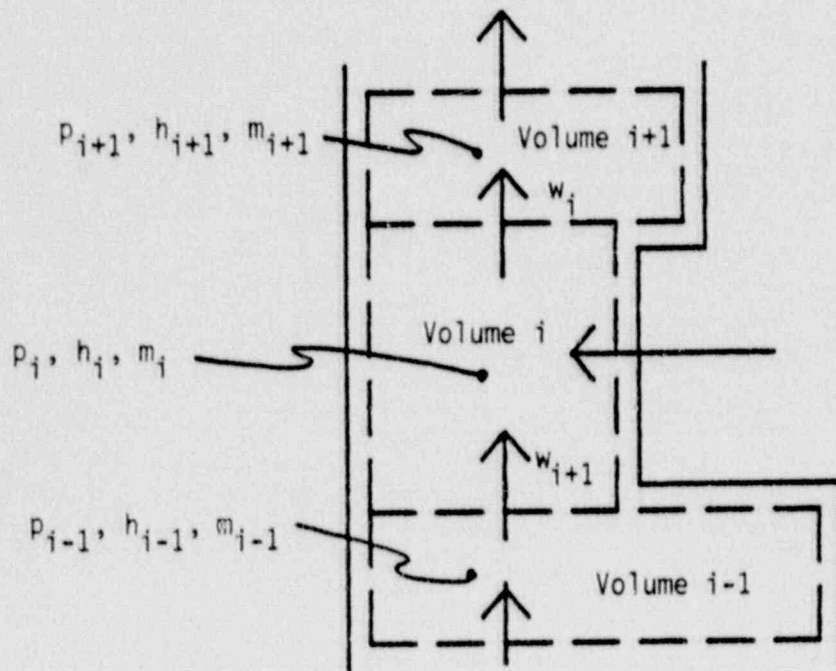


(b)

Figure 3-1 - Mass Balance Control Volume



(a)



(b)

Figure 3-2 - Energy Balance Control Volume

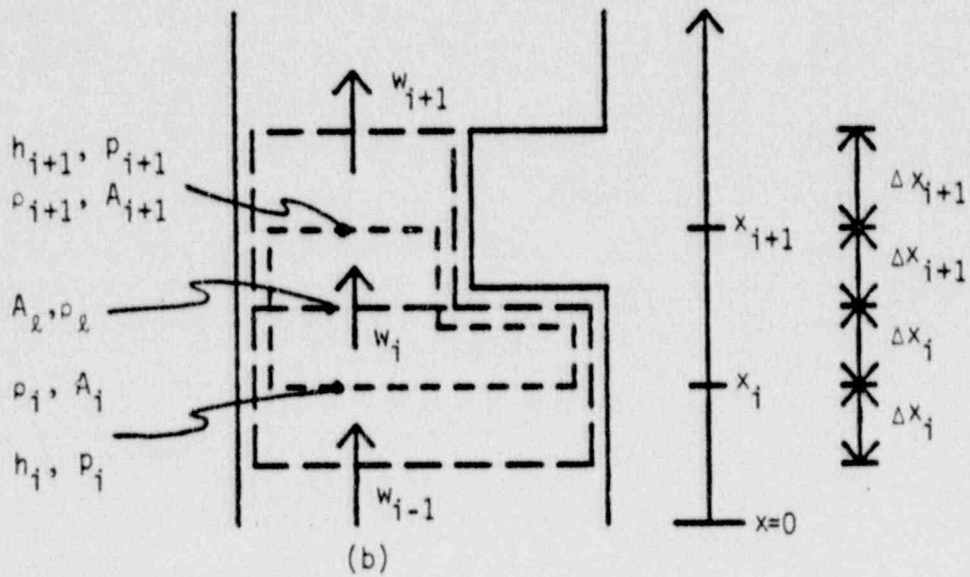
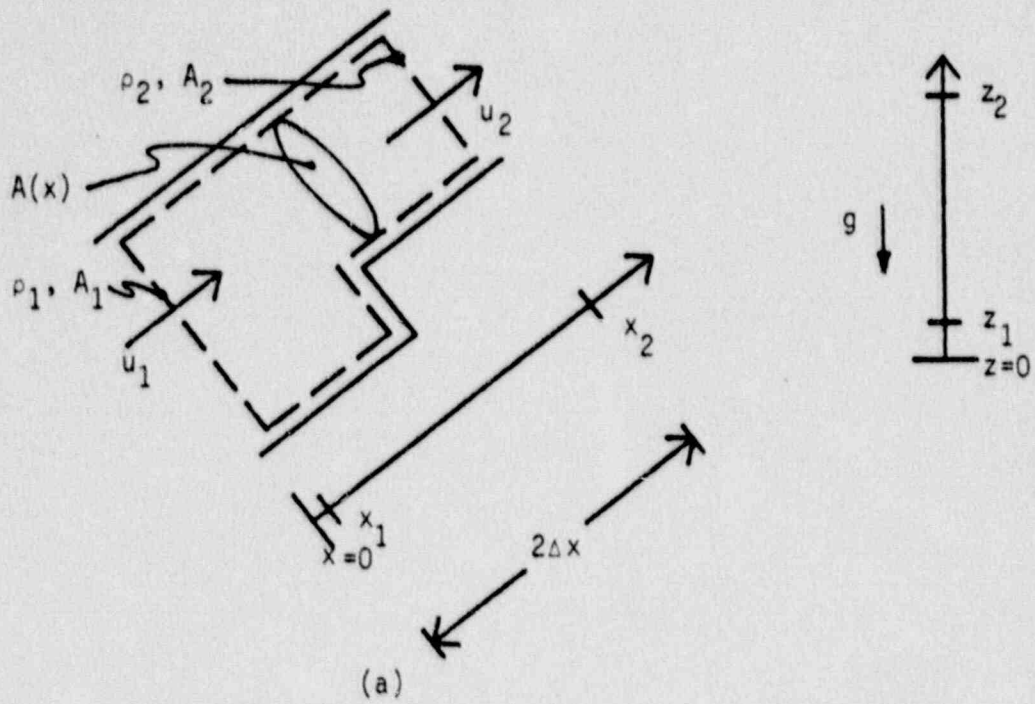


Figure 3-3 - Momentum Balance Control Volume



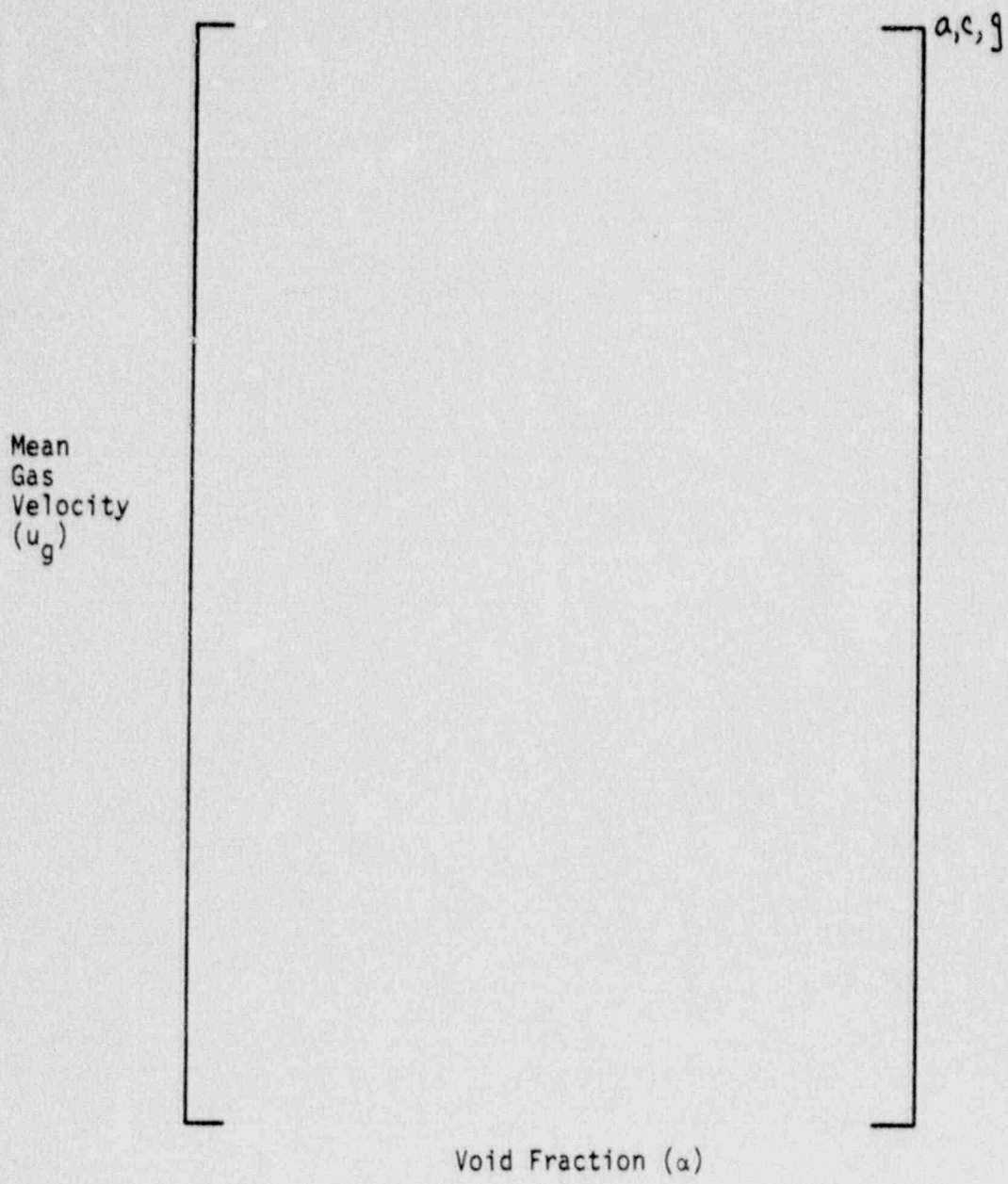


Figure 3-4 - Weighted Mean Rise Velocity of Steam Through Stagnant Water at Atmospheric Pressure

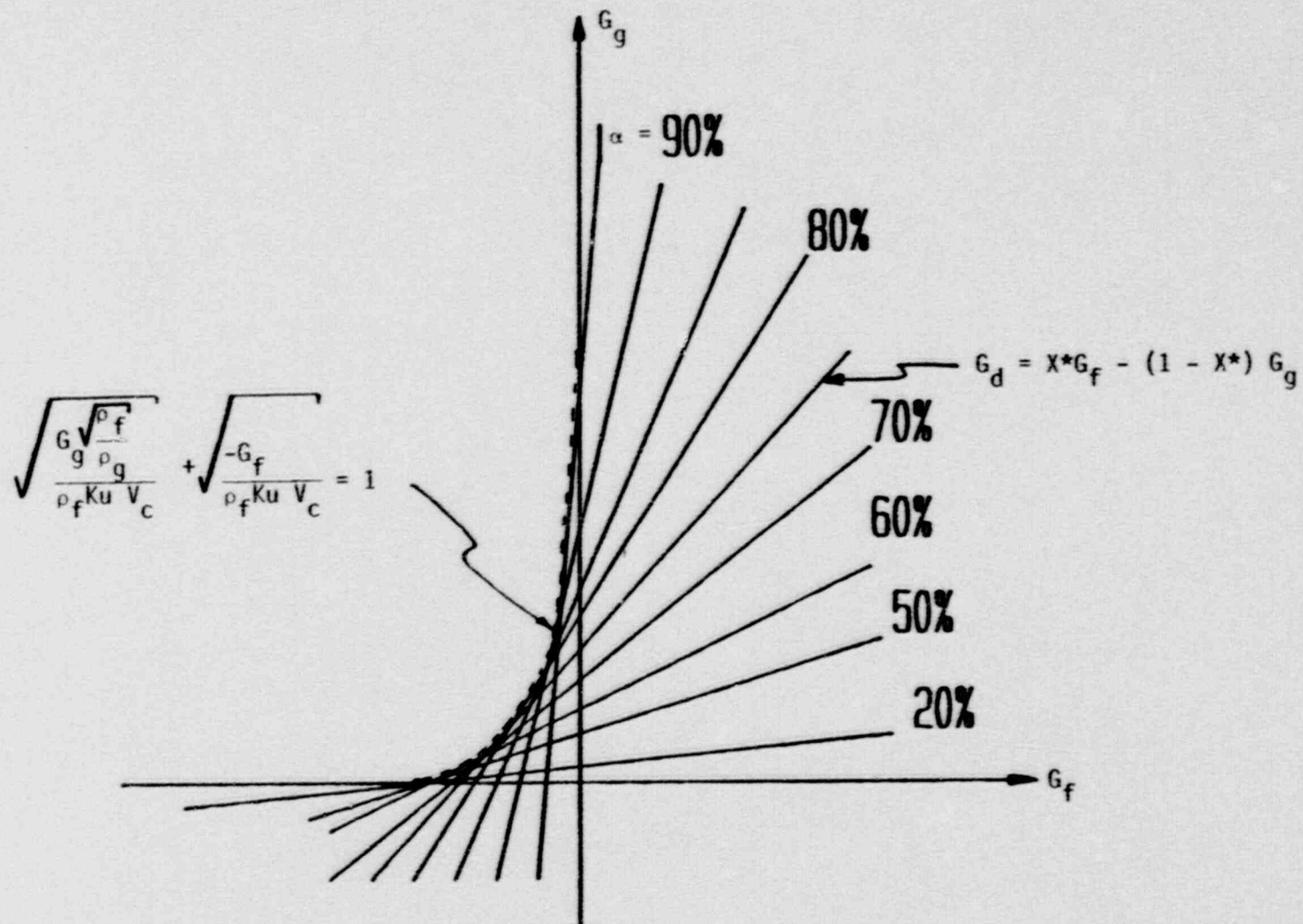


Figure 3-5 - Intersection of Driftflux and Countercurrent Flow Limitation Correlations

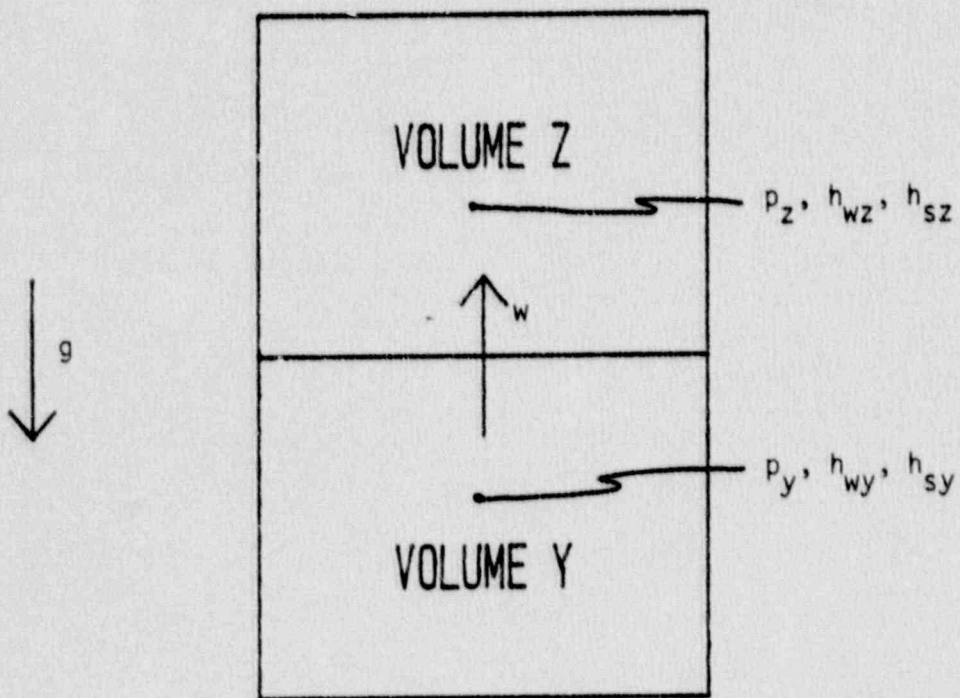


Figure 3-6 - Nomenclature Convention in Application of Drift Flux Model

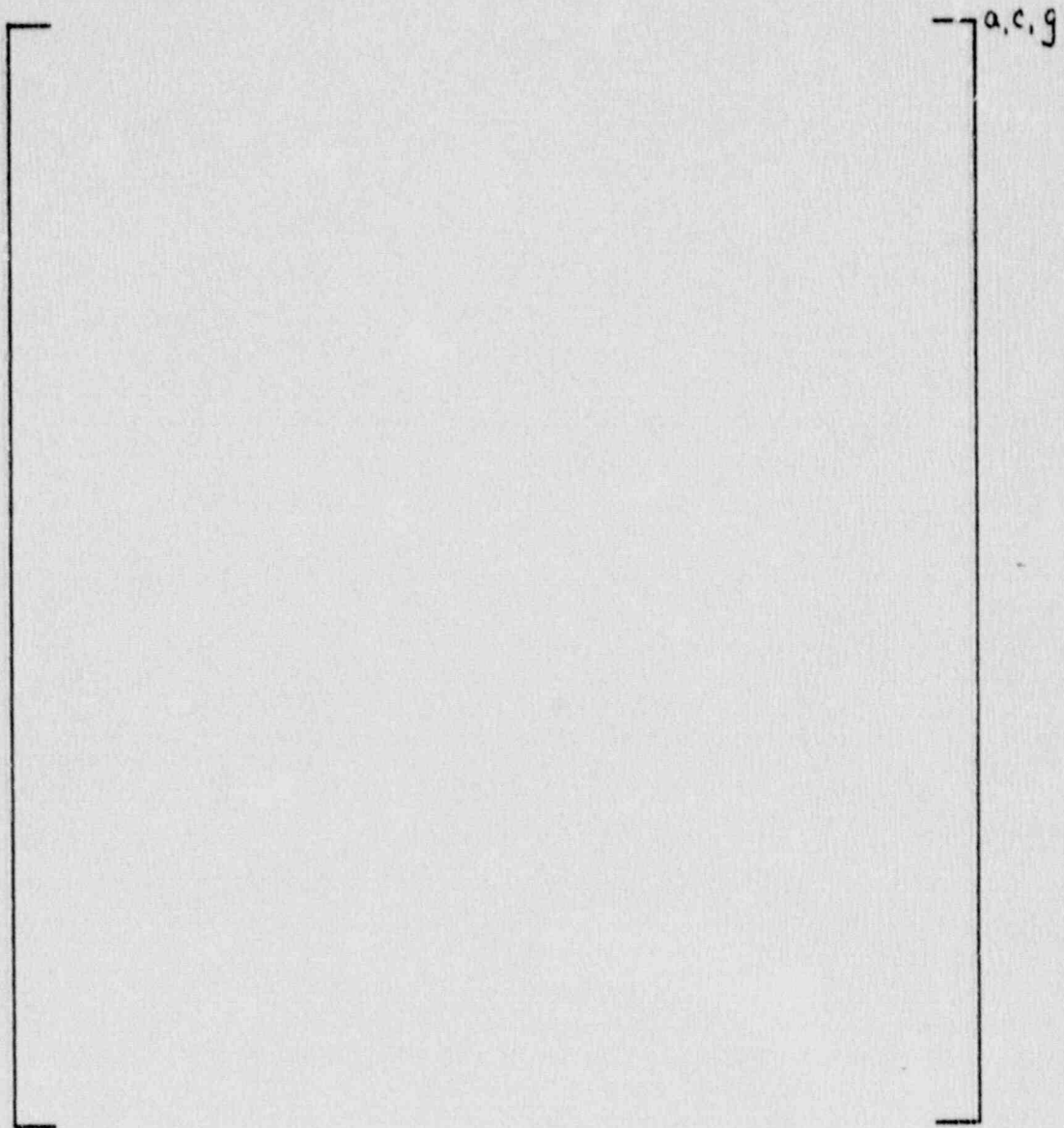


Figure 3-7 - Mass Drift Flux/CCFL Relation for  $\alpha_y \geq \alpha_z$

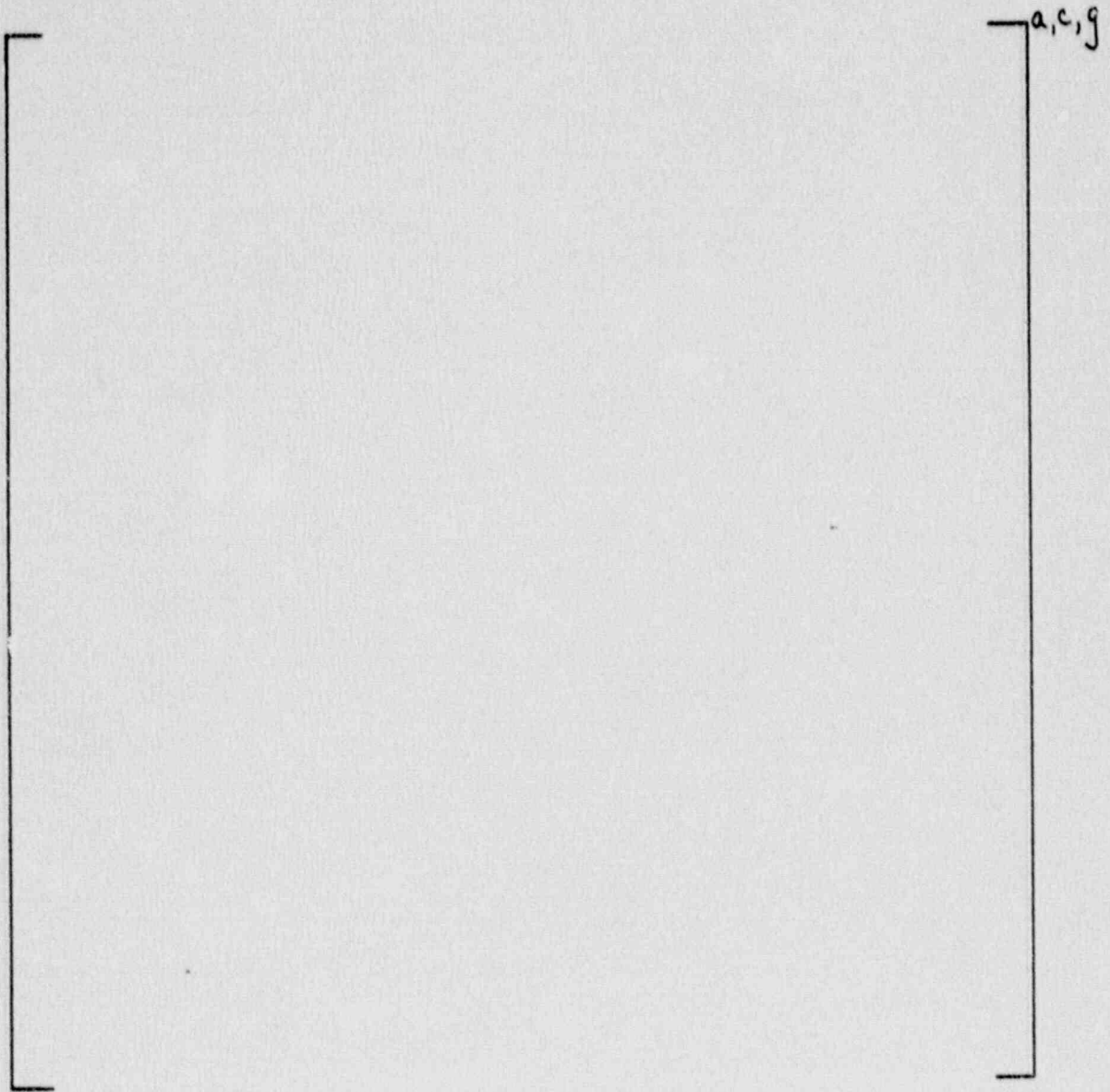
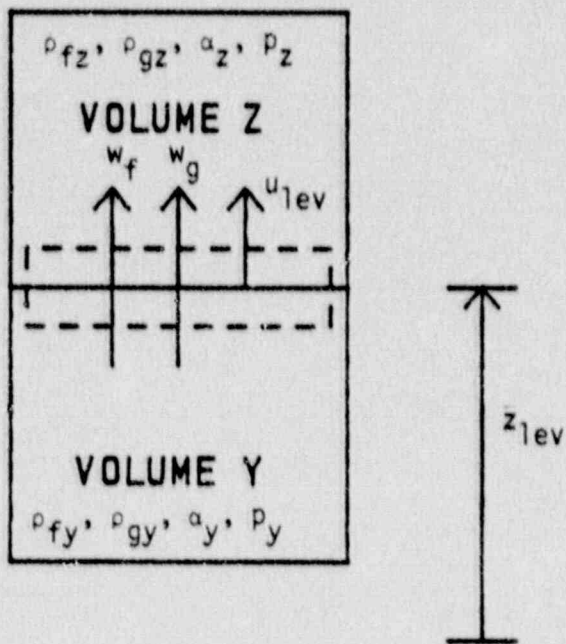


Figure 3-8 - Mass Drift Flux/CCFL Relation for  $\alpha_y < \alpha_z$

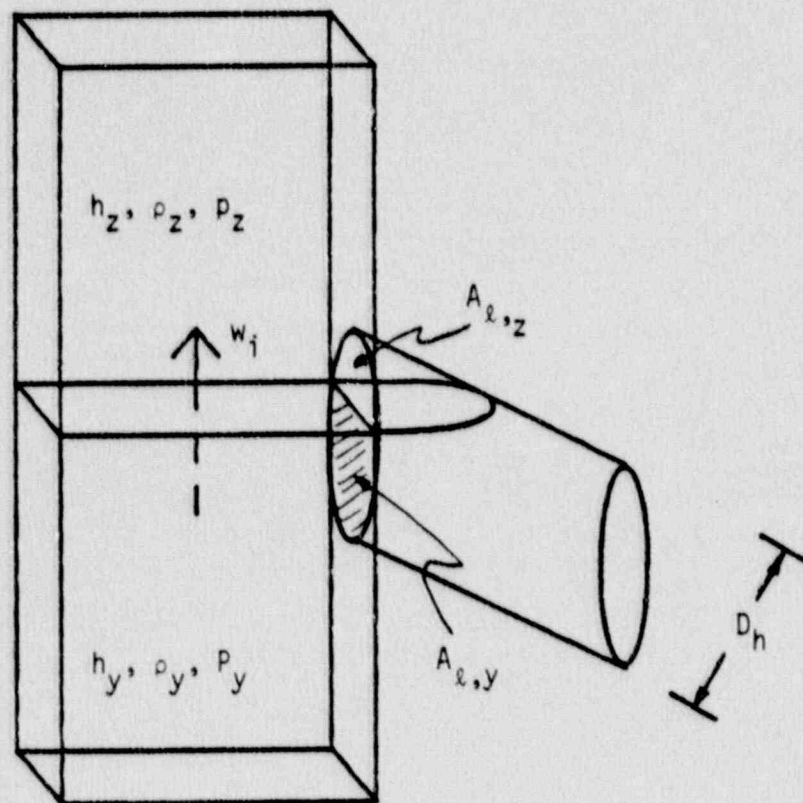


(a)



(b)

Figure 3-9 - Flow Conservation and Calculation at Two-Phase Level



(c)

Figure 3-9 (cont.) Flow Conservation and Calculation at Two-Phase Level

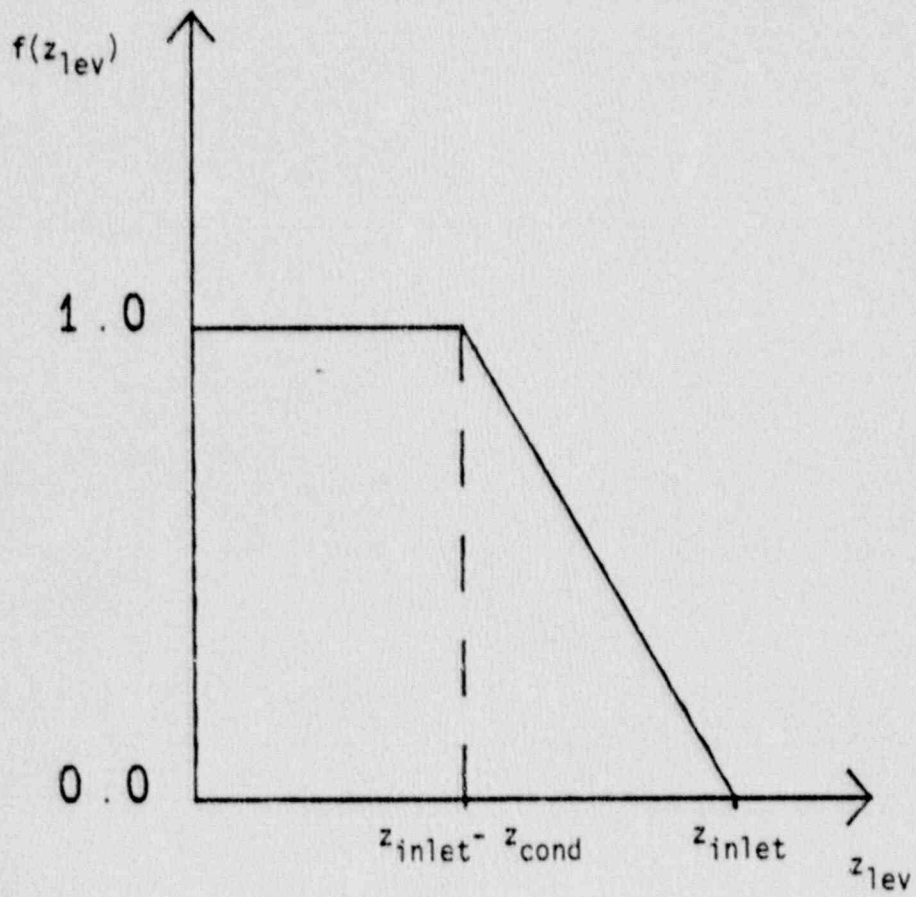


Figure 3-10 - Condensation Rate Function



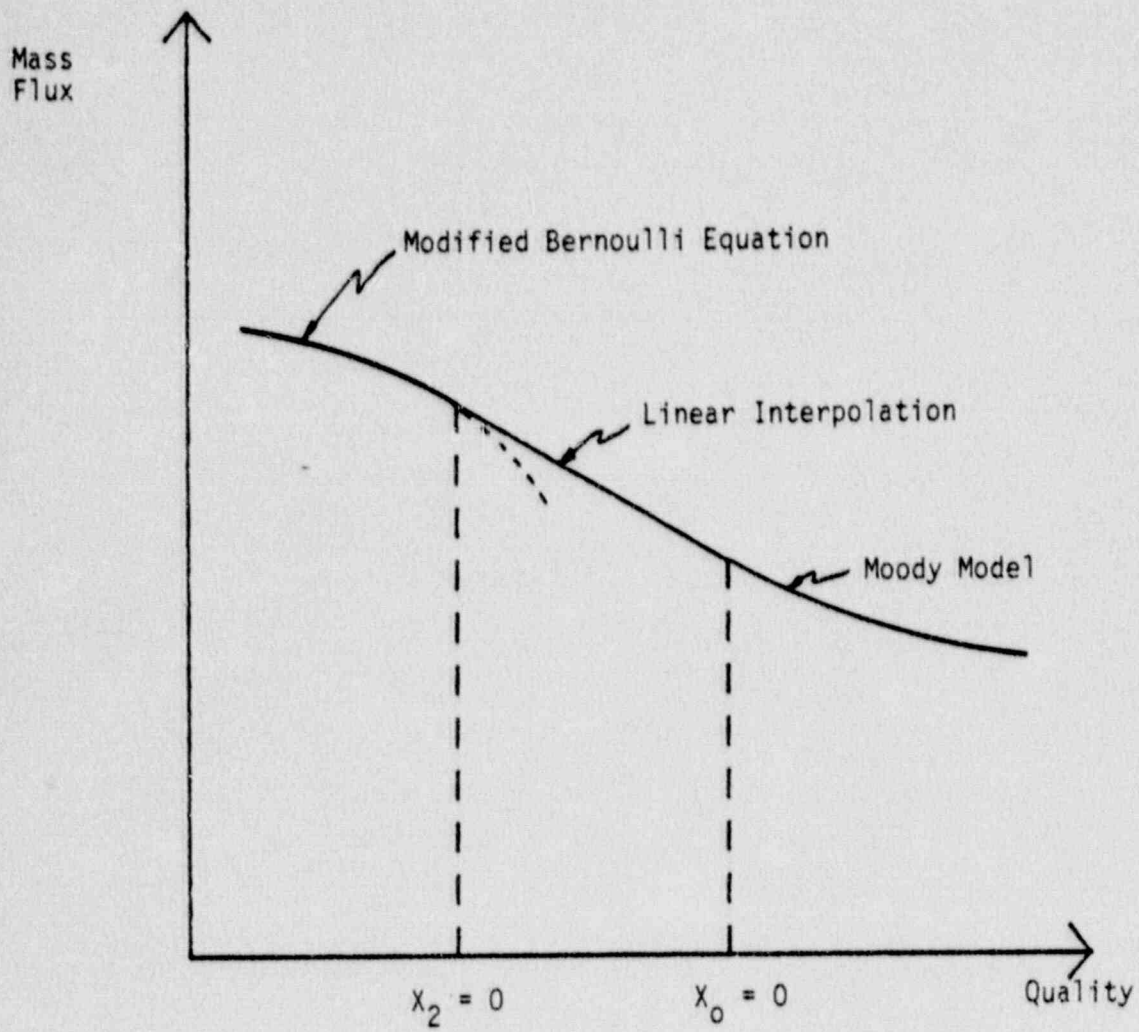


Figure 3-11 - Critical Break Flow Model Regimes

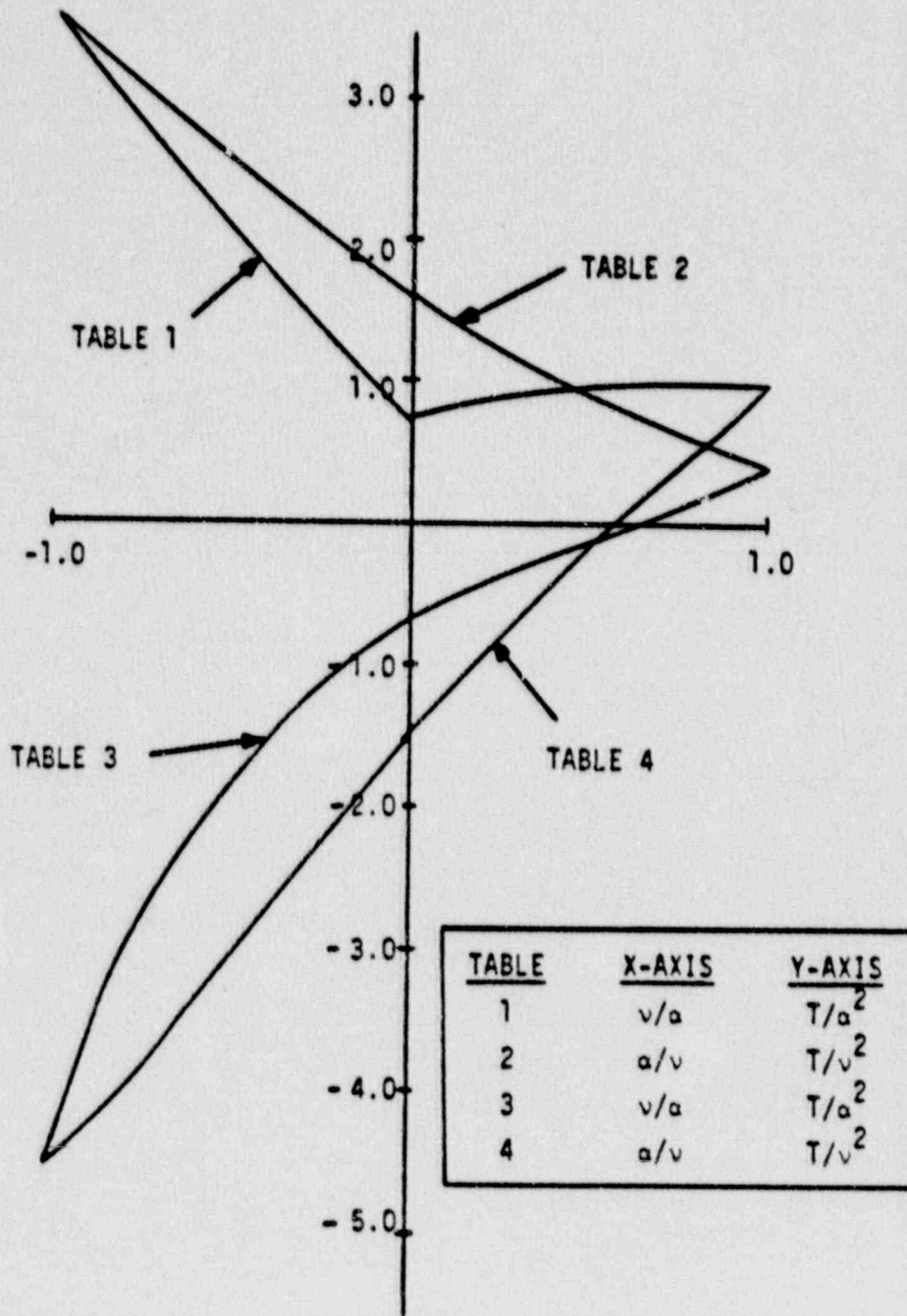


Figure 3-12 - Typical Homologous Hydraulic Torque Curve

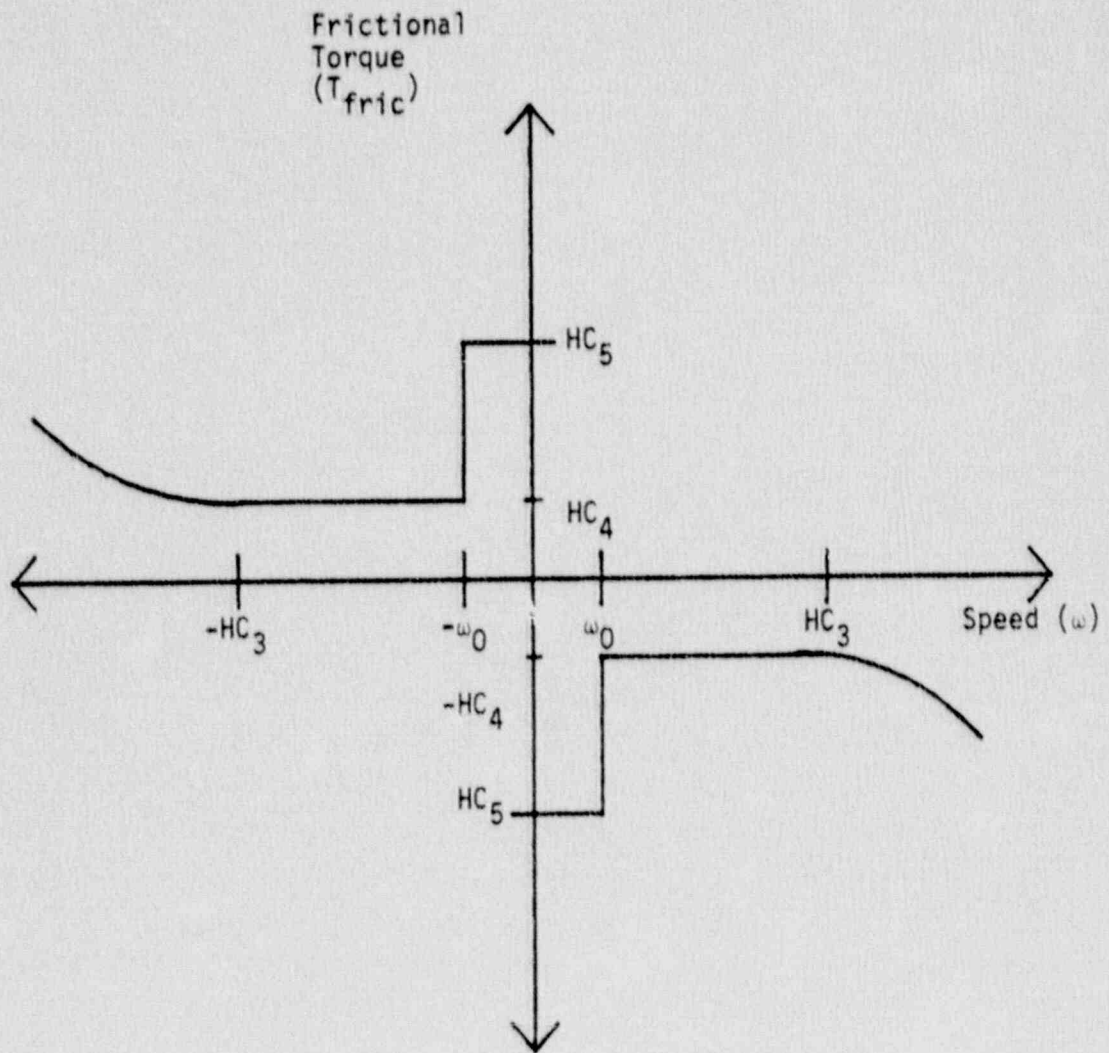


Figure 3-13 - Frictional Torque as Function of Pump Speed

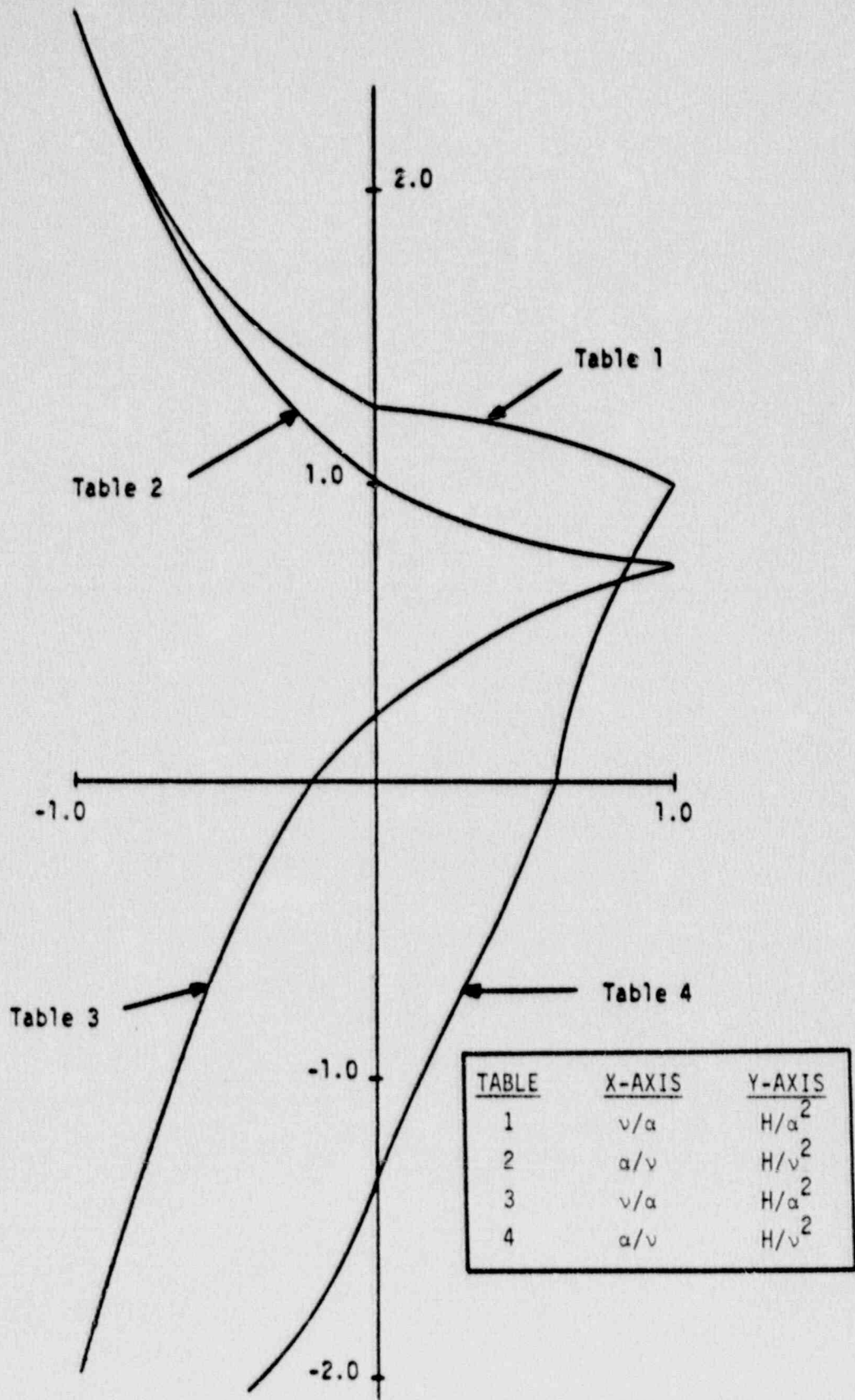


Figure 3-14 - Typical Homologous Pump Head Curves

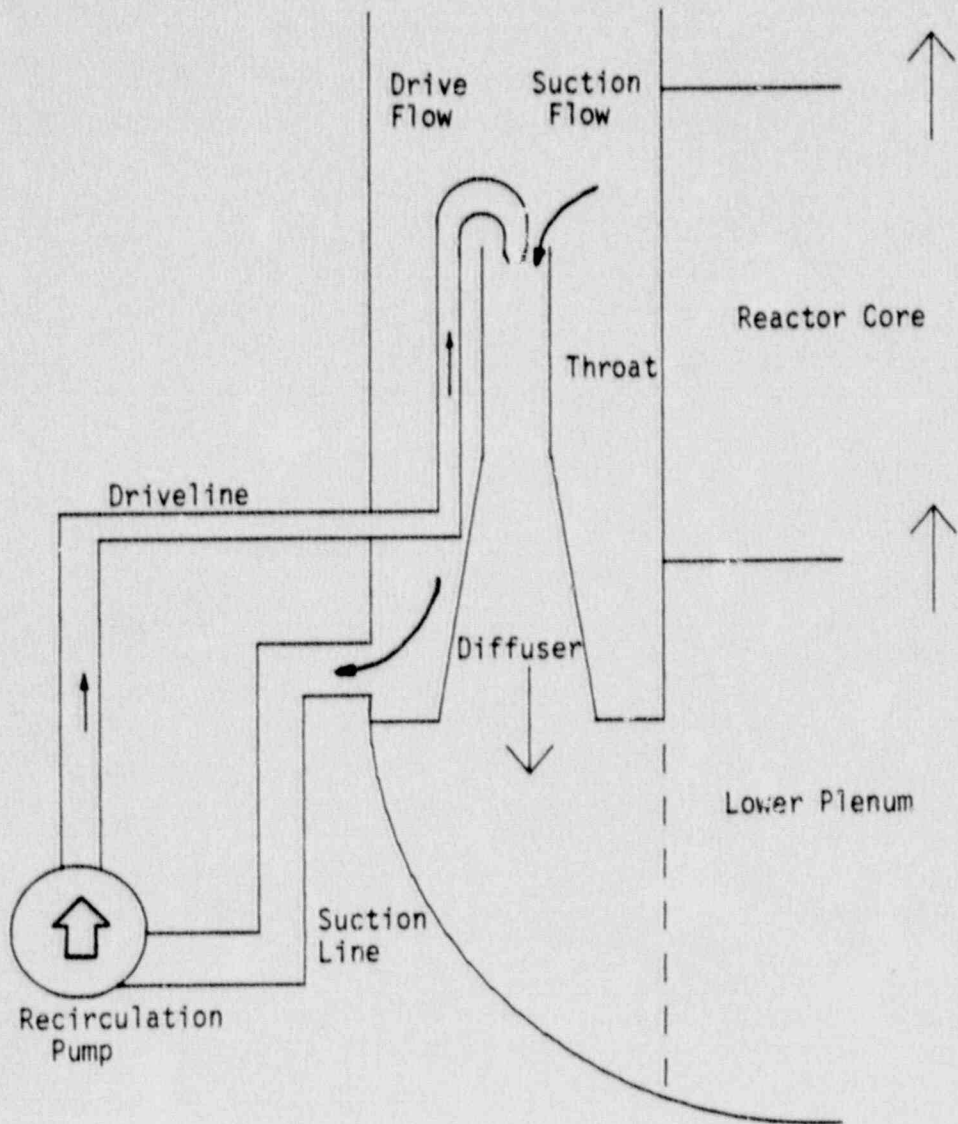


Figure 3-15 - Jet Pump Recirculation System

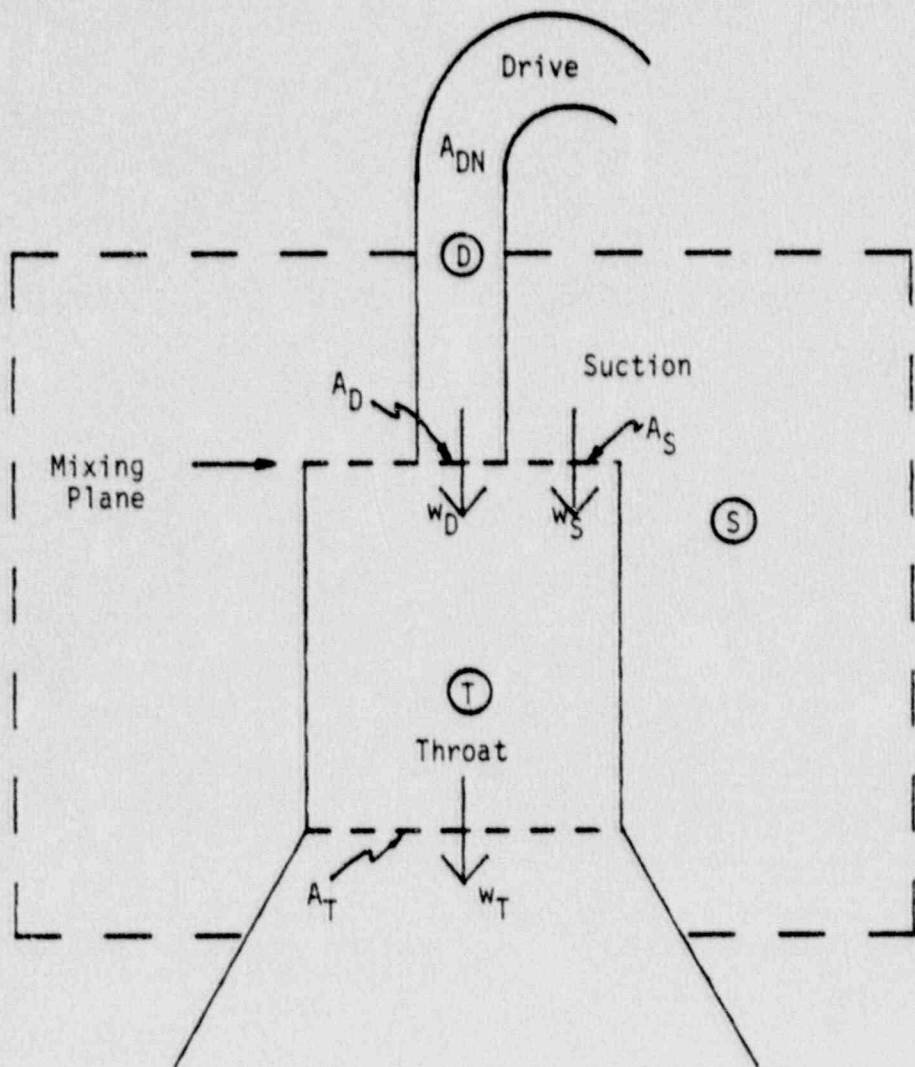


Figure 3-16 - Schematic of Jet Pump Model

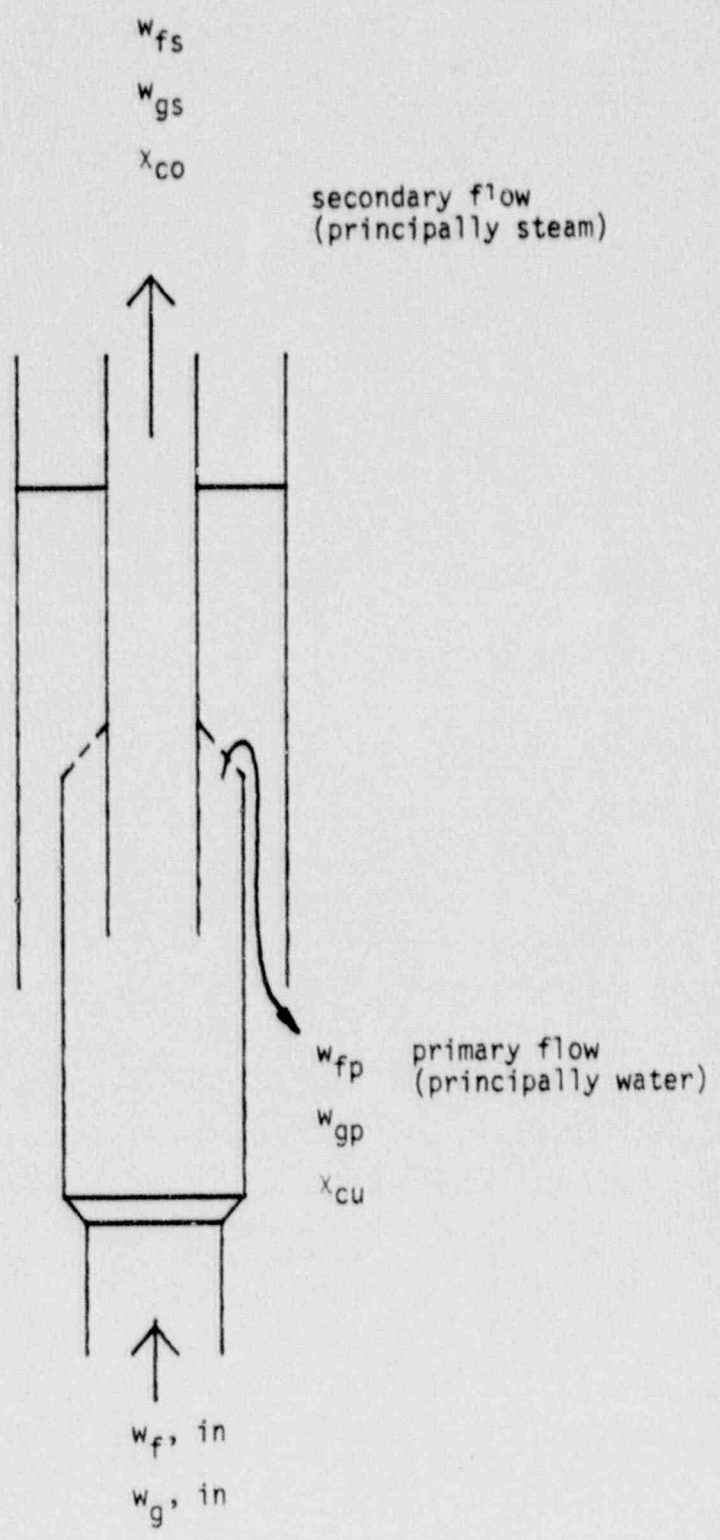


Figure 3-17 - Schematic of Steam Separator Model

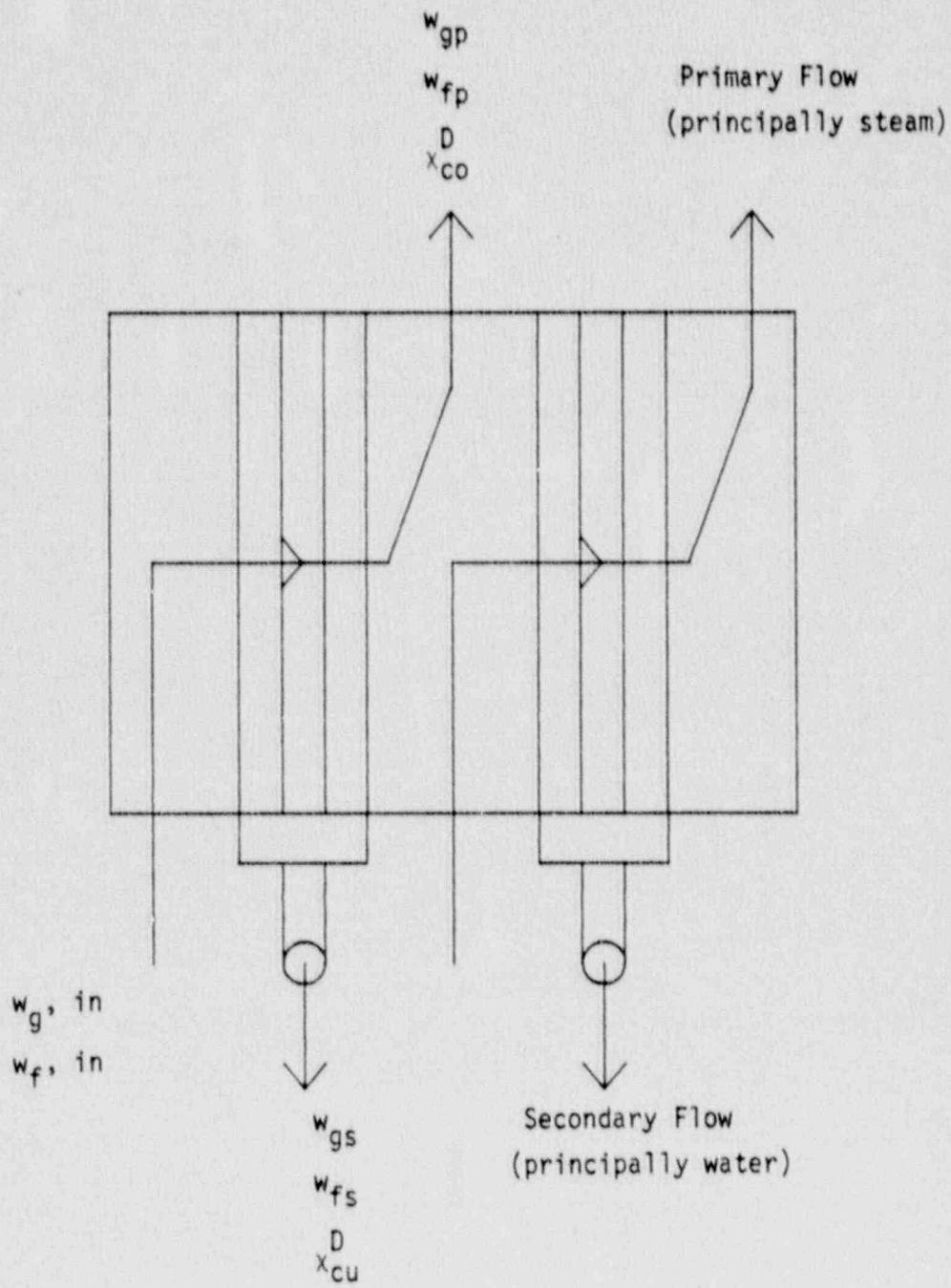
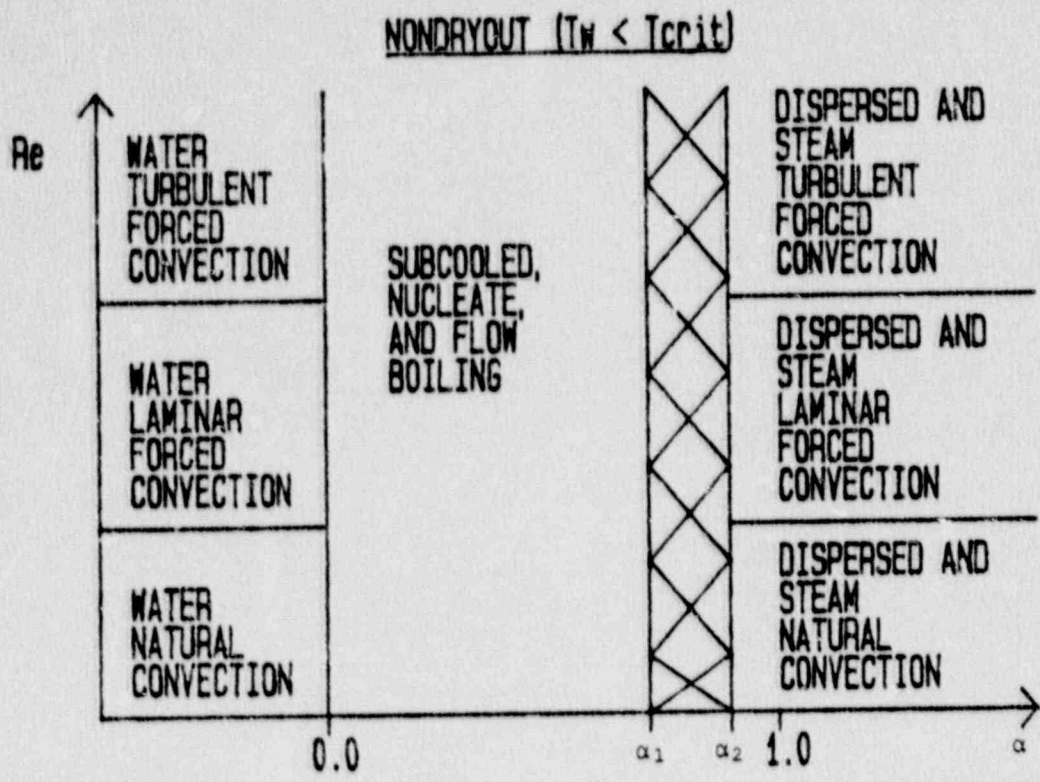


Figure 3-18 - Schematic of Steam Dryer Unit





UNSTABLE DRYOUT ( $T_{crit} < T_w < T_{leid}$ )  
 TRANSITION BOILING  
STABLE DRYOUT ( $T_w > T_{leid}$ )

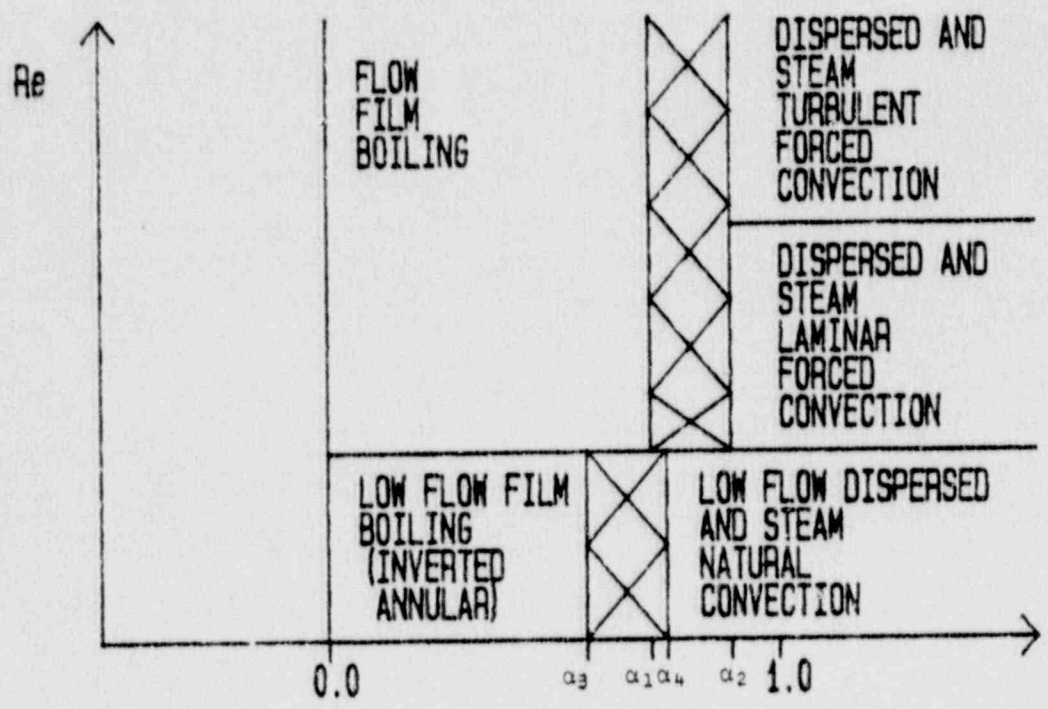


Figure 3-19 - Heat Transfer Flow Regime Map

3-129

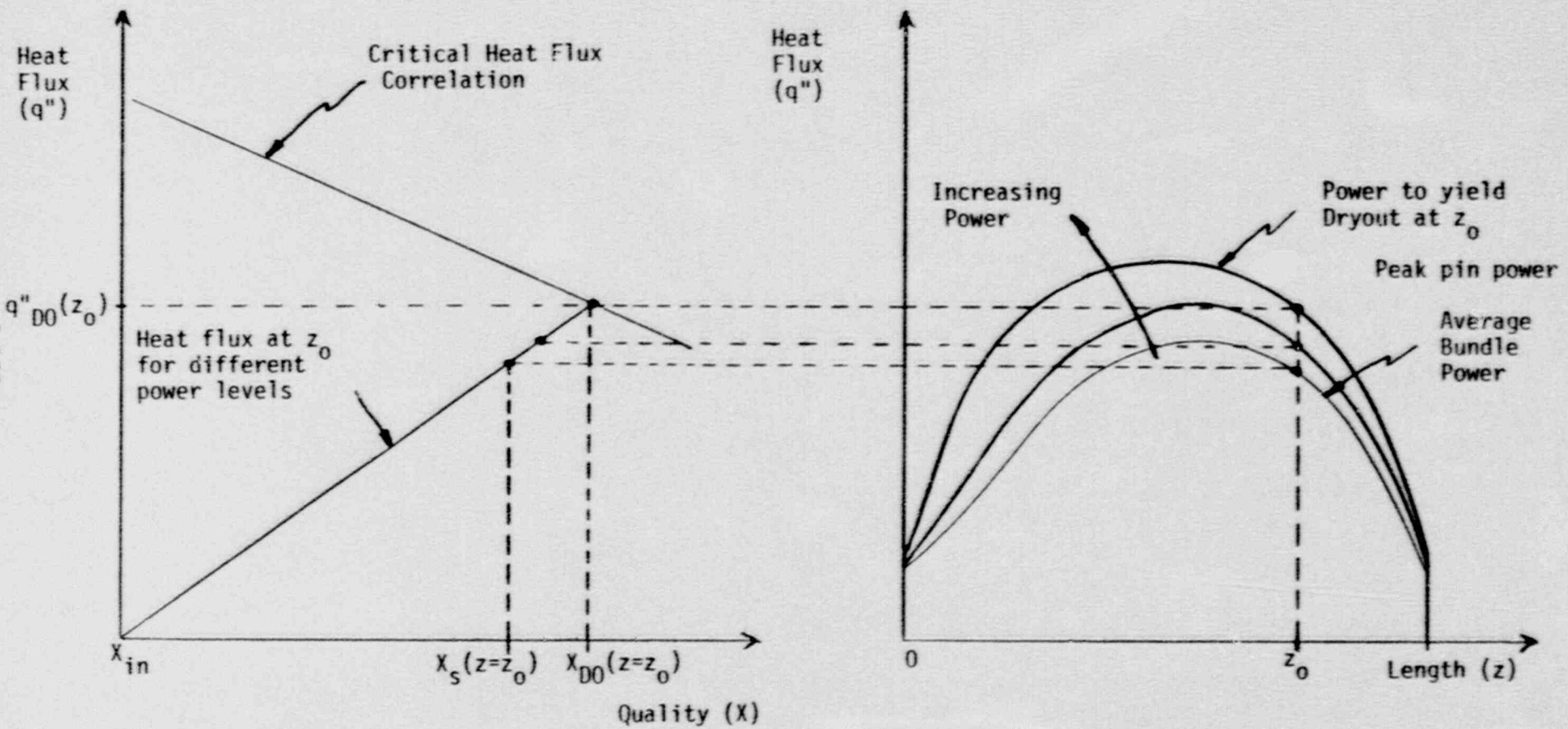


Figure 3-20 - Dryout Quality and Maximum Heat Flux Calculation Based on Critical Power Ratio

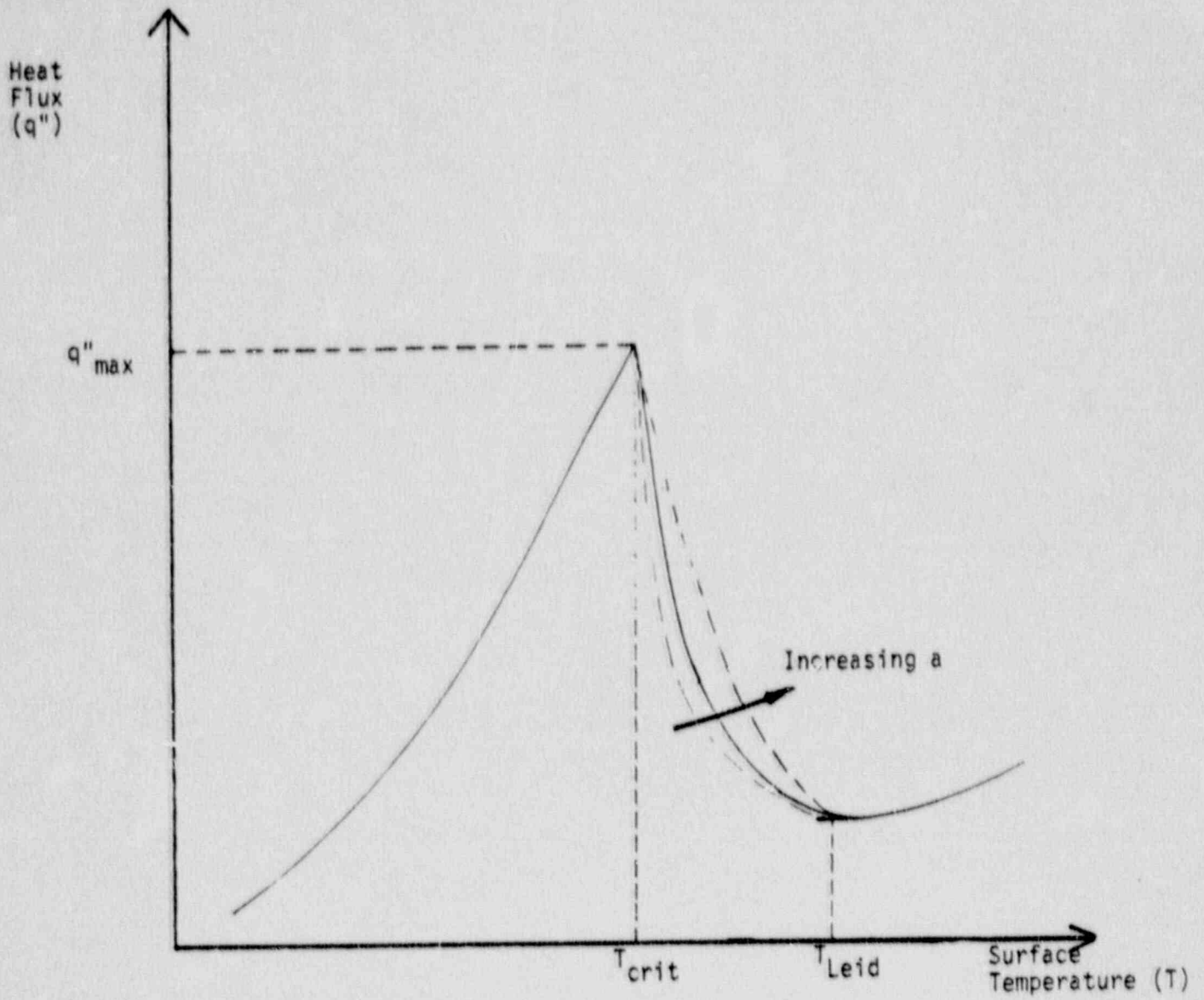


Figure 3-21 - Transition Boiling Model

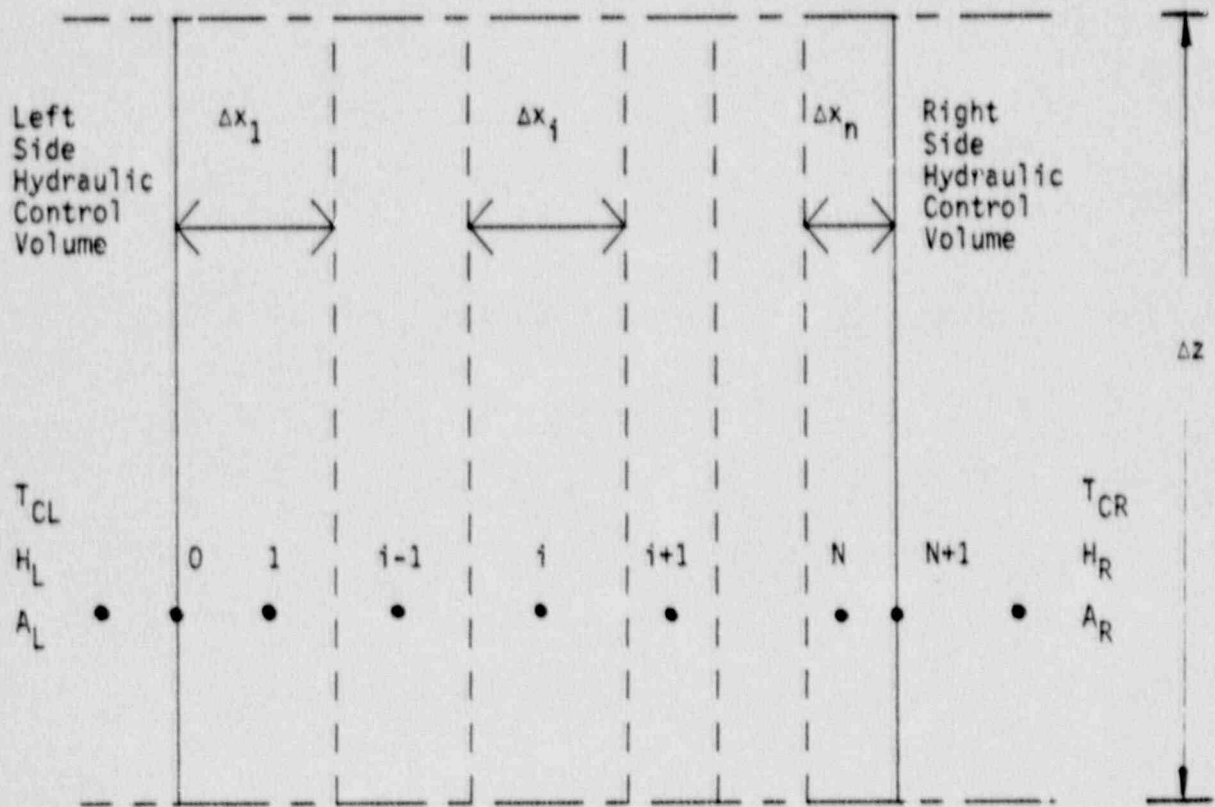


Figure 3-22 - Plate Heat Conduction Model Nodalization

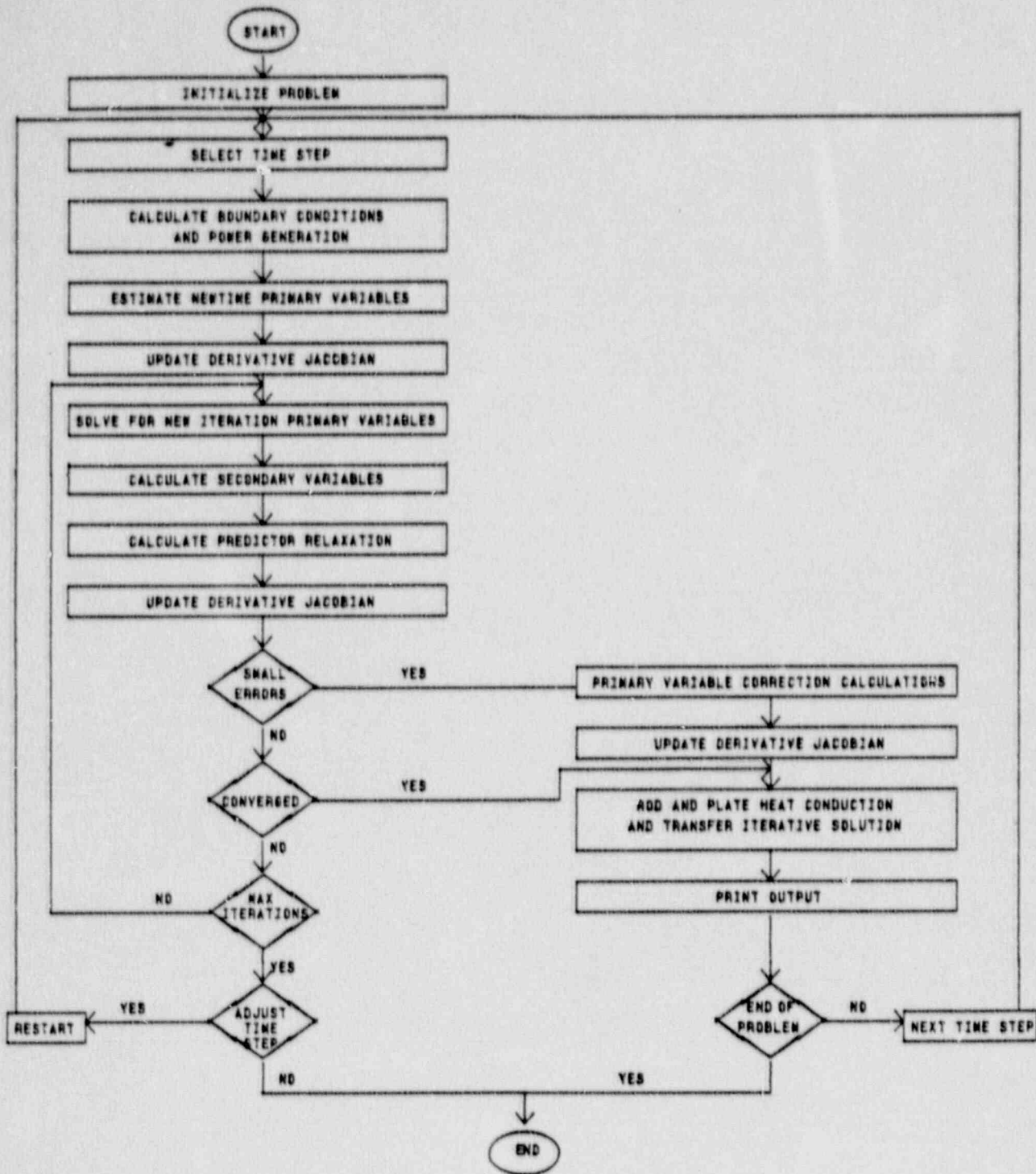


Figure 3-23 - Simplified Flow Chart of GOBLIN Calculational Sequence

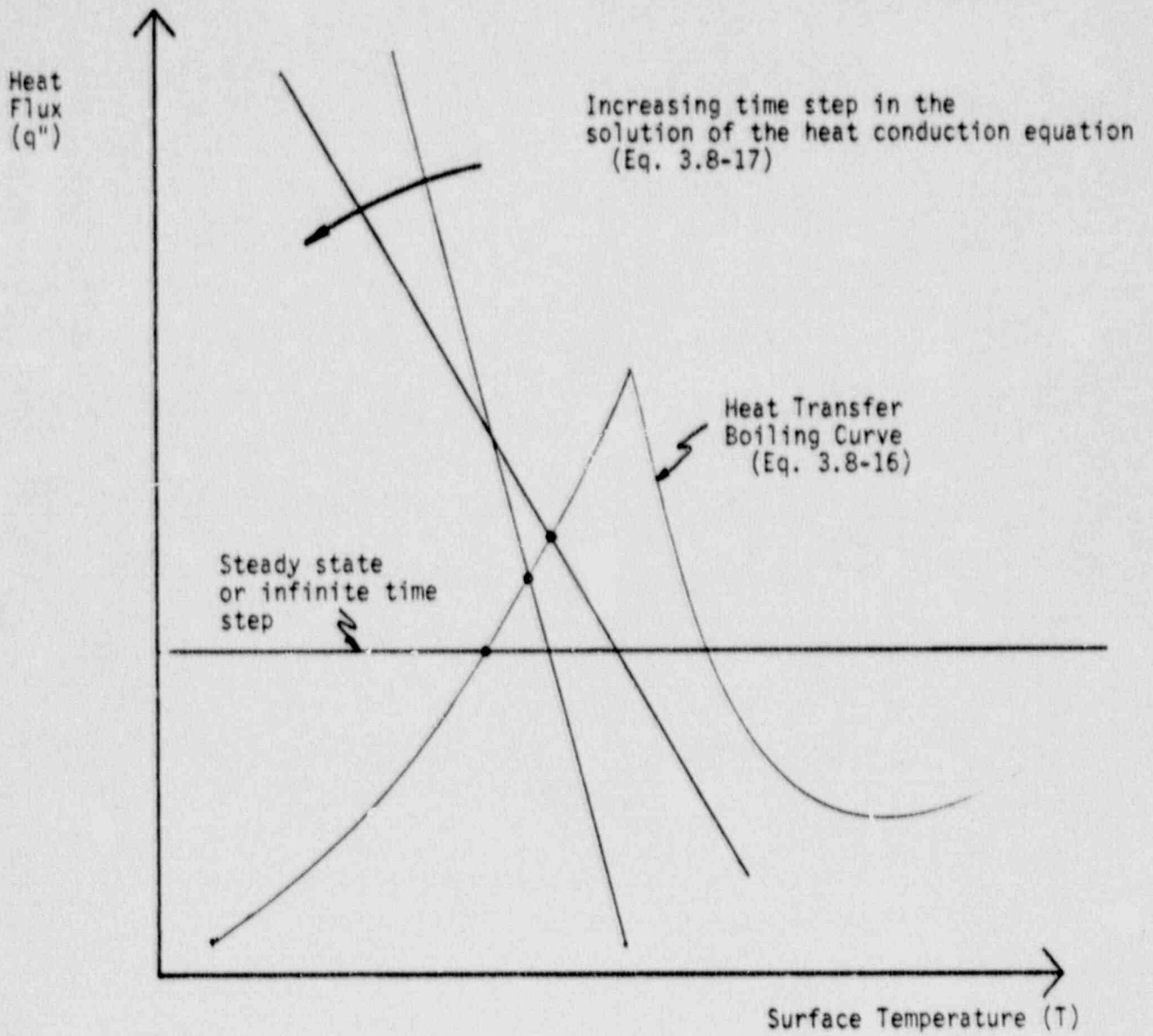
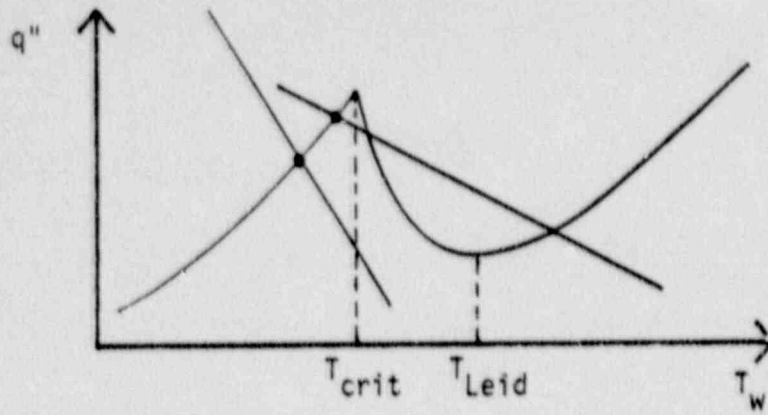


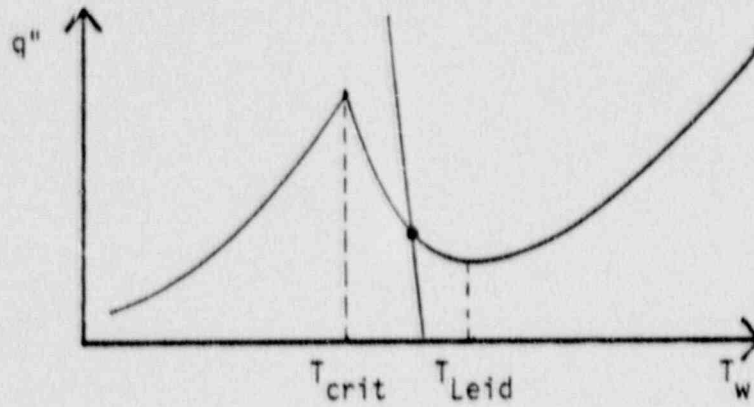
Figure 3-24 - Simultaneous Solution of Conduction and Convective Heat Transfer

NO DRYOUT

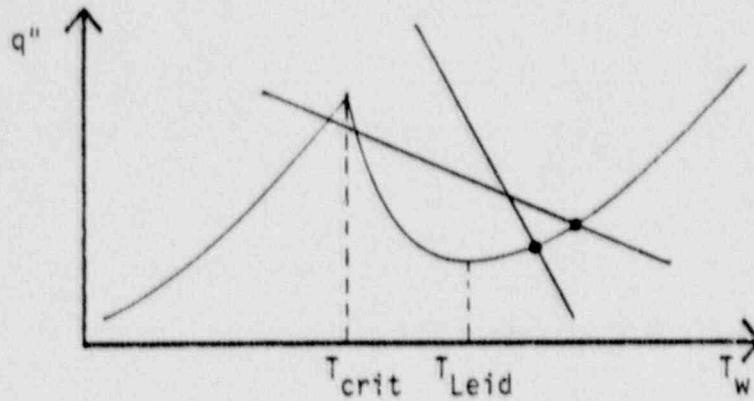


Only if there was no dryout last time step

TRANSITION BOILING

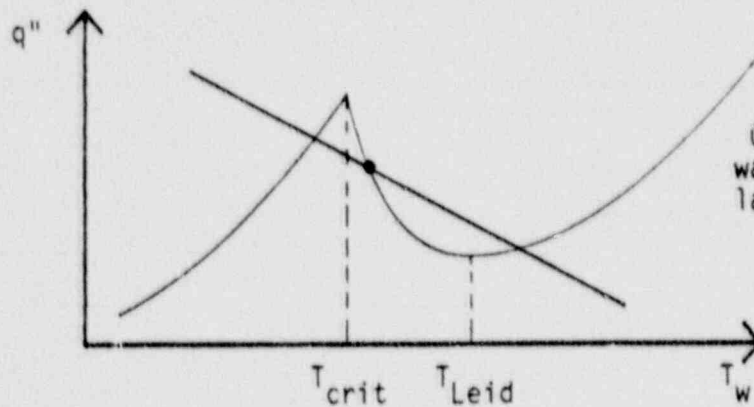


STABLE DRYOUT



Only if there was dryout last time step

HALF TIME STEP



Only if there was transition boiling last time step

Figure 3-25 - Conduction/Heat Transfer Solution for Various Heat Transfer Regimes

#### 4. ROD HEATUP CALCULATIONAL CODE

The detailed fuel rod heatup calculations are performed with the CHACHA-3C code, using boundary conditions supplied by DRAGON. The DRAGON values of coolant pressure and temperature are used directly as boundary conditions. The surface heat transfer coefficients calculated by DRAGON are modified prior to running CHACHA-3C, in order to be consistent with the requirements of 10CFR50, Appendix K.

The primary use of CHACHA-3C is to determine peak clad temperatures at the hottest axial plane in the peak power bundle. The code is also used to determine total hydrogen generation, by evaluating local cladding oxidation at a number of axial and radial locations in the core.

The major components of the CHACHA-3C code include the following models:

- Fuel Rod Conduction Model
- Channel Temperature Model
- Heat Generation Model
- Metal-Water Reaction Model
- Thermal Radiation Model
- Gas Plenum Temperature and Pressure Model
- Channel Rewet Model
- Pellet/Cladding Gap Heat Transfer Model
- Cladding Strain and Rupture Model

This section describes each of these models in detail.



#### 4.1 Fuel Rod Conduction Model

Heat transfer in a fuel rod during a LOCA can be characterized as a multi-region, transient, two dimensional conduction problem with volumetric heat generation and general boundary conditions. Since the axial temperature gradients in the fuel rod and cladding are much smaller than the radial temperature gradients, axial conduction is assumed to be negligible, and is ignored by CHACHA-3C.

With these assumptions the time dependent heat conduction equation may be written as

$$\rho C \frac{\partial T}{\partial t} = q''' + \frac{\partial k}{\partial r} \frac{\partial T}{\partial r} + k \left( \frac{\partial^2 T}{\partial r^2} + \frac{1}{r} \frac{\partial T}{\partial r} \right) \quad (4.1-1)$$

This equation is solved by CHACHA-3C using an implicit finite-difference method developed by Crank and Nicolson (Ref. 4-1). With this method it is assumed that  $\frac{\partial T}{\partial t}$  varies linearly with time so that

$$T \Big|_{t+\Delta t} = T \Big|_t + \frac{\Delta t}{2} \left( \frac{\partial T}{\partial t} \Big|_{t+\Delta t} + \frac{\partial T}{\partial t} \Big|_t \right) \quad (4.1-2)$$

In order to solve Eq. (4.1-1) for the fuel rod temperature distribution, the rod is first divided into a number of radial nodes as shown in Fig. 4-1. Eq. (4.1-1) is then multiplied by  $2\pi r \Delta Z$  and integrated:

$$\int_{r_i}^{r_{i+1}} 2\pi r \Delta Z \rho C \frac{\partial T}{\partial t} dr = \int_{r_i}^{r_{i+1}} 2\pi r \Delta Z q''' dr + \quad (4.1-3)$$

$$\int_{r_i}^{r_{i+1}} 2\pi r \Delta Z \left( \frac{\partial k}{\partial r} \frac{\partial T}{\partial r} + k \left( \frac{\partial^2 T}{\partial r^2} + \frac{1}{r} \frac{\partial T}{\partial r} \right) \right) dr \quad (3)$$

where

(1) - heat storage in node i

(2) - heat generation in node i

(3) - net heat conduction into node i

The average temperature in node i is given by

$$T_i = \frac{\int_{r_i}^{r_{i+1}} 2\pi r T dr}{\int_{r_i}^{r_{i+1}} 2\pi r dr} \quad (4.1-4)$$

It is assumed that the density and specific heat are constant in node i. The expressions for the density and specific heat are given in Appendix 4.A.

The heat storage term may now be integrated, yielding

$$\rho_i C_i \Delta Z \pi (r_{i+1}^2 - r_i^2) \frac{\partial T_i}{\partial t}$$

or

$$\rho_i C_i \Delta V_i \frac{\partial T_i}{\partial t} \quad (4.1-5)$$

Integrating the heat generation term results in:

$$\int_{r_i}^{r_{i+1}} 2\pi r \Delta Z q''' dr = q''' \Delta Z \pi (r_{i+1}^2 - r_i^2)$$

or

$$q''' \Delta V_i \quad (4.1-6)$$

Partial integration of the net conduction term results in:

$$2\pi \Delta Z (rk \frac{\partial T}{\partial r})_{r=r_{i+1}} - 2\pi \Delta Z (rk \frac{\partial T}{\partial r})_{r=r_i} \quad (4.1-7)$$

Eq. (4.1-3) may now be rewritten as:

$$\rho_i C_i \Delta V_i \frac{\partial T_i}{\partial t} = q''' \Delta V_i + 2\pi \Delta Z ((rk \frac{\partial T}{\partial r})_{r=r_{i+1}} - (rk \frac{\partial T}{\partial r})_{r=r_i}) \quad (4.1-8)$$

This equation together with the following boundary conditions is then solved using a finite-difference method.

At  $r = 0$  (centerline):

$$\frac{\partial T}{\partial r} \Big|_{r=0} = 0 \quad (4.1-9)$$

At  $r = r_{fs}$  (fuel surface):

$$(-k \frac{\partial T}{\partial r})_{r=r_{fs}} = h_{gap} (T_{fs} - T_{ci}) \quad (4.1-10)$$

At  $r = r_{ci}$  (cladding inner surface):

$$\left(-k \frac{\partial T}{\partial r}\right)_{r=r_{ci}} = h_{gap}(T_{fs} - T_{ci}) (r_{fs}/r_{ci}) \quad (4.1-11)$$

At  $r = r_{co}$  (cladding outer surface):

$$\left(-k \frac{\partial T}{\partial r}\right)_{r=r_{co}} = h_{co}(T_{surf} - T_{cool}) \quad (4.1-12)$$

### Finite difference formulation

The following finite difference approximations to the derivatives in Eq. (4.1-8) are used:

$$\frac{\partial T_i}{\partial t} = \frac{T_i^{n+1} - T_i^n}{\Delta t} \quad (4.1-13)$$

$$\left.\frac{\partial T_i}{\partial r}\right|_{r=r_i} = \frac{T_{i+1} - T_i}{0.5(\Delta r_i + \Delta r_{i+1})} \quad (4.1-14)$$

At the boundaries (fuel outer surface, cladding inner and outer surfaces) the following approximations are used (refer to Fig. 4-1):

$$\left.\frac{\partial T}{\partial r}\right|_{r_{fs}} = \frac{T_{fs} - T_M}{0.5 \Delta r_M} \quad (4.1-15)$$

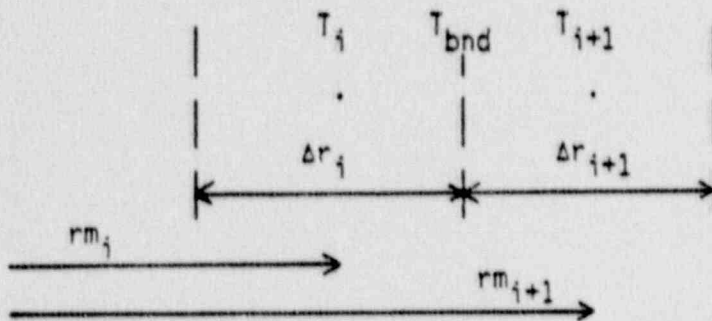
$$\left.\frac{\partial T}{\partial r}\right|_{r_{ci}} = \frac{T_{M+1} - T_{ci}}{0.5 \Delta r_{M+1}} \quad (4.1-16)$$

$$\left. \frac{\partial T}{\partial r} \right|_{r_{co}} = \frac{T_{surf} - T_N}{0.5\Delta r_N} \quad (4.1-17)$$

Calculation of composite thermal conductivities

In Eq. (4.1-8) the thermal conductivities are required at the boundaries of each node. The temperatures are calculated at the centers of the nodes. The following derivation of the composite thermal conductivities at the boundaries is based on the requirement that the heat flux should be continuous at the boundaries between each node.

Case 1: No gap between nodes



The requirement of a continuous heat flux at the boundary results in:

$$k_i \frac{T_{bnd} - T_i}{0.5\Delta r_i} = k_{i+1} \frac{T_{i+1} - T_{bnd}}{0.5\Delta r_{i+1}} \quad (4.1-18)$$

Furthermore we have:

$$k_i \frac{T_{bnd} - T_i}{0.5\Delta r_i} = K_i \frac{T_{i+1} - T_i}{0.5(\Delta r_i + \Delta r_{i+1})} \quad (4.1-19)$$

where  $K_i$  is the composite thermal conductivity. Solving

Eq. (4.1-18) for  $T_{\text{bnd}}$  yields:

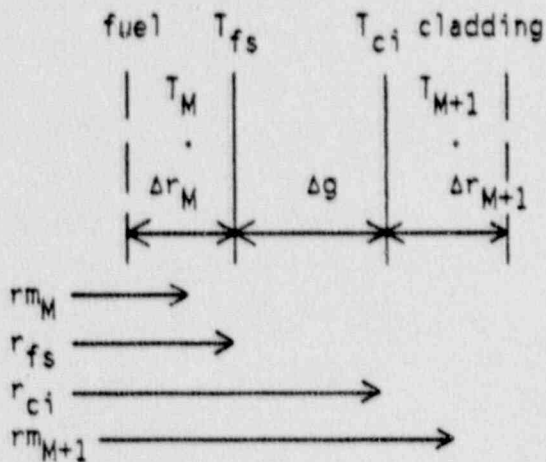
$$T_{\text{bnd}} = \frac{T_i k_i \Delta r_{i+1} + T_{i+1} k_{i+1} \Delta r_i}{k_i \Delta r_{i+1} + k_{i+1} \Delta r_i} \quad (4.1-20)$$

Substituting for  $T_{\text{bnd}}$  in Eq. (4.1-19) gives:

$$K_i = \frac{1}{\frac{1}{k_{i+1}} + \left(\frac{1}{k_i} - \frac{1}{k_{i+1}}\right) \frac{\Delta r_i}{\Delta r_i + \Delta r_{i+1}}} \quad (4.1-21)$$

The expressions for the thermal conductivities are given in Appendix 4.A.

Case 2: Gas gap between nodes



Heat transferred at the fuel surface is given by:

$$k_M \frac{T_{fs} - T_M}{0.5 \Delta r_M} = h_{\text{gap}} (T_{ci} - T_{fs}) \quad (4.1-22)$$

The gas in the gap is assumed not to store any energy. The gap heat transfer is based on the fuel surface area. With these assumptions the heat transferred at the cladding inner surface is given by:

$$r_{ci} k_{M+1} \frac{T_{M+1} - T_{ci}}{0.5 \Delta r_{M+1}} = r_{fs} h_{gap} (T_{ci} - T_{fs}) \quad (4.1-23)$$

The heat transferred between nodes M and M+1 is expressed as:

$$K_M \frac{T_{M+1} - T_M}{0.5 (\Delta r_M + \Delta r_{M+1}) + \Delta g} = h_{gap} (T_{ci} - T_{fs}) \quad (4.1-24)$$

Solving Eq. (4.1-22) and (4.1-23) simultaneously for  $T_{fs}$  and  $T_{ci}$  gives

$$T_{fs} = \frac{T_M (k_M k_{M+1} + k_M h_{gap} 0.5 \Delta r_{M+1} \frac{r_{fs}}{r_{ci}}) + T_{M+1} (h_{gap} k_{M+1} 0.5 \Delta r_M)}{k_M k_{M+1} + k_M h_{gap} 0.5 \Delta r_{M+1} \frac{r_{fs}}{r_{ci}} + h_{gap} k_{M+1} 0.5 \Delta r_M} \quad (4.1-25)$$

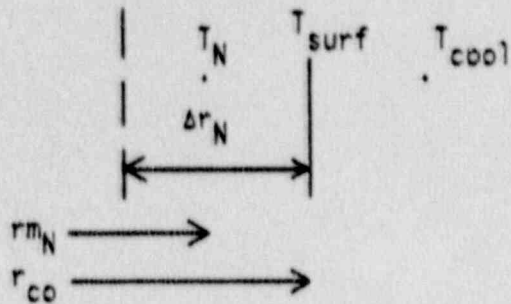
and

$$T_{ci} = \frac{T_M (k_M h_{gap} 0.5 \Delta r_{M+1} \frac{r_{fs}}{r_{ci}}) + T_{M+1} (k_M k_{M+1} + h_{gap} k_{M+1} 0.5 \Delta r_M)}{k_M k_{M+1} + k_M h_{gap} 0.5 \Delta r_{M+1} \frac{r_{fs}}{r_{ci}} + h_{gap} k_{M+1} 0.5 \Delta r_M} \quad (4.1-26)$$

Substituting these two equations into Eq. (4.1-24) will give the composite thermal conductivity as:

$$K_M = \frac{h_{gap} k_M k_{M+1} (0.5 (\Delta r_M + \Delta r_{M+1}) + \Delta g)}{k_M k_{M+1} + k_M h_{gap} 0.5 \Delta r_{M+1} \frac{r_{fs}}{r_{ci}} + h_{gap} k_{M+1} 0.5 \Delta r_M} \quad (4.1-27)$$

Case 3: Surface node adjacent to the coolant



The requirement of a continuous heat flux at the outer surface results in:

$$k_N \frac{T_N - T_{surf}}{0.5\Delta r_N} = h_{co} (T_{surf} - T_{cool}) \quad (4.1-28)$$

The heat transferred from the outermost node to the coolant is expressed as:

$$K_N \frac{T_N - T_{cool}}{0.5\Delta r_N} = h_{co} (T_{surf} - T_{cool}) \quad (4.1-29)$$

Solving Eq. (4.1-28) for the surface temperature gives:

$$T_{surf} = \frac{T_N \frac{k_N}{0.5\Delta r_N} + h_{co} T_{cool}}{\frac{k_N}{0.5\Delta r_N} + h_{co}} \quad (4.1-30)$$

Substituting into Eq. (4.1-29) gives:

$$K_N = \frac{h_{co} k_N}{\frac{k_N}{0.5\Delta r_N} + h_{co}} \quad (4.1-31)$$



Resulting set of equations to be solved

Steady-state

Center node:

$$R_1 K_1 (T_1 - T_2) = q_1'' \Delta V_1 \quad (4.1-32)$$

where  $R_1$  is given by Eq. (4.1-35) below.

Intermediate nodes (for  $i$  from 2 to  $N-1$ ):

$$-R_{i-1} K_{i-1} (T_{i-1} - T_i) + R_i K_i (T_i - T_{i+1}) = q_i'' \Delta V_i \quad (4.1-33)$$

Outermost node:

$$-R_{N-1} K_{N-1} (T_{N-1} - T_N) + R_N K_N (T_N - T_C) = q_N'' \Delta V_N \quad (4.1-34)$$

where

$$R_i = \frac{2\pi\Delta Z(rm_i + 0.5\Delta r_i)}{0.5(\Delta r_i + \Delta r_{i+1})} \quad (4.1-35)$$

except

$$R_M = \frac{2\pi\Delta Z r_{fs}}{0.5(\Delta r_M + \Delta r_{M+1}) + \Delta g} \quad (4.1-36)$$

$$R_N = \frac{2\pi\Delta Z r_{co}}{0.5\Delta r_N} \quad (4.1-37)$$

This set of equations can be written as

$$[CB] \cdot [T] = [ACB] \quad (4.1-38)$$

where [CB] is a symmetric tridiagonal matrix. The unknown temperatures are solved for using a Gaussian elimination technique. Since the thermal conductivities are temperature dependent, the solution of Eq. (4.1-38) must be done iteratively.

### Transient

Center node:

$$\begin{aligned} \Delta V_1 (\theta (\rho C)_1^{n+1} + (1-\theta) (\rho C)_1^n) \frac{T_1^{n+1} - T_1^n}{\Delta t} = \theta R_1 K_1^{n+1} (T_2^{n+1} - T_1^{n+1}) + \\ (1-\theta) R_1 K_1^n (T_2^n - T_1^n) + q_1'' \Delta V_1 \end{aligned} \quad (4.1-39)$$

Intermediate nodes:

$$\begin{aligned} \Delta V_i (\theta (\rho C)_i^{n+1} + (1-\theta) (\rho C)_i^n) \frac{T_i^{n+1} - T_i^n}{\Delta t} = \theta R_{i-1} K_{i-1}^{n+1} (T_{i-1}^{n+1} - T_i^{n+1}) + \\ (1-\theta) R_{i-1} K_{i-1}^n (T_{i-1}^n - T_i^n) + \theta R_i K_i^{n+1} (T_{i+1}^{n+1} - T_i^{n+1}) + \\ (1-\theta) R_i K_i^n (T_{i+1}^n - T_i^n) + q_i'' \Delta V_i + Q_{mwr,i} \end{aligned} \quad (4.1-40)$$

Outermost node:

$$\begin{aligned} \Delta V_N (\theta (\rho C)_N^{n+1} + (1-\theta) (\rho C)_N^n) \frac{T_N^{n+1} - T_N^n}{\Delta t} = \theta R_{N-1} K_{N-1}^{n+1} (T_{N-1}^{n+1} - T_N^{n+1}) + \\ (1-\theta) R_{N-1} K_{N-1}^n (T_{N-1}^n - T_N^n) + \theta R_N K_N^{n+1} (T_C^{n+1} - T_N^{n+1}) + \\ (1-\theta) R_N K_N^n (T_C^n - T_N^n) + q_N'' \Delta V_N + Q_{mwr,N} - Q_{rad} \end{aligned} \quad (4.1-41)$$

where  $Q_{mwr,i}$  is the heat addition in node  $i$  due to metal-water reaction, and, the "R" parameter is given by Eq. (4.1-35) through (4.1-37).

The implicitness parameter,  $\theta$ , is chosen to be 0.5 which gives the Crank-Nicolson method. The calculation of the terms  $Q_{mwr,i}$  and  $Q_{rad}$  is described in Sec. 4.4 and 4.5.

The volumetric heat generation rates are calculated from:

$$q'' = \int_t^{t+\Delta t} q''(\tau) d\tau / \Delta t \quad (4.1-42)$$

As in the steady-state case the set of equations can be written as:

$$[CB] \cdot [T] = [ACB] \quad (4.1-43)$$

The solution of this system is performed in the same way as in the steady-state case. Due to the temperature dependent material properties, iterations are performed until the user-specified convergence criteria are met.

## 4.2 Channel Temperature Model

The channel temperature throughout the transient is calculated based on the following assumptions:

- (1) No metal-water reaction takes place on the channel.
- (2) Axial heat conduction may be neglected.
- (3) The channel is at a uniform temperature at a given elevation.
- (4) Heat transfer to the control blades is neglected.

Under these conditions the energy balance for the channel is expressed as:

$$(\rho CV)_{ch} dT_{ch}/dt = -Q_{rrod} - Q_{conv} + Q_{gen} \quad (4.2-1)$$

where the heat generation due to gamma absorption,  $Q_{gen}$ , is a user input.

To solve this equation the time derivative is discretized in CHACHA-3C as:

$$(\rho CV)_{ch} dT_{ch} /dt = (\rho CV)_{ch}^{n+1} (T_{ch}^{n+1} - T_{ch}^n) / \Delta t \quad (4.2-2)$$

Eq. (4.2-1) is a non-linear equation for  $T_{ch}^{n+1}$  because  $Q_{rrod}$  and  $Q_{conv}$  are evaluated using channel and rod temperatures from time  $n+1$ . It is solved iteratively in CHACHA-3C using Newton's method.

Before uncover of the elevation of interest  $Q_{rrod}$  is set to zero.

Rewet of the channel is evaluated as described in Sec. 4.7. After the channel wall has rewetted at the elevation of interest the channel temperature is set equal to the saturation temperature.

### 4.3 Heat Generation Model

Heat generation rates in the fuel, cladding and channel are calculated by CHACHA-3C based on several key inputs. These inputs and the codes used to generate them are shown in Table 4-1. The heat generation in the cladding due to metal/water reaction is calculated separately, as described in Sec. 4.4.

As noted in Table 4-1, the hot bundle axial and radial (rod-wise) power distributions to be used in plant specific calculations will be based on POLCA and PHOENIX calculations. The radial bundle peaking factor will be determined based on maximum linear heat rate, and the bundle axial and rod-wise radial power distributions being used in the analysis. Sensitivity studies will be performed to identify limiting power distributions consistent with the maximum linear heat rate.

Typical pellet radial power distributions are shown in Fig. 4-2 for a  $UO_2$  pellet. The pellet radial power distribution becomes more nonuniform as burn-up increases, due to the nonuniform conversion of  $U^{238}$  to fissile  $Pu^{239}$ . The conversion rate is higher near the pellet surface than in the center of the pellet. Consequently the power density becomes highest near the surface as burnup increases. Transport theory based codes such as HAMMER, FOBUS and W-ANISN will be used to generate the radial power distributions for  $UO_2$  and  $UO_2/Gd_2O_3$  fuel pellets.

The user must specify the fraction of energy deposited in each of the fuel assembly components (fuel, cladding and channel) before and after scram. The values to be used in plant specific calculations will be selected based on nuclear considerations and sensitivity studies.

#### 4.4 Metal-Water Reaction Model

The reaction between zirconium and steam is expressed as:



The heat released by this reaction is

$$\Delta E = C_1 + C_2 (T_{\text{ox}}) \quad (4.4-2)$$

where,

$$\begin{aligned} C_1 &= 6.669 \times 10^6 \text{ J/kg} \\ C_2 &= -257 \text{ J/kg-}^\circ\text{K} \\ T_{\text{ox}} &= \text{temperature at the oxide front in } ^\circ\text{K} \end{aligned}$$

CHACHA-3C accounts for metal-water reaction on both sides of the cladding. Reaction on the inside is started when a cladding perforation is calculated to occur (see Sec. 4.9). The effect of plastic strain on the reaction rate due to the oxide layer becoming thinner when strained is accounted for.

There are two types of rate-limiting phenomena which represent the mechanism for the oxidation of zirconium in a steam environment:

- (1) The gas-phase diffusion of steam from the bulk stream toward the cladding surface, through gaseous hydrogen which must diffuse away from the zirconium dioxide product layer.
- (2) The solid-state diffusion of various ionic species through the zirconium dioxide product layer and into the base metal, a phenomena quantitatively expressed as the parabolic rate law.

As required by Appendix K, the reaction is conservatively assumed not to be steam-limited. The parabolic rate law expressing the solid-state diffusion is taken as that suggested by Baker and Just (Ref. 4-2), mathematically formulated as:

$$\frac{dS}{dt} = \frac{C_3}{S} \exp\left(\frac{C_4}{T_{ox}}\right) \quad (4.4-3)$$

where

$$C_3 = 3.937 \times 10^{-5} \text{ m}^2/\text{sec}$$

$$C_4 = -22899 \text{ }^\circ\text{K}$$

S = oxide thickness in meters

Integration of this equation over a time step gives:

$$\int_{S_1}^{S_2} S dS = \int_{t_1}^{t_2} C_3 \exp\left(\frac{C_4}{T_{ox}}\right) dt \quad (4.4-4)$$

If the expression  $\exp\left(\frac{C_4}{T_{ox}}\right)$  is assumed to be constant during the time step, then

$$S_2^2 - S_1^2 = 2C_3 \exp\left(\frac{C_4}{T_{ox}}\right) \Delta t \quad (4.4-5)$$

where

$$\Delta t = t_2 - t_1$$



$S_1$  = the depth the reaction has penetrated the cladding at the start of the time step

$S_2$  = the depth the reaction has penetrated the cladding at the end of the time step

If the right-hand side of Eq. (4.4-5) is called A, the equation may be rewritten as

$$S_2 = (S_1^2 + A)^{1/2} \quad (4.4-6)$$

The mass of zirconium per unit length that has reacted during the time step is calculated from

$$m_{Zr} = \pi \rho_{Zr} ((r_{co} - S_1)^2 - (r_{co} - S_2)^2) \quad (4.4-7)$$

which can be written using Eq. (4.4-6) as

$$m_{Zr} = \pi \rho_{Zr} A \left( \frac{2r_{co}}{S_1 + S_2} - 1 \right) \quad (4.4-8a)$$

In the case of reaction on the inside of the cladding the mass of zirconium reacted per unit length is calculated as

$$m_{Zr} = \pi \rho_{Zr} A \left( \frac{2r_{ci}}{S_1 + S_2} + 1 \right) \quad (4.4-8b)$$

Power generated by the reaction during the time step is calculated from:

$$Q_{mwr} = \Delta E \cdot m_{zr} / \Delta t \quad (4.4-9)$$

When solving the conduction equation this term is added as a heat source to the cladding node which contains the Zr-ZrO<sub>2</sub> interface.

To account for cladding strain Eq. (4.4-6) and (4.4-8) are used as follows, where primed quantities denote strained i.e. actual geometric dimensions and unprimed quantities denote nominal dimensions.

The strained geometric dimensions are

$$S_1' = S_1 / (1 + \epsilon) \quad (4.4-10a)$$

$$r_{co}' = r_{co} (1 + \epsilon) \quad (4.4-10b)$$

$$r_{ci}' = r_{ci} (1 + \epsilon) \quad (4.4-10c)$$

where  $\epsilon$  is the cladding tangential strain.

Eq. (4.4-6) gives

$$S_2' = (S_1'^2 + A)^{1/2} \quad (4.4-11)$$

and (4.4-8a) and (4.4-8b) can be written

$$m_{zr} = \pi \rho_{zr} A \left( \frac{2r_{co}'}{S_1' + S_2'} - 1 \right) \quad (4.4-12a)$$

$$m_{zr} = \pi \rho_{zr} A \left( \frac{2r_{ci}'}{S_1' + S_2'} + 1 \right) \quad (4.4-12b)$$

The nominal depth  $S_2$  at the end of the time step is then calculated from

$$S_2 = S_2' (1+\epsilon) \quad (4.4-13)$$

The initial oxide depth on the cladding outer surface is calculated using the fuel rod design code PAD. The initial oxide layer protects the cladding from subsequent oxidation in the same way as oxide which has been generated during the LOCA transient.

## 4.5 Thermal Radiation Model

The radiation model employed in the fuel rod heat-up calculation allows for anisotropic reflection. Following is the model derivation, and a description of the method used to calculate the gray body factors used by CHACHA-3C. The method used to obtain Appendix K - equivalent spray heat transfer coefficients for use with the anisotropic model is also discussed.

### 4.5.1 Model Derivation

The radiation model is formulated with the following assumptions:

- (1) All surfaces in the rod bundle are gray, diffuse and nontransparent.
- (2) The emission of radiation takes place isotropically.
- (3) Reflection of radiation is divided into an isotropic and an anisotropic component.
- (4) The anisotropic reflection reverts back to the origin of the radiation.
- (5) Absorption, emission and dispersion in the coolant are omitted.
- (6) All surfaces are in thermal quasi-equilibrium during each time step.

From assumption (1) the sum of the reflectivity and the absorptivity of surface  $i$  is unity

$$\rho_i + \alpha_i = 1 \qquad (4.5-1)$$

From assumption (6) the absorptivity and emissivity of surface  $i$  are equal

$$\alpha_i = \epsilon_i \quad (4.5-2)$$

The following relations therefore apply to surface  $i$  (refer to Fig. 4-3):

- o The radiation emitted is equal to the sum of the reflection and the gray body emission

$$\begin{aligned} B_i &= \rho_i H_i + \epsilon_i \sigma T_i^4 \\ &= (1-\epsilon_i) H_i + \epsilon_i \sigma T_i^4 \end{aligned} \quad (4.5-3)$$

- o The radiation emitted consists of an isotropic component,  $B_i^I$ , and an anisotropic component,  $B_i^A$ , where

$$B_i^I = (1-r_i) (1-\epsilon_i) H_i + \epsilon_i \sigma T_i^4 \quad (4.5-4)$$

$$B_i^A = r_i (1-\epsilon_i) H_i = \sum_{j=1}^N B_{ij}^A \quad (4.5-5)$$

Here  $r_i$  denotes the portion of the reflection from surface  $i$  which is anisotropic.

- o The total radiation incident to surface  $i$  is given by

$$\begin{aligned} H_i &= \sum_{j=1}^N H_{ji} \\ &= \sum_{j=1}^N (A_j B_j^I F_{ji} + A_j B_{ji}^A) / A_i \end{aligned} \quad (4.5-6)$$

The geometric view factor,  $F_{ji}$ , describes the fraction of the isotropically emitted radiation from surface  $j$  which strikes surface  $i$  directly.

The radiation model is developed from these relations as follows. Applying an energy balance to surface  $i$  in Fig. 4-3 yields

$$\begin{aligned} q''_{i,\text{rad}} &= (1-\epsilon_i) H_i + \epsilon_i \sigma T_i^4 - H_i \\ &= \epsilon_i \sigma T_i^4 - \epsilon_i H_i \end{aligned} \quad (4.5-7)$$

Solving Eq. (4.5-4) for  $H_i$  and substituting gives

$$q''_{i,\text{rad}} = \frac{\epsilon_i [(1-r_i (1-\epsilon_i)) \sigma T_i^4 - B_i^I]}{(1-\epsilon_i) (1-r_i)} \quad (4.5-8)$$

Substituting Eq. (4.5-6) in (4.5-5),

$$A_i B_{ij}^A = r_i (1-\epsilon_i) (A_j B_j^I F_{ji} + A_j B_{ji}^A) \quad (4.5-9)$$

Switching indices gives

$$A_j B_{ji}^A = r_j (1-\epsilon_j) (A_i B_i^I F_{ij} + A_i B_{ij}^A) \quad (4.5-10)$$

Inserting Eq. (4.5-10) into (4.5-9) and noting that  $A_j F_{ji} = A_i F_{ij}$  gives the following expression for  $B_{ij}^A$

$$B_{ij}^A = \frac{r_i (1-\epsilon_i) F_{ij} (B_j^I + r_j (1-\epsilon_j) B_i^I)}{1-r_i (1-\epsilon_i) r_j (1-\epsilon_j)} \quad (4.5-11)$$

Solving Eq. (4.5-5) for  $H_i$  and substituting into (4.5-4) gives

$$B_i^I = \frac{1-r_i}{r_i} \sum_{j=1}^N B_{ij}^A + \varepsilon_i \sigma T_i^4 \quad (4.5-12)$$

Eq. (4.5-11) is inserted into (4.5-12), yielding

$$B_i^I = \varepsilon_i \sigma T_i^4 + (1-r_i)(1-\varepsilon_i) \sum_{j=1}^N \frac{F_{ij} (B_j^I + r_j (1-\varepsilon_j) B_i^I)}{1-r_i (1-\varepsilon_i) r_j (1-\varepsilon_j)} \quad (4.5-13)$$

If we define

$$L_i = \sum_{j=1}^N \frac{r_j (1-\varepsilon_j) F_{ij}}{1-r_i (1-\varepsilon_i) r_j (1-\varepsilon_j)} \quad (4.5-14)$$

Eq. (4.5-13) may be rewritten as

$$B_i^I = \varepsilon_i \sigma T_i^4 + (1-r_i)(1-\varepsilon_i) L_i B_i^I + (1-r_i)(1-\varepsilon_i) \sum_{j=1}^N \frac{F_{ij} B_j^I}{1-r_i (1-\varepsilon_i) r_j (1-\varepsilon_j)} \quad (4.5-15)$$

Using Kronecker's delta function,  $a_{ij}$ , which has the property

$$a_{ij} = \begin{cases} 0 & \text{for } i \neq j \\ 1 & \text{for } i = j \end{cases}$$

Eq. 4.5-15 may be written as

$$\sum_{j=1}^N \left( \frac{F_{ij}}{1-r_i (1-\varepsilon_i) r_j (1-\varepsilon_j)} + a_{ij} \left( L_i - \frac{1}{(1-r_i)(1-\varepsilon_i)} \right) \right) B_j^I = - \frac{\varepsilon_i \sigma T_i^4}{(1-r_i)(1-\varepsilon_i)} \quad (4.5-16)$$

In matrix form this may be expressed as

$$\underline{G} \cdot \underline{B}^I = \underline{D} \quad (4.5-17)$$

a, c, g



[

] <sup>a,c,g</sup>  
(4.5-24)

Eq. (4.5-23) may be rewritten as

$$q_{k,\text{rad}}'' = \sum_{i=1}^N \text{GBF}_{ki} [\sigma T_k^4 - \sigma T_i^4] \quad (4.5-25)$$

The use of the term  $a_{ki} \epsilon_i$  in Eq. (4.5-24) gives the gray body factors the following characteristic:

$$\sum_{i=1}^N \text{GBF}_{ki} = \epsilon_k \quad (4.5-26)$$

#### 4.5.2 Gray Body Factor Code BILBO

The gray body factors (GBF) described in the previous section are calculated by the auxiliary code BILBO, which evaluates geometric view factors using the methodology described in Ref. 4-3. BILBO is run prior to the execution of CHACHA-3C. The output of BILBO consists of four sets of GBF for each of the symmetries which could be used in CHACHA-3C (i.e., full bundle, 1/2 symmetry, 1/4 symmetry and 1/8 symmetry). The four sets of GBF for each symmetry are calculated for the following conditions:

- 1) Rods in the nominal geometry, all surfaces dry
- 2) Same as 1, except the channel is wet
- 3) All rods strained to the diameter coincident with cladding perforation, all surfaces dry
- 4) Same as 3, except the channel is wet

For a reactor calculation, the emissivities of dry and wet surfaces are taken as 0.67 and 0.96, respectively. The anisotropic coefficients are set equal to 0.5 for fuel rods, and 0.15 for the channel, as recommended in Ref. 4-4. The rod diameters coincident with cladding perforation are calculated as described in Sec. 4.9.

#### 4.5.3 Derivation of Consistent Spray Heat Transfer Coefficients

Appendix K of 10CFR50 identifies convective heat transfer coefficients acceptable for use in analyses of 7x7 fuel under spray cooling conditions. Those coefficients were derived based on analyses of experimental data which were performed using an isotropic radiation model. This section describes the method by which those coefficients have been modified for QUAD+ fuel in order to account for the use of an improved, anisotropic radiation model, and for potential geometry effects.

Experimental spray cooling data obtained by ASEA-ATOM (A-A) in the GOTA test facility have shown that the Appendix K coefficients are applicable to the A-A 8x8 design, when the isotropic radiation model is used (Ref. 4-5). A-A has also determined the convective heat transfer coefficients which, when applied with the anisotropic model, would match the 8x8 temperature distributions calculated with the Appendix K coefficients and the isotropic radiation model. The resulting coefficients and the original Appendix K coefficients are shown in Table 4-2. The revised values represent Appendix K equivalent coefficients for use in analyses of A-A 8x8 fuel performed with the anisotropic model.

The heat transfer coefficients in Table 4-2 have been conservatively adjusted for application to QUAD+ fuel. The method of adjustment was to reduce each of the values in Table 4-2 by 15%, so that the QUAD+ bundle average heat transfer coefficient matches the A-A 8x8 bundle average heat transfer coefficient. The resulting values are shown in Table 4-3. These values represent Appendix K equivalent spray cooling convective heat transfer coefficients for use in analyses of QUAD+ fuel performed with the anisotropic radiation model.

#### 4.6 Gas Plenum Temperature and Pressure Model

In order to calculate the gas pressure in the rod, the temperature of the gas in the different regions of the rod has to be known. Three different regions are considered in CHACHA-3C, namely; the plenum volume, the gap volume and the free volume within the column of  $UO_2$  pellets. The initial sizes of these volumes are interpolated from an input table which is given as a function of linear heat generation rate and burnup.

The gas temperature in the gap volume is conservatively assumed to be equal to the gap temperature at the analyzed cross-section. The gas temperature in the free volume within the column of pellets is assumed to be equal to the volumetric average pellet temperature at the analyzed cross-section. The gas temperature in the plenum is calculated by the model described in Sec. 4.6.1.

The size of the gap volume increases during the course of the transient due to thermal and elastic expansion of the cladding. The effect of this increase is neglected which is conservative with respect to the rod gas pressure. The volume within the pellet column is also assumed to be constant in time.

In the calculation of the plenum volume the axial thermal expansion of the cladding is accounted for but thermal contraction of the pellet column is neglected. The axial thermal strain of the cladding is calculated by CHACHA-3C using the correlation given in Ref. 4-6:

$$\epsilon_z = \frac{\Delta Z}{Z_0} = A'\bar{T}^2 + B'\bar{T} + C' \quad (4.6-1)$$

$$A' = \begin{cases} 0. & \text{for } \bar{T} \leq 1073 \text{ } ^\circ\text{K} \\ 2.63 \times 10^{-8} & \text{for } 1073 \leq \bar{T} \leq 1273, \\ 0. & \text{for } \bar{T} \geq 1273 \end{cases}$$

$$B' = \begin{cases} 4.44 \times 10^{-6} & \text{for } \bar{T} < 1073 \text{ } ^\circ\text{K} \\ -7.25799 \times 10^{-5} & \text{for } 1073 \leq \bar{T} \leq 1273, \\ 9.7 \times 10^{-6} & \text{for } \bar{T} \geq 1273 \end{cases}$$

$$C' = \begin{cases} -1.24 \times 10^{-3} & \text{for } \bar{T} \leq 1073 \text{ } ^\circ\text{K} \\ 5.11224 \times 10^{-2} & \text{for } 1073 < \bar{T} \leq 1273, \\ -1.10 \times 10^{-2} & \text{for } \bar{T} \geq 1273 \end{cases}$$

The temperature used to evaluate the axial thermal strain over the heated length is set equal to the maximum of the coolant temperature and 0.8 times the cladding temperature at the analyzed cross-section, based on the BWR FLECHT test results noted in Ref. 4-7.

For the portion of the cladding above the pellet column the temperature calculated by the plenum temperature model is used to evaluate the thermal strain. The gas volume in the plenum is then calculated from

$$V_{gpln} = V_{gplni} Z_{plna}/Z_{plni} \quad (4.6-2)$$

where

$V_{gplni}$  = initial plenum gas volume

$Z_{plna}$  = current plenum length

$Z_{plni}$  = initial plenum length

#### 4.6.1 Plenum Temperature Model

A sketch of the top end of a fuel rod is shown in Fig. 4-4. The fission gas plenum is bounded by the top fuel pellet, the cladding and the end plug. A spring occupies a portion of the space within the plenum. The temperature of the plenum gas is determined by the heat transfer between each of these components and the gas itself.

The CHACHA-3C plenum temperature model considers seven components -- the end plug, the plenum gas, the spring, the center and outer portions of the top pellet, the cladding surrounding the top pellet, and the cladding surrounding the plenum. A heat balance is set up for each of these seven components:

$$\rho_i C_i V_i \frac{dT_i}{dt} + \sum_{j=1}^8 a_{ij} (T_i - T_j) = q_i'' V_i \quad (4.6-3)$$

where  $j=8$  corresponds to heat transfer to the coolant. Fig. 4-5 shows a schematic of the calculational model.

The  $\rho_i$ ,  $C_i$  and  $V_i$  for each component are specified in the input to CHACHA-3C. The volumetric heat generation rate in the top pellet is also input. There are 14 different heat transfer paths between the various components which corresponds to 28 nonzero elements in the  $(a_{ij})$  matrix. The heat transfer paths between the various components are defined via user input heat transfer areas ( $A_k$ ) and heat transfer coefficients ( $h_k$ ). If heat transfer path "k" goes from component "i" to component "j" then:

$$a_{ij} = A_k \times h_k \quad (4.6-4)$$

When the heat transfer path goes to the coolant a convective heat transfer coefficient ( $h_c$ ) is calculated internally and Eq. (4.6-4) is modified to read:

$$a_{ij} = A_k \frac{1}{\frac{1}{h_k} + \frac{1}{h_c}} \quad (4.6-5)$$

The convective heat transfer coefficient in Eq. (4.6-5) is set equal to the  $h_c$  at the studied axial cross-section before spray cooling starts. After spray cooling has started  $h_c$  is calculated from

$$h_c = h_{nb} + x_T (h_{film} - h_{nb}) \quad (4.6-6)$$

where

$$x_T = \begin{cases} 0 & ; T_j \leq T_{crit} \\ (T_j - T_{crit}) / (T_{leid} - T_{crit}) & ; T_{crit} < T_j \leq T_{leid} \\ 1 & ; T_{leid} < T_j \end{cases}$$

$j = pl, cu$  or  $cl$  (refer to Fig. 4-5)

$$T_{crit} = T_{sat} + 23.$$

$$T_{leid} = T_{sat} + 1 / (0.0090945 + 3696.3 / P_{cool})$$

$h_{nb}$  and  $h_{film}$  are specified in input.

The system of Eq. (4.6-3) is discretized in time in a fully implicit manner. The resulting equations read:

$$P_i C_i V_i \frac{T_i^{n+1}}{\Delta t} + \sum_{j=1}^7 a_{ij} (T_i^{n+1} - T_j^{n+1}) + a_{i8} T_i^{n+1} =$$

$$P_i C_i V_i \frac{T_i^n}{\Delta t} + a_{i8} T_{cool} + \dot{q}'' V_i ; i = 1, 2, \dots, 7 \quad (4.6-7)$$

This symmetric linear system of equations is solved by direct Gaussian elimination for the unknowns  $T_i^{n+1}$ ;  $i = 1, 2, \dots, 7$ .

#### 4.6.2 Internal Rod Gas Pressure Model

Given the gas temperatures in the plenum, the gap volume and the free volume within the pellet column, and the size of these volumes, the pressure in the rod is calculated from the amount of gas in the rod.

$$P_{gas} = \frac{n_{gas} R_{gas}}{\frac{V_{gpln}}{T_{gpln}} + \frac{V_{gap}}{T_{gap}} + \frac{V_{pelcol}}{T_{pelcol}}} \quad (4.6-8)$$

The initial volumes of the three gas regions and the number of moles of each component gas are interpolated from an input table as a function of linear heat generation rate and burnup.

Transient fission gas release may be neglected because only part of the pellets experience a temperature increase during the LOCA transient and because of the relatively short length of the transient. Power ramp testing of irradiated power reactor fuel rods has shown that significant release does not take place until at least half an hour after ramping (Fig. 4-6 and Ref. 4-8 and 4-9).



#### 4.7 Channel Rewet Model

This model calculates the channel wetting time, i.e. the time that it takes for a water film to propagate downwards along the channel wall to the studied axial location. The propagation of the water film is assumed to start simultaneously with the start of spray cooling.

The rewet time is calculated from consideration of the film front velocity,  $U_{ff}$ , and the film front temperature,  $T_{ff}$ .  $T_{ff}$  is the temperature of the channel wall just ahead of the film front. Yamanouchi (Ref. (4-10)) gives the film front velocity as:

$$U_{ff} = \frac{1}{(\rho C)_{ch}} \left( \frac{h_{NB} k_{ch}}{d_{ch}} \right)^{1/2} \left( \frac{T_{leid} - T_{sat}}{T_{ff} - T_{leid}} \right) \quad (4.7-1)$$

Assuming a constant, linear film front temperature profile, this equation can be integrated to give:

$$t_{wety} = (\rho C)_{ch} \left( \frac{d_{ch}}{h_{NB} k_{ch}} \right)^{1/2} \left( \frac{T_{ch} - T_{leid} - \left( \frac{dT}{dZ} \right) \frac{L}{2}}{T_{leid} - T_{sat}} \right) L \quad (4.7-2)$$

where,

$t_{wety}$  = Yamanouchi rewet time (sec)

$T_{ch}$  = channel temperature at the elevation of interest ( $^{\circ}\text{C}$ )

$\frac{dT}{dZ}$  = axial channel temperature gradient ( $^{\circ}\text{C}/\text{m}$ )

$L$  = distance to top of channel from the elevation of interest (m)

As recommended in Appendix K of 10CFR50, the rewet time predicted by the Yamanouchi correlation is modified based on the study reported in Ref. 4-9. The base correlation used in CHACHA-3C is:

$$t_{\text{rewet}} = 12 + \frac{158}{600} t_{\text{wety}} \quad (\text{sec}) \quad (4.7-3)$$

This correlation predicts rewet times equivalent to the correlation shown in Fig. D-11 of Ref. 4-9. The effective rewet time used by CHACHA-3C is Eq. (4.7-3) plus 60 seconds, consistent with Appendix K requirements.

#### 4.8 Pellet-Cladding Gap Heat Transfer Model

The heat flux at the pellet outer surface is given by:

$$q''_{fs} = h_{gap}(T_{fs} - T_{ci}) \quad (4.8-1)$$

$h_{gap}$  is calculated as a function of time, taking into account the gas composition in the gap and the dimensions of the gap.

The total gap heat transfer coefficient is calculated by CHACHA-3C as:

$$h_{gap} = h_{con} + h_{rad} \quad (4.8-2)$$

where  $h_{gas}$  is the gap conductance and  $h_{rad}$  is the radiation contribution to the total gap heat transfer. If an open gap is calculated by Eq. (4.9-8), CHACHA-3C calculates the gap conductance as:

$$h_{con} = \max(h_{con,1}, h_{con,2}) \quad (4.8-3)$$

where,

$$h_{con,1} = \left[ \quad \quad \quad \right]^{a,c} \quad \left( \frac{\text{Btu}}{\text{hr ft}^2 \text{ } ^\circ\text{F}} \right)$$

$$h_{con,2} = \left[ \quad \quad \quad \right]^{a,c} \quad \left( \frac{\text{Btu}}{\text{hr ft}^2 \text{ } ^\circ\text{F}} \right)$$

$$k_{mix} = \text{thermal conductivity of the gas mixture} \quad \left( \frac{\text{Btu}}{\text{hr ft } ^\circ\text{F}} \right)$$

$$\Delta r'_{gap} = \left[ \quad \quad \quad \right]^{a,c} \quad (\text{ft})$$

$\Delta r_{\text{gap}}$  = pellet/cladding gap size for the current time step, as calculated by Eq. (4.9-8)

$\Delta'$  = annular gap reduction factor  $\left[ \quad \right]^{a,c}$

$X$  = multiplier on Dean's surface roughness  $\left[ \quad \right]^{a,c}$

If  $k_{\text{mix}} < \left[ \quad \right]^{a,c} \frac{\text{Btu}}{\text{hr ft}^2 \text{ } ^\circ\text{F}}$ ,  $h_{\text{con}}$  is set equal to  $h_{\text{con},1}$ .

If a closed gap is calculated, i.e.,  $\Delta r_{\text{gap}} \leq 0.$ , the gap conductance is calculated as:

$$h_{\text{con}} = \left[ \quad \right]^{a,c} \left( \frac{\text{Btu}}{\text{hr ft}^2 \text{ } ^\circ\text{F}} \right) \quad (4.8-4)$$

where  $P_{\text{con}}$  is the pellet/cladding contact pressure in psi.

The thermal conductivity of the gas mixture is calculated based on the work of Brokaw (Ref. 4-11).

$$k_{\text{mix}} = \sum_{i=1}^n \frac{k_i}{1 + \sum_{\substack{j=1 \\ j \neq i}}^n \psi_{ij} \frac{y_j}{y_i}} \quad (4.8-5)$$

where:

$$\psi_{ij} = \phi_{ij} \left[ 1 + 2.41 \frac{(M_i - M_j)(M_i - .142 M_j)}{(M_i + M_j)^2} \right] \quad (4.8-6)$$

$$\phi_{ij} = \frac{[1 + (\frac{k_i}{k_j})^{0.5} (\frac{M_i}{M_j})^{0.25}]^2}{2 (2)^{0.5} (1 + \frac{M_i}{M_j})^{0.5}} \quad (4.8-7)$$

and:  $n$  = number of component gases in the mixture  
 $M$  = molecular weight of a component gas  
 $y$  = mole fraction of the gas  
 $k$  = effective thermal conductivity of a pure gas

The thermal conductivity equations of xenon and krypton were fit to the correlated data of Gandhi and Saxena (Ref. 4-12). The resulting expressions are:

$$k_{Xe} = 1.395 \times 10^{-5} TR^{0.872} \quad \left(\frac{\text{Btu}}{\text{hr ft}^{\circ}\text{F}}\right) \quad (4.8-8)$$

$$k_{Kr} = 1.588 \times 10^{-5} TR^{0.923} \quad \left(\frac{\text{Btu}}{\text{hr ft}^{\circ}\text{F}}\right) \quad (4.8-9)$$

where  $TR$  is the gas temperature in  $^{\circ}\text{R}$ .

The following conductivity equations for air and nitrogen were fit to the data found in Ref. 4-13 to 4-15. Thermal conductivity for hydrogen was fit to data in Ref. 4-13, 4-16 and 4-17.

$$k_{air} = 7.35 \times 10^{-5} TR^{0.846} \quad \left(\frac{\text{Btu}}{\text{hr ft}^{\circ}\text{F}}\right) \quad (4.8-10)$$

$$k_{N_2} = 7.35 \times 10^{-5} TR^{0.846} \quad \left(\frac{\text{Btu}}{\text{hr ft}^{\circ}\text{F}}\right) \quad (4.8-11)$$

$$k_{H_2} = 5.834 \times 10^{-4} TR^{0.8212} \quad \left(\frac{\text{Btu}}{\text{hr ft}^{\circ}\text{F}}\right) \quad (4.8-12)$$

The thermal conductivity of helium is based on Ref. 4-18. The resulting expression in units of Btu/hr ft °F is

$$k_{He} = \left[ \quad \right]^{a,c} \quad (4.8-13)$$

where P is the gas pressure in psia. When the gap size approaches the mean free path of the helium molecules, an accommodation coefficient must be used to reduce the thermal conductivity of the helium gas. The effective thermal conductivity of helium is therefore calculated as:

$$k_{He,eff} = k_{He}/f \quad (4.8-14)$$

where

$$f = \left[ \quad \right]^{a,c}$$

A = accommodation coefficient

$$= \left[ \quad \right]^{a,c}$$

$$R = \left[ \quad \right]^{a,c}$$

If rod burst is calculated during the transient, it is assumed that the gases in the gap are steam and hydrogen, in equal mole fractions. Conductivity of steam in the gap is calculated from a correlation of values based on the 1967 ASME steam tables. The expression derived is

$$k_{H_2O} = \left[ \quad \right]^{a,b,c} \left( \frac{\text{Btu}}{\text{hr ft } ^\circ\text{F}} \right) \quad (4.8-15)$$

where:

$$C = \left[ \right]^{a,b,c}$$

$P_{cool}$  = coolant pressure (psi)

The radiation contribution to the total gap heat transfer is calculated as:

$$h_{rad} = \frac{\sigma (T_p^4 - T_c^4)}{\frac{r_p + r_c}{2r_p} \left[ \frac{1}{\epsilon_f} + \frac{r_p}{r_c} \left( \frac{1}{\epsilon_c} - 1 \right) \right] (T_p - T_c)} \quad \left( \frac{\text{Btu}}{\text{hr ft}^2 \text{ } ^\circ\text{F}} \right) \quad (4.8-16)$$

where

$\sigma$  = Stefan - Boltzmann constant  $(0.1714 \times 10^{-8} \frac{\text{Btu}}{\text{hr ft}^2 \text{ } ^\circ\text{R}^4})$

$T_p$  = pellet surface temperature ( $^\circ\text{R}$ )

$T_c$  = cladding inner surface temperature ( $^\circ\text{R}$ )

$r_p$  = pellet radius for the current time step

$r_c$  = cladding inner radius for the current time step

$\epsilon_f$  = emissivity of fuel

$$= 1.2424 - 2.63 \times 10^{-4} (T_p - 459.7)$$

$\epsilon_c$  = emissivity of cladding

$$= \max (0.6, \left[ \right]^{a,c})$$

## 4.9 Cladding Strain And Rupture Model

Given the rod internal gas pressure, the coolant pressure, the pellet and cladding temperature distributions and the initial dimensions of the pellet and cladding this model calculates the cladding strain, the pellet cladding gap size, and possible cladding perforation.

### 4.9.1 Cladding Rupture Model

The maximum allowable cladding stress ( $\sigma_B$ ) is calculated as a function of the cladding temperature. If this stress is exceeded by the actual cladding stress ( $\sigma_C$ ) a rod perforation is assumed to occur.

The maximum cladding stress versus temperature relationship in CHACHA-3C is shown in Fig. 4-7. The cladding temperature used to evaluate the function is the arithmetic average of the cladding inner and outer surface temperatures. The actual cladding stress which is compared with  $\sigma_B$  is calculated based on nominal dimensions.

### 4.9.2 Cladding Strain Model

The cladding strain is the sum of the thermal, elastic and plastic strains:

$$\varepsilon = \varepsilon_t + \varepsilon_e + \varepsilon_p \quad (4.9-1)$$

The tangential thermal strain of the cladding is calculated by CHACHA-3C using the correlations given in Ref. 4-6:

$$\varepsilon_t = \frac{\Delta r}{r_{ci}} = A\bar{T}^2 + B\bar{T} + C \quad (4.9-2)$$



where,

$\Delta r$  = clad radius at elevated temperature minus clad radius at room temperature ( $r_{ci}$ )

$\bar{T}$  = clad average temperature ( $^{\circ}\text{K}$ )

A = 0. for  $\bar{T} \leq 1073$ ,  
 $1.49 \times 10^{-8}$  for  $1073 < \bar{T} < 1273$ ,  
0. for  $\bar{T} \geq 1273$

B =  $6.72 \times 10^{-6}$  for  $\bar{T} \leq 1073$ ,  
 $-4.61677 \times 10^{-5}$  for  $1073 < \bar{T} < 1273$ ,  
 $9.7 \times 10^{-6}$  for  $\bar{T} \geq 1273$

C =  $-2.07 \times 10^{-3}$  for  $\bar{T} \leq 1073$ ,  
 $3.75237 \times 10^{-2}$  for  $1073 < \bar{T} < 1273$ ,  
 $-9.45 \times 10^{-3}$  for  $\bar{T} \geq 1273$

The elastic strain of the cladding is calculated using the standard biaxial strain equation:

$$\epsilon_e = \frac{\sigma_c}{E} \left(1 - \frac{\nu}{2}\right) \quad (4.9-3)$$

The actual tangential stress is given by

$$\sigma_c = \frac{r_{ci,zr} P_{\text{gas}} - r_{co,zr} P_{\text{cool}}}{r_{co,zr} - r_{ci,zr}} \quad (4.9-4)$$

where,

$$r_{ci,zr} = r_{ci} + \Delta r_{oxi}$$

$$r_{co,zr} = r_{co} - \Delta r_{oxo}$$

$r_{ci}, r_{co}$  = nominal cladding inner and outer radii (m)

$\Delta r_{oxi}, \Delta r_{oxo}$  = oxide thickness on inner and outer surfaces (m)

$P_{gas}$  = rod internal gas pressure (Pa)

$P_{cool}$  = coolant pressure (Pa)

Young's modulus is given by

$$E = c E' \quad (4.9-5)$$

where,

$E'$  = Young's modulus in psi

$$= \left[ \quad \quad \quad \right]^{a,c}$$

TF = cladding average temperature (°F)

$c$  = conversion factor, 6900Pa/psi

Poisson's ratio is given by

$$\mu = \left[ \quad \quad \quad \right]^{a,c} \quad (4.9-6)$$

The tangential plastic strain is calculated using the method described in Ref. 4-7:

$$\epsilon_p = \epsilon_{p,final} f(T, T_{perf}) \quad (4.9-7)$$

The strain coincident with rod perforation,  $\epsilon_{p,final}$  is calculated as a function of the pressure differential over the cladding. The relationship used in CHACHA-3C is taken from Ref. 4-7, and is shown in Fig. 4-8.

The function used to evaluate plastic strain prior to cladding perforation,  $f(T, T_{perf})$ , is also taken from Ref. 4-7, and is shown in Fig. 4-9.

The perforation temperature used to evaluate this function is obtained from the perforation stress relationship shown in Fig. 4-7.

#### 4.9.3 Pellet/Cladding Gap Calculation

Following the calculation of the individual cladding strain components the pellet/cladding gap size is updated

$$\Delta r_{gap} = \Delta r_{gap,i} + (\epsilon_t + \epsilon_e + \epsilon_p - \epsilon_{clad,i}) r_{ci} - (\epsilon_{t,pellet} - \epsilon_{pellet,i}) r_{fs} \quad (4.9-8)$$

where,

$\Delta r_{\text{gap}}$  = gap size at current time (m)

$\Delta r_{\text{gap},i}$  = gap size at time zero (m)

$\epsilon_t$  = thermal strain of cladding at current time, from Eq. (4.9-2)

$\epsilon_e$  = elastic strain of cladding at current time, from Eq. 4.9-3)

$\epsilon_p$  = plastic strain of cladding at current time, from Eq. (4.9-7)

$\epsilon_{\text{clad},i}$  =  $\epsilon_t + \epsilon_e + \epsilon_p$  at time zero

$r_{ci}$  = nominal cladding inner radius (m)

$\epsilon_{t,\text{pellet}}$  = pellet thermal strain at current time

$\epsilon_{\text{pellet},i}$  = pellet thermal strain at time zero

$r_{fs}$  = nominal pellet radius (m)

The pellet thermal strain is given by

$$\epsilon_{t,\text{pellet}} = \left[ \dots \right]^{a,c} \quad (4.9-9)$$

where,

$\bar{T}$  = pellet volumetric average temperature in °C

#### 4.10 Nomenclature

<u>Variable</u>	<u>Description</u>	<u>Units</u>
$A_i$	Area of surface $i$	$(m^2)$
$A_k$	Heat transfer area for path $k$ in plenum temperature model	$(m^2)$
$B_i$	Radiation emitted from surface $i$	$(W/m^2)$
$B_i^A$	Anisotropic component of radiation emitted from surface $i$	$(W/m^2)$
$B_i^I$	Isotropic component of radiation emitted from surface $i$	$(W/m^2)$
$C$	Specific heat	$(J/kg-^{\circ}C)$
$d_{ch}$	Channel wall thickness	$(m)$
$E$	Young's modulus	$(Pa)$
$F_{ij}$	View factor from surface $i$ to surface $j$	
GBF	Gray Body Factor	
$H_i$	Radiation incident to surface $i$	$(W/m^2)$
$h_{film}$	Film boiling heat transfer coefficient	$(W/m^2)$
$h_k$	Heat transfer coefficient for path $k$ in in plenum temperature model	$(W/m^2-^{\circ}C)$
$h_{nb}$	Nucleate boiling heat transfer coefficient	$(W/m^2-^{\circ}C)$
$h_{rad}$	Radiative heat transfer coefficient	$(W/m^2-^{\circ}C)$
$K$	Composite thermal conductivity	$(W/m-^{\circ}C)$
$k$	Thermal conductivity (evaluated at node center)	$(W/m-^{\circ}C)$
$k_{mix}$	Thermal conductivity of gas mixture	$(W/m-^{\circ}C)$
$m_{zr}$	Mass of zirconium reacted per unit length	$(kg/m)$
$n_{gas}$	Number of moles of gas	
$P_{con}$	Pellet/cladding contact pressure	$(lb/in^2)$
$P_{cool}$	Coolant pressure	$(Pa)$
$P_{gas}$	Rod gas pressure	$(Pa)$
$Q_{conv}$	Convective heat transfer rate from the surfaces of the channel box	$(W)$
$Q_{gen}$	Heat generation in the channel box	$(W)$
$Q_{mwr,i}$	Heat generation from metal-water reaction in node $i$	$(W)$

<u>Variable</u>	<u>Description</u>	<u>Units</u>
$Q_{rad}$	Radiation heat rate for a rod	(W)
$Q_{rrod}$	Radiative heat transfer rate from the channel to the rods	(W)
$q''$	Heat flux	(W/m <sup>2</sup> )
$q'''$	Volumetric heat generation rate	(W/m <sup>3</sup> )
$R_{gas}$	Universal gas constant = 8.314	(J/mol-°C)
$r$	Node boundary radius	(m)
$r_c$	Cladding inner surface radius	(m)
$r_{ci,zr}$	Radius of zirc/oxide interface, cladding inner surface	(m)
$r_{co,zr}$	Radius of zirc/oxide interface, cladding outer surface	(m)
$r_m$	Node center radius	(m)
$r_p$	Pellet outer surface radius	(m)
$S$	Zirc oxide thickness	(m)
$T^n$	Temperature at time step n	(°C)
$T_{crit}$	Critical temperature	(°C)
$T_{leid}$	Effective Leidenfrost temperature = 274	(°C)
$T_{surf}$	Cladding outer surface temperature	(°C)
$t$	Time	(sec)
$t_{wety}$	Wetting time from Yamanouchi correlation	(sec)
$U_{ff}$	Water film front velocity	(m/sec)
$\alpha$	Absorptivity	(J/kg)
$\Delta g$	Gap size	(m)
$\Delta r_{gap}$	Current pellet/cladding gap size	(m)
$\Delta r_i$	Thickness of node i	(m)
$\Delta r_{oxi}$	Oxide thickness on inside of cladding	(m)
$\Delta r_{oxo}$	Oxide thickness on outside of cladding	(m)
$\Delta t$	Time step	(sec)
$\Delta V$	Volume	(m <sup>3</sup> )
$\Delta Z$	Axial distance	(m)
$\epsilon$	Total strain	

<u>Variable</u>	<u>Description</u>	<u>Units</u>
$\epsilon_c$	Emissivity of cladding	
$\epsilon_e$	Elastic strain	
$\epsilon_f$	Emissivity of fuel	
$\epsilon_i$	Emissivity of surface i	
$\epsilon_p$	Plastic strain	
$\epsilon_t$	Tangential thermal strain	
$\epsilon_z$	Axial thermal strain	
$\mu$	Poisson's ratio	
$\rho$	Density or reflectivity	(kg/m <sup>3</sup> , or dimensionless)
$\sigma$	Stefan-Boltzmann constant	(W/m <sup>2</sup> -°K <sup>4</sup> )
$\sigma_c$	Cladding stress	(Pa)
$\theta$	Implicitness parameter	
$\delta_{ij}$	Kronecker delta function	

<u>Subscript</u>	<u>Description</u>
bnd	Boundary
ch	Channel
ci	Cladding inside surface
co	Cladding outside surface
cool	Coolant
fs	Fuel outer surface
gap	Gas gap
i	Node or surface index
j,k	Surface indices
M	Outer fuel node index
M+1	Index of innermost cladding node
N	Index of outermost cladding node
ox	Oxide
rad	Radiation
sat	Saturation



#### 4.11 References

- 4-1 J. Crank and P. Nicolson, "A Practical Method for Numerical Evaluations of Solutions of Partial Differential Equations of the Heat Conduction Type", Proc. Cambridge Phil. Soc., Vol. 43, 1947.
- 4-2 L. Baker and L. C. Just, "Studies of Metal-Water Reactions at High Temperatures, III. Experimental and Theoretical Studies of the Zirconium-Water Reaction", ANL-6548, 1962.
- 4-3 G. L. Singer, "Viewpin. A Fortran Program to Calculate Viewfactors for Cylindrical Pins". Aerojet Nuclear Co. AT (10-1) - 1375, March 1972.
- 4-4 C. L. Tien, et.al., "Surface Radiation Exchange in Rod Bundles", Transactions of the ASME, Vol. 101, p. 378-379, 1979.
- 4-5 R. Pettersson, "GÖTA Data Analysis. Comparisons Between Test Data and Calculations," RCC-79-68, May 1979.
- 4-6 "MATPRO-Version 11: A Handbook of Material Properties for Use in the Analysis of LWR Fuel Rod Behavior", NUREG/CR-0497, 1979.
- 4-7 "General Electric Company Analytical Model for Loss-of-Coolant Accident Analysis in Accordance with 10 CFR 50 Appendix K, Volume I", NEDO-20566, January 1976.
- 4-8 B. Nilsson and B. Bivered, "Mekanisk vaxelverkan O1/R2-76/79 Exp R2 - FO 52R - FO53R EBU rapport avssende fissionsgasmatningar". SE K4-80/62.
- 4-9 B. S. Slifer and J. E. Hench, "Loss-of-coolant Accident and Emergency Core Cooling Models for General Electric Boiling Water Reactors". NEDO 10329, April 1971.
- 4-10 A. Yamanouchi, "Effect of Core Spray Cooling in Transient State After Loss of Coolant Accident", Journal of Nuclear Science Tech., Vol. 5, p. 547-558, 1968.

- 4-11 R. S. Brokaw, "Alignment Charts for Transport Properties, Viscosity, Thermal Conductivity and Diffusion Coefficients for Nonpolar Gases and Gas Mixtures at Low Density", Report NASA TR R-81, 1961.
- 4-12 J. M. Gandhi and S. C. Saxena, "Correlated Thermal Conductivity Data of Rare Gases and Their Binary Mixtures at Ordinary Pressures", Journal of Chemical and Eng. Data, Vol. 13, No. 3, July 1968.
- 4-13 J. M. Lenore, "Thermal Conductivity of Gases at Atmospheric Pressure", Bulletin No. 18, Engineering Experiment Station, University of Arkansas, Fayetteville, Arkansas.
- 4-14 Y. S. Touloukian, et. al., "Thermal Conductivity of Non-Metallic Liquids and Gases".
- 4-15 National Bureau of Standards - Circular 564-1955.
- 4-16 S. C. Saxena, "Transport Properties of Gases and Gaseous Mixtures at High Temperatures", High Temperature Science Journal, March 1971.
- 4-17 R. W. Powell, et. al., "Thermal Conductivity of the Elements", Journal of Physical Chemistry, 1972.
- 4-18 N. V. Tsederburg, "Thermal Conductivity of Gases and Liquids", MIT Press, 1965.

Appendix 4.A Fuel Bundle Material Properties

Uranium Dioxide (with and without Gd<sub>2</sub>O<sub>3</sub>)

Density

The general equation used to evaluate density for fuel pellets with and without Gd<sub>2</sub>O<sub>3</sub> is

$$\rho_{\text{UO}_2} = \text{TD} \left( \frac{\text{AD}}{100} \right)$$

where,

TD = theoretical density at room temperature

AD = actual density at room temperature, expressed as a percentage of TD

For fuel without Gd<sub>2</sub>O<sub>3</sub> the theoretical density is 10960 kg/m<sup>3</sup>. TD for gadolinium bearing fuel is given by

$$\text{TD}_{\text{UO}_2/\text{Gd}_2\text{O}_3} = \left[ \quad \right]^{a,c} \text{ (kg/m}^3\text{)}$$

where Wg is the weight percent of Gd<sub>2</sub>O<sub>3</sub>.

## Thermal Conductivity

For fuel without gadolinium the thermal conductivity is given by:

$$k_{UO_2} = \left( \frac{1 - P}{1 + \beta P} \right) k_{100}$$

where,

$k_{100}$  = thermal conductivity at 100% of theoretical density  
= [ ]<sup>a,c</sup> (W/cm°C)

TC = fuel node temperature (°C)

P = fractional porosity of the fuel

$\beta$  = [ ]<sup>a,c</sup>

For fuel containing  $Gd_2O_3$  the thermal conductivity is evaluated as:

$$k_{UO_2/Gd_2O_3} = \frac{1}{A + BT} + CT^3 \left( \frac{W}{m^3C} \right)$$

where,

A = [ ]<sup>a,c</sup>

B = [ ]<sup>a,c</sup>

C = [ ]<sup>a,c</sup>

T = fuel node temperature (°K)

Wg = weight percent of  $Gd_2O_3$

This model is valid for  $Wg \leq 12$ .

### Specific Heat

The specific heat for fuel with and without  $Gd_2O_3$  is given by

$$\left[ \right]^{a,c}$$

where,

$T$  = fuel node temperature ( $^{\circ}K$ )

Zircaloy-2 (Cladding) and Zircaloy-4 (Channel)

### Density

Density of Zr is given by

$$\rho_{Zr} = \frac{410.1}{1 + 9.66 \times 10^{-6} TF} \quad (\text{lbm/ft}^3)$$

where  $TF$  is the node temperature in  $^{\circ}F$ .

### Thermal Conductivity

The thermal conductivity is evaluated as

$$k_{Zr} = A + B (TF) \quad (\text{Btu/hr ft}^{\circ}\text{F})$$

where,

TF = node temperature ( $^{\circ}\text{F}$ )

A = 7.404 for  $32 \leq TF \leq 743$ ,  
5.621 for  $TF > 743$

B = 0.0029 for  $32 \leq TF \leq 743$ ,  
0.0053 for  $TF > 743$

### Specific Heat

The specific heat of Zr is defined for four different temperature ranges:



Zirconium Oxide

### Density

The density of  $\text{ZrO}_2$  is taken as  $347 \text{ lbm/ft}^3$ .

### Thermal Conductivity

The thermal conductivity of  $ZrO_2$  is calculated as

$$k_{ZrO_2} = \left[ \quad \quad \quad \right]^{a,c} \quad (\text{Btu/hrft}^\circ\text{F})$$

where TF is the oxide temperature in  $^\circ\text{F}$ .

### Specific Heat

The specific heat of  $ZrO_2$  is evaluated as

$$(C_p)_{ZrO_2} = \left[ \quad \quad \quad \right]^{a,c} \quad (\text{Btu/lb}_m^\circ\text{F})$$

Table 4-1

Inputs Required to Calculate Heat Generation Rates

<u>Input</u>	<u>Source</u>
Core average power vs time	GOBLIN
Axial peaking factor	Distribution from POLCA
Rod-wise radial power distribution	PHOENIX
Radial bundle peaking factor	Based on maximum kw/ft
Pellet radial power distribution	HAMMER, FOBUS, <u>W</u> -ANISN
Energy deposition in fuel, cladding and channel	See Saction 4.3



Table 4-2

Appendix K Spray Heat Transfer Coefficients for A-A 8x8 Fuel

<u>Rod Type</u>	<u>Isotropic Radiation Model (W/m<sup>2</sup>-°C)</u>	<u>Anisotropic Radiation Model (W/m<sup>2</sup>-°C)</u>
Inner	8.5	[ ] <sup>a,c</sup>
Side	19.9	
Corner	17.0	
Channel Wall	28.4	

Table 4-3

Appendix K Spray Heat Transfer Coefficients for QUAD+ Fuel \*

<u>Rod Type</u>	<u>h<sub>conv</sub> (W/m<sup>2</sup>-°C)</u>
Inner	[ ] <sup>a,b,c</sup>
Side	
Corner	
Channel Wall	

\* Anisotropic radiation model

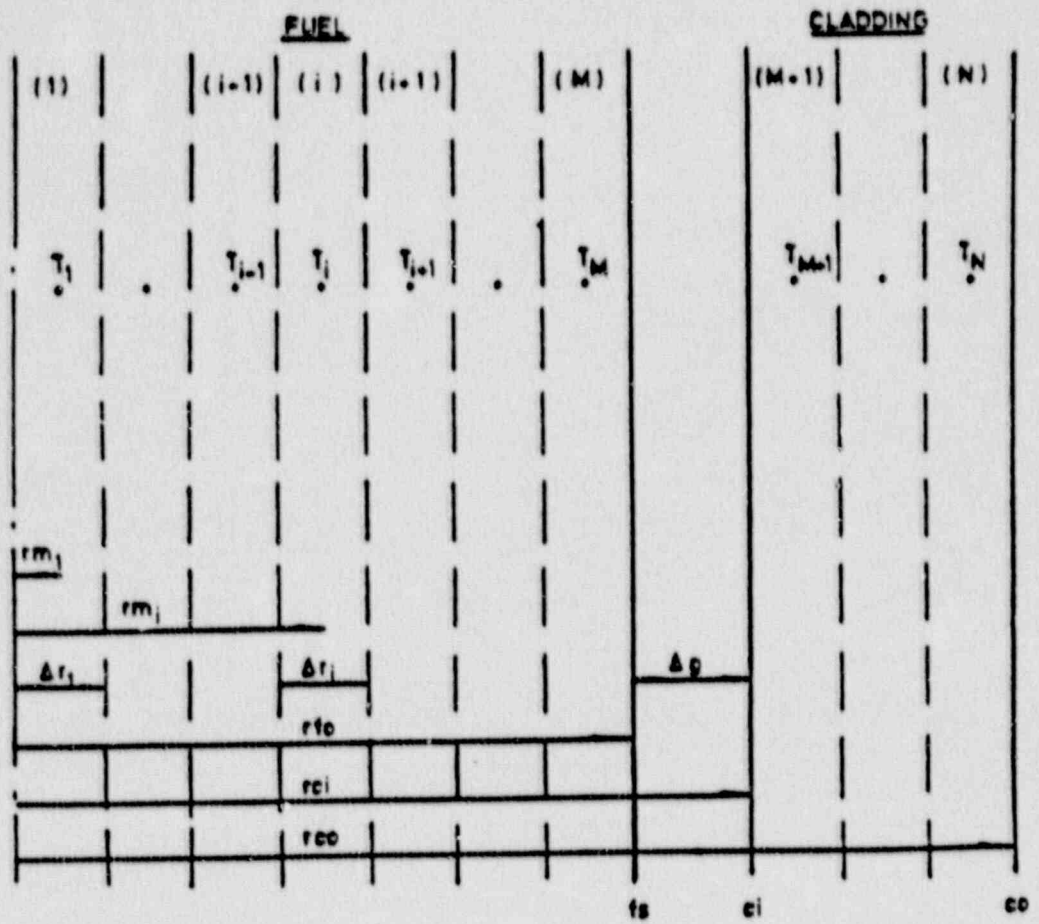


Figure 4-1 - Fuel Rod Conduction Model Nodalization



Figure 4-2 -  $UO_2$  Pellet Radial Power Distribution

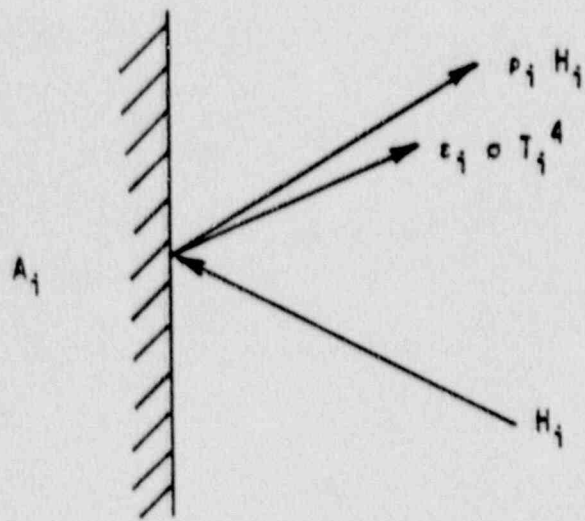


Figure 4-3 - Components of Radiation at Surface  $i$

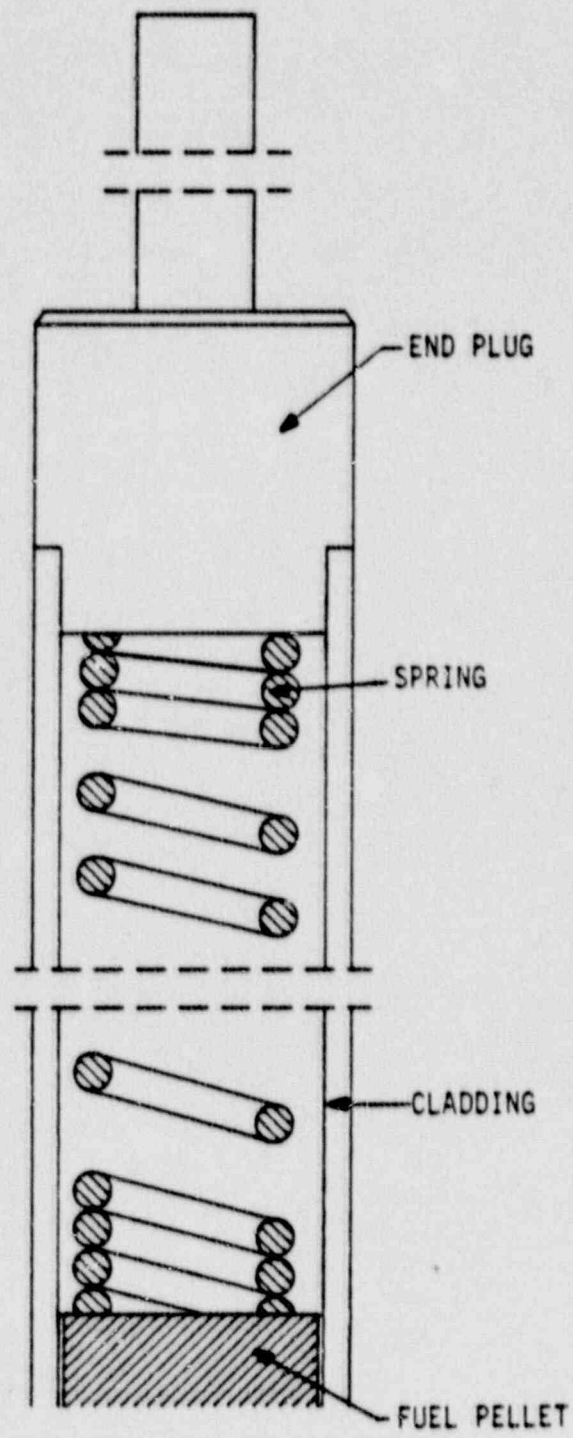


Figure 4-4 - Top End of Fuel Rod

KEY

- pi - end plug
- cu - upper portion of cladding
- cl - lower portion of cladding
- ga - plenum gas
- sp - spring
- fc - center portion of top pellet
- fr - outer portion of top pellet
- co - coolant

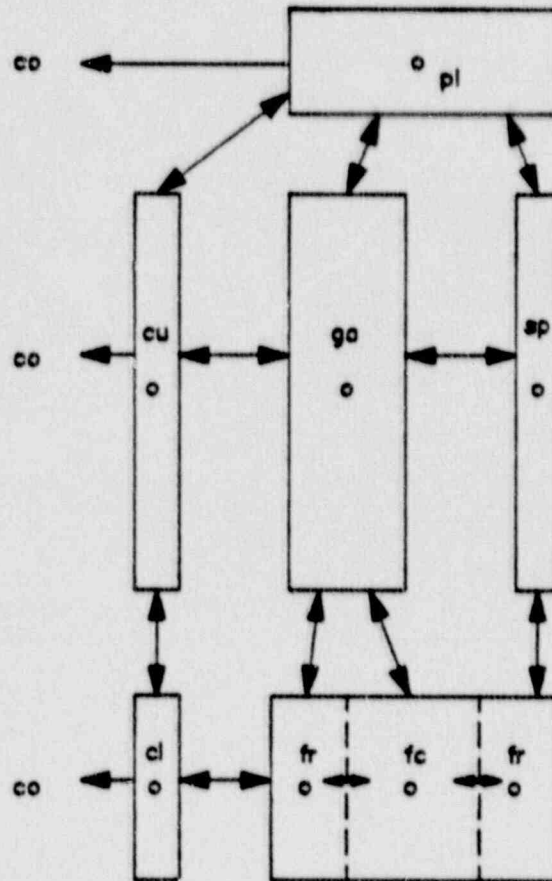


Figure 4-5 - Heat Transfer Paths for Plenum Temperature Model

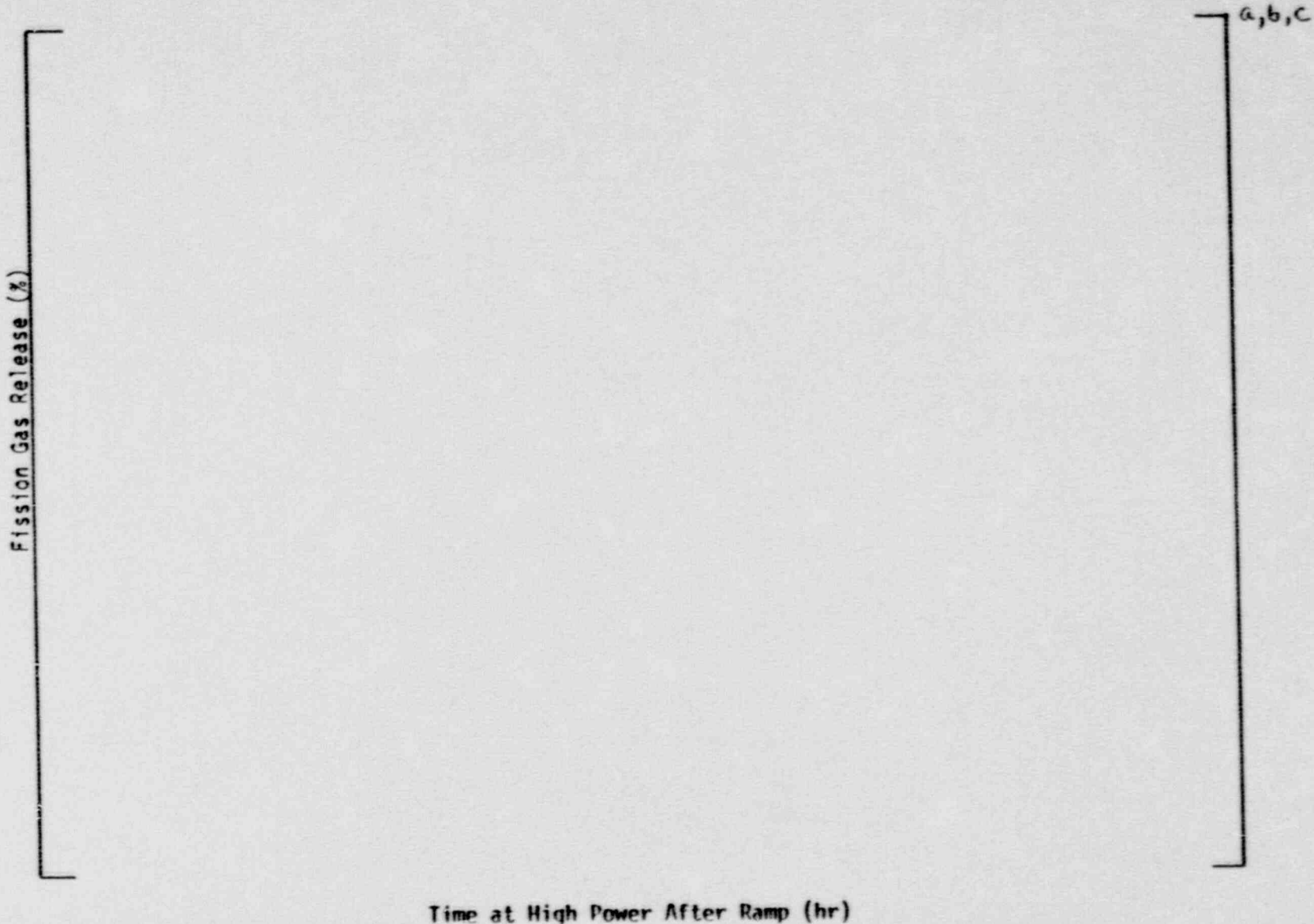


Figure 4-6 - Fission Gas Release vs. Time at High Temperature

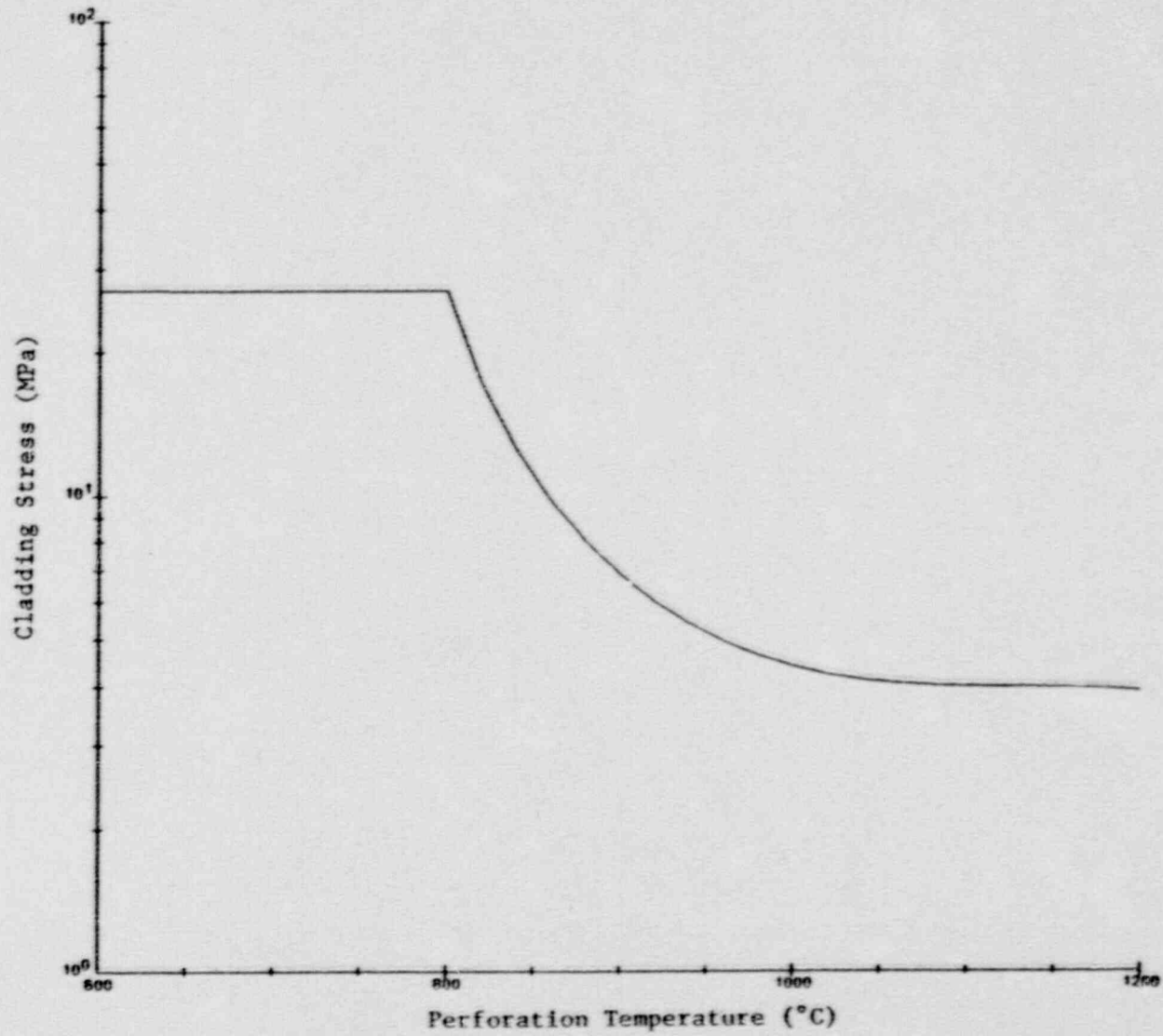


Figure 4-7 - CHACHA-3C Rod Burst Correlation



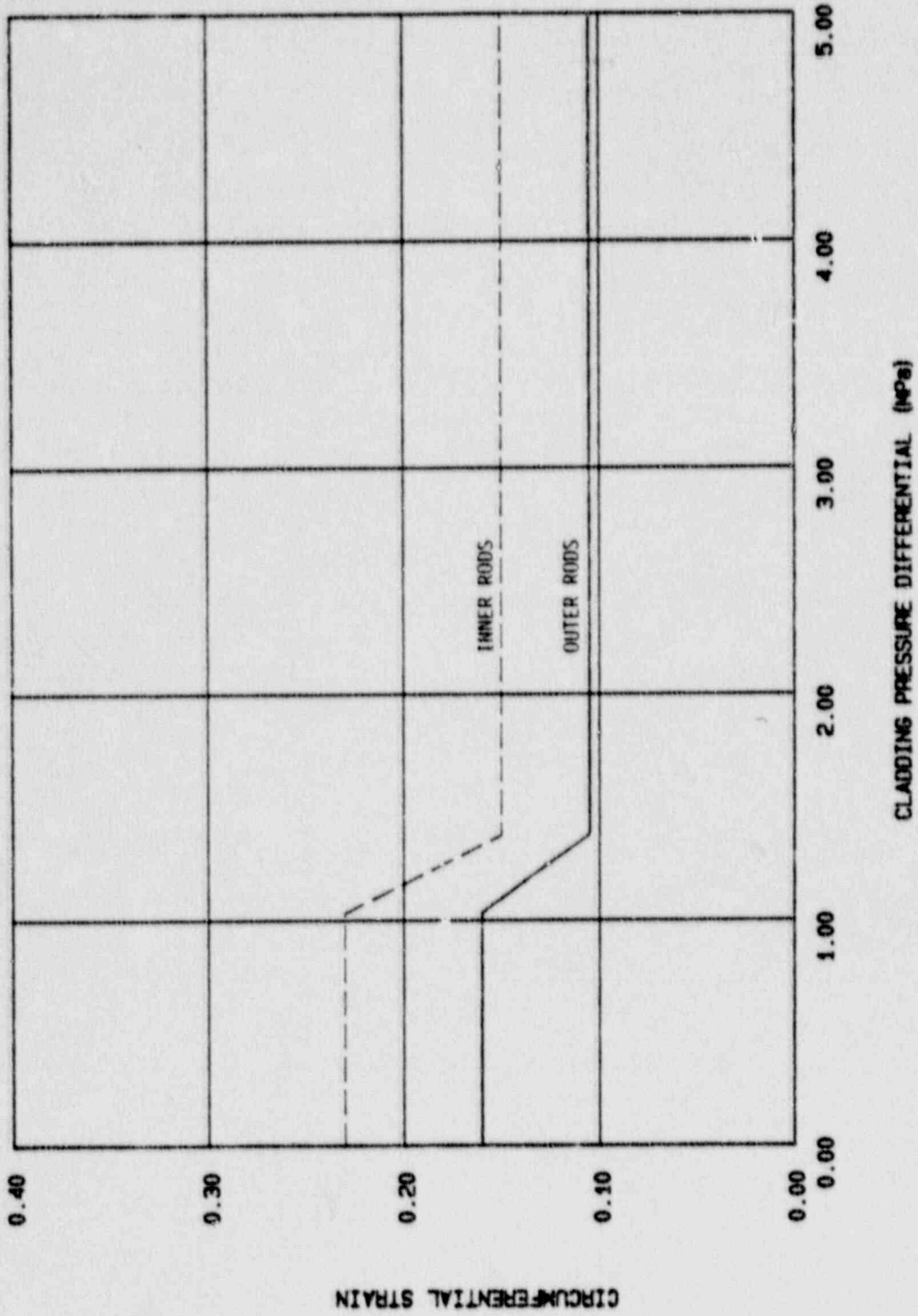


Figure 4-8 - Cladding Strain After Perforation (from Ref. 4-7)

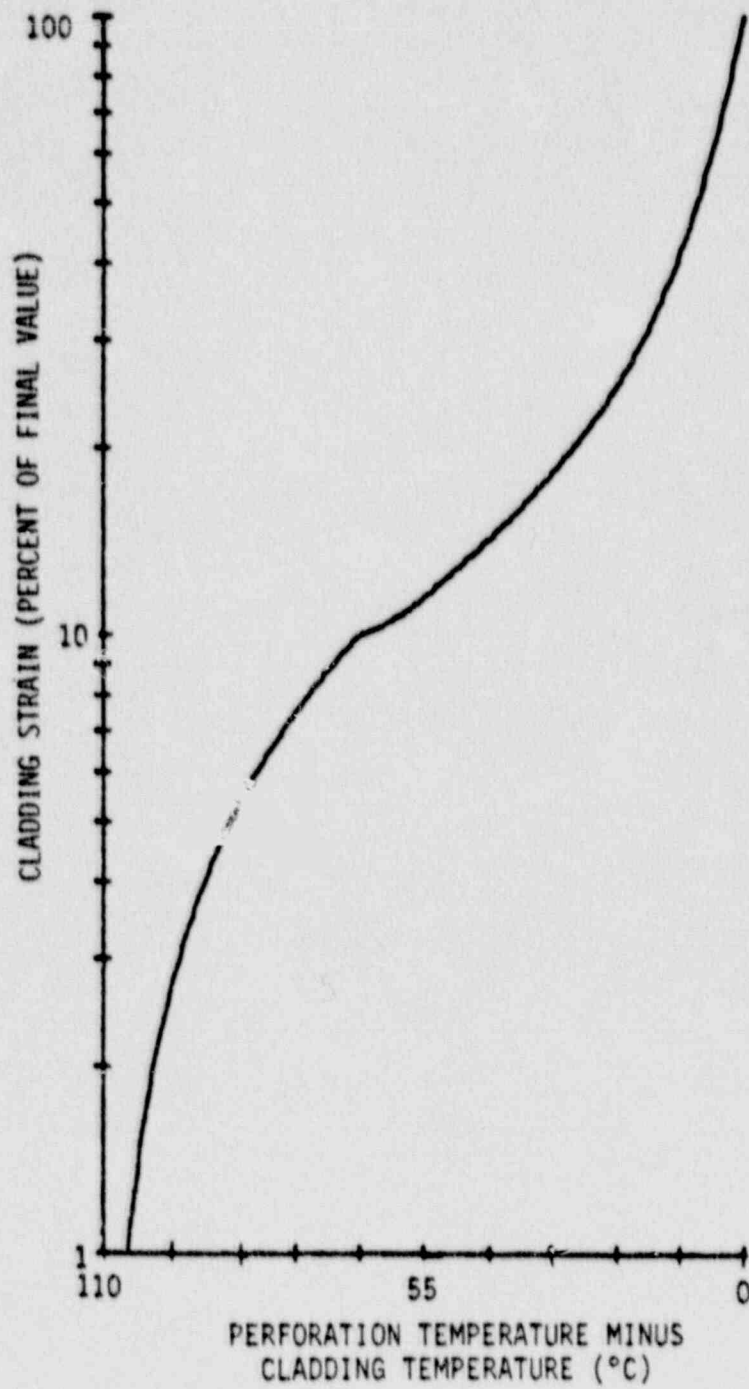


Figure 4-9 - Plastic Strain Prior to Cladding Perforation  
(from Ref. 4-7)



## 5. EVALUATION MODEL COMPLIANCE WITH 10CFR50 APPENDIX K

### 5.1 Introduction

This section is provided to show the conformance of the GOBLIN series of computer codes (GOBLIN, DRAGON, and CHACHA-3C) to the requirements for Evaluation Models specified in Title 10, Code of Federal Regulations, Part 50 (10 CFR 50) Appendix K (Ref. 5.1). For convenience, the subdivision alpha-numeric identifiers are the same as those in Appendix K. Since there are several paragraphs in Appendix K which do not apply to boiling water reactors, in some cases the numbering scheme is non-sequential.

Each applicable Appendix K paragraph is typed verbatim, enclosed in quotation marks, and is followed by a discussion of how the GOBLIN codes conform to the requirement.

In part 2 of Appendix K, Evaluation Model documentation requirements are defined. Sections 1 through 4 of this report comply with the documentation requirement by describing the technical details of the Evaluation Model. Section 6 of this report presents results of Evaluation Model comparisons with test data as required in part 2.4 of Appendix K. An additional topical report will be submitted in June of 1987. This report will contain results of the Evaluation Model sensitivity studies and document the Westinghouse methodology for boiling water reactor LOCA ECC system analysis.

### 5.2 Specific Compliance with Appendix K Requirements

#### 5.2.1 Appendix K Section I.A Sources of Heat During the LOCA

##### I. Required and Acceptable Features of the Evaluation Models

###### A. Sources of Heat During the LOCA.

"For the heat sources listed in paragraphs 1 to 4 below it shall be assumed that the reactor has been operating continuously at a power level at least 1.02 times the licensed power level (to allow for such uncertainties as instrument error), with the maximum peaking factor allowed by the technical specifications. A range of power distributions that may occur over the core lifetime shall be studied and the one selected should be that which results in the most severe calculated consequences, for the spectrum of postulated breaks and single failure analyzed."

#### Westinghouse Evaluation Model Compliance with I.A.

In all LOCA calculations it is assumed that the reactor has been operating continuously at a power level 1.02 times the licensed power level.

A sensitivity study of LOCA results to different power distributions was conducted. The power distributions to be used in the LOCA calculations and their justification is provided separately in the evaluation methodology topical report (Ref. 5-4). This report will also explain the methodology used to account for uncertainties in specific plant input and in modeling assumptions.

#### 5.2.2 Appendix K Section I.A.1 The Initial Stored Energy in the Fuel

"The steady-state temperature distribution and stored energy in the fuel before the hypothetical accident shall be calculated for the burnup that yields the highest calculated cladding temperature (or, optionally, the highest calculated stored energy). To accomplish this, the thermal conductivity of the  $UO_2$  shall be evaluated as a function of burnup and temperature, taking into consideration differences in initial density, and the thermal conductance of the gap between

the  $UO_2$  and the cladding shall be evaluated as a function of the burnup, taking into consideration fuel densification and expansion, the composition and pressure of the gases within the fuel rod, the initial cold gap dimension with its tolerances, and cladding creep."

#### Westinghouse Evaluation Model Compliance with I.A.1

The thermal conductivity of the fuel pellets is calculated as described in Appendix 4.A of this report. Temperature and density effects are accounted for. Burnup effects are neglected, since burnup has a negligible impact on the thermal conductivity of  $UO_2$  above about 500°C.

The thermal conductance of the pellet/cladding gap is evaluated using the model described in Section 4.8. An input table is used to supply CHACHA-3C with all of the data describing the fuel rod conditions at the initiation of the postulated LOCA (e.g., gap size, gas volumes, gas composition and the number of moles of each component gas). These data are generated by the fuel rod design code PAD for a full range of linear heat rates and burnups. CHACHA-3C interpolates the appropriate information for each rod, based on the rod-wise power and burnup distributions specified in input.

Evaluations will be performed to determine the burnup which yields the highest calculated cladding temperatures (or, optionally, the highest calculated stored energy). The results of these evaluations is provided in the evaluation methodology topical report (Ref. 5-4).

### 5.2.3 Appendix K Section I.A.2 Fission Heat

"Fission heat shall be calculated using reactivity and reactor kinetics. Shutdown reactivities resulting from temperature and voids shall be given their minimum plausible values, including allowance for uncertainties for the range of power distribution shapes and peaking factors indicated to be studied above. Rod trip and insertion may be assumed if they are calculated to occur."

#### Westinghouse Evaluation Model Compliance with I.A.2.

The fission heat is calculated by a reactor point kinetics model as described in Sec. 3.7. The model includes feedback effects from voiding, Doppler broadening, moderator temperature and control rod worth. The point kinetics parameters shall be generated from the nuclear design code PHOENIX for a range of power distributions, peaking factors, and void fractions throughout the fuel life. Conservative values for these parameters, i.e., those which yield the highest fission heat generation shall be used in the GOBLIN model. Specifically:

- o The delayed neutron fraction ( $\beta$ ) will be given its highest calculated value, typically corresponding to beginning of life conditions.
- o The void and Doppler reactivity coefficients will be given their highest calculated value (lowest absolute value).
- o The reactivity worth of the control rods will be given a conservative (low) value.

- o The reactor scram will be assumed to occur at a conservative (late) time in the LOCA transient.

The methodology and sensitivity studies demonstrating the conservatism of the fission heat generation is provided in the topical report WCAP-11427 (Ref. 5-4).

The average fission and decay heat generation curve calculated by the GOBLIN code is used with appropriate peaking factors in the DRAGON hot channel analysis and CHACHA-3C peak axial plane heat-up analysis.

#### 5.2.4 Appendix K Section I.A.3 Decay of Actinides

"The heat from the radioactive decay of actinides including neptunium and plutonium generated during operation, as well as isotopes of uranium, shall be calculated in accordance with fuel cycle calculations and known radioactive properties. The actinide decay heat chosen shall be that appropriate for the time in the fuel cycle that yields the highest calculated fuel temperature during the LOCA."

#### Westinghouse Evaluation Model Compliance with I.A.3.

The heavy-element (i.e., actinides) decay-energy release contribution is determined by calculating the equilibrium concentrations of the isotopes  $U^{239}$  and  $Np^{239}$ , and then using the energy per disintegration and half-life for these isotopes to evaluate the time dependence of the energy release after shutdown. While the fission product decay energy release determines the energy release of a localized point due to the fissions that have occurred at that point the heavy-element calculation relates the  $U^{238}$  absorptions



The elements  $U^{239}$  and  $Np^{239}$  are the only significant activation products that contribute to the decay energy release in the time range of interest for LOCAs. The energy release from the activation products of  $U^{235}$  (namely,  $U^{236}$  and  $U^{237}$ ) are insignificant, approximately a factor of 20-30 less, when compared to the energy release of  $U^{239}$  and  $Np^{239}$  for this time range.

The actinide decay power is determined from the decay rate equations as described in the American Nuclear Society standard 5.1 (Ref. 5-2) and is modeled in GOBLIN as the decay power groups 12, 13, and 14 (see Sec. 3.7.1).

The  $U^{239}$  production per fission,  $C_r \sigma_{25} / \sigma_{f25}$ , is chosen to yield the highest actinide decay power throughout the fuel life, typically end of life.

#### 5.2.5 Appendix K Section I.A.4 Fission Product Decay

"The heat generation rates from radioactive decay of fission products shall be assumed to be equal to 1.2 times the values for infinite operating time in the ANS Standard (Proposed American Nuclear Society Standard - "Decay Energy Release Rates Following Shutdown of Uranium-Fueled Thermal Reactors", Approved by Subcommittee ANS-5, ANS Standards Committee, October 1971). The fraction of the locally generated gamma energy that is deposited in the fuel (including the cladding) may be different from 1.0; the value used shall be justified by a suitable calculation."

#### Westinghouse Evaluation Model Compliance with I.A.4.

Decay of  $U^{235}$  fission products is computed by a relationship in the form of the summation of eleven decay equations. The fission product decay model is described in Section 3.7.1. Comparison with the tabulated 1971 ANS proposed standard (Ref. 5.1) is shown in Table 3-3. The agreement is excellent. The local decay heat power calculated by this model is multiplied by 1.2 in accordance with the requirement in paragraph I.A.4. The fraction of gamma energy deposited in the fuel along with gamma and neutron and gamma deposition in the coolant may be specified with time through the transient. The actual deposition fractions is described and justified in the topical report WCAP-11427 (Ref. 5-4).

#### 5.2.5 Appendix K Section I.A.5 Metal-Water Reaction Rate

"The rate of energy release, hydrogen generation, and cladding oxidation from the metal-water reaction shall be calculated using the Baker-Just equation (Baker, L., Just, L.C., "Studies of Metal Water Reactions at High Temperatures, III. Experimental and Theoretical Studies of the Zirconium-Water Reaction," ANL-6548, Page 7, May 1962). The reaction shall be assumed not to be steam limited. For rods whose cladding is calculated to rupture during the LOCA, the inside of the cladding shall also be assumed to react after rupture. The calculation of the reaction rate on the inside of the cladding shall also follow the Baker-Just equation, starting at the time when the cladding is calculated to rupture, and extending around the cladding inner circumference and axially no less than 1.5 inches each way from the location of the rupture, with the reaction assumed not to be steam limited."

#### Westinghouse Evaluation Model Compliance with I.A.5

The requirement to account for the effects of local metal water reaction as described in Section I.A.5 is met. This additional heat source is considered in the cladding temperature calculation as described in Section 3.7.2 for GOBLIN/DRAGON and Section 4.4 for CHACHA-3C. In these models the reaction rate between Zircaloy cladding and steam is assumed to follow the parabolic rate law of Baker and Just as specified by the criterion.

#### 5.2.7 Appendix K Section I.A.6 Reactor Internals Heat Transfer

Heat Transfer from piping, vessel walls, and non-fuel internal hardware shall be taken into account.

#### Westinghouse Evaluation Model Compliance with I.A.6

Heat transfer from piping, vessel walls, and non-fuel internal hardware are accounted for, according to the methods described in Sec. 3.5 and 3.6.

#### 5.2.8 Appendix K Section I.B Swelling and Rupture of the Cladding and Fuel Rod Thermal Parameters

"Each evaluation model shall include a provision for predicting cladding swelling and rupture from consideration of the axial temperature distribution of the cladding and from the difference in pressure between the inside and outside of the cladding, both as functions of time. To be acceptable the swelling and rupture calculations shall be based on applicable data in such a way that the degree of swelling and incidence of rupture are not underestimated. The degree of swelling and rupture shall be taken into account in calculations of gap conductance, cladding oxidation and embrittlement, and hydrogen generation.

The calculations of fuel and cladding temperatures as a function of time shall use values for gap conductance and other thermal parameters as functions of temperature and other applicable time-dependent variables. The gap conductance shall be varied in accordance with changes in gap dimensions and other applicable variables."

#### Westinghouse Evaluation Model Compliance with Section I.B

CHACHA-3C is in compliance with this requirement. As discussed in qualification Sec. 6.1.10, comparisons with applicable data and other correlations used in the industry have shown that the CHACHA-3C rod burst correlation is conservative. The evaluation of swelling and final cladding strain is consistent with the established industry methodology, which was developed based on experimental data. The effect of cladding strain on the zircaloy/water reaction rate is accounted for, as required.

The method used to evaluate gap conductance throughout the transient is described in Sec. 4.8. The gap size used to evaluate gap conductance and the temperature-dependent material properties are updated at each time step in the calculation of the fuel rod temperature transients.

#### 5.2.9 Appendix K Section I.C.1.a Break Spectrum Analysis

"In analyses of hypothetical loss-of-coolant accidents, a spectrum of possible pipe breaks shall be considered. This spectrum shall include instantaneous double-ended breaks ranging in cross-sectional area up to and including that of the largest pipe in the primary coolant system. The analysis shall also include the effects of longitudinal splits in the largest pipes, with the split area equal to the cross-sectional area of the pipe."

coolant system. The analysis shall also include the effects of longitudinal splits in the largest pipes, with the split area equal to the cross-sectional area of the pipe."

#### Westinghouse Evaluation Model Compliance with I.C.1.a

The LOCA sensitivity study topical report (Ref. 5-4) reports the results of a break spectrum analysis including the double ended guillotine break of the largest pipe in a typical boiling water reactor design for which this model is employed. The study will also include various break locations and will be used to justify the selection of the worst case in a plant specific LOCA analysis.

#### 5.2.10 Appendix K Section I.C.1.b Discharge Model

"For all times after the discharging fluid has been calculated to be two-phase in composition, the discharge rate shall be calculated by use of the Moody model (F. J. Moody, "Maximum Flow Rate of a Single Component, Two-Phase Mixture," Journal of Heat Transfer, Trans American Society of Mechanical Engineers, 87, No. 1, February 1965). The calculation shall be conducted with at least three values of a discharge coefficient applied to the postulated break area, these values spanning the range from 0.6 to 1.0. If the results indicate that the maximum clad temperature for the hypothetical accident is to be found at an even lower value of the discharge coefficient, the range of discharge coefficients shall be extended until the maximum clad temperature calculated by this variation has been achieved."

Westinghouse Evaluation Model Compliance with I.C.1.b.

The Moody model is used to calculate the two-phase discharge rate. The application and integration of the Moody model into the complete break flow model for all regimes is described in Sec. 3.3.6.

The results of a study showing PCT sensitivity to break area is presented in the Evaluation Model sensitivity study topical report (Ref. 5-4). The sensitivity study results will be used to justify the worst case break flow area and discharge coefficients used in plant specific evaluation model LOCA analyses.

5.2.11 Appendix K Section I.C.1.d Noding Near the Break and the ECCS Injection Points

"The noding in the vicinity of and including the broken or split sections of pipe and the points of ECCS injection shall be chosen to permit a reliable analysis of the thermodynamic history of these regions during blowdown."

Westinghouse Evaluation Model Compliance with I.C.1.d

The topical report WCAP-11427 (Ref. 5-4) shows the LOCA peak clad temperature sensitivity to noding near the break. These results will demonstrate that the break noding used in the Evaluation Model is sufficient to adequately represent the thermal hydraulic behavior and reactor vessel geometry in the vicinity of the break.

#### 5.2.12 Appendix K Section I.C.2 Frictional Pressure Drops

"The frictional losses in pipes and other components including the reactor core shall be calculated using models that include realistic variation of friction factor with Reynolds number, and realistic two-phase friction multipliers that have been adequately verified by comparison with experimental data, or models, that prove at least equally conservative with respect to maximum clad temperature calculated during the hypothetical accident. The modified Baroczy correlation (Baroczy, C.J., "A Systematic Correlation for Two-Phase Pressure Drop," Chem. 1965) or a combination of the Thom correlation (Thom, J.R.S., "Prediction of Pressure Drop During Forced Circulation Boiling of Water." Int. J. of Heat and Mass Transfer, 7,709-724, 1964) for pressure equal to or greater than 250 psia and the Martinelli-Nelson correlation (Martinelli, R.C. and Nelson, D.B., "Prediction of Pressure Drop During Forced Circulation Boiling of Water, Transaction of ASME, 695-702, 1948) for pressures lower than 250 psia is acceptable as a basis for calculating realistic two-phase friction multipliers."

#### Westinghouse Evaluation Model Compliance with I.C.2

The frictional losses are calculated using models that include a realistic variation of the friction factor with Reynolds number and realistic two-phase friction multipliers that are based on acceptable open literature correlations and test data (Sec. 3.3.3).

#### 5.2.13 Appendix K Section I.C.3 Momentum Equation

"The following effects shall be taken into account in the conservation of momentum equation: (1) temporal change of momentum, (2) momentum convection, (3) area change momentum flux, (4) momentum change due to compressibility, (5) pressure loss resulting from wall friction, (6) pressure loss resulting from area change, and (7) gravitational acceleration. Any omission of one or more of these terms under stated circumstances shall be justified by comparative analyses or by experimental data."

#### Westinghouse Evaluation Model Compliance with I.C.3

The momentum equation used in the GOBLIN and DRAGON codes includes all of the terms specified above (see Sec. 3.1.3).

#### 5.2.14 Appendix K Section I.C.4 Critical Heat Flux

- a. "Correlations developed from appropriate steady-state and transient-state experimental data are acceptable for use in predicting the critical heat flux (CHF) during LOCA transients. The computer programs in which these correlations are used shall contain suitable checks to ensure that the physical parameters are within the range of parameters specified for use of the correlations by their respective authors.
- b. Steady-state CHF correlations acceptable for use in LOCA transients include, but are not limited to, the following:



- (1) L.S. Tong, "Prediction of Departure from Nucleate Boiling for an Axially Non-uniform Heat Flux Distribution,": Journal of Nuclear Energy, Vol. 21, 241-248, 1967.
  - (2) J.S. Gellerstedt, R.A. Lee, W.J. Oberjohn, R.H. Wilson, and L.J. Stanek, "Correlation of Critical Heat Flux in a Bundle Cooled by Pressurized Water," Two-Phase Flow and Heat Transfer in Rod Bundles, ASME, New York, 1969.
  - (3) J.M. Healzer, J.E. Hench, E. Janssen, and S. Levy, Design Basis for Critical Heat Flux Condition in Boiling Water Reactors, APED-5186, GE Company Private Report, July 1966.
  - (4) R.V. Macbeth, "An Appraisal of Forced Convection Burnout Data," Proceedings of the Institute of Mechanical Engineers, 1965-1966.
  - (5) P.G. Barnett, A Correlation of Burnout Data for Uniformly Heated Annuli and Its Uses for Predicting Burnout in Uniformly Heated Rod Bundles, AEEW-R 463, 1966.
  - (6) E.D. Hughes, A Correlation of Rod Bundle Critical Heat Flux for Water in the Pressure Range 150 to 725 psia, In-1412, Idaho Nuclear Corporation, July 1970.
- c. Correlations of appropriate transient CHF data may be accepted for use in LOCA transient analyses if comparisons between the data and the correlations are provided to demonstrate that the correlations predict values of CHF which allow for uncertainty in the

experimental data throughout the range of parameters for which the correlations are to be used. Where appropriate, the comparisons shall use statistical uncertainty analysis of the data to demonstrate the conservatism of the transient correlation.

- d. Transient CHF correlations acceptable for use in LOCA transients include, but are not limited to, the following:
  - (1) B.C. Slifer and J.E. Hench, Loss-of-Coolant Accident and Emergency Core Cooling Models for General Electric Boiling Water Reactors, General Electric Company, Equation C-32, April 1971 (NEDO-10329).
- e. After CHF is first predicted at an axial fuel rod location during blowdown, the calculation shall not use nucleate boiling heat transfer correlations at that location subsequently during the blowdown even if then calculated local fluid and surface conditions would apparently justify the reestablishment of nucleate boiling. Heat transfer assumptions characteristic of return to nucleate boiling (rewetting) shall be permitted when justified by the calculated local fluid and surface conditions during the reflood portion of a LOCA."

Westinghouse Evaluation Model Compliance with I.C.4

The critical heat flux correlation currently available in GOBLIN/DRAGON is the AA-74 correlation described in Sec. 3.5. This correlation is based on experimental data taken with simulated ASEA-Atom BWR fuel bundles. The correlation is modified for low flow conditions by a pool boiling

correlation, as discussed in Sec. 3.5. This method of determining critical heat flux may be modified using experimental data recently obtained by Westinghouse for the QUAD+ fuel design. Justification for the method used to determine CHF for QUAD+ fuel will be provided in a future topical report.

5.2.15 Appendix K Section I.C.5 Post-CHF Heat Transfer Correlations

- "a. Correlations of heat transfer from the fuel cladding to the surrounding fluid in the post-CHF regimes of transition and film boiling shall be compared to applicable steady-state and transient-state data using statistical correlation and uncertainty analyses. Such comparison shall demonstrate that the correlations predict values of heat transfer coefficient equal to or less than the mean value of the applicable experimental heat transfer data throughout the range of parameters for which the correlations are to be used. The comparisons shall quantify the relation of the correlations to the statistical uncertainty of the applicable data.
  
- b. The Groeneveld flow film boiling correlation (equation 5.7 of D.C. Groeneveld, "An Investigation of Heat Transfer in the Liquid Deficient Regime, "AECL-3281, revised December (1969), the Dougall-Rohsenow flow film boiling correlation (R.S. Dougall and W.M. Rohsenow, "Film Boiling on the Inside of Vertical Tubes with Upward Flow of the Fluid at Low Qualities, "MIT Report Number 9079-26, Cambridge, Massachusetts, September 1963), and the Westinghouse correlation of steady-state transition boiling ("Proprietary Redirect/Rebuttal Testimony of Westinghouse Electric Corporation, "U.S.A.E.C. Docket RM-50-1, page 25.1, October 26, 1972)

are acceptable for use in the post-CHF boiling regimes. In addition the transition boiling correlation of McDonough, Milich, and King (J.B. McDonough, W. Milich, E.C. King, "Partial Film Boiling with Water at 2000 psig in a Round Vertical Tube" MSA Research Corp., Technical Report 62 (NP-6976), (1958) is suitable for use between nucleate and film boiling. Use of all of these correlations shall be restricted as follows:

- (1) The Groeneveld correlation shall not be used in the region near its low-pressure singularity,
- (2) the first term (nucleate) of the Westinghouse correlation and the entire McDonough, Milich, and King correlation shall not be used during the blowdown after the temperature difference between the clad and the saturated fluid first exceeds 300°F,
- (3) transition boiling heat transfer shall not be reapplied for the remainder of the LOCA blowdown, even if the clad superheat returns below 300°F, except for the reflood portion of the LOCA when justified by the calculated local fluid and surface conditions."

#### Westinghouse Evaluation Model Compliance with I.C.5

The convective heat transfer correlations and regimes modeled in GOBLIN are described in detail in Sec. 3.6. The post critical heat flux (dryout) convective heat transfer coefficient is calculated using the Groeneveld 5.7 correlation, NRC approved Westinghouse UHI correlation, modified Bromley correlation, and single-phase steam correlations.

The Groeneveld correlation is used for flow film boiling in the higher pressure range. For lower pressures, where the Groeneveld correlation has a singularity, a transition is made to the Westinghouse UHI correlation. This NRC approved correlation is more conservative than the Doughall-Rohsenow correlation, which is nonconservative when compared against some heat transfer data.

The lower limit to the heat transfer coefficient is calculated using the modified Bromley correlation, which is based on zero flow. The modified Bromley correlation has been demonstrated to be a conservative lower limit when compared against a wide range of tests. A more detailed discussion of the applicability of these correlation is given in the qualification section (see 6.1.7).

Once dryout is calculated to occur, the heat transfer is conservatively forced to remain in the post-dryout regime, even if rewet and transition boiling is calculated to occur.

#### 5.2.16 Appendix K Section I.C.6 Pump Modeling

"The characteristics of rotating primary system pumps (axial flow, turbine, or centrifugal) shall be derived from a dynamic model that includes momentum transfer between the fluid and the rotating member, with variable pump speed as a function of time. The pump model resistance used for analysis should be justified. The pump model for the two-phase region shall be verified by applicable two-phase pump performance data. For BWR's after saturation is calculated at the pump suction, the pump head may be assumed to vary linearly with quality, going to zero for one percent quality at the pump

suction, so long as the analysis shows that core flow stops before the quality at the pump suction reaches one percent."

#### Westinghouse Evaluation Model Compliance with I.C.6

The recirculation pump model is described in Sec. 3.4.1. An angular momentum balance is solved for the pump including all contributing torques. Single-phase and degraded two-phase pump performance are modeled through user specified performance curves. The justification of specific pump resistances, single-phase, and two-phase performance curves shall be addressed in a future topical report.

The two-phase performance degradation to zero pump head once the pump suction has a quality of one, can be specified by the user through the two-phase performance curves. However, it is expected that for the jet pump BWRs the pump performance will degrade to zero before saturation conditions reach the pump suction, due to the draining of the downcomer and uncovering of the jet pump suction. The degradation of pump performance will be addressed on a plant-specific basis.

"(Appendix K Section I.C.7 - Not applicable to BWR)"

#### 5.2.17 Appendix K Section I.D.1 Single Failure Criterion

"An analysis of possible failure models of ECCS equipment and of their effects on ECCS performance must be made. In carrying out the accident evaluation the combination of ECCS subsystems assumed to be operative shall be those available after the most damaging single failure of ECCS equipment has taken place."

### Westinghouse Evaluation Model Compliance with I.D.1

The evaluation of the loss-of-coolant accident is performed assuming the single active component failure that results in the most severe consequences. The combination of ECC subsystems assumed to be operating are those remaining after the component failure has occurred.

The topical report WCAP-11427 (Ref. 5-4) includes results showing LOCA peak clad temperature sensitivity to various single failure assumptions. Previous evaluations by the NSSS vendor identifying the worst single failure in the ECC systems will also be reviewed to determine the limiting component failure assumed in a plant specific LOCA analysis.

### 5.2.18 Appendix K Section I.D.2 Containment Pressure

"The containment pressure used for evaluating cooling effectiveness during reflood and spray cooling shall not exceed a pressure calculated conservatively for this purpose. The calculation shall include the effects of operation of all installed pressure-reducing systems and processes."

### Westinghouse Evaluation Model Compliance with I.D.2

The containment pressure used for determining the cooling effectiveness and flow rates of the ECC system during reflood and spray cooling is assumed to be 1 bar (approximately 1 atmosphere). This is a conservative assumption since, as was shown in Ref. 5-3, the effect of increased pressure will improve the heat transfer during both the flooding and spray cooling process. Also the

increased containment pressure realistically expected will increase ECC pump flows for a given value of reactor pressure (improving spray cooling and mass inventory recovery).

"(Appendix K Sections I.D.3 through I.D.5 - Not applicable to BWR)"

5.2.19 Appendix K Section I.D.6 Convective Heat Transfer Coefficients for BWR Fuel Rods Under Spray Cooling

"Following the blowdown period, convective heat transfer shall be calculated using coefficients based on appropriate experimental data. For reactors with jet pumps and having fuel rods in a 7x7 fuel assembly array, the following convective coefficients are acceptable:

- (a) During the period following lower plenum flashing but prior to the core spray reaching rated flow, a convective heat transfer coefficient of zero shall be applied to all fuel rods.
- (b) During the period after core spray reaches rated flow but prior to reflooding, convective heat transfer coefficients of 3.0, 3.5, 1.5, and 1.5  $\text{Btu}\cdot\text{hr}^{-1}\cdot\text{ft}^{-2}\cdot\text{°F}^{-1}$  shall be applied to the fuel rods in the outer corners outer row, next to outer row, and to those remaining in the interior, respectively, of the assembly.
- (c) After the two-phase reflooding fluid reaches the level under consideration, a convective heat transfer coefficient of 25  $\text{Btu}\cdot\text{hr}^{-1}\cdot\text{ft}^{-2}\cdot\text{°F}^{-1}$  shall be applied to all fuel rods."



### Westinghouse Evaluation Model Compliance with I.D.6.

The rod surface heat transfer coefficients used by CHACHA-3C for the period prior to the end of lower plenum flashing are those calculated by DRAGON using the models described in Sec. 3.5. After this period, the DRAGON values are replaced as follows:

- (1) To comply with the requirement that the convective heat transfer coefficient be zero following lower plenum flashing, the convective heat transfer coefficient will be set to zero whenever the heat transfer coefficient based on the GOBLIN/DRAGON heat transfer package described in Sec. 3.5, shows a marked degradation in heat transfer as a consequence of high voiding and reduced flow rates at the axial plane of interest.
- (2) For the period after core spray reaches rated flow but prior to reflooding, the spray cooling convective heat transfer coefficients in Table 4.3 will be used. These heat transfer coefficients are derived from the Appendix K recommended values. Experimental data will be used to verify their applicability (Sec. 6.1.12). The time needed for the ECC system to reach the rated spray flow rate is calculated in GOBLIN/DRAGON.
- (3) For the period after the two-phase reflooding fluid reaches the core elevation of interest, the reflood heat transfer coefficient specified in Appendix K will be used. The time of reflooding the core elevation of interest will be based on the local void fraction.

### 5.2.20 Appendix K Section I.D.7 The Boiling Water Reactor Channel Box Under Spray Cooling

"Following the blowdown period, heat transfer from, and wetting of, the channel box shall be based on appropriate

experimental data. For reactors with jet pumps and fuel rods in a 7x7 fuel assembly array, the following heat transfer coefficients and wetting time correlation are acceptable.

- (a) During the period after lower plenum flashing but prior to core spray reaching rated flow, a convective coefficient of zero shall be applied to the fuel assembly channel box.
- (b) During the period after core spray reaches rated flow, but prior to wetting of the channel, a convective heat transfer coefficient of  $5 \text{ Btu-hr}^{-1}\text{-ft}^{-2}\text{-}^\circ\text{F}^{-1}$  shall be applied to both sides of the channel box.
- (c) Wetting of the channel box shall be assumed to occur 60 seconds after the time determined using the correlation based on the Yamanouchi analysis (Loss-of-Coolant Accident) and Emergency Core Cooling Models for General Electric Boiling Water Reactors, General Electric Company Report NEDO-10329, April 1971).

Westinghouse Evaluation Model Compliance with I.D.7

Calculation of the channel wall temperature is described in Section 4.2. The following channel wall heat transfer coefficients and rewet model are used:

- (1) For the period prior to the end of lower plenum flashing, the convective heat transfer coefficients calculated by DRAGON will be used (Sec. 3.5).
- (2) For the period after lower plenum flashing but prior to core spray reaching rated flow, the channel convective heat transfer coefficient will be set to zero.

- (2) For the period after lower plenum flashing but prior to core spray reaching rated flow, the channel convective heat transfer coefficient will be set to zero.
- (3) For the period after core spray reaches rated flow but prior to wetting of the channel, the convective heat transfer coefficient in Table 4-3 will be applied to both sides of the channel. This heat transfer coefficient is derived from the Appendix K recommended value. Experimental data will be used to verify its applicability (Sec. 6.1.12).
- (4) The channel wetting time will be determined based on the modified Yamarouchi correlation plus 60 seconds, as described in Sec. 4.7.

### 5.3 References

- 5-1 Code of Federal Regulations, 10 Part 50, Office of the Federal Register, National Archives and Records Administration, 1986.
- 5-2 Proposed American Nuclear Society Standard 5.1 "Decay Energy Release Rates Following Shutdown of Uranium-Fueled Thermal Reactors," Oct. 1971, Revised Oct. 1973.
- 5-3 "BWR standby cooling heat transfer performance under simulated loss-of-coolant conditions between 15 and 300 psia," GEAP-13190, May 1972.
- 5-4 Westinghouse Boiling Water Reactor Emergency Core Cooling System Evaluation Model: Code Sensitivity, WCAP-11427 (Proprietary), June 1987.

## 6. QUALIFICATION

The GOBLIN series of codes were originally developed by ASEA-ATOM of Sweden, in the late 1970's. Over the past decade extensive qualification of the codes has been performed. Westinghouse has performed additional independent qualification of the codes which is included here. The qualification is presented in two parts: Separate effects and integral test qualification.

Separate effects qualification is presented for the following models and phenomena:

- o Drift flux model
- o Level swell
- o Countercurrent flow limitation
- o Core pressure drop
- o Jet pump model
- o Critical heat flux
- o Post-dryout heat transfer
- o Reactor power generation model
- o Rod heat conduction model
- o Rod swell and rupture
- o Surface to surface radiation

An integral qualification against the Two Loop Test Apparatus (TLTA) large break blowdown with emergency core cooling (ECC) test series (TLTA-5A, Ref. 6-1) is presented. The simulations include an average power/average ECC flow rate case (Run 6425/2) and a high power/low ECC flow rate case (Run 6423/3).

Several other integral qualifications of GOBLIN have been performed against experimental data. Specifically the code has been qualified against the TLTA-5C small break series of test (Ref. 6-2), the TLTA-4 blowdown series, (Ref. 6-3) and the FIX-II Loss of Coolant Accident Test Series (Ref. 6-4). A summary of these previous qualifications is also presented.

## 6.1 Separate Effects Qualification

### 6.1.1 Drift Flux Model

The drift flux model determines the volume fraction of vapor flow for a given total mass flow rate. The model used in GOBLIN is described in detail in Sec. 3.3.1. It was developed from and qualified against a large data base taken in the FRIGG test apparatus (Ref. 6-5). Figures 6-1 and 6-2 show two comparisons of void fraction versus steam quality for the drift flux model with data from the FRIGG loop. The conditions for these void measurement tests are shown in Table 6-1. The figures show excellent agreement between the measured and calculated void fraction for a range of qualities, flow rates, and pressures.

An independent qualification of the drift flux model performed by Westinghouse is described below.

#### Objective

This section describes an independent assessment of the GOBLIN/DRAGON drift-flux model which was performed by Westinghouse. Void fraction distributions calculated by GOBLIN/DRAGON are compared with data from two of the boil-off tests which were conducted in the Two-Loop Test Apparatus (TLTA).

#### Test Description

The boil-off tests were performed using the same TLTA-5A test facility configuration as was used to perform the integral blowdown/ECC experiments. A description of the TLTA-5A facility is contained in the integral system qualification section of this report (Sec. 6.2).

The feedwater, ECC, and recirculation systems of TLTA-5A were not used for the boil-off tests under consideration here. The tests were performed by applying constant power to the test bundle and measuring the system response under the conditions of constant pressure and no forced flow. During the tests, natural

circulation flow into the bundle was established due to the density differences between the bundle, the bypass, and the downcomer regions. Measurements taken throughout the experiments included heater rod temperatures and differential pressures from several elevations in the bundle. The tests were terminated when either the peak rod temperature reached 1000°F or the upper plenum temperature reached 800°F. Void fraction distributions throughout the tests were determined from the differential pressure measurements.

A total of five boil-off tests were performed, using different combinations of system pressure and bundle power. The test runs with the lowest and highest pressures, Runs 5 and 7, were selected for evaluation. Run 5 was performed at 195 psia with a constant bundle power of 250 kW. Run 7 was performed at 790 psia, with the same power level. Additional information on these tests and the entire boil-off test program may be found in Ref. 6-6.

#### Model Simulation

The test bundle nodalization used for these GOBLIN/DRAGON simulations is shown in Fig. 6-3. The heater rods were modeled by a single rod group. The axial power distribution used to simulate the actual chopped cosine distribution from the tests is shown in Fig. 6-4.

The boil-off tests were characterized by a slow depletion of the system liquid inventory. An examination of the void distributions reported in Ref. 6-6 showed that the bundle two-phase level movement throughout the transient was very slow, typically on the order of 0.1-0.2 inch/sec. The change in void fraction with time for elevations below the two-phase level was also very small. Therefore, it was decided that the transients could be treated as quasi-steady state, and the GOBLIN/DRAGON simulations were aimed at calculating the bundle axial void distribution at a single point in time for each experiment. The conditions chosen for the simulations correspond to 200 seconds into the transient for Run 5 and 100 seconds into the transient for Run 7.

The pressure boundary condition used in each simulation was the measured system pressure. The inlet subcooling was calculated from the non-boiling length shown in the reported (Ref. 6-6) void distributions. The inlet flow rate was determined such that the calculated two-phase level matched the measured two-phase level. The inlet flow rates determined with this method were within the uncertainty band of the reported values, which were based on a mass balance of the system. Therefore their use is judged to be appropriate.

### Discussion of Results

The axial void distribution calculated by GOBLIN/DRAGON for Run 5 (195 psia) is compared to the measured distribution in Fig. 6-5. The agreement is very good. Fig. 6-6 shows the same comparison for Run 7 (790 psia). The agreement is reasonable, but not as good as the low pressure case. However, the conditions of the Run 7 test (high pressure and very low flow) will not be experienced during a postulated LOCA. Therefore, the agreement in Fig. 6-6 is judged to be acceptable.

Based on the comparison results shown in these figures and the previous qualification results (Fig. 6-1 and 6-2), it is concluded that the drift-flux model used in GOBLIN/DRAGON is acceptable for use in BWR LOCA analyses.

## 6.1.2 Level Swell

### Objective

As the reactor vessel blows down during the initial phase of a loss of coolant accident the rapid decrease in pressure causes a sharp rise in the void fraction. This initial increase in void fraction causes the liquid regions of the vessel to swell as the mixture level increases. The objective of this separate effects qualification is to demonstrate the ability of GOBLIN to predict the level swell through the drift flux and level tracking models incorporated in GOBLIN (see Sec. 3.3.1). A comparison is made with level swell tests performed by General Electric (Ref. 6-7).

### Test Description

Tests were run by General Electric (GE) to simulate a boiling water reactor vessel steam break blowdown. The test measured the resulting pressure and level swell transient in the vessel. The tests were run in a cylindrical vessel that was approximately 14 feet in length, one foot in diameter with a volume of 10 cubic feet. Connected to the vessel was a 3 inch diameter, with a blowdown line located at an elevation of 12.89 feet. Figure 6-7 shows a schematic diagram of the vessel. Tests were conducted at saturated conditions with the vessel pressurized to approximately 1000 psia. The tests measured the decrease in pressure and initial increase in level swell after a break in the steam region of the vessel was initiated. Tests were run at varying initial water level and orifice size.

### Simulation Model

A GOBLIN model was set up to simulate a 14 foot high cylindrical vessel with a one foot diameter. The model consisted of 8 control volumes in the vessel and 2 control volumes in the blowdown line. The blowdown line was simulated as approximately 25 feet in length and 3 inch in diameter. The Moody break flow model was used to calculate the two-phase break flow. Critical flow was checked at both the orifice and blowdown pipe exits. The initial fluid



conditions of pressure, enthalpy, and mass were specified. The tests were initiated and allowed to reach steady-state conditions before the break was initiated in the steam region of the vessel at 5 seconds.

### Discussion of Results

Two of the GE tests were simulated using the GOBLIN model. Test number 1 had an orifice size of 1/2 inch and an initial water level of 9.59 feet. Test number 2 used the same model with an initial level of 11.77 feet and an orifice size of 3/8 inch. Figure 6-8 shows the pressure decrease for test 1 following the break initiated at 5 seconds. The pressure decrease predicted by GOBLIN shows good agreement with the data from the GE test results (Ref. 6-7). Figure 6-9 shows the level swell predicted by GOBLIN versus the GE test data. Level was initially at 9.59 feet and swelled to the level of the break, 12.89 feet. When level reached the break, it stabilized as flow out the orifice changed from single-phase steam to two-phase flow. The flow out the break returned to single-phase steam as level began to fall. As can be seen from Fig. 6-9 the GOBLIN prediction of the initial level swell and the following level decrease agrees well with that which is shown by the GE test data.

As can be seen in Fig. 6-10 the total mass depletion predicted by GOBLIN also compares well with the test number 1 results. This demonstrates the applicability of the break flow model used. Figures 6-11 and 6-12 show respectively, the pressure and level simulation for test number 2 versus the GE test data. Again both figures show good agreement with the GE test data. These two simulations confirm the level swell predictive capability of GOBLIN/DRAGON.

### 6.1.3 Countercurrent Flow Limitation

#### Objective

During a loss of coolant accident the bundle and lower plenum regions of the vessel experience a condition where the steam generated is moving in the opposite direction of the water and thus limits the amount of water that enters the bundle and lower plenum regions. This phenomena is known as countercurrent flow limitation (CCFL). The objective of this separate effects qualification is to compare the comprehensive countercurrent flow limitation correlation used in GOBLIN with specific CCFL correlations developed by K. H. Sun (Ref. 6-8) and General Electric (Ref. 6-9).

#### Correlation Description

The basis countercurrent flow formulation as described by Wallis (Ref. 6-10) can be expressed as:

$$j_g^* + M j_f^* = C \quad (6.1-1)$$

where  $j_g^* = j_g \rho_g^{1/2} [gD(\rho_f - \rho_g)]^{-1/2}$  (6.1-2)

$$j_f^* = j_f \rho_f^{1/2} [gD(\rho_f - \rho_g)]^{-1/2} \quad (6.1-3)$$

The coefficients M and C vary and may depend on the geometry in question. These coefficients have been correlated by Sun (Ref. 6-8) for the upper tie plate and side entry orifice regions, and have been used in TRAC-BWR assessments (Ref. 6-26). Coefficients for the bypass region, have been reported by GE in Ref. 6-9. The coefficients given in Ref. 6-8, for the side entry orifice, are

$$M = 1.0$$

$$C = 2.14 - 0.008 \cdot P_w^* \quad (6.1-4)$$

where

$$P_w^* = P_w / (\sigma/g\Delta\rho)^{1/2}$$

and  $P_w$  is the wetted perimeter and  $\sigma$  is the surface tension.

The coefficients given for the upper tie plate were  $C = 1.0$  and  $M = 4.2$ . For the bypass region Ref. 6-9 recommends a coefficient of  $M = 1.0$ , while the value for  $C$  was expressed as:

$$C = 0.47 \text{ ft}^{1/4} [\sigma/g (\rho_f - \rho_g)]^{-1/8} \quad (6.1-5)$$

For this qualification these coefficients were used in Eq. (6.1-1) and values of  $j_f^*$  and  $j_g^*$  over a range of pressures were calculated for each geometry. The values for  $j_g^*$  and  $j_f^*$  were then plotted and compared to the values of  $j_g^*$  and  $j_f^*$  from the CCFL correlation used in GOBLIN/DRAGON.

The CCFL correlation in GOBLIN/DRAGON uses the same basic equation as that described by Wallis (Eq. (6.1-1)). The coefficients  $C$  and  $M$  used are not only dependent on geometry but dependent on void fraction as well. The coefficients are described in Sec. 3.3.1, where

$$C = Ku^{1/2} \text{ and } M = K_1.$$

The correlations for the side entry, bypass, and upper tie plate geometries were compared with the comprehensive GOBLIN/DRAGON correlation for a range of void fractions between 0 and 1.0 and pressures between 14.7 and 1000 psia.

## Discussion of Results

In general, the CCFL correlation in GOBLIN/DRAGON compared well with the correlations by the Sun and GE (see Fig. 6-13, 6-14, and 6-15). Particularly noteworthy were the results from the upper tie plate comparison (Fig. 6-13) which showed the GOBLIN/DRAGON prediction of CCFL is more conservative (more restrictive) than the Sun calculation of CCFL for all ranges of void fractions and pressures. For the bypass region it was determined that the GOBLIN/DRAGON calculation of CCFL is more conservative than GE in the region of low void fraction. With increasing void fraction the GOBLIN/DRAGON curve approaches the GE curve and in a few cases exceeds it. However, only low voiding is expected in the bypass region during CCFL situations. In the case of the side entry orifice it is conservative to have a less restrictive liquid flow. At higher pressures the GOBLIN calculation of CCFL was less restrictive than that predicted by the Sun. At lower void fractions and high values of  $j_f^*$ , the GOBLIN/DRAGON curve becomes more restrictive than the Sun curve. A possible reason for this is that the data base used to develop Sun's coefficients was based only on relatively low values of  $j_f^*$ . Thus the coefficients developed by Sun may not be applicable for the complete range of the comparison.

In summary, the comprehensive CCFL correlation in GOBLIN/DRAGON compares well with the referenced correlations developed for specific geometries, hence it is expected to predict other geometries well.

Any potential impact on CCFL due to the Westinghouse QUAD+ fuel design is addressed in the response to NRC request for additional information.

#### 6.1.4 Fuel Bundle Pressure Drop

The fuel bundle pressure drop correlations in GOBLIN/DRAGON are described in Sec. 3.3.3 and 3.3.4 of this report. These correlations are based on full-scale rod bundle pressure drop measurements taken by ASEA-ATOM. Westinghouse has recently taken single-phase and two-phase pressure drop measurements for the QUAD+ fuel design. These new data will be used to verify that the current correlations are applicable to QUAD+ fuel, or to modify the correlations if necessary. Any modifications would be completed and documented prior to plant-specific applications of the Westinghouse Evaluation Model.

### 6.1.5 Jet Pump

#### Objective

The objective of this study is to verify the accuracy of the GOBLIN/DRAGON jet pump model predictive capability against the Idaho National Engineer Laboratory 1/6th-scale jet pump tests (Ref. 6-11 and 6-12). The accuracy of the jet pump model determines the ability of the GOBLIN code to correctly represent core flow rates during on and off-normal operating conditions. The jet pump model is described in detail in Sec. 3.4.2.

#### Test Description

The jet pump tests were performed at the LOFT Test Support Facility (LTSF) by attaching a 1/6th scale stainless steel jet pump supplied by General Electric. The scaling basis for the jet pump was a BWR/4 jet pump of the 218 inch vessel size, Browns Ferry class. Reference 6-12 contains a detailed description of the test facility, flow control valve configurations and jet pump dimensions. Data, for the various flow regimes, (see Fig. 6-17) were obtained by manually adjusting flow through the various flow control valves. One flow control valve for each of the primary jet pump regions was adjusted (discharge region, drive region and suction region) to obtain the desired range of flows. The drive, suction, and discharge flow rates and fluid conditions were measured and the results presented in the form of M-N ratios where,

M = suction flow/drive flow

N =  $(H_{dg} - H_{su}) / (H_{dr} - H_{dg})$

H = Total Head =  $[z + (p/\rho g_o \times 10^{-6}) + u^2/2g_o]$

p = static pressure (MPa)

$\rho$  = density ( $\text{kg/m}^3$ )

$g_0$  = acceleration due to gravity =  $9.80665 \text{ m/s}^2$

$u$  = fluid velocity (m/s)

$z$  = elevation

and the subscripts, dg, su, and dr are discharge, suction, and drive, respectively.

### Simulation Model

The test simulation was performed with a simplified GOBLIN/DRAGON nodalization scheme. This model consisted of six control volumes, three primary volumes made up of the jet pump throat, diffuser, tail section and three boundary volumes representing the jet pump drive, discharge and suction regions. Figure 6-16 presents the GOBLIN nodalization used for this test simulation.

The qualification runs were performed by providing the GOBLIN model with the appropriate test conditions (from Ref. 6-12) for the three boundary nodes. The GOBLIN jet pump model calculations were then compared to the measured test data for the six flow regimes which are presented in Fig. 6-17. The measured test data results were obtained from Tables A4 and A5 of Ref. 6-12.

### Discussion of Results

Figure 6-17 presents the comparison between the GOBLIN predicted and the measured test data results for the six various flow regimes. The test data and GOBLIN predictions are presented in the form of M-N curves where M and N are described in the Test Description section. As can be seen from the figure, the GOBLIN model displays good agreement with the test data up to the point where  $M = -0.8$ . This is not a major concern due to the significant data scatter which was predicted to occur during the jet pump tests in this region

of interest. Section 7.1 of Ref. 6-12 does not recommend the use of this data base for positive drive flow and M less than -0.8 for the development and assessment of analytical models. It states:

The effect of potential pressure imbalance cannot be fully removed from the data base: therefore, the data for positive drive flow with M less than -0.8 is highly suspect. The remaining data base does not appear to be significantly influenced by flow or pressure measurement errors.

Therefore, the calculated jet pump performance of the GOBLIN/DRAGON code is in good agreement with test data where applicable and is adequate for application to BWR LOCA analyses.



#### 6.1.6 CHF Correlation

The critical heat flux correlation currently used in GOBLIN/DRAGON is described in Sec. 3.5 of this report. This correlation is based on experimental data taken with simulated ASEA-ATOM BWR fuel bundles. Westinghouse is currently conducting a series of critical heat flux experiments using a simulated QUAD+ mini-bundle. A new correlation specifically for the QUAD+ fuel will be developed from these data. Westinghouse will incorporate the new correlation into GOBLIN/DRAGON after it has been finalized. Justification for the method used to determine critical heat flux for QUAD+ fuel will be provided in a future topical report.

### 6.1.7 Post-Dryout Heat Transfer

#### Objective

The post-dryout heat transfer is calculated from several correlations-- Groeneveld, Westinghouse UHI, modified Bromley, convective steam cooling-- depending on the void fraction, pressure, and flow rate. The complete package is described in detail in Sec. 3.5.

Each of these correlations have been qualified against a large experimental data base of transient conditions typical of a LOCA. These correlations also have been previously approved by the NRC for LOCA analysis. A confirmation of the conservatism of this integrated post-dryout heat transfer package in GOBLIN is presented here. The calculated heat transfer is compared against experimental transient post-dryout heat transfer data.

#### Test Data Description

Three experimental data bases are used to confirm the conservatism of the GOBLIN post-dryout heat transfer. They are: the Westinghouse G-1 and G-2 tests and the FLECHT low flow reflooding tests (Ref. 6-13 through 6-16). These tests cover the range of post-dryout heat transfer conditions typical of a LOCA transient.

The G-1 test series were cocurrent downflow blowdown tests described in detail in Ref. 6-13. The range of flow conditions in the tests are:

	<u>Units</u>
$30 <  G $	$\text{lbm/ft}^2 \text{ sec}$
$100 < p < 800$	psia
$0 < X < 0.90$	-

Over 6500 data points were used in the comparison.

The G-2 test series (Ref. 6-15) were concurrent and countercurrent flow test at lower pressures than conducted in the G-1 series. A comparison was made with 103 points of the test data. The data range is

	<u>Units</u>
$0.5 <  G $	$\text{lbm/ft}^2 \text{ sec}$
$20 < p < 100$	psia
$0.0 < X < 0.32$	-

Last a comparison with FLECHT reflood tests at low flow rates was made (Ref. 6-16). The data consisted of 21 time-averaged data points for the following range of conditions:

	<u>Units</u>
$4.41 <  G  < 25.9$	$\text{lbm/ft}^2 \text{ sec}$
$20 < p < 58$	psia
$0.14 < X < 0.81$	-

### Description of Results

Figures 6-18, 6-19, and 6-20 show the ratio of the measured heat transfer coefficient to the calculated value as a function of quality. As can be seen the experimentally measured heat transfer coefficients are significantly larger than the GOBLIN calculated heat transfer coefficients (the ratio is much greater than one). This comparison includes calculated heat transfer coefficients that cover the transition between Groeneveld, Westinghouse UHI, and modified Bromley correlations as the pressure and flow rate decreased in each test.

This comparison confirms that the GOBLIN heat transfer package conservatively calculates the post-dryout heat transfer during a LOCA transient.

### 6.1.8 Reactor Power Generation Model

#### Objective

A reactor point kinetic model and 14 group decay model is used in GOBLIN/DRAGON to calculate the reactor power generation. A detailed description of the model is given in Sec. 3.7. The objective of this qualification is to demonstrate that the point kinetics model in GOBLIN/DRAGON can calculate the fission power accurately following a LOCA. A simulation was made of a recirculation pump trip start up test performed at the TVO-1 plant in Finland was made. The resultant fission power transient was compared with the calculated power from GOBLIN/DRAGON.

#### Test Description

The TVO-1 plant is a 2000 MWt boiling water reactor designed by ASEA-ATOM. The plant is an internal recirculation pump plant design as shown in Fig. 6-21. The plant has six recirculation pumps imbedded in the lower downcomer, that force flow through the reactor core. The test consisted of a trip of all six recirculation pumps from a steady state condition at 62 percent power. The core flow rate dropped rapidly from an initial core flow rate of 6310 kg/sec ( $5.0 \times 10^7$  lbm/hr) to natural circulation conditions. The pump coastdown was very rapid due to the low inertia design of the ASEA-ATOM internal recirculation pumps. This feature creates a severe power transient compared to other ASEA-ATOM and General Electric boiling water reactor designs.

The decrease in core flow rate increases reactor voiding through the negative void reactivity coefficient  $\left[ \frac{\partial \rho}{\partial V} \right]^{a,c,g}$  and consequently decreases the fission power. The increasing fuel temperature also reduces the fission power through the Doppler reactivity coefficient  $\left[ \frac{\partial \rho}{\partial T} \right]^{a,c,g}$ .

Following coastdown of the pumps the plant reached a new steady state at approximately 20 percent rated power and a natural circulation flow of 2100 kg/sec ( $1.67 \times 10^7$  lbm/hr).

### Simulation Model

The GOBLIN model used to simulate the TVO-1 plant pump trip was a standard model used previous for loss of coolant analyses. A nodalization diagram is shown in Fig. 6-22. The active core was modelled with six axial control volumes and fuel rod segments. Two fuel rod groups were modelled to reflect the two different fuel rod diameters present in the core.

An initial steady state was established at the initial plant conditions. Then, following tripping of all the recirculation pumps, the feedwater and steamline pressure were controlled to follow the test transient. Parameters such as the reactor power, water level, pump speed and head were calculated with GOBLIN.

### Discussion of Results

Figure 6-23 shows the calculated and measured reactor core flow rate throughout the transient. The calculated flow coastdown compares well with the measured flow. Figure 6-24 shows a comparison of the fission power throughout the transient. The point kinetic model calculates the drop in fission power quite well. It should be noted that in this comparison best estimates of the void and Doppler reactivity coefficients were used. In an Appendix K LOCA analysis Westinghouse intends to use the most conservative value for each reactivity coefficient throughout the life of the fuel, thus ensuring a conservatively high calculation of the fission power.

In summary, it has been demonstrated that the point kinetics model in GOBLIN/DRAGON can sufficiently and conservatively calculate the fission power transient following a LOCA.

### 6.1.9 Fuel Rod Conduction Model

#### Objective

This section describes the qualification of the fuel rod conduction model described in Sec. 4.1 of this report. Temperature transients calculated by CHACHA-3C will be compared with analytical solutions for two cases representative of nuclear fuel geometries.

#### Description of Analytical Solutions

Analytical solutions to the conduction equation exist for a limited number of simple problems. Two of these have been selected to demonstrate the accuracy of the fuel rod conduction model in the GOBLIN series of codes. Both are based on cylindrical geometry. The first case describes the temperature response to a step change in surface temperature. The second describes the temperature response to a step change in coolant temperature, with a constant convective heat transfer coefficient. In both cases the cylindrical rod is assumed to be a solid material of infinite length, with constant material properties.

Given the problem statements above, Ref. 6-17 gives the exact solutions to the temperature responses as:

CASE I: Step change in surface temperature

$$\frac{T(r,t) - T_o}{T_i - T_o} = 2 \sum_{n=1}^{\infty} \frac{J_0(\lambda_n r) \exp[-(\lambda_n r_o)^2 (at/r_o^2)]}{(\lambda_n r_o) J_1(\lambda_n r_o)}$$

where,

$T(r,t)$  = temperature at radius  $r$  at time  $t$

$T_i$  = initial surface temperature

$T_o$  = final surface temperature

$r_o$  = outer radius of rod

$\lambda_n$  =  $n$ th solution of  $J_o(\lambda_n r_o) = 0$

$\alpha$  = thermal diffusivity =  $k/\rho c$

$k$  = thermal conductivity

$\rho$  = density

$c$  = specific heat

Case II: Step change in coolant temperature with convection

$$\frac{T(r,t) - T_{c,o}}{T_{c,i} - T_{c,o}} = 2A \sum_{m=1}^{\infty} \frac{J_o(\lambda_m r) \exp[-(\lambda_m r_o)^2 (at/r_o^2)]}{[(\lambda_m r_o)^2 + A^2] J_o(\lambda_m r_o)}$$

where,

$T_{c,i}$  = initial coolant temperature

$T_{c,o}$  = final coolant temperature

$A$  =  $hr_o/k$

$h$  = heat transfer coefficient

$\lambda_m$  =  $m$ th solution of  $\lambda_m r_o J_1(\lambda_m r_o) = A J_o(\lambda_m r_o)$

### Simulation Model

A solid, cylindrical rod with an outer diameter of 1.1623 cm (representative of QUAD+ fuel) was divided into ten radial nodes of equal volume in the CHACHA-3C model. Constant material properties typical of uranium dioxide were assumed:

$$k = 2.5 \text{ W/m-}^\circ\text{C}$$

$$\rho = 9600 \text{ kg/m}^3$$

$$c = 310 \text{ J/kg-}^\circ\text{C}$$

For Case I an initial surface temperature of 500°C and a final surface temperature of 1000°C were used. For Case II an initial coolant temperature of 500°C and a final coolant temperature of 1000°C were used. The convective heat transfer coefficient for Case II was selected such that  $A=hr_o/k = 0.5$  (i.e,  $h = 215.09 \text{ W/m}^2\text{-}^\circ\text{C}$ ).

### Discussion of Results

Figure 6-25 shows the comparison of the Case I calculated and exact temperature transients for four different radial nodes. The agreement is good, with all calculated temperatures matching the exact values to within 8°C throughout the transient.

Figure 6-26 shows the comparison of the Case II calculated and exact temperature transients for the same four radial nodes. The agreement is excellent, with all calculated temperatures matching the exact values to within 2°C throughout the transient.

From this study it is concluded that the fuel rod conduction model in the GOBLIN series of codes is well suited for use in BWR LOCA analyses.



#### 6.1.10 Clad Strain and Rupture Model

##### Objective

This section provides the qualification of the CHACHA-3C rod burst model described in Sec. 4.9 of this report. The rod burst model is compared to publicly available data taken with heat-up rates representative of BWR fuel cladding during a postulated LOCA. The model is also compared to a General Electric model which has been benchmarked against additional data which are not available to Westinghouse.

The plastic strain model used in CHACHA-3C is taken from Ref. 6-9. The qualification of the model is discussed in that reference, and is not repeated here.

##### Data Used for Comparison

A number of researchers have noted the dependence of cladding rupture stress on heat-up rates. The general trend is an increase in maximum allowable stress as heat-up rate increases. The cladding heat-up rates calculated for a postulated BWR LOCA are typically less than 10°F/sec. The data comparisons will therefore be limited to data taken with heat-up rates of  $\leq 10^\circ\text{F}/\text{sec}$ .

The data selected for comparison with the CHACHA-3C rod burst model were taken from Ref. 6-18 through 6-21. The data sources are summarized in Table 6-2.

##### Discussion of Results

The CHACHA-3C rod burst correlation is plotted with the rod burst data base in Fig. 6-27. The correlation is clearly conservative with all of the measured data falling above the predicted burst curve.

Figure 6 of Ref. 6-22 contains a rod burst correlation which was proposed by General Electric for use in BWR LOCA analyses. This correlation is based on additional rod burst data not available to Westinghouse. As shown in Fig. 6-28, the CHACHA-3C correlation is more conservative than the proposed GE correlation for all cladding temperatures.

From these comparisons it is concluded that the rod burst correlation in CHACHA-3C will provide conservative predictions of the maximum allowable cladding stress during a postulated BWR LOCA.

### 6.1.11 Radiation Heat Transfer Model

#### Objective

This section contains the qualification of the anisotropic radiation heat transfer model described in Sec. 4.5 of this report. Surface temperatures calculated by CHACHA-3C will be compared to experimental results from a radiation-only test performed with a simulated ASEA-ATOM 8x8 BWR fuel bundle.

#### Test Description

The ASEA-ATOM 8x8 radiation-only test was one of a series of full-scale BWR emergency core cooling tests performed in the GOTA loop located at the Studsvik Thermal Engineering Laboratory. The test under consideration here was designated as DSF-P1/87, and is reported in detail in Ref. 6-23. A cross-section of the test bundle is shown in Fig. 6-29.

Test No. 87 was conducted using a constant power level of 70.3 kW. Water cooling was applied to the outside of the channel box, maintaining the channel at saturation temperature. The temperatures of the heater rods were recorded until steady state conditions were clearly established.

#### Simulation Model

The CHACHA-3C model was set up for the bundle midplane elevation. All 64 rods were explicitly modelled using the measured rod-wise power distribution. The anisotropic radiation heat transfer model was used, with the anisotropic coefficients set to 0.5 for the rods and 0.15 for the channel.

#### Discussion of Results

The calculated temperatures along the two rod bundle diagonals are compared with the measured temperatures in Fig. 6-30. The variation of the temperatures measured for rods in symmetric locations does not appear in the

calculated results, but the agreement between the measured and calculated values is generally very good. There is a tendency towards overprediction of the rod temperatures as the channel wall is approached.

From this comparison it is concluded that the anisotropic radiation model used in the GOBLIN series of codes is capable of accurately predicting radiation heat transfer in BWR fuel bundles. Additional spray cooling and radiation-only tests are currently being conducted by ASEA-ATOM in the FRIGG loop, using a mini-bundle design very similar to QUAD+. These tests will be evaluated by Westinghouse to provide additional qualification for using the anisotropic radiation model for QUAD+ analyses.

### 6.1.12 Spray Cooling and Channel Wetting

Spray cooling convective heat transfer coefficients which are compatible with the anisotropic radiation model have been derived for QUAD+ fuel (Sec. 4.5.3). The resulting values, shown in Table 4-3, are equivalent to the spray cooling convective heat transfer coefficients recommended in Appendix K for use in analyses of BWR fuel. Spray cooling tests of a water-cross fuel geometry are currently being conducted by ASEA-ATOM in Sweden. These tests will be evaluated by Westinghouse to provide additional justification for using the coefficients in Table 4-3 for QUAD+ fuel, under spray cooling conditions.

The channel wetting model used in CHACHA-3C is the one recommended in Appendix K (Sec. 4.7). The ASEA-ATOM spray cooling test data will also be used to demonstrate the applicability of this model to QUAD+ fuel.

## 6.2 TLTA-5A Integral System Qualification

### 6.2.1 Objective

The objective of this section is to present comparisons of a GOBLIN computer code simulation to test data to verify the code's ability to correctly predict a design basis LOCA transient. The test data used in these comparisons is the publically available data from the BWR blowdown heat transfer test program sponsored by the NRC, EPRI, and GE.

The purpose of the BWR blowdown heat transfer test program was to develop a data base of thermal hydraulic and heat transfer test data that is characteristic of a BWR under loss of coolant accident conditions. To achieve this objective a test loop was built which was scaled from a typical jet-pump BWR and included all the major components of a BWR such as recirculation loops, jet pumps, upper and lower plenums, steam separator, downcomer, and rod bundle. The test loop, known as the two loop test apparatus (TLTA) was scaled on a volume basis with the test rod bundle simulating one complete rod bundle from the reference BWR.

It was concluded that the test data obtained from the TLTA runs provided a good global simulation of BWR system LOCA conditions and thus was suitable for use in code verification. This section will show that GOBLIN can correctly predict global thermal hydraulic conditions during a LOCA transient in a jet pump BWR.

### 6.2.2 TLTA Facility Description

The original TLTA facility which was scaled to a BWR/4, with 560 fuel bundles, was modified to represent a reference BWR/6, with 624 fuel bundles. Each bundle consists of 64 fuel rods arranged in an 8 x 8 square matrix. A detailed description of the TLTA facility is provided in the facility description report (Ref. 6-24). Reviewed below is a basic description of the facility (TLTA-5A) as it was used to simulate large break tests with emergency core cooling (ECC). A simplified schematic representation of the TLTA-5A facility is shown in Fig. 6-31.

The TLTA-5A consists of a pressure vessel with two external recirculation loops, a feedwater system, steamline with pressure regulation, blowdown valves and piping, and ECC systems. All the basic components and flow paths of the reference BWR have been built into the vessel, including a steam dome, downcomer, jet pumps, lower plenum, core region, upper plenum, steam separators, control rod guide tubes, and a core bypass region. The core region is simulated with a full length, full power heater rod bundle. The facility is designed to operate at typical BWR temperatures and pressures. The primary objective in designing the TLTA was to achieve a real time response during testing.

The reference BWR/6 contains 624 fuel bundles whereas the TLTA has one full size bundle. This 1/624 ratio is the basis for scaling the regional volumes within the vessel. Several compromises were made on regional volumes to accommodate the full size bundle while maintaining a real-time response. These scaling considerations are discussed in Ref. 6-1 and 6-24, and are reviewed here. The larger than scale recirculation loop volume in the TLTA can act to retard the system depressurization as a result of additional fluid mass available for flashing. The TLTA-5A configuration includes isolation valves on the intact recirculation loop suction and drive lines that are used to reduce this effect. The downcomer and lower plenum regions have a larger flow area to volume ratio than the reference BWR. This causes lower fluid velocities in the TLTA, but is not considered significant since velocities are typically very low. The boundary surface area to volume ratio is also higher in the TLTA, which can lead to greater heat transfer from the vessel metal mass. To counter this effect, insulation was installed on the inside of the lower plenum.

Following a postulated LOCA, core reflood and subsequent cooling of the fuel rods is strongly influenced by countercurrent flow limitation (CCFL) phenomena. For this reason, the CCFL characteristics of restricted flow areas at the bundle and bypass inlet and exit in the TLTA were matched to those in the reference BWR. This was accomplished through appropriate design of the side entry orifice and upper tie plate. Long term core cooling depends on the reflood height which in turn is determined by the pump throat elevation. In the reference BWR, this elevation corresponds to two-thirds of the height of

the active fuel. However, the requirement that fluid volumes be scaled on a 1/624 basis to achieve real time thermal hydraulic response in the TLTA results in a downcomer annulus too small to accommodate a full scale jet pump. Thus, the TLTA jet pumps were linearly scaled in height and diameter resulting in a much shorter overall length. The scaling basis for the jet pumps was chosen to preserve the mass flux between reference BWR and the TLTA recirculation pumps. The break area is also scaled on a 1/624 basis. The main break flowpath is through the recirculation pump suction line. The limiting break area in the reference BWR is the pipe flow area. It was not possible to scale the pipe area directly in TLTA, so a venturi type flow limiter with a scaled throat area was installed in the recirculation suction piping. The second break flow path is through the recirculation pump drive line, but the limiting flow area is in the jet pump nozzle. To compensate for the larger nozzle areas in the TLTA jet pump drives, a scaled flow limiting orifice was inserted in the blowdown line. The recirculation pump initial coastdown strongly affects the core flow during the early blowdown portion of a LOCA. For this reason, the TLTA pump and motor combinations were designed so that their dynamic inertia characteristics match those of the reference BWR.

The ECC systems in the TLTA-5A were designed to provide mass flow rates scaled on a 1/624 basis, with specific energy scaled on a one to one basis. Included are both high and low pressure core spray and low pressure core injection. The ECC system pumps were capable of providing variable flow rates, thus permitting such limiting test sequences as high core power/low ECC flow rates at elevated ECC temperatures.

It is felt that the TLTA-5A tests will closely simulate the system response expected from the reference BWR/6, and therefore provide a good source of qualification data for the GOBLIN computer code.



### 6.2.3 Average Power/Average ECC Test

#### Test Conditions

The reference test for the blowdown/ECC test series that was performed with the TLTA-5A facility is experiment 6425, Run 2. This test was performed at average bundle power with average ECC spray rates at nominal temperatures. Initial bundle power was 5.05 MW, with the bundle decay power controller started at the time of break. The blowdown transient was initiated when the blowdown valves were opened, and the power to the recirculation and feedwater pumps was tripped. The test was continued to 400 seconds with the bundle quenching at approximately 150 seconds.

#### GOBLIN Model of TLTA-5A

A GOBLIN model of the TLTA-5A facility was constructed with boundary conditions taken from test 6425, run 2. The test loop was modelled with 55 control volumes connected by 61 flow paths. A diagram of this noding scheme is shown in Figure 6-32. The core is modelled by a rod group divided axially into nine parts, one for each fluid volume in the bundle. The broken recirculation loop is divided into five control volumes incorporating two break locations, a recirculation pump, and jet pump drive nozzle. The intact loop volumes are isolated during the blowdown transient to prevent excessive vapor flashing from the intact loop liquid volume. Thirty six heat slabs were used to model the stored heat in the pressure vessel and internal components. The following initial and boundary conditions were taken from measured test data.

- o Bundle power input
- o Intact loop pump speed
- o Steam dome pressure
- o Initial downcomer water level

- o Feedwater flow rate and enthalpy
- o Steamline flow rate
- o Initial jet pump flow rates

The calculation was done using best estimate input for the GOBLIN code, since it was felt that this would give a true comparison with test data for the purposes of code qualification. Specifically, the homogeneous equilibrium model (HEM) was used for predicting discharge flow. Separate experiments have shown that the discharge flow for nozzles of the type used in TLTA are well predicted using the HEM. (Ref. 6-9 and 6-25) The actual measured bundle power was used and rod rewet was permitted, again with the intent of providing the more realistic comparison to actual test results. The GOBLIN simulation model thus described differs in several important respects from the more conservative evaluation model of GOBLIN that will be used in a licensing calculation meeting the Appendix K requirements. The specific Appendix K changes include:

- o Decay heat based on 1971 ANS standard plus 20%
- o Moody critical flow model used to predict break flow
- o Rod rewet following dryout will not be permitted

The evaluation model calculation uses the Moody model for critical flow as required by Appendix K. In Ref. 6-9 break flow calculations based on the Moody critical flow model and the homogeneous equilibrium model are compared to experimental data. These results show that the Moody model predicts significantly higher break flow rates than the homogeneous equilibrium model (HEM) and that the HEM predictions agree well with the measured break flow.

The GOBLIN code has the ability to track rod dryout and to preclude rod rewetting by the selection of the appropriate code input. If the predicted local thermal hydraulic conditions are consistent with rod rewetting and the

code input to preclude rewetting has been selected, GOBLIN will apply a convective heat transfer coefficient based on film boiling. Because film boiling heat transfer coefficients are typically several orders of magnitude lower than nuclear boiling heat transfer coefficients, this assumption can lead to significantly higher peak clad temperatures than measured.

#### GOBLIN Simulation of Test 6425, Run 2

The results of this simulation are presented in Fig. 6-33 through 6-39. The early portion of the blowdown transient is governed by the break flow and the changing mixture elevation in the downcomer. Within one second after opening the blowdown valves to initiate the test sequence, the flow reverses in the broken jet pump, followed shortly thereafter with bypass flow reversal. The jet pump suction inlet uncovers at approximately 7 seconds (Fig. 6-39) with an initial downcomer level of 1.4 meters above this inlet. Following the loss of jet pump flow in the broken loop, the bundle inlet flow drops and approaches zero when the jet pump suction is uncovered. These phenomena are well predicted by the GOBLIN code with the jet pump suction uncover occurring at approximately nine seconds. Figure 6-33 compares the measured and predicted bundle mass flow rates which show generally good agreement. Figure 6-37 shows that GOBLIN slightly underpredicts the pressure transient as measured from the TLTA. This is attributed to the slightly higher break flow predicted by GOBLIN in the first several seconds of the blowdown transient. Estimated break flows were inferred by comparing mass depletion rates in the downcomer, bundle (Fig. 6-34), bypass (Fig. 6-35), and lower plenum regions (Fig. 6-36). The results of the inferred break flow are shown in Fig. 6-38. The higher predicted break flow by GOBLIN early in the transient is, however, a conservative prediction.

As the pressure drops further and reaches the saturation pressure of the lower plenum fluid, the resultant vapor generation from flashing causes a redistribution of mass within the system. The bundle and bypass inlet and outlet areas are geometrically restrictive and as such can cause countercurrent flow limiting (CCFL) conditions to occur when high vapor mass flow exists in these regions. Liquid inventory is held up in the upper

regions because of the upflowing vapor generated during bulk lower plenum flashing. This behavior is predicted by GOBLIN as can be seen from Fig. 6-34. The bundle mass inventory initially drops during the first few seconds of blowdown. As vapor is generated in the lower plenum, CCFL conditions are established at the bundle inlet and the bundle mass inventory remains fairly constant until approximately 25 seconds into the transient. At this time, the lower plenum liquid mass begins to significantly reduce and at approximately 40 seconds the jet pump exit plane is uncovered, providing another path for the lower plenum vapor to escape from. Consequently, this causes a reduction in vapor flow through the bundle with a gradual breakdown of CCFL conditions. As seen from Fig. 6-34, during this time bundle liquid mass reduces to nearly zero and is correctly predicted by GOBLIN.

Figure 6-35 shows the lower plenum mass inventory with the reduction in liquid mass occurring during the later stages of CCFL at the bundle inlet. Again it is well predicted by the GOBLIN code. The fairly constant lower plenum mass inventory that exists after 40 seconds is a result of ECC System injection flow draining through the bundle and replenishing that which is lost through the jet pumps. The bypass flow behavior (Fig. 6-36) during this time period is also strongly governed by the CCFL effects. The bypass mass is kept from draining into the guide tube region by CCFL conditions at the bypass inlet, while the upper plenum inventory is kept from draining into the bypass by the CCFL conditions at the top of bypass. During this time, the bypass region gradually loses mass to the bundle through the leakage path at the bottom of the core. This behavior is clearly seen by examining Fig. 6-36. The combination of the low pressure spray and injection at approximately 65 seconds and the ensuing breakdown of CCFL at the top of bypass causes the bypass to begin refilling rapidly and is again seen from the bypass fluid mass shown in Fig. 6-36.

As the bypass region refills, leakage flow into the bundle drains through the side entry orifice into the lower plenum. Once the lower plenum level rises to the jet pump exit plane, the jet pump discharge liquid mass fraction increases. The reduced vapor flow through the jet pump is compensated for by an increased vapor flow through the bundle inlet thus creating CCFL conditions

and holding up bypass leakage flow in the bundle. Hence the bundle begins to refill, lagging behind the bypass region. This expected behavior is predicted by both TLTA and GOBLIN as can be seen from Fig. 6-34 and 6-36. Finally, CCFL breakdown at the upper tie plate allows the upper plenum liquid to drain into the bundle completing the reflooding process. Following this period, the ECC liquid flows through the bundle, into the lower plenum, out the jet pump and finally into the downcomer where it spills through the break.

In general, it is seen that the GOBLIN code can well predict the integral behavior during the blowdown transient. The significant events mentioned above occur at nearly the same times as measured in the TLTA experiment. In addition, the correct prediction of mass redistribution following the break is a good indication that the code realistically models the BWR component behavior under different thermal hydraulic conditions.

#### 6.2.4 High Power/Low ECC Test

##### GOBLIN Model for Test 6423, Run 3

The nodalization for the GOBLIN simulation of the high power, low ECC test was identical to that employed in modelling the average power, average ECC case. However, different boundary conditions were applied, these being taken from the available test data. The main differences were in the initial power which was 6.46 MW, the lower ECC spray and injection flow rates, and the higher ECC fluid temperatures. As such, this case should represent an upper bound for evaluating the system response to a design basis loss of coolant accident.

##### GOBLIN Simulation of Test 6423, Run 3

The results of this simulation run are presented in Fig. 6-40 through 6-46. During the blowdown portion of this transient, the system behavior is basically the same as that seen for the average power, average ECC case. The broken jet pump flow reverses almost immediately as shown in Fig. 6-46, followed shortly thereafter by the bypass flow reversal. Bundle inlet flow drops to nearly zero when the jet pump suction is uncovered followed by

flashing of the lower plenum liquid. These events and the mass redistribution are all predicted correctly by GOBLIN as can be seen from Fig. 6-40 through 6-46. The system behavior is strongly governed by CCFL conditions present at the bundle and bypass inlets and outlets, as was previously discussed. As with the average power/average ECC case, GOBLIN overpredicts the break flow and underpredicts the pressure during the first few seconds of the transient. The low ECC flow rates and higher temperatures show their effects when the bundle and bypass regions begin to refill. The bundle only partially refills due to the lower ECC flow and less limiting CCFL conditions at the bundle inlet due to reduced vapor mass flow. These conditions result in a reduced pressure difference between the lower plenum and steam dome and allows the lower plenum level to rise above the jet pump exit plane. This behavior is well predicted by GOBLIN as evidenced by the good comparisons to the TLTA data as shown in Fig. 6-41 and 6-42.

#### 6.2.5 Summary

From these comparisons of GOBLIN computer code predictions to the measured TLTA data for the average power/average ECC and high power/low ECC test sequences, it is concluded that the GOBLIN code can well predict the global thermal hydraulic behavior of a BWR system under design basis LOCA conditions. It is seen from the preceding discussion that GOBLIN predicts the correct trends for pressure response, break flow, mass redistribution, bundle inlet flow, and jet pump flow rates. Use of the GOBLIN code to predict the thermal hydraulic behavior of a BWR system together with conservative input assumptions that are in compliance with Appendix K requirements will undoubtedly result in a conservative calculation of the BWR LOCA transient.

### 6.3 Additional Integral Systems Qualification

Additional integral systems qualification has been performed by ASEA-ATOM, including simulations of TLTA-4 blowdown heat transfer tests 6007 Run 26 and 6006 Run 3, the TLTA-5B and TLTA-5C small break LOCA tests, and the Studsvik FIX-II break spectrum tests. This section summarizes the results of these qualification programs.

#### 6.3.1 TLTA-4 Blowdown Heat Transfer Tests

The TLTA-4 blowdown heat transfer tests are described in Ref. 6-27. Test 6007 Run 26 was the reference test, conducted at 5.05 kW. Test 6006 Run 3 was a peak power test, conducted at 6.49 kW.

Figure 6-47 shows the calculated and measured system pressure during the first 20 seconds of the blowdown for Test 6007 Run 26. The calculated depressurization rate is somewhat faster than in the experiment after the recirculation suction becomes uncovered. This can be attributed to water entrainment in the break flow which is not modelled in the calculation. The faster depressurization rate in the calculation leads to lower plenum flashing slightly earlier in the transient, as shown in Fig. 6-48. Figure 6-49 shows that the calculated flow rates for the intact and broken loop jet pumps agree very well with the measured values. The calculated transient rod temperatures are also in good agreement with the data, as shown in Fig. 6-50.

Similar agreement was found for other important system parameters throughout the transient. The simulation of Test 6006 Run 3 also showed generally good agreement between calculated and measured system response. Details of the GOBLIN/DRAGON simulations are available in Ref. 6-28.

### 6.3.2 TLTA Small Break Tests

The TLTA-5B and TLTA-5C small break LOCA tests are described in Ref. 6-29. TLTA-5B simulated a small break LOCA with all ECC systems available. TLTA-5C simulated a small break LOCA with high pressure core spray unavailable. Low pressure core spray and low pressure coolant injection were used to replenish the system inventory, following depressurization by the automatic depressurization system.

Figure 6-51 shows a comparison of the measured and calculated steam dome pressure for TLTA-5C. The agreement is excellent. The level swelling in the upper plenum and downcomer regions due to activation of the automatic depressurization system was also well-predicted, as shown in Fig. 6-52.

Similar agreement was found for other important system parameters. The simulation of the TLTA-5B test also showed good agreement. Details of the GOBLIN/DRAGON simulations are available in Ref. 6-30.

### 6.3.3 FIX-II Break Spectrum Tests

The FIX-II facility is a scaled test loop in Studsvik, Sweden, used to simulate LOCA transients of an ASEA-ATOM external recirculation pump plant design (similar to a General Electric BWR/2 design). The facility was used to simulate a spectrum of split and double-ended guillotine breaks ranging from 10 to 150 percent of a full recirculation line area. The core was simulated by a 36 rod bundle. Both average and peak power bundles were simulated. The blowdown tests measured coolant flow rates, coolant and rod temperatures, and differential pressures. A detailed description of the facility and tests are given in Ref. 6-4.

Five tests were simulated with GOBLIN/DRAGON. Figure 6-53 shows the steam dome pressure comparison for Test 3061, which is a 100 percent break with an average initial bundle power of 2.51 kW. The agreement is excellent. Figure 6-54 shows a comparison of the rod temperatures at the midplane with the



simulation. The heatup, peak, and rewet rates are all simulated well with GOBLIN/DRAGON. Similar agreement was obtained for all important parameters for the other break sizes and power levels simulated. Details of the GOBLIN/DRAGON simulations are reported in Ref. 6-31.

#### 6.4 Nomenclature

<u>Variable</u>	<u>Definition</u>
A	$hr_o/k$
C	CCFL correlation constant
c	Heat capacity
D	Diameter
G	Mass flux
g	Gravitation constant
h	Heat transfer coefficient
J	Bessel function
$j_f$	Superficial liquid velocity
$j_g$	Superficial vapor velocity
k	Thermal conductivity
M	CCFL constant
$P_w$	Wetted perimeter
P	Pressure
r	Radius
T	Temperature
$T_w$	Wall temperature
t	Time
X	Quality
$\lambda$	Solution of Bessel Function
$\alpha$	Void fraction
$\rho$	Density
$\sigma$	Surface tension

## 6.5 References

- 6-1 BWR Large-Break Simulation Tests - BWR Blowdown/Emergency Core Cooling Program, Vol. 1, NUREG/CR-2229, EPRI-NP-1783, April 1982.
- 6-2 BWR Small-Break Simulation Tests With and Without Degraded ECC Systems, EPRI NP-1782, April 1982.
- 6-3 BWR 64-Rod Bundle Blowdown Heat Transfer Final Report, GEAP/NUREG-23977.
- 6-4 L. Nilsson and P. A. Gustavsson, "FIX-II-LOCA Blowdown and Pump Trip Heat Transfer Experiments: Summary Report for Phase 2--Description of Experimental Equipment," NR-83/238, Studsvik, Sweden, Feb. 1983.
- 6-5 "OF-64: Results of Void Measurement," ASEA-ATOM report number FRIGG-PM-69, Feb. 1970.
- 6-6 "BWR Low-Flow Bundle Uncovery Test and Analysis" EPRI-NP-1781, NUREG/CR-2231, June 1982.
- 6-7 Loss-of-Coolant Accident and Emergency Core Cooling Models for General Electric Boiling Water Reactors, NEDO-10329, April 1971.
- 6-8 K. H. Sun, "Flooding Correlations for BWR Bundle Upper Tieplates and Bottom Side-Entry Orifices," Multiphase Transport: Fundamentals, Reactor Safety, Applications; Hemisphere Publishing, 1979, Pg. 1615-1635.
- 6-9 General Electric Company Analytical Model for Loss of Coolant Analysis in Accordance with 10CFR50, Appendix K, NEDO-20566, 1976.
- 6-10 G. B. Wallis, One-Dimensional Two-Phase Flow, McGraw-Hill, Inc., 1969.
- 6-11 H. S. Crapo, "LOFT Test Support Branch Data Abstract Report: One-Sixth Scale Model BWR Jet Pump Test," EGG-LOFT-5063, Nov. 29, 1979.

- 6-12 G. E. Wilson, "INEL One-Sixth Scale Jet Pump Data Analysis," EGG-CAAD-5357, Feb. 1981.
- 6-13 "ECCS Heat Transfer Experiment with Upper Head Injection," WCAP-8400.
- 6-14 "W Emergency Core Cooling System Evaluation Model Application to Plants Equipped with Upper Head Injection," WCAP-8479-P, Rev. 2.
- 6-15 "G-2 17 x 17 Refill Heat Transfer Tests and Analysis," WCAP-8793-P, August 1976.
- 6-16 FLECHT Low Flooding Rate Cosine Tests Series Data Report, WCAP-8651, Dec. 1975.
- 6-17 G. E. Myers, "Analytical Methods in Condition Heat Transfer," McGraw-Hill, NY, NY 1971.
- 6-18 D. A. Powers and R. O. Myers, "Cladding Swelling and Rupture Models for LOCA Analysis," NUREG-0630, April 1980.
- 6-19 F. J. Erbacher, et. al., "Burst Criterion of Zircaloy Fuel Claddings in a Loss-of-Coolant Accident," Fifth International Conference on Zirconium in the Nuclear Industry, Boston, August 1980.
- 6-20 E. F. Juenke and J. F. White, "Physico-Chemical Studies of Clad  $UO_2$  Under Reactor Accident Conditions," GEMP-731, April 1970.
- 6-21 M. F. Osborne and G. W. Parker, "The Effect of Irradiation on the Failure of Zircaloy - Clad Fuel Rods," ORNL-TM-3626, January 1972.
- 6-22 Letter, R. H. Bauchholz (GE) to L. S. Rubenstein (NRC), Subject: General Electric Fuel Clad Swelling and Rupture Model, May 15, 1981.
- 6-23 R. Harju and R. Pettersson, "GÖTA Loop ECCS Test. Data Analysis and Test Results, Test No. 87," Studsvik/E4-79/43, 1979.

- 6-24 W. J. Letzing et. al., BWR Blowdown Emergency Core Cooling Program Preliminary Facility Report for the BD/ECC-1A Test Phase, GEAP-23592, Dec. 1977.
- 6-25 A. F. Morrison, Blowdown Flow in the BHDT Test Apparatus, GEAP-21656, Oct. 1977.
- 6-26 Lecture notes from TRAC-BWR Workshop at EG&G Idaho, Idaho Falls, Sept. 17-20, 1985.
- 6-27 W. S. Hwang, et. al., "BWR 64-Rod Bundle Blowdown Heat Transfer," GEAP-NUREG-23977, September 1978.
- 6-28 H. Wijkström, "GOBLIN and DRAGON Calculations Compared with BWR BDHT Experiments 6007 Run 26 and 6006 Run 3," ASEA-ATOM Report RCC-81-114, August 1981.
- 6-29 W. S. Hwang, "BWR Small-Break Simulation Tests With and Without Degraded ECC Systems," GEAP-24963, March 1981.
- 6-30 H. Wijkström and M. Makinen, "Comparison Between Calculations and TLTA Small-Break Tests - Final Report," ASEA-ATOM Report KPA-84-138, August 1984.
- 6-31 H. Wijkström, "GOBLIN - Comparison with FIX-II Break Spectrum Tests," ASEA-ATOM Report KPA-85-71, May 1985.

TABLE 6-1

FRIGG Void Measurement Test Conditions

<u>Run</u>	<u>Pressure</u> (MPa)	<u>Power</u> (MW)	<u>Average</u> <u>Heat Flux</u> (W/cm <sup>2</sup> )	<u>Mass</u> <u>Flux</u> (Kg/m <sup>2</sup> -sec)	<u>Subcooling</u> (°C)
713-038	4.8	5.14	57.1	745	24.6
713-032	4.8	3.54	39.4	1245	9.6
713-040	6.8	5.14	57.1	759	8.9
713-039	6.8	3.54	39.4	1249	9.1

TABLE 6-2

Rod Burst Data Sources

<u>Data Source</u>	<u>Test Description</u>	<u>Number of Data Points</u>	<u>Heat-Up Rates (°F/sec)</u>
Ref. 6-18, Table F	Single rod in steam	6	0-9
Ref. 6-18, Table H	Single rod in steam	1	5
Ref. 6-18, Table I	Single rod in steam	9	0-9
Ref. 6-18, Table J	Single rod in steam	11	1-3
Ref. 6-19, Figure 4	Single rod in steam	27	1-3
Ref. 6-20, Table 1	Single rod in steam	3	1-9
Ref. 6-21, Table 4.1	Irradiated single rod in steam	4	9-10

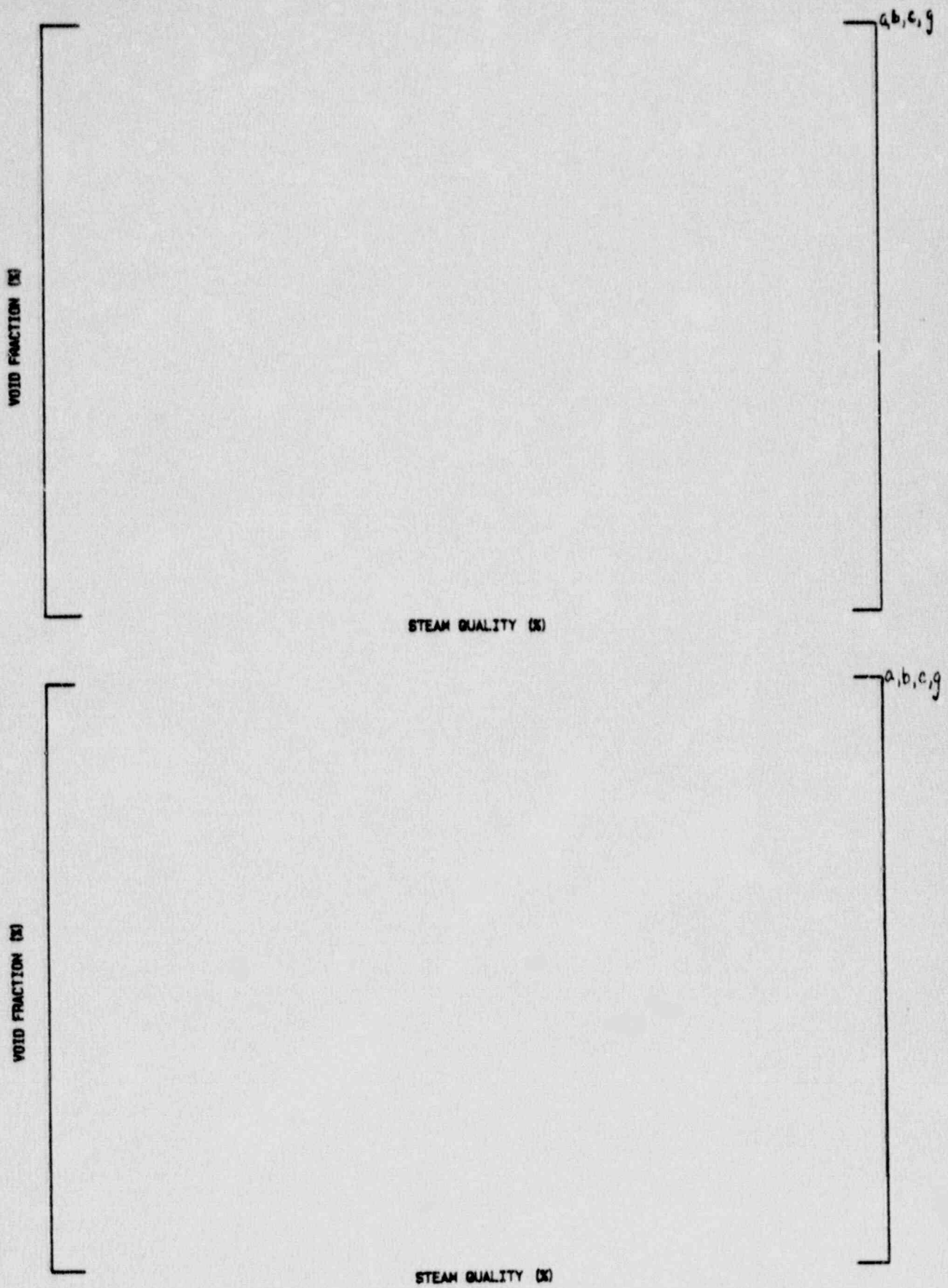


Figure 6-1 - Comparison of Drift Flux Model with FRIGG Data at 6.8 MPa (990 psia)



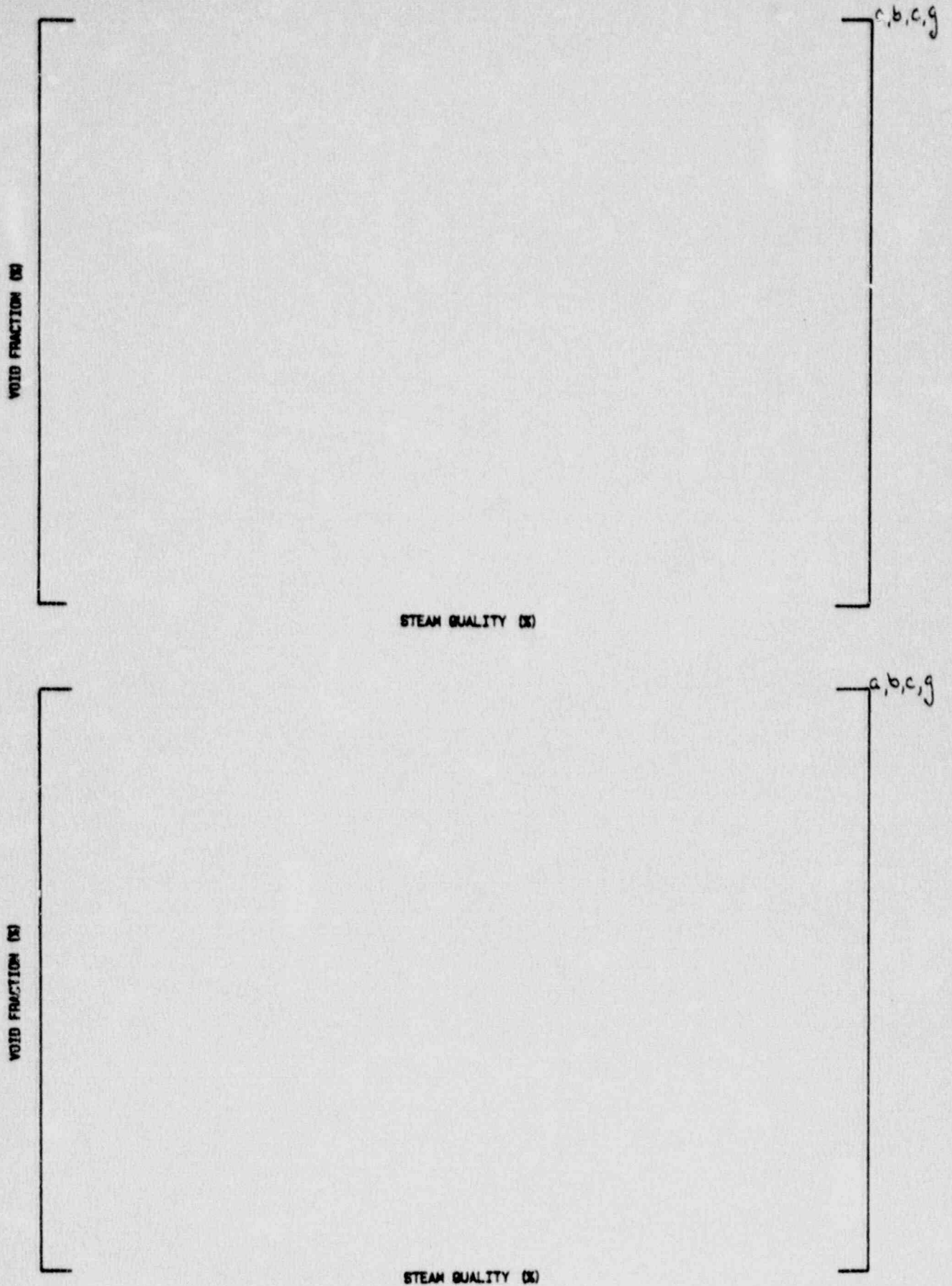


Figure 6-2 - Comparison of Drift Flux Model with FRIGG Data at 4.8 MPa (700 psia)

		ELEVATION FROM BHL (INCHES)
■	L20	
	L19	150.0
	L18	146.0
	L17	141.0
	L16	131.1
	L15	120.9
	L14	110.6
	L13	100.8
	L12	90.6
	L11	80.7
	L10	70.5
	L9	60.2
	L8	50.4
	L7	40.2
	L6	30.3
	L5	20.1
	L4	13.0
	L3	5.5
	L2	0.0
■	L1	

■ Boundary Nodes

Figure 6-3 - DRAGON Nodalization of TLTA Bundle

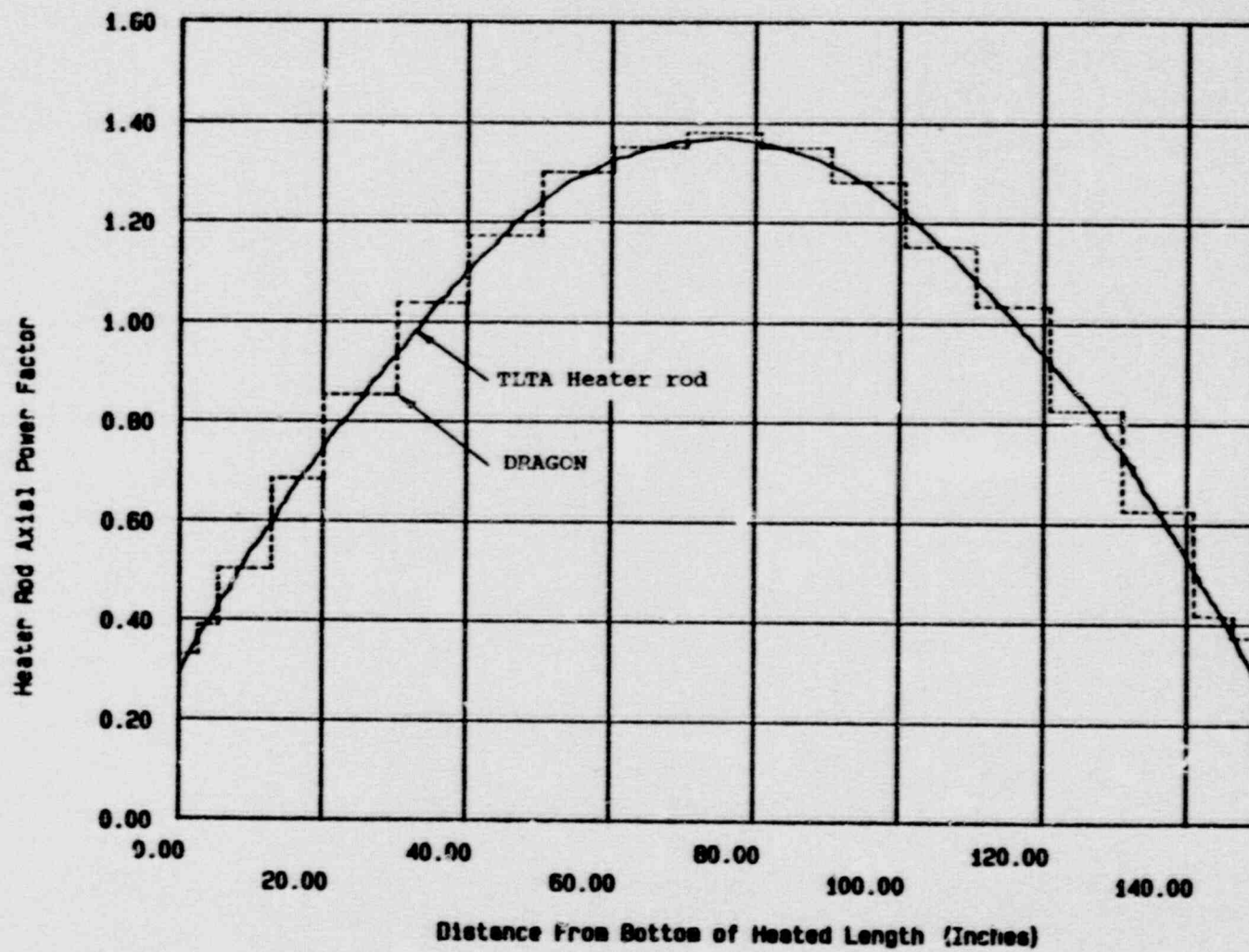


Figure 6-4 - Axial Power Distribution for TLTA Bundle

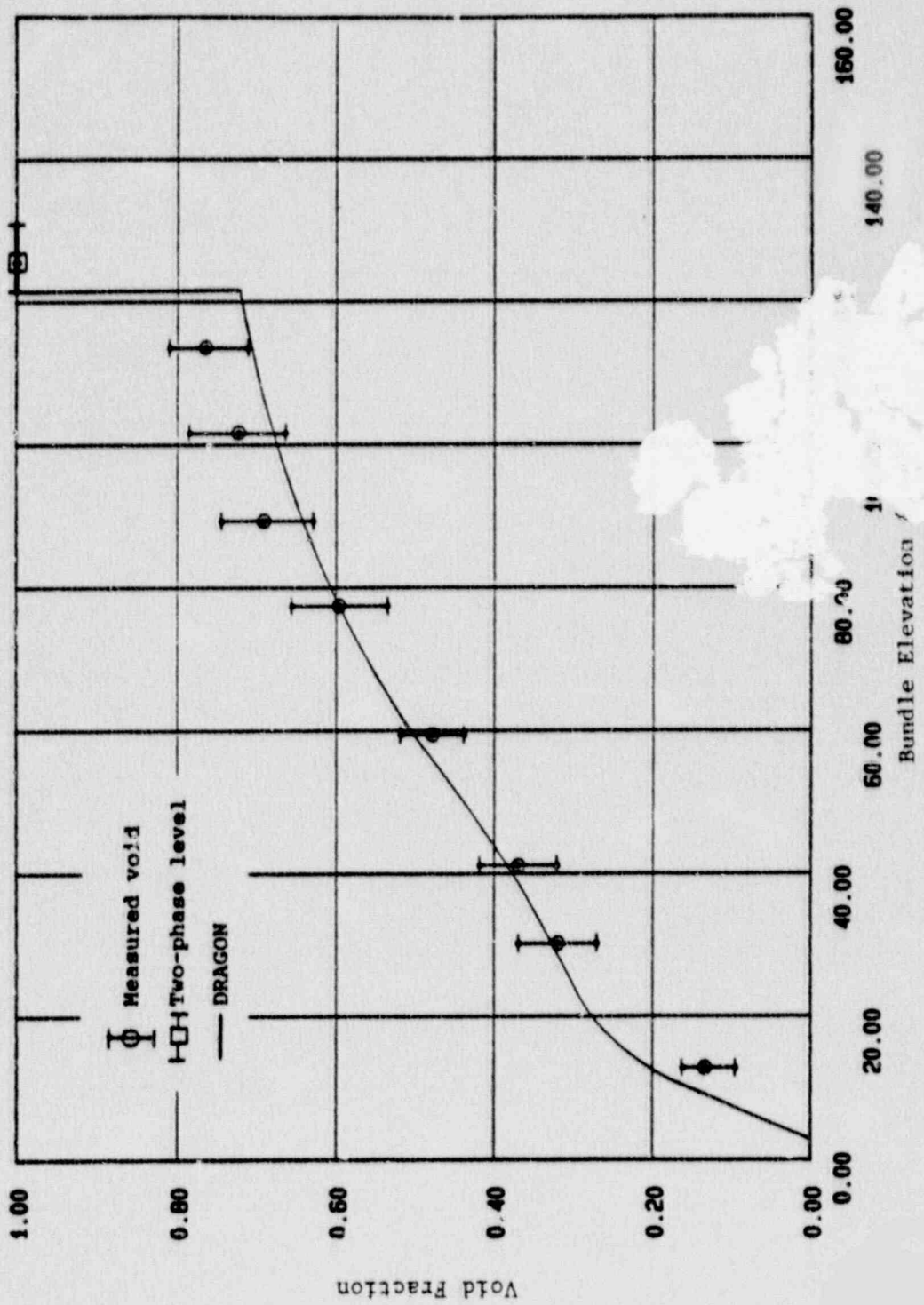


Figure 6-5 - Comparison of Void Fractions for 1" Bundle (200 sec.)

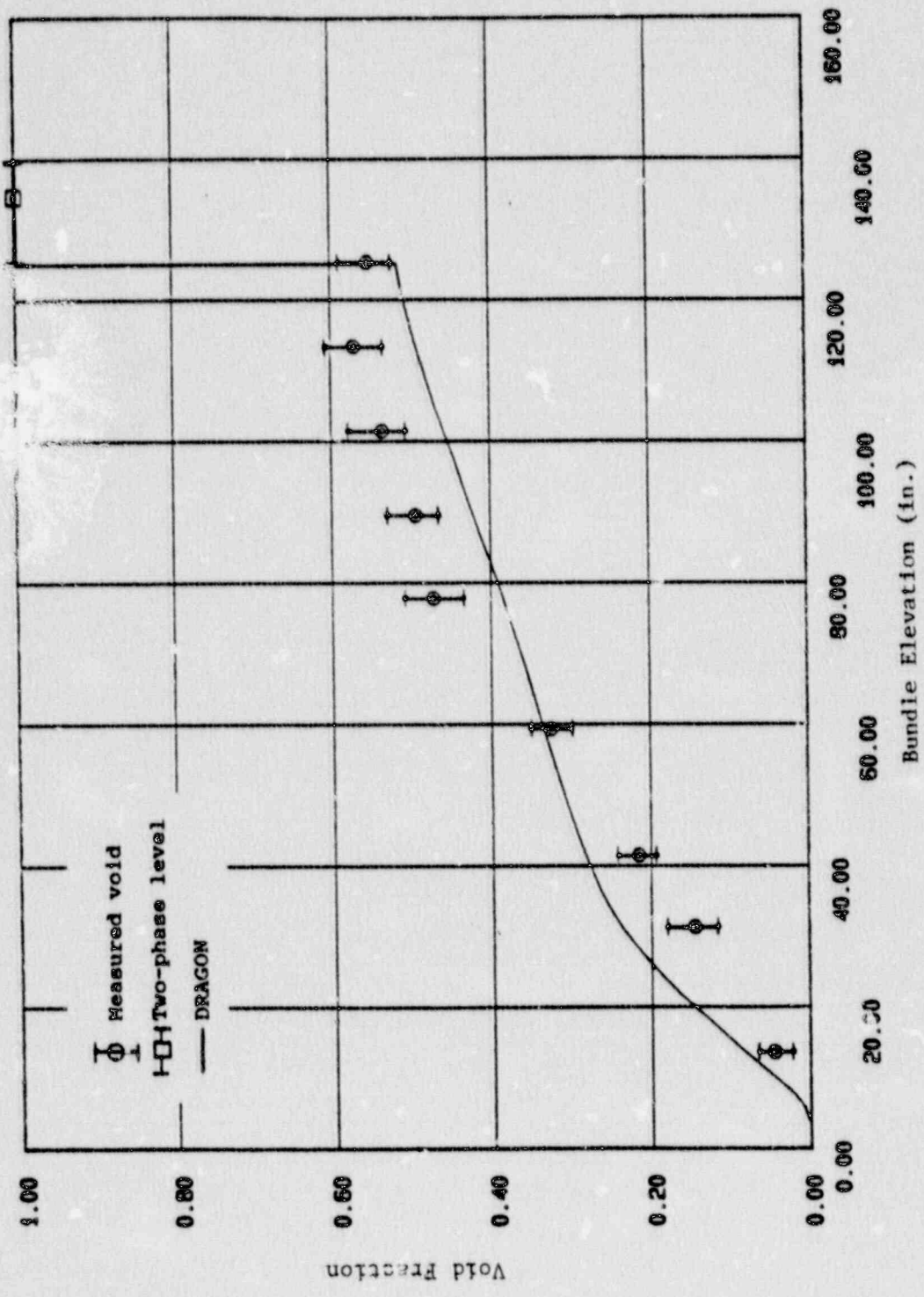


Figure 6-6 - Comparison of Void Fractions for 790 psia Test (100 Sec.)

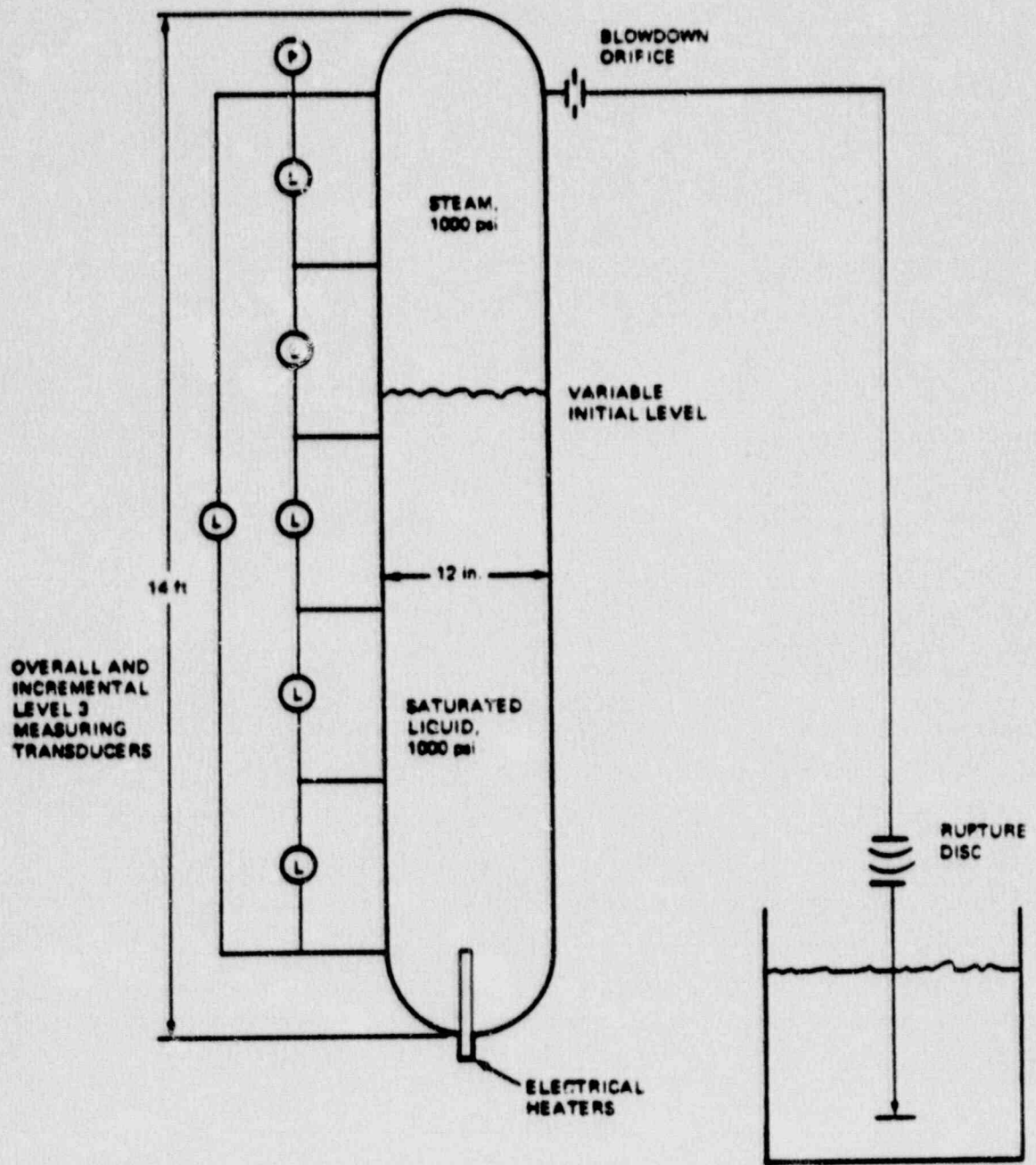


Figure 6-7 - Level Swell Test Apparatus (from Ref. 6-7)

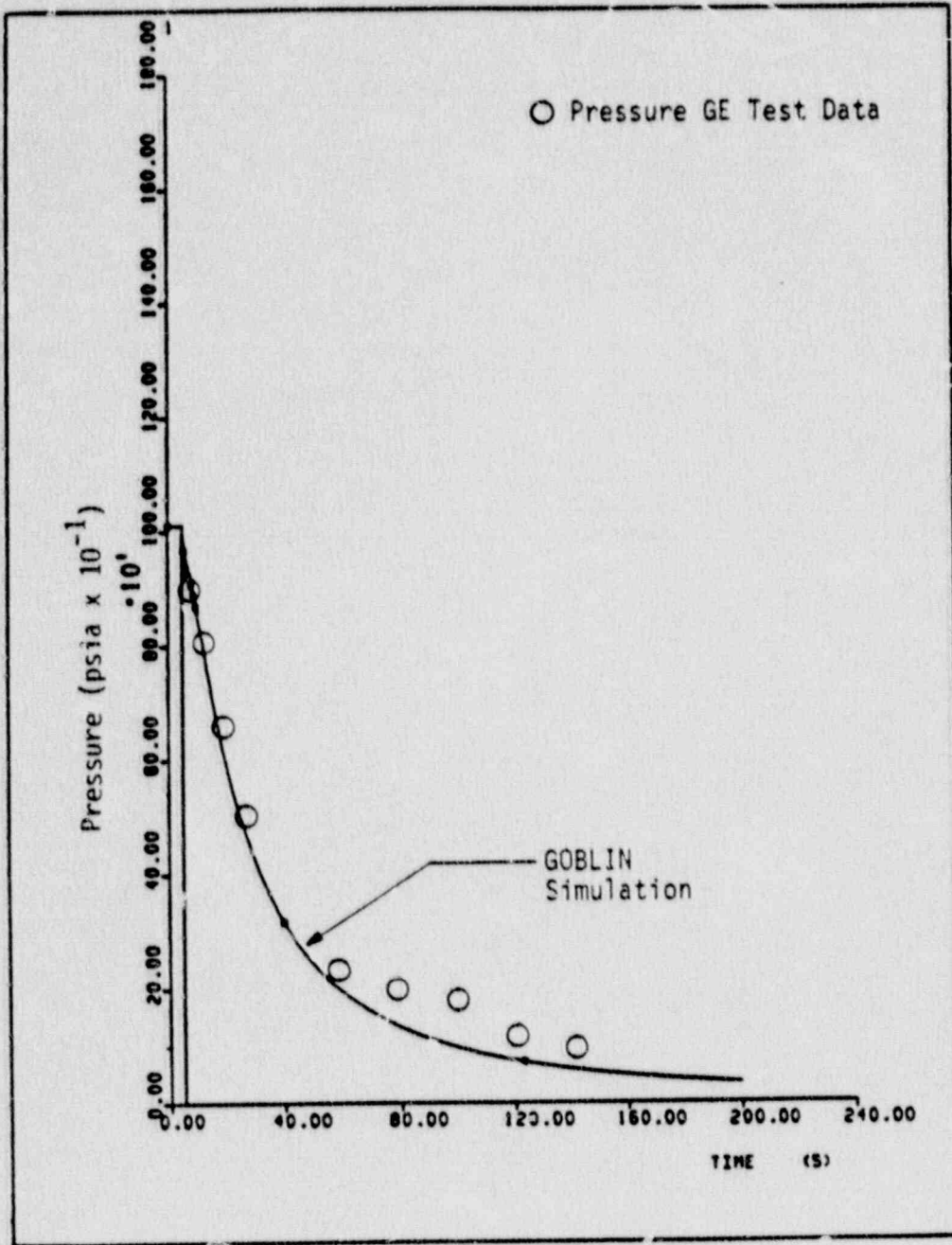


Figure 6-8 - Level Swell Qualification, Pressure Transient for Test 1

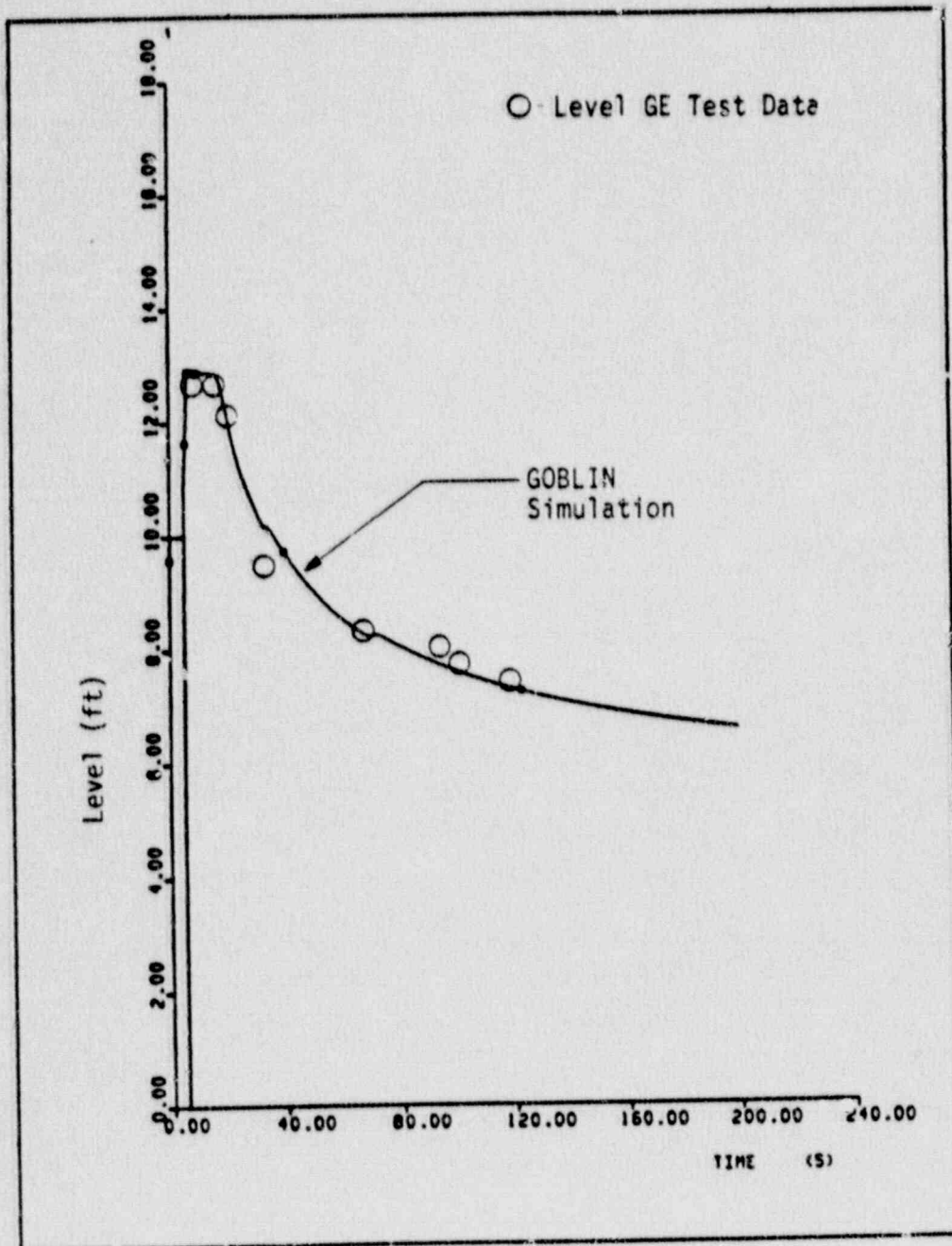


Figure 6-9 - Level Swell Qualification, Level Transient for Test 1



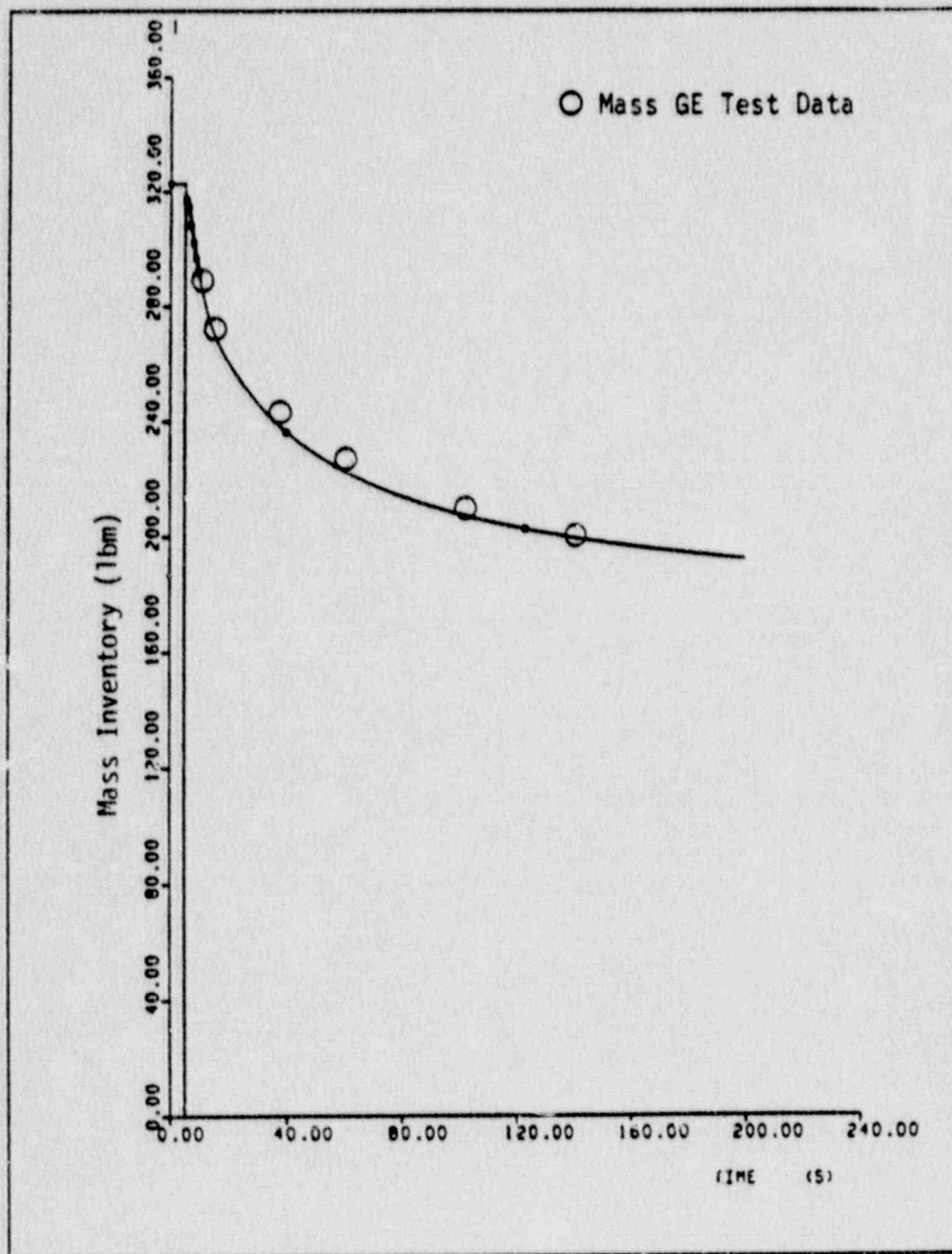


Figure 6-10 - Level Swell Qualification; Mass Transient for Test 1

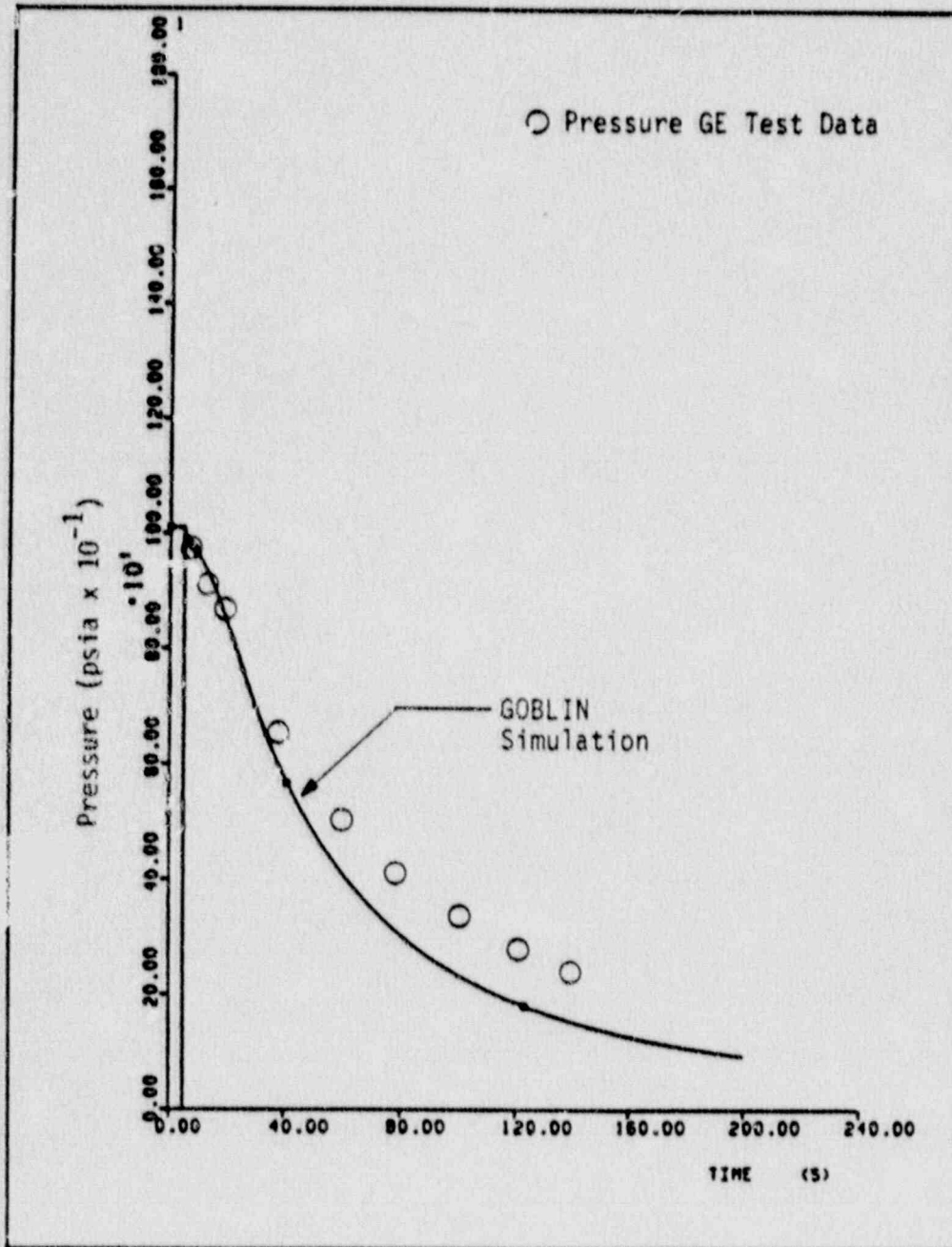


Figure 6-11 - Level Swell Qualification; Pressure Transient for Test 2

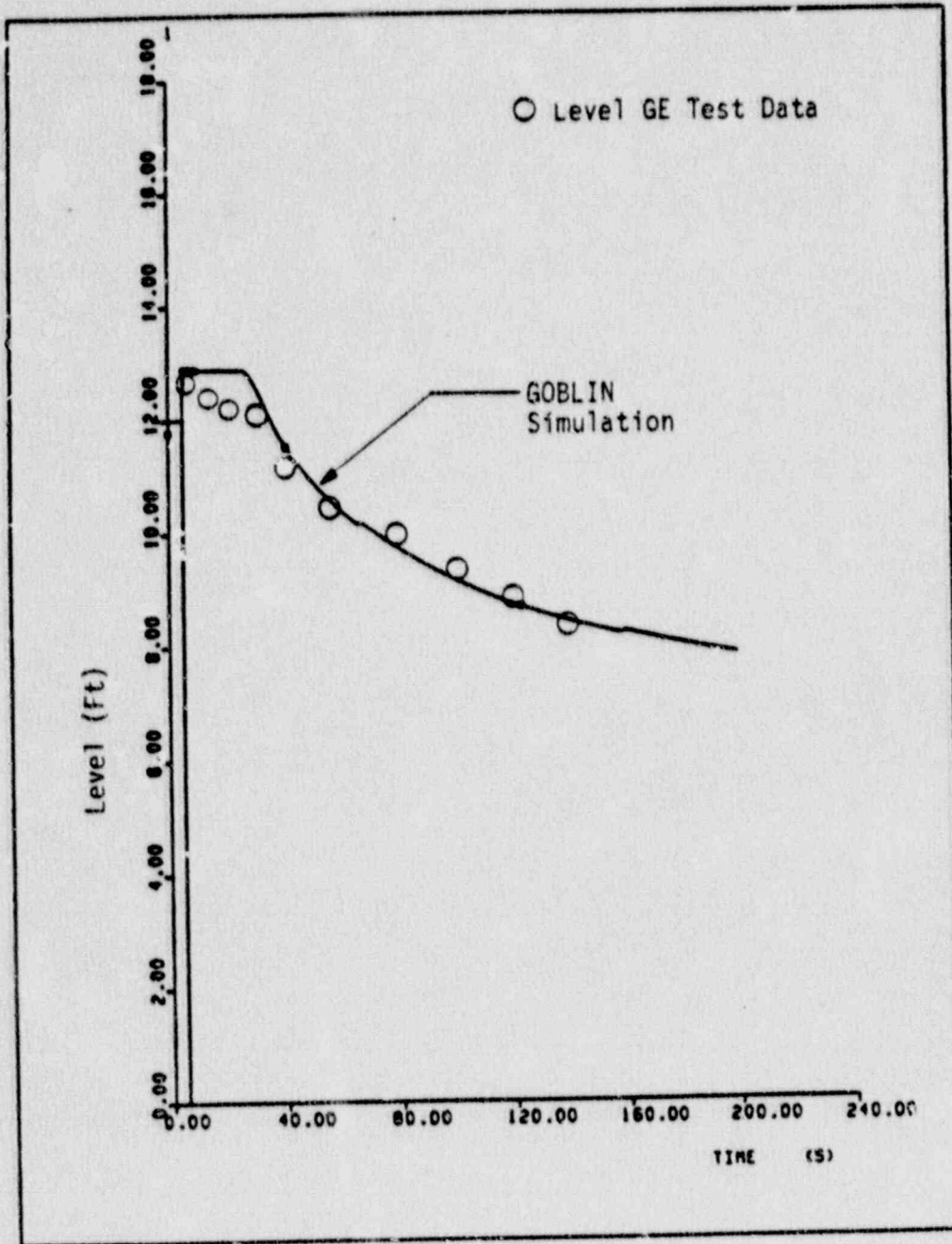


Figure 6-12 - Level Swell Qualification; Level Transient for Test 2

6-57

DIMENSIONLESS VELOCITY OF GAS

DIMENSIONLESS VELOCITY OF LIQUID

a.c.g

Figure 6-13 - CCFL Correlation Comparison for the Upper Tie Plate Region

DIMENSIONLESS VELOCITY OF GAS

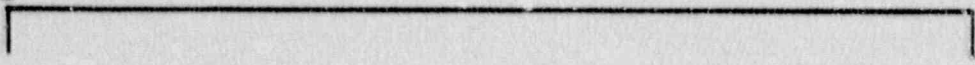


a.c.g.

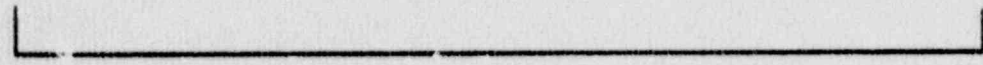
DIMENSIONLESS VELOCITY OF LIQUID

Figure 6-14 - CCFL Correlation Comparison for the Bypass Region

a, c, g



DIMENSIONLESS VELOCITY OF GAS



DIMENSIONLESS VELOCITY OF LIQUID

Figure 6-15 - CCFL Correlation Comparison for the Side Entry Orifice Region

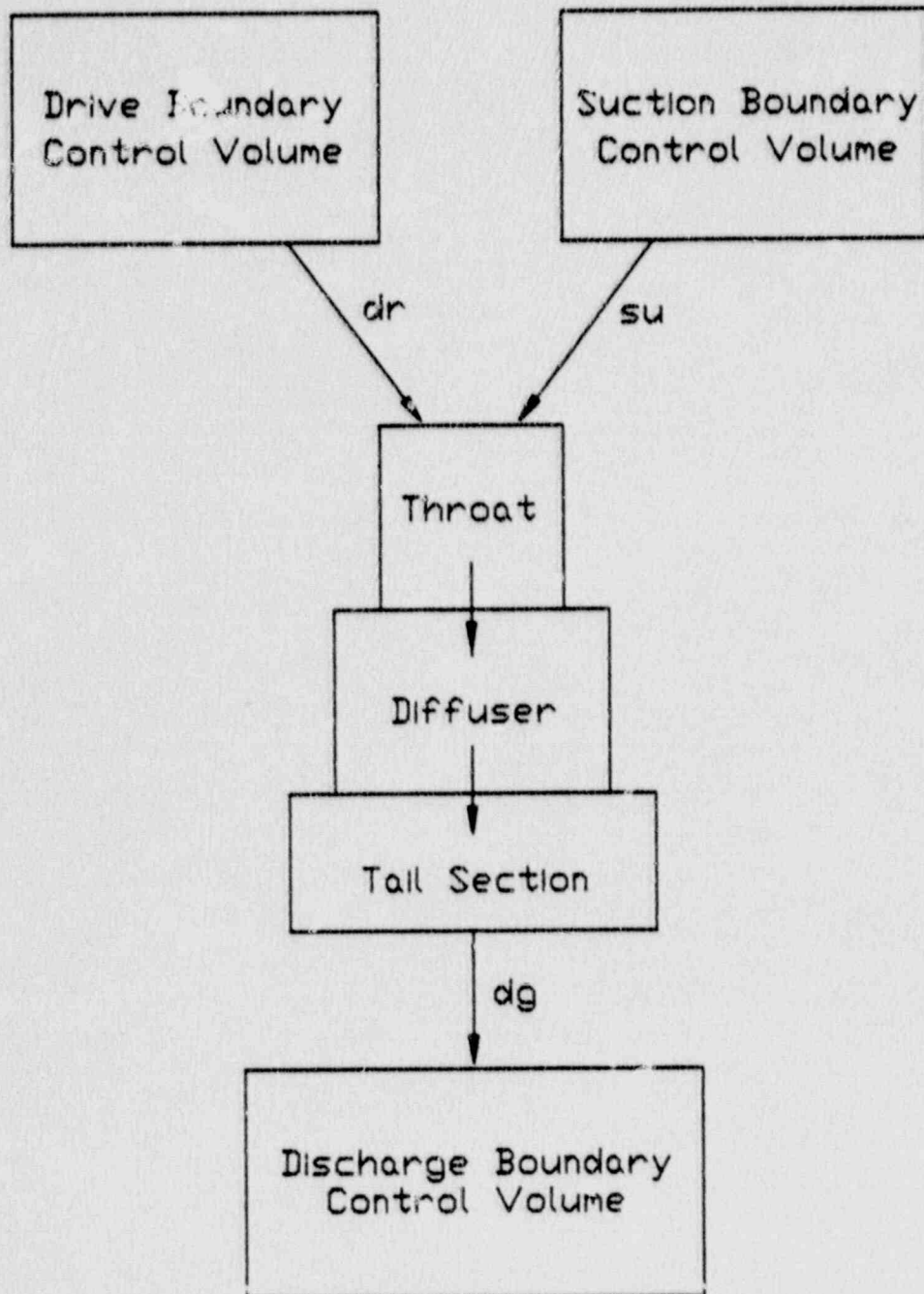


Figure 6-16 - Nodalization for Jet Pump Qualification

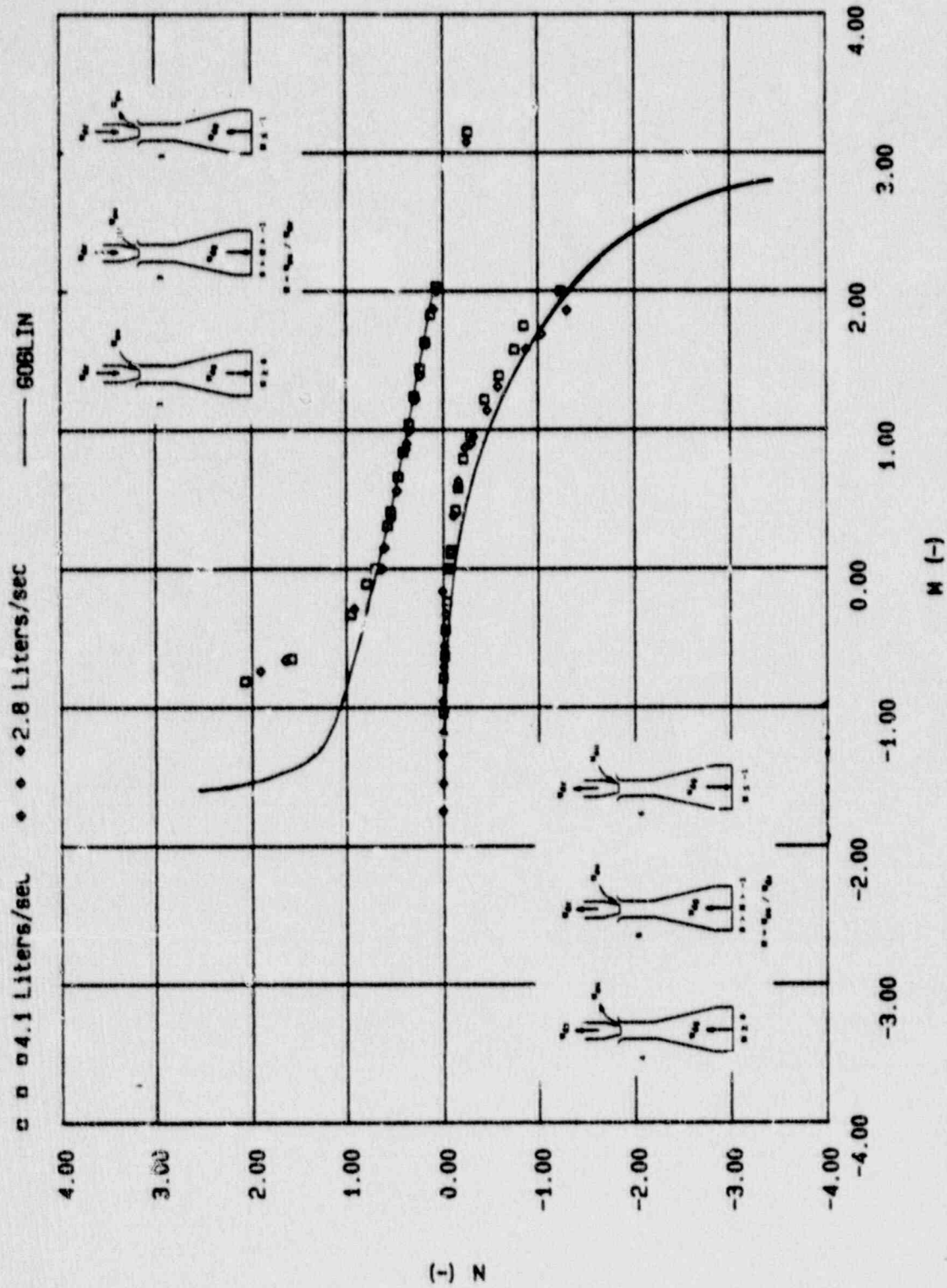
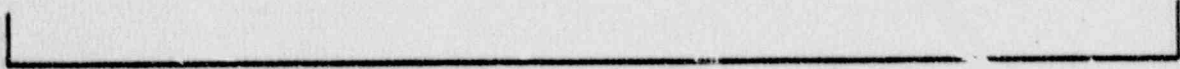
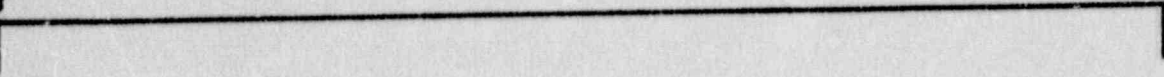


Figure 6-17 - Comparison of Measured and Calculated Jet Pump Performance



a,b,c



H  
Data /  
Correlation

QUALITY

Figure 6-13 - Post-Dryout Heat Transfer Coefficient Comparison with G-1 Test Data

a, b, c



$H_{Data}/H_{Correlation}$

QUALITY

Figure 6-19 - Post-Dryout Heat Transfer Coefficient Comparison with G-2 Test Data (Cocurrent flow)

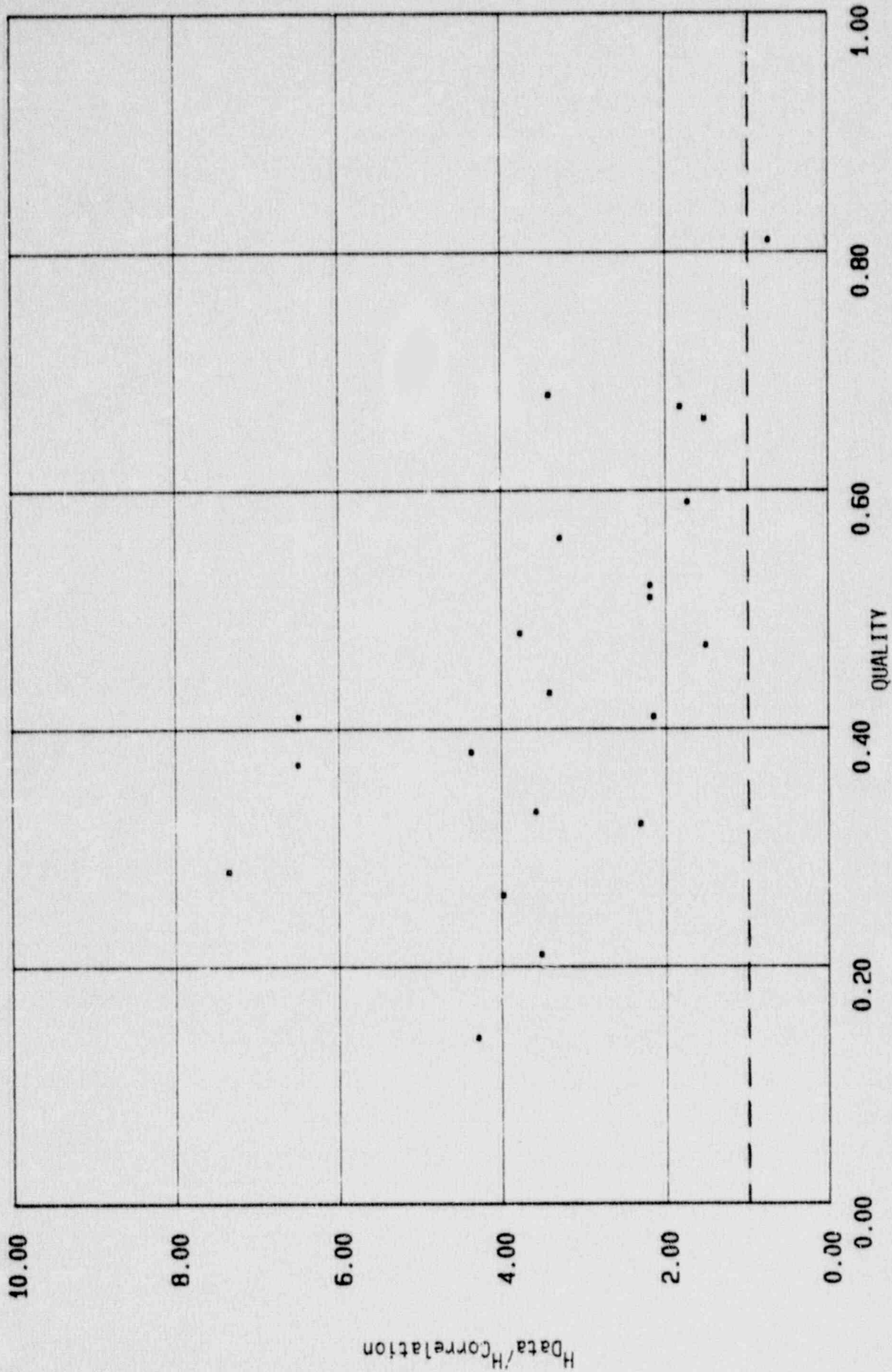


Figure 6-20 - Post-Dryout Heat Transfer Coefficient Comparison with FLECHT Low Flow Reflooding Data

$H_{Data}/H_{Correlation}$

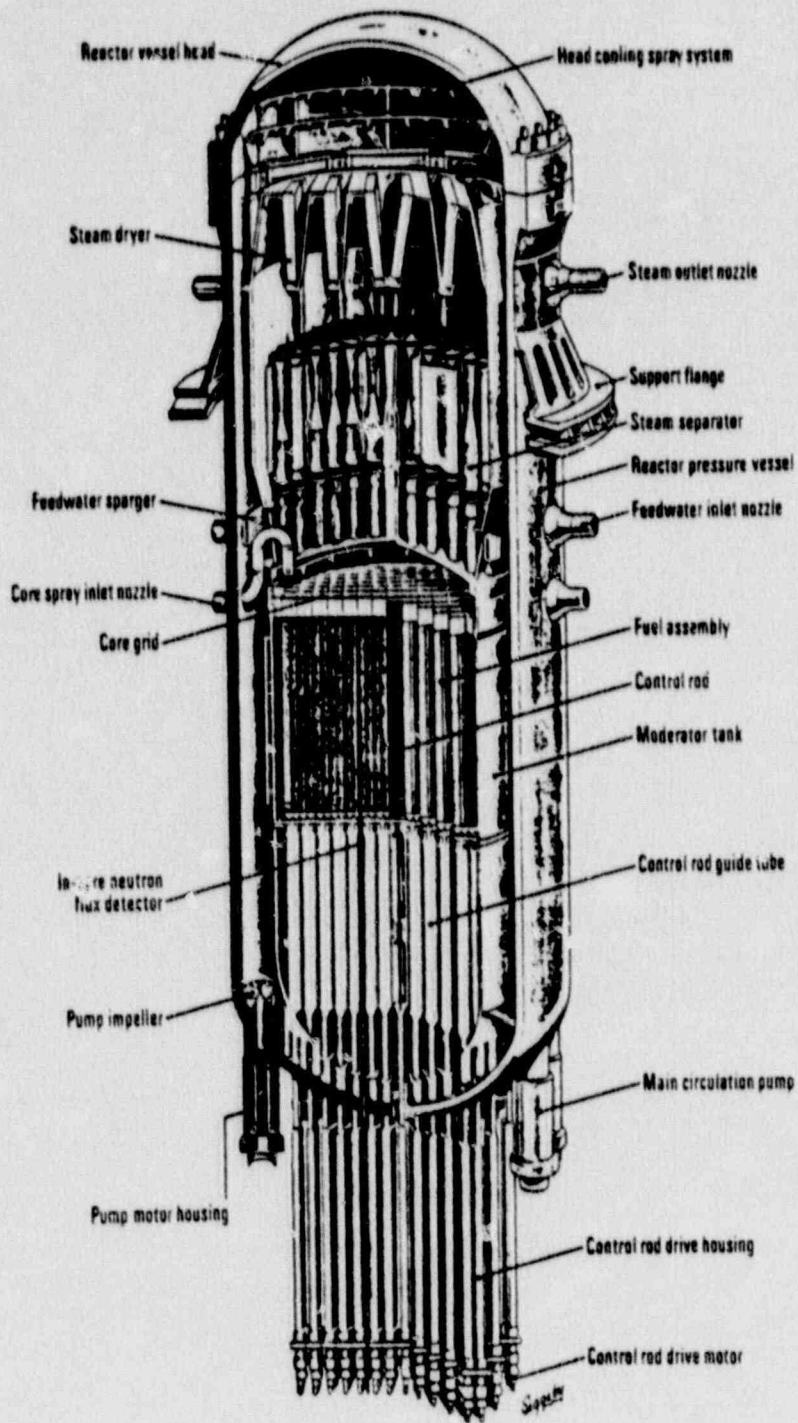


Figure 6-21 TVO-1 Internal Recirculation Pump Plant

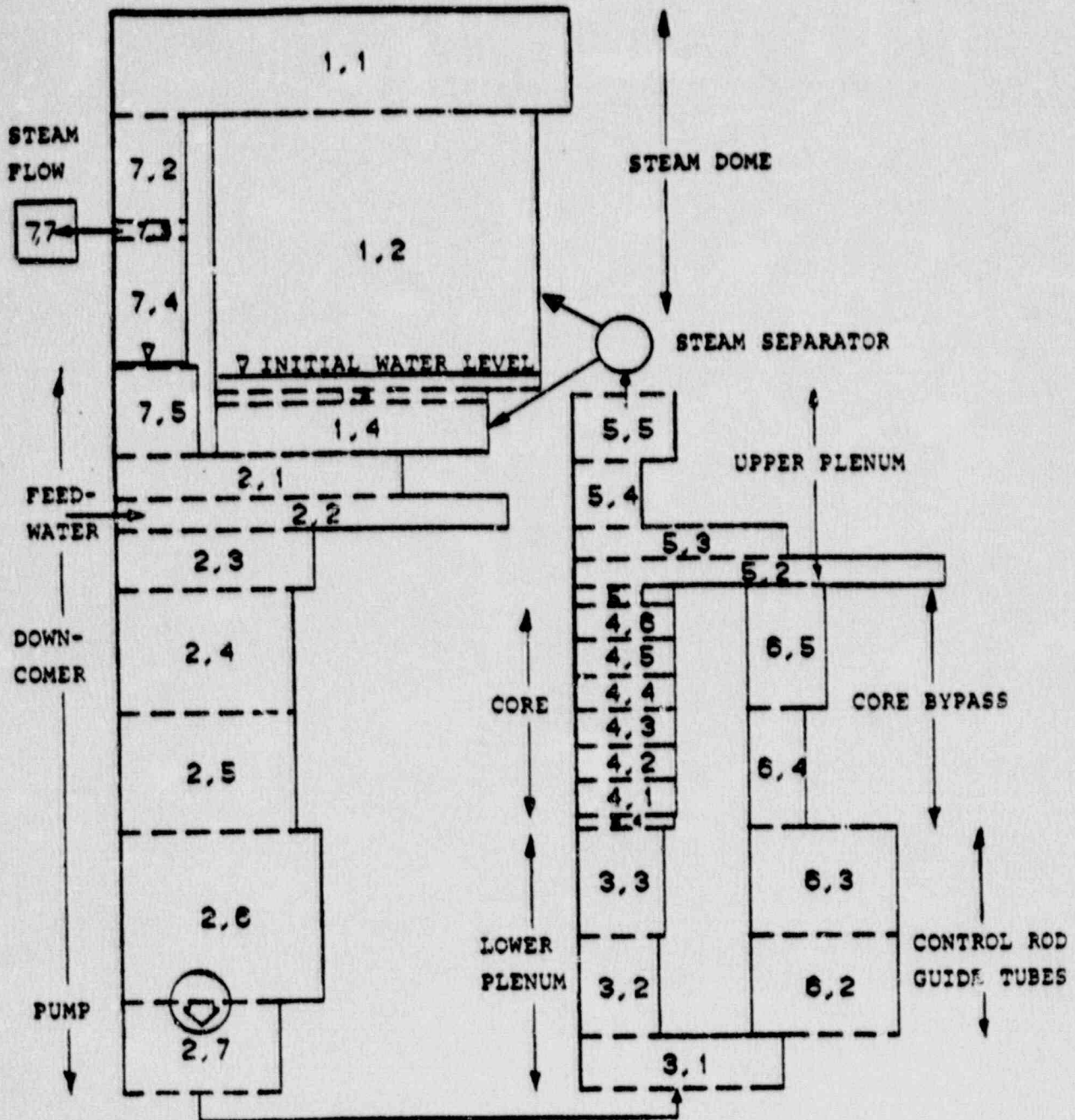


Figure 6-22 - GOBLIN Nodalization of TVO-1 for Pump Trip Transient

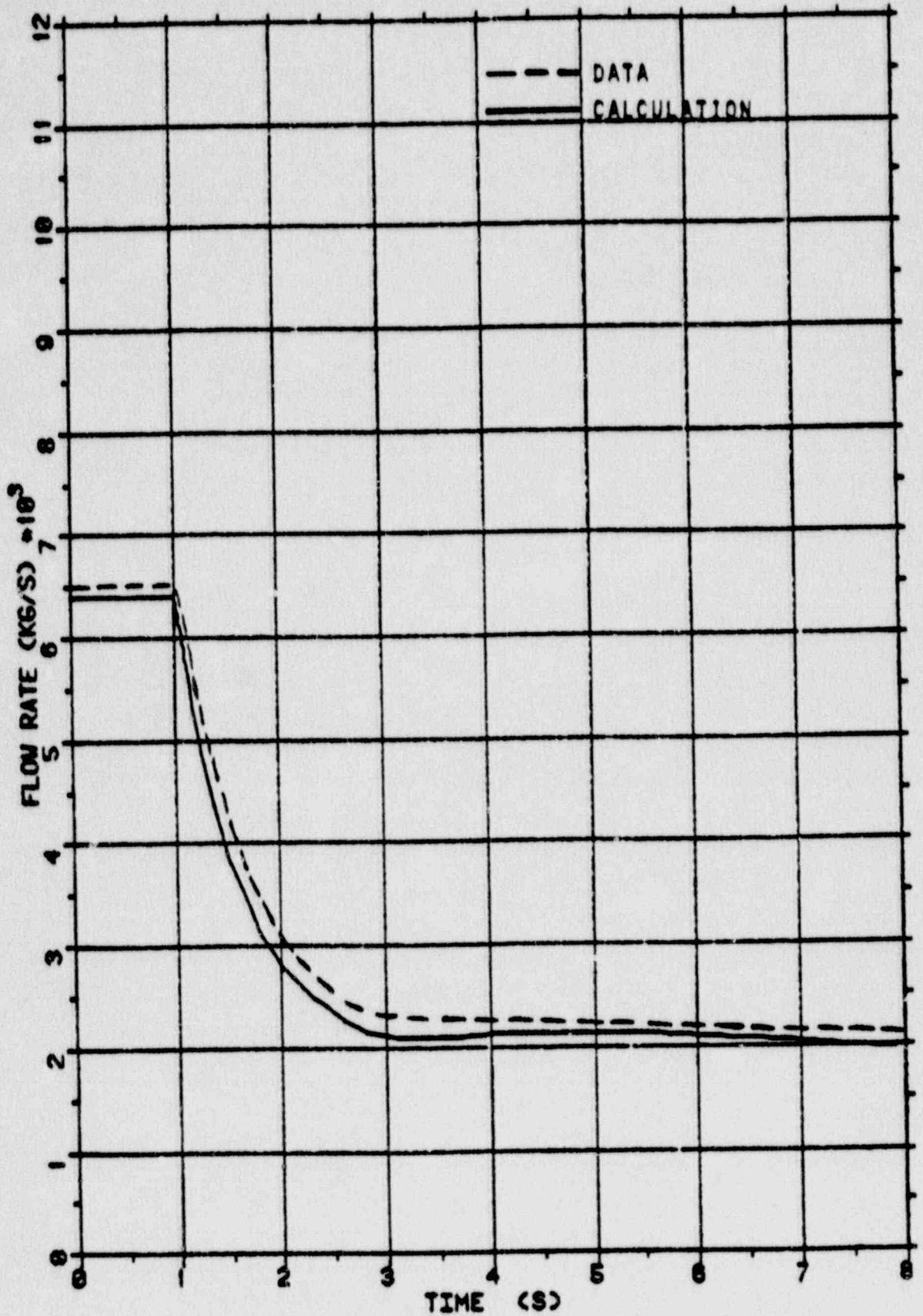


Figure 6-23 - Comparison of Core Channel Inlet Flow Rate for TVO-1 Pump Trip Transient

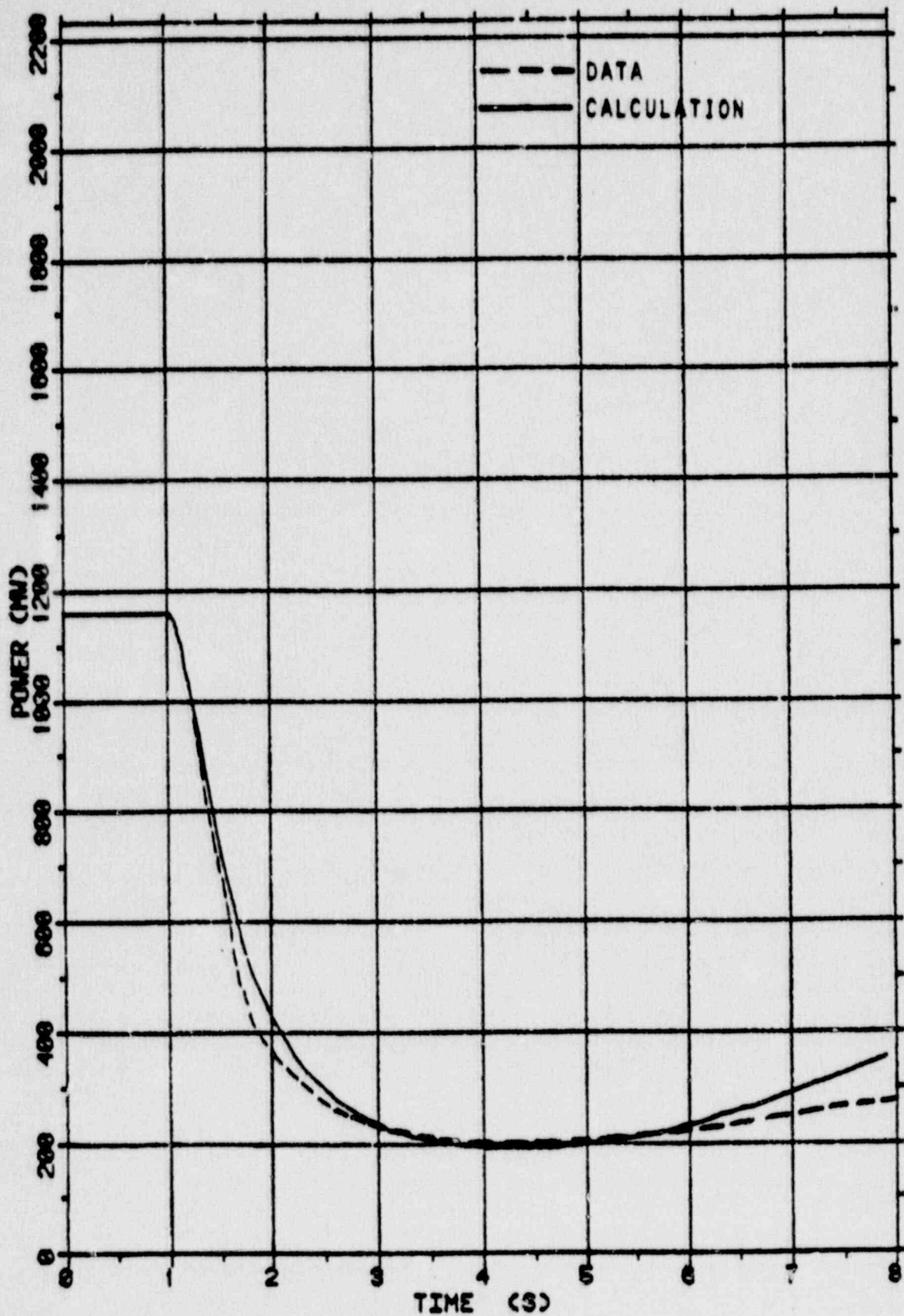
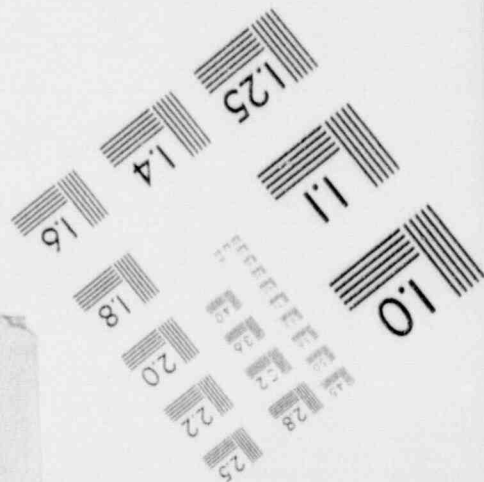
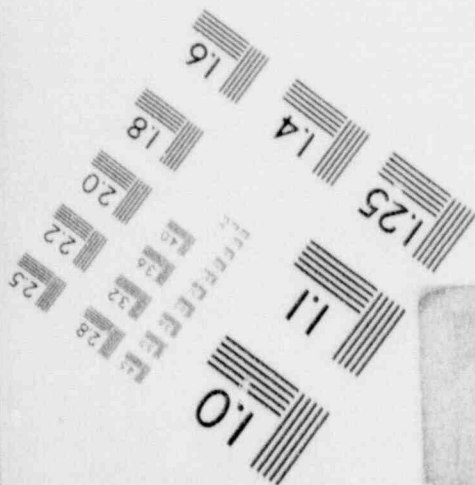
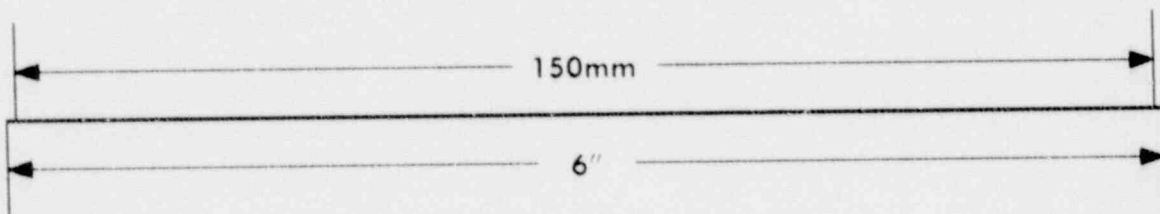
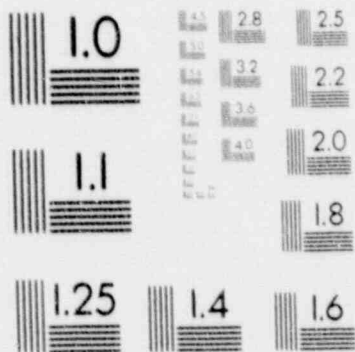
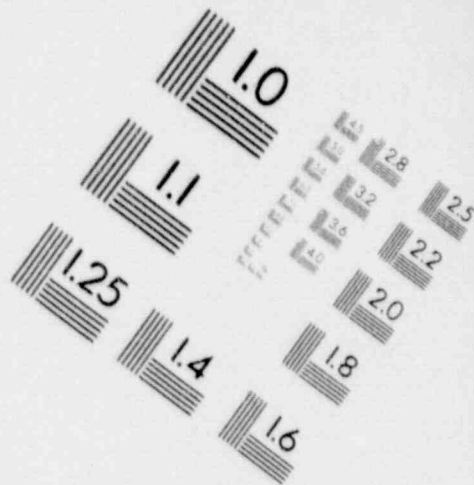
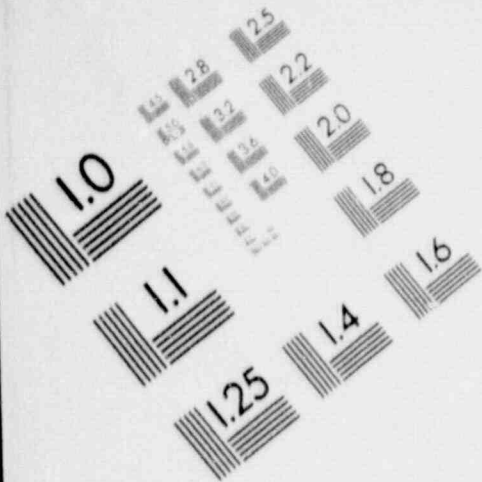


Figure 6-24 - Comparison of Fission Power for TVO-1 Pump Trip Transient

# 1

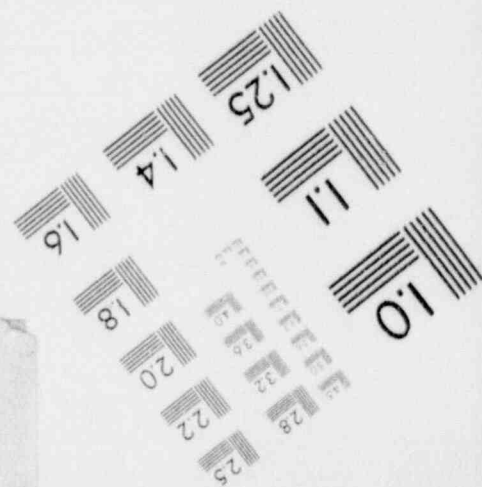
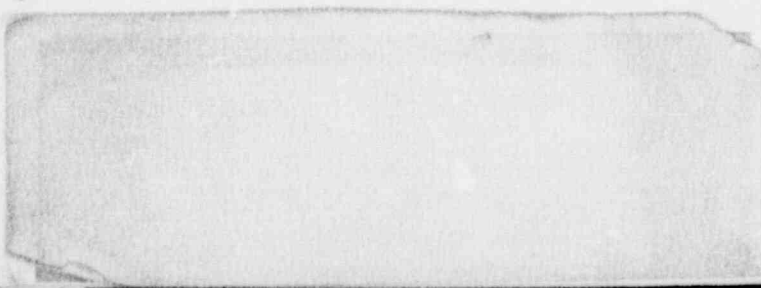
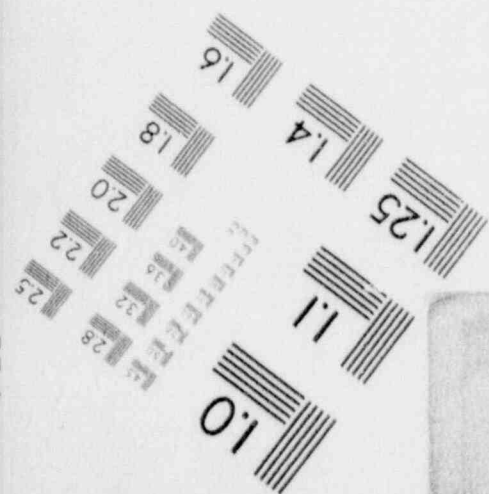
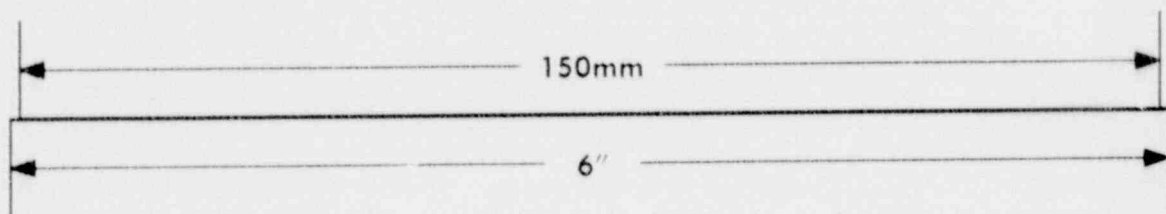
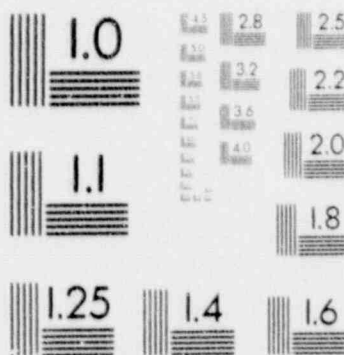
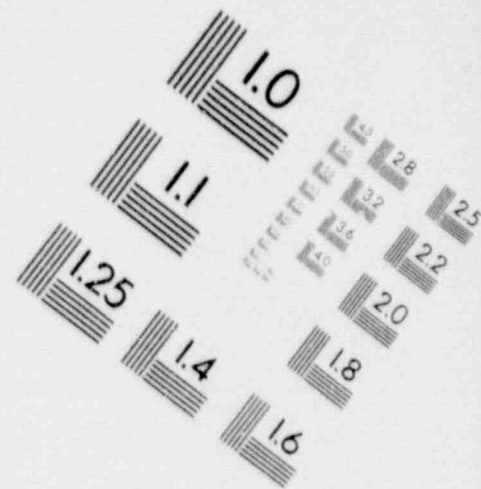
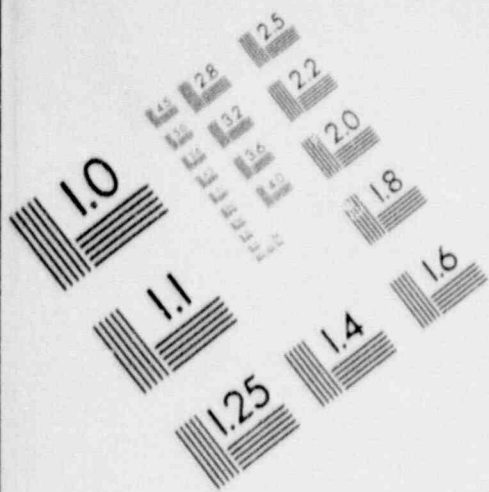
## IMAGE EVALUATION TEST TARGET (MT-3)





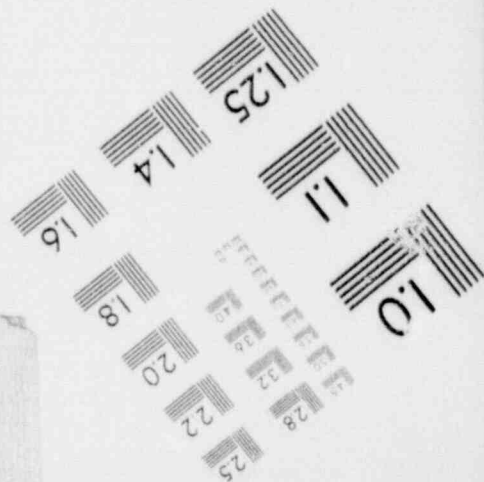
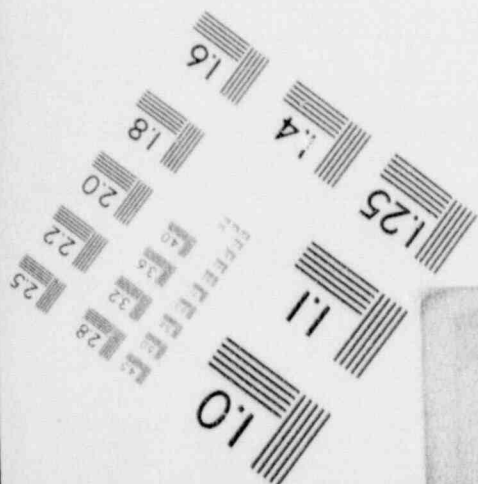
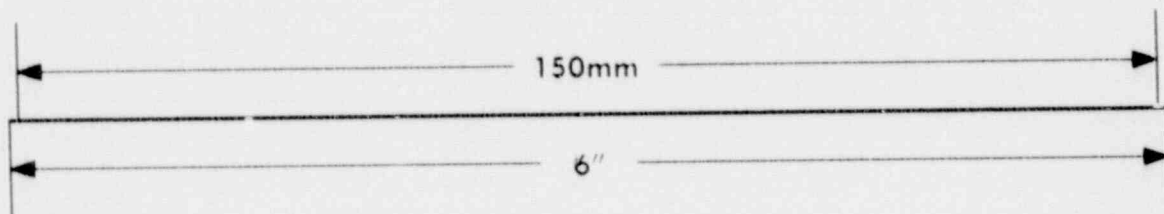
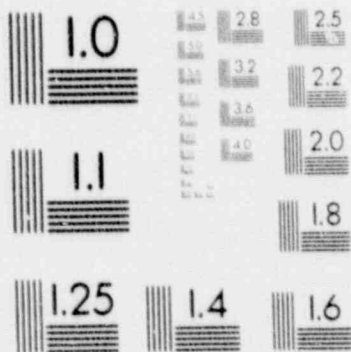
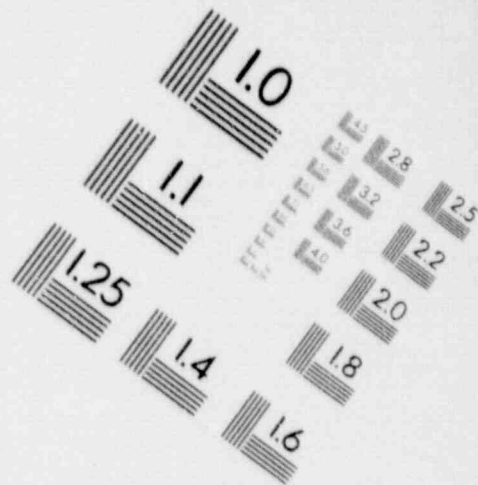
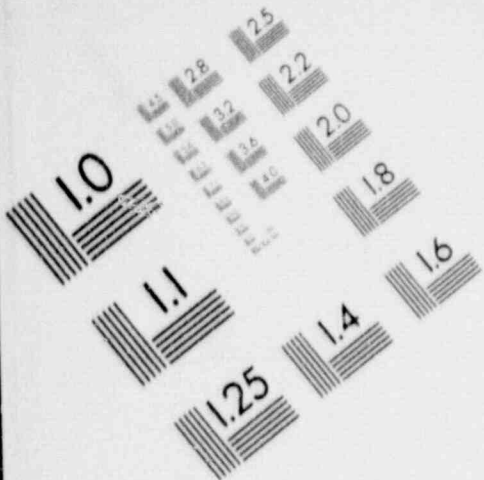
# 1

## IMAGE EVALUATION TEST TARGET (MT-3)



# 1

## IMAGE EVALUATION TEST TARGET (MT-3)



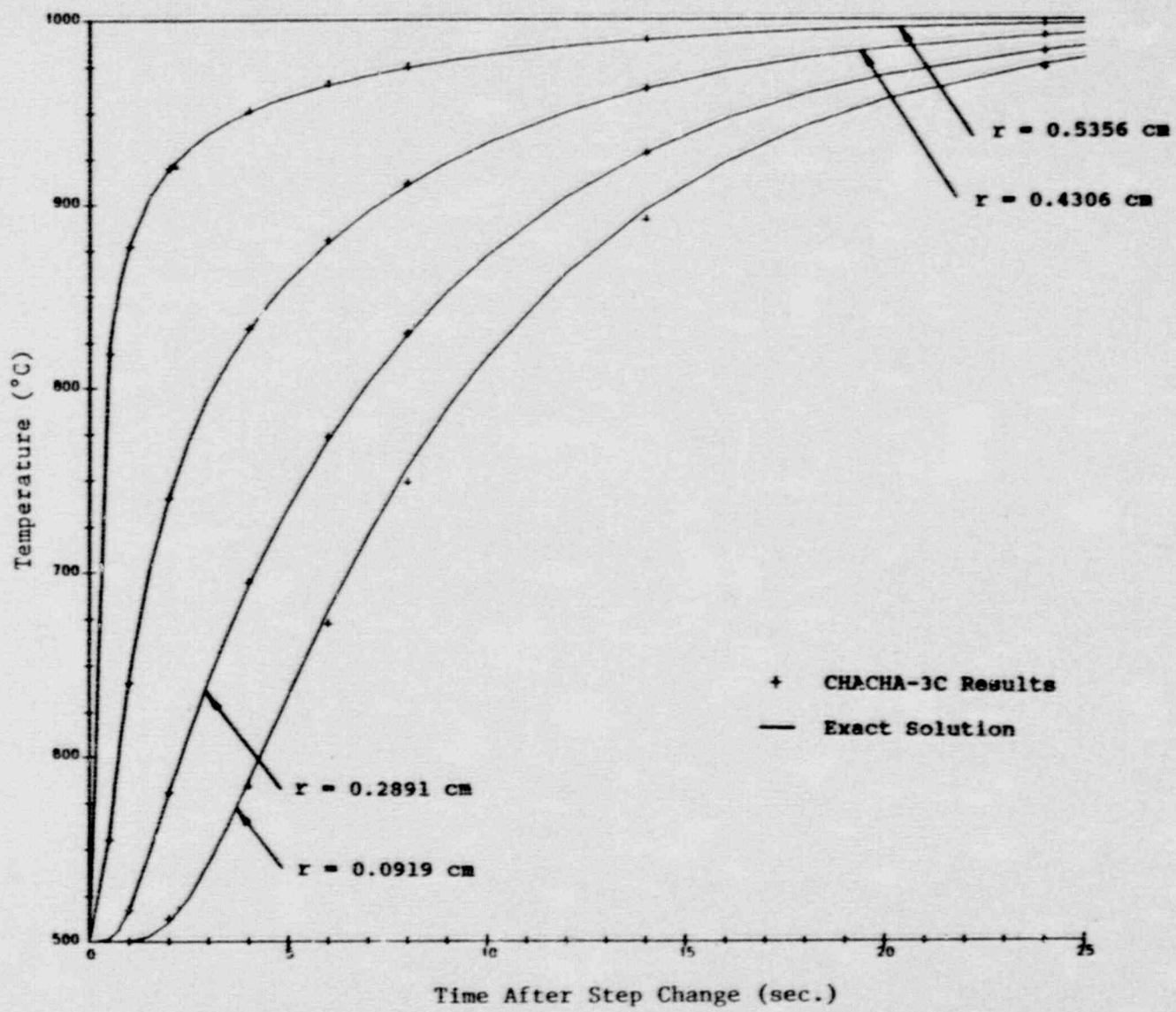


Figure 6-25 - Conduction Model Qualification - Step Change in Surface Temperature

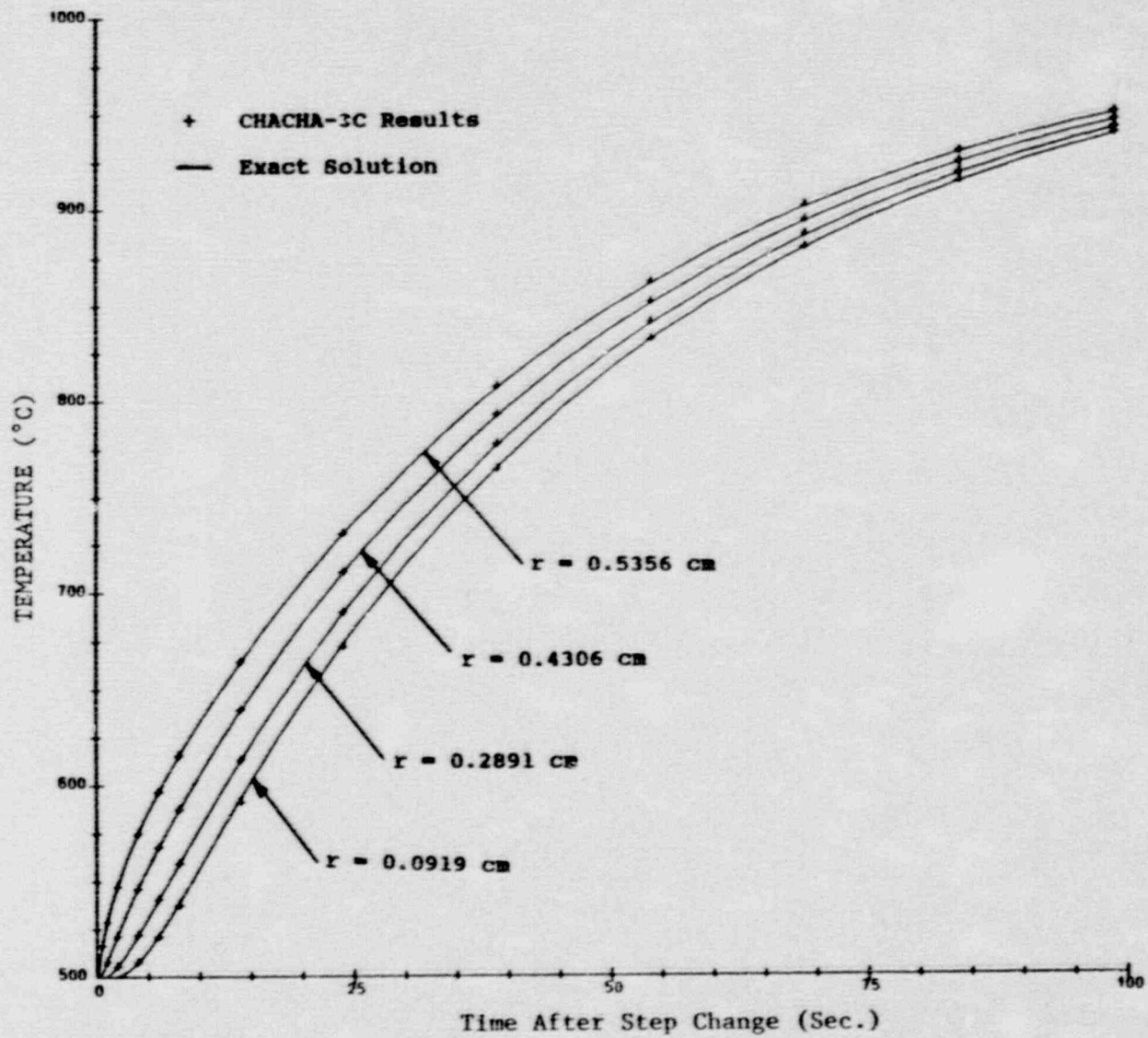


Figure 6-26 - Conduction Model Qualification - Step Change in Coolant Temperature with Convection

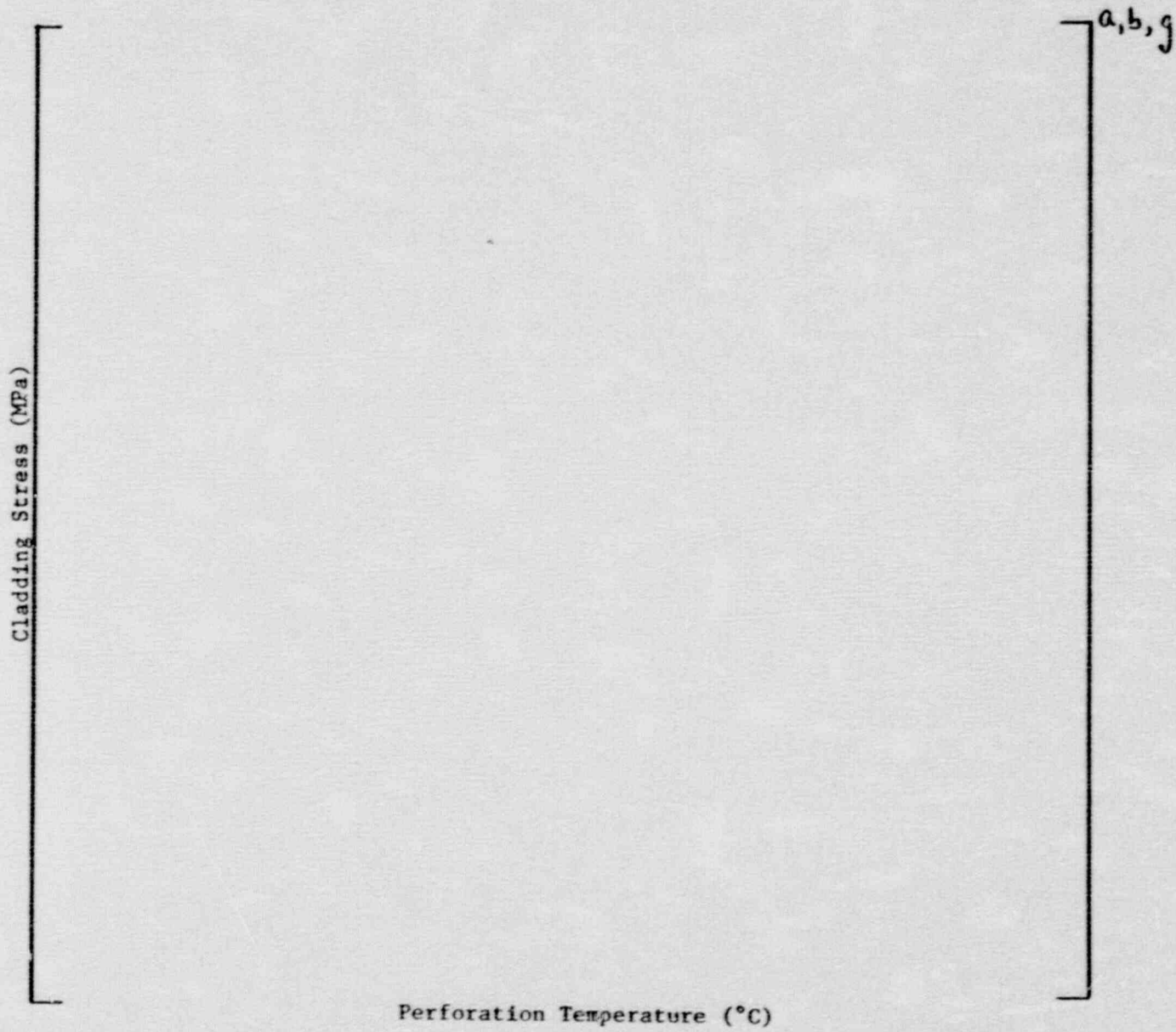


Figure 6-27 - Comparison of Rod Burst Correlation with Data

6-72

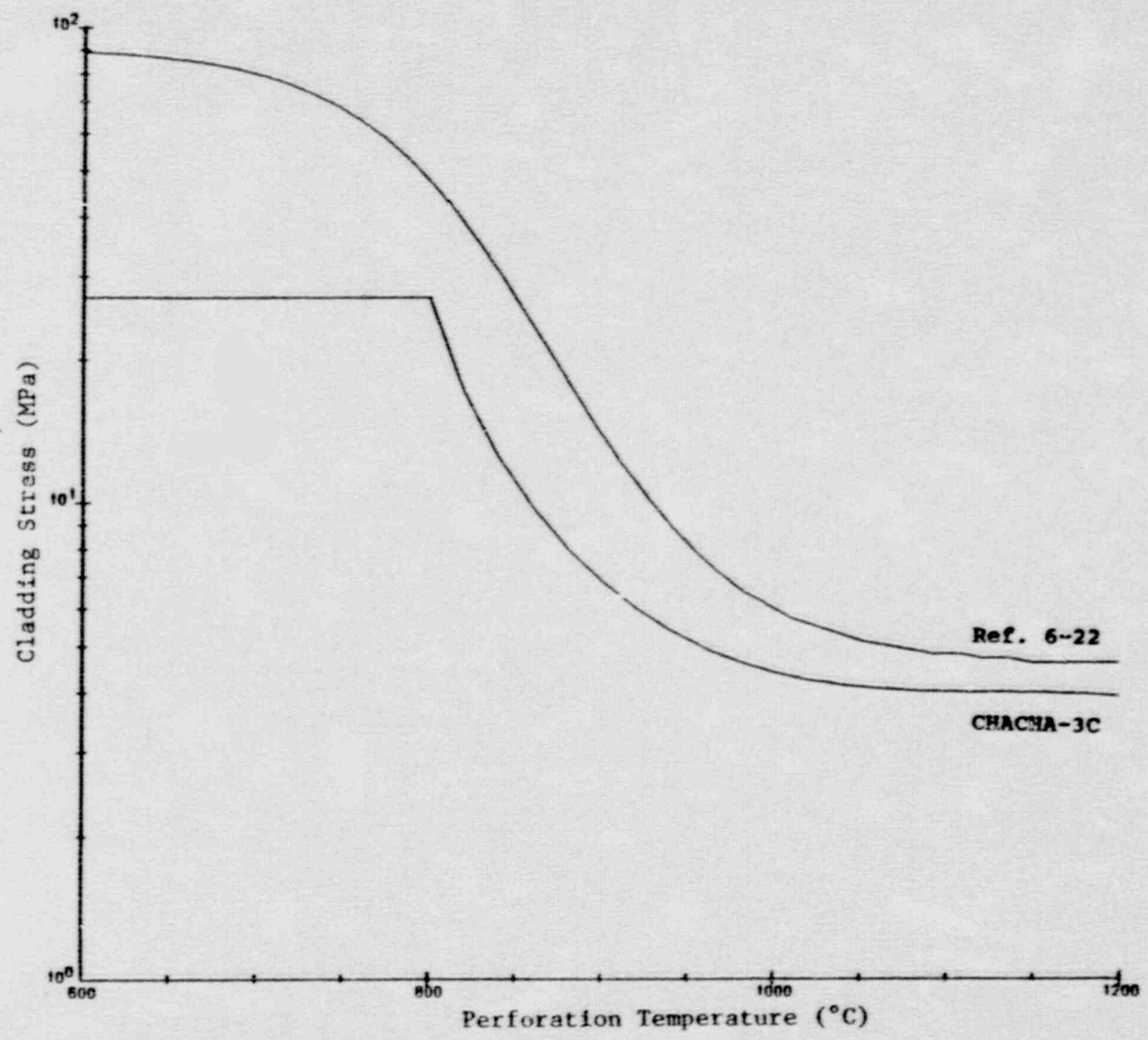
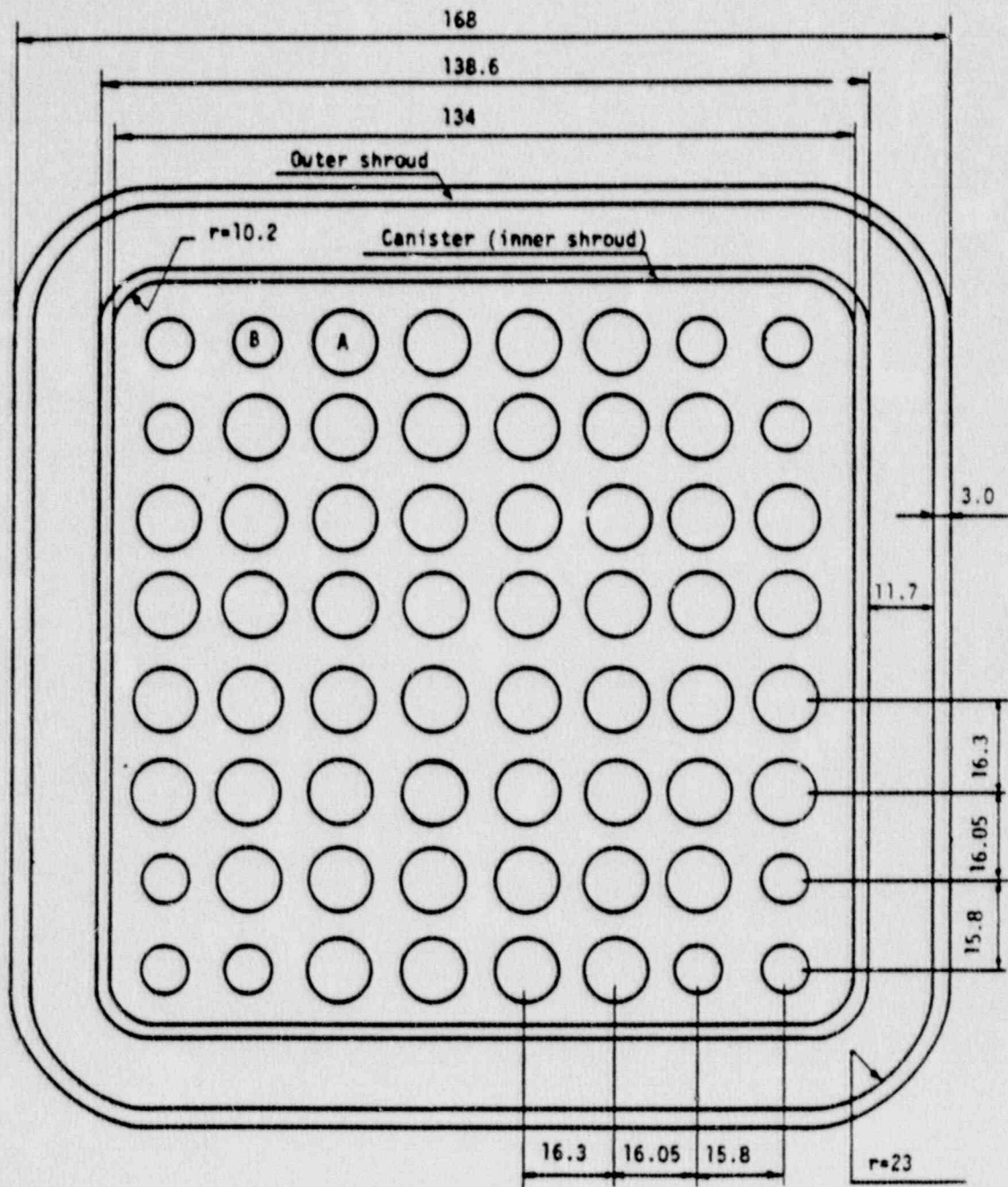


Figure 6-28 - Comparison of Rod Burst Correlations



A:  $\phi = 12.25$

B:  $\phi = 11.75$

(dimensions in mm.)

Figure 6-29 - Cross-Section of Bundle Used for Radiation-Only Test

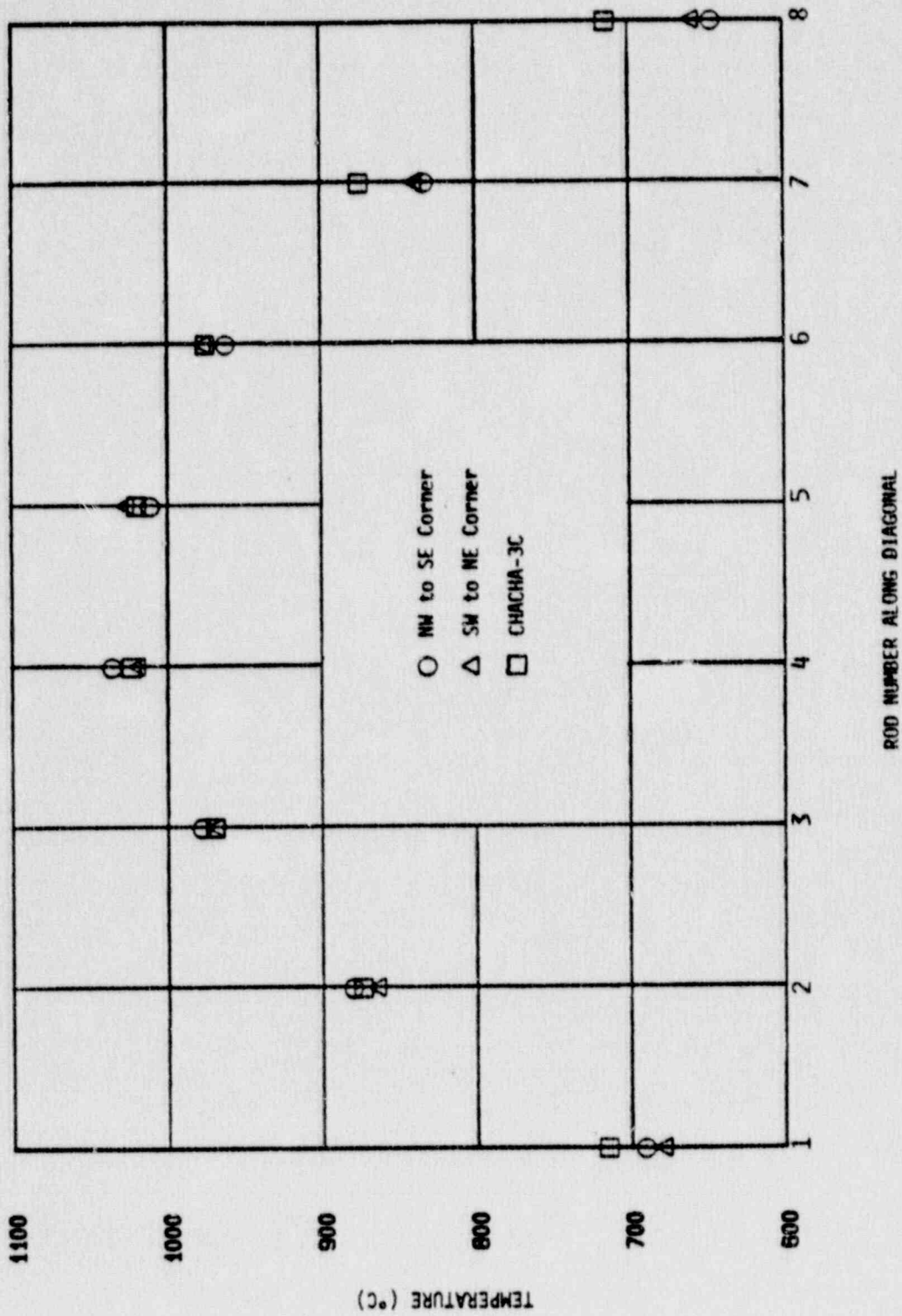


Figure 6-30 - CHACHA-3C Comparison with Radiation Only Data



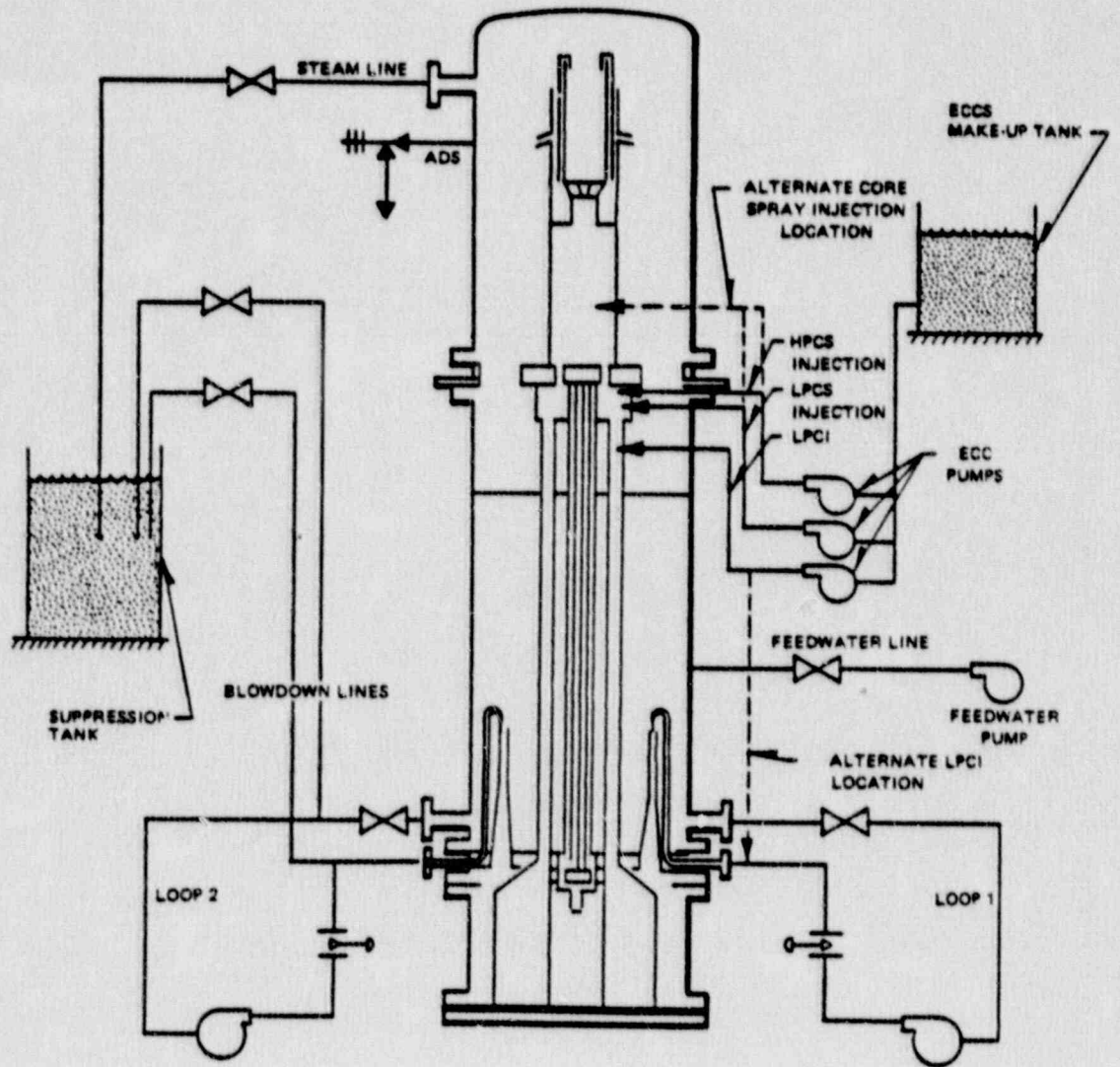


Fig. 6-31 TLTA Facility Schematic (from Ref. 6-24)

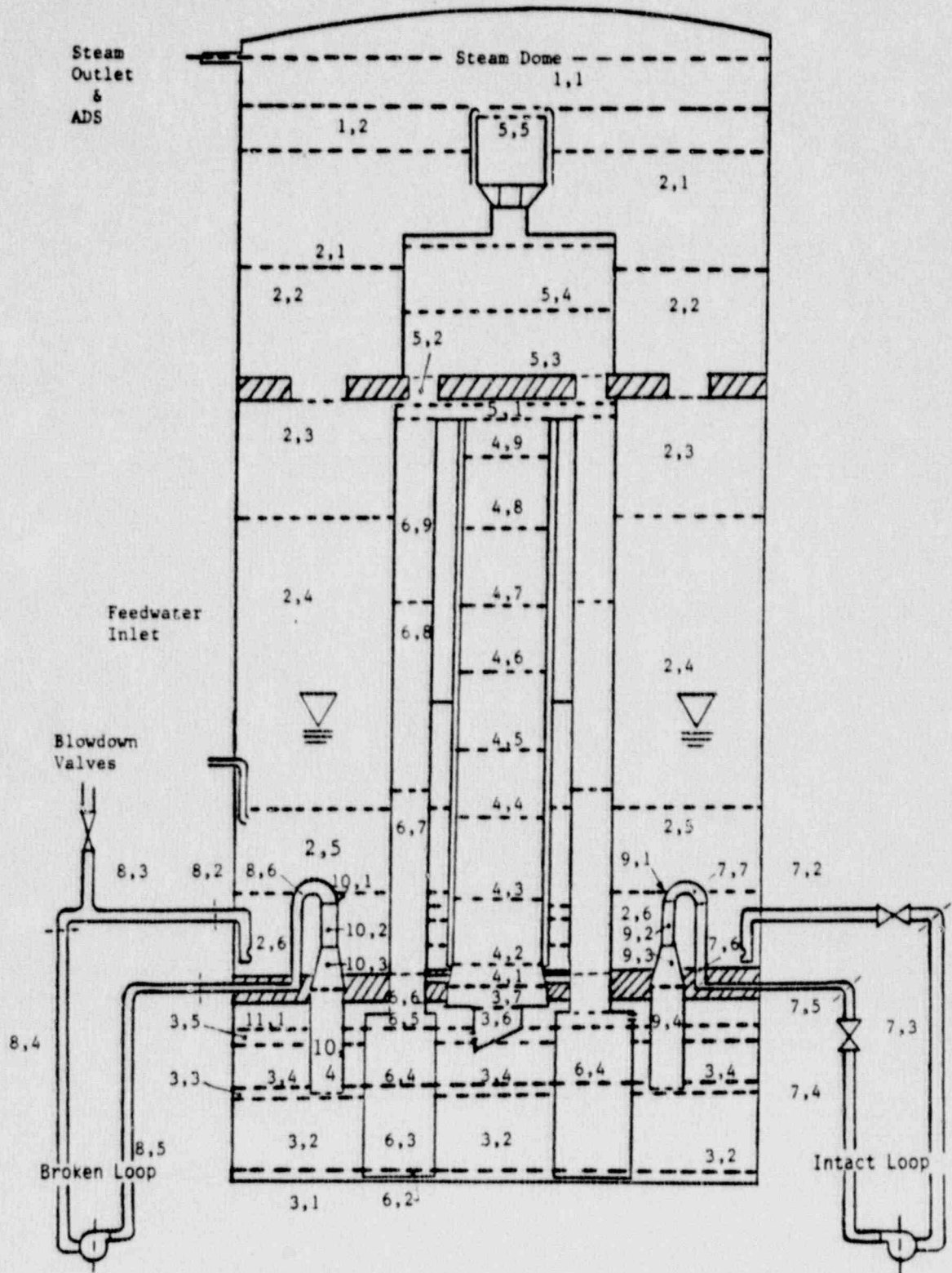


Fig. 6-32 Goblin Noding Diagram for TLTA5A

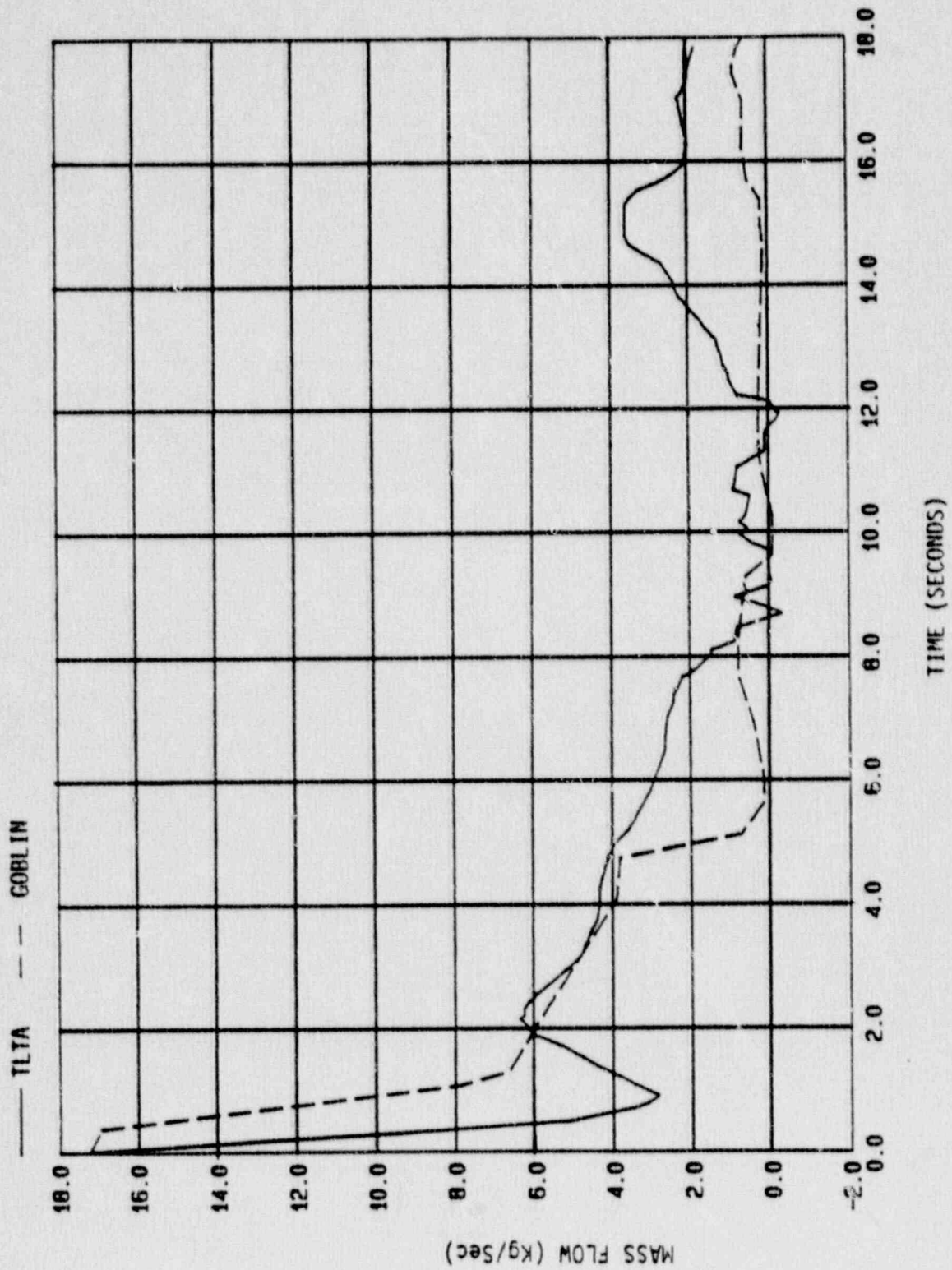


Figure G-33 - Bundle Flow Rate for TLIA5A Test 6245/2

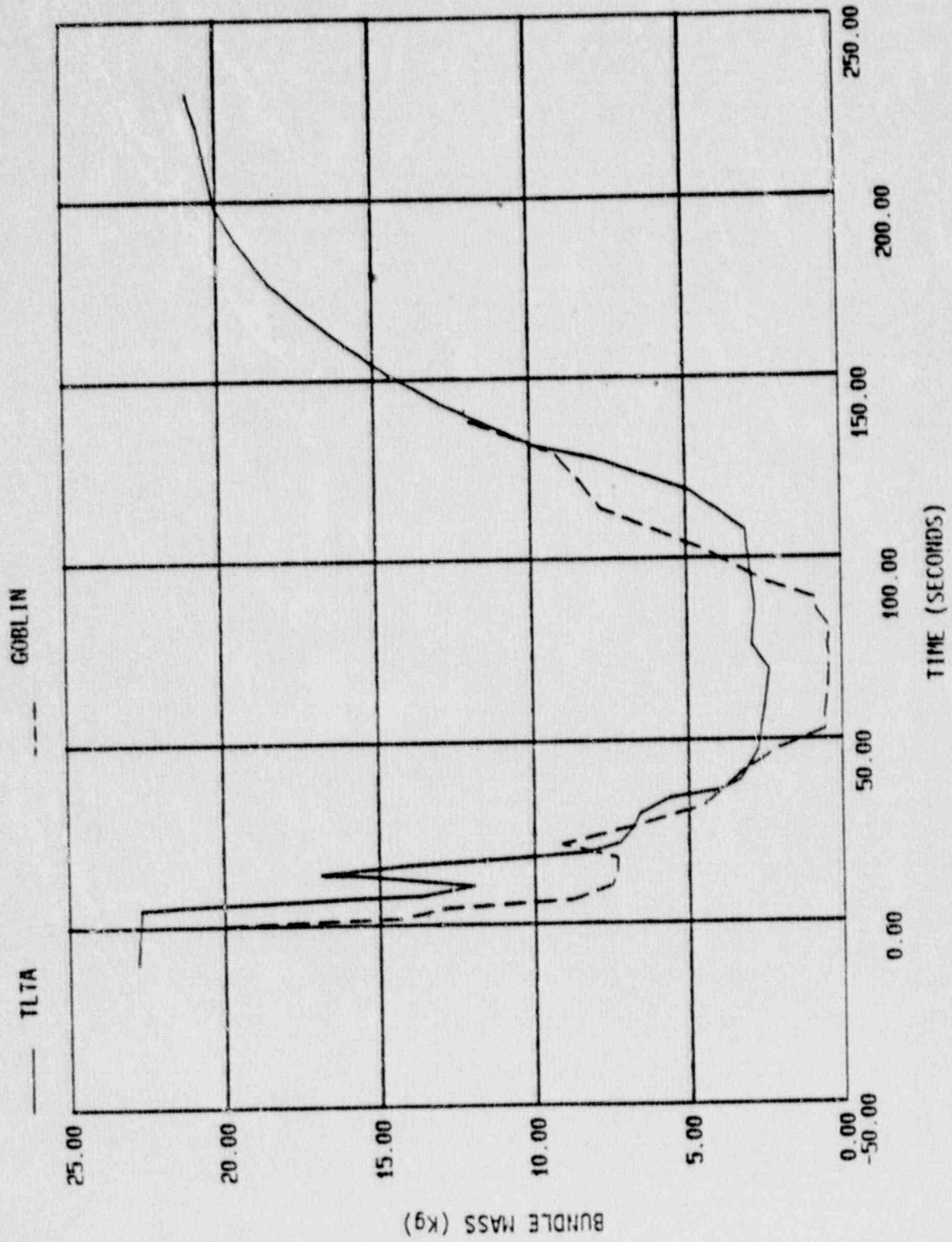


Figure 6-34 - Bundle Mass for TLTA5A Test 6425/2

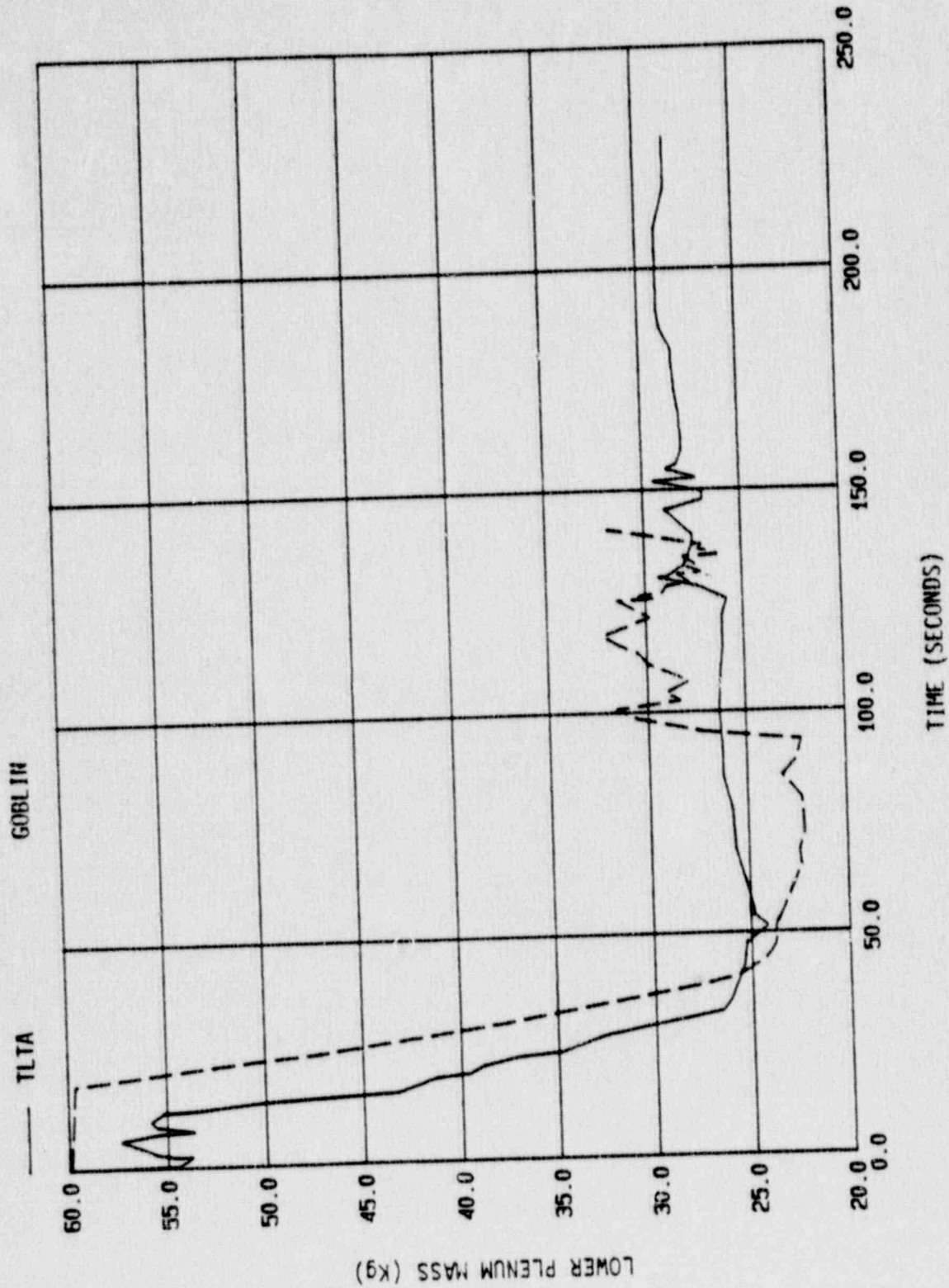


Figure 6-35 - Lower Plenum Mass for TLTA5A Test 6425/2

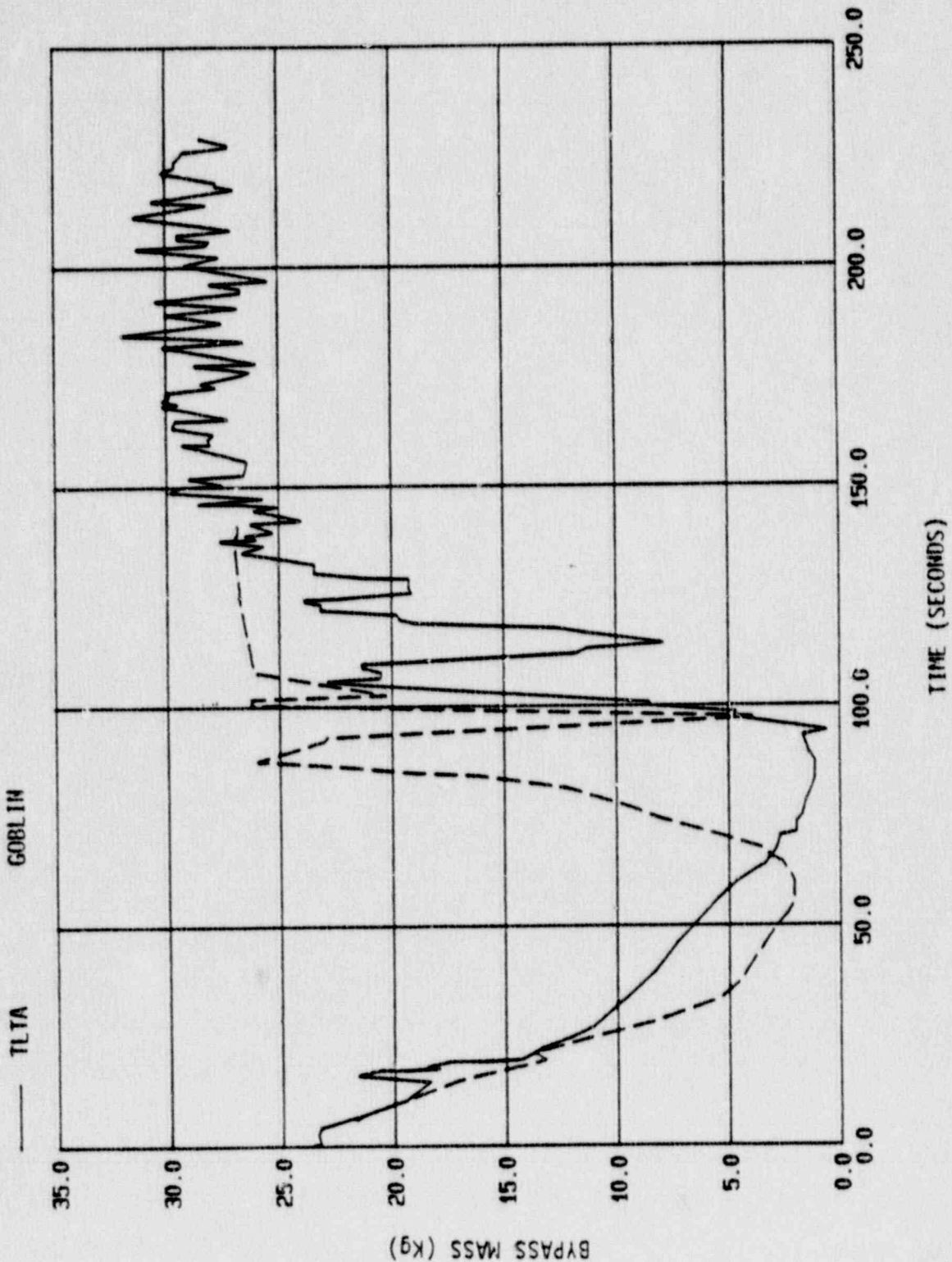


Figure 6-36 - Bypass Mass for TLTA5A Test 6425/2

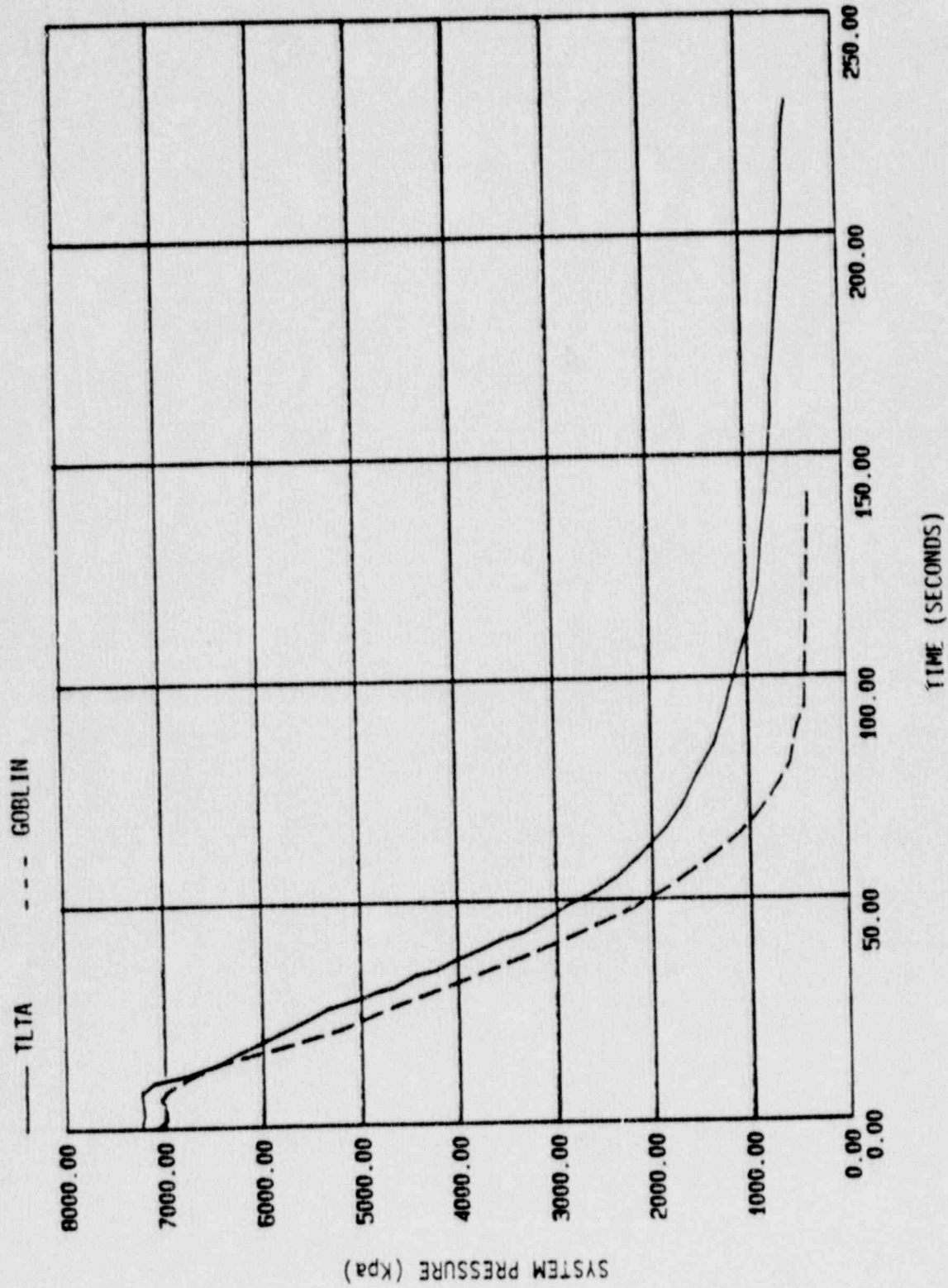


Figure 6-37 - System Pressure for TLTA5A Test 6425/2

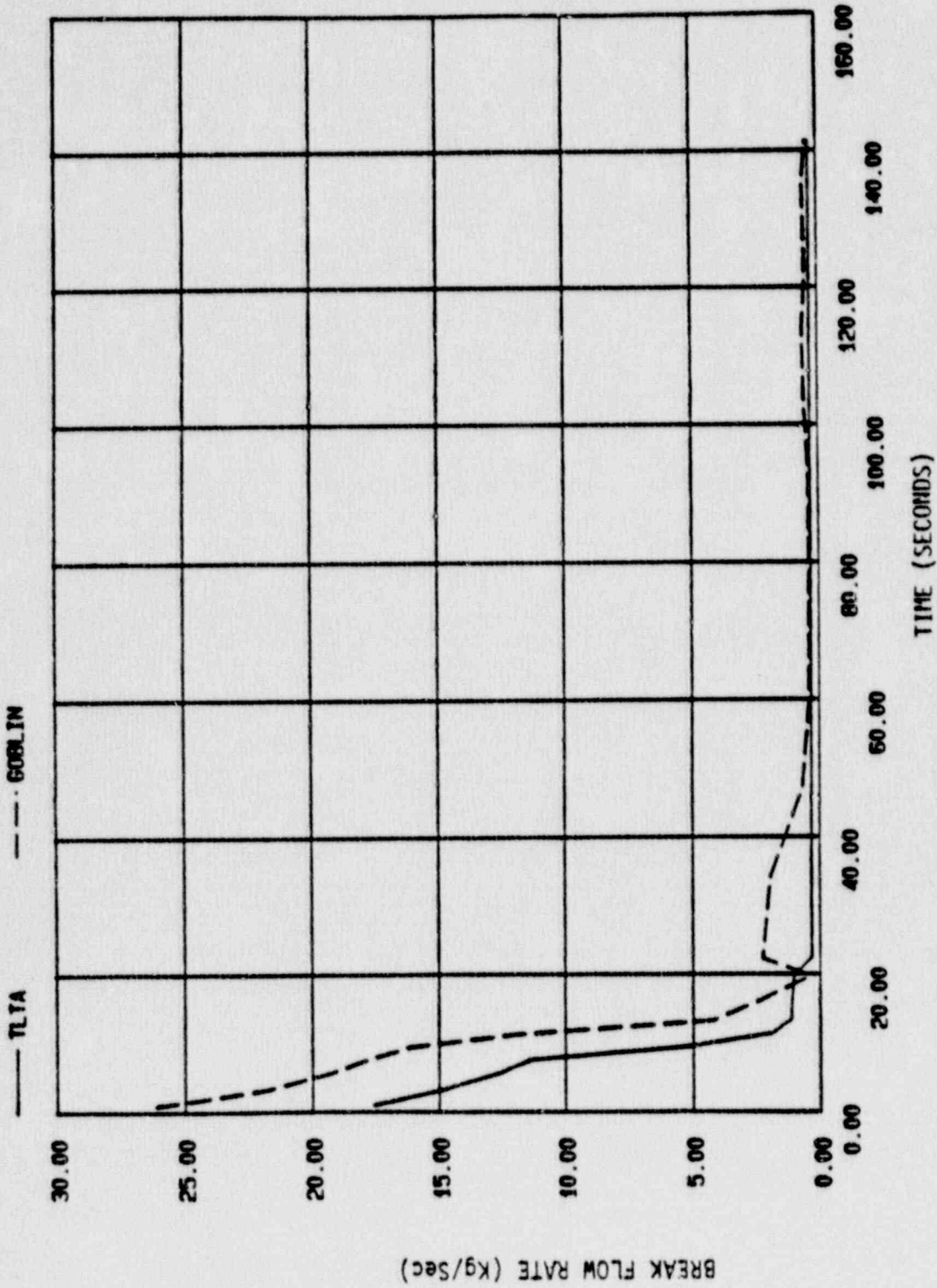


Figure 6-38 - Break Flow for TLTA5A Test 6425/2



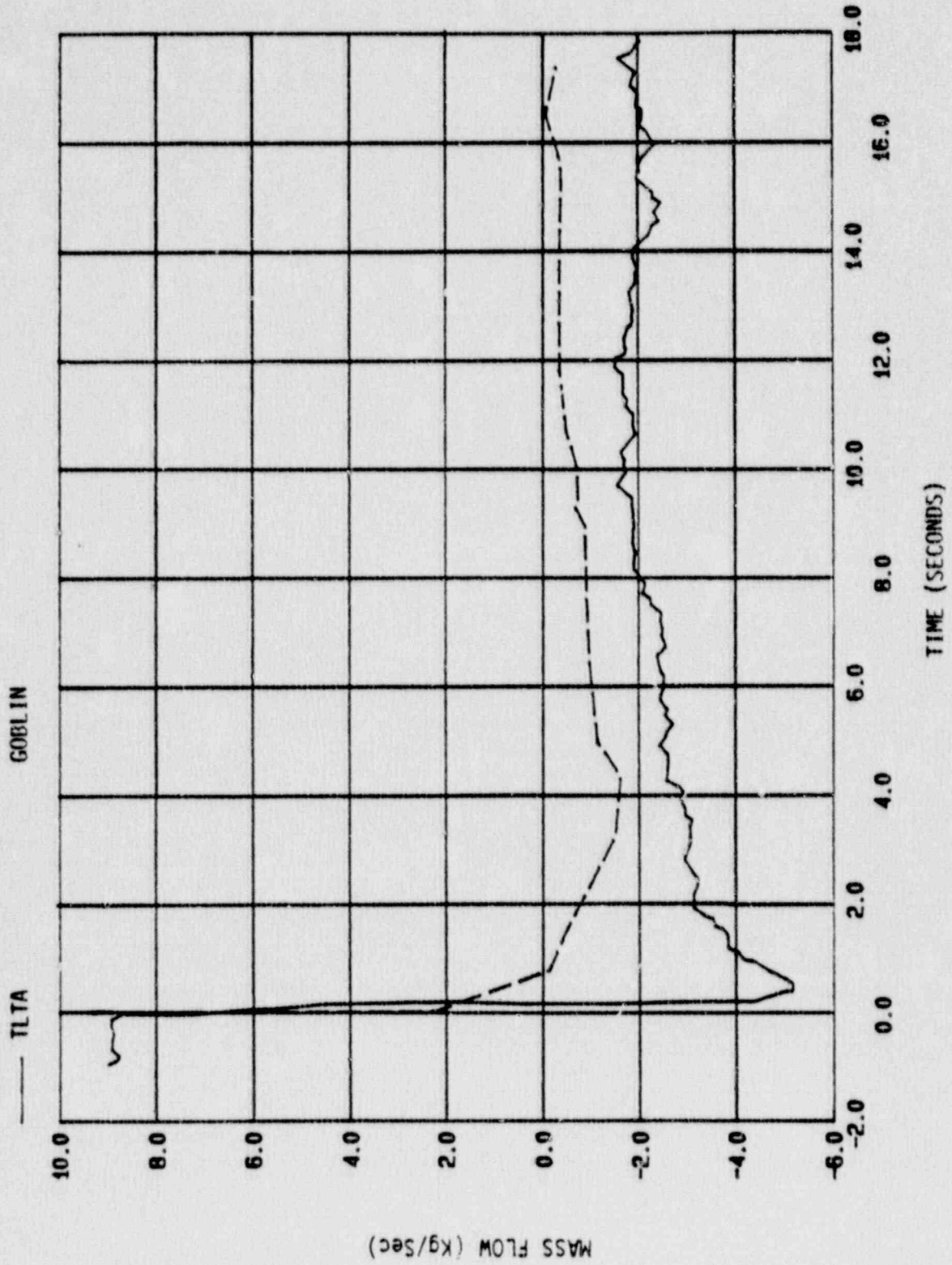


Figure 6-39 - Broken Jet Pump Flow Rate for TLTA5A Test 6425/2

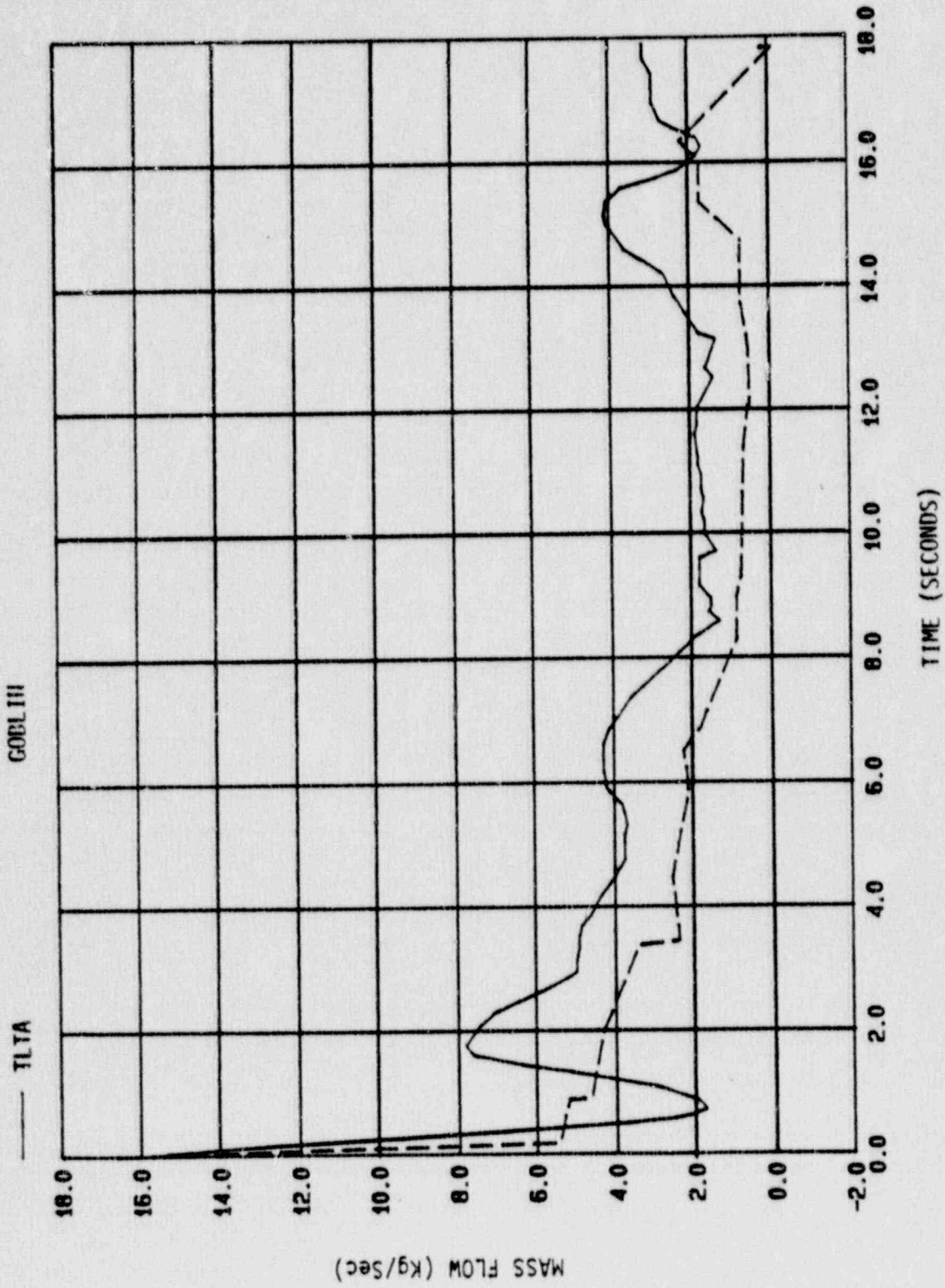


Figure 6-40 - Bundle Flowrate for TLTA5A Test 6423/3

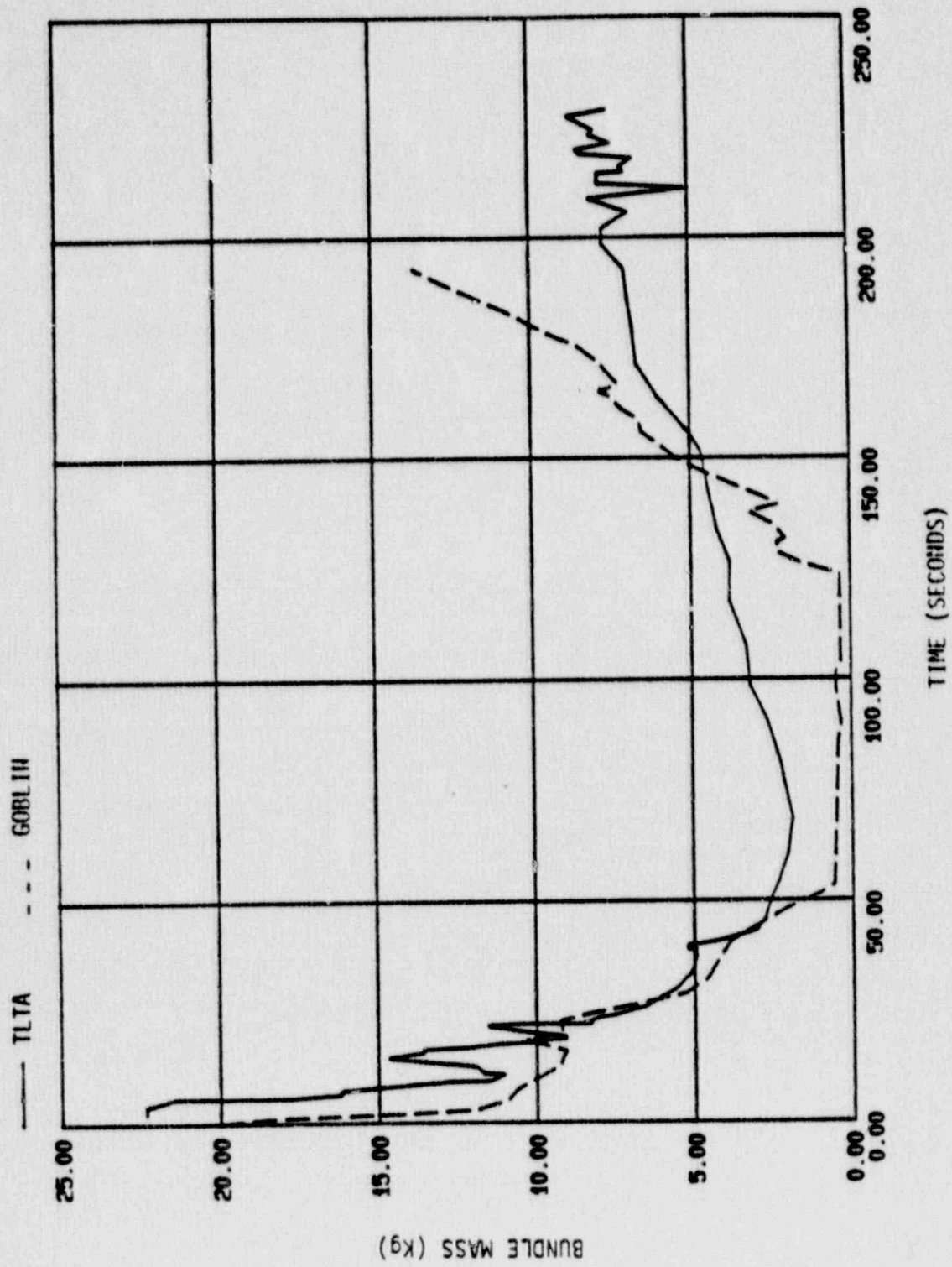


Figure 6-41 - Bundle Mass for TLTA5A Test 6423/3

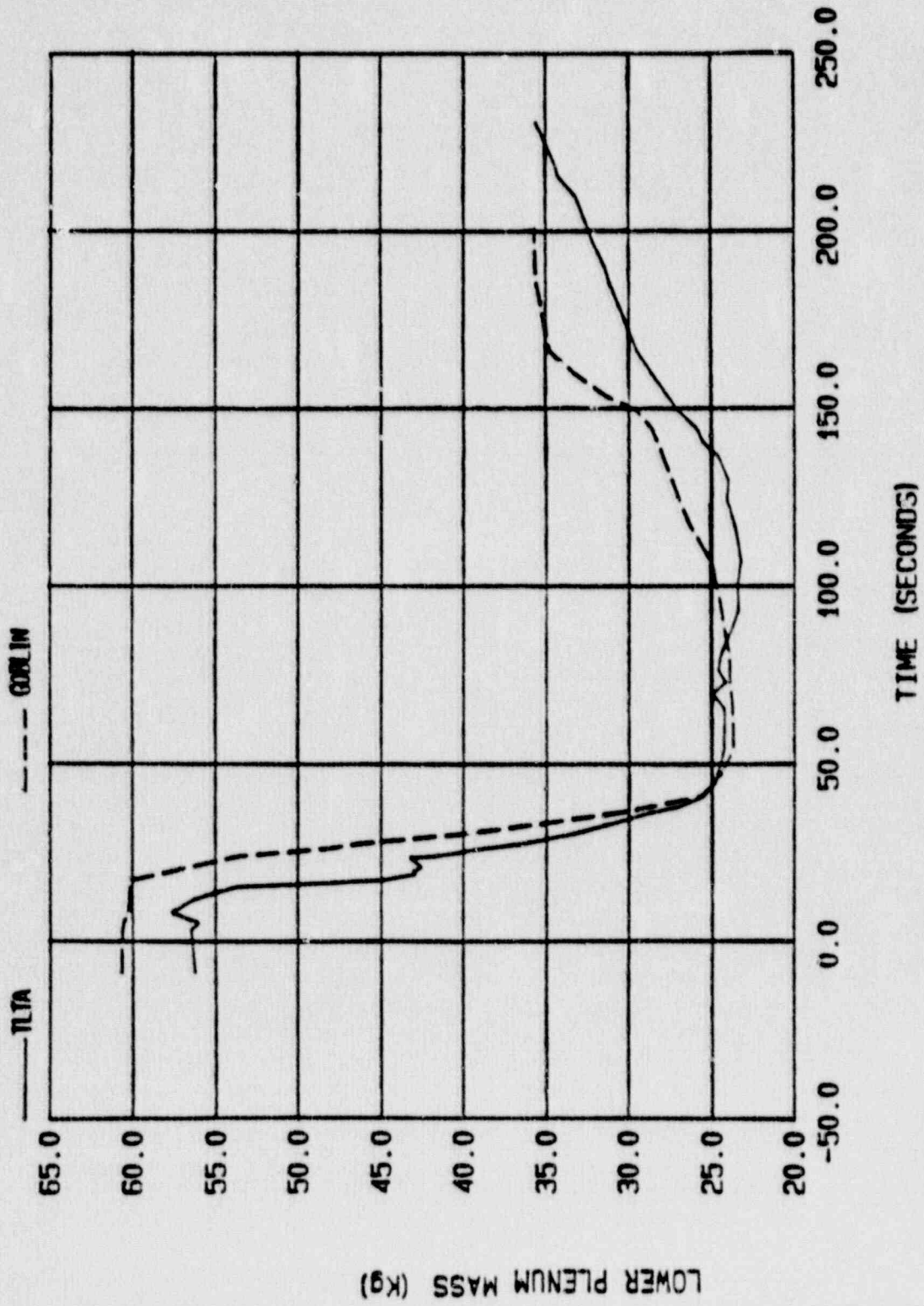


Figure 6-42 Lower Plenum Mass for TLTA5A Test 6423/3

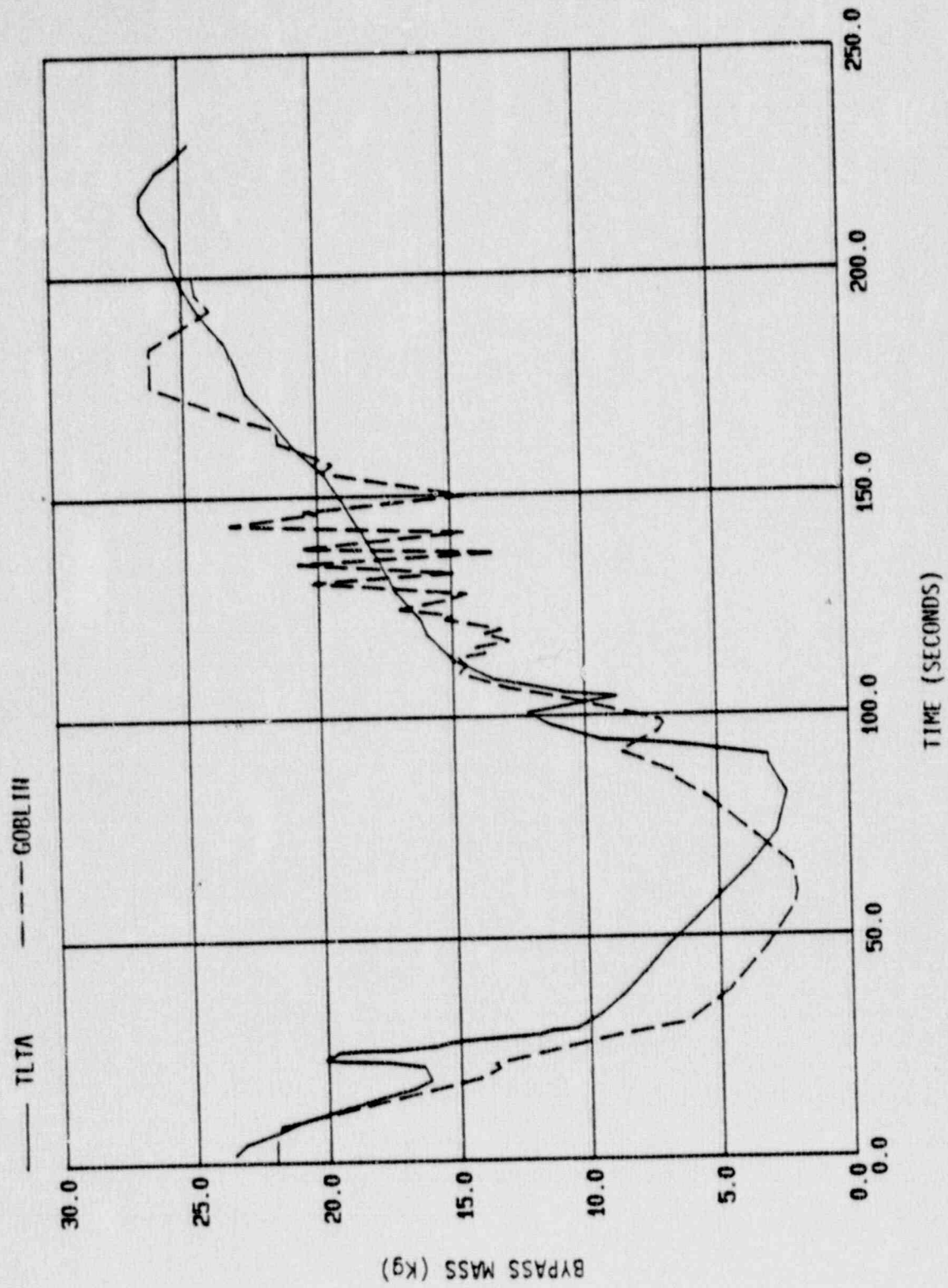


Figure 6-43 - Bypass Mass for TLTA5A Test 6423/3

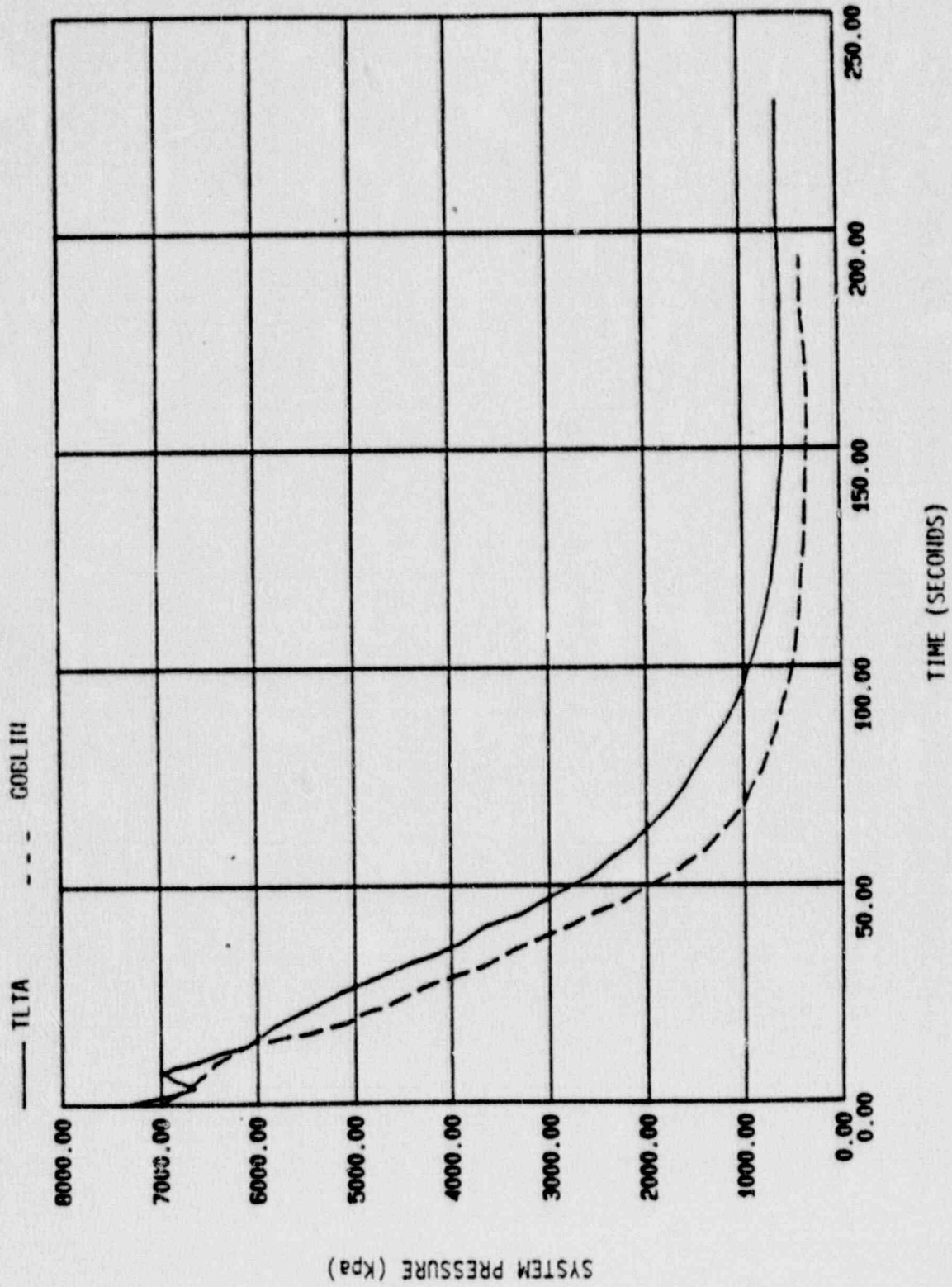


Figure 6-44 - System Pressure for TLTA5A Test 6423/3

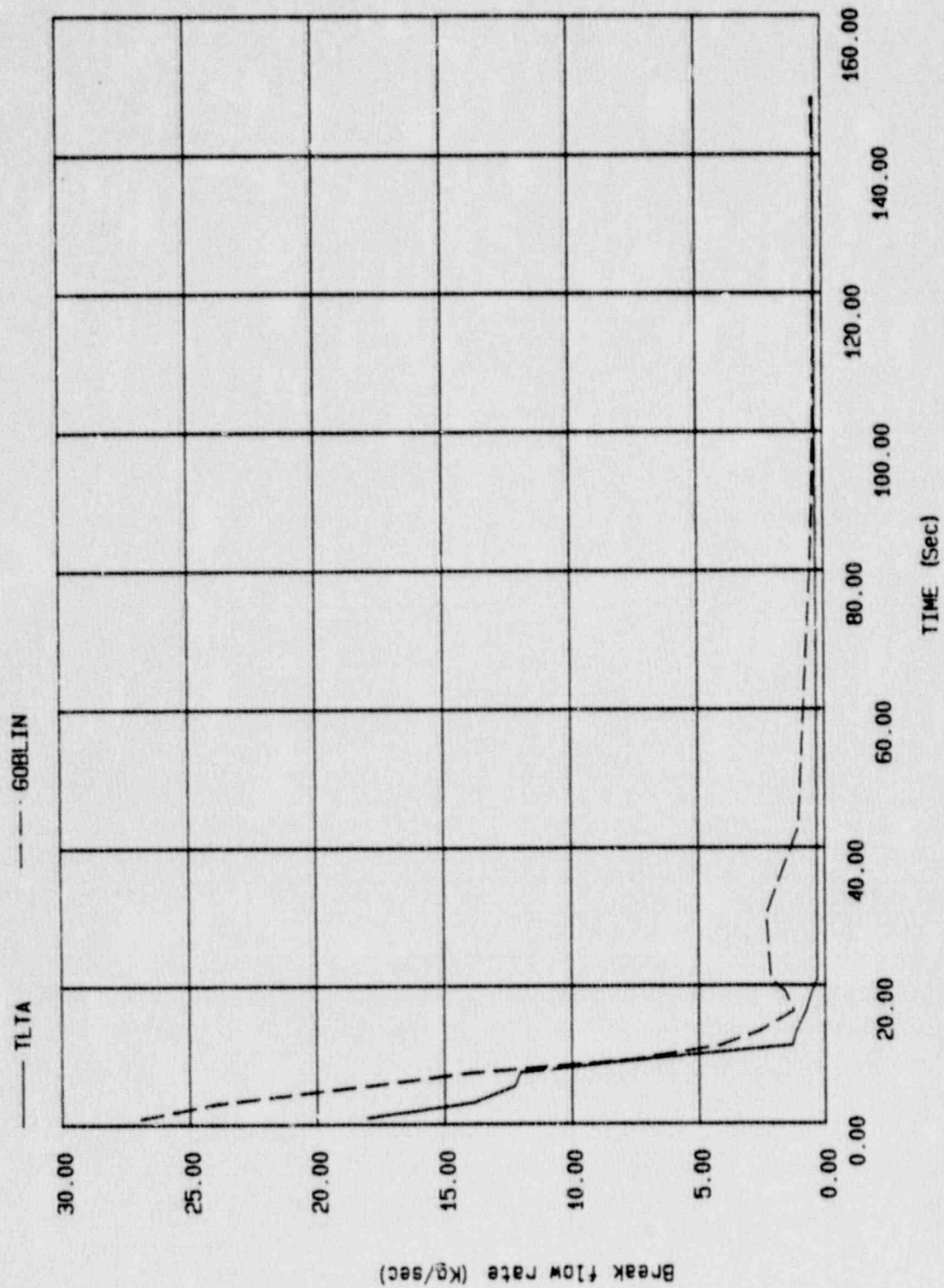


Figure 6-45 - Break Flow for TLTA5A Test 6423/3

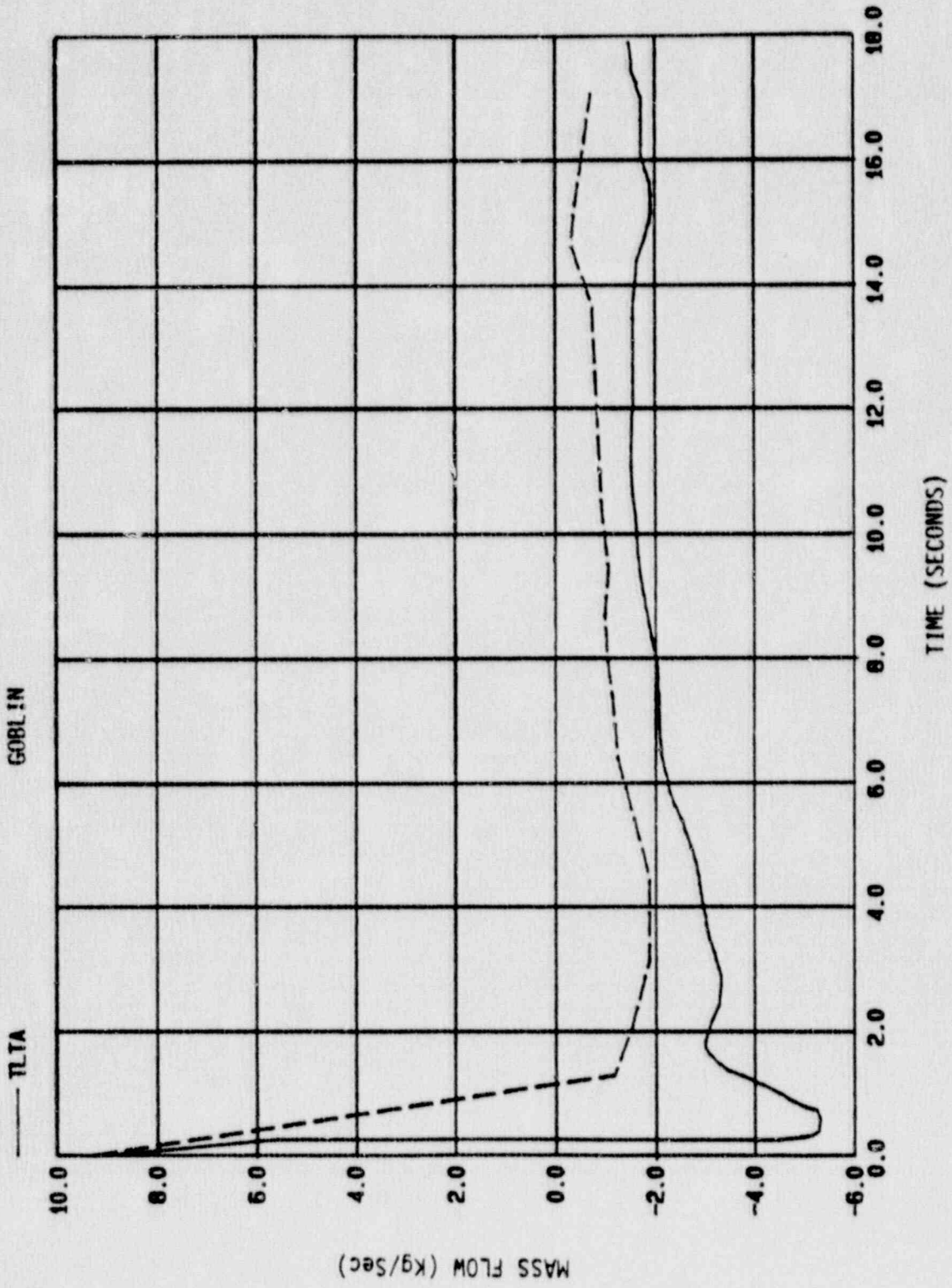


Figure 6-46 - Broken Jet Pump Flow Rate for TLTA5A Test 6423/3



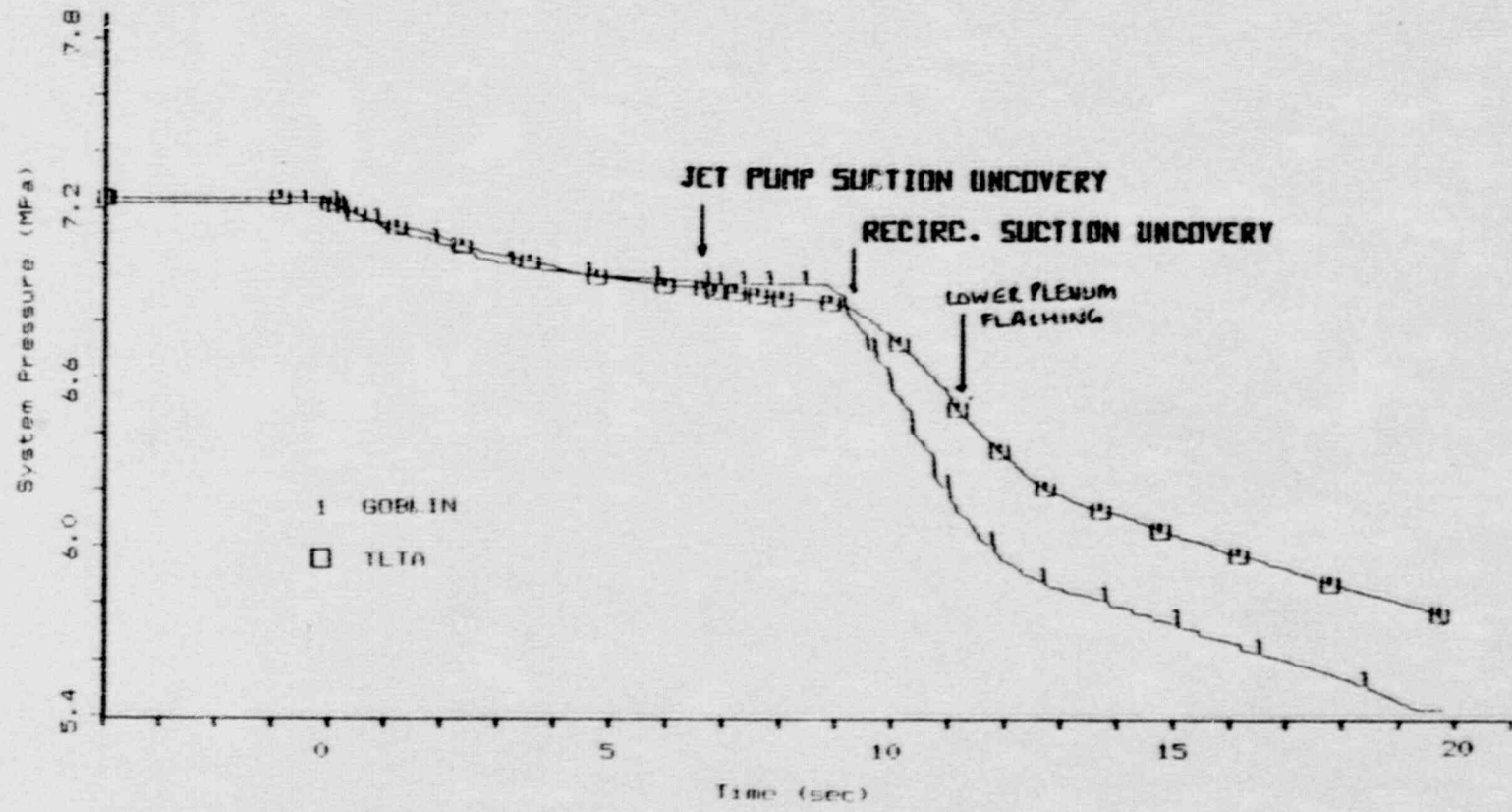


Figure 6-47 - System Pressure Transient for TLTA-4 Test 6007 Run 26

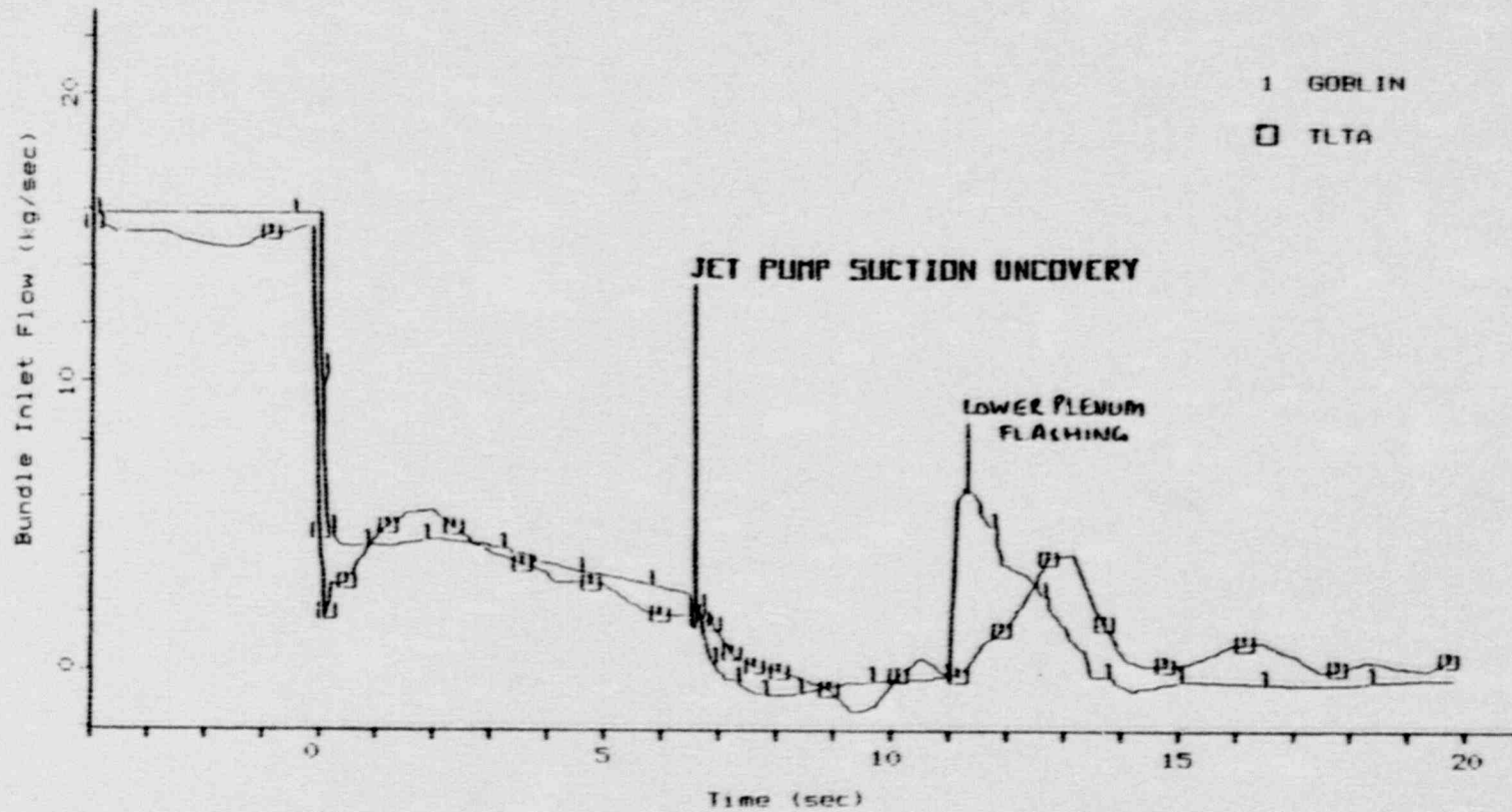


Figure 6-48 - Bundle Inlet Flow for TLTA-4 Test 6007 Run 26

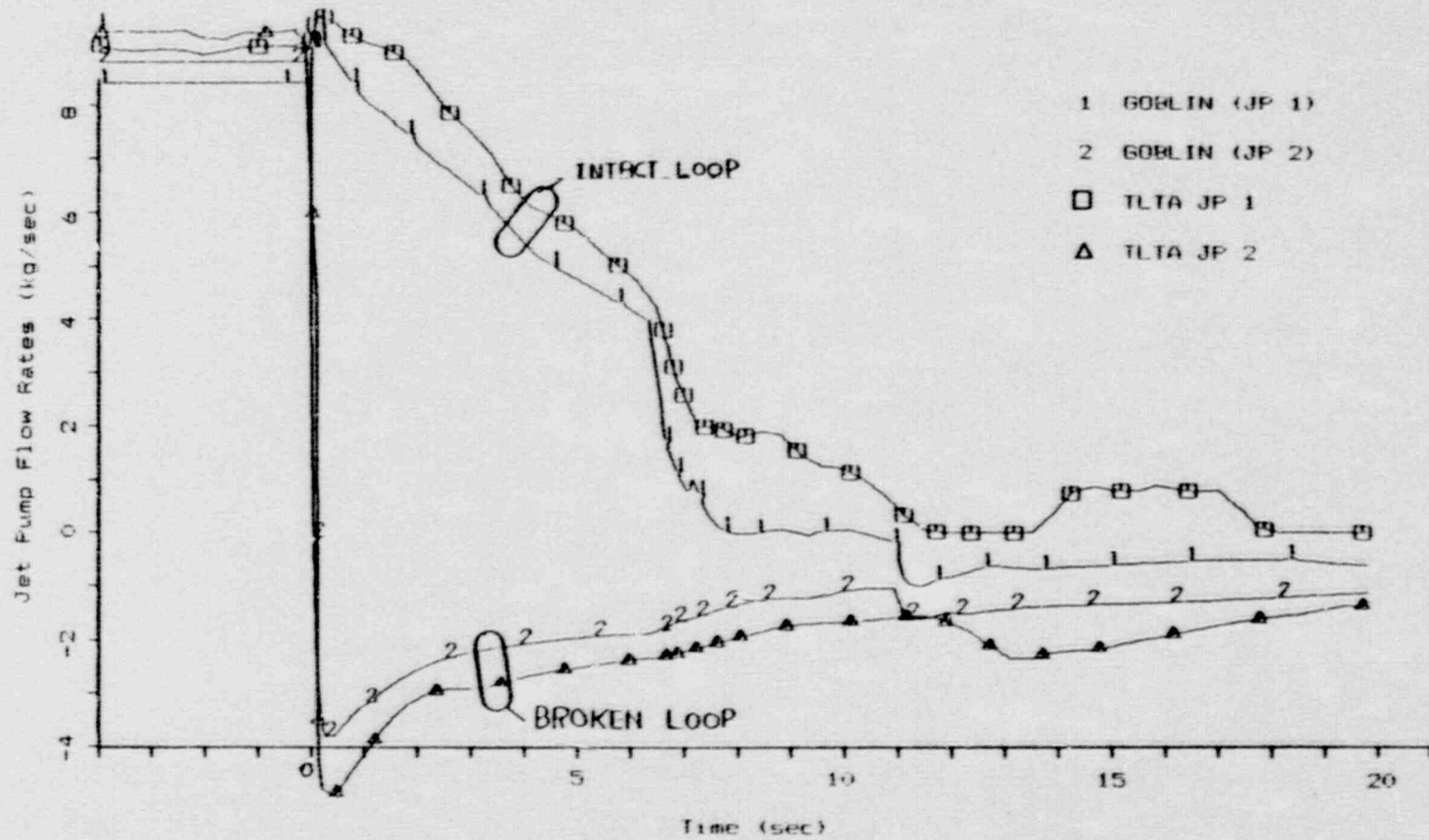


Figure 6-49 - Jet Pump Flow Rates for TLTA-4 Test 6007 Run 26

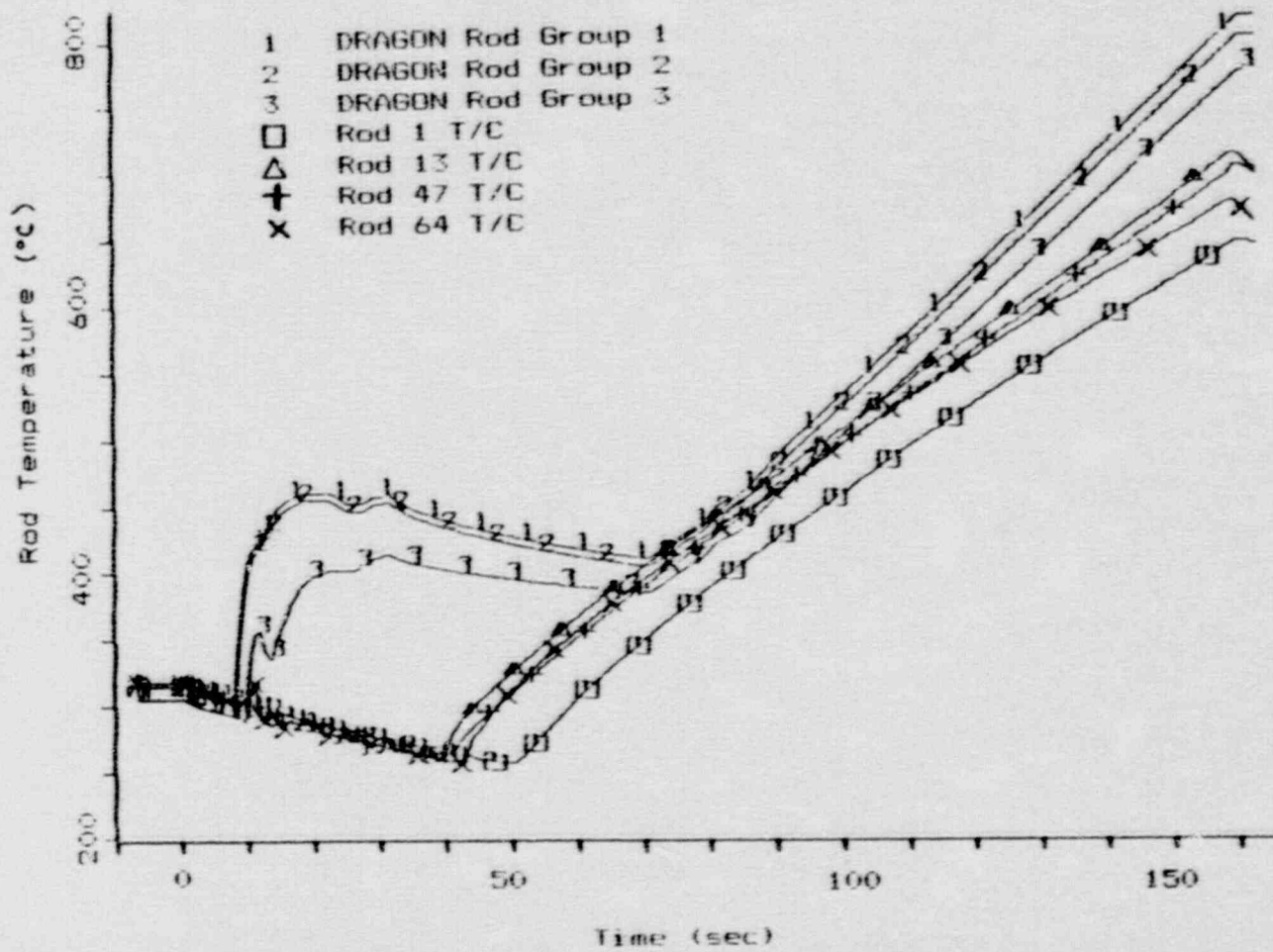


Figure 6-50 - Rod Temperatures at 79 Inch Elevation for TLTA-4 Test 6007 Run 26

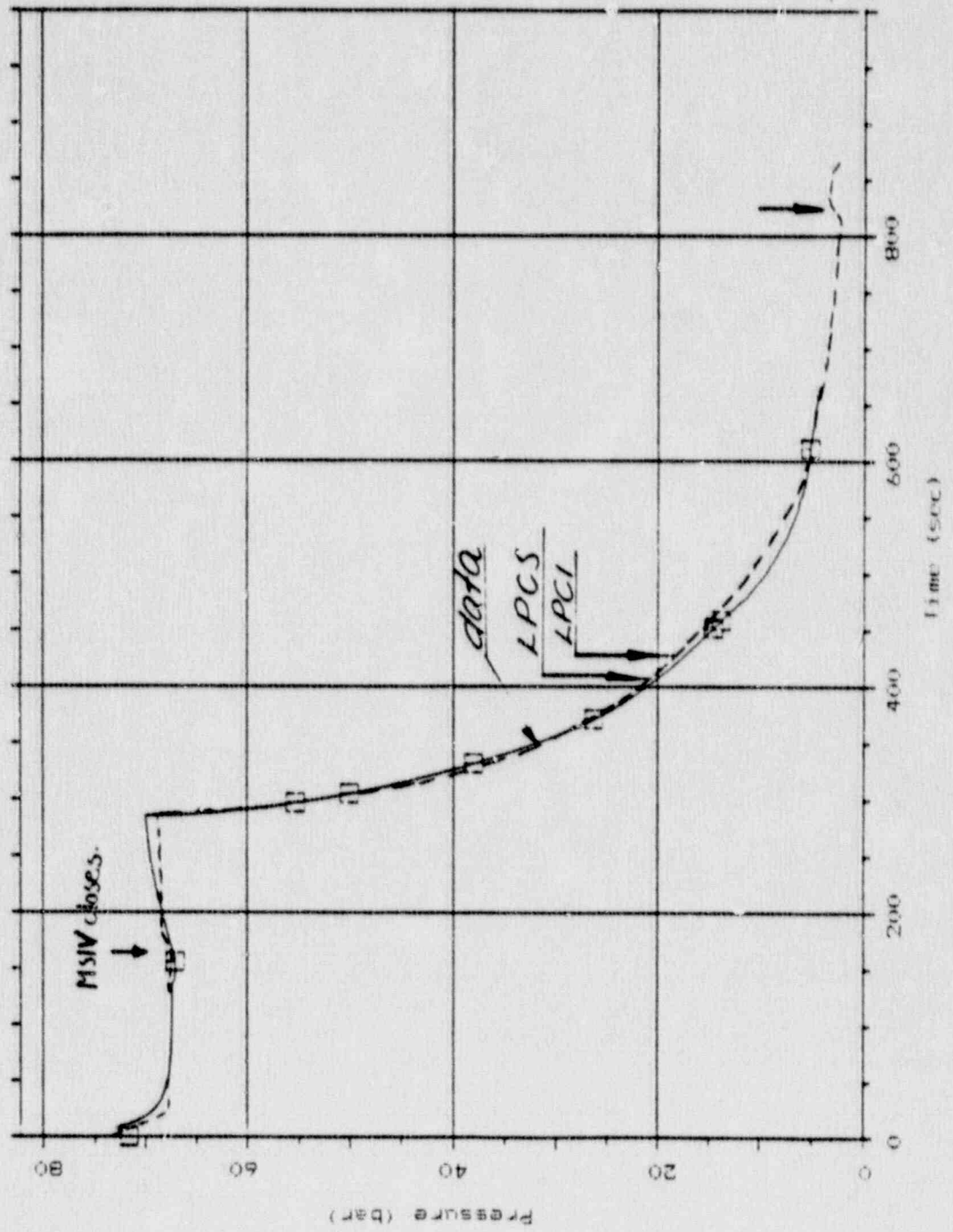


Figure 6-51 - Steam Dome Pressure TLIA-5C

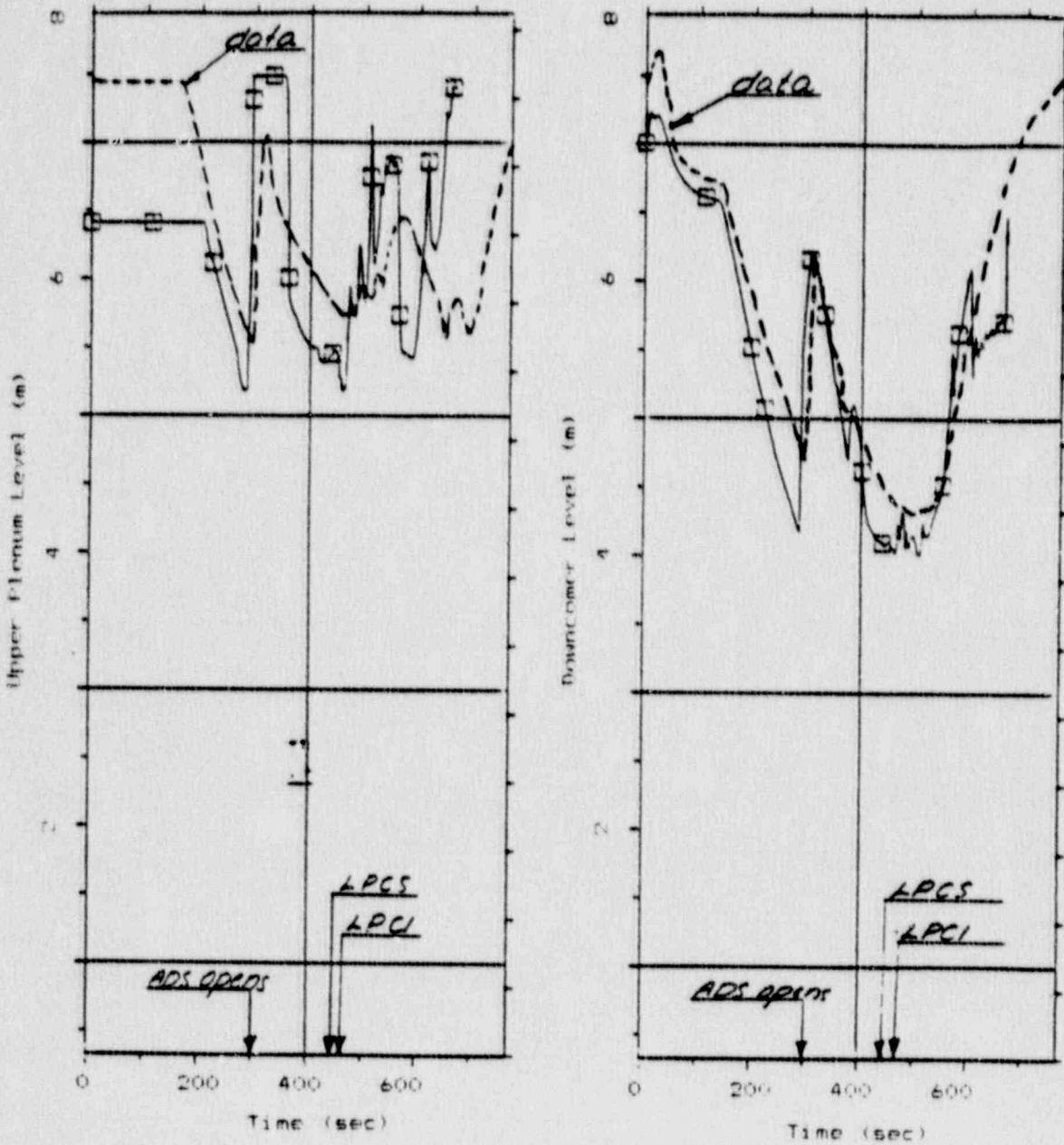


Figure 6-52 - Upper Plenum and Downcomer Levels for TLTA-5C

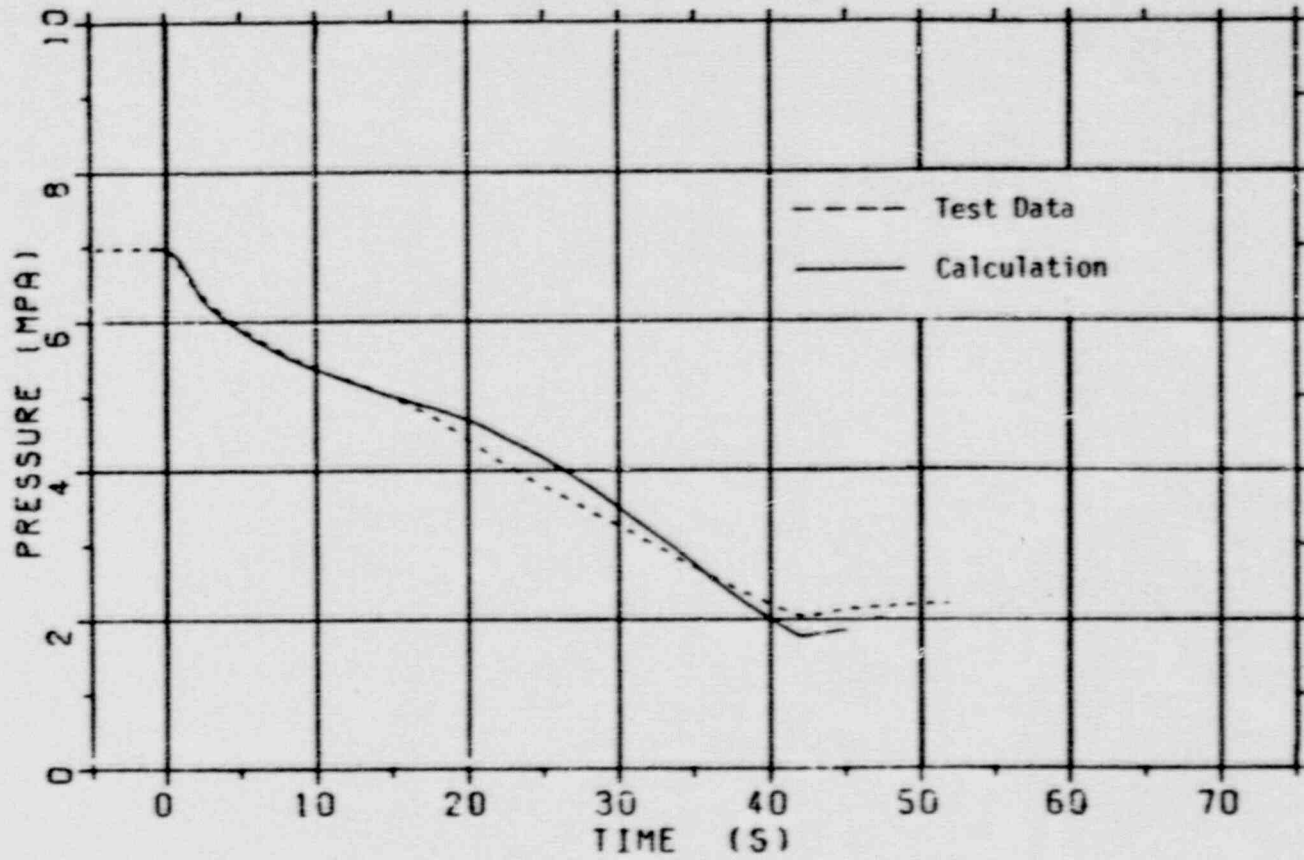


Figure 6-53 - Steam Dome Pressure for FIX-II Test 3061,  
100% Break at 2.51 kw

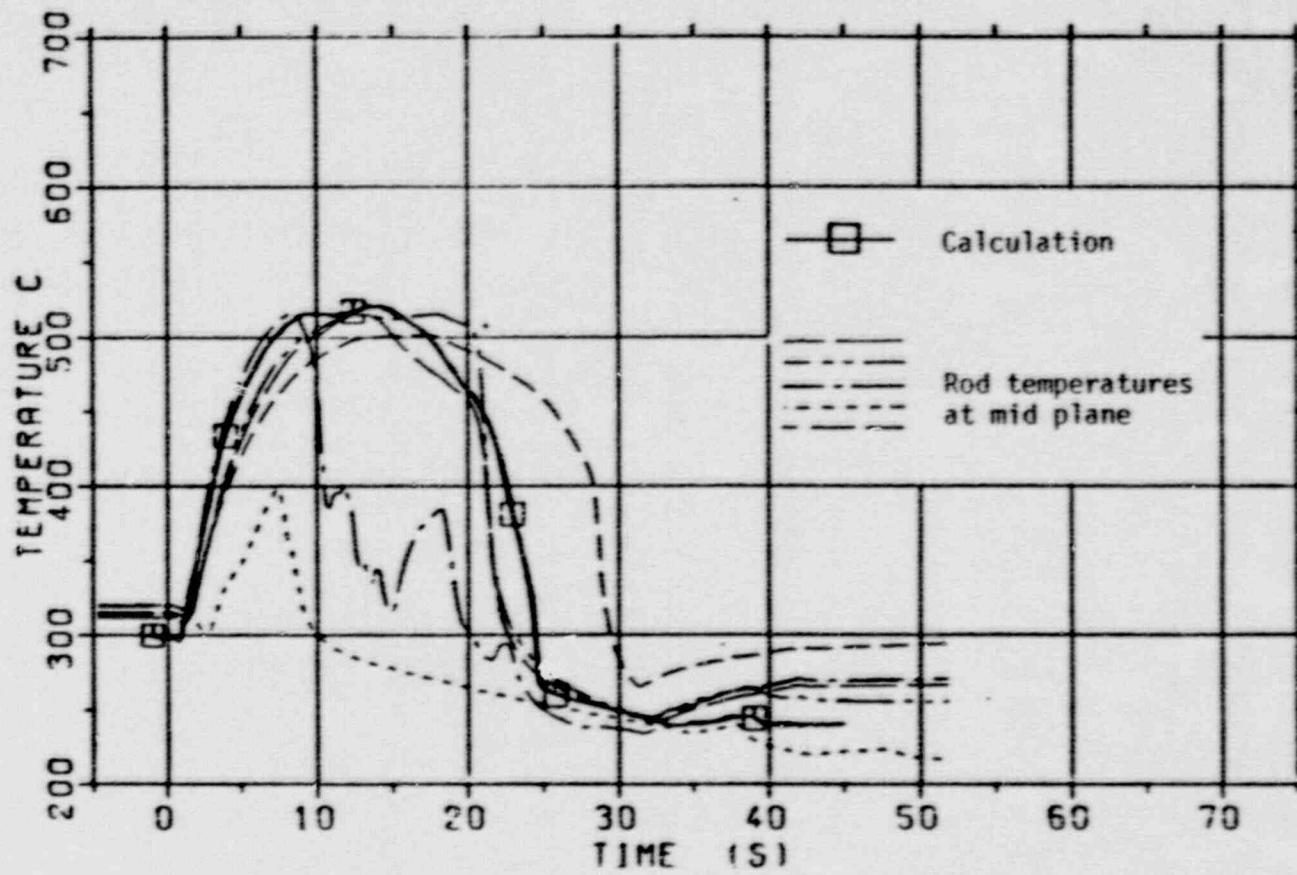


Figure 6-54 - Midplane Rod Temperature for FIX-II Test 3061,  
100% Break at 2.51 kw



## 7. CONCLUSIONS

This document described in detail the Westinghouse boiling water reactor emergency core cooling system evaluation model for compliance with 10 Part 50.46 and Appendix K of the Code of Federal Regulations. The report includes a description of the GOBLIN series of computer codes, an evaluation of the model's compliance with Appendix K, and a demonstration of the model's applicability for LOCA analysis through separate effects and integral qualification tests.

The detailed code description demonstrates that the GOBLIN series of codes are developed from first principle conservation equations that include models for all components and systems that are affected during a postulated LOCA accident, and that the numerical solution techniques are all proper and acceptable.

The Appendix K compliance evaluation shows that the GOBLIN series of codes contains all the mandated models and correlations to address the thermal hydraulic phenomena as required under Appendix K.

The results of the separate effects comparisons demonstrate that the individual calculational models in the GOBLIN series of codes are implemented correctly and the individual models compare favorably with the available separate effects test data.

The integral system comparison against TLTA-5A, along with the previously completed qualification performed by ASEA-ATOM for other integral system facilities, shows that the GOBLIN series of codes can accurately simulate the LOCA transient response of a BWR integral facility. This demonstrates that the models in the GOBLIN codes are programmed and integrated properly and include the necessary details to predict the thermal hydraulic phenomena and response for a boiling water reactor during a postulated design basis LOCA.

In addition the GOBLIN series of codes have been used by ASEA-ATOM of Sweden, for LOCA analysis over the past decade. The methods presented in this document are an accumulation of ASEA-ATOM and Westinghouse's experience over this period. On the basis of these past experience and qualification, and the additional qualification presented here, Westinghouse concludes that the GOBLIN series of codes conform to all the requirements for Evaluation Models as specified in Title 10, Part 50 and Appendix K of the Code of Federal Regulations. The GOBLIN series of codes are therefore suitable for boiling water reactor loss of coolant accident analyses.

A future topical report shall present Evaluation Model methodology and supply supporting sensitivities studies for the methodology.

Addendum to  
Westinghouse Boiling Water Reactor Emergency  
Core Cooling System Evaluation Model:  
Code Sensitivity

The following are responses to twelve questions pertaining to the review Westinghouse Topical Reports WCAP-11284 and WCAP-11427. The topical reports are refer to here in as:

- Ref. 1: Westinghouse Boiling Water Reactor Emergency Core Cooling System Evaluation Model: Code Description and Qualification, WCAP-11284, September 30, 1985, and
- Ref. 2: Westinghouse Boiling Water Reactor Emergency Core Cooling System Evaluation Model: Code Sensitivity, WCAP-11427, June 30, 1987

### Question 1

Page 4-27, Ref. 1. The use of a lower surface emissivity would result in a higher peak clad temperature in the DBA when radiation heat transfer becomes significant. Discuss the conservatism of the input values of 0.67 [dry surface] and 0.96 [wet surface], taking into consideration the oxide layer buildup.

### Response

Dry surface emissivity - The dry surface value of 0.67 is conservative, based on comparisons with the model described in Reference (1-1) below. This model, based on data reported in References (1-2) through (1-4), gives

$$\epsilon = 0.325 + 0.1246 \times 10^6 d \text{ for } d < 3.88 \times 10^{-6} \text{ m}$$

$$\epsilon = 0.808642 - 50.0d \text{ for } d \geq 3.88 \times 10^{-6} \text{ m}$$

where  $d$  is the oxide layer thickness in meters. The best-estimate for the standard error of the model prediction is quoted as  $\pm 0.1$ .

CHACHA-3C uses the best-estimate oxide thickness correlation described in Appendix A of Reference (1-5) to obtain the initial cladding oxide thickness for each rod being analyzed. Expressed as a function of local burnup, this correlation gives:

$$\Delta r_{\text{oxide}} = \left[ \quad \quad \right]^{a,c}$$

where the oxide thickness is in  $\mu\text{m}$  and the local burnup, BU, is in GWD/MTU. Examination of the above equations shows that incorporating the Reference (1-1) emissivity correlation in CHACHA-3C would give emissivities in excess of 0.67 for all local burnups greater than  $\left[ \quad \right]^{a,c}$ . For burnups below  $\left[ \quad \right]^{a,c}$ , an oxide layer quickly builds up due to zirc-water reaction. Use of the Reference (1-1) correlation for these cases would show that the emissivity would increase rapidly and exceed 0.67 by the time the clad temperatures reach the level at which radiation heat transfer becomes significant. A review of CHACHA-3C analyses performed at low burnups shows that use of the Reference (1-1) correlation would result in emissivities in excess of 0.67 by the time the cladding temperature reaches 1700°F.

The dry surface value of 0.67 is also conservative relative to the correlation given in Equation 4.8-16 of Ref. 1. This correlation, based on Reference (1-6), gives

$$\epsilon = \left[ \quad \right]^{a,c}$$

where T is the Zircaloy temperature in °R. Use of this correlation gives emissivities in excess of 0.67 for Zircaloy temperatures above  $\left[ \quad \right]^{a,c}$ .

Wet surface emissivity - The wet surface value of 0.96 is consistent with Table D-3 of Reference (1-7), which quotes emissivities of 0.95 - 0.97 for water films.

### References

- (1-1) "MATPRO Version 11: A Handbook of Materials Properties for Use in the Analysis of Light Water Reactor Fuel Rod Behavior," NUREG/CR-0497, 1979.
- (1-2) E. F. Juenke and L. H. Sjodahl, "Physical and Mechanical Properties: Emittance Measurements," GEMP-1008, pp. 239-242, 1968.

- (1-3) E. V. Murphy and F. Havelock, "Emissivity of Zirconium Alloys in Air in the Temperature Range 100-400°C," Journal of Nuclear Materials, Vol. 60, pp. 167-176.
- (1-4) T. B. Burgoyne and A. Garlick, OECD-CSNI Meeting on the Behavior of Water Reactor Fuel Elements Under Accident Conditions, Spind, Norway, September 13-16, 1976.
- (1-5) "Westinghouse Reference Safety Report for BWR Fuel," WCAP-11500 (Proprietary), August 1987.
- (1-6) J. F. White, et al., Eighth Annual Report, "AEC Fuels and Materials Development Program," GEMP-1012, Pt. II, 1969.
- (1-7) J. A. Adams and D. F. Rogers, "Computer Aided Heat Transfer Analysis," McGraw-Hill, 1973.

## Question 2

Page 5-6, Ref. 1. What is the assumed fraction of the locally generated gamma energy that is deposited in the fuel and cladding? This fraction needs to be justified if not unity.

## Response

The Westinghouse LOCA evaluation model assumes that the total gamma energy deposition fraction outside of the fuel rod is 2% of the total power generation. Evaluations have been performed which show this energy is partitioned as follows:

Active Channel Steam Fraction	Channel/ Watercross	Active Channel Coolant	Outer Water Gaps	Coolant in Watercross
0.40	0.8%	0.6%	0.4%	0.2%
0.70	0.9%	0.4%	0.5%	0.2%
1.00	1.1%	0.1%	0.6%	0.2%

This table is applicable for unrodded conditions. Control rod insertion would reduce each of these values.

The evaluation model fuel rod heatup calculations (CHACHA-3C) assume 96% of the total power generation occurs in the pellets until 0.1 second after the break. After that time, 98% of the total power generation is assumed to occur in the pellets. This modelling is based on the conservative assumption that the neutron moderation energy (initially taken as 2%) goes to zero within 0.1 seconds. The CHACHA-3C calculation also assumes gamma energy deposition of 1.5% of the total power generation occurs within the channel/watercross structure throughout the transient, which bounds the above values for all steam fractions.



Two CHACHA-3C sensitivity studies were performed to investigate the impact of the energy deposition fractions on PCT. In the first, the increase in pellet power generation from 96% to 98% of the total generation was delayed until 1 second after the break. This corresponds to the time at which the fission power has decreased to approximately half of the initial fission power, and is a more realistic approximation of the pellet power generation behavior. The power generation in the channel/watercross was also reduced to 1.1%, consistent with the maximum value under rodded or unrodded conditions. These changes reduced PCT by [ ]<sup>a.c</sup>, which is considered to be a negligible change.

The second sensitivity study reduced the reference case pellet power generation by 1% and added this power generation to the cladding. The result was a decrease in PCT of [ ]<sup>a.c</sup>. This result demonstrates that it is more conservative to model the fuel rod power generation as occurring entirely in the pellet, rather than partitioning the energy to the pellet and cladding to account for gamma energy deposition in the cladding.

Based on the above discussion it is concluded that the treatment of energy deposition fractions in the evaluation model is slightly conservative. The sensitivity of PCT to the gamma energy deposition treatment is seen to be small.

### Question 3

Page 3-7, Ref. 2. Provide additional discussion of the determination of the maximum oxidation fraction of 0.031 in the CHACHA-3C reference transient calculation. What percent of fuel rods is assumed to be perforated in the DBA analysis? Discuss the effect of water blockage from perforated rods on PCT.

### Response

The Westinghouse LOCA evaluation model uses the maximum circumferential strain versus hoop stress relation shown on page I-161 of Reference (3-1) to calculate the maximum oxidation fraction. This relation gives a maximum circumferential strain of 0.39 for cladding hoop stresses below 1500 psi and a maximum circumferential strain of 0.31 for hoop stresses in excess of 1500 psi. For the reference transient in Ref. 2, the cladding hoop stress exceeds 1500 psi ( $1.03 \times 10^7$  Pa). (See Figure 7-5 in the response to Question 7). The initial cold cladding thickness is 29 mils. The strained cladding thickness for use in the maximum oxidation thickness is therefore

$$29 \text{ mils} / 1.31 = 22.1 \text{ mils}$$

The final oxide thicknesses for the reference transient are 0.47 mils for the outer surface and 0.27 mils for the inner surface. The maximum oxidation fraction is then

$$\frac{0.47 \text{ mils} + 0.27 \text{ mils}}{22.1 \text{ mils}} = 0.033$$

All of the fuel rods in the hot minibundle were calculated to perforate in the DBA analysis presented in Ref. 2. This analysis used an average planar burnup of 22 GWD/MTU. At this burnup the rod internal pressures are sufficiently high that the final cladding strains are 0.15 for inner rods and 0.105 for outer rods (See Figure 4-8 of Ref. 1). The resulting blockage fraction is calculated as follows:

$$\text{Nominal flow area} = 3.877 \text{ in}^2 \text{ per minibundle}$$

Nominal clad outer radius = 0.2288 in

$$\begin{aligned} \text{Blocked flow area} &= 4\pi (1.15 \times 0.2288 \text{ in})^2 + 12\pi (1.105 \times 0.2288 \text{ in})^2 \\ &\quad - 16\pi (0.2288 \text{ in})^2 = 0.648 \text{ in}^2 \end{aligned}$$

$$\text{Blockage fraction} = 0.648/3.877 = 0.17$$

The maximum blockage fraction may be calculated assuming fresh fuel with all rods perforated. (Low burnup calculations have shown that not all rods perforate in the hot mini-bundle. However, this assumption is made to quantify the maximum possible blockage.) With fresh fuel the final cladding strains are 0.23 for inner rods and 0.16 for outer rods. The resulting blockage fraction would be 0.26.

Several investigators have examined the impact of flow blockage on heat transfer under conditions representative of a BWR LOCA. In BWR-FLECHT test Zr-2, a full-scale simulated 7 x 7 fuel bundle was used to determine the effect of rod swelling, rod burst and the resulting flow area blockage on PCT under top spray cooling conditions (Reference (3-2)). The results indicated that "the effectiveness of the BWR ECCS core spray will not be significantly impaired by even very substantial flow area reduction at the worst elevation" (p. III-13 of Reference (3-1)). General Electric estimated the total bundle blockage fraction in that test to be 0.29 to 0.33 (p. I-86 of Reference (3-1)), with local blockages of up to 50 percent. With a nominal test bundle flow area of 15.6 in.<sup>2</sup>, this corresponds to an effective flow area of 11.1 in.<sup>2</sup> or less. This bounds the minimum effective flow area of a QUAD+ assembly, which is  $4(1-0.26)(3.877 \text{ in}^2) = 11.5 \text{ in}^2$  assuming a fresh assembly with all rods burst.

General Electric also has evaluated the impact of flow blockage on BWR LOCA heat transfer during bottom flooding (p. III-14 of Reference (3-1)). Their conclusion was that "the effectiveness of the bottom-flooding mode of ECCS cooling will not be significantly affected by flow area reductions

considerably larger than these expected in an actual LOCA. These investigations have indicated that the bundle-wide flow area reduction would need to be in excess of approximately 90 percent before the bottom-flooding method would be impaired."

Kraftwerk Union has investigated the impact of up to 70 percent flow blockage on heat transfer under spray cooling conditions. The results of these tests indicated a slight reduction in PCT relative to a nominal (no blockage) experiment (Reference (3-3)).

Based on the experiments and evaluations described above, it is concluded that no flow blockage penalty is required for QUAD+ LOCA analyses in which rod bursts are calculated to occur.

#### References

- (3-1) "General Electric Company Analytical Model for Loss-of-Coolant Analysis in Accordance with 10CFR50 Appendix K. Volumes I-III," NEDO-20566, January 1976.
- (3-2) J. D. Dunlon and J. E. Leonard, "Thermal Response and Cladding Performance of an Internally Pressurized, Zircaloy-Clad, Simulated BWR Fuel Bundle Cooled by Spray Under Loss-of-Coolant Conditions," GEAP-13112, April 1971.
- (3-3) H. Schweickert, "Final Report - Emergency Cooling Program, Low Pressure Tests. Blocked Cooling Channels with BWR Configuration (Translation)," Project BMFT-RS-194, Kraftwerk Union Reaktortechnik, October 1978.

#### Question 4

Pages 6-2 and 6-8, Ref. 2. Provide the following information related to the determination of the limiting power shape for use in the DBA analysis:

- a. Identify the physical location of the dryout and uncover times in Table 6.2.

#### Response

The dryout and uncover times in Table 6.2 of Ref. 2 correspond to the peak power elevation. This elevation is presented in the table under the heading "Location of Axial Peak".

- b. Discuss why Case 2 is not included in the PCT calculation; Case 2 dries out and uncovers sooner than Case 4.

#### Response

Cases 2 and 5 both used peaked-to-top power shapes. The peak power elevation was found to dry out and uncover slightly earlier in Case 5 than in Case 2. Since both cases had the same initial stored energy at the peak power elevation (axial peaking factor times bundle relative power equals constant), this implies that the Case 5 PCT would bound the Case 2 PCT. Therefore, only Case 5 was evaluated with CHACHA-3C.

- c. Provide bases for selecting the axial peaking factor/bundle relative power ratios of 1.63/1.47 and 1.50/1.60. Were any other combinations considered?

#### Response

During steady state operation, axial peaking factors for a BWR/5 can normally be expected to be no higher than 1.5 to 1.6. A bundle relative power of 1.40 is also a realistic upper limit. Axial and radial power distributions for typical QUAD+ 24-month cycle BWR/5 transition and equilibrium cycle cores are

presented in Section 3.5.2 of Reference (4-1). These distributions confirm that the peaking factors used in the LOCA power distribution study can be considered as reasonable upper bound values.

Note that it is necessary to use large axial peaking factors and bundle relative powers to achieve the 14.5 kw/ft MLHGR assumed in the LOCA analysis. Comparisons of Case 1 versus Case 4, and Case 2 versus Case 5, show that the cases with the higher bundle relative power are slightly more limiting (earlier dryout and uncover). These cases used a bundle relative power of 1.60, which clearly bounds the values reported in Section 3.5.2 of Reference (4-1). Therefore it is concluded that the axial peaking factor/bundle relative power combination of 1.50/1.60 is more limiting than the other bounding relative power combination and combinations which would actually occur during operation of a BWR/5.

- d. Five cases were studied for various axial peaking factor/bundle power combinations. Discuss why the case of 1.63/1.47 with peaked-to-bottom power is left out of the sensitivity study.

#### Response

Comparisons of the five cases shown in Table 6.2 of Ref. 2 support the following conclusions:

- Dryout and uncover times are delayed as the peak plane is moved downward in the bundle (Case 1 versus Case 2, and Case 3 versus Case 4 versus Case 5).
- Given the same location of the peak power plane, the axial peaking factor/bundle relative power combination of 1.63/1.47 is less limiting (later dryout and uncover) than the 1.50/1.60 combination (Case 1 versus Case 4, and Case 2 versus Case 5).

From these conclusions it is apparent that the case of 1.63/1.47 with peaked-to-bottom power would be less limiting than the five cases in Table 6.2. Therefore this case was not analyzed.

e. Complete the PCT data tabulation in Table 6.2 to support the statement, "The results are seen to be relatively insensitive to the power distribution."

Response

CHACHA-3C analyses of Cases 1 and 3 have been performed to augment the information provided in Table 6.2 of Ref. 2. Using a reflood time of 142 sec, the Case 1 PCT was [ ]<sup>a,c</sup>. A PCT of [ ]<sup>a,c</sup> was calculated for Case 3, using a reflood time of [ ]<sup>a,c</sup> sec. These results confirm that, for the small changes in dryout, uncover and reflood time observed in the power distribution sensitivity study, the impact on PCT is relatively small.

Peaked-to-top power shapes in a BWR are indicative of some degree of control rod insertion. Under these conditions, the peak LHGR is typically well below the 14.5 kw/ft MLHGR assumed in the LOCA analysis. Figures 3-28 through 3-41 of Reference (4-1) show typical QUAD+ axial power shapes throughout 24-month transition and equilibrium cycles. The corresponding peak LHGR are shown in Figures 3-42 and 3-43. For cases with peaked-to-top power shapes the corresponding peak LHGR are seen to be on the order of 11 to 12 kw/ft. Since limiting MLHGR and MAPLHGR are not consistent with peaked-to-top power distributions, these shapes (including Cases 2 and 5) were removed from final consideration as the design basis shape. Therefore, a PCT calculation has not been performed for Case 2.

f. The statement that "the inherent tendency of BWRs operating with slightly peak-to-bottom power shapes" does not justify the use of the 1.5 cosine shape. Provide results from analyses with more peak-to-bottom power shapes.

Response

As previously discussed, peaked-to-bottom shapes are less limiting than cosine shapes with the same axial peaking factor because the peak power plane dries out and uncovers later, and reloads earlier. This effect was quantified in

response to item (e) above, and was shown to be a [ ]<sup>a,c</sup> benefit for Case 3 versus Case 4. The discussion in response to item (c) explains why the axial peaking factor bundle relative power combination of 1.50/1.60 can be considered bounding for BWR/5. Therefore, it is concluded that analyses of additional peaked-to-bottom power shapes is not required.

#### Reference

- (4-1) "Westinghouse Reference Safety Report for BWR Fuel," WCAP-11500 (Proprietary), August 1987.



## Question 5

Page 9-3, Ref. 2. Justify that the use of results from analyzing a 1/3-core 8 x 8 and a 2/3-core QUAD+ fuel is adequate to represent generic mixed-core characteristics.

## Response

The QUAD+ fuel assembly is designed to be hydraulically compatible with the resident fuel assemblies in the core (e.g., GE 8 x 8R fuel). An in depth description of the fuel hydraulic compatibility is given in Section 4.2.2 of Reference (5-1). The QUAD+ fuel assembly total pressure drop across the assembly is the same as that of the GE 8 x 8R assembly during normal operation. However, the component pressure drops do differ. The grid spacers for the QUAD+ fuel were designed to be less restrictive than the 8 x 8R spacers. In order to improve stability margin and reduce CCFL concerns, the QUAD+ upper tie plate was designed to be less restrictive than the 8 x 8R, and the lower tie plate was designed to be more restrictive (for the same flow conditions). Due to these design differences, the question arises whether the presence of the QUAD+ fuel in a mixed core would adversely alter the blowdown response, ECCS cooling, or the reflood time of the 8 x 8R fuel. To address these concerns, a mixed core analysis was performed using a core configuration of 2/3 QUAD+ fuel and 1/3 GE 8 x 8R fuel. The purpose was to evaluate the impact of a mixed core on the fuel assembly response for the reference transient of Ref. 2.

The attached figures present a comparison of the mixed core response to the full core response for each fuel type. Figure 5-1 shows the normalized total core differential pressure during the blowdown for the mixed core and both full core analyses. The core responses compare very well. Figure 5-2 shows the side entry orifice flow (per assembly) for each analysis which also compare very well. These figures demonstrate that the blowdown response is essentially the same for the three transients.

The normalized component differential pressures along the fuel assembly are shown in Figures 5-3 through 5-6. Figure 5-3 shows the pressure difference

across the side entry orifice for the different fuels. As expected, they agree well. The pressure drop across the lower tie plate is shown in Figure 5-4. The magnitude of the responses are different due to the different tie plate designs, but the same trend is followed for each fuel design. Figure 5-5 presents the pressure drop across the heated length of the assembly. Again the trends are the same, although the QUAD+ grid spacers are less restrictive than the 8 x 8R spacers. Figure 5-6 presents the upper tie plate response for the three transients. The less restrictive upper tie plate for the QUAD+ design is prominent at 10 seconds when lower plenum flashing begins. These figures show that although the individual component pressure drops may vary between fuels, the transient trends are essentially the same.

Figure 5-7 shows a comparison of the void distribution throughout the fuel assemblies at 20 seconds into the transient. Twenty seconds is just prior to midplane dryout, when the mass distribution in the bundle is important. It can be seen that since the transients are very similar, the mixed core does not significantly alter the individual assembly mass distributions. Because the mass distribution does not vary considerably, the dryout times for each transient are comparable, as seen in Table 9.1 of Ref. 2.

The midplane reflood portion of the transient is presented in Figure 5-8. Figure 5-8 shows the normalized total core differential pressure for the three transients from 130 to 150 seconds. The midplane reflood times for each case are indicated in the figure. These times compare well due to the similarity in the system mass distributions for each case. It can be seen that the driving force for reflooding the core is essentially the same for each transient.

The QUAD+ fuel is designed to be hydraulically compatible with the GE 8 x 8R, hence the LOCA system responses for a full core of either fuel type are very similar. Also, the system responses for one mixed core configuration has been shown to very closely follow the full core system responses for each respective fuel. It may be concluded any other mix of QUAD+ and 8 x 8R fuel would yield comparable results. Therefore, the MAPLHGR limits based on a full core analysis are directly applicable to mixed core configurations, since the mixed core configuration has no detrimental effect on the LOCA analysis.

It can be concluded from the above information that the core differential pressure response is relatively independent of local assembly differences. Highly localized effects would not alter the core average response. One example of a local effect is rod perforation. Varied degrees of localized rod perforations would have no impact on the global results for a mixed core.

Reference

- (5-1) "Westinghouse Reference Safety Report for BWR fuel," WCAP-11500, August 1987.

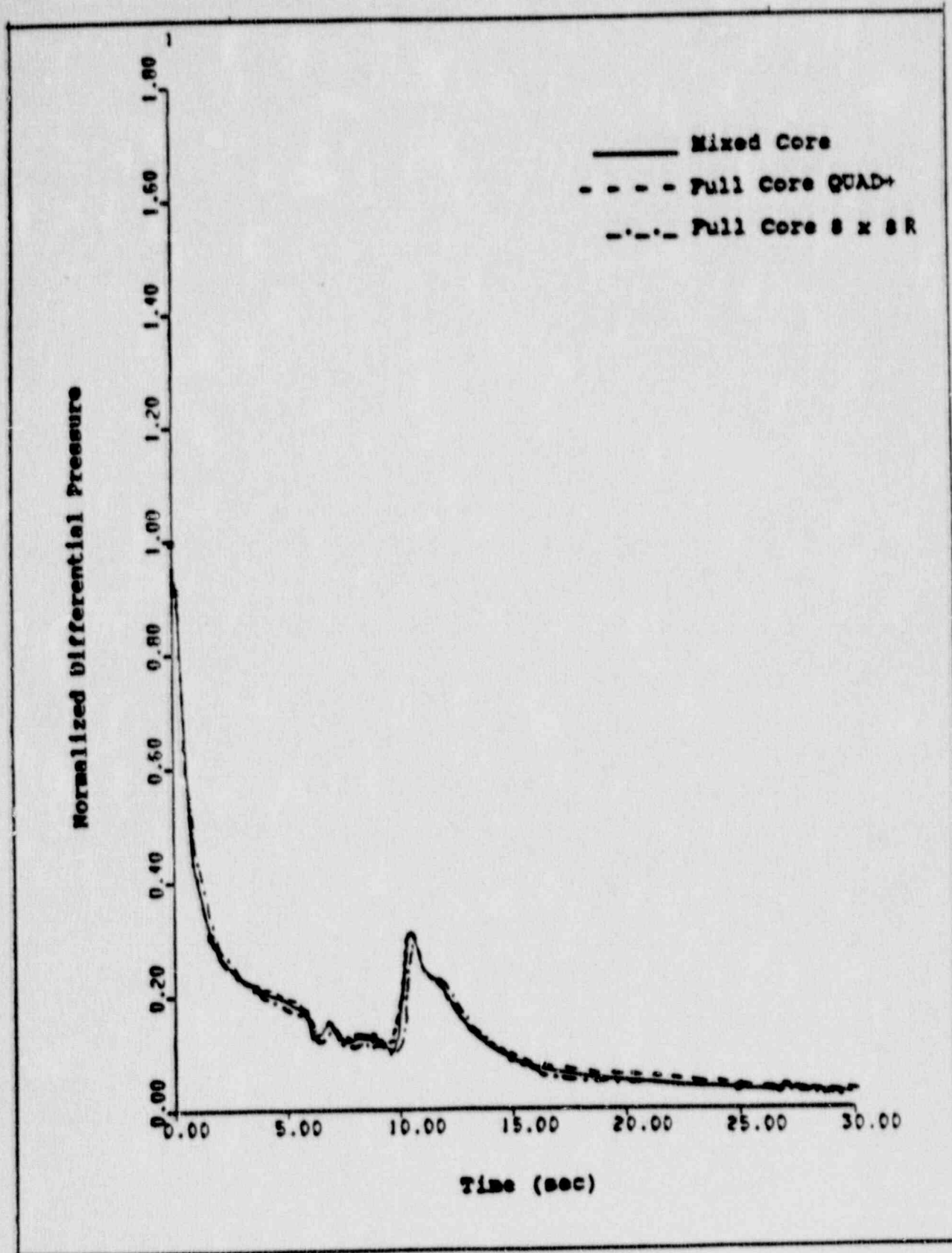


Figure 5-1 Normalized Assembly Differential Pressure vs Time

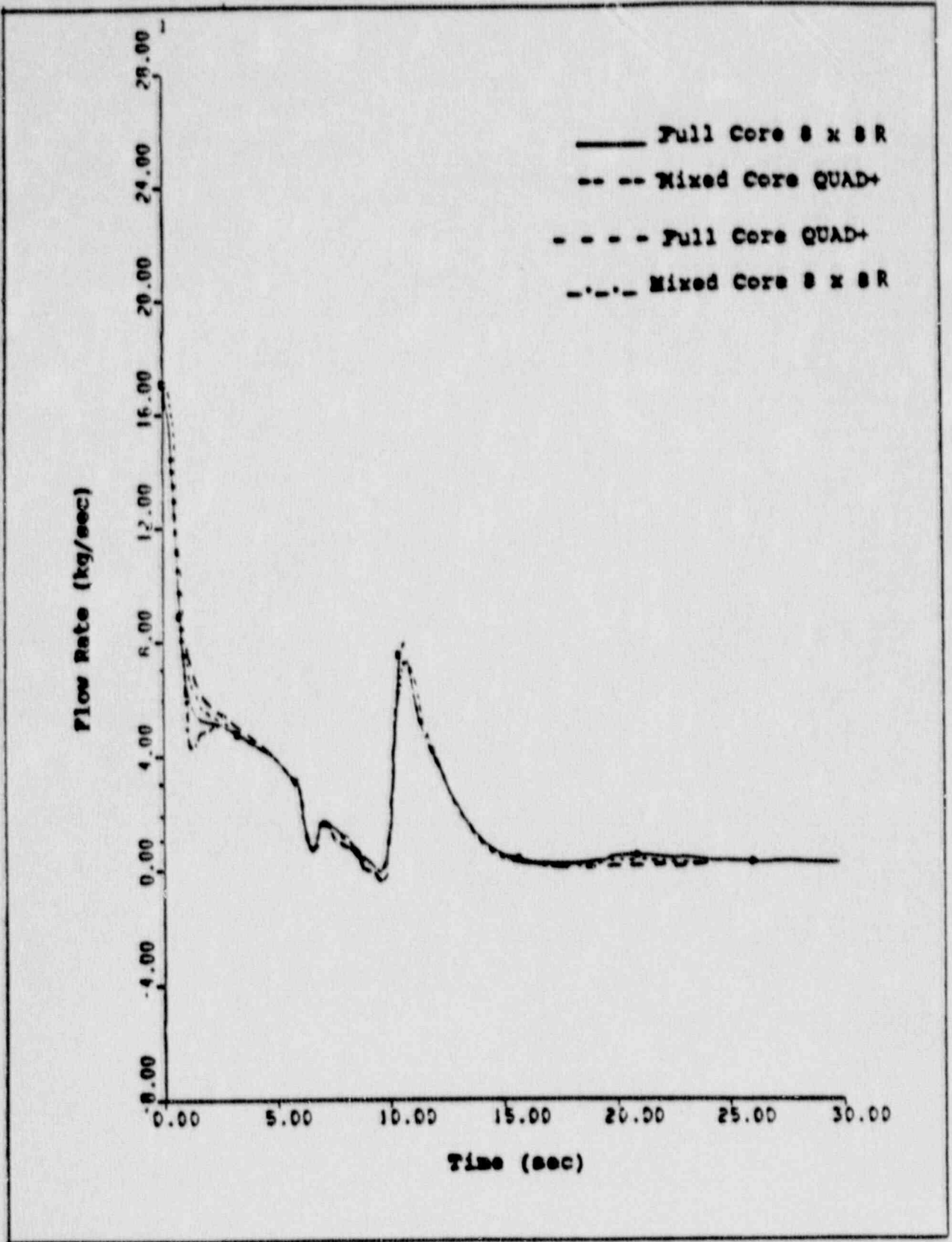


Figure 5-2 Side Entry Orifice Flow Per Assembly vs Time

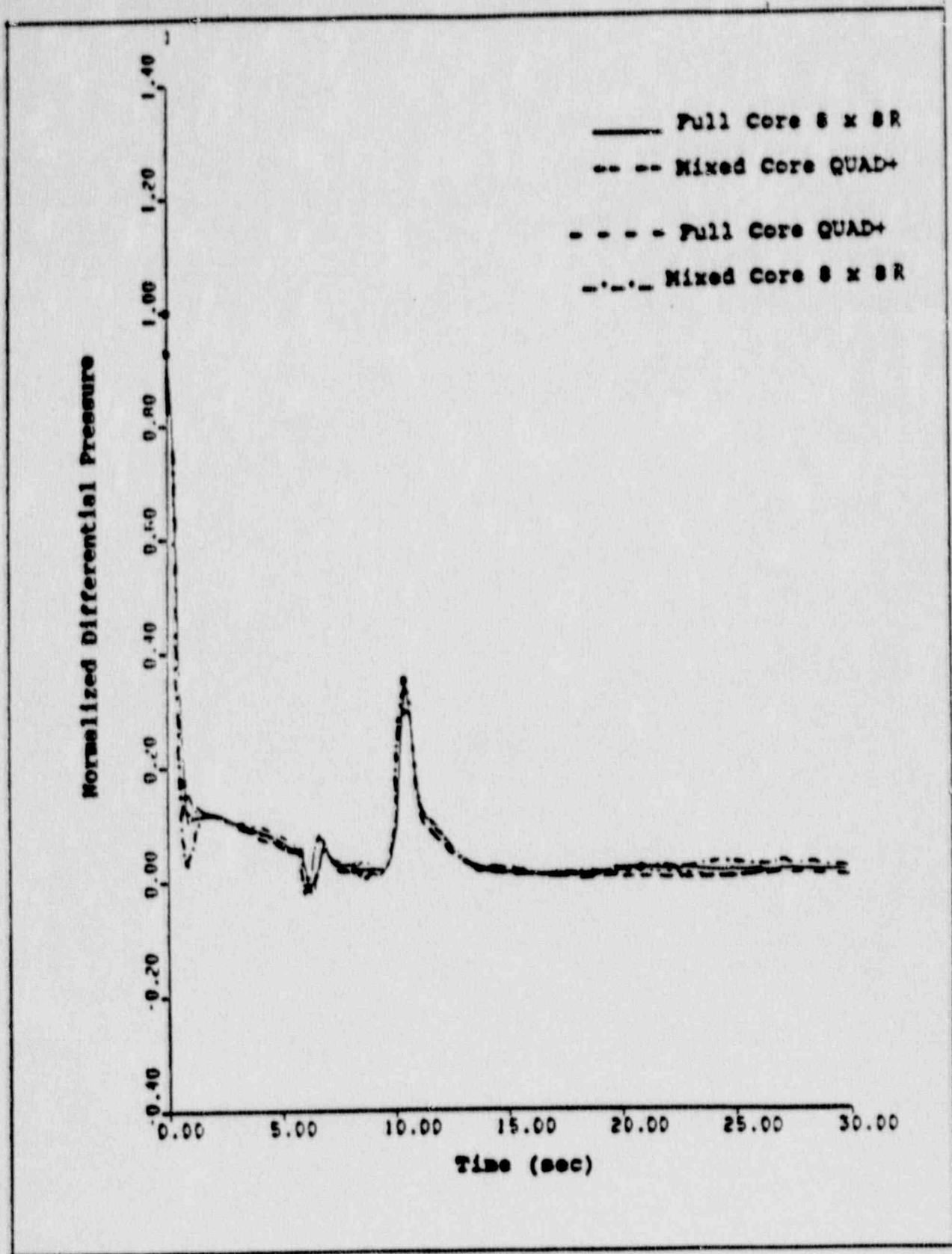


Figure 5-3 Normalized Side Entry Orifice Differential Pressure vs Time

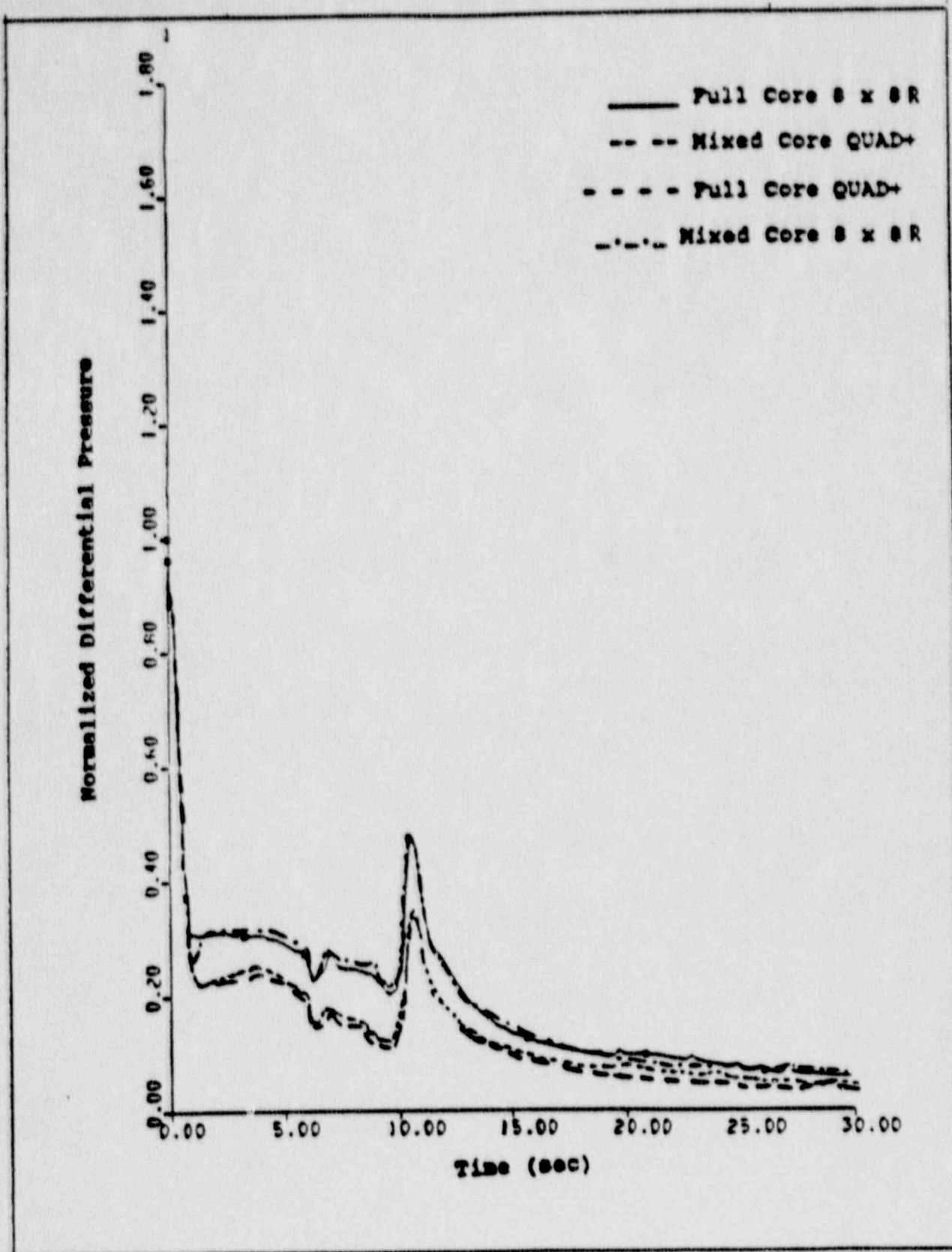


Figure 5-4 Normalized Lower Tie Plate Differential Pressure vs Time

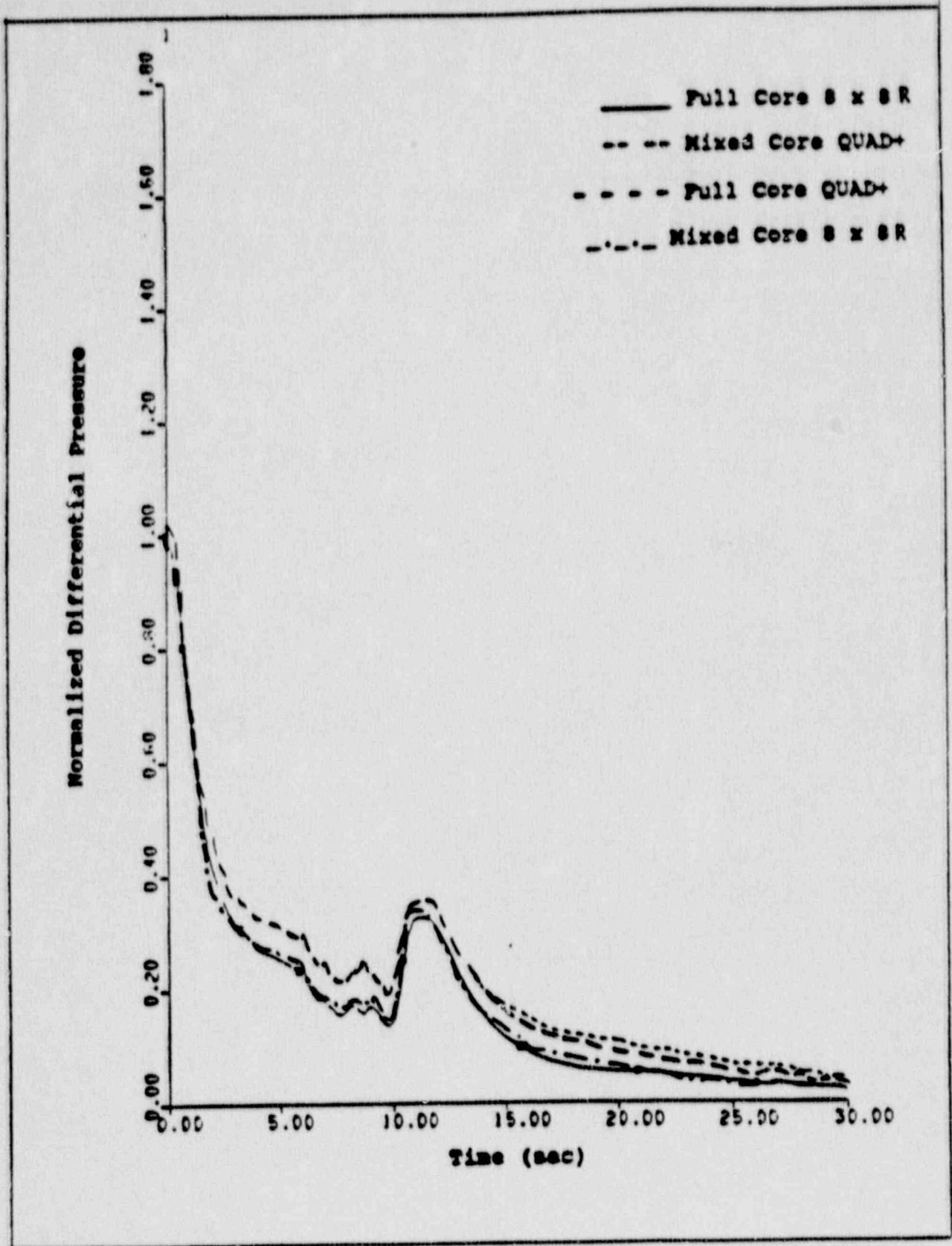


Figure 5-5 Normalized Heated Length Differential Pressure vs Time



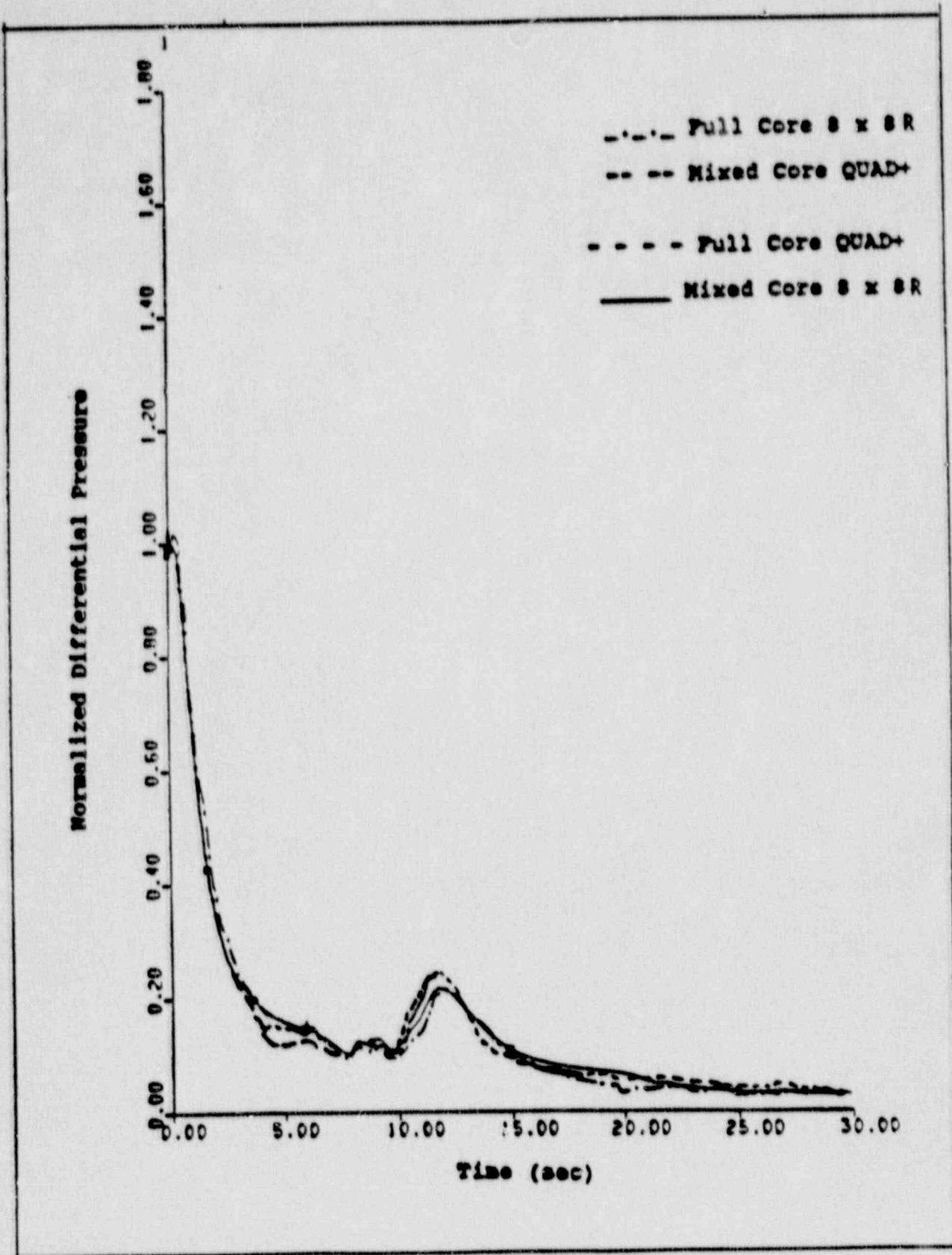


Figure 5-6 Normalized Upper Tie Plate Differential Pressure vs Time

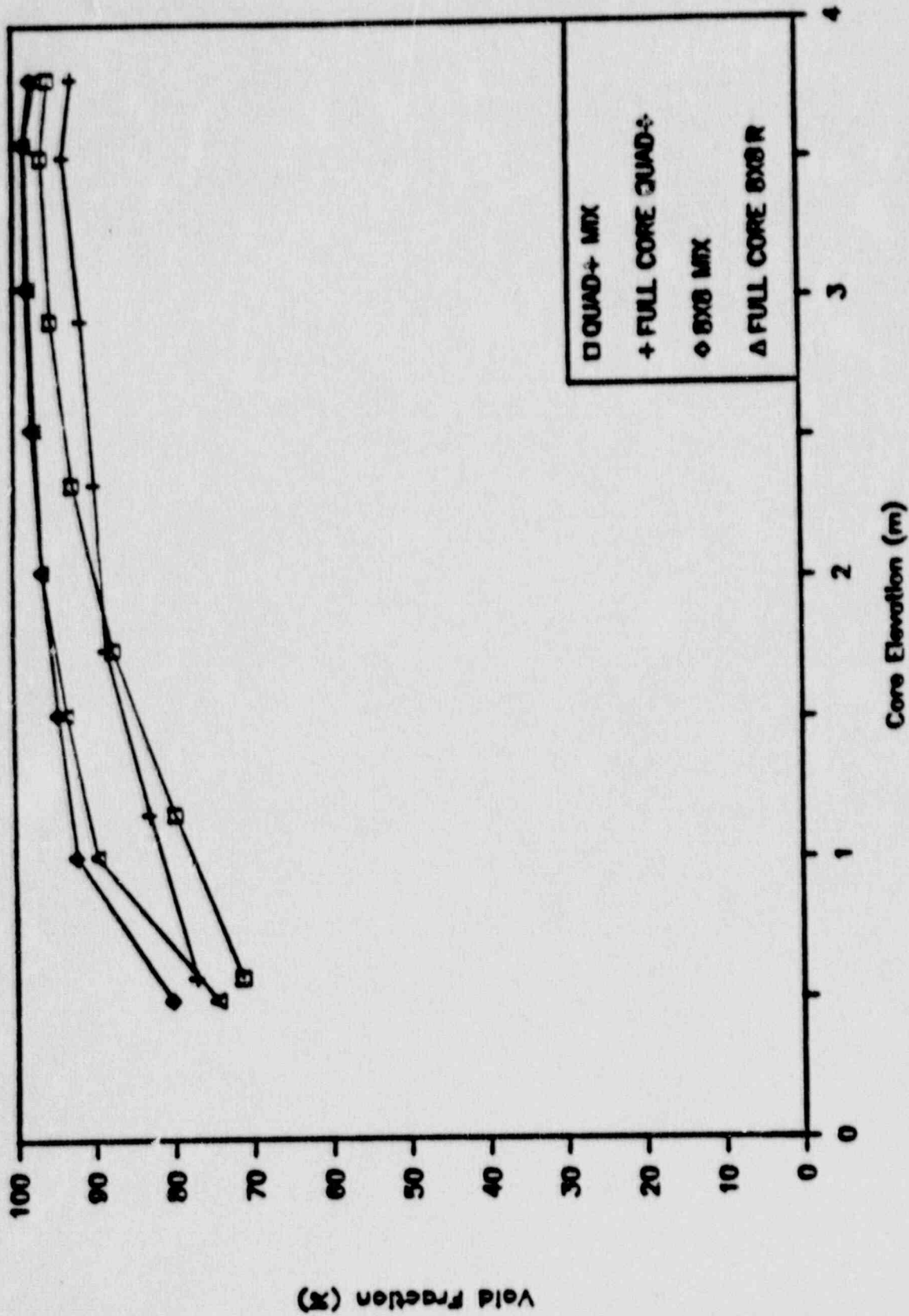


Figure 5-7 Core Void Fraction at 20 Seconds vs Core Elevation

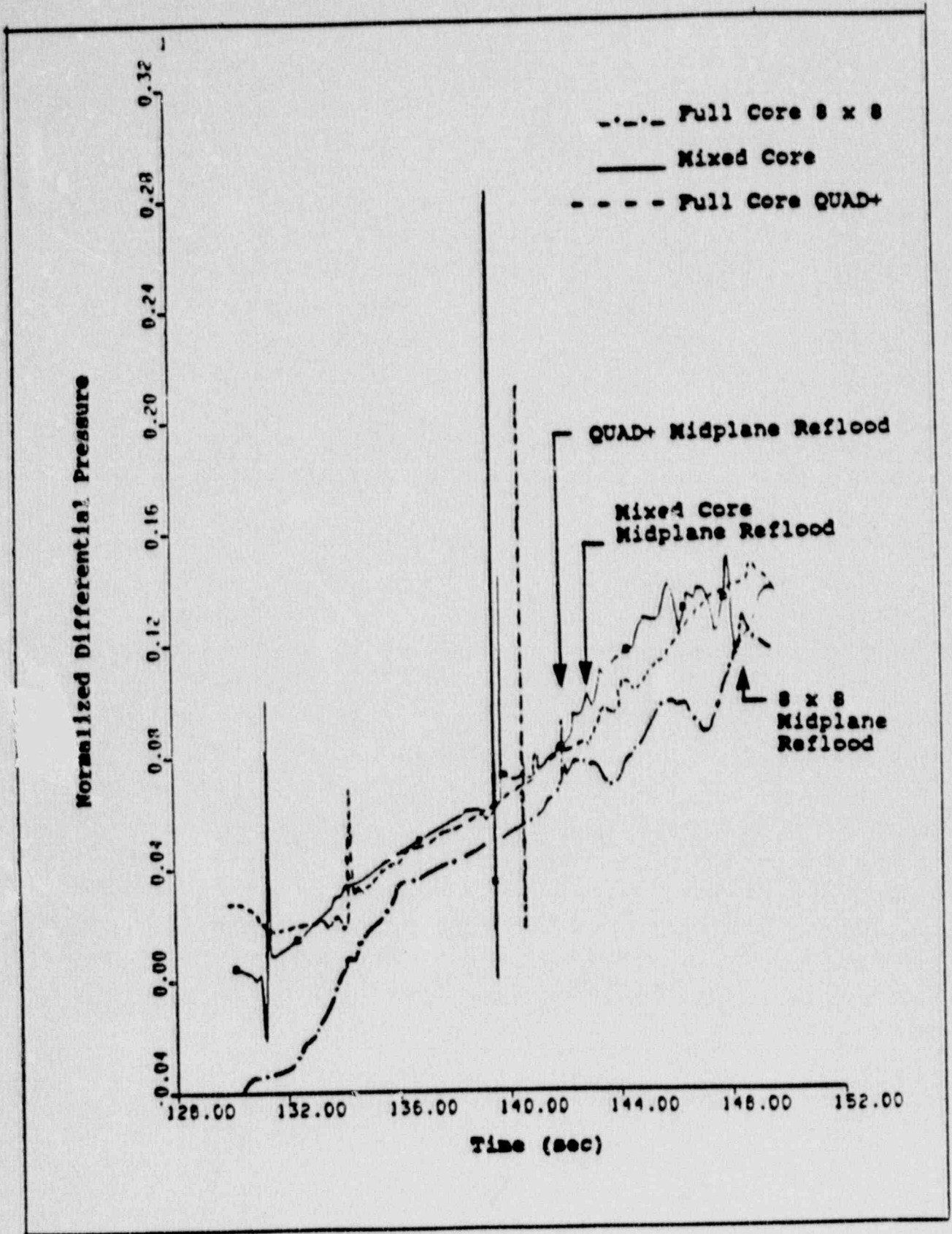


Figure 5-8 Normalized Assembly Differential Pressure vs Time

## Question 6

Sec. 4-8, Ref. 1. Discuss the effect of radiation heat transfer on the PCT when rods start to perforate and the core geometry starts to change, including the possibility of the rod bowing.

## Response

Upon the calculated perforation of the first rod, the gray body factors used in the radiation heat transfer calculation are modified to reflect the strained bundle geometry. For conservatism, the modified gray body factors are calculated assuming all rods are at their final strained dimensions.

Two CHACHA-3C sensitivity studies were performed to evaluate the impact of the strained bundle geometry on the radiation heat transfer for the reference transient. The first case used gray body factors corresponding to the nominal (no strain) geometry for the entire transient. The second case used gray body factors after the first perforation which corresponded to all rods strained such that the rod-to-rod gap is reduced to 1% of the nominal value. For the QUAD+ geometry, with a cladding outer diameter of 0.4576 inch and a rod pitch of 0.609 inch, this corresponds to a final strain of 0.33 for all rods.

Based on comparisons of the reference transient and the parametric runs described above, the effect of the strained bundle geometry on radiation heat transfer and PCT may be summarized as follows:

Outer rods - The temperatures of the 12 peripheral rods in a QUAD+ minibundle decrease as strain increases. This result is due to the increase in radiation heat transfer from the outer rods to the channel as the effective heat transfer area of the rods increases.

Inner rods - The temperatures of the 4 central rods in a QUAD+ minibundle increase as the strain increases. This result is due to the decrease in radiation heat transfer from the inner rods to the channel as the strained

outer rods "block" more and more of the radiation view factor. The increase in radiation heat transfer from the inner to outer rods does not completely compensate for this effect, since the outer rods are still significantly hotter than the channel wall.

For the reference transient, the no strain gray body factors resulted in a PCT of [ ]<sup>oC</sup>. The gray body factors corresponding to all rods strained to 99% gap closure resulted in a PCT of 1039°C. These differences would be more pronounced if the channel had rewetted prior to reflood, or if the reference transient had resulted in higher PCT.

The QUAD+ fuel assembly is designed to resist bowing of fuel rods, as described in Section 4.4.1 of Reference (6-1). Even allowing for the possibility of some degree of rod bow, the impact on PCT would clearly be bounded by the second case described above, which used gray body factors corresponding to all rod-to-rod gaps reduced to 1% of the nominal gap.

#### References

- (6-1) "Westinghouse Reference Safety Report for BWR Fuel," WCAP-11500 (Proprietary), August 1987.

### Question 7

Page 3-7, Ref. 2. In order to demonstrate a proper integration of material and hydraulic models, provide the major steps to arrive at the result of peak cladding burst at 98 seconds.

### Response

The cladding heatup for the hot rod for 0 to 100 seconds of the reference case is shown in Figure 7-1. The core midplane coolant pressure transient is shown in Figure 7-2. The rod internal pressure is shown in Figure 7-3. A comparison of Figures 7-2 and 7-3 shows that the rod internal pressure exceeds the coolant pressure after 30 seconds. This is reflected in the cladding stress, shown in Figure 7-4. This figure also shows the allowable cladding stress versus time, and the intersection of the actual and allowable stress curves at 98 seconds. The swelling of the cladding prior to burst is shown in Figure 7-5. The rapid swelling from 73 to 98 seconds is due to the plastic deformation of the cladding.

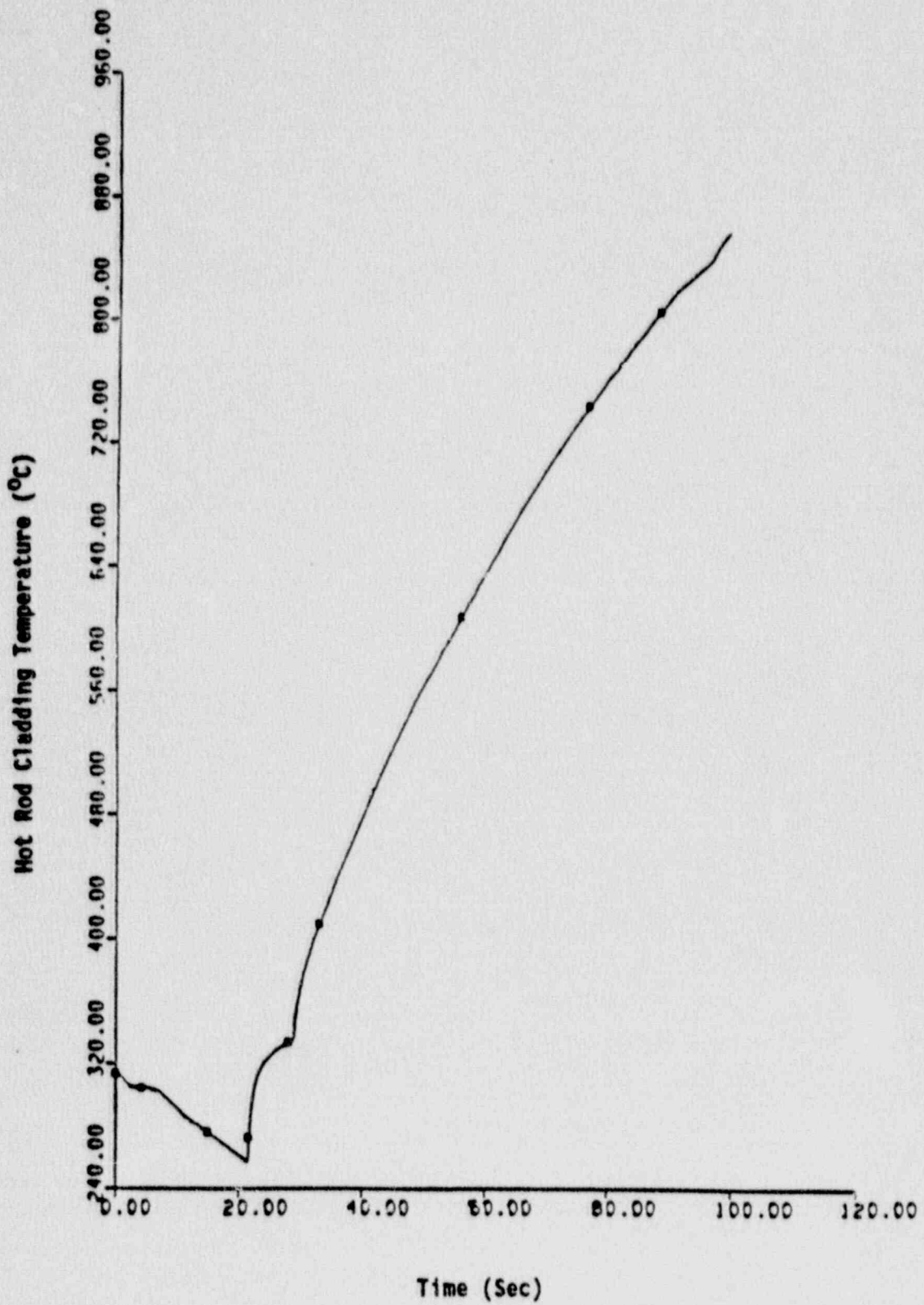


Figure 7-1 Hot Rod Cladding Temperature for Reference Transient

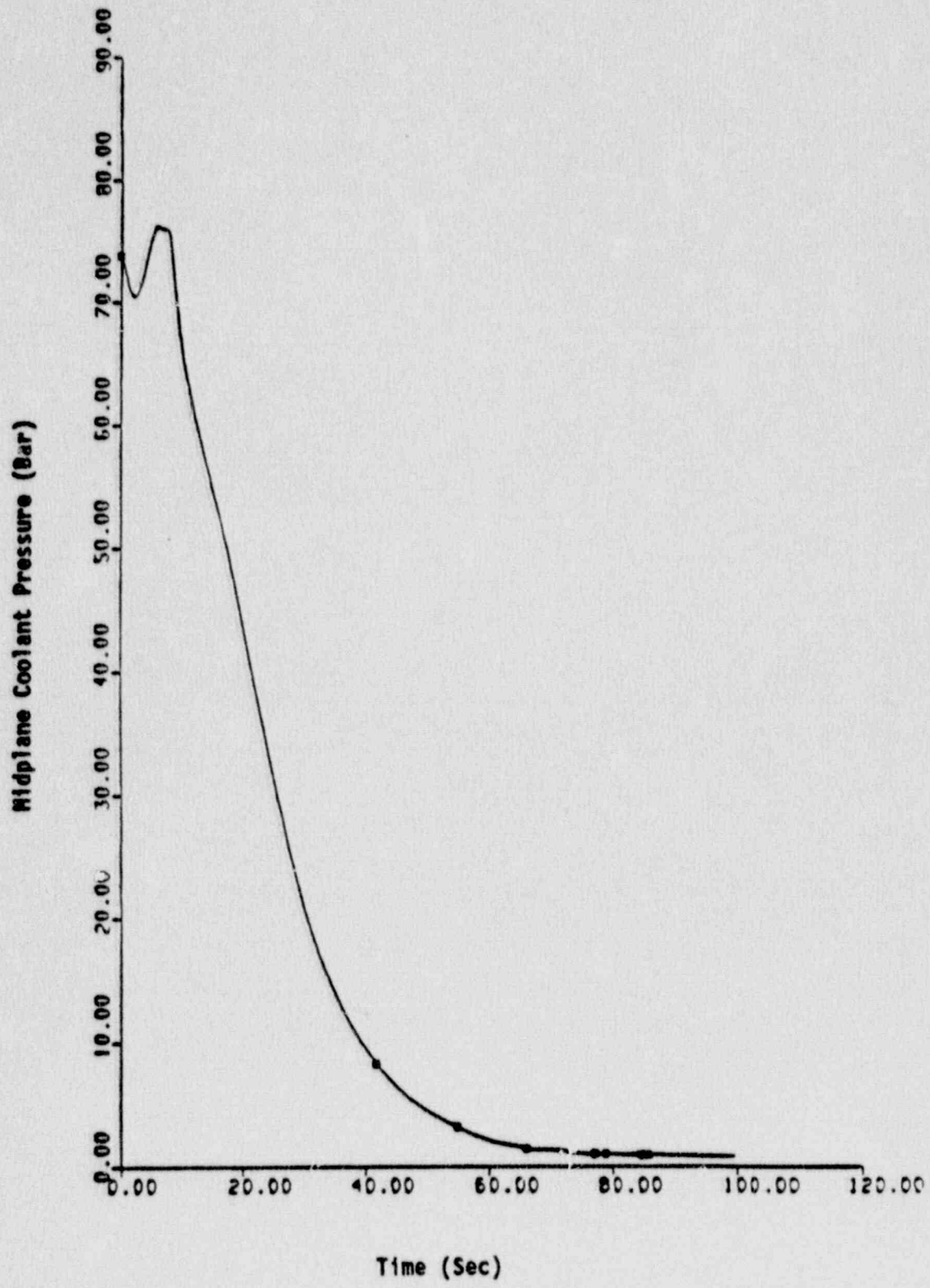


Figure 7-2 Midplane Coolant Pressure for Reference Transient



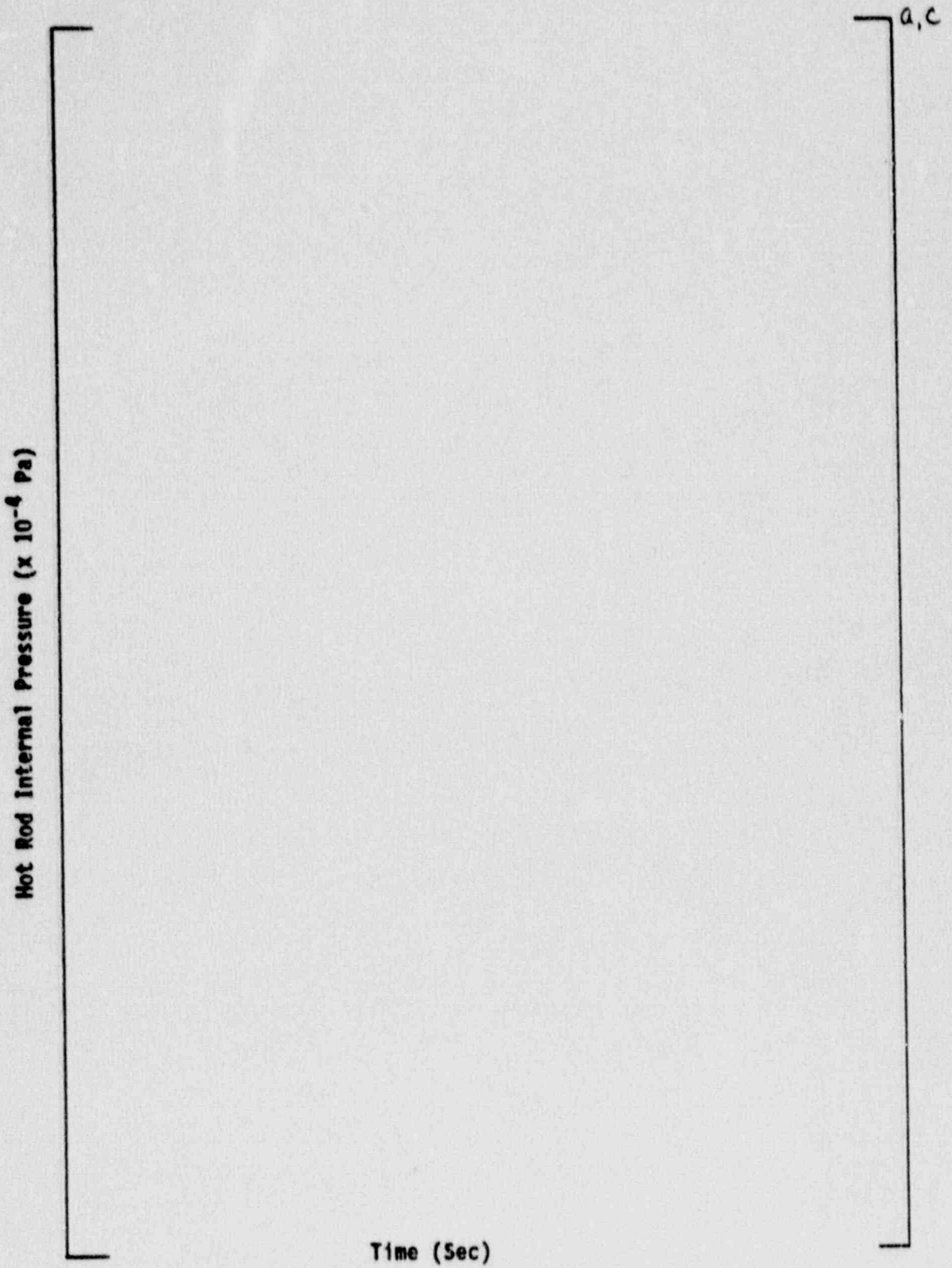


Figure 7-3 Hot Rod Internal Pressure for Reference Transient

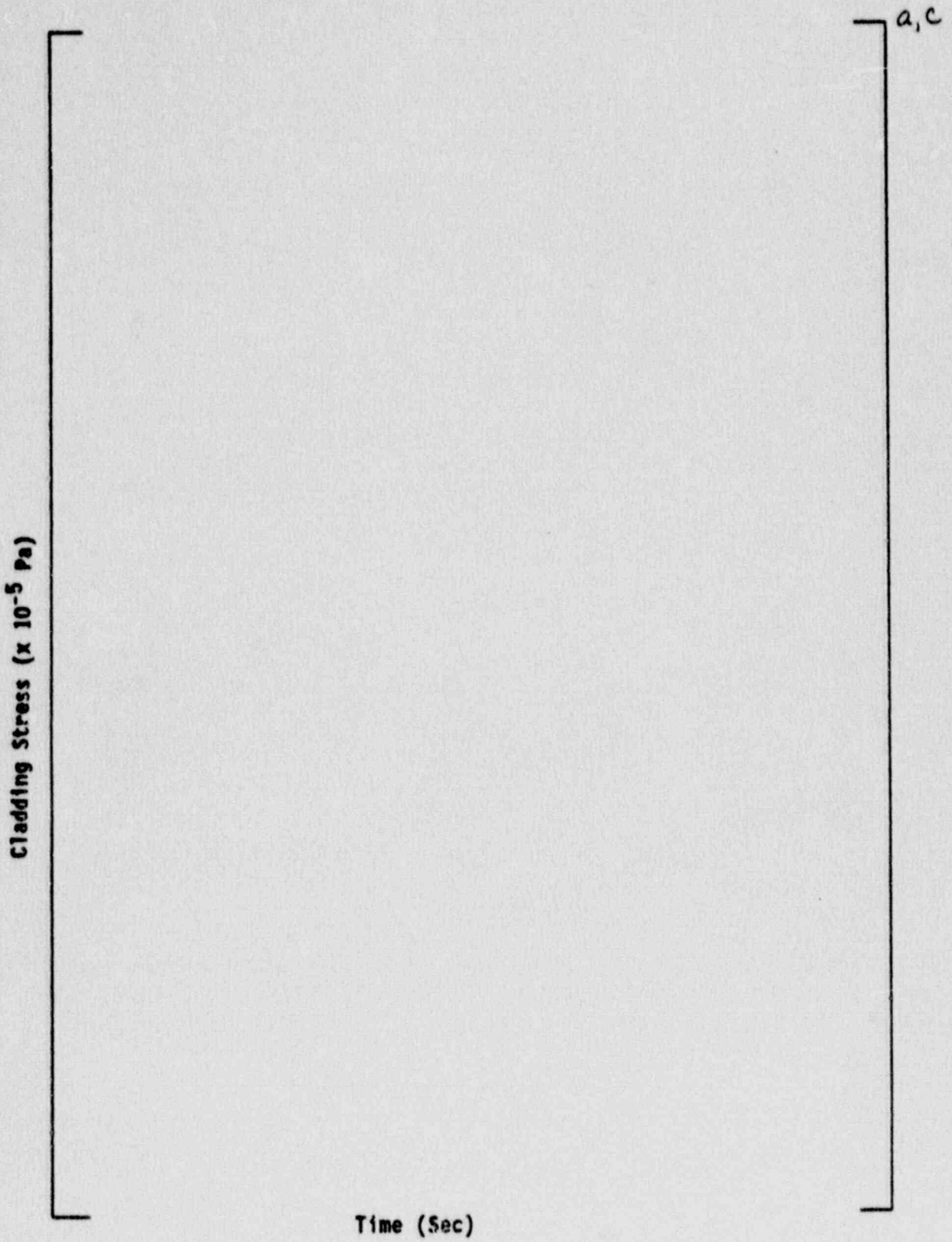


Figure 7-4 Hot Rod Cladding Stress for Reference Transient

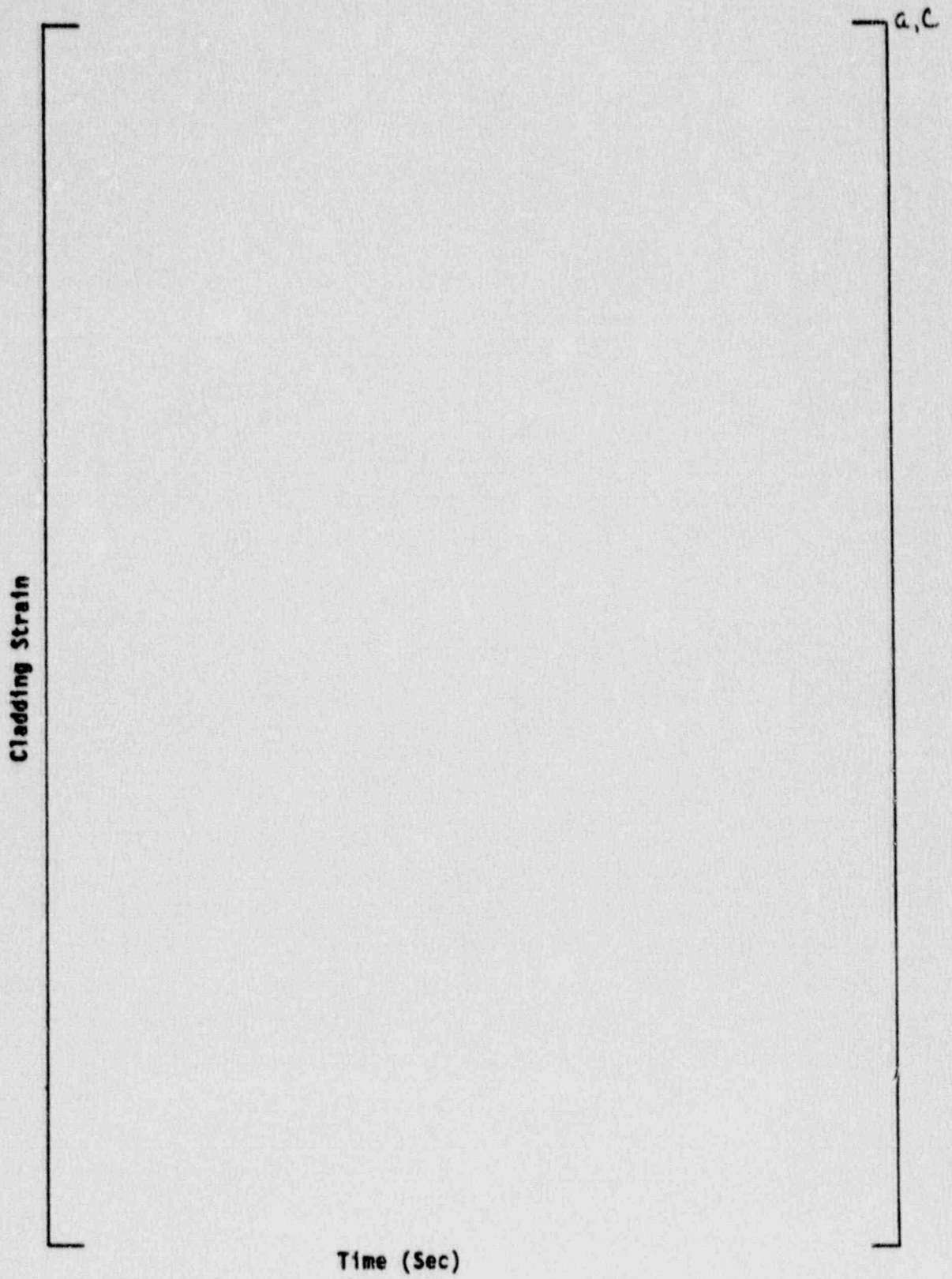


Figure 7-5 Hot Rod Cladding Strain for Reference Transient

### Question 8

Page 3-22, Ref. 1; Pages 5-1, 5-2, Ref. 2. Values of  $K_L$  and  $K_U$  determine the liquid phase and gas phase fluxes in the CCFL correlation. Justify that the use of  $K_L$  and  $K_U$  that best fit the A-A 8 x 8 bundle geometry would also be appropriate for the QUAD+ geometry. Describe the experimental geometry and provide results that are used to justify the statement "The correlation conservatively calculates a 25 percent less liquid penetration into the fuel bundle than was observed in the test." In particular, data for liquid draining rate and gas upflow rate are needed.

### Response

The countercurrent flow limitation (CCFL) correlation used in GOBLIN/DRAGON contains two correlating coefficients  $K_L$  and  $K_U$ . These coefficients were originally determined based on formulations and data by Bailey and Eriksson (Reference (8-1) and (8-2) below).

A CCFL experiment was conducted using prototypical QUAD+ hardware to demonstrate the appropriateness of the GOBLIN/DRAGON CCFL correlation for QUAD+ fuel. A description of the test and summary of the results are presented below.

Nitrogen/water tests were performed on a full-scale model of the upper half of the BWR QUAD+ fuel assembly to determine the countercurrent flow limiting (CCFL) characteristics of the rod bundle top spacer and upper tie plate. A schematic of the test facility is shown in Figure 8-1. The atmospheric tests were carried out for 5 and 10 gpm spray water injection rates and a range of gas flow rates to obtain data covering the CCFL performance of the fuel assembly from the onset of CCFL to flooding.

The tests were repeated with several different gas/water injection techniques. Tests were run without gas flow up the watercross and with sufficient gas flow to create flooding at the watercross exit. Tests also were run with two different methods of introducing the injected water. A

spillover method was used where the water entered the bundle by spilling over the channel lip. The other method used a shower head to spray the injected water above the bundle.

Figure 8-2 shows the liquid drain rate as a function of gas flow for the 5 and 10 gpm tests with and without gas flow in the watercross. The spillover method was used in the collection of these data. The influence of the watercross flooding is negligible. At low gas flows the water drain rate reaches a plateau due to the limited injection flow rate, not due to CCFL.

Figure 8-3 shows a comparison of the two water injection methods. The shower head water introduction method produced slightly more restrictive CCFL, than the spillover method. This is attributed to the smaller drops created in the shower head. These two methods examine the two limiting water injection configurations. An actual reactor situation would be expected to be some combined condition.

All the data presented above was compared to the CCFL correlation in GOBLIN/DRAGON. The general form of the correlation is

$$\text{where } K_g^{1/2} + K_l^{1/2} = K_u^{1/2}$$

$$K_g = \rho_g^{1/2} j_g / (\sigma g_c (\rho_l - \rho_g))^{1/4}$$

$$K_l = \rho_l^{1/2} j_l / (\sigma g_c (\rho_l - \rho_g))^{1/4}$$

and  $j_l$  is positive downward.

Evaluating the GOBLIN/DRAGON correlation for the conditions and geometry of the CCFL test gives  $K_u = \left[ \frac{a_1 c}{\rho_l} \right]^{1/2}$ . A comparison of the GOBLIN/DRAGON correlation with the data is shown in Figure 8-4. The correlation is more restrictive over the range of liquid flows,  $K_l^{1/2}$ , where the facility water flow rate was not limiting ( $K_l^{1/2} < 0.4$ ). In a typical LOCA analysis calculation  $K_l^{1/2}$  is much less than 0.4 (less than 0.05). Hence in

a LOCA analysis calculation a more restricted upper bundle CCFL is conservative because it limits the amount of injection water available for cooling the bundle and draining into the lower plenum for refilling the vessel.

In summary, the Westinghouse CCFL tests conducted for the QUAD+ fuel geometry demonstrates that the CCFL correlation in GOBLIN/DRAGON is conservative. The correlation is 25 percent more restrictive in the liquid drain flow rate than observed in the test for typical LOCA analysis conditions (see Figure 8-4)).

#### References

- (8-1) Bailey, R. V., et al, "Transport of Gases Through Liquid-Gas Mixtures," Paper presented at the AIChE New Orleans Meeting, 1956.
- (8-2) Eriksson, S. O., et al, "Experiment Med Motriktade Ångflöden i strilkyliningskretsen, GÖTA, Studsvik, AEA-15, 1977.

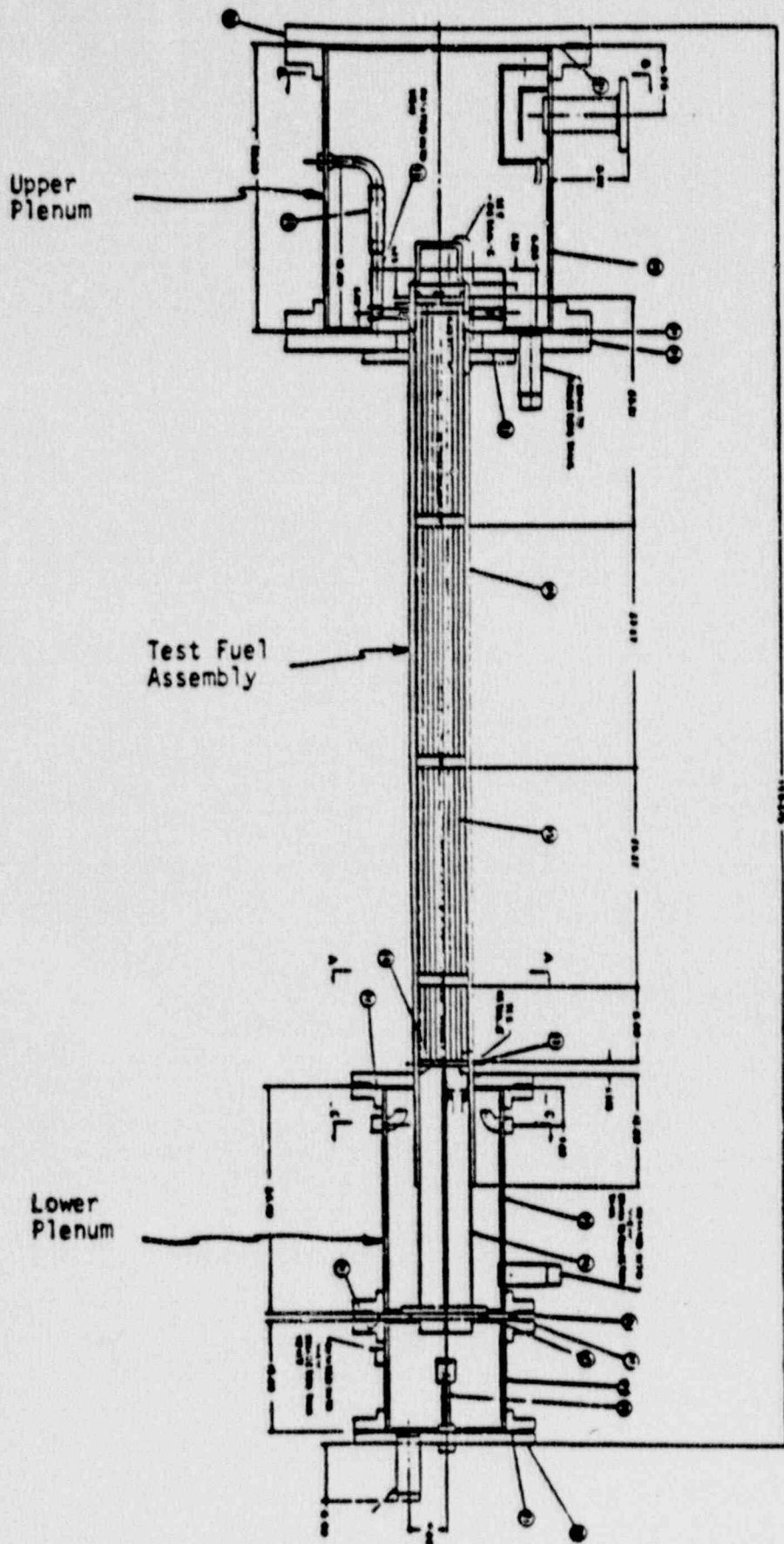
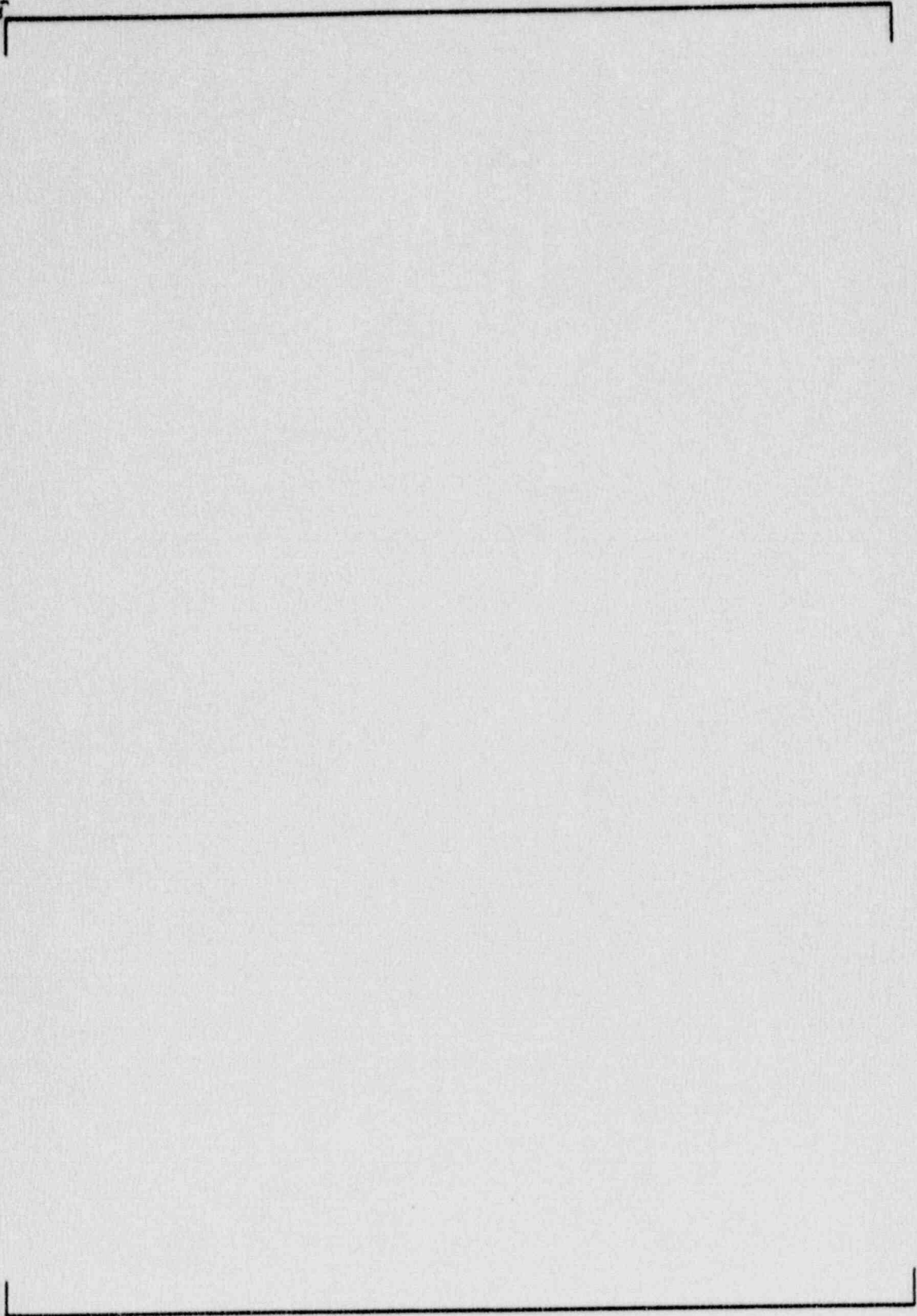


Figure 8-1 QUAD+ Counter Current Flow Test Facility

Figure 8-2 Spillover Water Injection

BWR QUAD+ ROD BUNDLE CCFL DATA  
WATER INJECTION TO FUEL ASSEMBLY: 5 GPM AND 10 GPM  
WATER CROSS NITROGEN FLOW: 0.0 AND FLOODING

a, b, c



WATER FLOW IN ROD BUNDLES (LBM/SEC)

NITROGEN FLOW IN ROD BUNDLES (LBM/SEC)



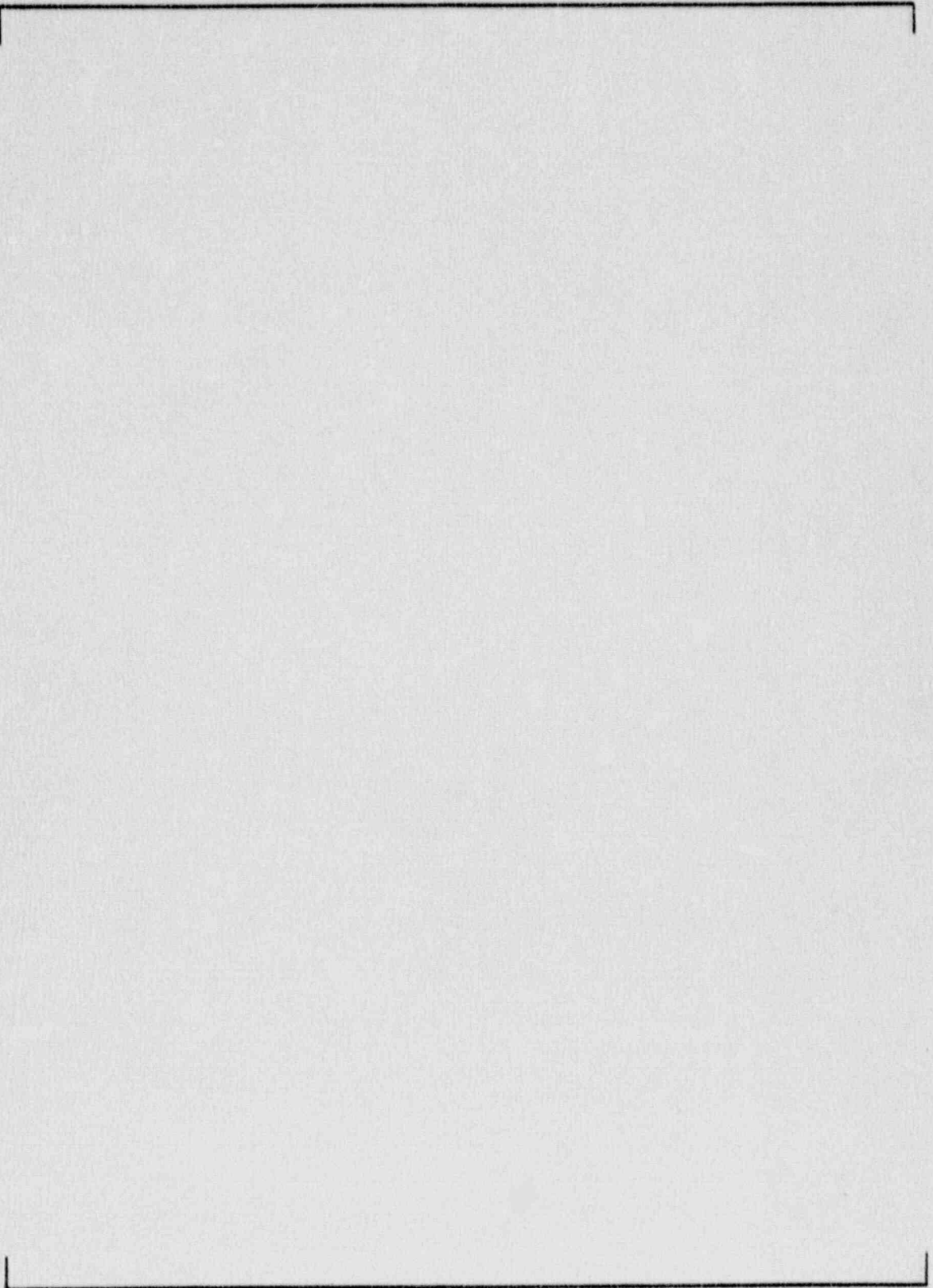
**Figure 8-3 Shower Head Water Injection**

**BWR QUAD+ ROD BUNDLE CCFL DATA**

**WATER INJECTION TO FUEL ASSEMBLY: 5 GPM AND 10 GPM**

**WATER CROSS NITROGEN FLOW: 0.0 AND FLOODING**

a,b,c



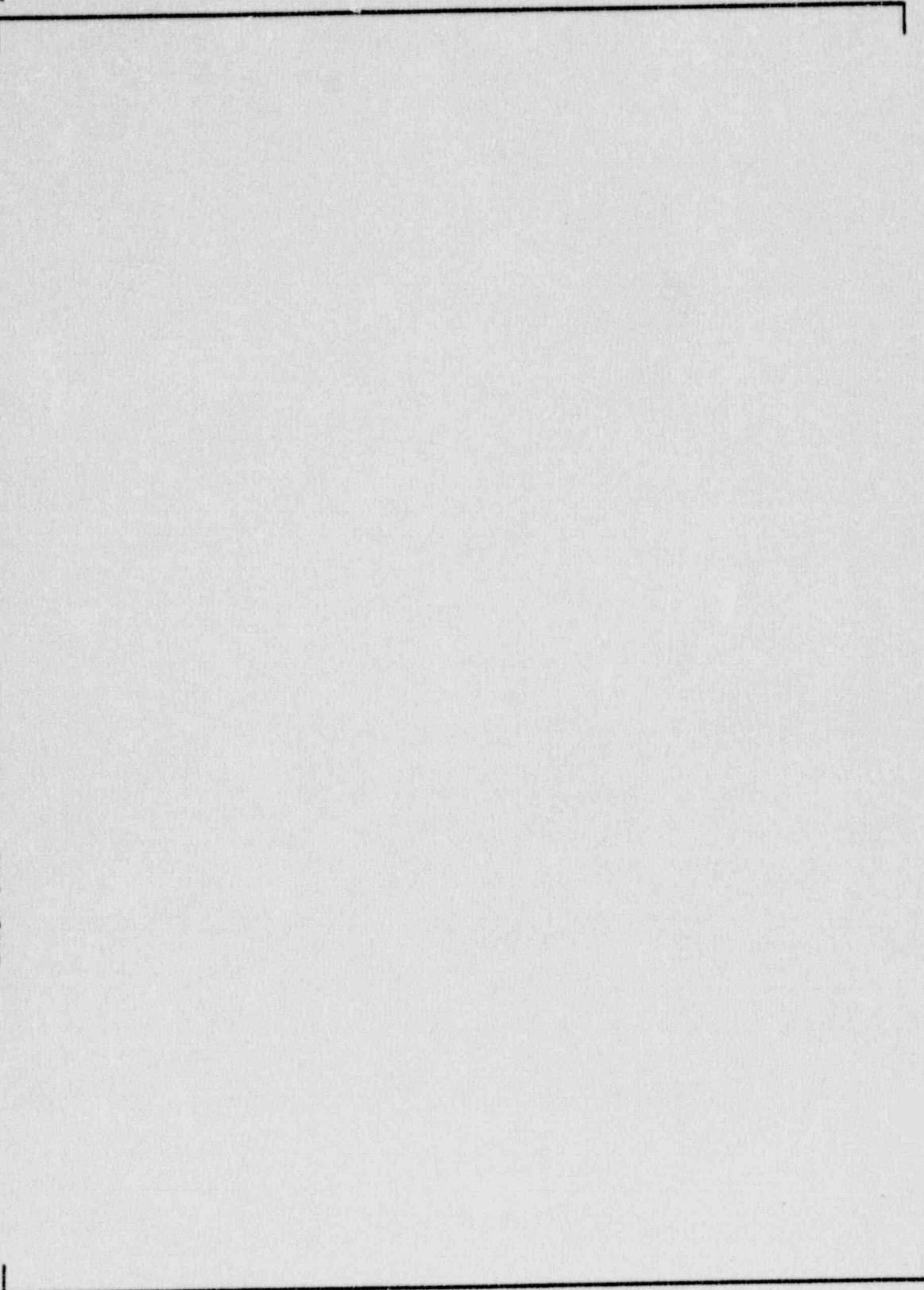
WATER DOWNFLOW IN ROD BUNDLES (LBM/SEC)

NITROGEN UPFLOW IN ROD BUNDLES (LBM/SEC)

Figure 8-4 Data Correlation Comparison

BWR QUAD+ ROD BUNDLE CCFL DATA  
WATER INJECTION TO FUEL ASSEMBLY: 5 GPM AND 10 GPM  
WATER CROSS NITROGEN FLOW: 0.0 AND FLOODING  
WATER INJECTION METHOD: SPILLOVER AND SHOWER HEAD

a,b,c



### Question 9

Page 3-36, Ref. 1. Reference 1 characterizes the modified Bernoulli equation as providing a conservative prediction of subcooled break flow. Identify the reference to the modified Bernoulli equation which discusses the conservatism. In the Westinghouse model, what guidance is provided to a user for critical flow checks so that the consistency of solutions is ensured?

### Response

The modified Bernoulli equation is conservative for the prediction of the maximum subcooled break flow rate (calculated using equation 3.3-57 of Ref. 1) because friction is neglected. The flow resistance coefficient ( $\xi$ ) from the stagnation point to the exit is set equal to zero in the Westinghouse LOCA evaluation model.

The GOBLIN critical flow check compares the flow rate determined by the solution of the momentum equation and the flow rate determined from the applicable critical flow model. Critical flow is used when the flow rate calculated by the momentum equation is greater than the critical flow rate for that flowpath.

For recirculation line breaks, the Westinghouse evaluation model methodology uses critical flow checks at three locations. Each critical flow check is in the broken recirculation line at the location of greatest physical restriction or largest pressure drop (i.e., the locations where choked flow is expected to occur). Two of the locations are at each side of the break point and the third is at the jet pump drive nozzle.

The critical flow check is used at two locations where a two-phase level may uncover the flowpath. These locations are the drive nozzle of the broken jet pump and the vessel side of the guillotine break in the recirculation line. The two-phase level is the downcomer level, which drops rapidly during the initial blowdown. The description of the two-phase level includes the position or height and the quality of the fluid in the appropriate regions.

When the two-phase level uncovers a flowpath, the level is traced within the height of the flow path. As the level moves, the conditions above the level are mixed with the conditions below the level to accurately model the quality of the fluid at the break location.

### Question 10

Page 3-63, Ref. 1. Identify the new correlation to replace or modify the A-A correlation for the critical heat flux in order to reflect the QUAD+ fuel design.

### Response

Steady-state and transient CHF tests have been conducted by Westinghouse using a simulated QUAD+ minibundle. The resulting test data were used to develop and verify the WB-1 correlation, which uses the critical quality-boiling length formulation. The correlation description and comparisons with steady-state and transient test data are reported in Reference (10-1). The WB-1 correlation has been incorporated into GOBLIN/DRAGON and replaces the AA-74 correlation for use in QUAD+ fuel analysis. (Note that when fluid conditions are outside of the range of the WB-1 correlation Equation 3.5-34 is replaced with  $q_{crit}'' = q_{pc}''$ .)

### Reference

(10-1) "QUAD+ BWR Critical Power Correlation Development Report," WCAP-11287 (Proprietary), September 1986.

### Question 11

Page 6-77, 6-84, 6-92 and Sec. 6.2.4, Ref. 1. GOBLIN significantly overestimates early bundle flow rate (0 to 2 s) for all the cases presented (Figs. 6-33, 6-40, and 6-48,) which is a nonconservative result. Rod temperature test results for TLTA test 6423 indicate early rod dryout in the upper regions of the core (Ref: US Nuclear Regulatory Commission report NUREG/CR-3633, EGG-2294, Vol. 4, p. 65). The GOBLIN analysis might miss this early dryout because of an excessive core flow rate. The TLTA test results mentioned above are not available in the Westinghouse report. It is essential that rod temperature analysis results be supplied so that the effect of overestimated bundle flow rate can be assessed.

### Response

Part of the qualification of the GOBLIN/DRAGON code presented in Ref. 1 consisted of simulations of two integral tests conducted in the two-loop test apparatus (TLTA) (Ref. 1). The tests (Reference (11-1)) simulated were an average power bundle with nominal emergency core cooling (case 6425 run 2) and a high power bundle with degraded emergency core cooling (case 6423 run 3). The more severe transient, case 6423 run 3, was repeated with several refinements included to reaffirm the initial integral qualification assessment and provide additional detail regarding the simulation.

TLTA case 6423, run 3 is an integral simulation of a full guillotine break of the recirculation line in a jet pump boiling water reactor. The test models a single, full length 8 x 8 fuel assembly at a peak power of 6.46 MW. The high and low pressure core spray systems were degraded from their nominal flow rates and emergency core cooling fluid temperature was increased from nominal to 200°F.

The primary difference between the simulation of case 6423 run 3 presented here and that documented in Ref. 1 is in the initial and boundary conditions. An effort was made to much more closely match the test initial and boundary conditions to confirm that observed deviations in the original simulation were a consequence of these initial condition differences. Table 11-1 summarizes the test, original simulation, and revised simulation initial conditions. The significant changes are better matches of initial downcomer mass inventory and lower plenum enthalpy. The downcomer mass affects the initial depressurization through break uncover timing and the lower plenum enthalpy affects the timing of lower plenum flashing.

One key boundary condition is the steamline flow rate. Modelling of the steam line valve closure was also modified to better match the measured steam line flow (See Figure 11-1). This change noticeably improved the early pressure transient as will be seen in the results presented below.

The GOBLIN simulation of TLTA case 6423 run 3 excluded several Appendix K evaluation model requirements in order to properly evaluate the code. The Appendix K requirements excluded from the system simulation are:

- o Rewetting of the fuel rods was allowed
- o The best estimate homogeneous equilibrium critical flow model with subcooled flow multipliers based on TLTA orifice critical flow data, was used, replacing the Appendix K required Moody model.
- o The actual test power history was used whereas Appendix K requires the ANS 1971 decay heat curve plus 20 percent conservatism.

A comparison of the GOBLIN system simulation with test measurements is presented first. Then an additional heatup calculation is presented, which includes some Appendix K conservatism, to demonstrate the conservative margin inherent in the LOCA evaluation model.

The GOBLIN simulation system pressure response is shown in Figure 11-2. The simulation agrees very well with the measured pressure. The initial depressurization is due to the subcooled break flow. The pressure recovery from about 4 to 7 seconds is a consequence of the rapid steamline valve closure (See Figure 11-1). At 7 seconds the downcomer level uncovers the jet pump allowing vapor to flow out the drive line side of the break and causing a return of the system depressurization. The jet pump uncover is shown in the downcomer level plot of Figure 11-3 and is apparent in Figure 11-4 where the intact jet pump performance is severely degraded after 7 seconds. A more rapid depressurization occurs at about 10 seconds once the downcomer is empty and vapor also flows out the recirculation line suction side of the break. The remainder of the depressurization follows the test data very closely with a slightly lower final pressure.

The bundle inlet flow for the initial phase of the transient is shown in Figure 11-5. The general agreement with data is good. The initial drop in bundle flow is a little sharper in the test. This is a reflection of the initial flow reversal in the broken jet pump (Figure 11-6) which is attributed to the initial, rapid nonequilibrium break flow out the broken jet pump drive line. The GOBLIN equilibrium code does not fully capture this small nonequilibrium effect. The start of lower plenum flashing also is visible in Figure 11-5 in the rise in bundle inlet flow at about 15 seconds.

The total vessel mass inventory is shown in Figure 11-7. The good agreement of the total mass inventory and system pressure responses confirms the accurate calculation of the break flow throughout the transient. (Accurate direct measurements of the break flow in the test were not available).

A comparison of the mass inventory distribution throughout the transient are shown in Figures 11-8 and 11-9. The agreement in the trends and timing of event is quite good. The downcomer mass inventory agreement is excellent. The bypass and guide tube also agree well when considering the offset in the initial and final all liquid states. The larger initial guide tube mass and smaller bypass mass is attributed to the deviation in the definition of the boundary between the guide tubes and bypass for the simulation versus the test.



The upper plenum, bundle, and lower plenum mass distributions also have good agreement with the data. (Please note that level tracking in the GOBLIN simulation continuously redefined the control volumes in the upper plenum/separator region, therefore, comparison of the upper plenum mass over the exact same region of measured in the test was not possible). In summary, GOBLIN does an excellent job of predicting the mass inventory distribution through the vessel during the LOCA transient.

Comparisons of the test rod thermocouple measurements at various elevations with the GOBLIN predictions are shown in Figures 11-10, 11-11, and 11-12. The GOBLIN simulation gives a good prediction of the average rod temperature response throughout the bundle. Note that the simulation provides average hydraulic and rod conditions, hence, all the local thermocouple variations are not predicted. The simulation generally does an excellent job of predicting the rod dryout, heatup, and rewet. The blowdown dryout occurring high in the bundle is calculated to be later in time and more pronounced. This is a consequence of the later and longer drop in calculated bundle inlet flow discussed earlier and shown in Figure 11-5. The lower temperatures following rewet at the lower bundle elevations are a result of the lower predicted system pressure reducing the fluid saturation temperature.

The test simulation comparison presented here shows the ability of GOBLIN to calculate the average thermal-hydraulic response during a LOCA transient. To demonstrate that substantial conservative margin above the peak TLTA measured temperature is inherent in LOCA evaluation model, the Appendix K required rod heat transfer was introduced in a hot plane heatup calculation of the TLTA simulation. The prescribed rod heat transfer coefficients as a function of time are shown in Figure 11-13. The Appendix K requirements are no rewetting of the rods, zero heat transfer following uncover and prescribed heat transfer during spray cooling and after reflood. The resultant rod temperature transient is shown in Figure 11-14. Clearly, the conservatism from the above stated Appendix K requirements introduces a large peak cladding temperature margin above the rod temperature measurements for the TLTA simulation. Additional PCT margin is inherent in the evaluation model due to other conservative assumptions excluded from this simulation (e.g., break flow model and decay heat curve).

Figures 11-15 through 11-21 are replotted results of the original TLTA case 6423 run 3 simulation reported in Ref. 1. These figures supersede the original Figures 6-40 through 6-46 of Ref. 1 and shall be incorporated in the final (approved) version of the topical report.

#### Reference

- (11-1) W. J. Letzing et.al., BWR Blowdown Emergency Core Cooling Program Preliminary Facility Report for the BD/ECC-1A Test Phase, GEAP-23592, December 1977.

TABLE 11-1  
COMPARISON OF TLTA 6423 RUN 3 INITIAL CONDITIONS

	GOBLIN		
	<u>Test</u>	<u>Original</u>	<u>Revised</u>
Bundle Power (MW)	6.46	6.46	6.46
Steam Dome Pressure (psia)	1037 ± 5	1016	1031
Lower Plenum Enthalpy (Btu/lbm)	518 ± 5	451	518
Feedwater Enthalpy (Btu/lbm)	41 ± 2	41	41
Feedwater Flow (lbm/sec)	1.0 ± 0.3	1.0	1.2
Jet Pump 1 Flow (lbm/sec)	17 ± 2	20	18.5
Jet Pump 2 Flow (lbm/sec)	19 ± 2	20	19.0
Bundle Inlet Flow (lbm/sec)	33 ± 5	37	34
Downcomer Mass (lbm)	310	460	312
Initial Water Level (inch elev.)	123 ± 6	122	122

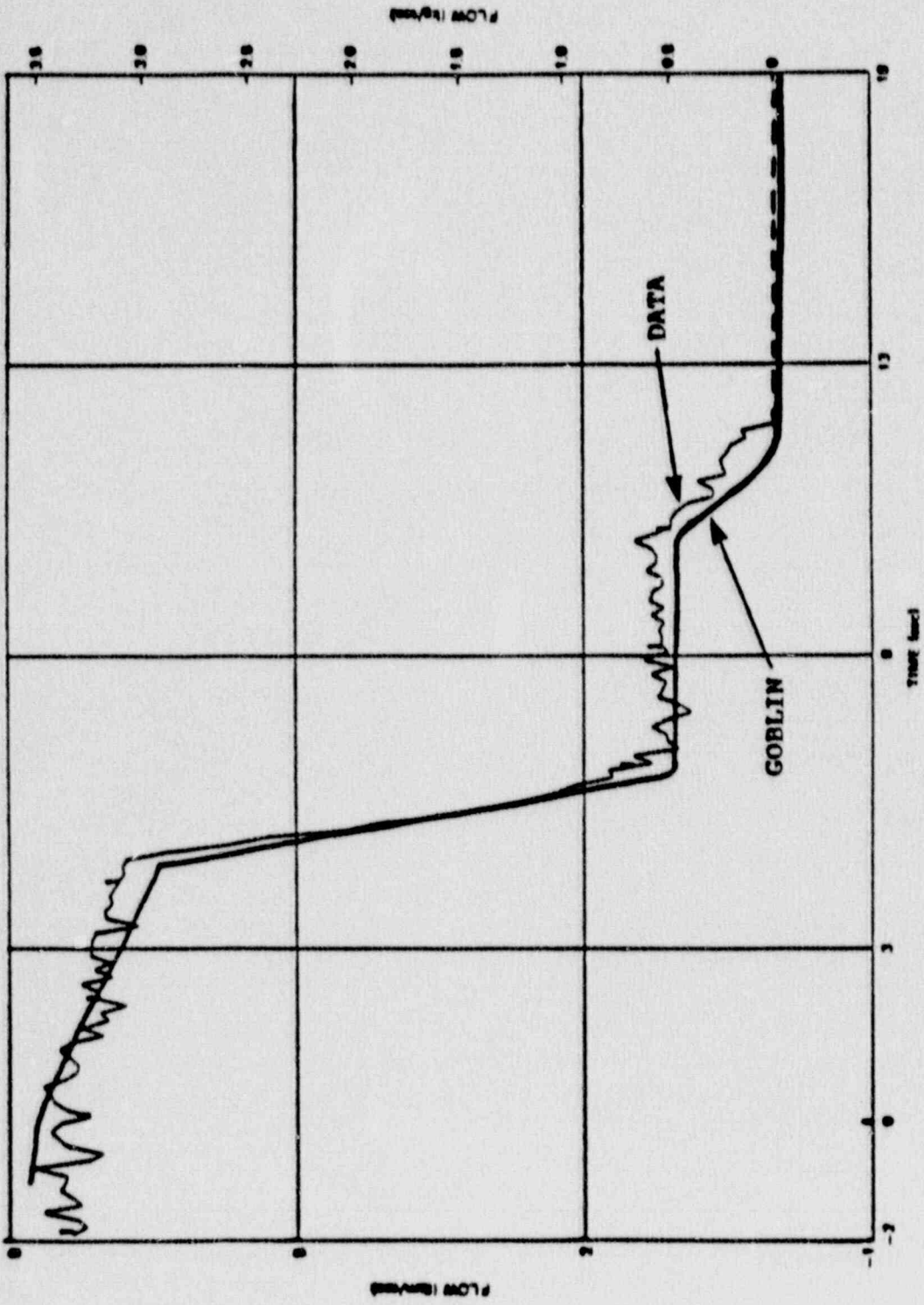


Figure 11-1 TLTA 6423/3 Steamline Mass Flow Rate Boundary Condition

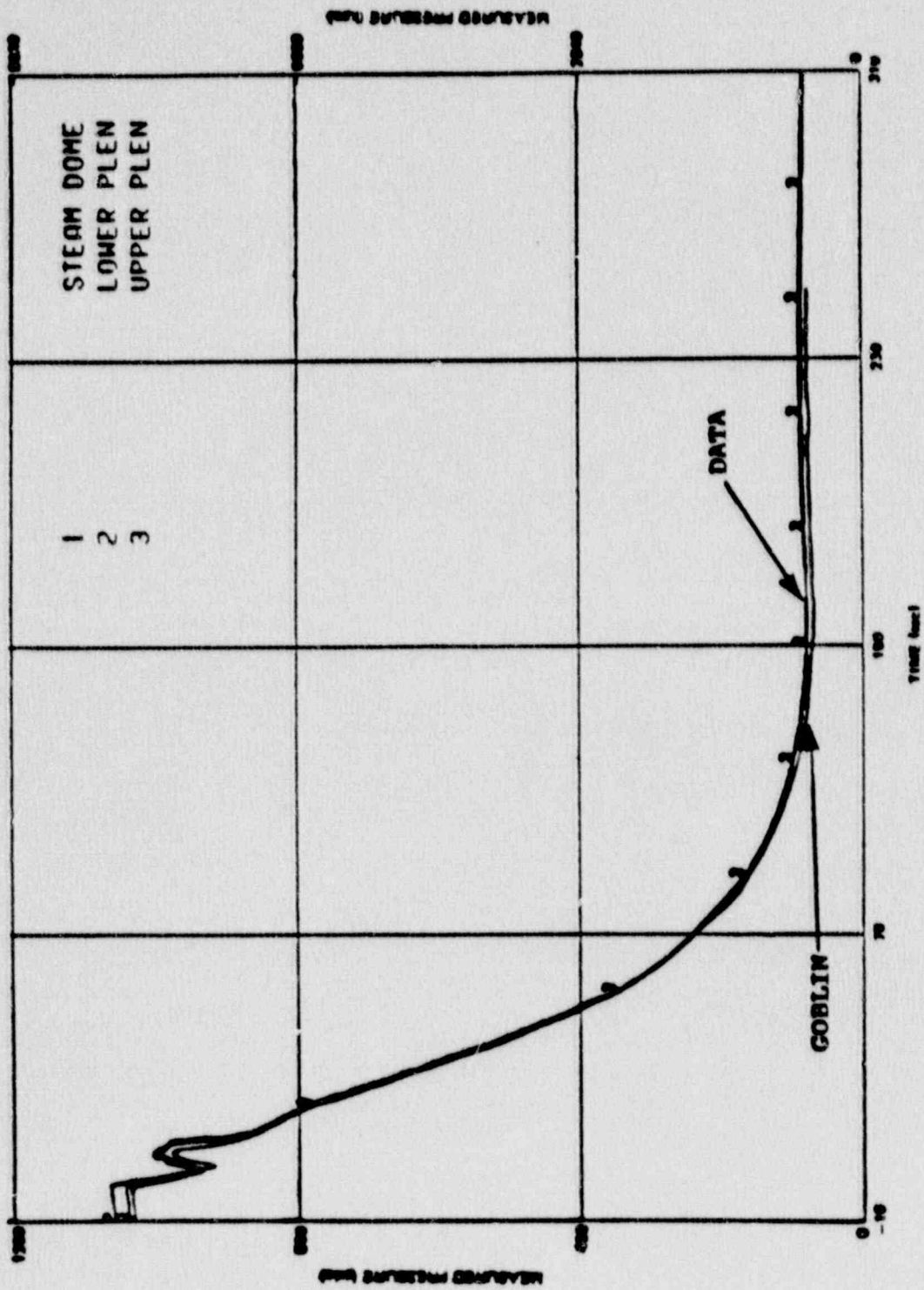


Figure 11-2 TLTA 6423/3 System Pressure Response

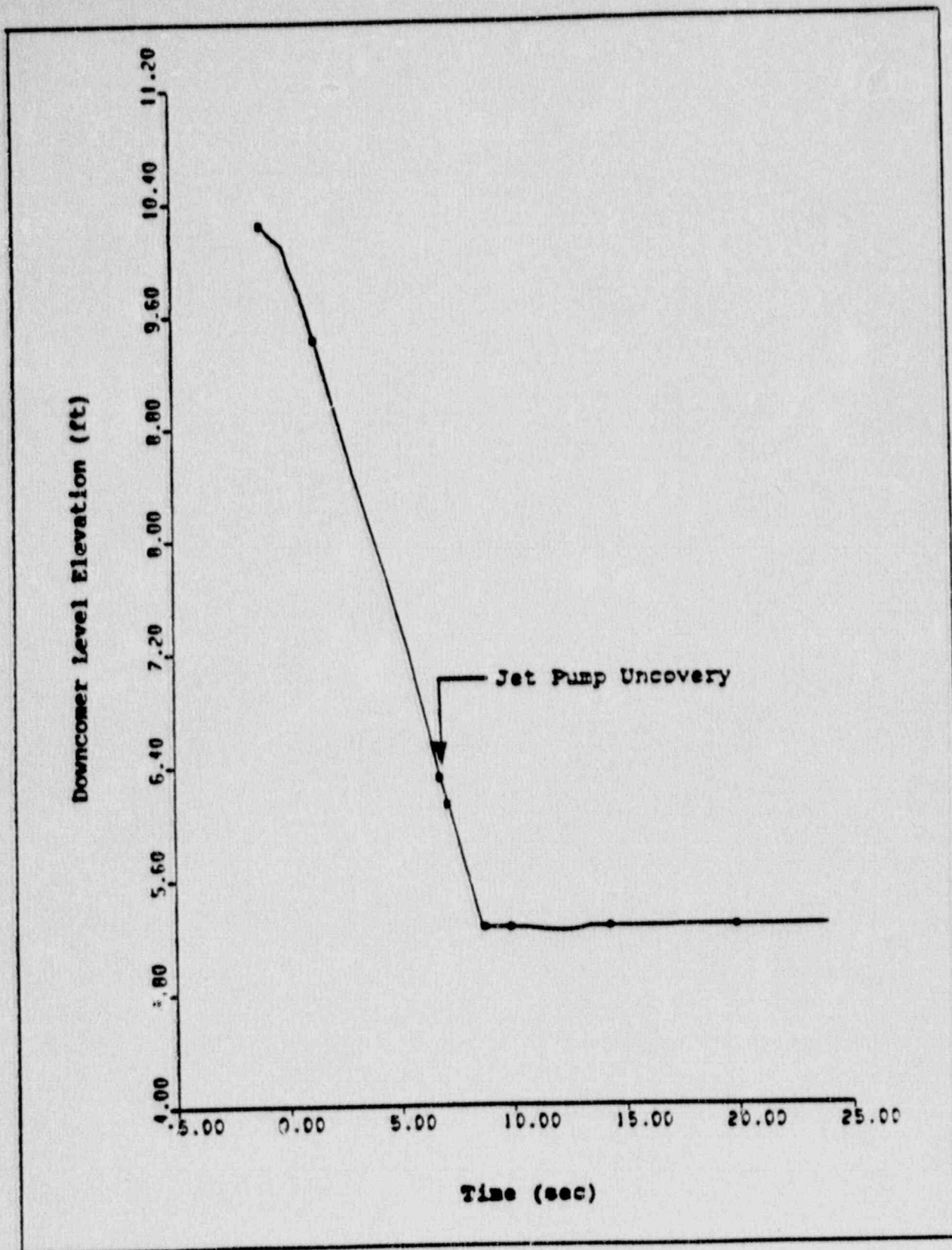


Figure 11-3 TLTA 6423/3 Downcomer Level Transient Response

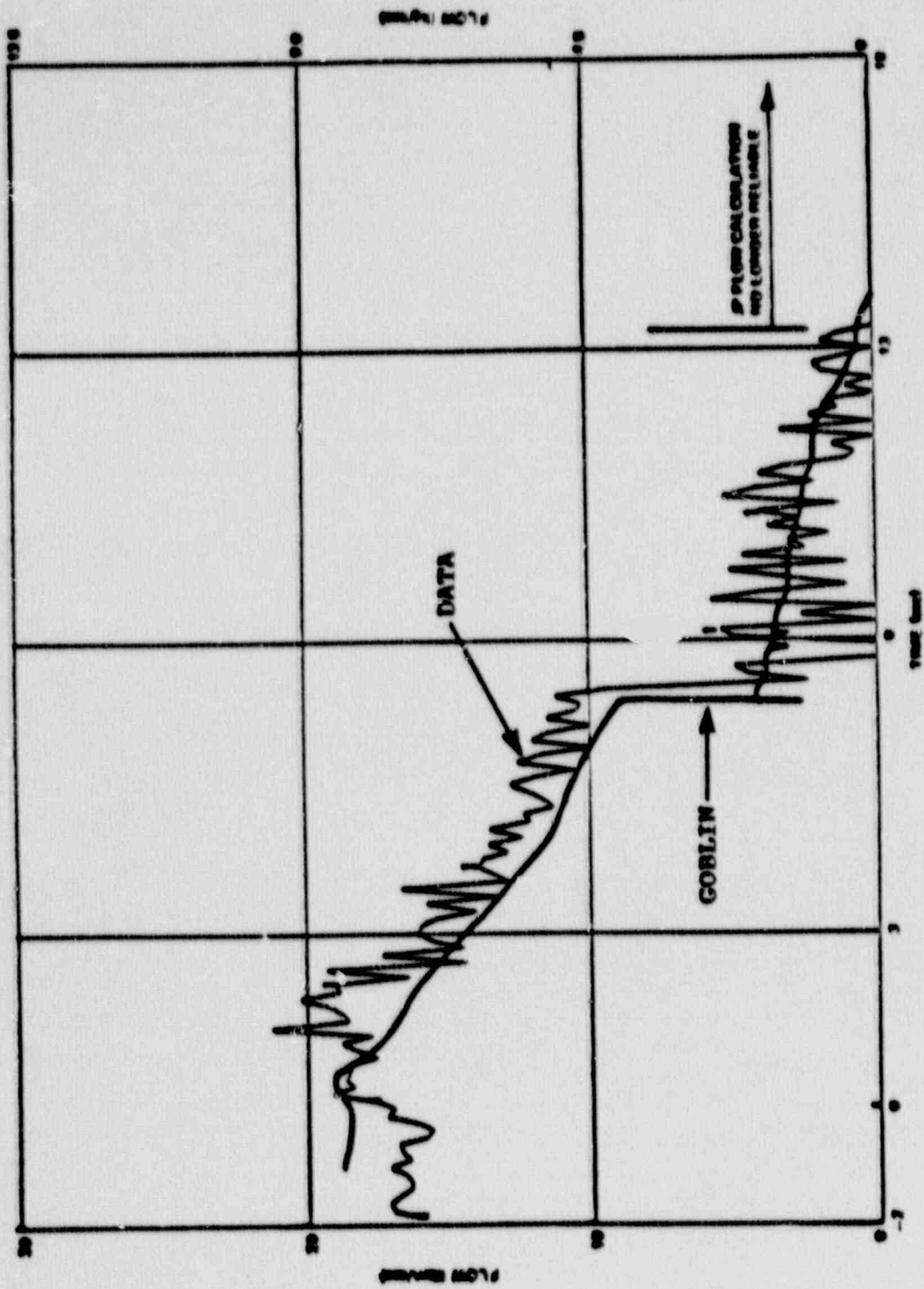


Figure 11-4 TLTA 6423/3 Intact Loop Jet Pump Mass Flow Rate

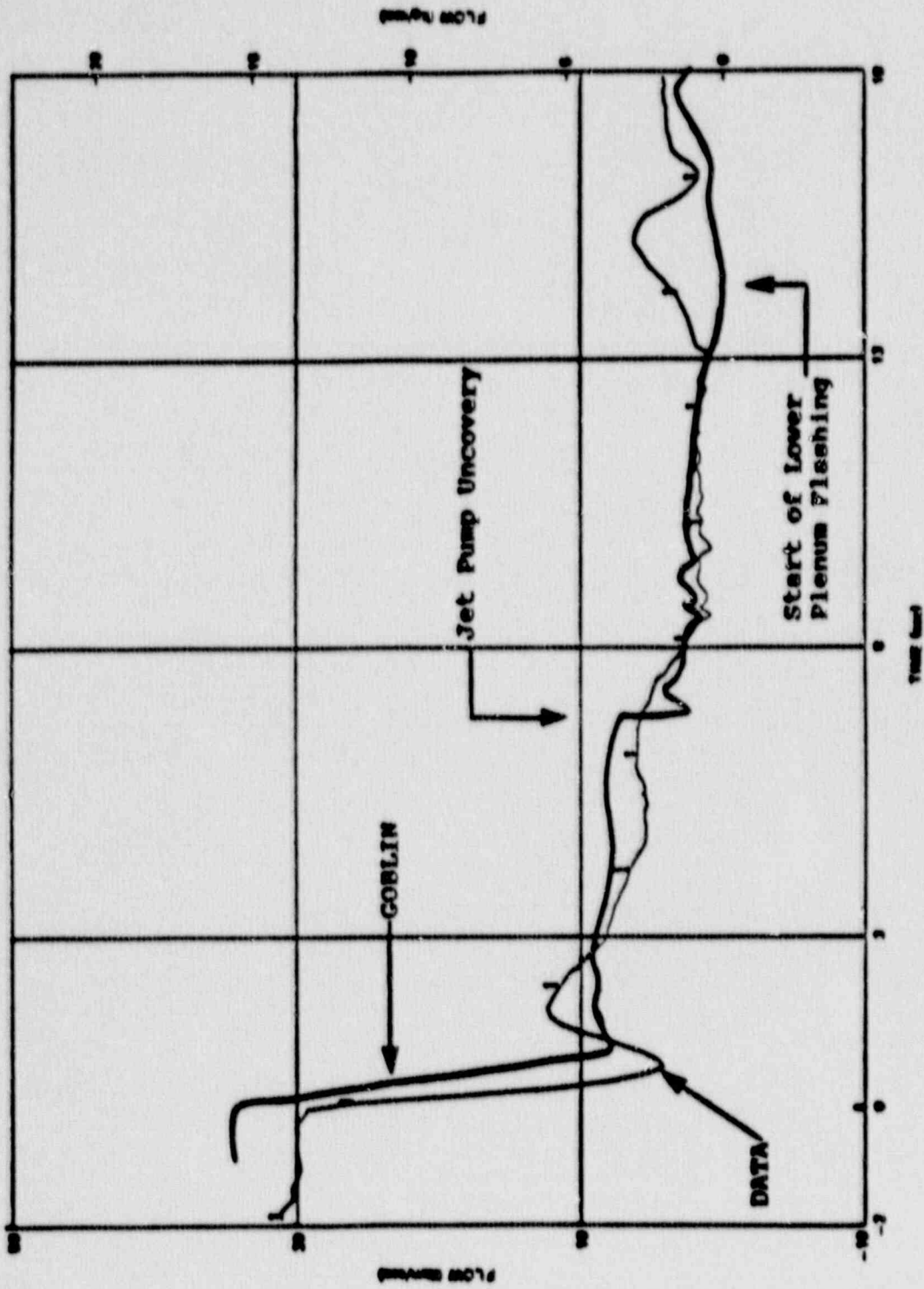


Figure 11-5 TLTA 6423/3 Bundle Inlet Mass Flow Rate



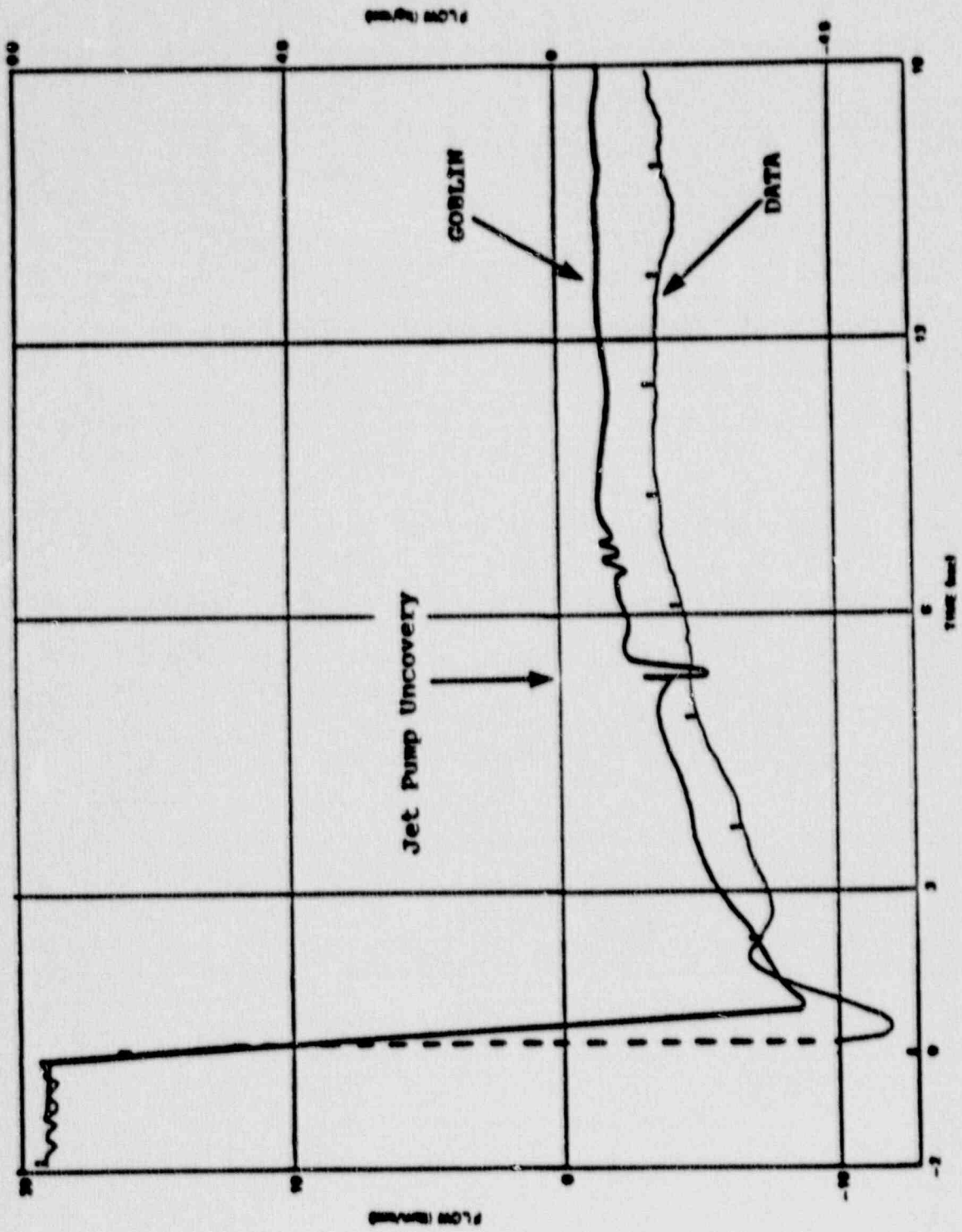


Figure 11-6 TLTA 6423/3 Broken Loop Jet Pump Mass Flow Rate

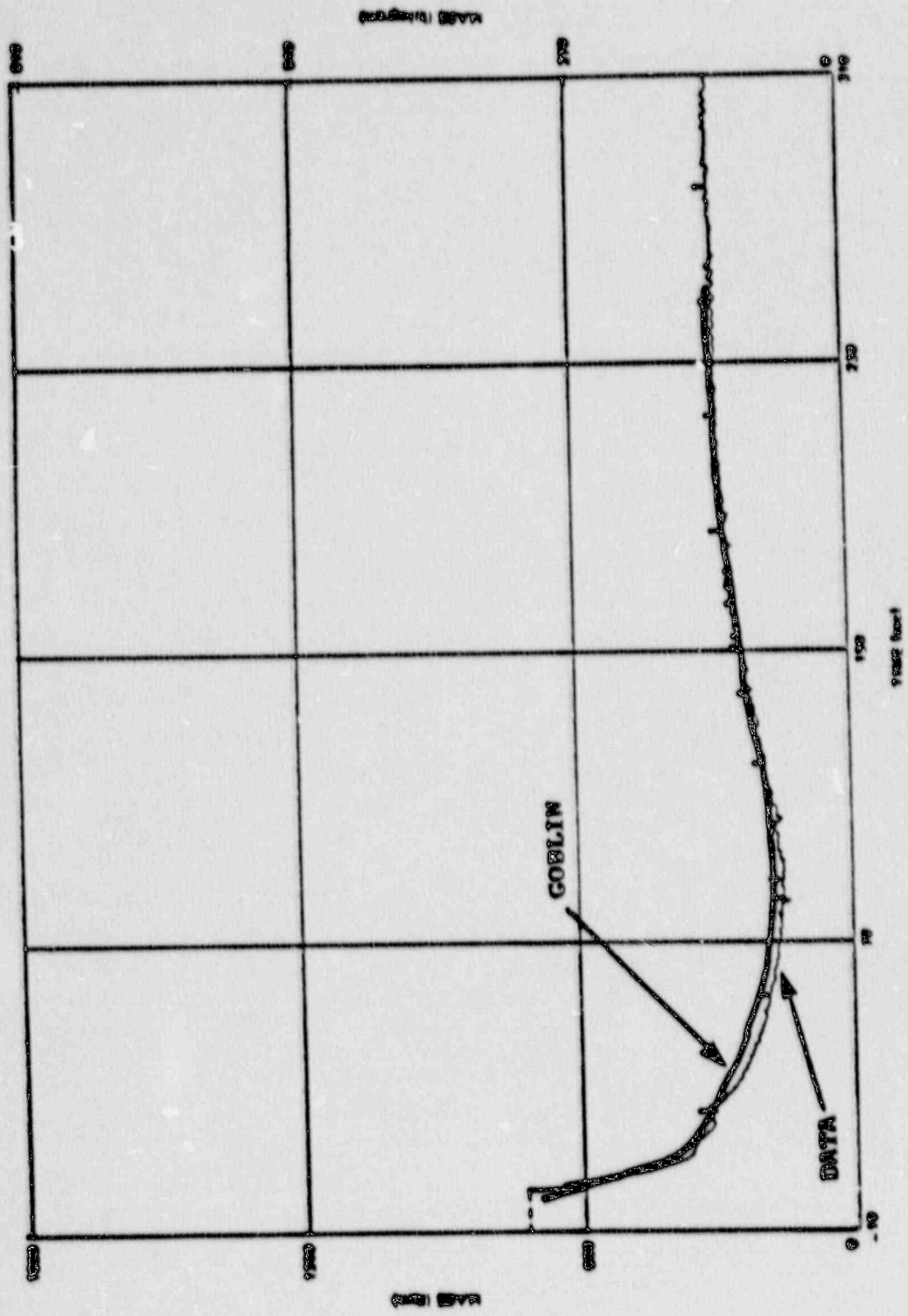


Figure 11-7 TLTA 6423/3 Total Vessel Fluid Mass Inventory

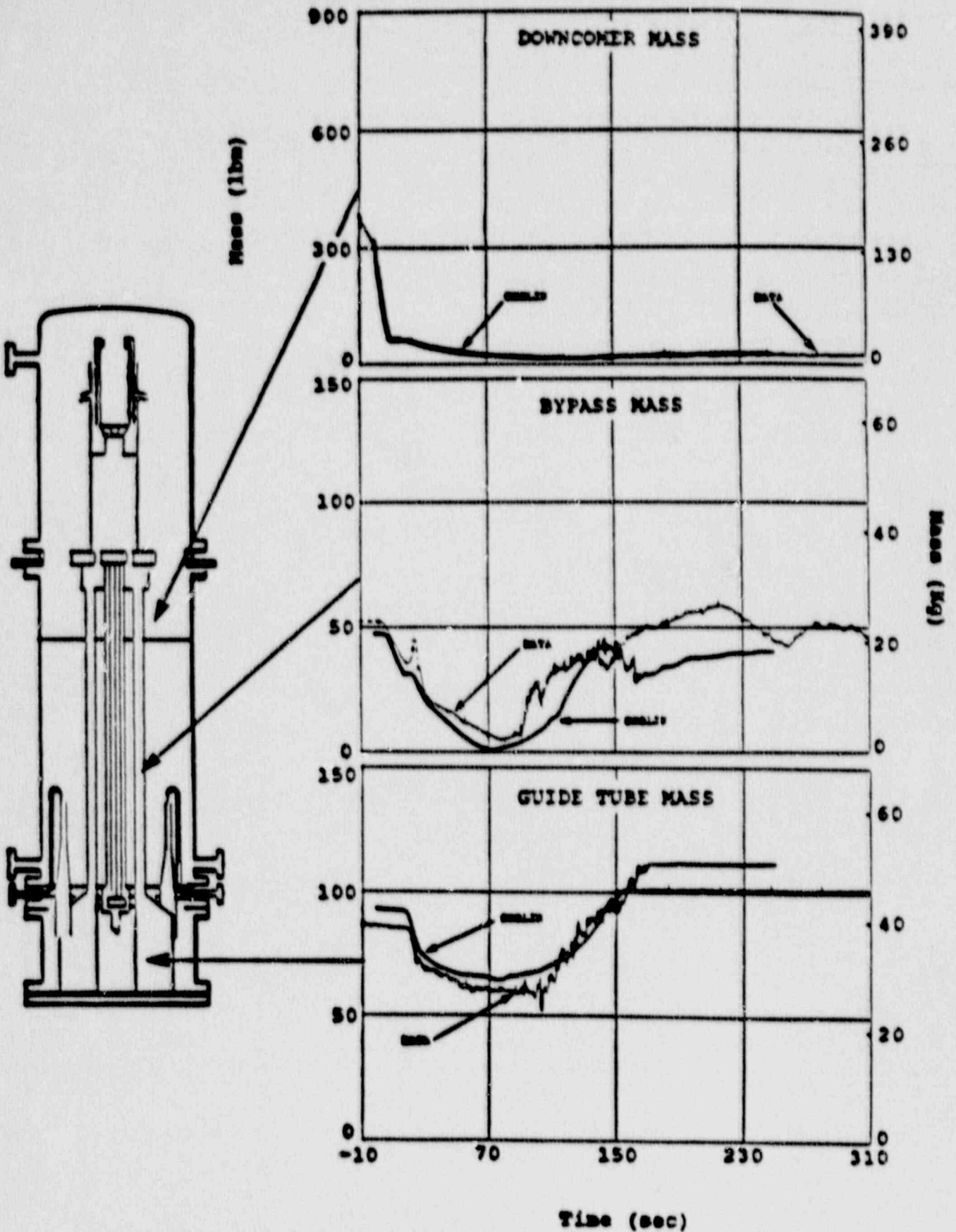


Figure 11-8 TLTA Run 6423/3 Mass Inventory Distribution (Downcomer Bypass, and Guide Tubes)

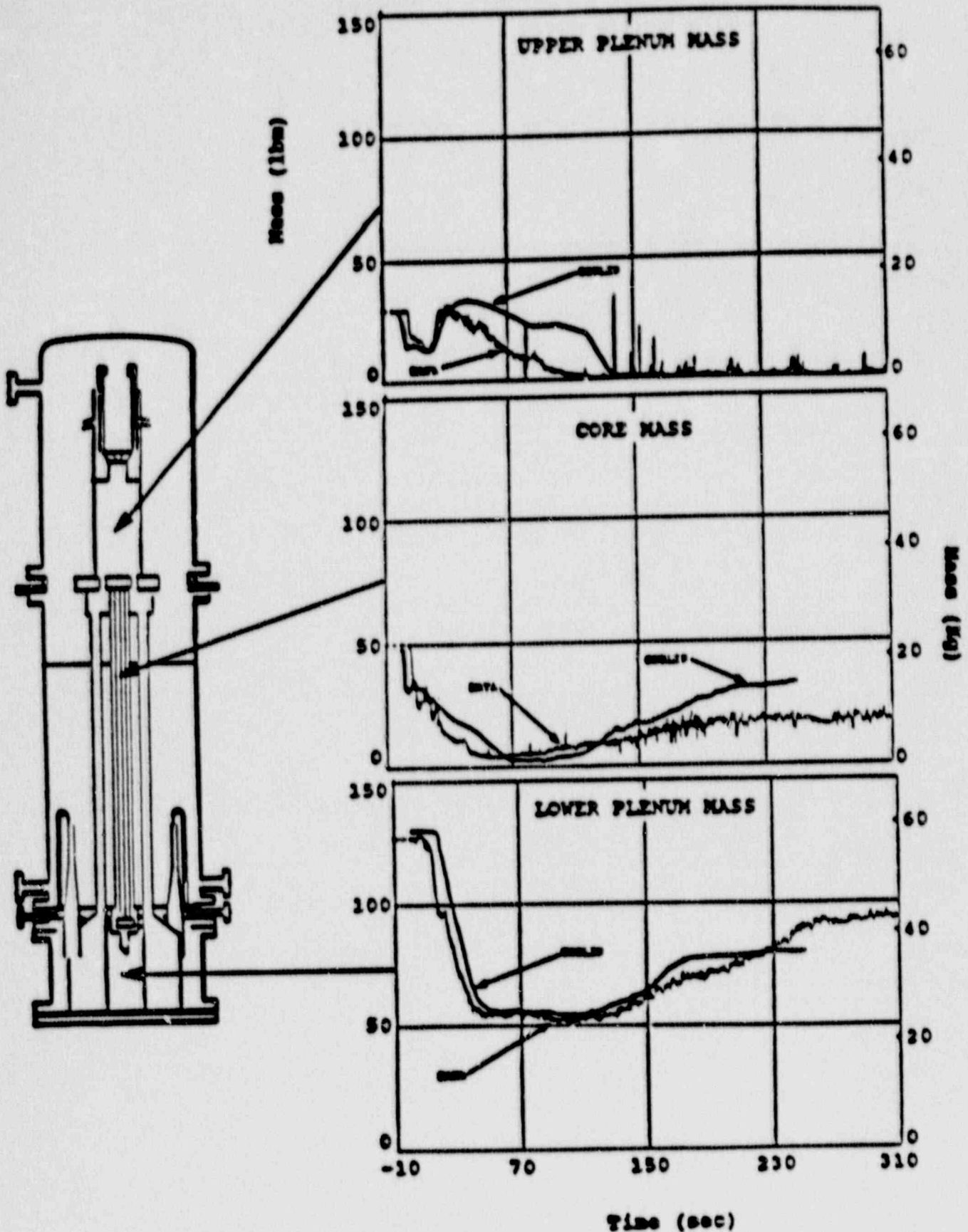


Figure 11-9 TLTA Run 6423/3 Mass Inventory Distribution (Upper Plenum, Core, and Lower Plenum)

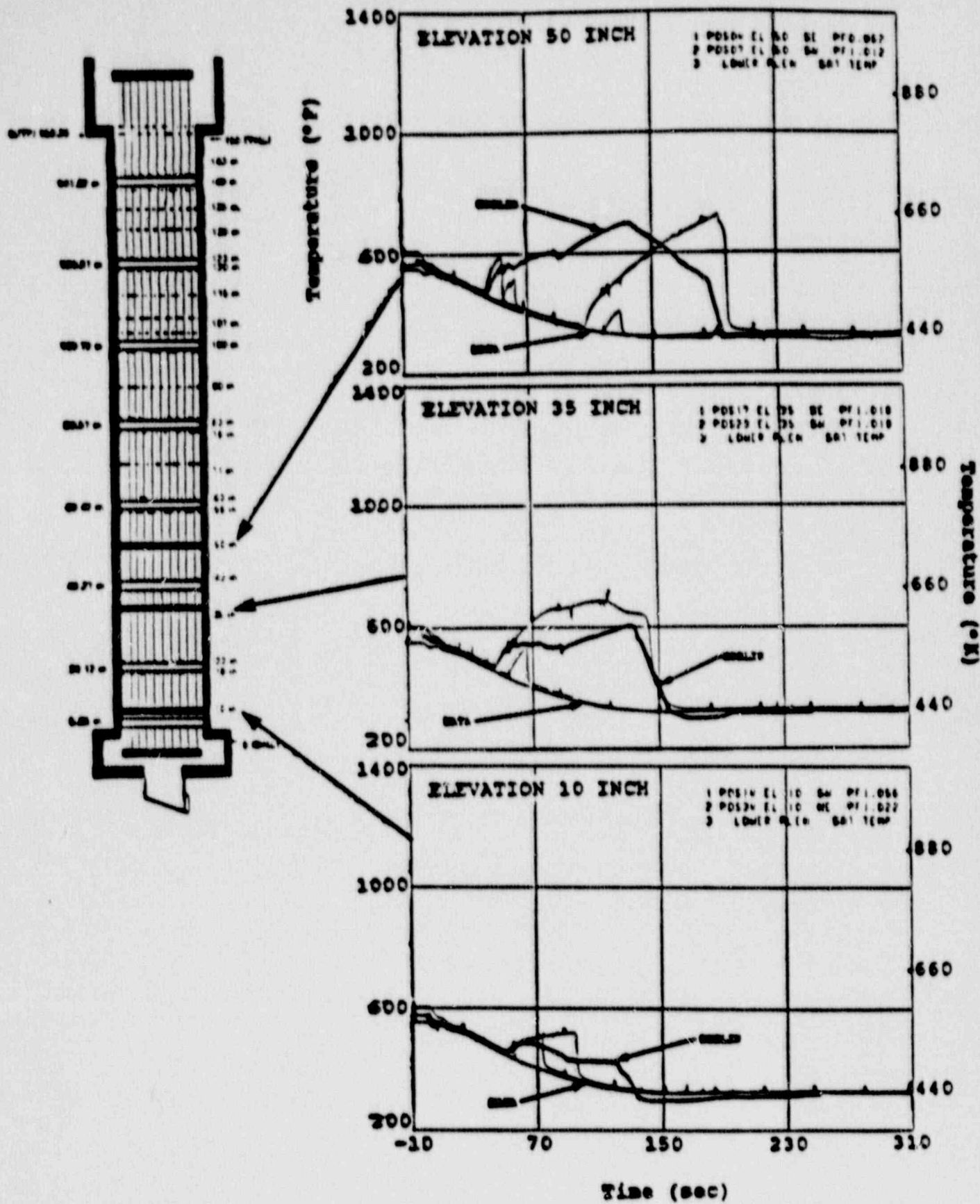


Figure 11-10 TLTA 6423/3 Lower Elevations Rod Temperature Response

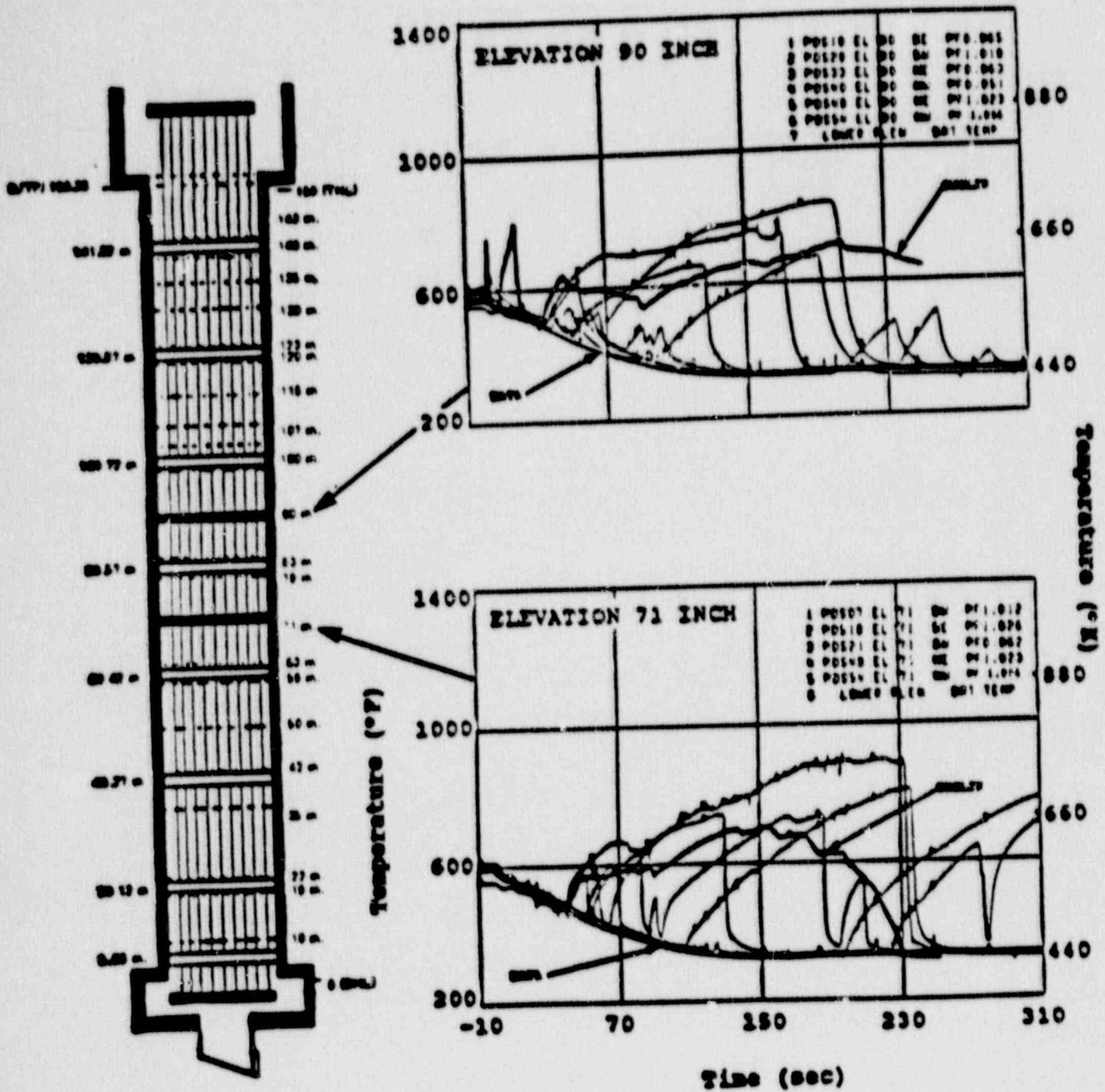


Figure 11-11 TLTA 6423/3 Middle Elevations Rod Temperature Response

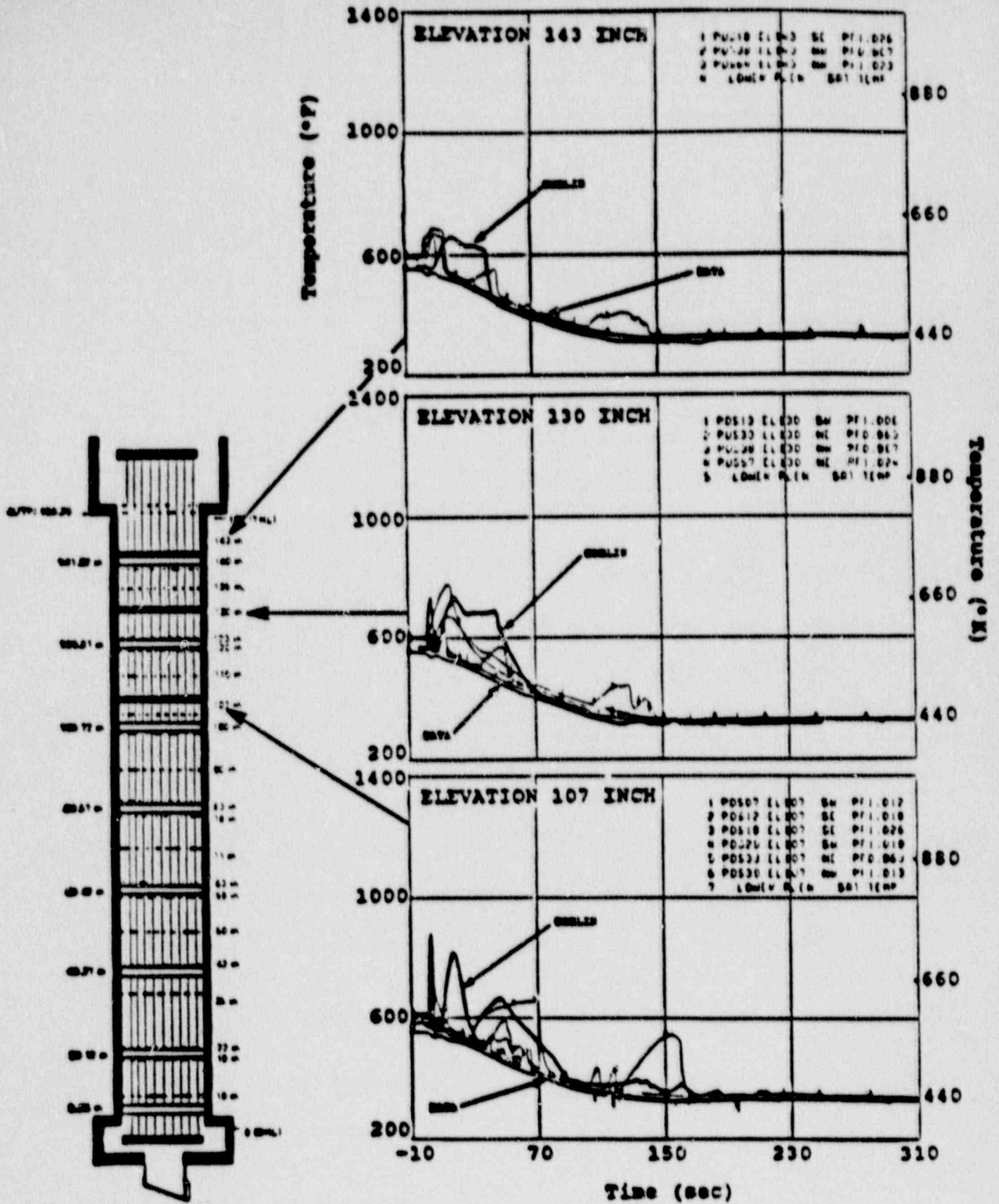


Figure 11-12 TLTA 6423/3 Top Elevations Rod Temperature Response

a,c

Figure 11-13 Conservative Hot Plane Calculation Prescribed Rod Surface Heat Transfer Coefficients



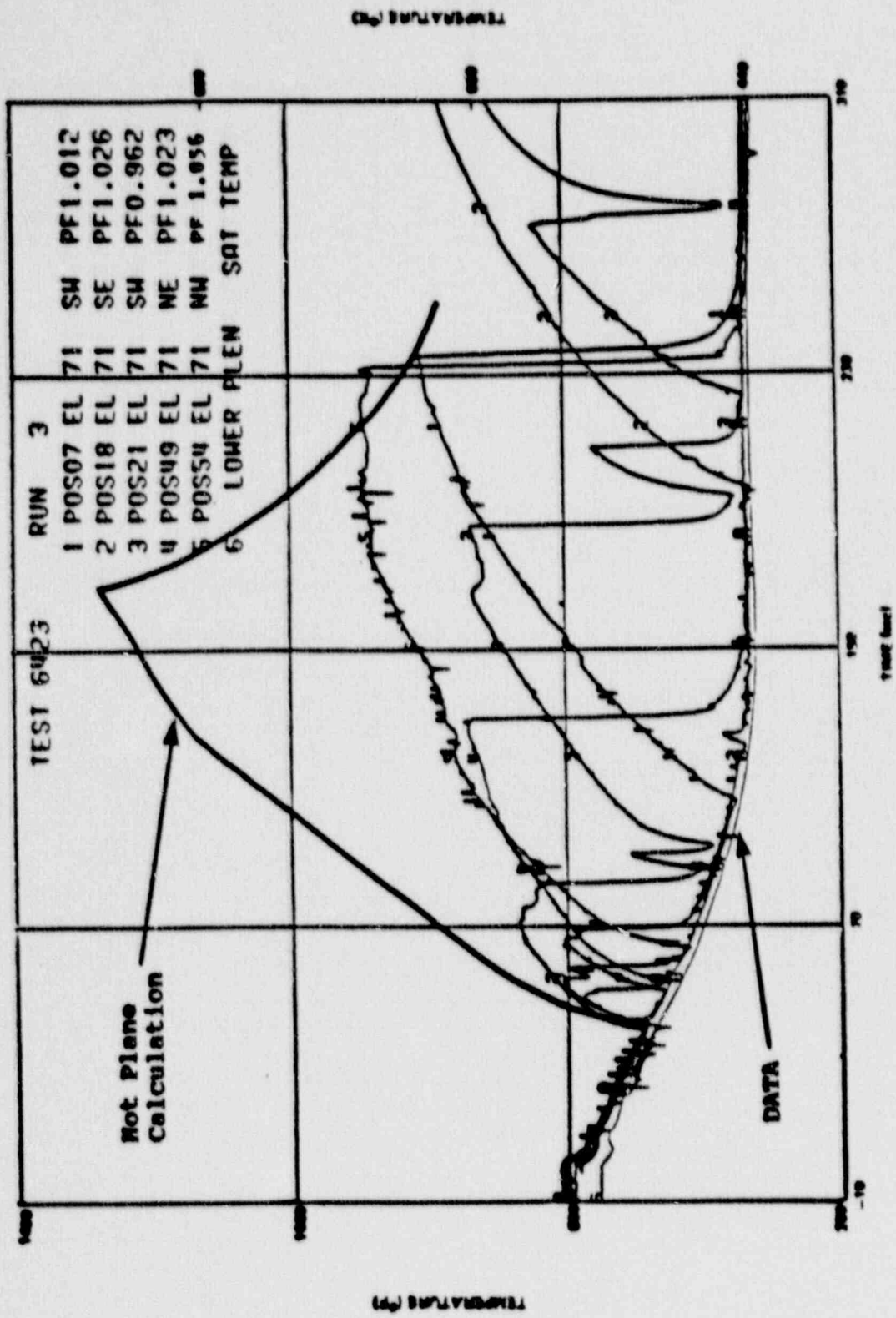


Figure 11-14 Conservative Hot Plane Calculation Peak Cladding Temperature Comparison

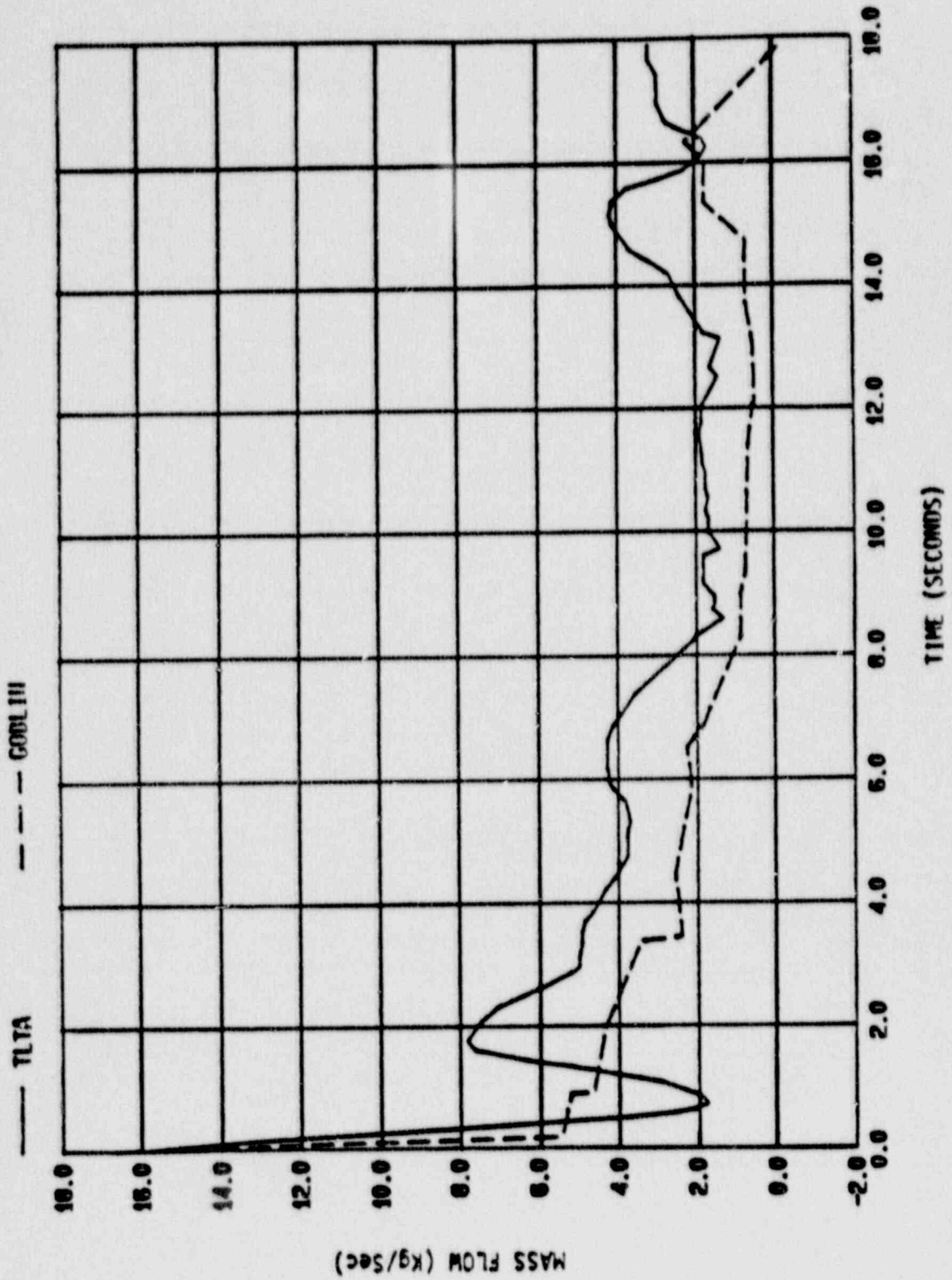


Figure 11-15 Bundle Flowrate for TLTASA Test 6423/3

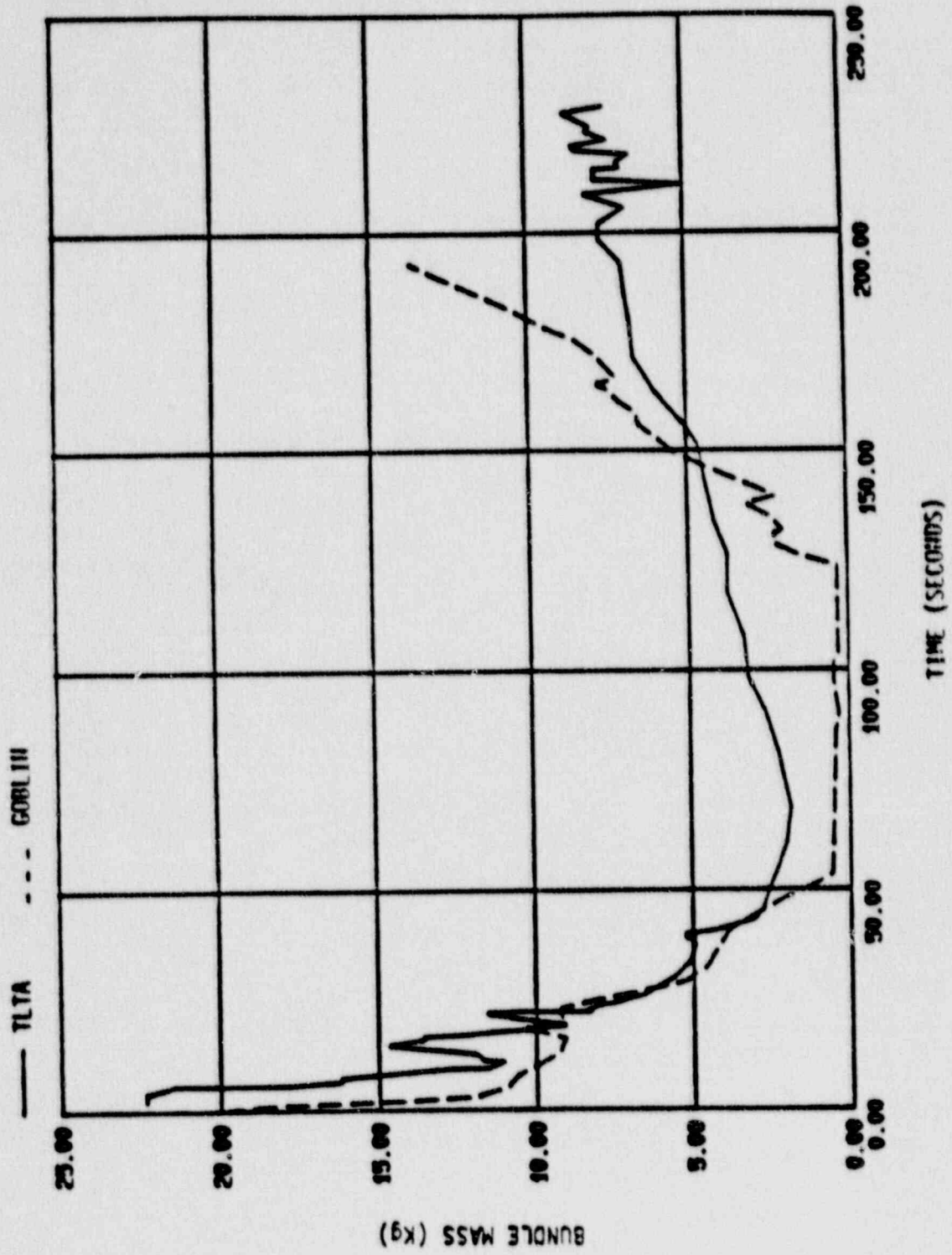


Figure 11-16 Bundle Mass for TLTA5A Test 6423/3

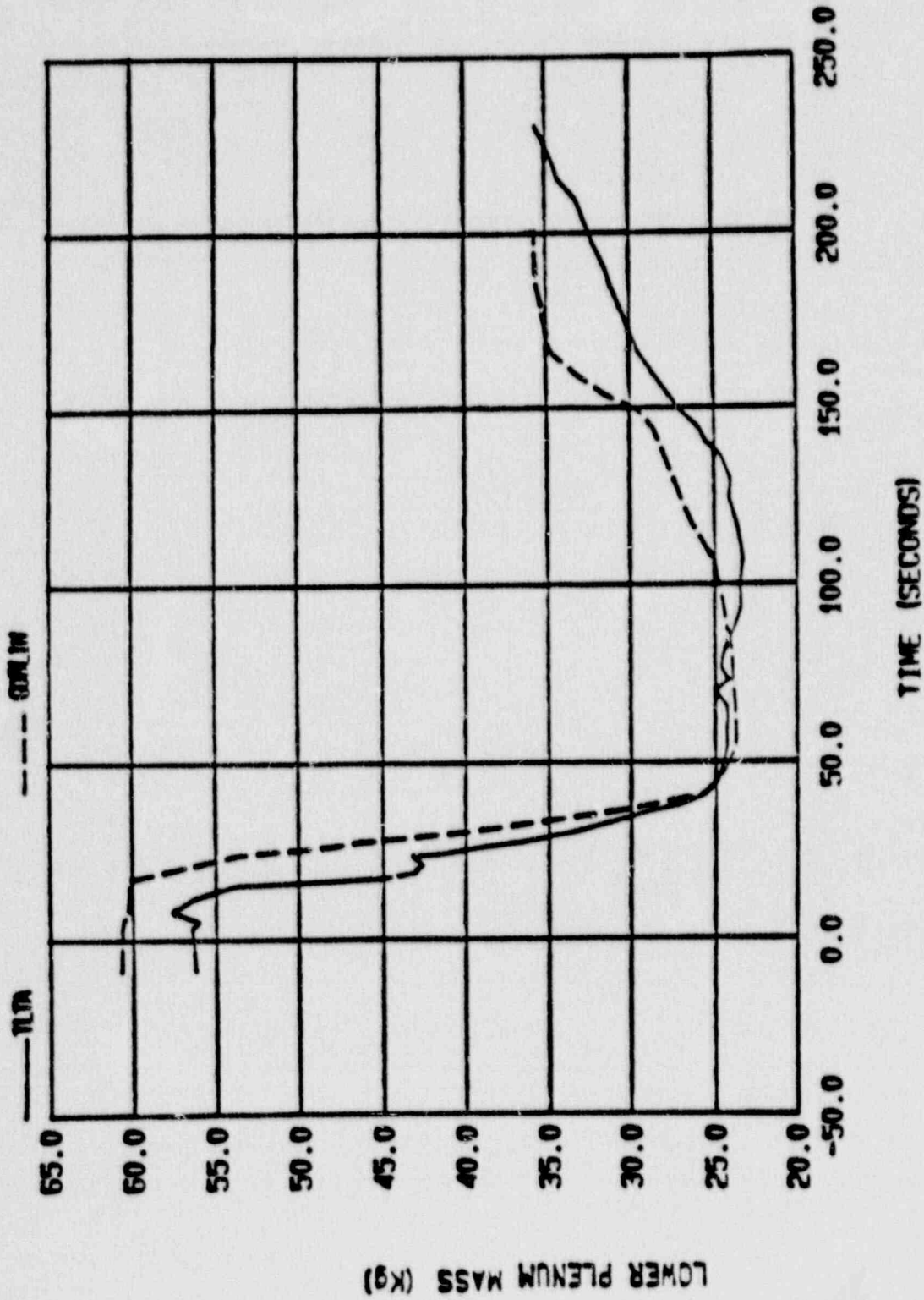


Figure 11-17 Lower Plenum Mass for TLTA Test 6423/3

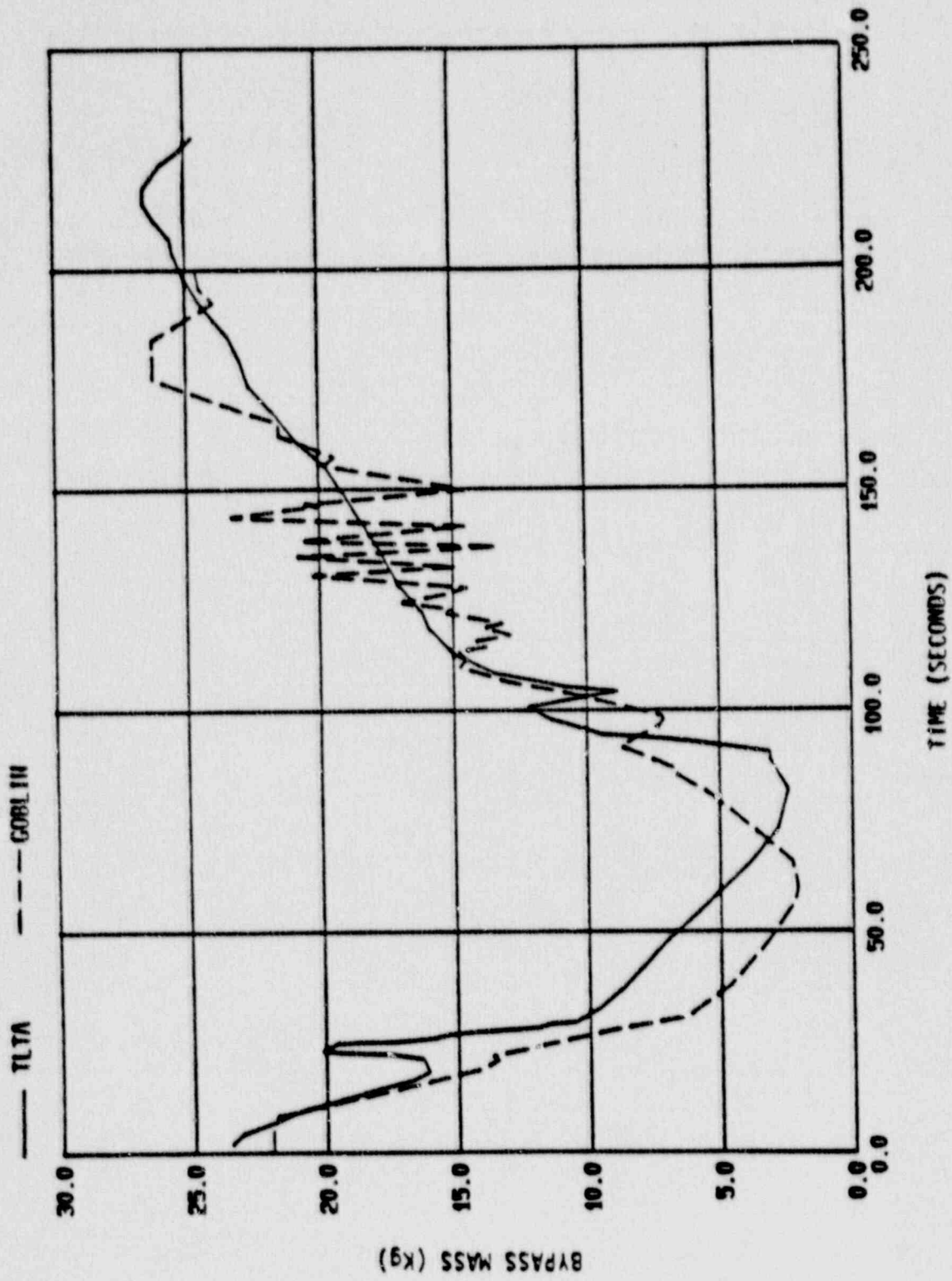


Figure 11-18 Bypass Mass for TLTA5A Test 6423/3

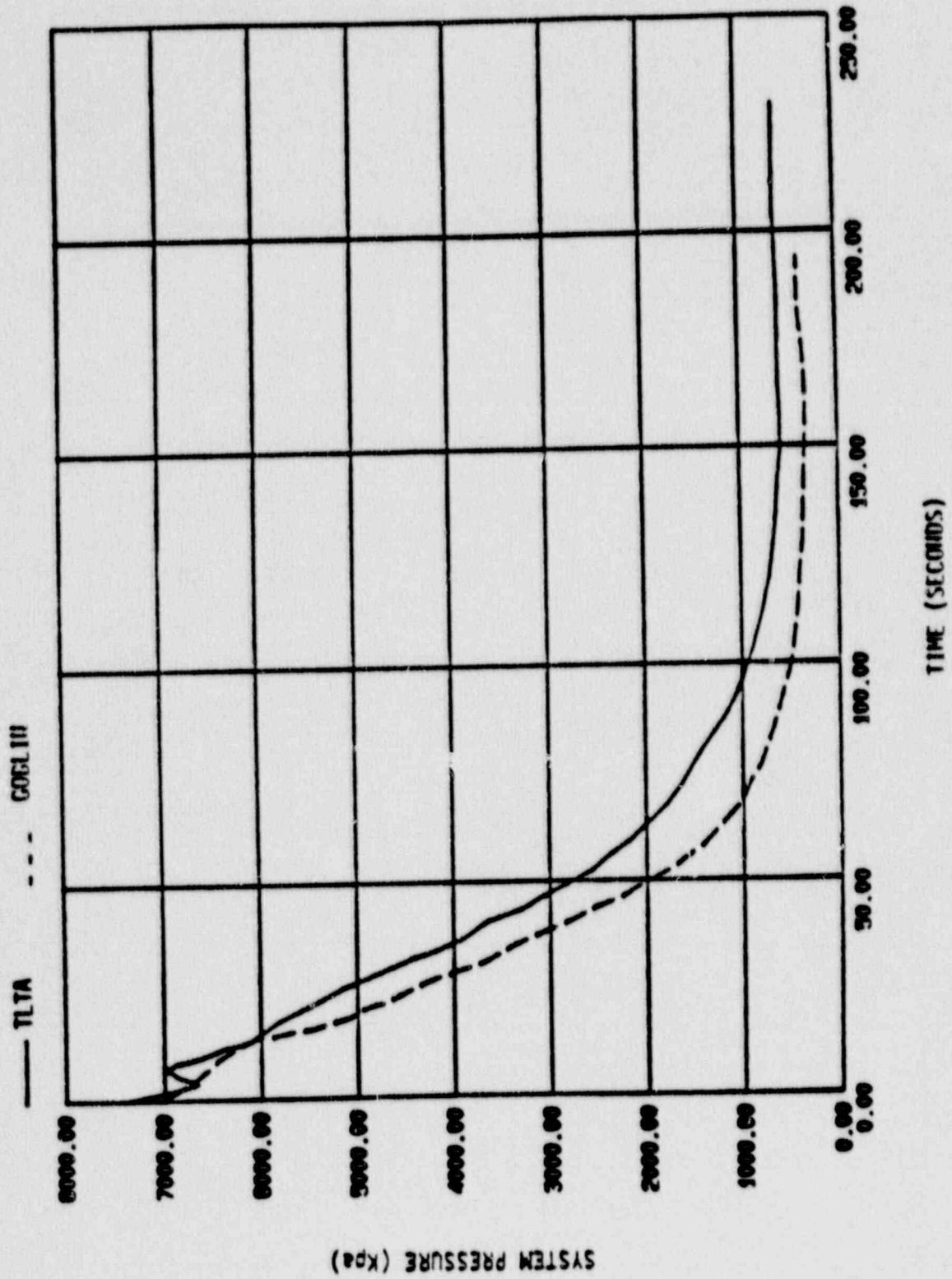


Figure 11-19 System Pressure for TLTA5A Test 6423/3

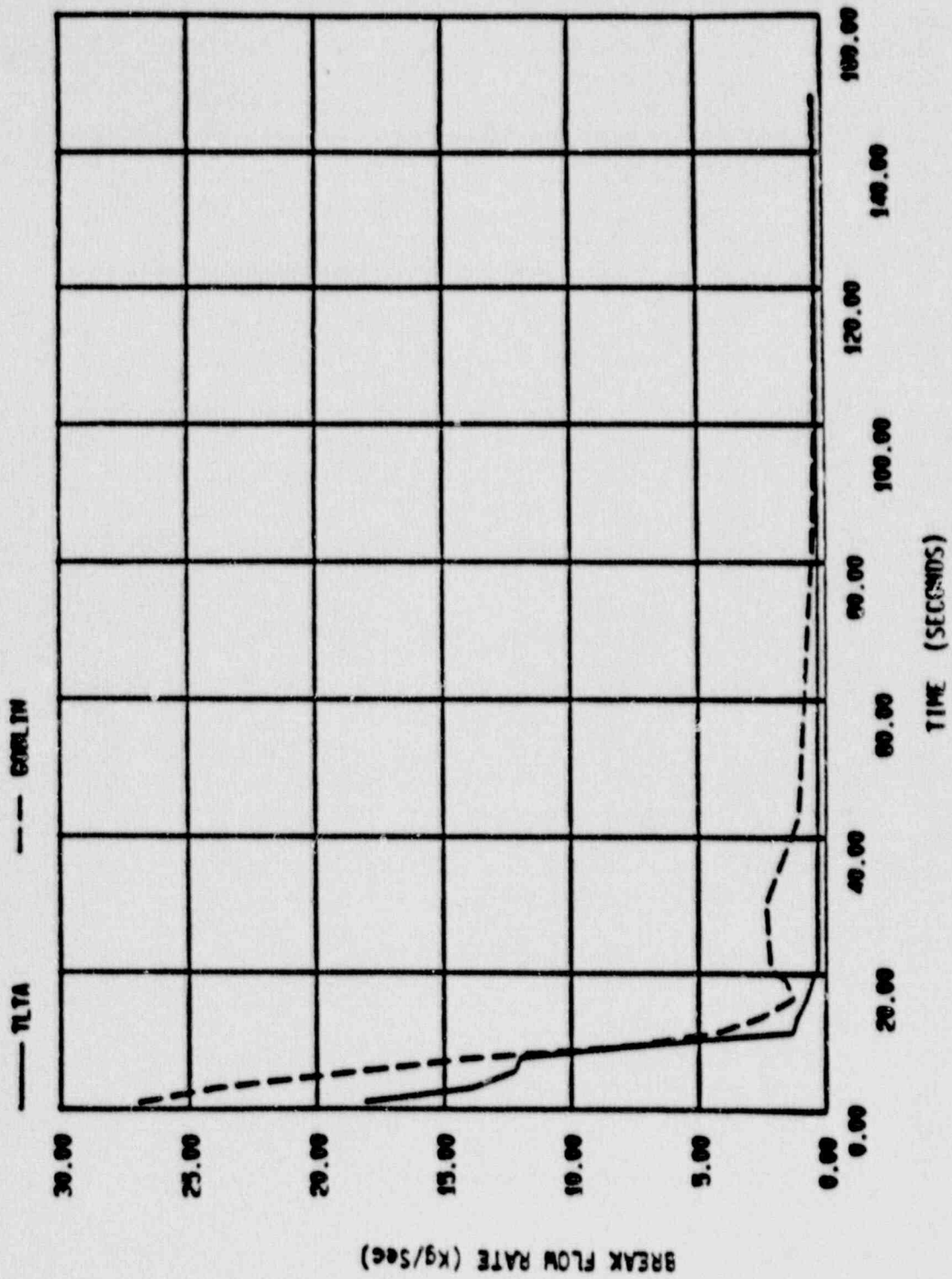


Figure 11-20 Break Flow for TLTA5A Test 6423/3

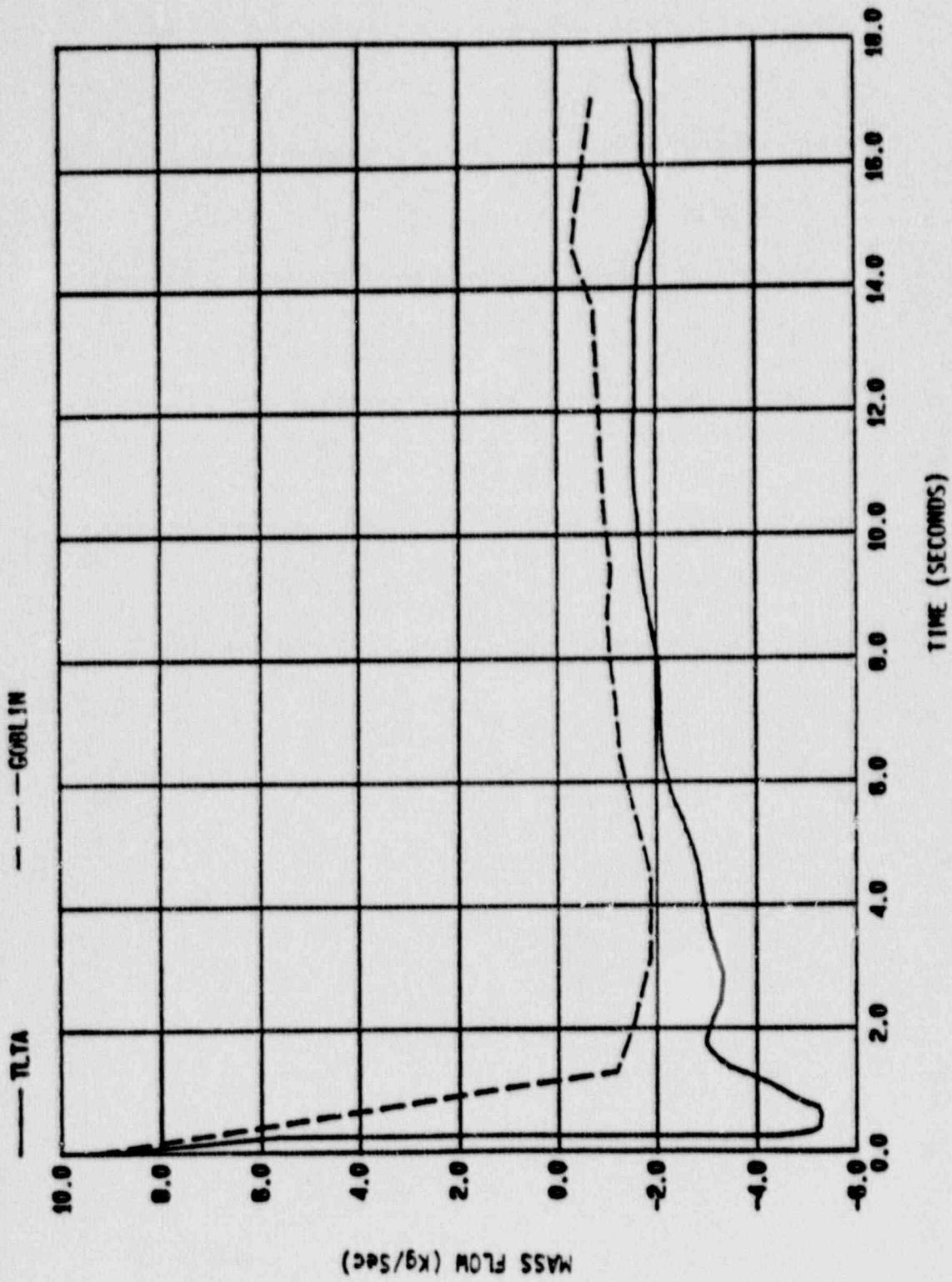


Figure 11-21 Broken Jet Pump Flow Rate for TLTA5A Test 6423/3



## Question 12

Pages 6-94, 6-98 and Sec. 6.2.3, Ref. 1. The rod temperature results are missing in the Westinghouse analysis of TLTA test 6425. In effect, these analyses have been presented in the form of separate-effects tests to demonstrate the correct response of the fuel rods. Based on Figs. 6-50 and 6-54, it appears that the code has no conservative margin in terms of PCT. In fact, the code predicts a cooldown from 40 s to 70 s in Fig. 6-50, and the data indicate a heatup. The observed differences need to be explained. Fig. 6-54 does not indicate which test rod the computational rod was simulating or what the differences are between the curves for the measured data. The rod locations for the measurement curves and which rod(s) were being simulated with the computational rod need to be identified.

## Response

The TLTA integral qualification simulation results of case 6425 run presented in Ref. 1 are repeated here. Table 12-1 shows the initial conditions for the test and simulation. Figures 12-1 through 12-7 are replotted comparisons of the transient hydraulic response. These figures supersede Figures 6-33 through 6-39 of Ref. 1. Figure 12-8 shows the corresponding rod temperature response.

The calculated rod temperature response compare reasonably well with the test data. The deviations in the simulation are a result of the variation in the initial conditions as demonstrated in the addition simulation of case 6423 run 3 presented in the response to Question 11.

Figure 6-50 of Ref. 1 shows the comparison of the rod temperature response for the TLTA case 6007 run 26. The GOBLIN/DRAGON simulation predicts a early dryout at the midplane after the initial drop in bundle flow rate. This is a consequence of the slightly sharper predicted depressurization following the jet pumps uncover (as shown in Figure 6-47 of Ref. 1). The rod heatup is terminated by the subsequent lower plenum flashing. Because of the

conservatively low calculated minimum stable film boiling temperature, the rod heat transfer did not return to nucleate boiling resulting in sustained higher rod temperatures than is the test.

At approximately 40 seconds the lower plenum drains enough to allow steam venting out the jet pumps, resulting in a rapid draining of the bundle and upper plenum coolant through the side entry orifices and subsequent rod dryout. The GOBLIN/DRAGON simulation had a prolonged draining period due to overpredicted mass inventory in the upper plenum and bundle at 40 seconds. The overpredicted upper plenum mass inventory in the simulation is attributed to an overpredicted initial mass and to the prolonged dryout in the bundle from 10 to 50 seconds.

Additional TLTA qualification simulations presented in Ref. 1 and in response to Question 11 demonstrate that the rod temperature deviation is unique to this simulation.

Figure 6-54 of Ref. 1 shows a comparison of the predicted and measured midplane rod temperatures for FIX II test 3061. Attached is Figure 12-9, a copy of Figure 6-54 with the rod numbers of the five thermocouples indicated. The midplane is at a distance of 71.5 inches from the bottom of the heated length. This elevation corresponds to node 14 in the GOBLIN simulation. The GOBLIN simulation modelled a single rod at the average planar power. This average rod temperature is compared to the rod temperature measurements at the same elevation.

The rod temperature comparisons presented here reaffirm the ability of the GOBLIN/DRAGON code to predict the average rod temperature response. The conservative margin in PCT of the Westinghouse LOCA evaluation model due to the 10CFR50 Appendix K requirements was not included in this simulation. (See the response to Question 11 for a discussion of the PCT conservatism resulting from the Appendix K requirements.)

The revised figures of Ref. 1 presented in this response will be incorporated into the final (approved) version of the topical report.

TABLE 12-1  
COMPARISON OF TLTA 6425 RUN 2 INITIAL CONDITIONS

	TLTA	GOBLIN
Bundle Power (Mw)	$5.05 \pm 0.03$	505
Steam dome pressure (psia)	$1044 \pm 5$	1031
Lower plenum enthalpy (Btu/lbm)	$528 \pm 5$	508
Feedwater enthalpy (Btu/lbm)	$41 \pm 2$	41
Feedwater flow (lbm/sec)	$1.4 \pm 0.3$	1.1
Jet Pump 1 flow (lbm/sec)	$22 \pm 2$	20
Jet Pump 2 flow (lbm/sec)	$20 \pm 2$	21
Bundle inlet flow (lbm/sec)	$39 \pm 5$	41
Downcomer Mass (lbm)	310	558
Initial Water level (inch elev.)	$123 \pm 6$	122

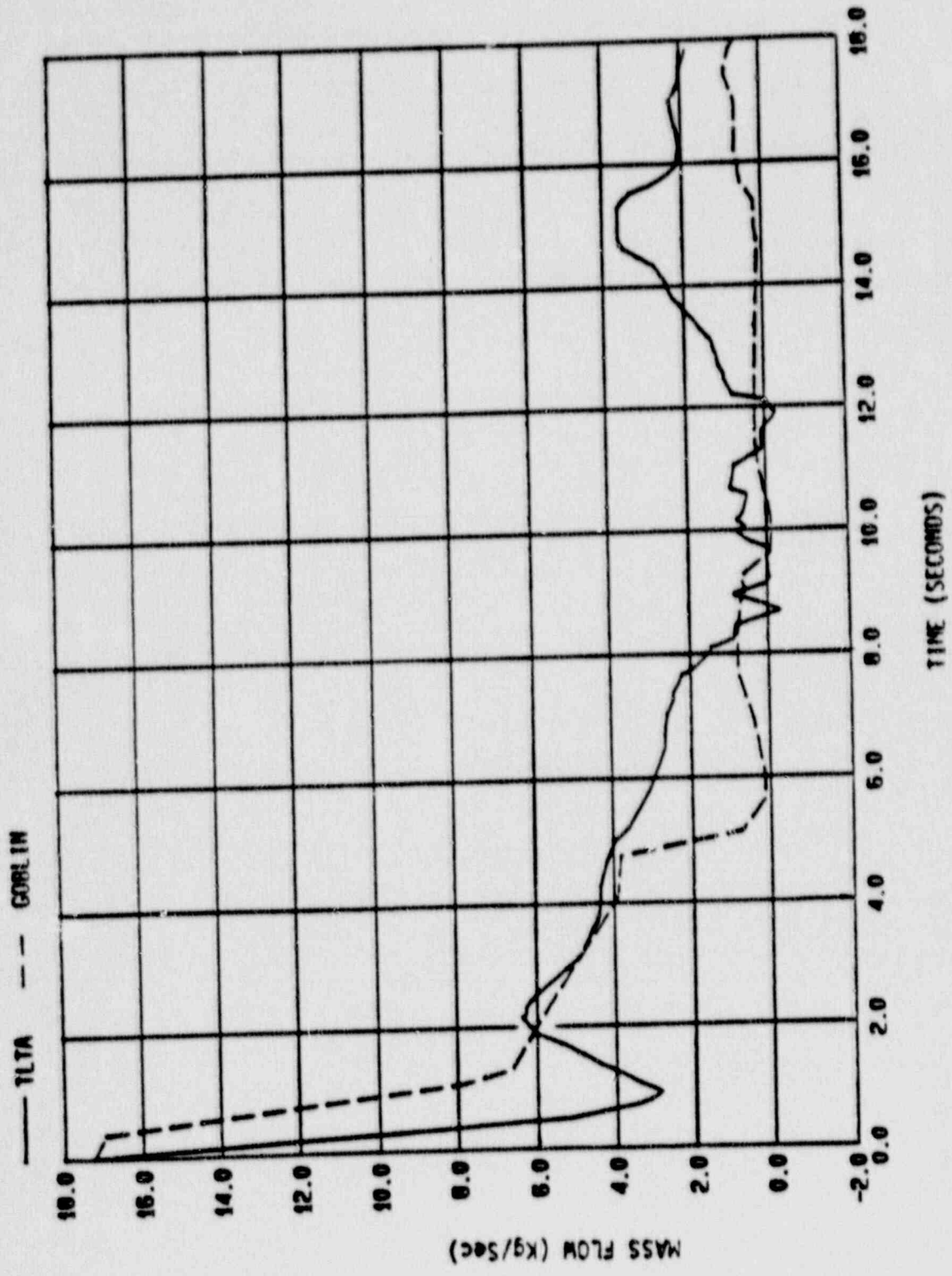


Figure 12-1 Bundle Flow Rate for TLTSA Test 6245/Z

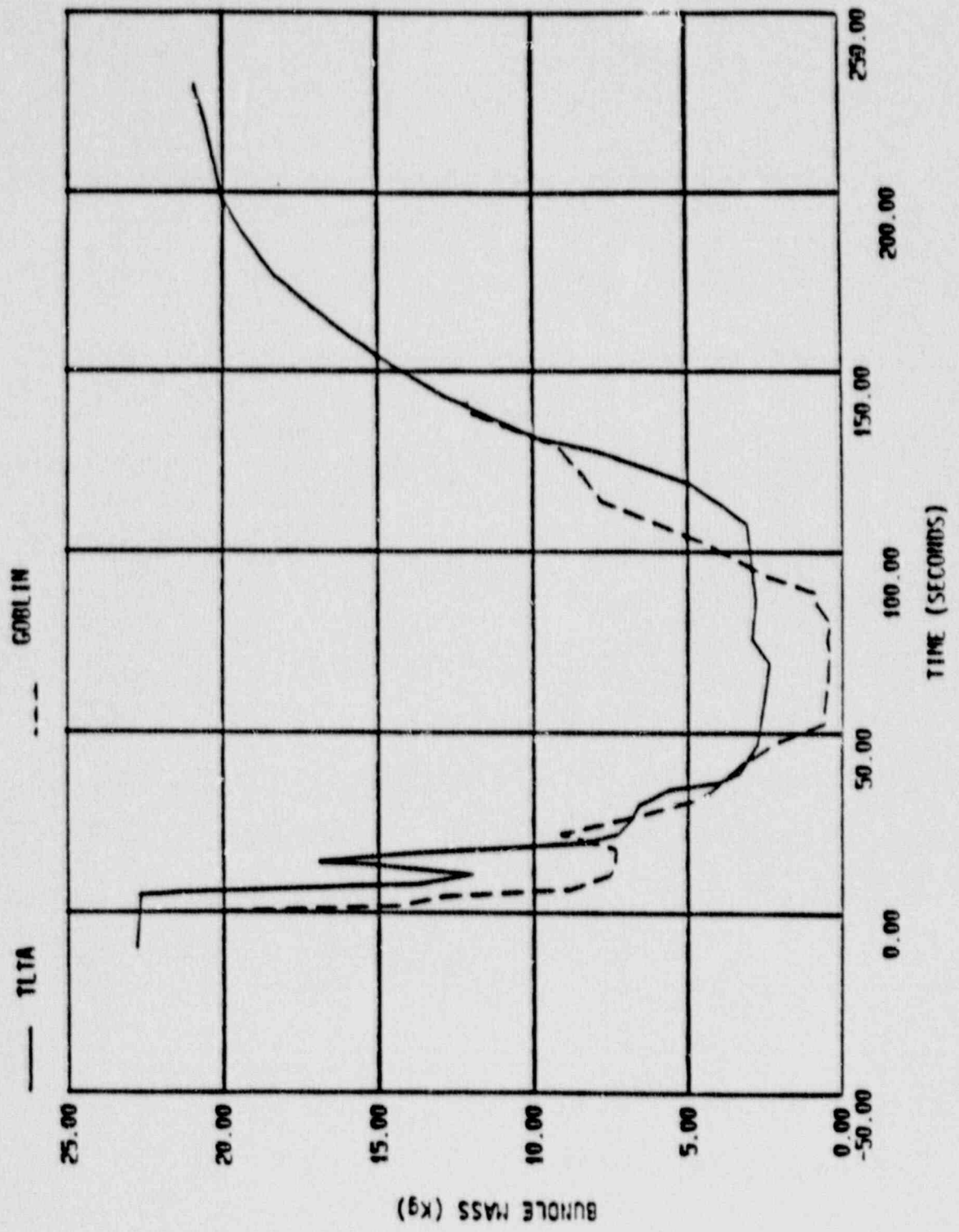


Figure 12-2 Bundle Mass for TLTA Test 6425/2

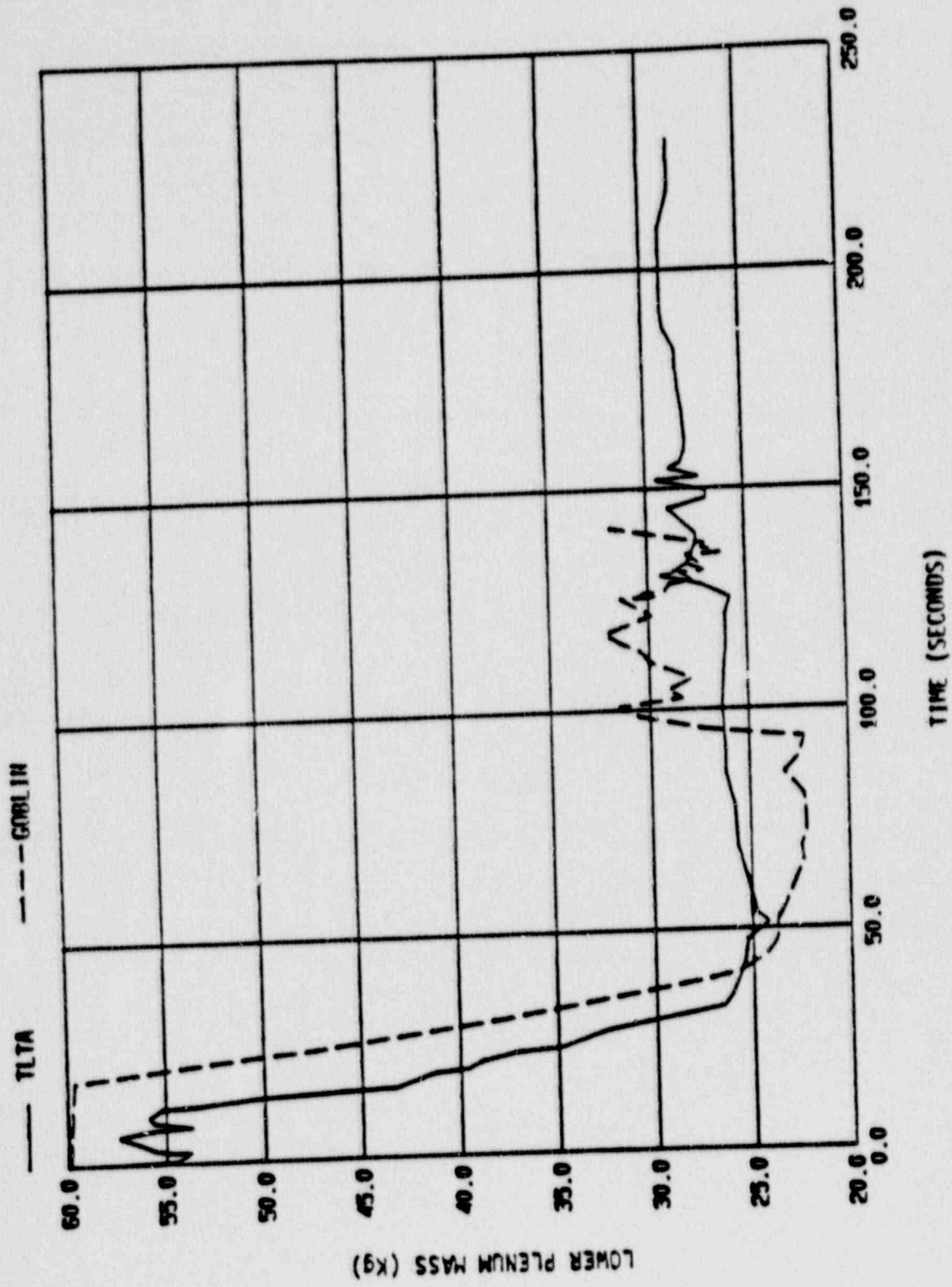


Figure 12-3 Lower Plenum Mass for TLTA5A Test 6425/2

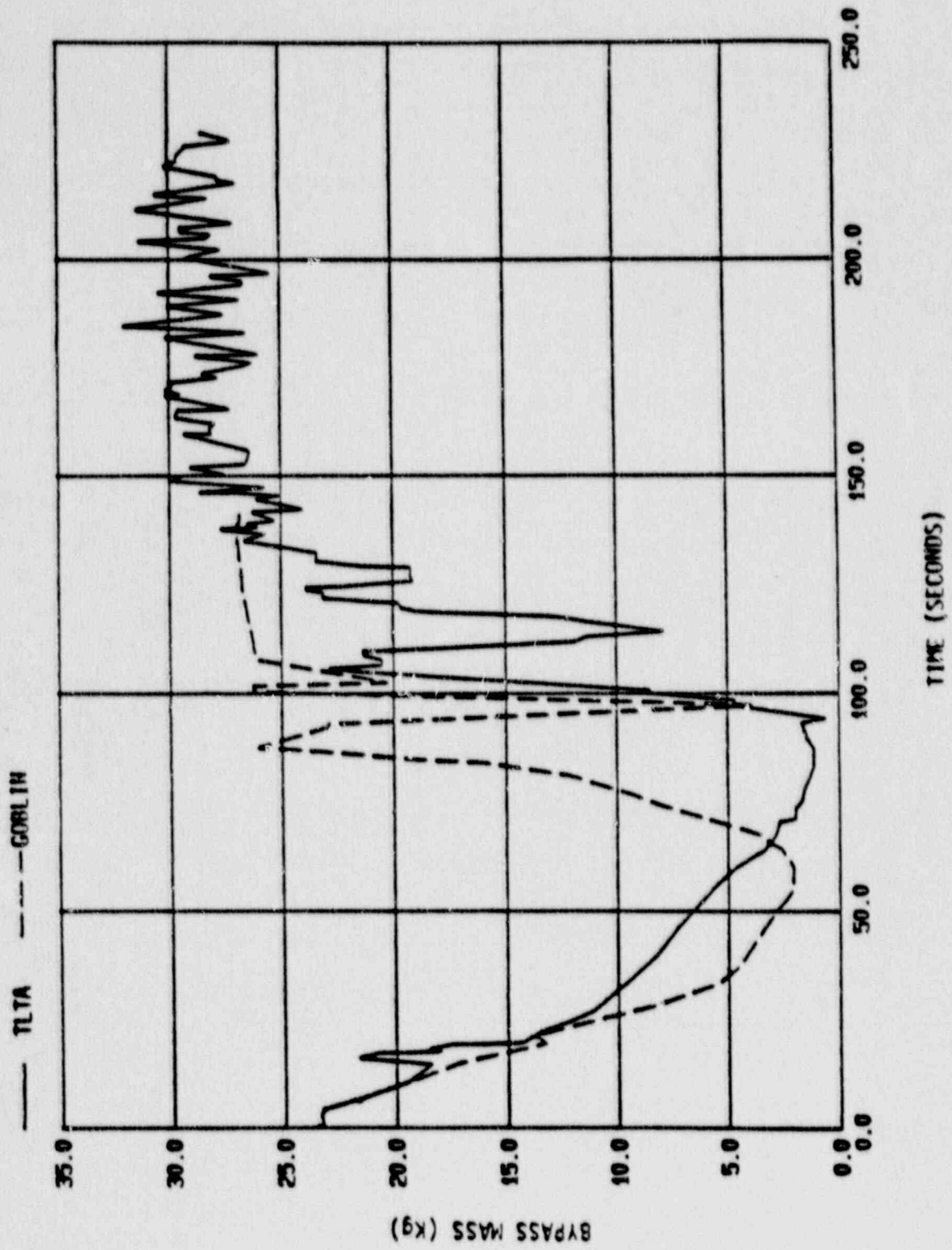


Figure 12-4 Bypass Mass for TLTASA Test 6425/2

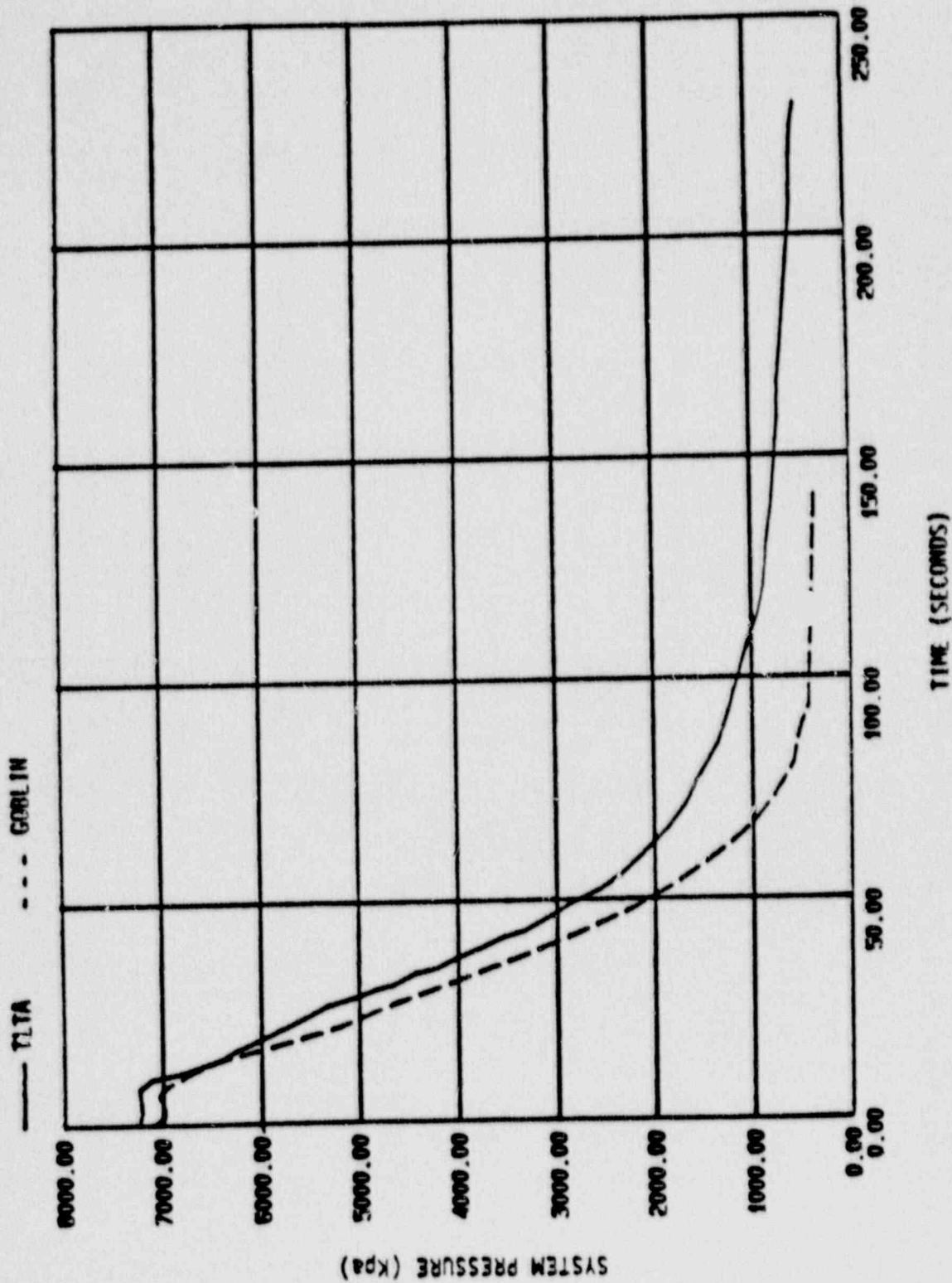


Figure 12-5 System Pressure for TLTA5A Test 6425/2



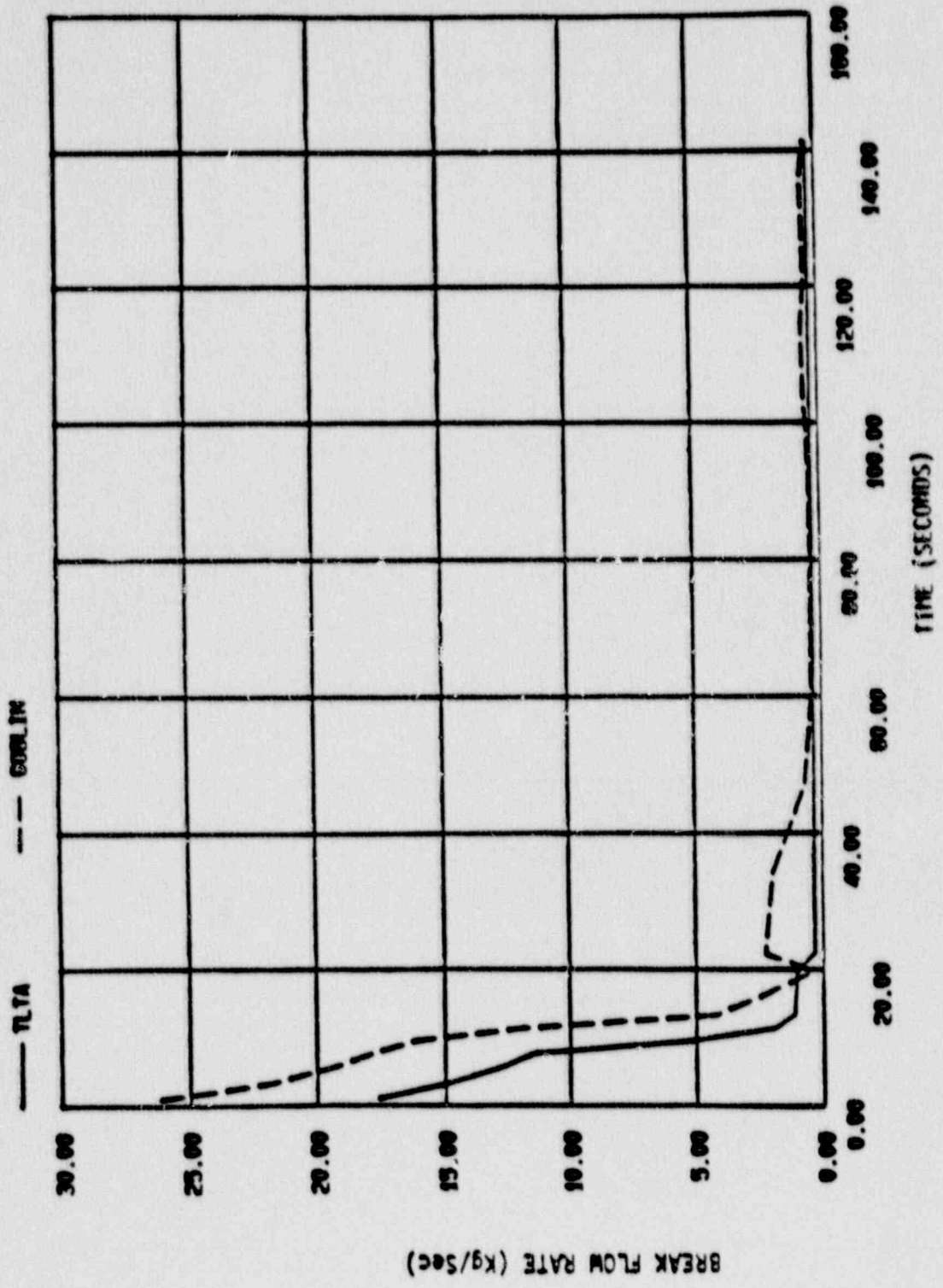


Figure 12-6 Break Flow for TLTASA Test 6425/2

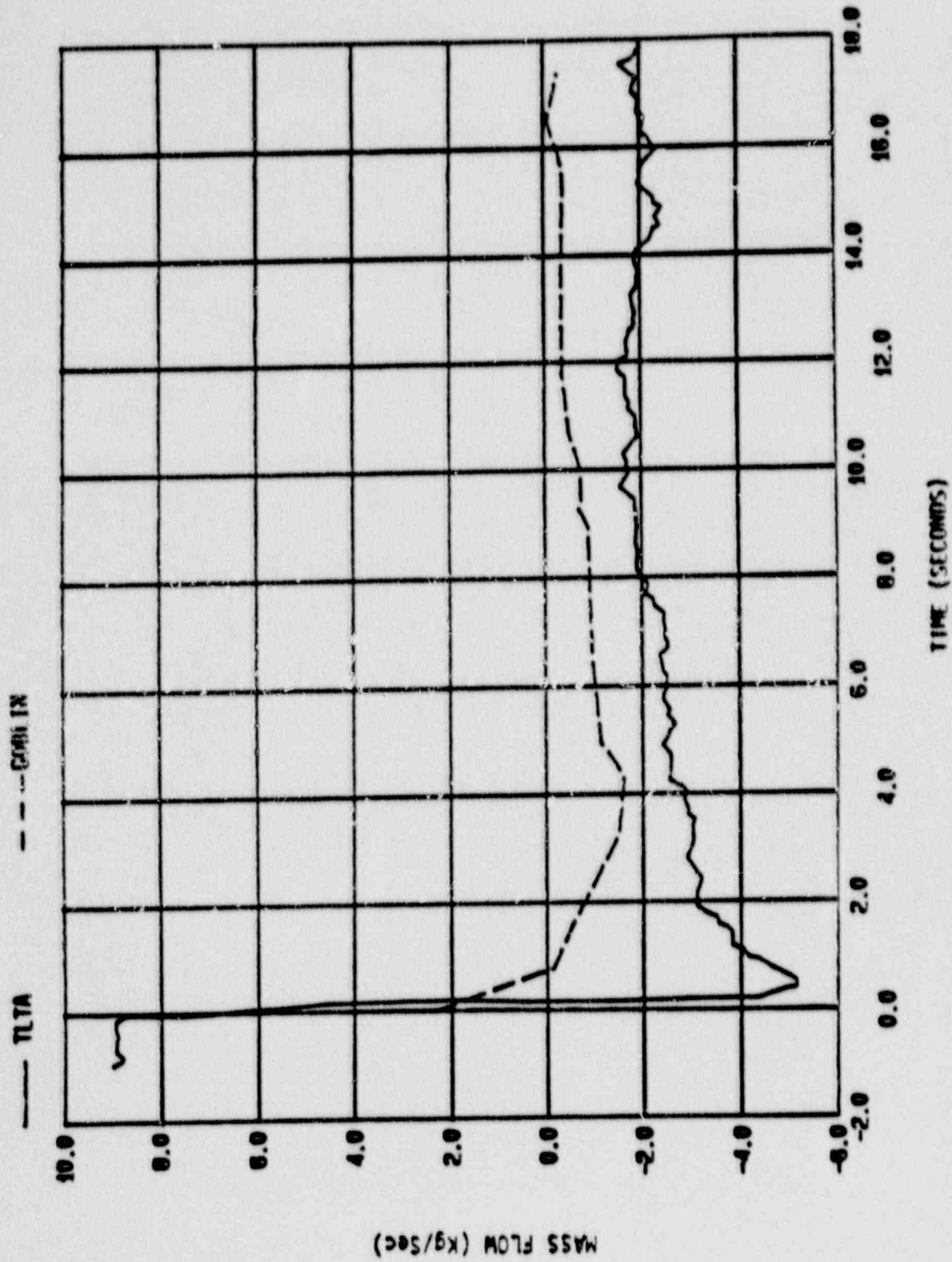


Figure 12-7 Broker Jet Pump Flow Rate for TLTASA Test 6425/2

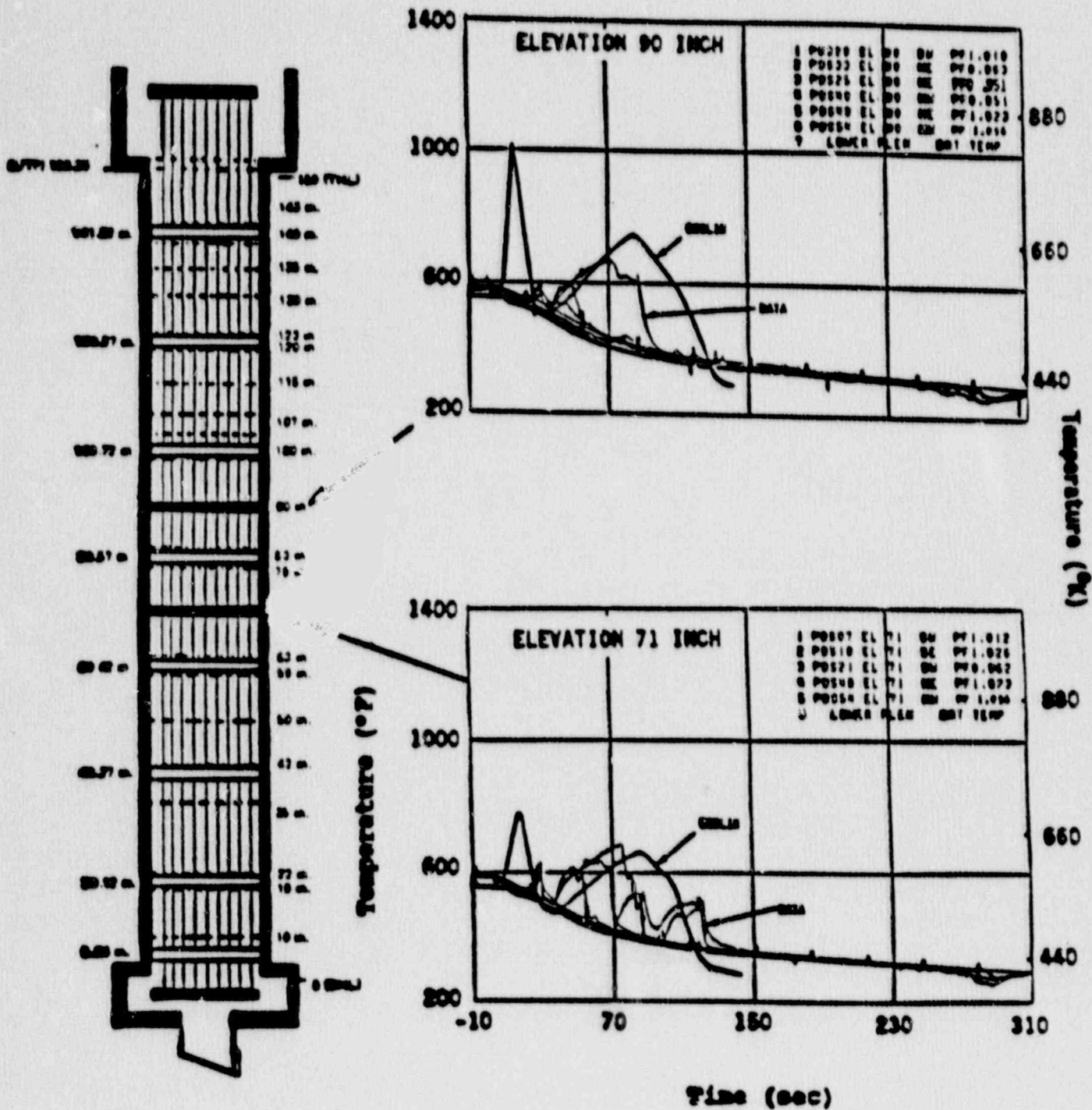


Figure 12-8 TLTA 6425/2 Rod Temperature Response

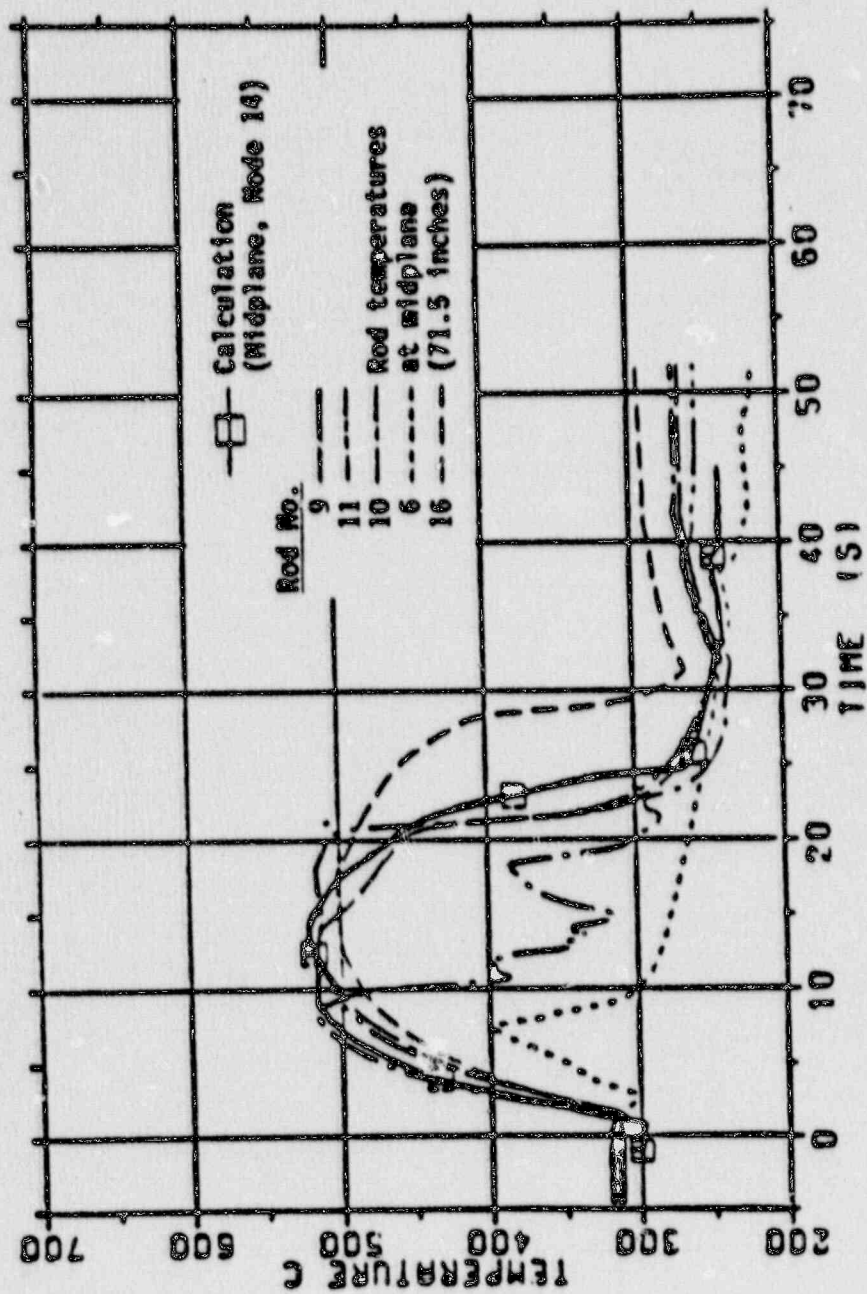


Figure 12-9 Midplane Rod Temperature for FIX-11 Test 3081,  
100% Break at 2.51 kw